Microtubule Organisation in Normal and Colon Cancer Cells

Jonathan Richard Gadsby

A thesis submitted to the University of East Anglia for the Degree of Doctor of Philosophy

School of Biological Sciences

Norwich Research Park

University of East Anglia

Norwich

NR4 7TJ

January 2014

Word Count: 82,105

© This copy of the thesis has been supplied on condition that anyone who consults it is understood to recognise that its copyright rests with the author and that use of any information derived there from must be in accordance with current UK Copyright Law. In addition, any quotation or extract must include full attribution.

Abstract

Apico-basal polarisation of epithelial cells is essential for normal function, with the rearrangement of the microtubule cytoskeleton on differentiation critical for the establishment of polarity. During this process, microtubules reorganise to form a stabilised array of apico-basal bundles via a release and capture mechanism. Disruption of this array can cause a loss of epithelial polarity, which can contribute to diseases such as cancer. Microtubule rearrangements are driven by their inherent dynamics, which are regulated by +TIP proteins. This project aims to examine the mechanisms behind apico-basal array formation, and how they may be compromised in colorectal cancer. It has focussed on two +TIPs; APC (which is mutated in most colorectal cancers), and EB2 (which has also been observed upregulated in cancer).

The role of APC at the cortex was examining using cell lines containing wild type or APC truncation mutations. Microtubule orientation at junctional sites was determined, with Nocodazole regrowth assays used to determine cortical approach. Additionally, the angle of the mitotic spindles was analysed in the different cell lines.

The impact of EB2 loss on microtubule organisation was determined by immunolabelling following siRNA treatment. A fluorescently tagged EB2 construct was created and used to rescue depleted phenotypes. The effect of EB2 depletion on microtubule stability was assessed by analysing live microtubule dynamics. The impact of EB2 overexpression on cell migration was assessed by creating a stable EB2 overexpressing cell line and live imaging sparsely seeded cells and scratch assays. Overexpressing cells were grown in 3D culture to study any effects on polarisation.

The TC7 cell line containing truncated APC possessed fewer microtubules orientated perpendicular to the cortex than wild-type expressing cells. This could be rescued with full length GFP-APC. Nocodazole regrowth showed microtubules in TC7 cells would approach the cortex perpendicularly, and then curl away. TC7 cells also had an increased proportion of misorientated spindles.

EB2 depletion caused a dramatic increase in cell size, and redeployment of EB1 and the microtubule-actin crosslinking protein ACF7 along the microtubule lattice. These effects could be rescued by transfection with mCherry-EB2. Analysis revealed EB2 depleted cells possessed less dynamic microtubules. The large depleted cells were found capable of division, although some appeared to fail during the process, with cell cycle analysis revealing suggesting the potential induction of a cell death pathway. Overexpressed EB2 could be located at the migratory leading edge, and was found to promote cell migration, with cells moving at an increased rate and wounds healing more quickly. There was also evidence of compromised tissue integrity in overexpressing cells grown in 3D culture

The results gathered identified a potential role for full length APC in stabilising cortical microtubule contacts, and helped identify EB2 as a central regulator of microtubule dynamics and organisation during polarisation. EB2 overexpression was found to increase cell migration, and may be able to induce EMT.

Table of Contents

Abstract ii

Table of Contents iii

List of Figures and Tables xi

Acknowledgements xv

Chapter I: Introduction 1

1.1: The Cytoskeleton and Cancer 2

1.2: Introduction to the Cytoskeleton 5

1.2.1: Cytoskeletal filaments 5

1.2.1.1: Actin 5

1.2.1.2: Intermediate filaments 7

1.3: Microtubules 8

1.3.1: Microtubule structure 8

1.3.2: Microtubule nucleation 10

1.3.3: Post-translational modifications 13

1.3.3.1: The tyrosination/detyrosination cycle 13

1.3.3.2: Acetylation 15

1.3.3.3: Glutamylation and glycylation 15

1.3.3.4: Other post translational modifications 16

1.3.3.5: Interactions of microtubule post translational modifications 16

1.4: The Centrosome 18

1.4.1: Structure & function 18

1.4.2: The pericentriolar matrix 18

1.4.2.1: Ninein 20

1.4.2.2: Other PCM proteins 23

1.5: Microtubule Dynamics and Microtubule Associated Proteins 25

1.5.1: Dynamic instability 25

1.5.2: Polymerases and depolymerises 25
1.5.3: Plus-end tracking proteins (+TIPs) 26
1.5.3.1: +TIP classification 27
1.5.3.1.1: The end binding proteins 28
1.5.3.1.2: Cytoskeleton-associated Gly-rich (CAP-Gly) proteins 33
1.5.3.1.3: Basic and serine rich sequence containing proteins 34
1.5.3.1.4: Other proteins 36
1.5.4: Cytoskeletal linking proteins 37
1.5.4.1: ACF7 38
1.5.5: Microtubule motors 39
1.6: Microtubule Reorganisation in Epithelial Cell Polarisation 41
1.6.1: Epithelial junctions 43
1.6.2: The polarised cytoskeleton in differentiated epithelial cells 46
1.6.3: Apico-basal array formation: the release and capture model 47
1.6.4: +TIPs in microtubule reorganisation and differentiation 50
1.7: Cell Cycle 51
1.7.1: Cell cycle control 52
1.7.2: The centrosome cycle 53
1.7.3: The cell and centrosome cycles in cancer 56
1.8: Colorectal Cancer 58
1.8.1: Colon biology 58
1.8.1.1: Crypt structure 59
1.8.2: Tumorigenesis 61
1.8.2.1: Staging and treatment of colorectal cancer 61
1.8.2.2: Molecular basis of the disease 62
1.8.3: APC 64
1.8.3.1: APC domain structure 64
1.8.3.2: The role of APC in Wnt signalling 65

1.8.3.3: In the cytoskeleton: APC a +TIP and cortical anchor 68

1.9: Cell Migration 70

1.9.1: Cytoskeletal organisation 70

1.9.2: EMT, invasion and metastasis 72

1.10: Summary 73

1.11: Aims and Objectives 75

Chapter II: Materials & Methods 77

2.1: Model Systems 78

2.1.1: Cell lines 78

2.1.1.1: Models of the epithelial cytoskeleton 78

2.1.1.2: Models of colorectal cancer 79

2.1.2: Human tissue 79

2.2: Cell Culture 80

2.2.1: Maintenance of cell lines 80

2.2.1.1: Passaging cells 81

2.2.1.2: Freezing & thawing cells 81

2.2.2: Seeding cells 82

2.2.3: 3D cell culture 83

2.3: Drug Treatments 84

2.3.1: Nocodazole regrowth 84

2.3.2: Double thymidine block 84

2.4: Cell Transfection 86

2.4.1: siRNA 86

2.4.2: Plasmid DNA 87

2.4.2.1: Creation of stable cell lines 87

2.5: Human Tissue Samples 89

2.5.1: Cryostat sectioning 89

2.6: Sample Staining 90
2.6.1: Fixatives 90
2.6.2: Immunofluorescent labelling 90
2.6.2.1: 2D culture 90
2.6.2.2: 3D culture 91
2.6.2.3: Cryostat sections 92
2.6.3: Haematoxylin and eosin (H & E staining) 93
2.7: Microscopy 96
2.7.1: Widefield 96
2.7.2: Confocal 96
2.7.3: Live Imaging 97
2.7.3.1: Microtubule dynamics analysis 97
2.8: Migration & Invasion Assays 99
2.8.1: Sparse cell tracking 99
2.8.2: Scratch assays 99
2.9: Construct Generation 100
2.9.1: Total RNA extraction 100
2.9.2: PCR 100
2.9.2.1: Primers 100
2.9.2.2: RT-PCR 101
2.9.2.3: GoTAQ PCR 102
2.9.2.4: High fidelity PCR 103
2.9.3: Agarose gel electrophoresis 103
2.9.4: Gel purification 104
2.9.5: Ethanol precipitation 104
2.9.6: Restriction digests 105
2.9.7: pGEM®-T ligation 105
2.9.8: DNA ligation 106

2.9.9: Bacterial transformation 106
2.9.10: Plasmid preparation 106
2.9.10.1: Mini-prep 107
2.9.10.2: Midi-prep 107
2.9.11: Sequencing 108
2.10: Western Blotting 109
2.10.1: Cell lysis 109
2.10.1.1: Polarisation sequence 109
2.10.2: Protein quantification 109
2.10.3: SDS-PAGE electrophoresis 110
2.10.3.1: Protein transfer 110
2.10.4: Protein detection 111
2.10.4.1: Antibody probing 111
2.10.4.2: Immunodetection 112
2.10.4.3: Re-probing 112
2.11: Cell Cycle Analysis 113
2.12: Statistical Analysis 114

Chapter III: Characterisation of Human Tissue Samples 115

3.1: Introduction 116
3.2: Results 119
3.2.1: Immunolabelling of normal frozen human colon tissue samples 119
3.2.2: Analysis of cancer patient matched pair tissue samples 119
3.3: Discussion 122
3.3.1: Cancer tissue exhibits extensive architectural change 122
3.3.2: Frozen tissue samples poorly preserve cytoskeletal architecture 123
3.3.3: Summary and future work 124

Chapter IV: APC and Microtubule Cortical Contact 132

4.1: Introduction 133

4.2: Results 137

4.2.1: Confirmation and further exploration of the TC7 cell lines as a model for the expression of truncated APC in polarised epithelial cells 137

4.2.2: Characterisation of HCT116 cells 138

4.2.3: GFP-APC expression in TC7 cells 140

4.2.4: Analysis of microtubule orientation at the cortex 141

4.2.5: Analysis of spindle orientation in TC7 and HCT116 cells 142

4.2.6: siRNA knockdown of the kinesin motor KIF17 145

4.3: Discussion 147

4.3.1: HCT116 cells are a model for expression of full length APC 147

4.3.2: Full length GFP-APC localises differentially from the APC truncation mutant in TC7 cells 148

4.3.3: APC truncations compromise microtubule cortical contacts 148

4.3.4: Truncated APC promotes abnormal spindle phenotypes 150

4.3.5: KIF17 colocalises with truncated and normal APC in colon cancer cell lines 152

Chapter V: EB2 Function in Microtubule Reorganisation & Bundle Formation 172

5.1: Introduction 173

5.2: Results 177

5.2.1: EB2 is expressed along microtubules in epithelial cell lines 177

5.2.2: EB2 is downregulated during mIMCD-3 polarisation 177

5.2.3: EB2 depletion causes distinctive phenotypic changes 178

5.2.4: Cloning of mouse EB2 179

5.2.5: Verification and characterisation of the mCherry-EB2 construct 181

5.2.6: Rescue of EB2 siRNA phenotypes 182

5.3: Discussion 184

5.3.1: EB2 is downregulated during epithelial polarisation 184

5.3.2: EB2 depletion alters microtubule organisation, results in EB1 and ACF7 recruitment, and leads to coordination with the actin cytoskeleton 184

5.3.3: mIMCD-3 cells express mouse EB2 variant 3 185

5.3.4: Mouse EB2 variant 3 was successfully cloned into pmCherry-C1 186

5.3.5: mCherry-EB2 can rescue the EB2 control phenotypes 187

5.3.6: Summary and further work 187

Chapter VI: The Role of EB2 in Microtubule Dynamics & Cell Division 202

6.1: Introduction 203

6.2: Results 206

6.2.1: EB2 depleted cells express detyrosinated tubulin in distinct microtubule bundles 206

6.2.2: EB2 depletion leads to less dynamic microtubules 206

6.2.3: Cell cycle analysis reveals a sub-G1 population on EB2 depletion 209

6.2.4: EB2 depleted cells divide but suffer increased division failures 210

6.3: Discussion 213

6.3.1: Loss of EB2 decreases microtubule dynamics 213

6.3.2: EB2 depleted cells have the ability to divide, but extended depletion causes increased cell death 213

6.3.3: Further work 216

Chapter VII: EB2 Overexpression in Polarisation & Migration 228

7.1: Introduction 229

7.2: Results 232

7.2.1: Generation of an MDCK-II EB2 overexpressing stable cell line 232

7.2.2: MDCK-mCherry-EB2 cells maintain EB2 expression during polarisation sequences 233

7.2.3: EB2 overexpression in MDCK-II 3D epithelial cultures 233

7.2.4: mCherry-EB2 localises to the leading edge of migratory cells 235

7.2.5: EB2 overexpression in MDCK-II cells causes an increase in speed of cell migration 235

7.2.6: EB2 depletion in ARPE-19 cells causes a decrease in speed of cell migration 237

7.2.7: EB2 overexpression in MDCK-II cells increases the rate of wound healing 237

7.3: Discussion 240

7.3.1: EB2 overexpressing cells are able to form apico-basal microtubules 240

7.3.2: EB2 overexpression causes increased invasion and migration 241

7.3.3: Summary and further work 243

Chapter VIII: General Discussion 265

8.1: Summary 269

8.2: APC Mediates Microtubule Cortical Interactions 270

8.2.1: Truncated APC compromises microtubule cortical capture 270

8.2.2: Truncated APC is associated with spindle misorientation 274

8.3: EB2 Plays an Important Role in Epithelial Differentiation 275

8.3.1: EB2 loss promotes microtubule stabilisation 275

8.3.2: EB2 is a central regulator of microtubule organisation in epithelial apico-basal polarisation 277

8.3.3: Regulation of EB2 expression levels in epithelial differentiation 278

8.3.4: Model for EB2 function in epithelial apico-basal array formation 280

8.4: EB2 Expression Promotes Cell Migration and Invasion 282

8.5: Future Work & Conclusions 284

Appendices 285

Appendix A: Reagents & Solutions 286

Appendix B: Construct Maps & Cloning 290

Appendix C: Supplementary Data 294

Abbreviations 304

References 308

List of Figures and Tables

Chapter I

Figure 1.1 Microtubule Structure 9

Figure 1.2 Microtubule nucleation by γ-tubulin complexes 12

Figure 1.3 Structure and organisation of a centrosome 19

Figure 1.4 Domain structure of ninein 22

Figure 1.5 Domain structures of +TIP proteins 29

Figure 1.6 Organisation of the epithelial cytoskeleton 42

Figure 1.7 The release and capture model for the formation of apico-basal microtubule arrays 49

Figure 1.8 The cell and centrosome cycle 54

Figure 1.9 Structure of the mitotic spindle 55

Figure 1.10 Structure of the large intestine and colonic crypts 60

Figure 1.11 Genetic model of colorectal cancer progression and correlation to TNM stage 63

Figure 1.12 Domain structure of APC 66

Figure 1.13 Simplified illustration of canonical Wnt signalling 67

Figure 1.14 Cytoskeletal organisation in cell migration 71

Chapter II

Table 2.1 List of cell lines, media and additives, and their origins 81

Table 2.2 List of siRNA sequences 86

Table 2.3 Details of human colon tissue samples 89

Table 2.4 Detailed list of primary antibodies 94

Table 2.5 Detailed list of secondary antibodies. 95

Table 2.6 Sequence of PCR primers for the cloning of mouse EB2. 101

Table 2.7 Details of sequencing primers. 108

Chapter III

Figure 3.1 Characterisation of control human tissue samples. 126

Figure 3.2 Characterisation of cancer patient tissue sections I: sample A (normal tissue) 127

Figure 3.3 Characterisation of cancer patient tissue sections II: sample A (tumour tissue) 128

Figure 3.4 Characterisation of cancer patient tissue sections III: sample B (normal tissue) 129

Figure 3.5 Characterisation of cancer patient tissue sections IV: sample B (tumour tissue) 130

Figure 3.6 Isolated rat crypts provide an improved model for cytoskeletal immunolabelling 131

Chapter IV

Figure 4.1 Cortical contact is an important step in the formation of apico-basal microtubule arrays 134

Figure 4.2 TC7 cell characteristics 154

Figure 4.3 Characterisation of TC7 polarisation and differentiation 155

Figure 4.4 Characterisation of HCT116 cells 157

Figure 4.5 APC western of colorectal cancer cell lines 159

Figure 4.6 Relative size of HCT116 and TC7 cells 159

Figure 4.7 GFP-APC expression in TC7 cells 160

Figure 4.8 Microtubule orientation and APC status 162

Figure 4.9 Microtubule orientation following nocodazole regrowth in TC7 cells 163

Figure 4.10 Optimisation of double thymidine block in TC7 cells 164

Figure 4.11 Analysis of spindle orientation in TC7 and HCT116 cells 165

Figure 4.12 TC7 cells exhibit three spindle morphologies 167

Figure 4.13 TC7s possess a greater proportion of the abnormal spindle morphologies than HCT116 cells 168

Figure 4.14 KIF17 localises along microtubules and colocalises with APC 169

Figure 4.15 KIF17 siRNA treatment alters ARPE-19 microtubule organisation 171

Chapter V

Figure 5.1 EB2 localisation in epithelial cell lines 190

Figure 5.2 Polarisation sequence in mIMCD-3 cells 191

Figure 5.3 EB2 is downregulated during mIMCD-3 epithelial differentiation 192

Figure 5.4 EB2 depletion in epithelial cell lines affects cell size and microtubule organisation 193

Figure 5.5 EB2 depletion causes EB1 to associate with the microtubule lattice 195

Figure 5.6 Cloning of mouse EB2 from mIMCD-3 cells 196

Figure 5.7 Verification of mCherry-EB2 protein expression 197

Figure 5.8 mcherry-EB2 characterisation in epithelial cell lines 198

Figure 5.9 Rescue of control cell size with expression of mCherry-EB2 in EB2 depleted cells 199

Figure 5.10 Rescue of EB1 comet localisation in mCherry-EB2 expressing EB2 depleted cells 200

Figure 5.11 ACF7 cytoplasmic dispersed distribution can be rescued by mCherry-EB2 expression in EB2 depleted ARPE-19 cells 201

Chapter VI

Figure 6.1 EB2 depleted ARPE-19 cells express detyrosinated tubulin in stable microtubule bundles 218

Figure 6.2 EB2 depletion alters the dynamic profiles of microtubules 219

Figure 6.3 EB2 depletion decreases microtubule dynamics 220

Figure 6.4 Dynamic profiles of selected microtubules 221

Figure 6.5 EB2 depletion causes increased microtubule pausing and reduces shrinking events 222

Figure 6.6 EB2 overexpression has no effect on microtubule dynamics 223

Figure 6.7 Cell cycle analysis of EB2 depleted ARPE-19 cells 224

Figure 6.8 EB2 depletion causes an accumulation of cells in sub G1 and reduction in G2/M phases 225

Figure 6.9 EB2 depleted cells are able to divide, but can fail to separate 226

Figure 6.10 EB2 depletion in ARPE-19 cells causes increased instances of division failure over time 227

Chapter VII

Figure 7.1 Establishment of a mCherry-EB2 expressing stable cell line 246

Figure 7.2 Polarisation sequence in MDCK-II cells stably overexpressing mCherry-EB2 247

Figure 7.3 3D culture of MDCK-II cells 248

Figure 7.4 3D culture of EB2 overexpressing MDCK-II cells 249

Figure 7.5 EB2 overexpression can cause cell protrusion and aggregation in 3D culture 250

Figure 7.6 mCherry-EB2 localises to the leading edge of epithelial cells 251

Figure 7.7 β-actin and IQGAP1 are exposed at the leading edge of migratory MDCK-II cells 252

Figure 7.8 mCherry-EB2 colocalises with IQGAP1, β-actin, and APC at the migratory leading edge 253

Figure 7.9 Single cell tracking of EB2 overexpressing MDCK cells 254

Figure 7.10 EB2 overexpression causes increased speed of random migration in subconfluent cells 257

Figure 7.11 Single cell tracking in EB2 depleted ARPE-19 cells 258

Figure 7.12 EB2 depletion causes decreased speed of random migration in subconfluent cells 259

Figure 7.13 Scratch wound assays in EB2 overexpressing cells 260

Figure 7.14 Measurement of area in scratch wound assays 261

Figure 7.15 EB2 overexpression causes increased area of closure in scratch wound assays 262

Figure 7.16 Single cell tracking during scratch wound assays 263

Figure 7.17 EB2 overexpression causes increased speed of cell migration in scratch wound assays 264

Chapter VIII

Figure 8.1 Speculative model for APC mediated microtubule cortical contact in the establishment of the extended radial array during the release and capture model 273

Figure 8.2 Model for EB2 in the release and capture mechanism and microtubule apico-basal bundle formation 281

Appendix C (Supplementary Figures & Movies)

Figure S1 pGEM®-T + EB2 carrier vector sequencing data 294

Figure S2 pmCherry-C1 + EB2 construct sequencing data 297

Figure S3 Cell Cycle Analysis Expt 2: EB2 depletion causes cells to accumulate in sub G1 300

Movie S1 Microtubule dynamics in a scramble treated ARPE-19 cell 301

Movie S2 Microtubule dynamics in an EB2 siRNA treated ARPE-19 cell 301

Movie S3 Cell division in scramble treated ARPE-19 cells 301

Movie S4 EB2 siRNA treated ARPE-19 cells are able to divide 301

Movie S5 EB2 depletion causes cell death in division 301

Movie S6 Cell tracking in subconfluent control MDCK cells 302

Movie S7 Cell tracking in subconfluent empty vector expressing MDCK cells 302

Movie S8 Cell tracking in subconfluent EB2 overexpressing MDCK cells 302

Movie S9 Cell tracking in subconfluent scramble siRNA treated ARPE-19 cells 302

Movie S10 Cell tracking in subconfluent EB2 siRNA treated ARPE-19 cells 302

Movie S11 Scratch assay and cell tracking in control MDCK cells 303

Movie S12 Scratch assay and cell tracking in empty vector expressing MDCK cells 303

Movie S13 Scratch assay and cell tracking in EB2 overexpressing MDCK cells 303

Acknowledgements

First and foremost I would like to thank my supervisors Mette Mogensen and Liz Lund for their support and guidance throughout, and for providing such an interesting project to work on. I'd like to thank all the current and former lab members; Ben, Jenny, Debbie, Chris, James and Zoe for putting up with me over the years, and providing help, advice and support throughout, as well as a fun environment to work in. Extra special thanks must go to Jenny and Debs for kicking me into shape, teaching me the ropes, and making sure I made the most out of the opportunity I had been given.

Many colleagues have provided invaluable assistance throughout, and I would particularly like to thank Paul Thomas for help with all things imaging, Andy Goldson and Darren Sexton for assistance with flow cytometry, and Penny Powell for providing reagents and extensive instruction in molecular cloning. Speaking of cloning, I'd also like to thank Uli Mayer for the tip that finally solved a particularly tricky ligation problem. Further, I'd like to thank the various people that provided instruction or use of equipment and reagents, including Louise Wakenshaw (IFR) and Rick Evans-Gowing for use and training on cryostat machines, James Sington (NNUH) for providing tissue samples and Jelena Gavrilovic and Mohammad Hajihosseini for general advice. I am also extremely grateful to BigC for supporting this project.

I'd also like to thank the many staff in the BMRC for making work such an enjoyable place to come. Extra special thanks go to Sally, Niels, and Jon, along with Cat and Rob of the 'extended' BMRC family, for their in-lab banter and after work fun. I am also extremely grateful to the various bands dotted around Norfolk (especially Amy, Jo, Mieke, and all of the other NCCB bandies,) for providing a sanity saving outlet, particularly during the rather extensive thesis writing bit.

Finally, I'd like to thank my entire family, particularly my grandparents but especially Mum and Dad. Without your endless support I wouldn't have made it to this point; thank you for being there for ranting at during the tricky times, and for pushing me to get the most out of myself at school, university and now. I hope that now it's all nearly over it you think it was all worth it, and that I've made you proud.

Chapter I

Introduction

1.1: The Cytoskeleton and Cancer

This project is focussed on the cytoskeleton in disease, and in particular the microtubule cytoskeleton and its role in the development of colorectal cancer. Cancer is a leading health issue worldwide, but especially in the developed world, where lifestyle and environmental factors promote a greater risk of developing disease. Meanwhile, improved healthcare systems mean the life expectancy of the population is increasing and so a greater number of people are likely to become affected. The approximate lifetime risk of developing a cancer of any sort is roughly one in four, with cancers of the colon or rectum being the third most common across both genders (Siegel et al., 2012).

The major difficulty with the treatment of cancers is their variety; by definition no two tumours are genetically identical and so can accumulate varying characteristics, although cancers originating within the same tissue type will often develop certain common defects. As such, there is a desire for treatment programmes to become more individualised to a tumour's particular characteristics. The more research, especially into novel areas that can be used to target the actual tumour, the more chance of developing novel treatment procedures suited to each individual case. Another important area of research is into the identification of prognostic markers. Generally, the earlier a tumour is discovered and its severity ascertained, the greater the chance of successful treatment. Therefore, findings that uncover disregulated proteins useful as a marker for disease presence and stability allow the disease to be discovered earlier and the treatments administered to be tailored more effectively to the case, even if the particular protein identified does not lend itself to being a potential drug target.

The cytoskeleton is a highly adaptable network of filaments that are vital to cell function; indeed, without it, cells lose viability. The cytoskeleton has been associated with many diseases, but is of particular interest in cancer due to the essential role it plays in cell division (which becomes uncontrolled in cancer) and in cell motility and invasion. This is particularly important, as the poorest outcomes are for patients where the tumour has escaped its original environment and undergone

metastasis to distant sites (Compton and Greene, 2004). Microtubules and their organising centres (known as centrosomes) play important parts in both of these cellular processes, as well as others implicated in tumour development. Due to the vast network of regulating and adaptor factors that mediate cytoskeletal activity, the exact mechanisms by which these processes are influenced by the cytoskeleton have not been fully elucidated. It is therefore important to develop a better understanding of the functions that the microtubule cytoskeleton plays under normal conditions, before examining the effects of disease.

Microtubules and microtubule dynamics are a long established target for anti-cancer chemotherapy; as an example, since initial clinical trials began in the 1980s, the microtubule binding drug paclitaxel (Taxol®) and its derivatives have become a commonly used treatment for breast, ovarian and lung cancers. Taxol works by stabilising the microtubule lattice and stimulating polymerisation, which causes microtubules to form bundles. Accordingly, this prevents the rapid dynamics required for successful rearrangement into the mitotic spindle, thereby blocking cell division and promoting tumour cell apoptosis, and thus impeding tumour growth. Another major group of microtubule targeting anti-cancer agents are the *Vinca* alkaloids such as vinblastine, which again inhibit microtubule dynamics and thus block cell division (Jordan et al., 1991; Jordan and Wilson, 2004; Schiff et al., 1979). An increasing number of recent investigations have identified the expression levels and distribution patterns of various important microtubule associated proteins as becoming altered in disease samples, opening a wider array of future drug targets and possible cancer markers (Bhat and Setaluri, 2007).

The colon is a particularly good model for examining microtubule reorganisation in normal epithelial cells and in colorectal cancers. This is because the cells are easy to observe in their natural environment, and have a rapid turnover rate, meaning the differentiation process that occurs as cells migrate to the surface epithelium from their origins in the stem cells zone located at the base of a colonic crypt has been well characterised (Sancho et al., 2004). Cells polarise during this differentiation, with the microtubule cytoskeleton extensively reorganising to form stable arrays that extend from apical to basal regions (Mogensen, 1999). Our lab has

historically focussed on the mechanism by which the microtubule network reorganises during this epithelial polarisation process, and is now looking to apply the models developed to disease phenotypes, especially cancers, in which the loss of apico-basal polarity and transition to a mesenchymal phenotype is an important step in the development of invasive characteristics. Of particular interest is the adenomatous polyposis coli (APC) protein, which is mutated in the majority of colorectal cancers, and is known to interact with the microtubule cytoskeleton (Nathke, 2004). Also of interest is EB2, a member of the end binding (EB) family of microtubule plus end tracking proteins (+TIPs), which has recently been shown upregulated in invasive pancreatic cancers (Abiatari et al., 2009). More generally, this project aims to investigate the mechanisms and effector proteins behind any defective microtubule rearrangements in cancer cells of the colonic epithelium.

1.2: Introduction to the Cytoskeleton

The cytoskeleton is essential for the survival of a cell. Like our own skeleton it provides structural support, whilst also allowing the cell to move and change shape, transport components along internal pathways, replicate, and generally perform its differentiated function.

1.2.1: Cytoskeletal filaments

Theories postulating an internal cytoskeleton initially arose in the 1930s, however it was the advent of the electron microscope, and later fluorescence microscopy, that allowed the fibres that make up the cytoskeleton to be visualised. We now know the cytoskeleton in eukaryotic cells is made up of three major networks of filaments; actin (microfilaments), intermediate filaments, and of main interest to this project, microtubules. Each filament is assembled into a polymer with specific properties, and associates with an array of accessory proteins, allowing them to perform their various functions (Frixione, 2000).

1.2.1.1: Actin

Actin was initially discovered as filaments coupled to myosin motors in the myofibrils responsible for mammalian muscle contraction (Frixione, 2000; Jakus and Hall, 1947), and has multiple functions in the cell, including an especially important role in the control of cell shape and motility (Alberts, 2002). It exists in the cytoplasm in its monomeric form G-actin, which is assembled head to tail into a polar alpha-helical filament approximately 5-9nm in diameter, termed F-actin. Both forms hydrolyse ATP to ADP, however the process is quicker in the polymer. The two ends of the filament are termed the barbed (plus) and pointed (minus) ends, with monomers generally being added at the fast growing barbed end bound to ATP, and departing following hydrolysis to ADP at the pointed end, in a process termed treadmilling (Dos Remedios et al., 2003). Actin filaments are further assembled into

a wide variety of distinctly organised arrays, such as lamellipodia and stress fibres, which are designed to perform differing roles within the cell. For example, the lamillipodia at the leading edge of a migrating cell contain a dense meshwork of actin filaments, which push on the membrane at the leading edge and drive the cell's forward movement. Meanwhile, at focal adhesion sites where cells are anchored to the substrate, filaments are instead organised into stress fibres; a bipolar array of F-actin coupled to myosin, which is able to contract and provide tension (Pollard and Borisy, 2003; Vinzenz et al., 2012).

The process of assembling G-actin into F-actin, and organising this further into different networks is controlled by a multitude of tightly regulated actin binding proteins (ABPs), which can act in several different ways and bind either at the end or along the side of a filament. Some proteins cap the ends of filaments to prevent either addition or loss of actin subunits (for example, at the barbed end capping protein CapZ). Others such as severing proteins and depolymerising proteins (including the ADF/cofilin family) promote filament shortening and turnover, whereas cross-linking and stabilising proteins lead to bundle and network formation. Important nucleation factors include the Arp2/3 complex and formins. Other ABPs include myosin motor proteins acting along actin filaments, and proteins linking actin to junctions and other elements of the cytoskeleton, including the microtubule network (Chhabra and Higgs, 2007; Cooper and Schafer, 2000; Dos Remedios et al., 2003).

Different ABPs are responsible for the assembly of the varying arrays, for example, the complicated actin network at the lamellipodia membrane is driven by Arp2/3 nucleation (Small et al., 2002; Vinzenz et al., 2012), whereas stress fibres are assembled by formins (Lee and Dominguez, 2010). A signalling cascade through and crosstalk between the Rho family GTPases Rho and Rac controls these processes. The Rac subfamily controls lamellipodia formation, whilst Rho promotes stress fibre induction via downstream myosin light chain phosphorylation. Rho family signalling can be induced by a number of cell surface receptors, including some adhesion proteins, such as cadherins (Burridge and Wennerberg, 2004).

1.2.1.2: Intermediate filaments

Intermediate filaments provide mechanical strength and the ability to resist external stresses. Unlike actin and microtubules, they are highly genetically diverse; in humans there are in excess of 50 intermediate filament genes, with different families expressed in different tissues. For example, epithelial cells express keratins, whilst mesenchymal fibroblasts express vimentins. Meanwhile, lamins are present in the nucleus of all cells (Alberts, 2002; Fuchs and Weber, 1994).

All intermediate filament families share a common structure, forming polymers composed of two different extended α-helical monomers that heterodimerise in parallel to form a polar coiled-coil structure. Two dimers associate in an anti-parallel fashion to form an apolar tetrameric soluble subunit. These subunits are assembled both laterally and longitudinally into protofilaments (around 2-3nm in diameter) and protofibrils (around 4-5nm in diameter). Between two and four protofibrils further intertwine into the complete intermediate filament lattice, which can thus consist of up to 32 monomers in cross-section. This large number of parallel polypeptides gives the final filament its characteristic strong rope-like properties; it is easy to bend, but very difficult to break (Alberts, 2002; Fuchs and Weber, 1994; Herrmann and Aebi, 2004).

The differences between intermediate filaments are mainly due to the diversity in head and tail regions surrounding the central α-helical domain of the protein, which allow them to associate with different factors. These factors include proteins that cross-link intermediate filaments with the other cytoskeletal filaments, and to junctional components at the plasma membrane. This variety of associated proteins tailor the arrangement of the intermediate filament network to its tissue environment. For example, the intermediate filament networks between neighbouring cells in simple epithelial sheets are linked to each other and to the basal lamina through specialist junctions, giving tensile strength across the entire epithelial sheet, and thus providing tissue integrity. Mutations in intermediate filaments and their adaptor proteins which result in the disruption of network assembly are known to cause many genetic diseases with symptoms related to a loss

of mechanical integrity, such as skin blistering (Alberts, 2002; Fuchs and Cleveland, 1998; Haines and Lane, 2012; Lane et al., 1992).

1.3: Microtubules

Microtubules have multiple functions in the cell. In particular, they play crucial roles in cell morphology by providing internal structure and support (Hawkins et al., 2010), cell motility (Vasiliev et al., 1970), organelle, vesicle and signalling trafficking where they provide tracks for transport (Cole and Lippincott-Schwartz, 1995; Gundersen and Cook, 1999), cell division as the spindle (Mitchison and Salmon, 2001), and of particular interest to this project, cell polarity (Drubin and Nelson, 1996).

1.3.1: Microtubule structure

Microtubules are polymers composed of α- and β-tubulin heterodimers, which assemble by binding head-to-tail into intrinsically polar linear protofilaments, with α-tubulin exposed at the minus end and β-tubulin at the plus end. These protofilaments further associate laterally, forming the wall of the hollow cylindrical microtubule. Microtubules walls can consist of between 10-15 protofilaments, however thirteen typically associate in parallel to form a tube approximately 25nm in diameter. The lateral interactions between protofilaments assemble into a B-type lattice, in which homologous subunits of adjacent protofilaments associate (i.e. α-α and β-β), offset at an angle to form a left handed helix that rises by three monomers for each turn. This helix is not symmetrical, resulting in a seam in the wall of the microtubule, where lateral α and β subunits interact (Figure 1.1 A). Microtubule polymerisation occurs in two phases; initial nucleation, followed by elongation. (Desai and Mitchison, 1997; Moritz and Agard, 2001).

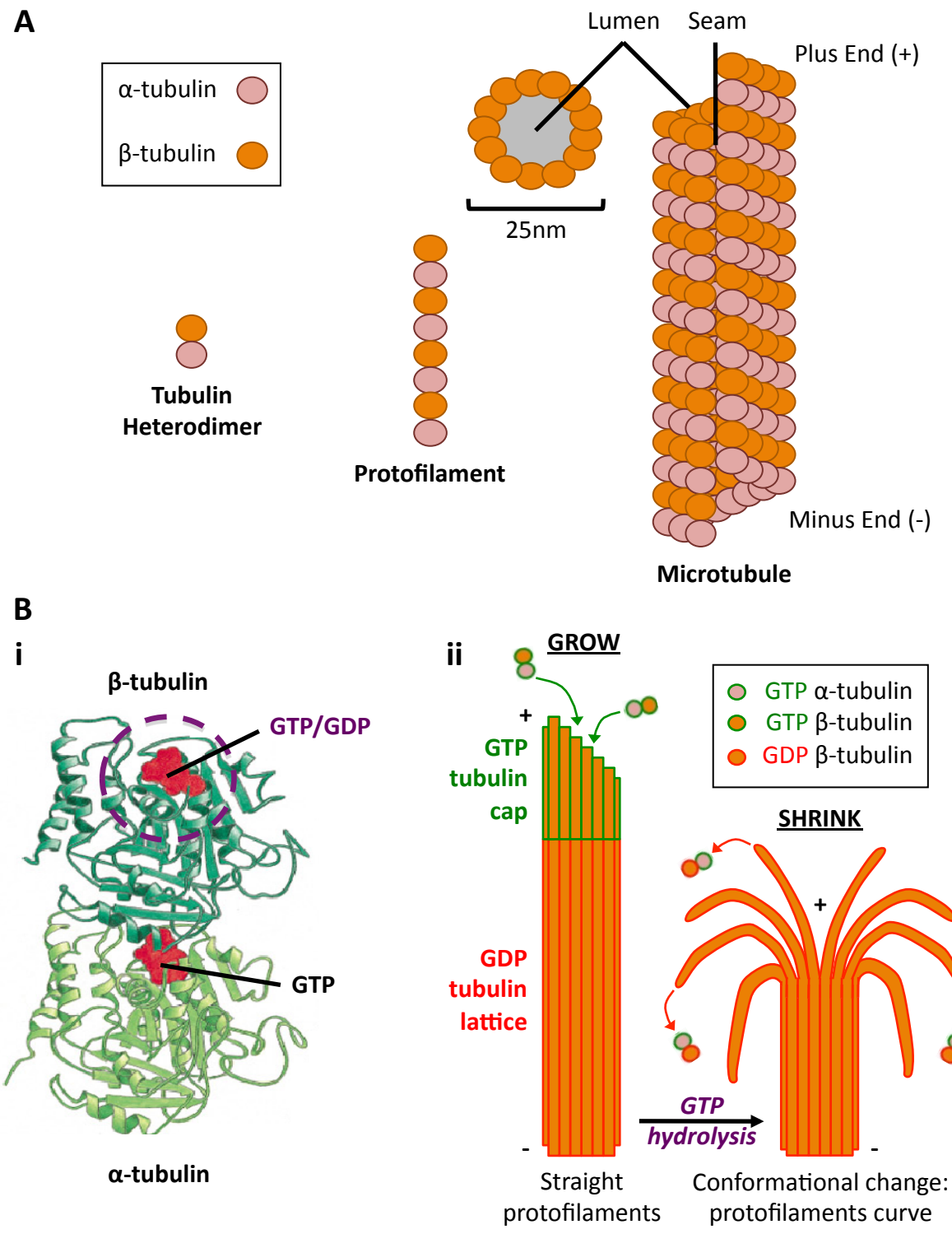

Figure 1.1 Microtubule Structure

(A) Microtubules are assembled from α and β-tubulin heterodimers, which form protofilaments. 13 protofilaments associate laterally in a non-symmetrical helix to form a hollow tube 25nm in width, which rises by 3 monomers every turn. Note the seam in the microtubule wall, and the polarity of the filament.

(B) [i] Structure of the αβ-tubulin heterodimer, highlighting GTP nucleotide binding sites. β-tubulin can hydrolyse GTP to GDP (circled). **[ii]** Growing microtubules possess a GTP tubulin cap. Protofilaments are straight and the lattice stable, allowing incorporation of GTP tubulin heterodimers at the plus end. Hydrolysis of β-tubulin in the cap causes protofilaments to curve and peel away, and the microtubule to shrink.

Adapted from (Alberts, 2002)

Elongation requires energy, and occurs by the addition of GTP-tubulin heterodimers to the end of growing microtubules. α and β-tubulin subunits are both able to bind GTP, however it can only be hydrolysed to GDP on β-tubulin. Heterodimer addition therefore occurs preferentially at the β-tubulin exposed plus end of microtubules, termed the fast growing end, with the minus end known as the slow growing end (Nogales et al., 1999). The nucleotide status of tubulin heterodimers in the microtubule lattice determines the level of curvature in the protofilament. GTP tubulin subunits incorporated in a cap at the growing end of a microtubule gives longitudinal strength to encourage straight protofilaments, thereby providing sufficient energy in the lattice to enable further subunits to be added and the microtubule to grow. The hydrolysis to GDP on β-tubulin causes a conformational change; the heterodimers and thus protofilaments curve outwards, leading to strain on lateral interactions and encouraging depolymerisation of the microtubule (Figure 1.1 B) (Nogales and Wang, 2006; Rice et al., 2008).

1.3.2: Microtubule nucleation

Although *in vitro* microtubules will undergo self-assembly at high enough tubulin concentrations, *in vivo* the heterodimer concentration is insufficient, and instead microtubule nucleation in eukaryotes is organised by microtubule organising centres (MTOCs), such as the fungal spindle pole body (SPB) or the animal centrosome. MTOCs can vary greatly in morphology; the SPB is embedded in the nuclear membrane and nucleates microtubules into both the cytoplasm and nucleus, whilst the centrosome, consisting of two centrioles surrounded by pericentriolar material (PCM), is free in the cytoplasm.

Despite their structural differences, all MTOCs share functional nucleating complexes containing another member of the tubulin family, γ-tubulin, along with several γ-tubulin complex proteins (GCPs). The basic γ-tubulin nucleating complex in animal cells is the γ-tubulin small complex (γTuSC), which comprises two γ-tubulin molecules linked to one copy of each of the highly conserved GCP2 and GCP3 (Figure

1.2 A). Several copies of the γTuSC are organised into the more potent γ-tubulin ring complex (γTuRC) linked by a cap of further accessory proteins, including GCP4, GCP5 and GCP6 (Figure 1.2 B) (Kollman et al., 2011).

Two initial models for how the γTuRC nucleates microtubules were developed (Figure 1.2 C). The 'protofilament' model suggests the ring could uncoil such that γ-tubulin subunits are organised longitudinally into a protofilament, which then nucleates α-tubulin and β-tubulin heterodimers through lateral contacts. Evidence now overwhelmingly supports the alternative 'template' model, in which the γTuRC caps the minus end of the microtubule, with the laterally organised γ-tubulin subunits nucleating longitudinal α-tubulin (Kollman et al., 2011; Wiese and Zheng, 2006). Initially there were doubts as to how the 'template' model could nucleate the thirteen-protofilament microtubule, as an even number (12 or 14) of γ-tubulins would have to be incorporated into the γTuRC in pairs through six or seven γTuSC complexes. Recent work has confirmed that thirteen γ-tubulins are present in the γTuRC, as the first and seventh γTuSC subunits overlap. This is believed to be controlled by lateral interactions between GCP proteins, in which GCPs 4, 5 and 6 are directly incorporated into the ring rather than acting as a mere scaffold for the γTuSC subunits, thus allowing the half overlap, and possibly dictating the position of the microtubule seam (Kollman et al., 2011).

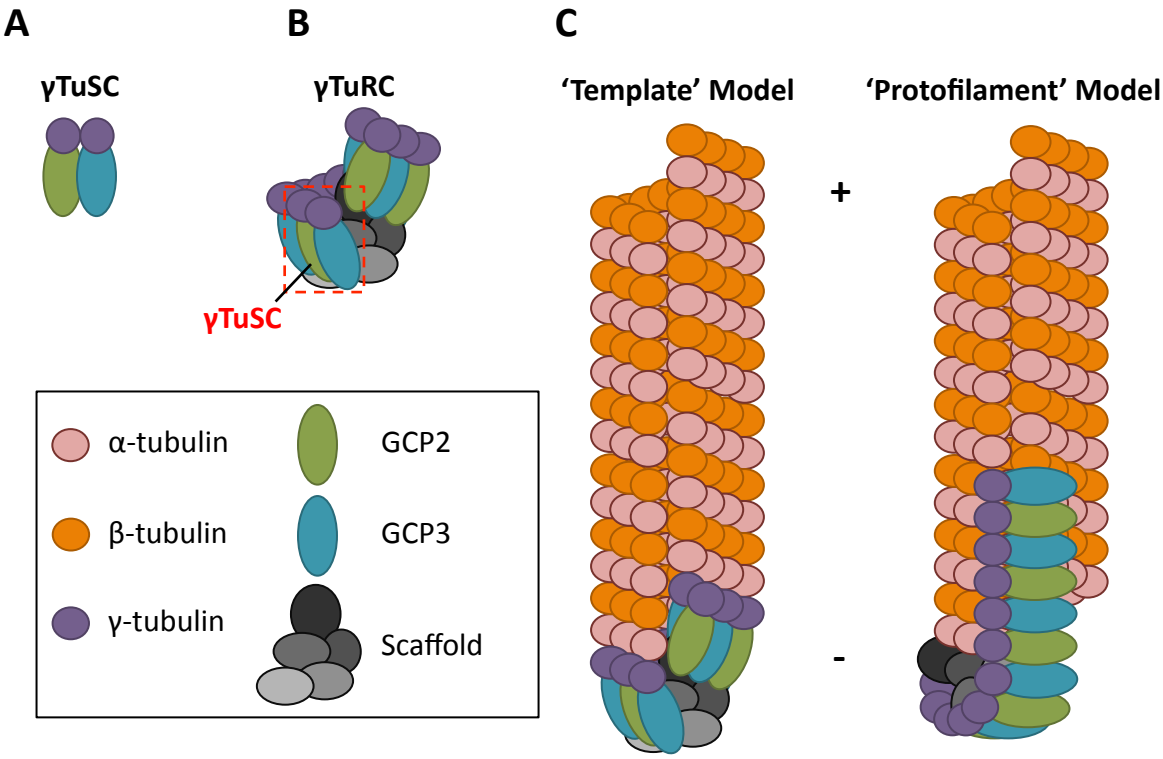

Figure 1.2 Microtubule nucleation by γ-tubulin complexes
(A) The basic arrangement of the microtubule nucleating complex is the γTuSC, which consists of two γ-tubulin molecules and one each of GCP2 and GCP3.
(B) Several copies of the γTuSC (boxed) are assembled into a ring complex including additional GCP proteins termed the γTuRC.
(C) In the presence of GTP, the γTuRC nucleates αβ-tubulin heterodimers to form the initial microtubule seed by either the 'protofilament' model, in which the ring unfurls to form a protofilament which makes lateral contact with α and β-tubulin; or by the more widely accepted 'template' model, in which a capping ring containing six and a half γTuSCs (13 γ-tubulins) incorporating GCPs 4,5 and 6 provides a template for nucleation.

Adapted from (Kollman et al., 2011)

1.3.3: Post-translational modifications

Microtubules are built from a simple αβ-tubulin heterodimer, yet have many functions within the cell. This functional diversity is controlled by the microtubule associated proteins (MAPs), which will be discussed in detail later, but include: structural proteins, molecular motors (which use microtubules as tracks for molecular trafficking), and plus end tracking proteins (+TIPs), which are important in microtubule dynamics. MAPs interact with the microtubule surface, with their functions thus influenced by the chemical variability of that surface; there are several isotypes of α and β-tubulin with variable expression patterns in different tissues, and which acquire a variety of post-translational modifications (PTMs) on the tubulin heterodimer. These PTMs generally occur on the C-terminal tail domains of α and β-tubulin which are exposed on the outer face of the polymer, and so are believed to provide a 'code' for appropriate MAP recruitment, thereby influencing the properties of the microtubule (particularly stability) and fine-tuning its function to the local environment. This allows microtubule subpopulations with distinct properties and specific roles to exist within the overall network, or indeed for a single microtubule to possess variable PTM signals along its length (Garnham and Roll-Mecak, 2012; Verhey and Gaertig, 2007).

1.3.3.1: The tyrosination/detyrosination cycle

The first modification identified was the tyrosination of α-tubulin (Arce et al., 1975; Barra et al., 1973), and in fact it was later discovered that the addition of a C-terminal tyrosine is encoded within most α-tubulin genes such that the natural form of the heterodimer is to be tyrosinated. It exists in a cycle of loss and re-addition known as the tyrosination-detyrosination cycle, with the removal of the tyrosine exposing a glutamic acid residue at the C-terminus (leading to its alternative name, Glu-tubulin). Whilst the exact carboxypeptidase enzymes responsible for detyrosination have yet to be identified (Garnham and Roll-Mecak, 2012; Janke and Bulinski, 2011), the reverse protein responsible for re-addition of tyrosine, termed tubulin-tyrosine ligase (TTL), has been well characterised; indeed it was the first

tubulin-modifying enzyme identified. TTL requires ATP for function and works exclusively to retyrosinate soluble heterodimers (Raybin and Flavin, 1977). Whilst the cycle is reversible in either direction, detyrosinated tubulin can be further permanently modified by the removal of the exposed glutamic acid residue from the C-terminus by CCP family deglutamylases to form Δ2-tubulin (Janke and Bulinski, 2011).

Tubulin exists in two distinct populations in undifferentiated cells at interphase; most are tyrosinated, however a small but distinct subset of microtubules are detyrosinated (Gundersen et al., 1984). These separate populations have been associated with microtubule stability; generally tyrosinated microtubules are dynamic, whilst detyrosination has been linked with stable long-lived microtubules (Webster et al., 1987). Whilst often used as a marker for microtubule stability, it is a matter of some debate as to whether detyrosination is a cause or consequence. Recent studies have suggested a mechanism in which the detyrosination of the lattice inhibits binding of depolymerising kinesin motors such as MCAK and KIF2A (Peris et al., 2009).

Kinesin motors (particularly kinesin 1 family members) have a preference to track along detyrosinated microtubules and this is known to be important in neuronal development where particular microtubule cargoes are required to accumulate asymmetrically. Motors targeting detyrosinated tubulin have also been shown to cross-link microtubules with vimentin intermediate filaments. Tyrosinated tubulin has roles related to its ability to recruit certain +TIPs (such as CLIP-170), which contain a CAP-Gly domain, but not those missing this region (including EB1). Mice missing TTL, (and therefore lacking tyrosinated tubulin) were unable to recruit CAP-Gly domain +TIPs, which affected their ability to mediate plus end cortical contact in astral microtubules, leading to a misorientated mitotic spindle. Due to these various roles, defective tyrosination/detyrosination has been implicated in disease, including inadequate organisation of neurones, and cancer tumorigenesis and invasion (linked to TTL reduction and decreased tubulin tyrosination) (Garnham and Roll-Mecak, 2012; Hammond et al., 2008).

1.3.3.2: Acetylation

Unlike the other modifications, the second to be discovered, acetylation, is likely to occur on the luminal face of the microtubule, at the N-terminus of α-tubulin on lysine 40 (L'Hernault and Rosenbaum, 1985). Acetylation is reversible and occurs courtesy of one of several acetyltransferase enzymes, a major example recently discovered being MEC17 (Akella et al., 2010). Two microtubule deactylases have been identified; HDAC6 (Hubbert et al., 2002) and SIRT2 (North et al., 2003), which tend to form a complex, but can function independently. The exact effects of tubulin acetylation are still not completely understood, however it is most commonly associated with stable microtubules. It has also been associated with membrane dynamics; acetylated tubulin interacts with a membrane ion pump, and provides tracks for movement of the endoplasmic reticulum (presumably via the dynein or kinesin-1 motors that can bind acetylated microtubules) (Garnham and Roll-Mecak, 2012; Janke and Bulinski, 2011). It has been suggested that deacetylation by HDAC6 located at the leading edge may play a role in cell migration, as overexpression of HDAC6 has been shown to increase cell motility (Hubbert et al., 2002), though this may be due to the enzyme acting on an alternative substrate. Recently, an additional acetylation site on lysine 252 of soluble β-tubulin has been discovered (Janke and Bulinski, 2011).

1.3.3.3: Glutamylation and glycylation

Glutamylation (Edde et al., 1990) and glycylation (Redeker et al., 1994) are poly-modifications involving the addition of glutamate or glycine chains of varying length to exposed C-terminal glutamate residues of either α or β tubulin by tubulin tyrosine ligase-like (TTLL) family enzymes (Janke et al., 2005). The TTLL family contains several enzymes, which differ in which residue they add, the specificity of their preferred tubulin target, and whether they would rather initiate a branch (by ATP dependent isopeptide bond formation) or elongate a poly-chain (by standard peptide bonding). Glutamate chains are usually between one and six (but can be as many as twenty) residues in length, whilst as many as thirty-four residues can make

up a poly-glycine chain. Removal of chains occurs by the same CCP family deglutamylases that produce Δ2-tubulin. Polymodifications are most commonly found in the axonemes of cilia and flagella, with loss of TTLLs causing defects in cilia formation and motility. Polyglutamylation is, as with the other PTMs, important for the control of transport within cilia and flagella by modulating motor activity, with different lengths of chain able to recruit different motors and therefore cargoes. This flexibility allows particularly fine-tuning of motor activity. It also promotes the activity of microtubule-severing enzymes such as spastin and katanin (Garnham and Roll-Mecak, 2012; Hammond et al., 2008).

1.3.3.4: Other post translational modifications

Microtubules can also be phosphorylated on serine and tyrosine residues by several kinases, some of which are involved in cell cycle regulation, although in general this has been poorly studied. Similarly tubulins can be palmitoylated, which adds fatty acids to the microtubule, possibly encouraging membrane contact, however little is known about the process (Verhey and Gaertig, 2007).

1.3.3.5: Interactions of microtubule post translational modifications

The complex pattern of PTMs on a microtubule increases over time, and adds great potential diversity to microtubule structure, allowing microtubules to serve a local environment; for example the microtubules orientated in the direction of a wound in cells of an epithelial sheet will be detyrosinated. Generally, the greatest quantity of PTMs are seen in the most complicated microtubule arrays, particularly those of neurones and cilia (which are acetylated and exceptionally poly-glutamylated and poly-glycylated) (Garnham and Roll-Mecak, 2012). The PTM profile is also important during division. Generally, the midbody and spindle microtubules are especially modified (detyrosinated, acetylated and polyglutymylated), in order to stabilise kinetochores and promote katanin severing

of chromatids or spastin severing in cytokinesis, whilst astral microtubules are detyrosinated and less modified (Janke and Bulinski, 2011).

The accumulation of a microtubule's PTM 'signature' must be tightly regulated, however little is known about the signalling processes behind its formation. It has been suggested that signalling through Rho GTPase family members acting through microtubule plus end tracking proteins can stimulate the formation of acetylated and detyrosinated tubulin, for example at the leading edge of migrating cells, although more work is required to confirm whether these small GTPases provide a more general mechanism by which PTM enzymes can be controlled. If incorrectly regulated, disorganised PTMs have been associated with several human diseases, including cancer (Verhey and Gaertig, 2007).

1.4: The Centrosome

1.4.1: Structure & function

The centrosome is the major MTOC in animal cells, responsible for both nucleation and anchorage of microtubule minus ends (Mogensen, 2004). It consists of a pair of centrioles surrounded by a protein matrix, the PCM. Centrioles are composed of nine sets of microtubules arranged in a radially symmetrical cylinder, and have polarity. Typically, the microtubule sets are arranged as triplets at the proximal (minus) end of the centriole and as doublets at the distal (plus) end. The two centrioles differ in terms of maturity; the older centriole (known as the mother) possesses distal and subdistal appendages, whilst the daughter centriole is younger, and has yet to develop appendages (Figure 1.3 A). In some differentiated cells centrioles act as the basal body of the primary cilium, which grows from the distal end (Bornens, 2002; Ou et al., 2004). In cell division, they separate to opposite poles of the spindle, and each become the new centrosome for one of the daughter cells (Nigg, 2006). Centrosomes can be inherited asymmetrically, for example in radial glial progenitor division in the mammalian neocortex, where one daughter cell remains a progenitor and the other migrates away to differentiate. In this process, the original mother centrosome is retained in the cell remaining in the stem cell niche, whilst the younger centrosome is inherited by the differentiating progeny (Wang et al., 2009).

1.4.2: The pericentriolar matrix

The PCM is highly dynamic and forms in a microtubule dependent manner around the centrioles, which organise its configuration. It has many different components, some of which associate intimately and specifically at the proximal and lateral regions of centrioles to form a tube, which links the centrioles with the rest of the PCM, and thus integrates centriole and PCM function (Ou et al., 2004). Key PCM proteins include ninein, γ-tubulin, centrin, PCM-1 and pericentrin, all of which can also localise to the cytoplasm (Figure 1.3 B) (Bornens, 2002).

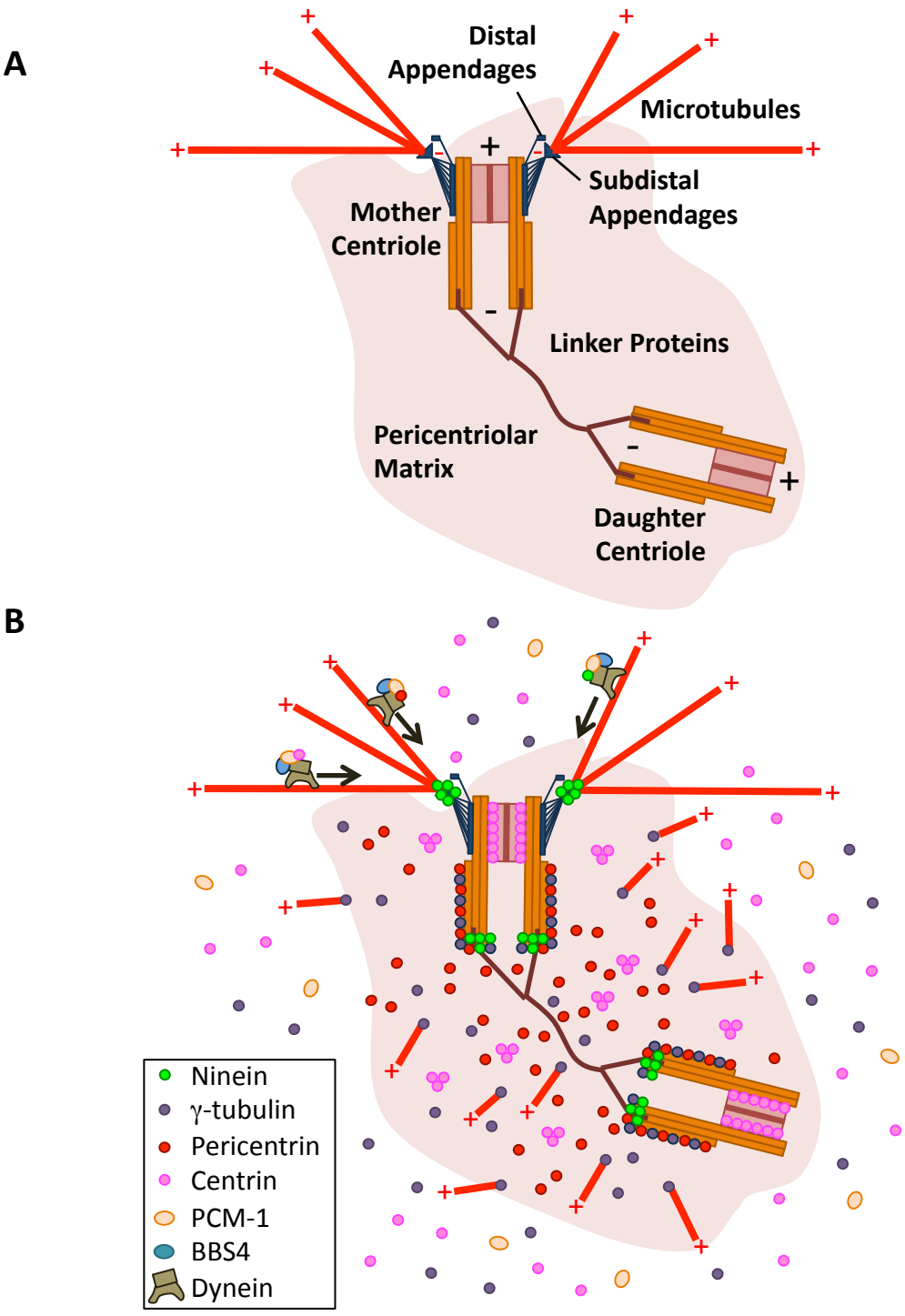

Figure 1.3 Structure and organisation of a centrosome

(A) The centrosome possesses two centrioles connected by an array of linker proteins. Only the mother centriole possesses appendages, from which a radial microtubule array is anchored. The PCM surrounds both centrioles.

(B) The PCM is composed of multiple proteins. Ninein (green) is localised to distal appendages of the mother centriole, and provides anchorage to the microtubule network. It can also be found at the proximal end of both centrioles. γ-tubulin in γTuRCs (purple) is located throughout the PCM to nucleate microtubules, and is also present in the cytoplasm. Pericentrin (red) is a structural component in the PCM, and co-ordinates with γ-tubulin to form a tube associated with the proximal and lateral regions of both centrioles. Centrin (pink) locates to the distal core structure of the centrioles, and is present as cytoplasmic speckles. The dynein/dynactin motor in complex with adaptor proteins like BBS4 (blue) transports PCM-1 (orange), ninein, pericentrin and centrin to the centrosome.

Adapted from (Bornens, 2002)

The main role of the PCM is to organise the complexes associated with microtubule nucleation and anchorage. The concept of two distinct complexes responsible for nucleation and anchorage is key to how the centrosome controls formation of different microtubule arrays. The theory was initially developed following studies in the pillar epithelial cells of the cochlea, which possess an extensive non-centrosomal array with microtubules anchored and elongating from apical sites (Mogensen et al., 1997). In these cells nucleation complexes are only present at the centrosome, leading to the initial theory that microtubules are first nucleated at the centrosome, then released and transported to dock at apical sites (Mogensen et al., 1997). This was later referred to as the release and capture mechanism (Mogensen, 1999), and will be discussed in greater detail later. These observations led to the theory that there are two major types of centrosomal PCM complexes; one for nucleation, and the other for minus end anchorage. This anchoring complex captures released microtubule minus ends and caps them, leading to stabilisation and anchorage at the centrosome. The complex itself could then be released from the PCM and transported with its captured microtubule to an alternate site. (Delgehyr et al., 2005; Mogensen, 1999; Mogensen, 2004).

γ-tubulin and pericentrin localise to the matrix, and are linked to nucleation; γ-tubulin incorporated into the γTuRC (as previously discussed) (Hannak et al., 2002), with pericentrin providing a lattice to recruit γ-tubulin complexes (Delaval and Doxsey, 2010). Ninein meanwhile is most strongly associated with anchorage (Mogensen et al., 2000), with the $p150^{GLUED}$ dynactin subunit also suggested to have a role (Quintyne et al., 1999).

1.4.2.1: Ninein

Human ninein has been mapped to chromosome 14q22 (Hong et al., 2000). It is a predominantly coiled-coil protein that is alternatively spliced to produce four known splice variants sized between 245-249kDa. The coiled-coil region extends through most of the protein, with the exception of around 50 C-terminal and 400 N-terminal residues. It also possesses EF-hand domains within the N-terminal region, a

GTP binding site, four leucine zipper domains, and multiple phosphorylation sites for cAMP/cGMP-dependant kinases, protein kinase C, casein kinase II, and tyrosine kinases (Bouckson-Castaing et al., 1996). Additionally, it is known to be phosphorylated at the C-terminus by GSK3β, at a site implicated in oligomerisation (Hong et al., 2000), and can directly bind γ-tubulin and $p150^{GLUED}$ (Delgehyr et al., 2005) (Figure 1.4).

Ninein has been identified as being responsible for anchorage at both the centrosome and at non-centrosomal sites. It accumulates at the mother centrosome, specifically at subdistal appendages, where it associates with the minus ends of microtubules; importantly, only the mother centrosome can support the radial array. Crucially, in cochlea pillar cells it is located at the apical non-centrosomal sites, specifically where the minus ends of the microtubule array are located. Unlike γ-tubulin, which remains centrosomal, ninein is released and translocates along microtubules to these apical sites, where it then stabilises the minus ends of the apical array. Thus, ninein is revealed to be crucial in the successful formation of apico-basal arrays by release and capture (Mogensen et al., 2000; Moss et al., 2007). Inhibition of ninein function prevented microtubule anchorage at the centrosome (Dammermann and Merdes, 2002), whilst ninein overexpression had no effect on the nucleation or elongation of microtubules but reduced their release from the centrosome (Abal et al., 2002), further confirming the key role of ninein in microtubule anchorage.

There is also evidence that ninein may aid nucleation, albeit indirectly. It is theorised that ninein can act at the centrosome by docking the γTuRC to the centriole; γ-tubulin can bind the N-terminus of ninein, whilst its C-terminus binds the centriole (Figure 1.4). Ninein may therefore provide a link between the two important complexes of the centrosome and thus is implicated in both nucleation and anchorage (Delgehyr et al., 2005).

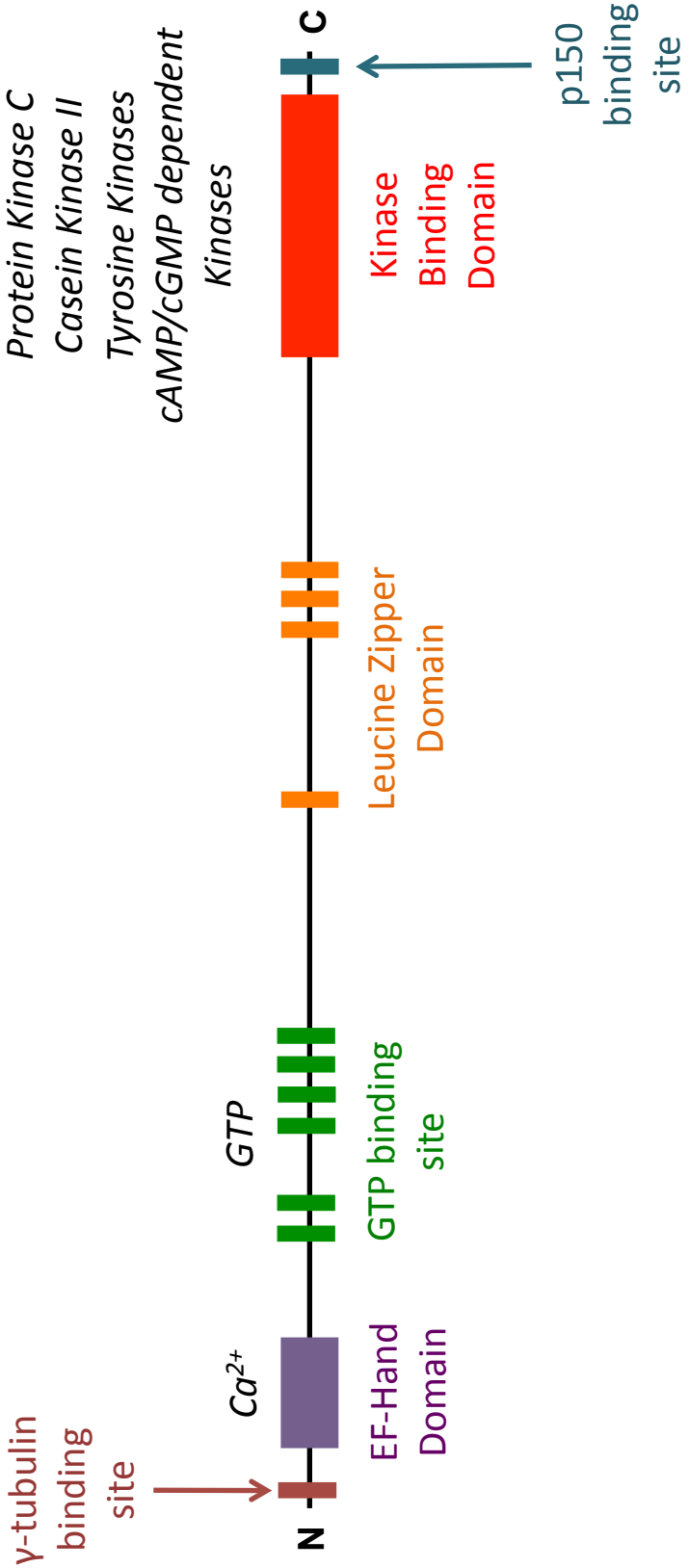

Figure 1.4 Domain structure of ninein
Ninein is predominantly coiled-coil in structure, with domains for calcium and GTP binding, a leucine zipper domain, multiple phosphorylation sites in C-terminal regions, and binding sites for γ-tubulin and the $p150^{GLUED}$ dynactin subunit.
Adapted from (Hong et al, 2000)

The ninein family consists of two proteins; ninein, and the related protein Nlp (ninein-like protein). Nlp is much smaller at 156kDa, and despite its C-terminus bearing no similarities with the ninein sequence, there is a 37% homology with the N-terminal domain of ninein (up until the beginning of the coiled-coil region). It is believed to recruit the γTuRC, and as for ninein, dock it at the centrosome. It is regulated by Plk1 phosphorylation, which removes it from the centrosome during division (Casenghi et al., 2003). Ninein is similarly removed from the spindle during division, before returning immediately after (Chen et al., 2003a). Like ninein, Nlp is targetted to the centrosome by the dynein-dynactin motor (Casenghi et al., 2005).

In addition to a role in epithelial polarisation, ninein has also been implicated in the reorganisation of the microtubule network that occurs in other cell types. An example of this is in neurones, which are highly polarised, and where nearly all microtubules are released from the centrosome. Ninein is known to be rich in the cytoplasm of these cells. It is also believed to relocate to dendrites where it acts as a microtubule anchor, thus aiding changes in cell morphology during neuronal migration (Baird et al., 2004; Ohama and Hayashi, 2009)

Ninein has been implicated in disease phenotypes, including cancer. It has been seen as a regulator of the microtubule organisation required for migration and 3D redistribution in endothelial angiogenic tip cells. Angiogenesis is the formation of new blood vessels, and is key in allowing cancers to invade and grow (Matsumoto et al., 2008). Phosphorylation of ninein by GSK3β (glycogen synthase kinase 3β) is blocked in some brain tumours (Howng et al., 2004), whilst Nlp has been suggested to be an oncogene; it is seen overexpressed in ovarian tumours, leading to an increased capacity for microtubule nucleation (Qu et al., 2008).

1.4.2.2: Other PCM proteins

There are many other PCM components with differing roles (Figure 1.3 B). The protein kinase Nek2 colocalises with the phosphatase PP1 and coiled-coil protein C-Nap1 at the proximal end of centrioles, where they are believed to be involved in

centriole assembly. CNap1 is controlled by the kinase and phosphatase to cap and protect the minus end of the centriole, and may regulate the protein tether between mother and daughter centrioles (Bornens, 2002). Nek2 may also control ninein release from the centrosome (Tyrrell, 2012).

Centrin is believed to be involved in centriole duplication and procentriole formation, as well as the establishment of cilia. It is detected in the distal part of the core centriole structure and is one of the earliest proteins detected at the site of a newly synthesising centriole. It is believed to act as a template for centriole synthesis, and moves distally as the new centriole elongates, where it then acts as the template for further development into the primary cilium (Salisbury, 2007).

PCM-1 is present in cytoplasmic granules known as 'centriolar satellites' that are transported by dynein to the centrosome. It has an important role in the assembly of the matrix, where it is involved in the transport of ninein, centrin and pericentrin to the centrosome. Depletion of PCM-1 compromised microtubule anchorage, but not nucleation (Dammermann and Merdes, 2002). BBS4 is also believed to be involved in PCM-1 function, as a potential adaptor between it and dynactin (Kim et al., 2004).

1.5: Microtubule Dynamics and Microtubule Associated Proteins

1.5.1: Dynamic instability

An essential characteristic of microtubules is their highly dynamic nature. They exhibit dynamic instability, defined as the ability to readily and rapidly switch between phases of pause, growth and shrinkage at the microtubule plus end (Mitchinson and Kirschner, 1984), allowing the microtubule to 'explore' the cytoplasm, and make contact with cellular structures such as kinetochores or the cell cortex (Galjart and Perez, 2003). This allows the microtubule network to be dramatically rearranged depending on cellular function, underpinning its adaptability, and enabling it to perform its various different roles. The switch by which a growing microtubule converts to a phase of continuous shrinkage is termed 'catastrophe', whilst a shrinking microtubule returning to a growing phase is known as 'rescue' (Howard and Hyman, 2003). Dynamic instability requires and is driven by the destabilising effect (as outlined earlier) that GTP hydrolysis of β-tubulin has on microtubule structure and stability (Hyman et al., 1992). The actual growth rate of an individual microtubule can fluctuate over time as the length of the GTP tubulin cap at the microtubule plus end varies. This fine balance requires a variety of MAPs to tightly control the flux between phases of growth and shrinkage. These can be grouped into polymerases, depolymerases, and the +TIP family of proteins (Howard and Hyman, 2009).

1.5.2: Polymerases and depolymerases

Polymerases and depolymerises act in conjunction at the microtubule plus end to help control the switch between growth and shrinkage. Kinesin-13 family proteins such as MCAK have been identified as depolymerisation factors that induce catastrophe. MCAK functions via an ATP hydrolysis dependent mechanism to bind and stabilise the depolymerisation favoured curved protofilament conformation, as described earlier, thus causing loss of GTP-tubulin heterodimers from the microtubule. Members of the kinesin-8 and kinesin-14 families have also been

shown to exhibit similar behaviours (Howard and Hyman, 2007; Hunter et al., 2003; Moores and Milligan, 2006).

The best studied polymerase is XMAP215, which catalyses a tenfold increase in the microtubule growth rate. It acts by suppressing pausing activity without affecting castastrophe rates (in contrast to some other growth promoting MAPs such as doublecortin, which act as anti-catastrophe agents). The exact mechanism by which XMAP215 functions has been debated; one popular theory was that it acted as a 'shuttle' to transport multiple heterodimers to the microtubule end. More recent work however has suggested that it acts in a processive manner in a similar fashion to how formins polymerise actin, whereby it tracks the end of the microtubule for an extended period of time, and catalyses multiple reactions by the stabilisation of a polymerisation favoured structural intermediate (Brouhard et al., 2008; Howard and Hyman, 2007; Howard and Hyman, 2009).

1.5.3: Plus-end tracking proteins (+TIPs)

The +TIPs are a diverse group of evolutionary conserved proteins defined by their ability to track the plus ends of growing microtubules. +TIP behaviour is complex, as in addition to accumulation on microtubule ends they also extensively interact with each other, as well as with signalling components and actin binding proteins, thus combining and organising a vast network at the microtubule tip. They are well known to regulate microtubule dynamics, but also have a role in cargo capture through interactions with motors, and mediate the interaction of microtubule ends with the cortex and other cellular structures (Galjart and Perez, 2003; Lansbergen and Akhmanova, 2006).

There are several mechanisms by which +TIPs track microtubule ends. The most studied is a process termed 'treadmilling,' which was described using live imaging of GFP tagged CLIP-170. In this, the +TIP molecule is transiently added at the very end of the microtubule, and dissociates shortly afterwards as the microtubule grows beyond the site of addition. It should be noted that the +TIP

itself does not move along the microtubule lattice, however to the observer, it appears as if the protein 'surfs' along the growing tip (Perez et al., 1999). The exact processes by which molecules are added and lost are not fully understood, although it is believed that some +TIPs such as CLIP-170 and $p150^{GLUED}$ may co-assemble with tubulin heterodimers, and that phosphorylation promotes their release from the microtubule. Other treadmilling +TIPs (which also include the end binding (EB) proteins) may utilise different mechanisms, such as preferential recognition for structural features or affinity for the GTP-tubulin cap (Carvalho et al., 2003; Galjart and Perez, 2003). The second method of plus end tracking is known as 'hitchhiking,' in which a +TIP interacts with the microtubule via an adaptor treadmilling +TIP. A well-studied example is the budding yeast protein Kar9p, a relative of the mammalian tumour suppressor protein adenomatous polyposis coli (APC), which depends on Bim1p (the orthologue of EB1) for recruitment to the microtubule. Finally, some +TIPs (including APC) are actively transported to microtubule ends by plus end directed kinesin family motor proteins, although this method is less common in mammals than other organisms such as budding and fission yeast (Carvalho et al., 2003; Jimbo et al., 2002).

A +TIP is not necessarily restricted to a single mechanism of plus end tracking; they can utilise several methods in combination, as demonstrated by APC (Carvalho et al., 2003), which can associate with microtubules in three distinct ways; by direct binding, by 'hitchhiking' through EB1 (Mimori-Kiyosue et al., 2000), and through directed transport via kinesin motors (Jaulin and Kreitzer, 2010; Jimbo et al., 2002). The contributions that each method of plus end targeting actually make in the case of APC is unclear, however as discussed later, it has multiple roles and is targeted to multiple locations within the cell, so the ability to interact with microtubules in several ways is likely to be important for its regulation and function.

1.5.3.1: +TIP classification

+TIPS are very diverse; they greatly range in size and structure, and yet share common binding locations and similar functions. This is because they share certain

conserved motifs and domains, which can be used to categorise them (Akhmanova and Steinmetz, 2008) (Figure 1.5).

1.5.3.1.1: The end binding proteins

The first, and most common group are the end binding (EB) proteins. In mammalian cells they comprise a highly conserved trio of proteins: EB1, EB2, and EB3. EB1 was initially discovered as an APC binding partner in a yeast two-hybrid screen, with its gene (named MAPRE 1) mapped to chromosome 20q11.2 in human cells (Su et al., 1995). Its cytoskeletal organisation was later characterised, where it was shown to associate with microtubules in both interphase and cell division independently from its interaction with APC (Morrison et al., 1998). Two further genes were later identified in humans (MAPRE 2 on chromosome 18q12.1 and MAPRE 3 on chromosome 2p23.3-p23.1) encoding EB2 (also known as RP1) and EB3 (also known as EBF3) respectively, both of which could (in contrast to EB1) be alternatively spliced to produce different transcript variants (Su and Qi, 2001).

The MAPRE genes are transcribed to produce small (32-39kDa) proteins, consisting of an N-terminal calponin homology (CH) domain linked to a coiled-coil region that extends into an end-binding homology (EBH) domain, and terminating with a C-terminal EEY/F acidic tail region. The CH domain allows the EBs to bind microtubules, whilst the EBH domain is important as the site at which they dimerise. The C-terminal acidic tail region allows various binding partners (especially other +TIPs) to interact. Some +TIPs, including APC, also utilise the coiled-coil region to bind (Figure 1.5 A) (Akhmanova and Steinmetz, 2008; Bu and Su, 2003). These interactions at the different domains have been implicated in different aspects of EB function. It has been shown that the ability of the EB proteins to dimerise via the EBH domain is essential for their plus end tracking ability (Slep and Vale, 2007). Meanwhile, in addition to being a site for protein binding, the C-terminal acidic tail has also been shown to be important for self-inhibition of EB activity (Akhmanova and Steinmetz, 2008; Hayashi et al., 2005).

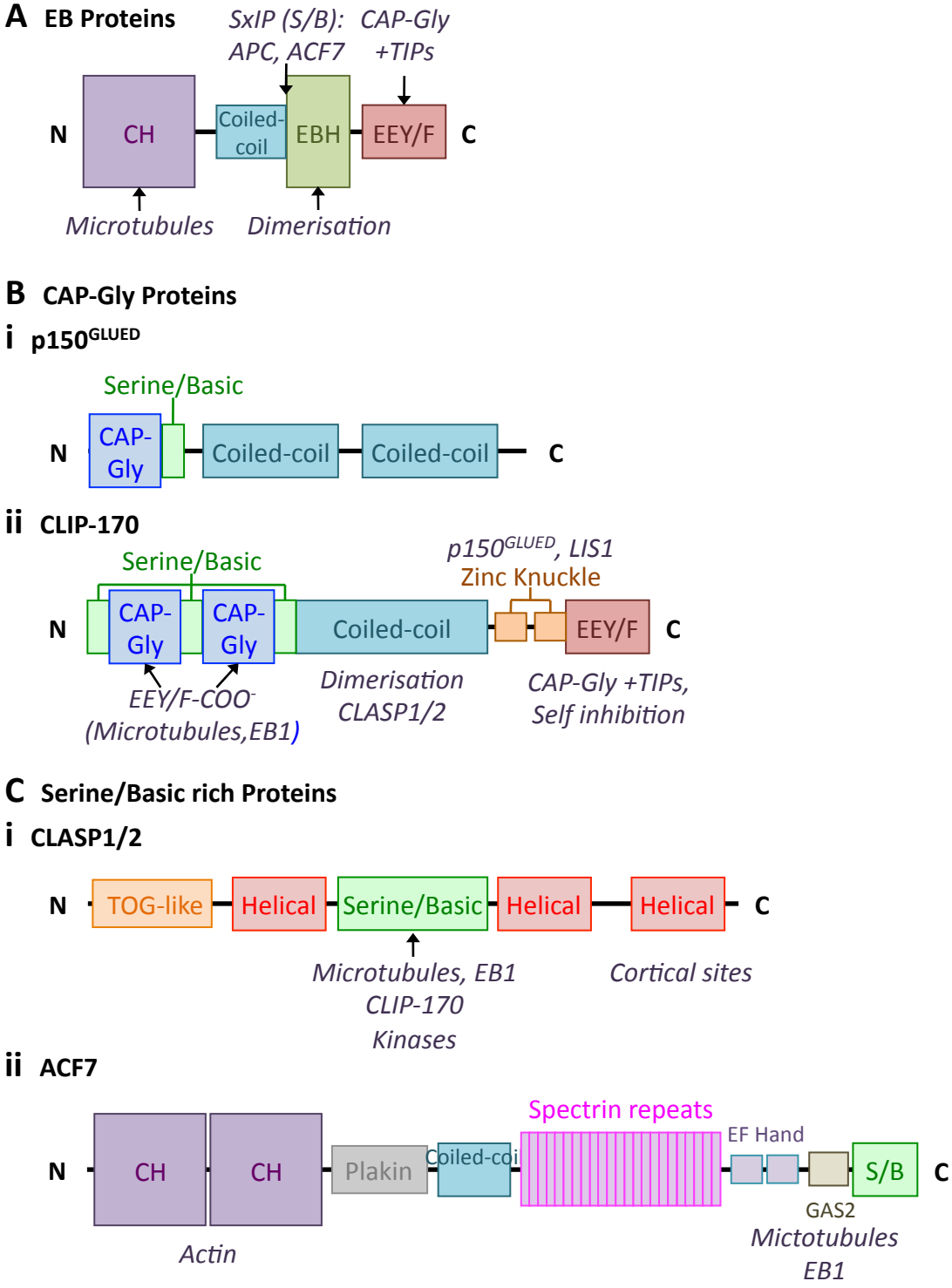

Figure 1.5 Domain structures of +TIP proteins
(A) The EBs bind microtubules through their C-terminal CH domain. They co-ordinate CAP-Gly +TIPs via the C-terminal acidic tail domain and recognise serine/basic regions throught the EBH region. They dimerise via a central coiled coil region.
(B) CAP-Gly +TIPs include p150^{GLUED} **[i]** and CLIP-170 **[ii]** and recognise the C-terminal tail of EB1 and microtubule through N-terminal domains. CLIP-170 can also bind further +TIPS through additional sites, and can self inhibit via its own C-terminal tail region.
(C) Serine/Basic rich +TIPs recognise EB1 through SxIP motifs and include CLASP1/2 **[i]** and ACF7 **[ii]**. ACF7 is a spectraplakin that cross-links actin and microtubules through N-terminal actin binding CH domains and its microtubule/EB1 binding C-terminal region.
Adapted from (Akhmanova and Steinmetz, 2008)

There have been several models proposed to explain the nature of the structure by which the growing plus ends of microtubules are recognised by the EB CH domain. Initially, there were suggestions that EBs may recognise extended sheets of tubulin at the tip, or that they may bind an A-lattice conformation similar to that found at the microtubule seam, however a more favoured model has recently been proposed in which the EBs recognise the GTP/GDP nucleotide status of the microtubule (Akhmanova and Steinmetz, 2011). Maurer and coworkers (2011, 2012) utilised microtubules incorporating GTPγS (a slowly hydrolysable analogue of GTP) to demonstrate that EBs recognise the tip of growing microtubules due to their high affinity for the particular structural conformation exhibited by the GTP-tubulin cap (or possibly by the process of GTP hydrolysis at this site). There they make contact with the corners of four tubulin heterodimers (in the B-lattice configuration; i.e. everywhere except the seam), thus bridging together two neighbouring protofilaments, increasing the strength of lateral interprotofilament contacts and stabilising the microtubule plus end (Maurer et al., 2011; Maurer et al., 2012). Interestingly, it has recently been discovered that mature microtubules retain 'islands' of GTP-tubulin within their lattice, which may serve as switch points for the rescue of a depolymerising microtubule (Cassimeris, 2009). It is likely that recognition of the exposed GTP-tubulin by EB proteins would aid in this process. Whilst the CH domain promotes microtubule binding at plus ends, the C-terminal tail also encourages the EB to bind at the very end of the microtubule as opposed to the lattice due to the repulsion between the negatively charged lattice and the acidic nature of the tail region (Buey et al., 2011). Despite the preference for the plus end, all three EB family proteins can associate along the entire microtubule lattice, as evidenced by their switch to such a distribution when they are transiently overexpressed (Bu and Su, 2001).

EB1 has been extensively studied and revealed to be exceptionally important in the regulation of the +TIP network. It has often been described as the 'master controller' of the +TIP family (Vaughan, 2005) due to its ability to bind, recruit and organise almost every other +TIP, including: CLIPs (Dixit et al., 2009; Komarova et al., 2005), CLASPs (Mimori-Kiyosue et al., 2005), APC, and spectraplakins such as the

microtubule-actin cross-linking protein ACF7 (Slep et al., 2005). Indeed, the ability of a +TIP to bind through EB1 usually determines its ability to interact with the microtubule. Thus, EB1 and the EB family play a fundamental role in the control of interactions at the microtubule plus end. They also mediate microtubule connections with internal cell structures (including the cortex, organelles and kinetochores), as well as with the actin cytoskeleton (Lansbergen and Akhmanova, 2006; Vaughan, 2005). Additionally, EB1 has been shown to be an active component of the centrosome (Louie et al., 2004), where it has been implicated in spindle formation (Rehberg and Graf, 2002), and has been suggested to have a role in a microtubule minus end anchoring complex (Yan et al., 2006). EB overexpression induces microtubule bundling, and thus EBs and other +TIPs have a role in microtubule assembly and reorganisation, an important process in differentiation and disease which will be discussed in greater detail later (Bu and Su, 2001; Jaworski et al., 2008).

The most important role of the EB family is in the regulation of microtubule dynamics, and this has been extensively studied in EB1 and its homologues at all stages of the cell cycle. It has been shown that the budding yeast homologue Bim1p promotes an increase in microtubule dynamics during the G1 phase of the cell cycle (Tirnauer et al., 1999), and that loss of the *Drosophila* homologue of EB1 leads to an increased number of microtubules stuck in a paused state during interphase, in addition to defects in spindle assembly and positioning (Rogers et al., 2002). Although the importance of the role is known, the exact mechanisms by which EB1 directly exerts this control are not fully understood. *In vitro* studies using purified tubulin and EB1 homologues have been contradictory; some have suggested that EB1 stimulates both rescue and catastrophe phases of microtubule dynamics (Bieling et al., 2007; Vitre et al., 2008), whilst another indicated catastrophe suppression (Manna et al., 2007), with others showing no effect at all. It has been suggested that this contradictory evidence may be due to the differing conditions used in each experiment (Dixit et al., 2009), or to the variety of tags (such as GFP) and purification techniques used to prepare the EB1 homologues for study, as these may significantly alter the complex binding patterns of EB family members with microtubules (Zhu et

al., 2009). It is most likely however that EB1 functions to stimulate microtubule growth by suppressing catastrophe; this has been seen *in vivo* in both *Xenopus* and the fission yeast homologue Mal3 (Busch and Brunner, 2004; Tirnauer et al., 2002). This is also supported by the structural data where the stabilising effect that EB1 has on lateral interprotofilamental contacts (as outlined above) discourages the peeling away of protofilaments that occurs in catastrophe, thus promoting microtubule growth (des Georges et al., 2008; Maurer et al., 2012; Sandblad et al., 2006). Recently, EB1 at the microtubule plus end has been shown to recruit the novel +TIP SLAIN2, which comes complexed with ch-TOG (the mammalian homologue of XMAP115), promoting processive microtubule growth (van der Vaart et al., 2011).

The majority of studies have concentrated on EB1, with the other two mammalian family members less well characterised. Komarova and coworkers (2009) recently explored how the domains of the different family members impacted on their ability to control microtubule growth. They found that the family members (particularly EB1 and EB3, but less so EB2) were required for persistent microtubule growth, and once again functioned by suppressing catastrophe rather than by directly increasing growth rate or rescue. The C-terminal acidic tail (and thus the recruitment of binding partners) was not required for this effect, however the ability to dimerise strongly was, as the presence of the EBH domain was found to be essential for function. Interestingly, EB1 and EB3 are able to heterodimerise. They also concluded that EB1 and EB3 were far more potent at suppressing catastrophe than EB2, as they were better able to compete with the other family members for access to microtubule tips. Due to this, there was a notable difference in localisation of EB2 when visualised by immunostaining; EB1 and EB3 possessed the classic +TIP firework-like distribution of comets, whereas EB2 was more associated with the microtubule lattice. This was shown to be due to crucial amino acid differences between EB2 and EB1/EB3 clustered at key CH domain residues important for plus end accumulation; replacing the first 29 amino-acids of the EB3 CH domain with the equivalent residues of EB2 dramatically reduced the ability of the EB3 to inhibit catastrophe (Komarova et al., 2009).

As mentioned, both EB2 and EB3 can be alternatively spliced. In the case of EB2, this produces three variants in mice (NCBI database; Variant 1: NM_153058, Variant 2: NM_001162941, and Variant 3: NM_001162942); the shortest variant (3) begins at a downstream start codon at the splice site, and as such is present in all three variants. It marks the start of the CH domain, and is equivalent to EB1 and EB3. The other two variants have completely separate N-terminal extensions that get added to the basic protein, one of 42 amino acids (variant 1), the other of 33 amino acids (variant 2). The purpose of these extensions has yet to be investigated, although they are not thought to affect the catastrophe inhibition behaviour of the protein, as when the extension from the human equivalent of variant 1 was added to the CH domain of EB3, it had no effect on its activity (Komarova et al., 2009).

1.5.3.1.2: Cytoskeleton-associated protein Gly-rich (CAP-Gly) proteins

This group includes the CLIP proteins (CLIP-170 and CLIP-115) and the structurally related $p150^{GLUED}$ subunit of dynactin. Their key distinguishing features are the CAP-Gly domains present in their N-terminal regions, which fold to form a hydrophobic cavity that recognises and binds microtubules and the EBs through the terminal aromatic residue of the acidic C-terminal EEY/F tail motif (EEY/F-COO^-) present in EBs and conserved in α-tubulin, and also interestingly in CLIP-170 itself. In fact the EEY/F-COO^- motif is restricted to these proteins, underlining its importance for CAP-Gly recruitment (Akhmanova and Steinmetz, 2008; Honnappa et al., 2006; Komarova et al., 2005).

Structurally, the CLIPs and $p150^{GLUED}$ are very similar containing two and one N-terminal CAP-Gly domains respectively, followed by coiled-coil regions that allow them to form parallel dimers. CLIP-115 and CLIP-170 (named as such because they 115kDa and 170kDa in size respectively) are virtually identical in the N-terminal region, however CLIP-115 lacks the C-terminal regions of CLIP-170, which contain additional features including the EEY/F-COO^- domain and two zinc knuckle motifs. The presence of an EEY/F domain means CLIP-170 can also bind the CAP-Gly domain of $p150^{GLUED}$, providing an additional method for the dynein/dynactin complex to

hitchhike to the microtubule plus end (in addition to direct binding and recruitment by EB1). In the case of CLIP-170, recruitment of $p150^{GLUED}$ depends on one of the zinc motifs, which is also targeted in a competitive manner by another +TIP, LIS1. Due to the presence of both a CAP-Gly and EEY/F at opposite ends of the protein, CLIP-170 can fold back on itself into an inactive conformation, and thus regulate itself in a dominant negative fashion (Akhmanova and Steinmetz, 2008; Lansbergen et al., 2004) (Figure 1.5 B).

CLIP-170 was the first +TIP identified, and thus the first protein observed to localise and be tracked live as comets at the end of microtubules (Perez et al., 1999). Although they directly bind microtubules, it has been shown that the plus end tracking activity of both CLIP proteins is dependent on the EBs, particularly EB1 and EB3. Simultaneous depletion of all three EBs or EB1 and EB3 together reduced the level of CLIP proteins present at the plus end by increasing their rate of dissociation from the microtubule. This effect could be rescued by transfection of an EB1 construct, but interestingly not by overexpression of EB2, again highlighting a difference in functionality between EB1/3 and EB2 (Komarova et al., 2005).

1.5.3.1.3: Basic and serine rich sequence containing proteins

A much larger and diverse group of proteins interact with microtubules via EBs through domains enriched with basic amino acids and serine and proline residues, including APC, CLIP associating proteins (CLASPs), spectraplakins like ACF7, amongst many others (additionally, both CLIPs and $p150^{GLUED}$ also have similar short regions in their N-terminal domains) (Akhmanova and Steinmetz, 2008). The small sequences involved in these interactions are known as SxIP motifs, and have also been described as a 'microtubule tip signal'. They consist of four residues (Serine/Threonine-Any-Isoleucine/Leucine-Proline), which are recognised by and bind to a hydrophobic groove formed by the EBH domain of the EBs. The hydrophobic contacts made by the isoleucine and proline residues are thought to be particularly important; mutations in them can prevent EB binding and plus end tracking. Proteins may contain several SxIP motifs to enhance their affinity for their

target. Although required for binding to EBs, SxIP motifs alone are insufficient; the regions either side of them also contribute to binding and plus end tracking behaviour and must be rich in basic amino acids, especially arginine residues, which can interact with the negatively charged C-terminal region of EBs. These interactions are particularly amenable to disruption by phosphorylation of serine residues, making them readily regulated by kinases. As the SxIP sequence is quite small, it is also quite common, and is being regularly identified in new proteins, leading to the possibility of many new +TIPs being uncovered in the future (Akhmanova and Steinmetz, 2010; Honnappa et al., 2009; Kumar and Wittmann, 2012).

+TIPs of this class are exceptionally diverse in both structure and function. A common role (exhibited for example by APC and the CLASPs) is to encase the microtubule end and act as a stabilising factor, preventing catastrophe and promoting pausing or rescue events (Akhmanova and Steinmetz, 2008). Several members have a role as a plus end adaptor linking the plus end with microtubule capture sites at locations around the cell, including the cell cortex. A good example of this behaviour is exhibited by CLASP proteins in cell migration, which stabilise microtubules orientated towards the leading edge of migratory cells. There are two mammalian CLASPS (CLASP 1 and CLASP2), which were identified through their ability to bind through the basic/serine rich regions to the coiled-coil region of CLIP proteins and co-localise with them at microtubule ends (Akhmanova et al., 2001) (Figure 1.5 Ci). They are able to localise to the cortex independent of microtubules via C-terminal regions, and their depletion led to disorganisation of the microtubule network, such that microtubules curled away from the cortex, and rather than approaching perpendicular to the cell membrane often ran parallel. It is believed the CLASPs act to mediate cortical capture by interacting with EB1 decorated growing microtubule ends; both cortical and EB binding domains were found to be required to rescue the depletion phenotype. Analysis of dynamics at the cortex suggests many microtubules are in fact still dynamic, but undergo constant and extremely rapid cycles of catastrophe and rescue (and thus appear to pause when viewed by live time lapse imaging). It was theorised by Mimori-Kiyosue and coworkers (2005) that contact with the cortical barrier causes catastrophe, and that CLASPs mediate

microtubule capture by promoting EB1 recruitment in the immediate vicinity of the cortex, and thus almost immediate microtubule rescue. CLASP depletion reduced the amount of time a microtubule stayed in close proximity (within 1μm) of the cortex. CLASP effects on dynamics are localised to the cortex; depletion had no effect on the rate of switching between growing and shrinking states in the general cytoplasm (Mimori-Kiyosue et al., 2005). Similar, but independent cortical capture mechanisms have also since been linked to both APC and ACF7 (Lansbergen and Akhmanova, 2006), as will be discussed in subsequent sections.

1.5.3.1.4: Other proteins

Many other +TIPs exist, and can be characterised according to more unique features. Often these can also be classified in one of the other +TIP or MAP classes already described; for example, the polymerase XMAP215 can also be characterised as a +TIP which binds microtubules through several N-terminal TOG domains (which are also present in CLASPs) (Slep and Vale, 2007). Various microtubule motors (both minus and plus end directed) also accumulate at plus ends so can be defined as +TIPs, often binding through domains outside their motor specific microtubule interacting regions. These include dynein and the depolymerising kinesin MCAK, which possesses basic/serine SxIP regions and can bind through EB1 (Akhmanova and Steinmetz, 2008).

LIS1, named for its causal role in the neuronal developmental disease lissencephaly acts as a +TIP via interactions with the C-terminal region of CLIP-170 through WD-40 repeats at its C-terminus, and is also thought to regulate dynein function. It is present at kinetochores and at the cortex of dividing cells, and is thought to be involved in spindle orientation. It also relocates to the leading edge of migrating cells (Akhmanova and Steinmetz, 2008; Vallee and Tsai, 2006).

1.5.4: Cytoskeletal linking proteins

It is becoming increasingly apparent that the different networks of cytoskeletal filaments do not function independently, and instead extensively co-operate with one another. They achieve this through a variety of adapter proteins, which are able to structurally bridge together, stabilise and regulate different networks, and so allow them to co-ordinate their activities (Fuchs and Karakesisoglou, 2001); for example, both CLASP proteins have been found to also interact with actin filaments (Tsvetkov et al., 2007). There are many groups of proteins which interact with two or more filaments, but for simplicity we will focus here on two: formins, and spectraplakins.

Formins are commonly associated with their role in the actin cytoskeleton as an actin assembling protein, however recent studies have shown they can also directly bind microtubules (Bartolini and Gundersen, 2010). The best-studied example is mDia, which binds microtubules via its FH2 domain, and has been shown to stabilise and bundle tyrosinated microtubules in migrating fibroblasts (Palazzo et al., 2001). This behaviour has been shown to be dependent on the +TIPs EB1 and APC, with which it formed a scaffolding complex, and was regulated by active Rho specifically restricted to the leading edge (Palazzo et al., 2004; Wen et al., 2004). Although mediated by the same site responsible for actin nucleation, the microtubule stabilisation activity of mDia was found to be independent of its roles in the actin cytoskeleton, as mutations in actin binding specific nucleotides had no effect on its microtubule activity (Bartolini et al., 2008). That said, Rho signals acting to stimulate microtubule bundling could also signal actin related activity too. There have been some indications of actin-microtubule co-alignment related to formin activity, although the evidence remains inconclusive. Formins are also believed to stabilise microtubules in neurones and cell division, and may be involved in reorientation of the centrosome in migrating cells (Bartolini and Gundersen, 2010).

Proteins of the spectraplakin family are known to cross-link actin and microtubule filaments. They are giant proteins that, as the name suggests, are members of both the spectrin and plakin superfamilies (Roper et al., 2002). Plakins

were originally identified as mediators of the interaction of intermediate filaments with junctional structures (for example, desmoplakin anchors keratins to desmosomes), and as such are important in the maintenance of tissue integrity. Another example, plectin is able to bind elements across the cytoskeleton, including intermediate filaments, actin, and microtubules, not to mention junction and structural components such as the nuclear envelope (Fuchs and Karakesisoglou, 2001; Leung et al., 2002). Spectrins meanwhile link actin with cell membranes. Spectraplakins contain structural elements from both superfamilies, and can both cross-link filaments, and link them to membrane proteins. *Drosophila* has a single spectraplakin known as *short stop*, or *shot,* whilst the analogous protein in mammalian cells is ACF7 (actin cross-linking factor 7, also known as microtubule-actin cross-linking factor 1, MACF1) (Roper et al., 2002).

1.5.4.1: ACF7

ACF7 was identified by PCR and found to have a very modular structure (Byers et al., 1995). Its size is roughly 608kDa, with the N-terminal region consisting of two CH domains responsible for actin binding, followed by the plakin domain. The central section contains a coiled-coil region followed by 23 spectrin repeats, with the microtubule binding C-terminal region consisting of two EF-hand domains, a GAS2 domain, and terminating in a Basic/Serine rich region with SxIP motifs (Akhmanova and Steinmetz, 2008; Karakesisoglou et al., 2000; Leung et al., 2002) (Figure 1.5 Cii). As such, ACF7/*shot* is able to bind EB1 and exhibits plus end tracking activity; it can decorate the length of microtubules but is enriched at the plus tip. Depletion of EB1 and CLIP-170 revealed that EB1 was essential for ACF7's +TIP behaviour, whilst CLIP-170 was not (Alves-Silva et al., 2012; Slep et al., 2005). The key role for ACF7 however, is to link microtubules with actin filaments. ACF7 was seen to align with actin particularly at sites were actin and microtubules co-localise, such as focal adhesions. Actin-microtubule bundling via ACF7 was particularly favoured adjacent to junctional sites (Karakesisoglou et al., 2000).

The cross-linking between actin and microtubules leads to microtubule stabilisation, as their growth is guided and aligned along bundles of actin. Depletion of ACF7 causes microtubules to unbundle, and the array to become disorganised and no longer orientate with actin filaments, although there is no effect on the distribution of EB1 or CLIP-170. EB1 depletion causes a similar phenotype, emphasising how ACF7 interacts with microtubules through EB1. Similar to CLASPs, ACF7 depletion also compromises cortical contact and alters microtubule dynamics; microtubules again spend more time growing rather than rapidly switching between phases of growth and catastrophe on cortical contact, and thus curl around parallel to the membrane. Depletion effects can be rescued by a shortened construct containing both actin and microtubule binding domains (Alves-Silva et al., 2012; Kodama et al., 2003). The formation of polarised microtubule bundles aligned along actin by ACF7 has been shown to be important in migration, targeting microtubules to focal adhesions (Wu et al., 2008), and may well link to the Rho regulated function of mDia on microtubule ends at similar sites as described earlier.

1.5.5: Microtubule motors

Microtubule motors utilise ATP to continuously travel along microtubules, using the intrinsic polarity of the microtubule to shuttle cargo in either direction between the centre and peripheral regions of cells with a radial array. Dynein travels towards the minus end (retrograde transport), whilst kinesin superfamily proteins (KIFs) are mainly plus end directed (anterograde transport), although some are minus end directed.

Since the discovery of the first kinesin (Vale et al., 1985), the number of KIFs has expanded to literally hundreds of members, which have been grouped into 14 kinesin families (Lawrence et al., 2004). Kinesins are complexes of two identical heavy and two light chains, which generally form a conserved globular catalytic core (the ‘head’) that hydrolyses ATP and drives stepping movements. This is linked through a short ‘neck’ (often important for family specific regulation or direction properties) to the ‘stalk’ responsible for dimerization and the ‘tail’ domains. These

include the light chains, are highly divergent, and are responsible for the specific function of the motor, such as recognition of its cargo. Generally 'head' domains are at the N-terminus of each heavy chain, driving motility in the plus-end direction, but this is occasionally reversed, with the catalytic region located at the C-terminus, and the motor driven towards the minus end. During movement, the head domains of each heavy chain are coupled, making alternate stepping movements to pull the motor and its cargo along the microtubule (Gennerich and Vale, 2009; Miki et al., 2005). KIFs of interest include the depolymerising kinesin-13 member MCAK, and members of the kinesin-2 family, including KIF3A, KIF3B/C and KIF17. The KIF3s are thought to act through the adaptor protein KAP3, which can bind APC for transport to microtubule plus ends (Jaulin and Kreitzer, 2010; Jimbo et al., 2002; Miki et al., 2005).

The exact mechanism by which dynein functions is not as well understood, although it is believed to process in small walking steps split alternating between the two identical heavy chains. The processive motor domain is again driven by ATP hydrolysis, with each heavy chain arranged into a ring of six AAA (ATPase associated) domains, linked via a coiled-coil stalk between the fourth and fifth AAA domain to a microtubule-binding site, with another link to a dimerisation domain. Only the first four AAA domains bind ATP, with just the first itself required for movement; the other three regulate function. Several additional chains also associated in the tail region, including the intermediate chains (Gennerich and Vale, 2009), which serve to recruit the dynactin adaptor complex via its pair of $p150^{GLUED}$ subunits, which are essential for function (Vaughan and Vallee, 1995). The dynactin complex is required for almost all dynein functions, and consists of 11 subunits. It links dynein to its cargo, targets it within the cell, and increases its rate of process along the microtubule (Kardon and Vale, 2009). Importantly, dynein has been shown to complex with β-catenin and E-Cadherin at adherens junctional sites in epithelial cells, where it is involved in the capture and tethering of microtubules at cortical sites. This is dependant on an intact cortical actin network (Ligon et al., 2001). Other dynein adaptors include the +TIP LIS1 and Bicaudel D, which is involved in the transport of mRNA and Golgi vesicles (Kardon and Vale, 2009).

1.6: Microtubule Reorganisation in Epithelial Cell Polarisation

In undifferentiated animal cells, microtubules typically exist in a radial network extending from a centrally located centrosome (Figure 1.6 A), where their minus ends are anchored and stabilised by ninein. On differentiation, many cell types lose their radial microtubule network, and reorganise into an array ideally suited for their specialised function. In the case of pillar cells of the cochlea and simple columnar epithelial cells such as those lining the intestine and kidney tubules, cells polarise along the apico-basal axis, with microtubules forming a non-centrosomal microtubule array (Figure 1.6 B) anchored by ninein at apical cortical sites (Bellett et al., 2009; Mogensen et al., 2000).

Polarisation is defined as "the asymmetric organisation of cell components," and allows different domains of the plasma membrane to have specialised functionality. It widely occurs throughout nature, and is important in both differentiation and cell migration, as well as for many other processes. The core mechanisms in establishing polarity are well conserved, and the cytoskeleton plays an important role, translating cues marked at the cell surface inside the cell to re-organise the molecular machinery according to the spatial signal, and then controlling the resultant change in cell shape (Drubin and Nelson, 1996).

Epithelial cells are arranged in sheets lining the outer layer of many tissues, and as such provide a protective barrier against external factors. These sheets are semi-permeable, allowing the transport of certain solutes into the organism, as required. The establishment of epithelial cell polarity is essential in maintaining barrier integrity and the creation of a trafficking gradient between the top and bottom of the cells. The cue for epithelial polarisation in mammalian cells is the establishment of junctional complexes with neighbouring cells, which effectively splits the plasma membrane into two separate compartments; an apical domain facing the outside environment and baso-lateral domains in contact with the basement matrix and neighbouring cells respectively (Drubin and Nelson, 1996; Gibson and Perrimon, 2003).

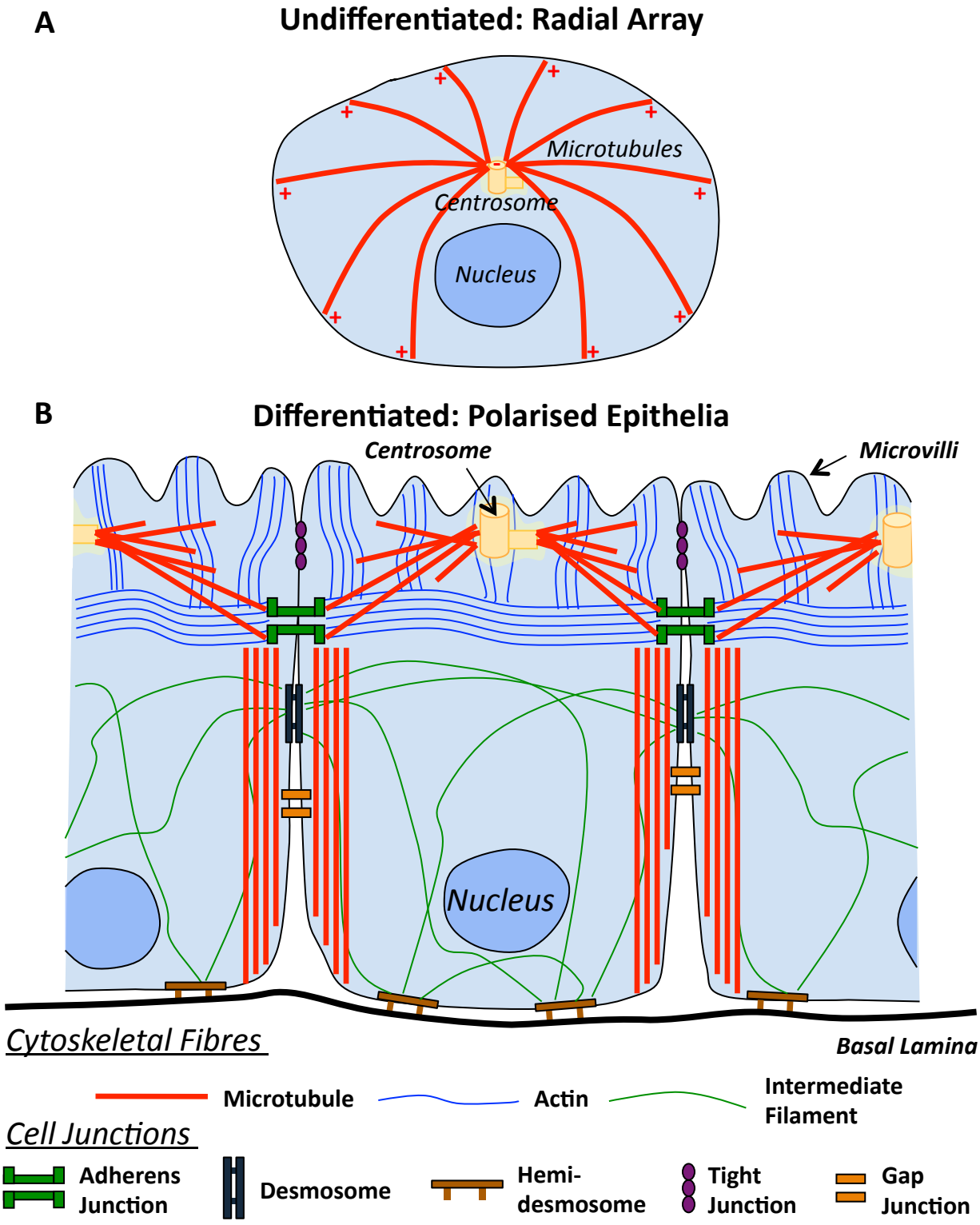

Figure 1.6 Organisation of the epithelial cytoskeleton
(A) Undifferentiated epithelial cells exhibit a radial microtubule array anchored at a centrally located centrosome with plus ends extending out to the cell periphery.
(B) On differentiation, epithelial cells polarise. Tight and adherens junctions form in apical regions, providing a semi-permeable barrier. The centrosome relocates to the top of the cell as the apical membrane forms microvilli. Actin filaments are organised in a continuous apical belt anchored at adherens junctions and extend into microvilli. Microtubules exist in a non-centrosomal apico-basal array anchored at junctional sites. Desmosomes link intermediate filaments between cells, with hemidesmosomes connecting them to the basal lamina. Gap junctions allow molecules to pass through channels between neighbouring cells.
Adapted from (Giepmans and van Ijzendoorn, 2009) and (Alberts, 2002)

1.6.1: Epithelial junctions

Junctions occur where contacts are made between cells, or between cells and the extracellular matrix. There are three main groups of junction: occluding, communicating and anchoring (Alberts, 2002).

Occluding junctions in vertebrates are known as tight junctions. They are located in a continuous belt at the very apical surface of epithelial cells, as a branching network of proteins that forms a tight semi-permeable seal between neighbouring cells of the epithelial sheet, preventing unwanted transport across the epithelial barrier between cells (Figure 1.6 B). They are primarily composed of integral membrane occludin and junction adhesion molecules (JAMs), which are linked to transmembrane claudins. On the cytoplasmic face, zonula occludens (ZO-1, ZO-2 and ZO-3) connect the junctions to the actin cytoskeleton through alpha-actinin (Giepmans and van Ijzendoorn, 2009; Schneeberger and Lynch, 2004). Importantly, the tight junctions define the apical and baso-lateral domains in epithelial polarisation, by preventing mixing of membrane proteins between the different regions (Gibson and Perrimon, 2003).

Communicating junctions allow small molecules to pass between cells, and include synapses and gap junctions. Epithelial gap junctions are small channels that allow small molecules no greater than 1kDa in size to diffuse between neighbouring cells, and have a role in, for example, electrical transduction, cell signalling and nutrition in the gut (figure 1.6 B). They are composed of connexin family integral membrane proteins, and can be opened and closed under tight levels of regulation. Various proteins interact at the cytoplasmic face of gap junctions, including signalling components and microtubules (Giepmans and van Ijzendoorn, 2009; Giepmans et al., 2001).

Anchoring junctions connect the cytoskeleton of a cell to that of a neighbour, or to the extracellular matrix (ECM). They are therefore especially important in epithelial sheet formation, and cell migration. There are two main forms of anchoring junctions; cadherin family transmembrane adhesion proteins make connections between cells in adherens junctions and desmosomes, whilst integrin

family proteins link cells with the ECM through focal adhesions and hemidesmosomes (Alberts, 2002).

Adherens junctions link the actin cytoskeleton of adjacent cells. In epithelial sheets, they cluster to form an encircling continuous belt termed the zonula adherens in the apical region of cells, just below the tight junctions (Figure 1.6 B). These belts line up in each cell of the sheet, linking contractile bundles together and allowing activity of myosin motors to contract the sheet. The transmembrane links are provided by E-Cadherin (amongst other proteins), which has two domains to bind separate catenins (β-catenin and p120) in a calcium dependent manner on the cytoplasmic face. These in turn act through a third catenin, α-catenin, to influence actin remodelling in the region of the junction. The catenins bind and regulate a variety of additional proteins (Hartsock and Nelson, 2008), including components of signalling pathways such as the Rho-family GTPases, which have been implicated in cytoskeletal regulation (Perez-Moreno et al., 2003; Wheelock and Johnson, 2003). β-catenin has an additional role as a signalling molecule in the Wnt signalling pathway, and can be mutated in colorectal cancer. It is believed its location at these different cellular compartments is regulated by phosphorylation (Nelson and Nusse, 2004).

Microtubules have also been linked to adherens junctions. It has been shown that p120 linked to vesicles containing cadherin-catenin complexes recruits kinesin motors for trafficking to the cell membrane and junctional complexes (Chen et al., 2003b). Adherens junctions also interact with microtubule plus ends, and can act as sites for minus ends anchorage (Stehbens et al., 2009); it has been shown that complexes associated with cadherins at cell-cell junctions can stabilise the minus ends of non-centrosomal microtubules and affect microtubule organisation (Chausovsky et al., 2000). Plus end interactions with adherens junctions have been shown to be an important method of microtubule anchorage. Dynein colocalises with β-catenin and E-cadherin at junctional sites, where it captures and tethers microtubule ends and links the microtubule cytoskeleton with actin in peripheral regions (Ligon et al., 2001). This process does not require dynactin, and is essential for efficient junction formation via the kinesin-mediated delivery of junctional components. Many other +TIPs have also been associated with cortical regions,

including APC and ACF-7, and may be involved with initial microtubule docking at the membrane, before dynein tethers them to junctions (Ligon and Holzbaur, 2007; Perez-Moreno et al., 2003).

Desmosomes link the intermediate filaments of cells in the entire epithelial sheet together to withstand mechanical stress; the desmosome-intermediate filament complex exhibits a unique property termed 'hyper-adhesion,' making it particularly strong (Figure 1.6 B). This helps protect against the shearing forces exerted on an epithelial sheet, and so desmosomes are particularly highly expressed in tissues that undergo a lot of stress, such as the epidermis and heart muscle. Hyper-adhesion can be modulated in circumstances where flexibility is required, such as in wound healing. Unlike adherens and tight junctions, they are not strictly located to an apical band, and instead are interspersed with gap junctions in lateral regions. The intermediate filaments are connected to the transmembrane desmosomal cadherins, which interact in the intracellular space through adaptor proteins including desmoplakin and plakoglobin (Garrod and Chidgey, 2008; Green and Jones, 1996). Desmoplakin has also been found to recruit ninein to desmosomes in epidermal stratified squamous epithelial cells, and so may be involved in microtubule rearrangement in the skin (Lechler and Fuchs, 2007).

Hemidesmosomes act through transmembrane integrins (specifically, a heterodimer of α6-β4 integrin) to link the extracellular matrix protein laminin-5 of the basal lamina in an epithelial sheet to intermediate filaments, via an anchoring cytoplasmic plaque that structurally resembles the desmosome plaque and contains adaptor proteins such as plectin (Figure 1.6 B). This strengthens the epithelial sheet, preventing shearing stresses from lifting the epithelium from the underlying tissue (Green and Jones, 1996; Jones et al., 1998).

1.6.2: The polarised cytoskeleton in differentiated epithelial cells

Polarisation mechanisms are well conserved between organisms such as flies and vertebrates, and are driven by polarity proteins. In both groups the initial establishment of junctional complexes between neighbouring cells serves as the cue for apico-basal polarisation (Gibson and Perrimon, 2003). Establishment of adherens junctions in mammalian epithelial cells triggers the formation of a complex consisting of PAR-3, PAR-6 and aPKC, which is responsible for the formation of tight junctions at the apical surface, and thus establishes the separate baso-lateral and apical membrane domains (Joberty et al., 2000). The apical membrane often folds into numerous protrusions termed microvilli, which increase the surface area of the apical surface. Rearrangements of the cytoskeleton transfer this polarisation signal to the rest of the cell. Actin becomes arranged in a distinct apical acto-myosin ring, with extensions into the microvilli crosslinked by villin and fimbrin proteins. It is also present along baso-lateral membranes (Yeaman et al., 1999) (Figure 1.6 B).

Polarisation is driven by rearrangements of the microtubule cytoskeleton believed to be controlled by mammalian PAR-1 (Cohen et al., 2004). The centrosome migrates to the apical cell surface (where it may extend and act as the basal body of a primary cilium) (Rizzolo and Joshi, 1993). The radial microtubule array is reorganised into a primarily non-centrosomal array consisting of microtubule bundles orientated apico-basally, in which the minus ends are located and anchored at apical junctional sites close to the plasma membrane, and the plus ends extend down to the base of the cell. An extended radial microtubule network associated with the centrosome remains in the apical region (Bacallao et al., 1989), along with a disorganised web in basal regions (Figure 1.6 B). As such, the rearranged microtubules are organised perfectly to transport cargo such as Golgi vesicles longitudinally along the cell towards either the apex or base. Accordingly, following establishment of the microtubule array, secretory machinery including the Golgi apparatus is relocalised towards apical regions, below the centrosome (Musch, 2004; Yeaman et al., 1999).

Microtubules organised in apico-basal arrays show an increase in stability (Pepperkok et al., 1990), and as may be expected accumulate PTMs, including detyrosination, which are more resistant to drug induced depolymerisation. It is doubtful the modification is a cause of stability, and is instead believed to be an effect of increased microtubule longevity, although this is open to debate (Bre et al., 1987). A recent study by Quinones and coworkers (2011) has suggested acetylated microtubules become more prominent and detyrosination reduces on polarisation. They theorised that different microtubule motors may prefer different microtubule PTM decoration (Quinones et al., 2011), although more work is required to confirm the findings and theory.

1.6.3: Apico-basal array formation: the release & capture model

The mechanism by which epithelial apico-basal arrays form is not fully understood, however our lab has generated a model following many years of study. As discussed earlier initial investigations in the outer pillar cells of the organ of Corti, which have extensive apico-basal arrays consisting of a great number of microtubules (Henderson et al., 1994), revealed that γ-tubulin and pericentrin remained localised at the centrosome rather than relocating to the apical sites where microtubule minus ends were located. These observations gave rise to the initial release and capture model for the formation of apico-basal microtubule arrays in polarised epithelial cells (Mogensen, 2004; Mogensen et al., 1997). The model has subsequently been modified and expanded with new discoveries over several years (Bellett et al., 2009; Mogensen, 1999; Mogensen et al., 1997; Mogensen et al., 2000; Mogensen et al., 2002; Moss et al., 2007).

The central protein in the model is the anchoring protein ninein. As previously mentioned, it has been found at the apical sites where microtubule minus ends are anchored (Mogensen et al., 2000). Importantly, it has been seen to travel along microtubules as speckles towards these sites, where it co-localised with the adherens junction component β-catenin (Moss et al., 2007). Microtubule regrowth

assays revealed that nucleation occurs at the centrosome and not apical sites, and that an initial extended apical array arises from the centrosome, with the plus ends (marked by EB1 or CLIP-170) targeting adherens junctions. As already discussed, the +TIPs promote microtubules extension, and allow interaction with dynein recruited to adherens junctions at the cortex (Bellett et al., 2009). As such, in the model, the first step involves the nucleation of microtubules at the centrosome, followed by extension towards the cortex as +TIPs associate with growing plus ends. The intermediate step in the process is the formation of an extended radial array, with the +TIPs targeting dynein at junctional sites. This allows centrosomal proteins; specifically ninein, to be transported by microtubule plus end directed motors to these apical sites. The dynein motor exerts force on the microtubule plus end providing sufficient tension for the microtubule to be released from its centrosomal anchor. There has been speculation as to the nature of what controls minus end release, with the leading candidate currently being phosphorylation by the kinase Nek2. Following release, dynein translocates the microtubule downwards towards the basal regions of the cell, until the minus end is captured by the relocated ninein at the apical site, and the plus end reaches the bottom of the cell. The apico-basal microtubules are then stabilised into bundles, completing array formation (Bellett et al., 2009) (Figure 1.7). APC is located along lateral sites and near the basal membrane where the microtubule plus ends terminate, and may help to stabilise the array as it forms (Mogensen et al., 2002). It may also be involved with cortical capture by dynein at junctional sites.

An alternative model for apico-basal array formation has been proposed, suggesting that intermediate filaments are able to anchor non-centrosomal γ-TuRC via GCP6 interactions with keratins in apical regions, which would allow nucleation and subsequent extension of microtubules into basal regions (Oriolo et al., 2007). It should be noted that the two models are not necessarily mutually exclusive, with the potential for either to occur to a greater or lesser extent in different cell types.

Figure 1.7 The release and capture model for the formation of apico-basal microtubule arrays
[1] Microtubules are nucleated at the centrosome. **[2]** They elongate towards the cortex, with +TIPS accumulating at plus ends. **[3]** An extended radial array forms, with plus ends captured by dynein at adherens junctions. **[4]** Ninein is transported along microtubules to apical adherens junction associated sites. **[5]** Dynein motors release the microtubules from the centrosome and translocates them towards basal regions. **[6]** Microtubule minus ends are captured and anchored by ninein at adherens junction associated sites. Plus ends elongate towards the cell base.

Adapted from (Bellett et al., 2009)

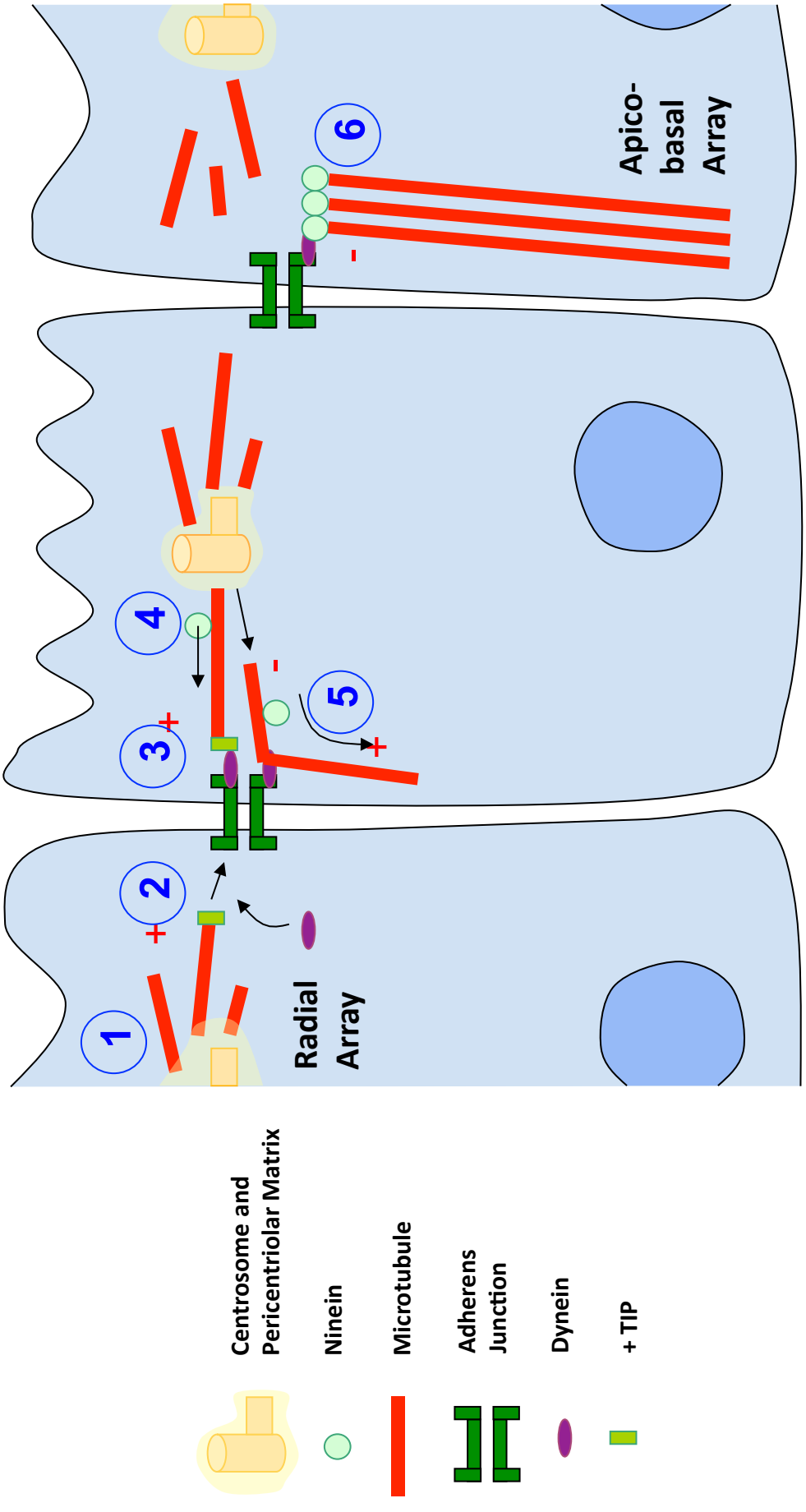
1
2
3
4
5
6
Radial Array
Apico-basal Array
Centrosome and Pericentriolar Matrix
Ninein
Microtubule
Adherens Junction
Dynein
+ TIP

1.6.4: +TIPs in Microtubule Reorganisation & Differentiation

It is known that EB1 overexpression is involved in the formation of stable microtubules and microtubule bundling (Bu and Su, 2001). It has been observed to have a role in migrating fibroblasts (where it is linked to APC, mDia and Rho GTPase family signalling) (Wen et al., 2004), and in the differentiation of skeletal myoblasts, where like in epithelial cells there is a significant rearrangement of the microtubule array as myoblasts differentiate into myotubes containing parallel bundles of non-centrosomal microtubules (Zhang et al., 2009). EB3 has also been identified with an important role in cortical microtubule dynamics in muscle cell differentiation (Straube and Merdes, 2007). Intriguingly, unlike EB1 (whose levels remained constant) and EB3 (which was up-regulated), EB2 was markedly down-regulated during the early stages of the muscle differentiation process (Straube and Merdes, 2007), and does not induce microtubule bundling on overexpression (Bu and Su, 2001). The EB family may therefore also play an important role in the formation of stable microtubule arrays in the apico-basal array formed during epithelial differentiation, with the tantalising observation that EB2 once again behaves in a markedly different fashion than its siblings, and may in fact need to be down-regulated for induction of a stable array.

+TIPS have also been extensively characterised in neurons, which possess long axons, with many released non-centrosomal microtubules cross-linked into bundles that extend along axons (where they exhibit uniform polarity) and dendrites (which can exhibit mixed polarity). They have been shown to be vital at various stages of development, including in neuronal cell migration (where LIS1 and CLIP-170 are important), axon growth, neurotransmitter transport, and neuronal cell death. As such, +TIPs have been associated with several neuronal disorders such as lissencephaly (LIS1), motor neuron disease (dynein/dynactin) and Williams Syndrome (CLIP-115) (Jaworski et al., 2008)

1.7: Cell Cycle

Cell proliferation is controlled by the cell cycle, which ensures the duplication of cellular components and accurate division into two daughter cells. Cells switch between interphase, a period of preparation in which DNA and all cellular components are replicated, and mitotic division (M phase). Progression through the cycle is tightly controlled by a series of regulatory checkpoints, which monitor whether conditions are suitable for division, and whether the cell has correctly duplicated its components, including the centrosome. Interphase can be split into three periods, S phase, and two gap phases (G1 and G2). Cells generally spend the majority of their time in G1 phase, during which cells will grow and perform their normal functions. They may enter a quiescent phase G0, and come out of the cell cycle, particularly in cells that are fully differentiated. Those cells embarking on a division cycle exit G1 into S phase, during which the entire genetic content of the cell is replicated, after which they transfer into the second growth phase, G2, during which the cell prepares for a mitotic division, replicating and duplicating cell components as required. Division itself is subdivided into several further steps. Mitosis begins in prophase, during which chromosomes condense and the mitotic spindle begins to form. The nuclear membrane breaks down in prometaphase, after which cells pass into metaphase, where the spindle attaches to chromosomal kinetochores. Once all chromosomes are aligned at the plane of division, anaphase occurs, in which the spindle rapidly pulls sister chromatids apart to opposite poles, reaching telophase where the cell membrane pinches in. Finally cytokinesis occurs, the cells separate, the nuclear membranes reform in each daughter cell, and the chromosomes decondense as the cells re-enter G1 (Alberts, 2002; Tyson and Novak, 2008) (Figure 1.8 A).

Spindles are composed of microtubules following a dramatic reorganisation of the interphase network, and are driven by their dynamics. Microtubules originate from centrosomes located at each spindle pole and consist of three types: kinetochore microtubules, interpolar microtubules and astral microtubules. Kinetochore microtubules are all orientated in the same direction within each half spindle, with minus ends anchored at the pole and plus ends docked to

kinetochores, arranging chromosomes at the equator. Interpolar microtubules emanating from each pole overlap in the spindle midzone, forming an antiparallel array bundled by kinesin motors. Finally, astral microtubules extend out from each centrosome to the cortex, where they interact with cortical dynein to orientate the spindle (Figure 1.9). Microtubules in the spindle exist in a state of flux, whereby they constantly polymerise at plus ends and depolymerise at minus ends, whilst disassembly at both ends drives chromatid separation in anaphase. Spindle microtubules are highly regulated by a multitude of proteins to both generate and maintain the structure, including polymerases, depolymerises, stabilising MAPs and severing proteins. Motors push apart the antiparallel arrays, encouraging the poles to separate, whilst also aiding both focus at the poles and attachment at kinetochores. +TIPs are important in the capture and anchorage of microtubule ends at both kinetochores and the cortex (Gadde and Heald, 2004; Mitchison and Salmon, 2001; Wittmann et al., 2001). Recently a non-centrosomal method termed microtubule-dependent microtubule nucleation, controlled by the novel protein augmin, has been shown to be important in the generation of spindle microtubules (Goshima et al., 2008).

1.7.1: Cell cycle control

A series of checkpoints monitor conditions and allow passage through the cell cycle. In particular, during the G1/S checkpoint cells confirm the external and internal environment is suitable for division, and either commit to S phase entry, delay division, or exit the cell cycle into G0. The second checkpoint (G2/M) controls entry to mitosis and checks that the cells genome has been correctly replicated, and that the cell is ready to divide (Novák et al., 2001). Finally, the spindle checkpoint at the metaphase-anaphase transition ensures that chromosome kinetochores have correctly attached to the bipolar spindle prior to daughter cell segregation (Musacchio and Hardwick, 2002). Passage through these checkpoints is regulated by cyclin-dependant kinases (CDKs), via their interactions with cyclins. Where conditions are unsuitable for progress the cell cycle is arrested, or if any damage is

sufficiently severe, apoptosis is triggered. Loss of cell cycle control leads to cancer (Malumbres and Barbacid, 2009).

1.7.2: The centrosome cycle

The maturation process of centrioles is tightly controlled by the centrosome cycle. Just as with DNA, centriole duplication is semi-conservative, and occurs once every cell cycle, with one centrosome segregated into each daughter cell. Immediately following division the centrosome consists of one mother centriole tightly bound to a perpendicular elongated new centriole. At the exit of M phase, a key process called disengagement occurs, where the two centrioles separate (Figure 1.8 B). This involves the enzyme separase, and also leads to the creation of a protein tether (composed of proteins such as rootletin), linking the two centrioles together. It is believed that this acts as a 'licensing' step, to ensure that duplication occurs only once per cell cycle (in the tightly bound 'engaged' conformation, further duplication is prevented) (Bahe et al., 2005; Tsou and Stearns, 2006). Duplication occurs during S phase, with a single new procentriole forming next to both original centrioles. Procentrioles elongate in G2 phase until the centrosome has two pairs of centrioles. These separate on M phase entry as the protein link breaks, and the original daughter centriole undergoes maturation, developing appendages. The two centriole pairs migrate to opposite poles of the spindle, thus ending up in different cells following division (Nigg, 2006; Strnad and Gonczy, 2008) (Figure 1.8 B).

Like the chromosome cycle, the centriole cycle is tightly regulated; Cdk2-Cyclin A/E is involved in the duplication of both centrosomes and chromosomes, with other kinases also involved, including Plk1, Aurora A, and Nek2. Proteolysis also plays a key role; separase, which separates chromatids in division, is key to the disengagement process (Nigg, 2006; Strnad and Gonczy, 2008; Zyss and Gergely, 2009).

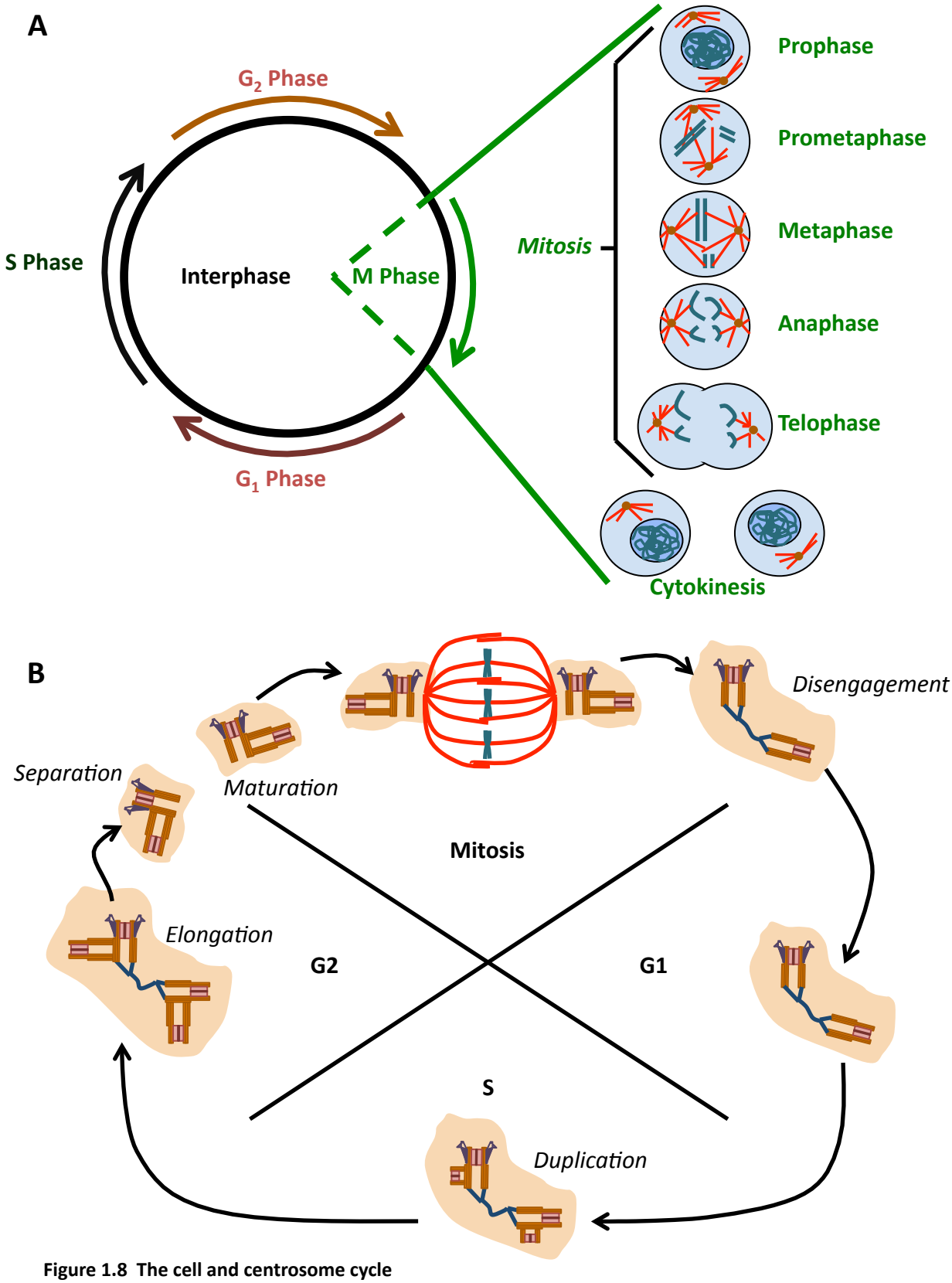

Figure 1.8 The cell and centrosome cycle
(A) The cell cycle consists of two gap phases (G1 and G2) during which the cell grows and checks conditions are suitable for division, S phase where cells duplicated their DNA, and M phase (mitosis). **(B)** Centrosome duplication occurs once per cycle. On mitotic exit, the tightly linked centrioles disengage. Procentrioles form perpendicular to mother and daughter centrioles in S phase, and elongate in G2. On entry to mitosis, centrioles separate and the daughter centriole undergoes maturation, generating appendages. Centrioles migrate to opposite poles of the spindle, and are segregated into separate cells on division.

Adapted from (Alberts, 2002) **(A)** and (Nigg, 2006) **(B)**

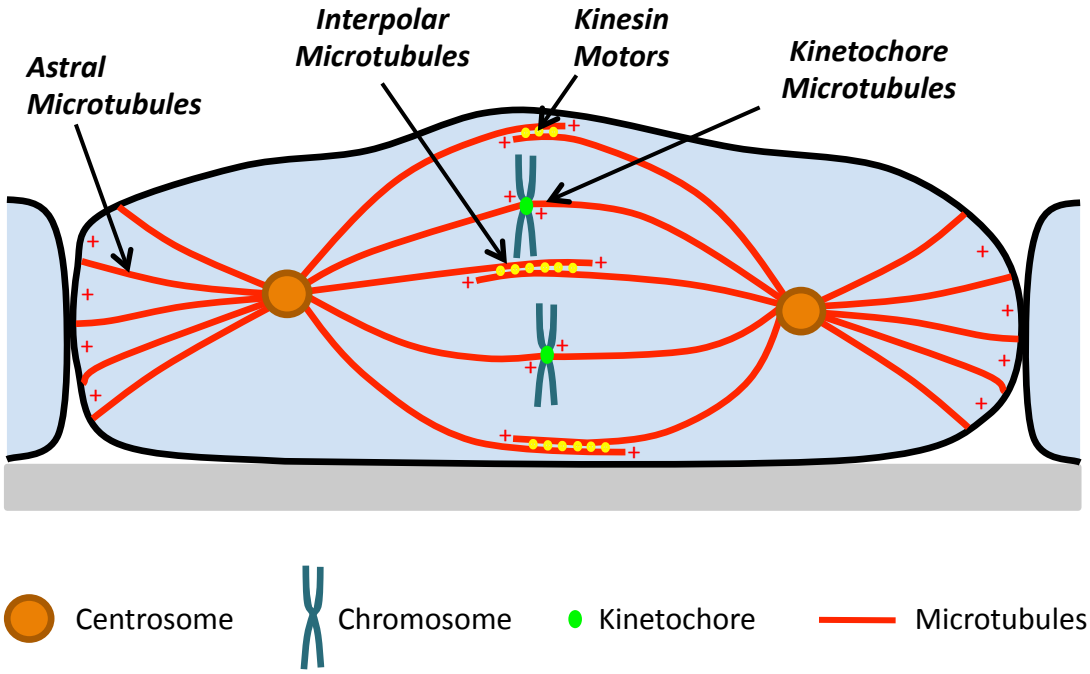

Figure 1.9 Structure of the mitotic spindle
The spindle consists of three classes of microtubule, all anchored at their minus ends by centrosomes located at the spindle poles. Kinetochore microtubules target kinetochores to organise chromosomes at the plane of division. Interpolar microtubules interdigitate at the spindle midzone, where motor proteins organise them into antiparallel bundles. Finally, astral microtubules extend out to make contact with the cell periphery, where cortically anchored dynein helps to orientate the spindle.

Adapted from (Alberts, 2002)

1.7.3: The cell and centrosome cycles in cancer

Cancers exhibit genetic instability, and can develop aneuploidy, where abnormal chromosome copy numbers can develop. There are two pathways by which they can develop; chromosomal instability (CIN) causes aneuploidy, and accounts for the majority of tumours, whilst mismatch repair deficiency (MIN) prevents the repair of point mutations within chromosomes. MIN tumours account for around 15% of colorectal tumours, and exhibit a near normal number of chromosomes (Lengauer et al., 1997).

The centrosome organises the spindle in dividing cells. In diploid MIN tumours, the centrosome appears normal and the ability of the centrosome to nucleate microtubules appears intact. However, in aneuploid neoplasms, centrosomes are fragile, leading to gross changes in their structure and number. Accordingly, the ability of centrosomes to nucleate microtubules is severely impaired (Ghadimi et al., 2000). These centrosomal defects have been studied and shown to be widely varying. Defective centrosomes appear larger in diameter, with increased accumulation of PCM components. They have been implicated in the formation of disorganised mitotic spindles, and therefore are associated with the aberrant division that can lead to further genomic instability (Pihan et al., 2001). As an example, pericentrin has been seen overexpressed and disorganised in cancers, where it has been associated with abnormal nucleation of both mitotic spindles and astral microtubules and thus has been associated with defective spindle orientation (Delaval and Doxsey, 2010). +TIPs also play an important role; EB1, with its many roles including kinetochore attachment, centrosomal anchorage and astral microtubule elongation has been reported to be upregulated in breast cancer (Dong et al., 2010).

The centrosome cycle is part of the cell cycle, and defects in centrosome duplication can lead to CIN and aneuploidy. There are many points at which defects can occur, for example, the kinases and phosphatases involved in separation and maturation of centrioles (including Plk1, Aurora A and Nek2) have been seen mutated in some tumours (Hayward and Fry, 2006). Perhaps the most extreme case

is the development of supernumerary centrosomes, which has been associated with loss of key cancer markers including p53 and BRCA1/2. The exact cause is hard to determine. It is possible that centrioles are overduplicated, or may be newly generated. They can lead to the formation of multipolar spindles, which on division can lead to unequal chromosomal divisions. If the cells subsequently survive, this can lead to far greater CIN, and so drive tumours to malignancy (Nigg, 2006). Multipolar division is often lethal, so cancer cells usually either inactivate the supplementary centrosomes, or cluster them at the two poles, to retain bipolarity of the spindle. This can lead to abnormal microtubule-kinetochore attachments and therefore divisions. Junctional proteins, dynein and polarity proteins are all involved, as the motors and MAPS help cluster centrosomes together to try and avoid multipolar divisions (Kwon et al., 2008; Zyss and Gergely, 2009).

Disruptions to spindle organisation are also associated with cancer. Compromised microtubule kinetochore capture can prevent correct chromosome segregation; chromosomes lag behind during metaphase, and are then left in the midzone during cytokinesis, thus contributing to CIN (Green and Kaplan, 2003). Meanwhile interactions of astral microtubules with the cell cortex can control spindle orientation, which is particularly important for the maintenance of epithelial monolayers. Microtubule plus ends are targetted to cortically anchored dynein, which exerts forces on the astral microtubules to correctly align the spindle. Compromised cortical capture of astral microtubules can thus cause incorrectly orientated division and thereby contribute to the disruption of the epithelial monolayer in cancers (Busson et al., 1998; Fleming et al., 2009).

1.8: Colorectal Cancer

Cancers of all types are one of the leading causes of mortality worldwide. They are driven by the accumulation of genetic mutations in oncogenes and tumour suppressor genes that lead to loss of control over cell proliferation (neoplasia), resulting in malignant tumour growth. Mutations occur over time as the tumour acquires key characteristic traits; they become both self-sufficient in growth signals and lose their sensitivity to opposing anti-growth signals, develop the potential for unlimited replication and the ability to avoid apoptosis, become able to support angiogenesis, and develop the ability to migrate and invade through tissues (Hanahan and Weinberg, 2000).

Colorectal cancers are one of the most common forms of cancer in the western world, responsible for an estimated 9% of all new incidences and deaths due to cancer in the U.S.A in 2012 (Siegel et al., 2012). They are particularly associated with age (around half the population will develop a benign adenoma by the age of 70) and environmental factors; especially diet, with other risk factors including a sedentary lifestyle, smoking, and conditions that cause inflammation of the bowel such as Crohn's disease. Additionally, genetic predispositions account for about a quarter of all cases (Cardoso et al., 2007).

1.8.1: Colon biology

The large intestine is the penultimate section of the lower gastrointestinal tract, and is around 1.5 metres long in humans of which most is the colon, with the final 15cm being the rectum, which connects to the anal canal. The colon can be divided into several sections; at its proximal end the ascending colon is attached to the small intestine through the caecum, off which the appendix also protrudes. It, as the name suggests, ascends up the right of the abdomen, before turning into the transverse colon, which extends across to the left side of the abdomen before turning down into the descending colon. A final twist, the sigmoid colon, connects to the rectum (Figure 1.10 A). Its role is to absorb water and any remaining

nutrients, and to remove indigestible matter. It takes the form of a tube composed of several layers; the innermost mucosa which lines the lumen, the connective tissue of the submucosa, longitudinal and circular muscle layers (the muscularis propria) which drive matter through the tract by peristaltic contraction, and the outer membrane, the serosa. The mucosa can be subdivided further into a very thin muscle layer (the muscularis mucosae), the connective tissue of the lamina propria, and the innermost single cell layer of epithelial cells, which line the lumen (Seeley et al., 2008) (Figure 1.10 B).

1.8.1.1: Crypt structure

The epithelial layer of the mucosa folds into distinctive crypts, and constantly regenerates itself from stem cells located at the bottom of each crypt. These newly synthesised proliferative progenitor cells divide and migrate through the bottom two-thirds of the crypt, differentiating into epithelial cell types: enterocytes, goblet cells, and enteroendocrine cells. Goblet cells and enteroendocrine cells secrete protective mucus and regulatory hormones respectively into the gut lumen, whilst enterocytes make up the bulk of cells and absorb water and nutrients across the epithelium. By the time they reach the top third of the crypt and migrate out into the surface epithelium, cells are fully differentiated, with their cell cycles arrested. There is a very high turnover rate; cells at the surface are shed into the lumen where they undergo apoptosis (Figure 1.10 C). Each crypt produces around 200 cells every day, and the entire epithelial layer is replaced every 4-5 days. As such they are an excellent model for studying epithelial proliferation and differentiation. Several signalling pathways are involved in crypt cell renewal; Wnt signalling has been associated with the promotion of progenitor cell proliferation, whilst Notch signalling is implicated in cell fate determination and differentiation (Sancho et al., 2004; van der Flier and Clevers, 2009; Wang et al., 2006).

Figure 1.10 Structure of the large intestine and colonic crypts
(A) The colon connects to the small intestine via the caecum, extending through ascending, transverse, descending and sigmoid colon to terminate at the rectum. **(B)** The colon wall consists of five main layers; the luminal mucosa, the submucosa, the smooth muscle layer of the muscularis propria and the membrane lining of the subserosa and serosa. The mucosa can be further divided into a small muscle layer, the muscularis propria, and the basal lamina upon which epithelial cells sit. **(C)** Stem cells lie at the bottom of the colonic crypt. These divide asymmetrically to produce proliferative progenitor cells, which differentiate and further divide. Around two-thirds of the way up the crypt, cells terminally differentiate, and are further pushed up and out to the surface epithelium, where they eventually apoptose and are shed.

Adapted from (Seeley et al., 2008) **(A)**, (Alberts, 2002) **(B)** and (Soncho et al., 2006) **(C)**

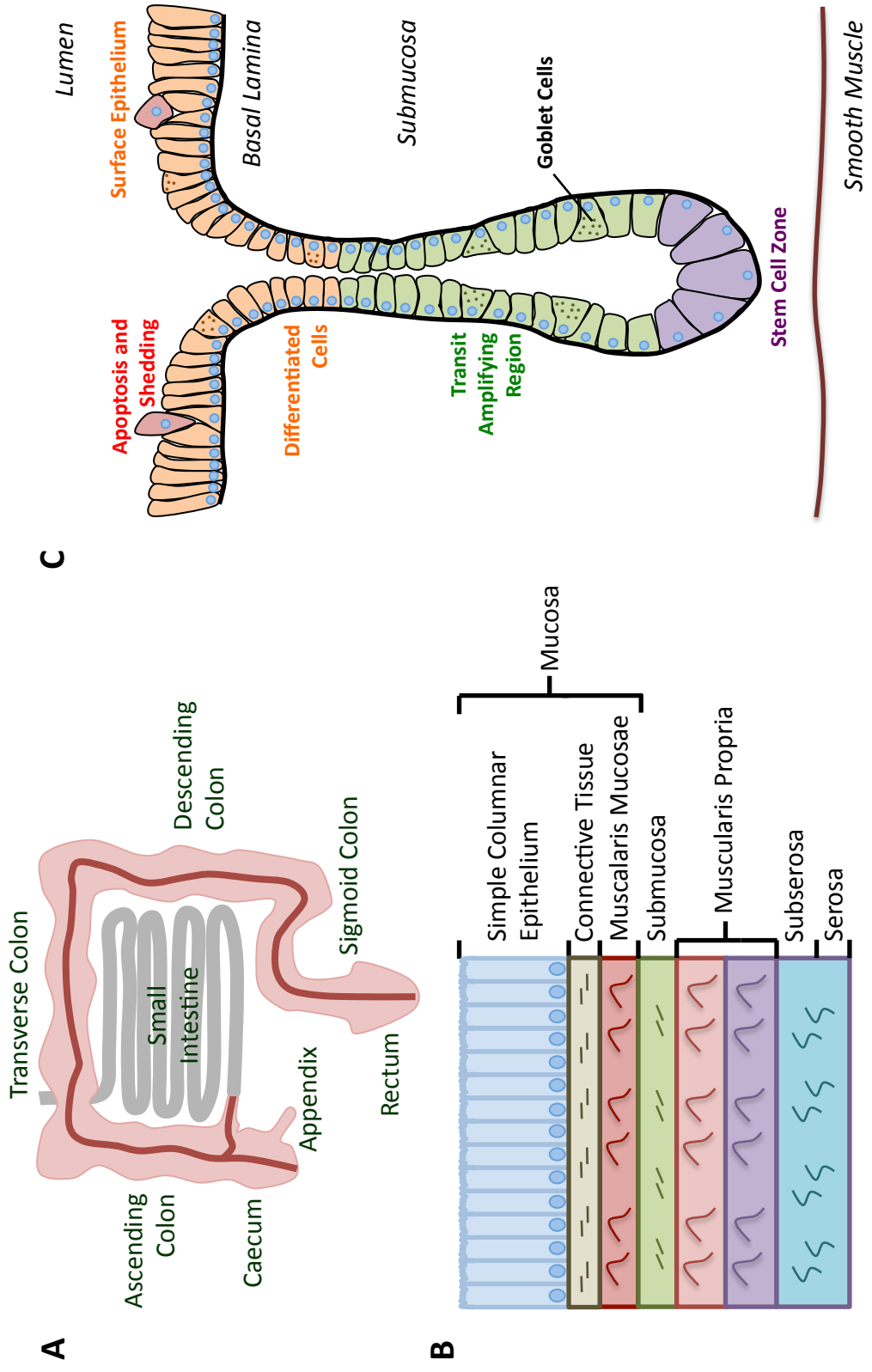
A
Transverse Colon
Descending Colon
Sigmoid Colon
Small Intestine
Appendix
Rectum
Ascending Colon
Caecum
B
Mucosa
Simple Columnar Epithelium
Connective Tissue
Muscularis Mucosae
Submucosa
Muscularis Propria
Subserosa
Serosa
C
Lumen
Surface Epithelium
Basal Lamina
Submucosa
Goblet Cells
Smooth Muscle
Apoptosis and Shedding
Differentiated Cells
Transit Amplifying Region
Stem Cell Zone

1.8.2: Tumorigenesis

Colorectal tumours originate from this epithelial layer, and progress over time in a very specific pattern, termed the adenoma-carcinoma sequence. Initial defects cause the epithelium to become hyperproliferative, from which a future tumour begins as a tiny polyp less than 1cm in diameter, protruding from the epithelium of the colon or rectum. This benign adenoma initially resembles normal epithelial tissue. Over many years these polyps grow monoclonally and become more abnormally differentiated, until eventually breaching through the basal lamina of the mucosa, and invading into the muscularis propria. At this point the tumour has gone from being a benign adenoma to a malignant adenocarcinoma. Finally, metastasis occurs, and neoplastic cells migrate into other tissues, particularly local lymph nodes, the liver, and the lungs (Fearon and Vogelstein, 1990) (Figure 1.11).

1.8.2.1: Staging and treatment of colorectal cancer

Depending on the severity at diagnosis, it is possible to cure the disease. Progression through the adenoma-carcinoma sequence is slow; polyps can stay in the benign yet detectable (by colonoscopy) stage for as many as 35 years before malignancy. The danger arises when the tumour undergoes metastasis and invades other tissues. Treatment generally involves surgical excision of the primary tumour, and in more advanced cases subsequent adjuvant chemotherapy (Wang et al., 2006).

The severity of the disease is classified using staging systems such as the TNM system. TNM is based on the invasion achieved by the tumour in the immediate vicinity (T), into lymph nodes (N) or distant metastasis (M). Staging systems allow a prognosis to be produced for each patient and thus enable more appropriate treatment management, according to disease severity (Compton and Greene, 2004) (Figure 1.11). Detection at an earlier stage leads to a significant improvement in prognosis; whilst around 90% of patients undergoing surgery at stage I are cured without requiring adjuvant therapy (Wang et al., 2006), a patient with stage IV metastatic disease has a survival chance of just 8% (Cardoso et al., 2007). Thus,

methods of detection at an early stage, and the identification of prognostic markers to allow better application of treatments are particularly important areas of research.

1.8.2.2: Molecular basis of the disease

Due to the accessibility and distinct progression sequence, it has been possible to study the genetic changes that correlate with each stage in the disease. Fearon and Vogelstein presented this model in 1990. The key theory they outlined was that progression through the sequence requires the accumulation of mutations in several oncogenes and tumour suppressor genes, and that it is this accumulation of mutations rather than the order in which they occur that is particularly important. That said, mutations in a number of key genes were observed in a relatively high percentage of cases, and these generally tended to occur in a preferred order along the sequence (Fearon and Vogelstein, 1990). The first of these, the tumour suppressor and +TIP APC is discussed below. The second major mutation, usually occurring slightly later than APC, is the activation of the oncogene K-Ras. This is detected in 58% of adenomas larger than 1cm in diameter, and up to 50% of all colorectal cancers, and may be able to activate Wnt signalling by inhibiting GSK3β. Inhibition of this oncogene has been suggested to halt tumour growth by increasing the transcription of the cell cycle protein p53 and thus apoptosis (Wang et al., 2006). Later still in the progression is the inactivation of the TGF-β signalling pathway (which normally acts to control proliferation and activate differentiation or apoptosis), particularly Smad4 (lost in around 30% of tumours), leading to a growth advantage in mutated cancer cells. The final common mutation is the loss of p53, and most often corresponds with the transition from benign adenoma to malignant carcinoma (Figure 1.11). This is observed in the vast majority of cancers due to its key role in cell cycle regulation and initiation of apoptosis. Once lost, cancer cells are able to avoid the apoptosis normally caused by extensive DNA damage, and thus quickly acquire numerous further mutations and genetic instability (Sancho et al., 2004).

Figure 1.11 Genetic model of colorectal cancer progression and correlation to TNM stage
Colorectal cancer progresses through a distinctive sequence involving the accumulation of common mutations over several years. The earliest of these is a loss of function mutation in APC. Severity of the disease is staged by methods such as the TNM system, which examines the degree of invasion of the tumour.
Adapted from (Fearon and Vogelstein, 1990) and (Compton and Greene, 2004)

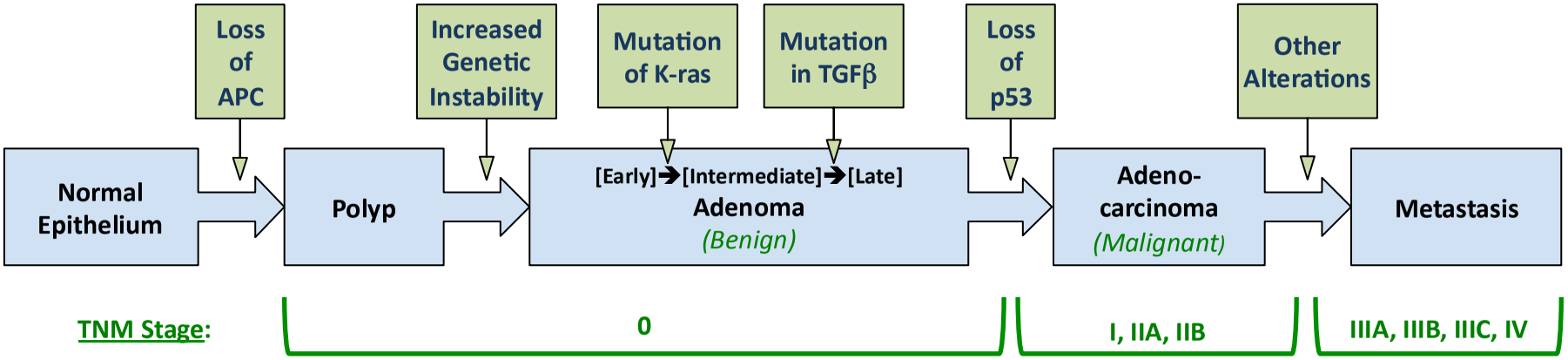

STAGE	DESCRIPTION
0	No evidence of tumour / no growth beyond mucosa.
I	Invasion into submucosa / muscularis propria.
IIA	Invasion beyond muscularis propria. No spread to lymph nodes or distant sites.
IIB	Invasion through colon wall into neighbouring tissue. No spread to lymph nodes or distant sites.
IIIA	Invasion to muscularis propria and metastasis to 1-3 lymph nodes. No spread to distant sites.
IIIB	Invasion through colon wall and metastasis to 1-3 lymph nodes. No spread to distant sites.
IIIC	Metastasis to 4 or more lymph nodes but no spread to distant sites.
IV	Metastasis to distant sites

Colorectal cancer progression follows Darwinian evolution; a mutation that gives a cell a selective advantage allows it to divide and dominate the population (Sancho et al., 2004). Thus the above defects are the most common, as consistently they confer the greatest advantages. However it is important to note that they are not essential; many other defects are observed, and not all of the above have to be present for a tumour to be malignant (though most possess at least two of the four identified by Fearon & Vogelstein). Nor do they have to occur in the order outlined in the progression, it is the accumulation of defects that is important, and the quicker this occurs, the faster the tumour develops to malignancy (Fearon and Vogelstein, 1990).

1.8.3: APC

Mutations in APC are the earliest common defects in the colorectal cancer progression sequence outlined above. They were identified in the inherited syndrome familial adenomatous polyposis (FAP), in which hundreds of adenomas develop and line the gut epithelium (leading to an increased predisposition to colorectal cancer at a younger age). In this disease, the tumour suppressor APC is deleted or mutated. APC has roles in both the cytoskeleton as a +TIP, and in the Wnt signalling pathway, which also involves β-catenin (Giles et al., 2003; Sancho et al., 2004).

1.8.3.1: APC domain structure

APC is large, at around 310kDa, with the N-terminal, middle and C-terminal of the polypeptide distinct in terms of structure. The N-terminus is well ordered and contains coiled-coil domains allowing oligomerisation. Of more interest is the set of seven armadillo repeats that bind to several proteins of cytoskeletal interest (Nathke, 2004), including IQGAP1 (Gundersen, 2002), and the kinesin adaptor protein KAP3 (Jimbo et al., 2002). The middle segment contains regions required for Wnt signalling, specifically β-catenin and axin binding domains. The C-terminal

section provides a basic/serine region allowing direct microtubule interaction and EB1 binding via a mechanism conserved with ACF7 (Akhmanova and Steinmetz, 2008; Nathke, 2004; Slep et al., 2005). APC can also interact with actin filaments through the basic region and mDia, via interactions with Asef (an exchange factor linked to Rho family GTPases) in the armadillo repeat region, and through DLG-1 via the C-terminal PDZ domain (Figure 1.12). APC has been shown to cluster at the leading edge of migrating cells (Hanson and Miller, 2005; Nathke, 2004).

APC mutations in cancer generally involve a truncation mutation in the mutation cluster region located in the central section of the protein, resulting in the loss of the C-terminus and thus the direct microtubule and EB1 binding domains. It can however still associate with kinesin motors and junctional sites through its armadillo repeats (Nathke, 2004) (Figure 1.12).

1.8.3.2: The role of APC in Wnt signalling

Over 90% of colorectal tumours have a mutation in a component of the Wnt signalling pathway; usually in APC, but alternatively often in β-catenin. The pathway regulates the phosphorylation status of β-catenin. In the absence of Wnt ligand, the degradation complex forms, with APC and Axin forming a scaffold for the protein kinases GSK3β and CK1α (Casein Kinase 1α) to specifically phosphorylate free cytoplasmic β-catenin. This targets it to the β-TrCP ubiquitination complex, and results in its subsequent proteosomal degradation. A Wnt ligand binding the Frizzled/LRP receptor complex activates the signal transducer Dishevelled. It inhibits GSK3β, which leads to the disassociation of the degradation complex. This leaves free unphosphorylated β-catenin able to translocate into the nucleus, displace the transcription repressor Groucho, and act as a cofactor for the TCF transcription factor, resulting in expression of Wnt target genes (Figure 1.13). In colorectal cancer, mutations in both copies of the APC gene or sometimes a single copy of the β-catenin gene itself result in β-catenin failing to be phosphorylated and degraded, allowing accumulation in the nucleus and thus activity of Wnt genes. In

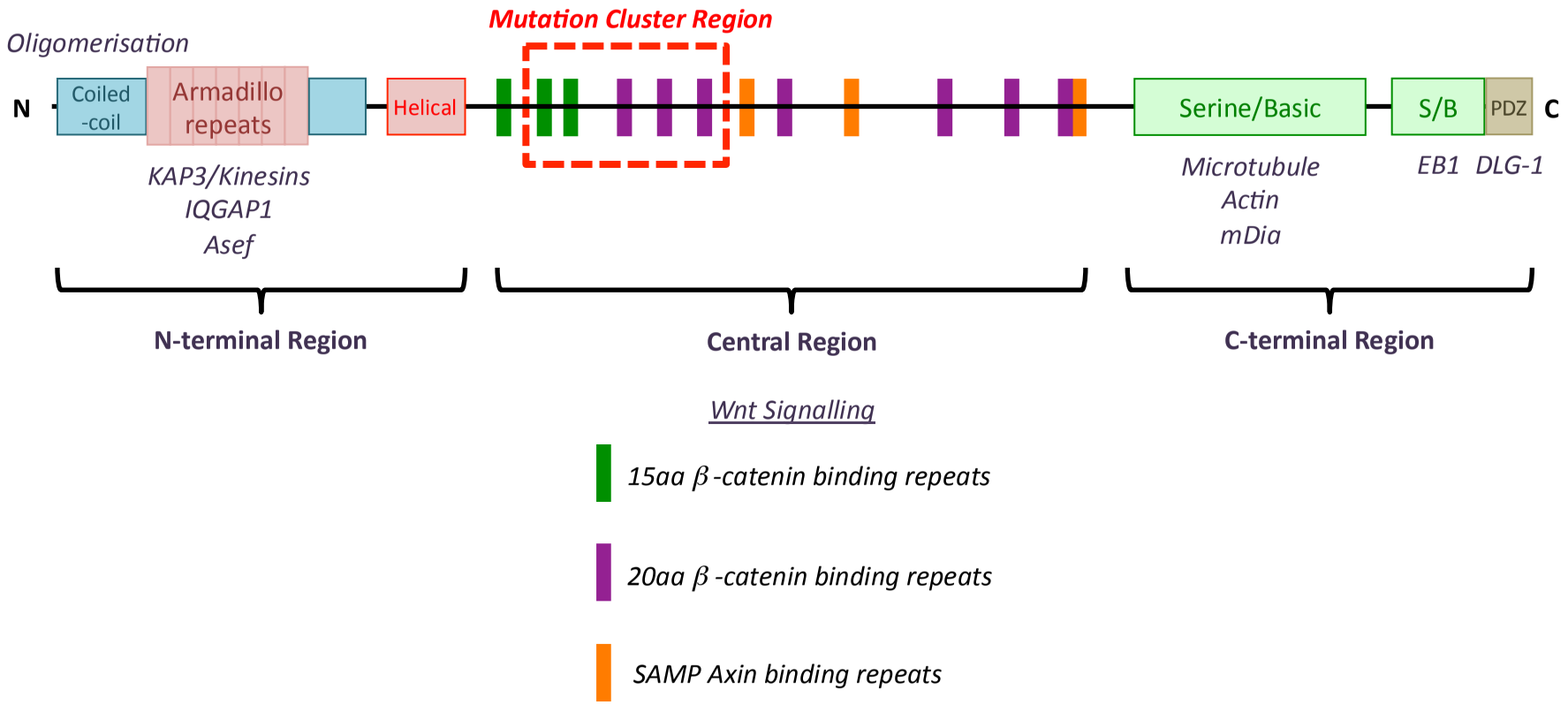

Figure 1.12 Domain structure of APC

APC is able to interact with microtubules both directly at its serine/basic region, and indirectly, through EB1 at the C-terminus, and via IQGAP1 and kinesin motors through N-terminal regions. The middle region contains domains related to Wnt signalling. APC can also bind actin, directly or through adaptors iike DLG-1 or Asef. The APC truncation mutation common in colorectal cancers usually occurs within the mutation cluster region, between amino acids 1284-1580.

Adapted from (Akhmanova and Steinmetz, 2008) and (Näthke, 2004)

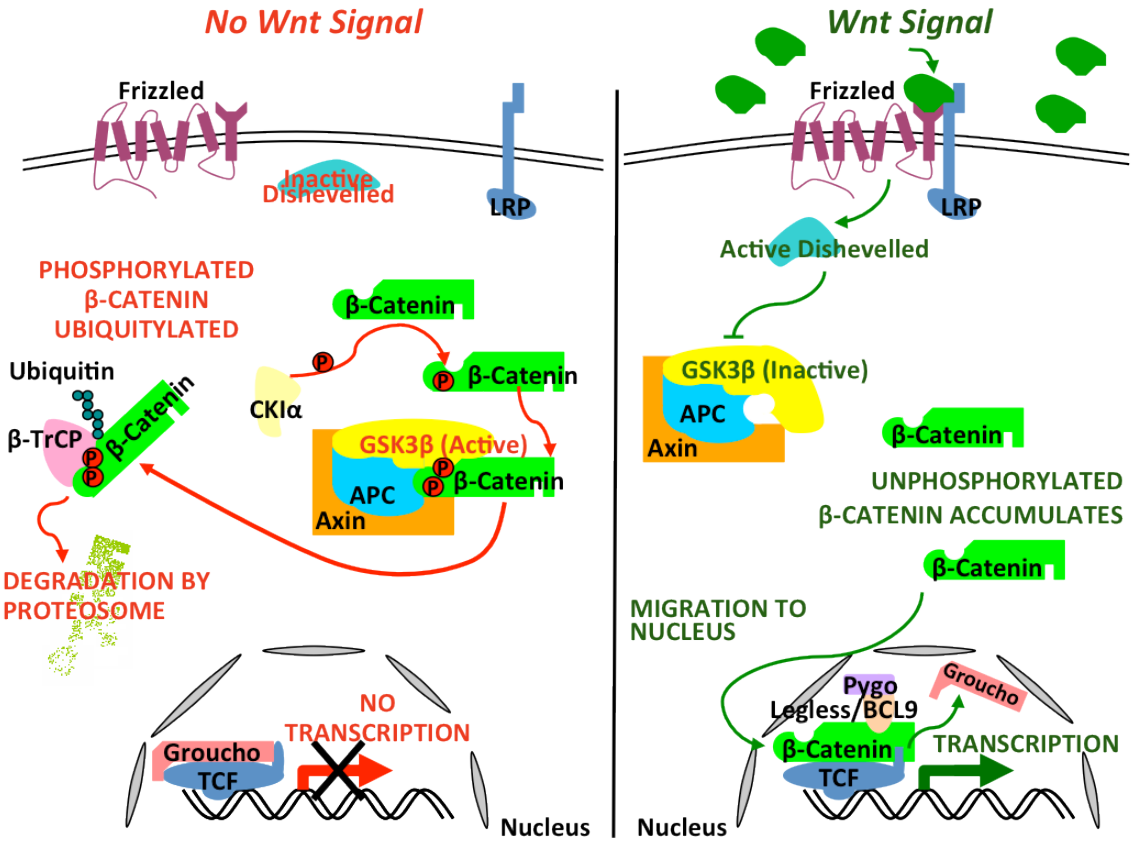

Figure 1.13 Simplified illustration of canonical Wnt signalling
In the absence of Wnt signal, β-catenin is phosphorylated by the degradation complex (GSK3β, APC and Axin) and targeted to be ubiquitinylated and subsequently degraded by the proteosome. A Wnt ligand activates the Frizzled receptor and thus Dishevelled, which inactivates GSK3β. β-catenin is no longer phosphorylated and degraded, and is therefore free to translocate to the nucleus, displace the transcription repressor Groucho, and activate the transcription of Wnt target genes.

Adapted from (Giles et al., 2003)

cells of the upper third of the crypt and surface epithelium, this can result in differentiated cells reverting to a more crypt progenitor-like phenotype (Giles et al., 2003). Interestingly, ACF7 has also been shown to be involved in Wnt signalling where it is believed to recruit the degradation complex to the LRP co-receptor at the cortex (Chen et al., 2006).

1.8.3.3: In the cytoskeleton: APC a +TIP and a cortical anchor

As mentioned in earlier sections, APC can interact with microtubule ends in several ways through multiple associating proteins. As is typical for a +TIP, it accumulates at the microtubule plus end, but can also bind along the lattice (Hanson and Miller, 2005; Mimori-Kiyosue et al., 2000). Binding to microtubules has been shown to increase their stability, and the C-terminal domain is required for this behaviour. It has also been shown that phosphorylation by GSK3β, required for β-catenin binding in Wnt signalling, reduces microtubule association suggesting that APC exists in separate pools for its signalling and cytoskeletal roles, with the switch between these regulated by its phosphorylation status (Zumbrunn et al., 2001).

APC has been associated with polarisation processes in cell-cell adhesion and the formation of the apico-basal microtubule array in epithelial cells, as well as cell migration (Hanson and Miller, 2005). In polarised epithelial cells it is recruited to the lateral membrane in an actin dependant manner (Rosin-Arbesfeld et al., 2001), and clusters at microtubule tips in basal regions in a microtubule dependant fashion, where it is important in establishing the parallel apico-basal microtubule bundles as microtubules are translocated to the cell base. Interestingly, in the highly polarised pillar cochlea cells, APC was only detected in basal regions, possibly suggesting the great number of microtubules in bundles sequesters the available APC (Mogensen et al., 2002). The ability of APC to stabilise microtubules and interact with actin is also important in its role in cell motility, where it locates to microtubule plus ends at the leading edge, and promotes migration (Barth et al., 2008). Switches between

promoting cadherin-mediated adhesion and cell migration may be controlled by Rho family GTPases such as Cdc42, via the interaction between APC and Asef (Kawasaki et al., 2003).

Due to its location at cortical sites APC is associated with cortical capture, with the loss of its ability to anchor microtubules at cellular structures and cortical sites believed to be important in the development of neoplasms, including colorectal cancer. One area where this has been particularly investigated is in the mitotic spindle. The loss of microtubule direct and indirect binding sites in the truncated APC protein product can lead to a failure of kinetochore capture, and thus prevent correct chromosome segregation (Green and Kaplan, 2003). Additionally, the mutation has been associated with spindle misalignment due to compromised cortical capture of astral microtubules. Mice heterozygous for the APC truncation have free astral microtubules and abnormally orientated spindles, leading to divisions occurring at incorrect orientations and disruption of the epithelial monolayer (Fleming et al., 2009).

APC can also bind IQGAP1, which can associate with CLIP-170 and is a receptor at the cortex, where it is suggested to be involved in microtubule plus end capture at the leading edge of migrating cells (Gundersen, 2002), and at junctions. IQGAP1 is also an important regulator of actin, and generally links the cytoskeleton to signalling pathways. IQGAP1 misregulation has been implicated in cancer cell motility and invasion, as well as angiogenesis (Briggs and Sacks, 2003; Johnson et al., 2009).

As cortical capture is an important intermediary step in the formation of apical-basal microtubule arrays, it is interesting to speculate as to whether APC could also be involved in the microtubule anchorage at cortical sites important for ninein redeployment, and whether this process is therefore disrupted in cancer cells expressing the APC truncation.

1.9: Cell Migration

Migration of both single cells and entire sheets is essential during initial embryonic development, and remains important in the mature organism. Migration is also important in wound healing, leukocyte motility, and diseases, especially cancer cell invasion. Like in epithelial differentiation, migrating cells are polarised, with very different morphologies from front to rear. Migration occurs in a multistep process. First, the membrane at the leading edge protrudes or extends forwards in lamellipodia (broad sheets) or filopodia (thin extensions). These extensions then make attachments with the basal matrix at the leading edge known as focal adhesions, which are stabilised and act through integrins. These connect the extracellular matrix with the internal cytoskeleton, allowing contraction driven by acto-myosin activity to pull the cell over the matrix. Finally, adhesions at the rear are disassembled as it retracts to allow a new cycle to begin (Figure 1.14 A). Migration can be directional, driven by external factors such as chemokines that attract a cell to a particular course (Lauffenburger and Horwitz, 1996; Ridley et al., 2003).

1.9.1: Cytoskeletal organisation

Rearrangement of the cytoskeleton is fundamental to the mechanism of migration. The leading edge of lamellipodia is characterised by extensive actin nucleation by the Arp2/3 complex, forming a complex stabilised actin network that pushes forward the membrane (Pollard and Borisy, 2003; Small et al., 2002; Vinzenz et al., 2012). The centrosome and Golgi apparatus relocate to a location in front of the nucleus, with microtubules involved in trafficking and turnover of key proteins and structures, such as components of focal adhesions. Stable microtubules extend forwards into the leading edge, whilst at the rear microtubules are destabilised (Kaverina and Straube, 2011; Ridley et al., 2003) (Figure 1.14 B). Some microtubules are released from the centrosome, and are believed to encourage the directionality of motility (Abal et al., 2002).

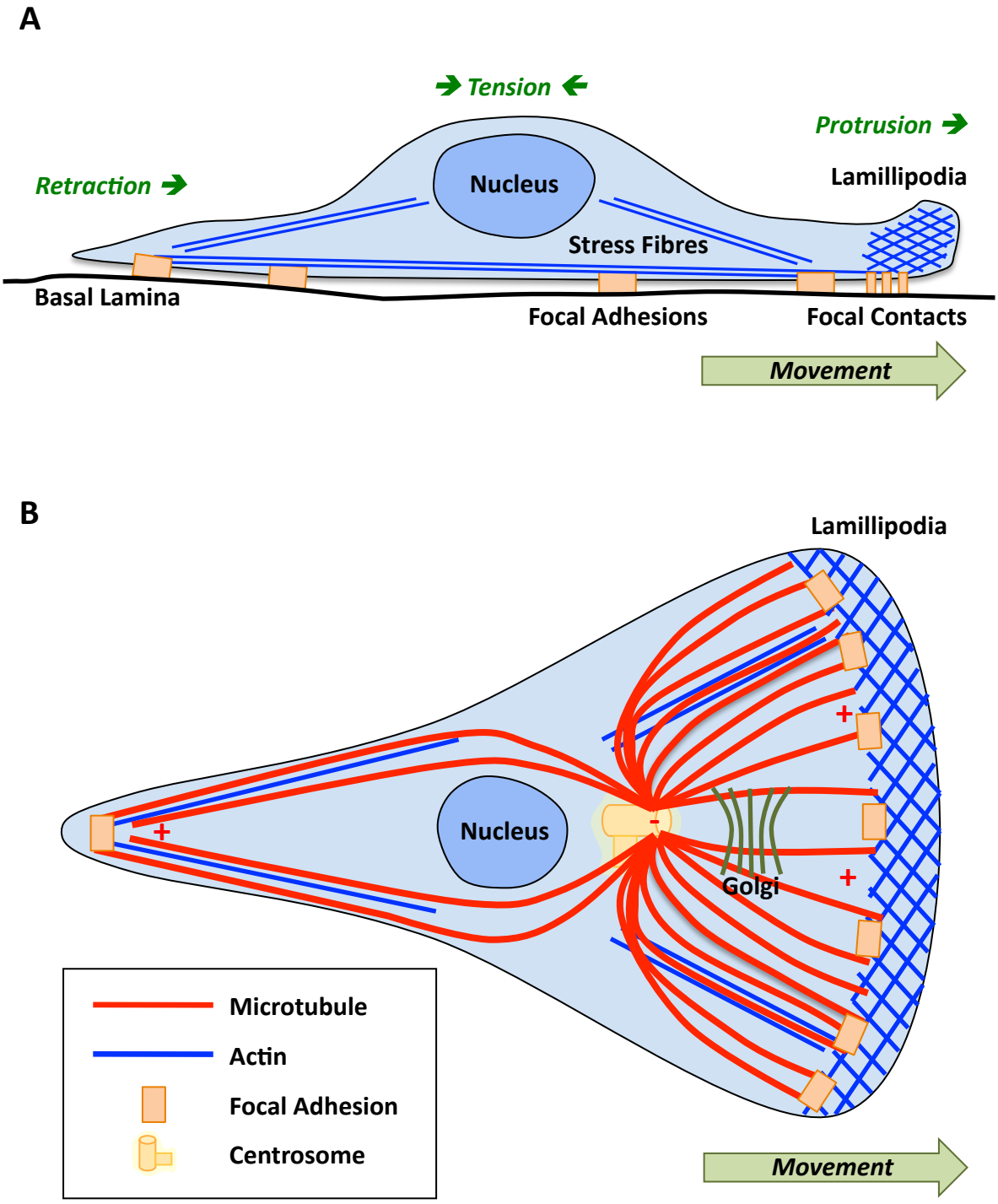

Figure 1.14 Cytoskeletal organisation in cell migration
(A) Cell migration occurs in a stepwise manner. Actin polymerisation in lamellipodia push forwards the plasma membrane at the leading edge. Focal adhesions are established with the ECM, allowing tension exerted by acto-myosin contraction in stress fibres to pull the cell forward. Finally, the rear of the cell retracts.
(B) The microtubule cytoskeleton re-organises in migration. The centrosome and Golgi apparatus relocate forwards of the nucleus as microtubules extend to the leading edge and are stabilised. Less stable microtubules also extend to the rear of the cell.
Adapted from (Lauffenburger and Horwitz, 1996) and (Ridley et al., 2003)

Rho GTPase family proteins (in particular Rho, Rac and Cdc42) control migration by co-ordinating the changes in cytoskeleton and adhesion required for motility. They particularly regulate the mobilisation of the actin cytoskeleton; Rac is required for lamellipodia formation and stimulates actin polymerisation, amongst other effects. It is also required for formation of focal adhesions. Rho controls the acto-myosin contraction in the main cell body (Ridley, 2001). The activity of Rho family GTPases can be modulated by microtubules. Many +TIPs (including APC, CLIPs and CLASPs) can interact with Rac and Cdc42 via IQGAP1. ACF7 has been associated with the disassembly of focal adhesions (Kaverina and Straube, 2011; Wittmann and Waterman-Storer, 2001). The Rho GTPases also feed back to regulate the organisation of the microtubule cytoskeleton, for example nocodazole treatment activates RhoA signalling through ROCK (Rho associated kinase) to trigger the release of the Rho effector GEF-H1 from microtubules, destabilising them and causing microtubule depolymerisation (Chang et al., 2008). In contrast, inhibition of ROCK or RhoA has been seen to cause microtubules to stabilise and bundle (Gao et al., 2004). Importantly, these various roles across both networks mean Rho signalling is able to mediate crosstalk between the actin and microtubule cytoskeletons (Krendel et al., 2002).

1.9.2: EMT, invasion and metastasis

The final stage of colorectal cancer progression is the invasion through the colon wall, and metastasis to distant sites. This involves the tumour cells changing from an epithelial phenotype to a migratory one, and acquiring the ability to survive outside their natural niche. This process is known as epithelial-mesenchymal transition (EMT), in which cells lose their apico-basal polarity, and their junctional associations with neighbours (Natalwala et al., 2008). This requires the alteration of multiple cellular processes. For example, tumours often start producing matrix metalloproteases (MMPs) to digest the extracellular matrix, as well as modulate the tumour microenvironment (Kessenbrock et al., 2010). Cancer cells can move in the mesenchymal method described above, in an amoeboid fashion similar to leukocytes

where they are more able to squeeze through gaps in the matrix, or indeed in sheets or clusters of cells (Sahai, 2005).

1.10: Summary

The microtubule cytoskeleton is essential for the function of cells. It is highly adaptable and can readily rearrange to suit cellular function. Its highly dynamic nature allows it to perform roles in trafficking, migration, division, and polarisation, and it is regulated by a multitude of proteins, especially +TIPs, which have an impact on its dynamics and stability. It can also cross-link via proteins such as ACF7 to other networks and structures of the cytoskeleton, including actin.

In the epithelial cells that line the colon, microtubules rearrange to form an apico-basal array most likely by a release and capture mechanism, in which the microtubules are anchored by ninein at junctional sites. An important intermediary step in this mechanism is the formation of an extended radial array in which microtubule plus ends dock with adherens junction associated sites.

Cancers are caused by the accumulation of mutations over time in key genes. Mutations affect the expression pattern of genes and contribute to the development of cancer phenotypes. For example, the loss of adhesion complexes is involved in allowing cancer cells to migrate and undergo metastasis. Colorectal epithelial cells polarise on cell-cell contact following differentiation, which is the result of a change in the gene expression profile in key signalling pathways, including Wnt signalling. These pathways are known to be mutated in colorectal cancer, with constitutive activation in the absence of an activating ligand returning the cell to a more crypt like morphology (Sääf et al., 2007). Cell polarity and junctional integrity (often marked by E-cadherin) is known to be lost in cancer as cells undergo EMT. Often the polarity proteins that drive epithelial differentiation are altered in cancers (Tanos and Rodriguez-Boulan, 2008; Wodarz and Nathke, 2007).

It is reasonable to suppose that any alterations that disrupt the apico-basal array that normally forms on polarisation could contribute to a return to a less

differentiated state, with diminished adhesion and a more migratory phenotype. An interesting avenue of research therefore is to examine the distribution of key proteins involved in the formation of the apico-basal microtubule array, such as the centrosomal protein ninein and +TIPs like the EBs and APC, and determine whether they are abnormally distributed in colorectal cancer cells. If these proteins are organised incorrectly, what effect does it have on the microtubule array and cell morphology, and can any effects be used as specific markers for the stage of disease?

This study aims to examine these ideas as to whether the formation of the microtubule array is disrupted in models of colorectal cancer, and determine what effect this may have on the correct maintenance of the gut epithelial monolayer.

1.11: Aims & Objectives

The establishment of the apico-basal microtubule array is essential during epithelial differentiation for the maintenance of cell polarity. The overall aim of the project was therefore to investigate whether the formation of apico-basal arrays in polarised colon epithelial cells is disrupted in colorectal cancer, and how the mechanism controlling array formation is compromised. A particular focus was on the role of certain +TIP proteins, initially examining their normal role in microtubule reorganisation, and then how they may contribute to aberrant phenotypes in cancer cells.

There were three main avenues of investigation, each with specific objectives.

1. Examination of cytoskeletal organisation in normal and tumour human tissue samples.
    - Initially, develop techniques for cryostat sectioning and immunolabelling procedures.
    - Use these to examine the general epithelial architecture in normal and human matched pair tissue samples, with particular focus on the distribution of centrosomal proteins, especially ninein.

2. Examine the role of APC in microtubule cortical capture
    - Characterise the HCT116 cell line as a suitable full length APC expressing control cell line compared to TC7 cells.
    - Analyse whether the APC truncation mutation disrupts microtubule cortical approach and capture.
    - Analyse whether truncated APC could lead to spindle misorientation due to compromised targeting of astral microtubules to cortical sites.
    - Attempt to deplete the KIF17 motor, as a way of removing all APC from cortical sites.

3. Examine the role of EB2 as a regulator of microtubule reorganisation in epithelial differentiation.
    - Examine further initial data suggesting EB2 is downregulated during epithelial polarisation.
    - EB2 depletion in ARPE-19 cells has been found to produce a distinct phenotype. Verify these effects in HCT116 cells as an additional cell line.
    - Create a fluorescently tagged EB2 construct by cloning mouse EB2 from mIMCD-3 cells into the pmCherry-C1 expression vector, to be used in rescuing the EB2 depletion phenotype.
    - EB2 depletion appears to cause microtubule bundling, suggesting increased stability. Assess microtubule dynamics EB2 depleted cells.
    - EB2 siRNA treated cells also appear larger in size. Examine whether such cells are capable of division, and perform cell cycle analysis.
    - As EB2 appears downregulated during epithelial polarisation, examine whether its overexpression could contribute to cancer progression, with particular focus on whether cell polarisation is compromised, and whether rates of cell migration and invasion are increased.

Chapter II

Materials & Methods

2.1: Model Systems

2.1.1: Cell lines

The majority of work in this project utilises cell lines modelling different aspects of colon biology and microtubule organisation in epithelial cells. Cell lines are easy to work with, and readily manipulated by transfection with constructs, or depletion with small interfering RNAs. The cell lines outlined below were used in this study.

2.1.1.1: Models of the epithelial cytoskeleton

Human retinal pigmented epithelial (ARPE-19) cells are widely used as a model for the undifferentiated radial microtubule array in epithelial cells. They have been reported to polarise (Dunn et al., 1996), although have not been seen to in our experience. They are flat and easy to image, with their distinctive radial array anchored at the centrosome, and their ends radiating out to the cell periphery. Ninein is located at the centrosome and as speckles in the cytoplasm, with EB1 in a classic plus tip firework pattern at microtubule plus ends (Bellett et al., 2009).

Two kidney cell lines have been used to model polarised epithelia. Madin-Darby Canine Kidney cells (MDCK-II) were isolated from the distal kidney tubule of a cocker spaniel (Leighton et al., 1969), and are widely used as a model for epithelial differentiation as they polarise when grown on a tissue culture insert (Bre et al., 1987). We use them as a model for the formation of the apico-basal microtubule array (Bellett et al., 2009). When grown as a subconfluent monolayer they demonstrate a disorganised microtubule array, with some plus end cortical contact, however when polarised on a filter insert, they form an apico-basal array. Mouse terminal inner medullary connecting duct (mIMCD-3) cells (Rauchman et al., 1993) present a similar phenotype (Tyrrell, 2012), and are used particularly for depletion and cloning experiments, as mouse genetics are easier to manipulate than dog.

2.1.1.2: Models of colorectal cancer

Two human colorectal cancer cell lines were used. TC7 cells are used as a model for the APC truncation mutation. They are a derivative of the commonly used Caco-2 cell line, which was originally isolated from the adenocarcinoma of a 72 year old male, and possess a truncation mutation at residue 1367 of one APC allele, whilst lacking the other (Rowan et al., 2000). When grown as a subconfluent monolayer they exhibit a disorganised microtubule array. They express β-catenin and E-cadherin at cell junctions, and a split centrosome. TC7 cells polarise when grown on filters, forming an apical-basal microtubule array (Keynton, 2011).

HCT-116 cells by contrast are a model for human colon cancer cells with full length APC, instead possessing a deletion in a single residue of β-catenin, serine 45, which is part of the GSK3β recognition site and phosporylated by Casein Kinase I (Morin et al., 1997).

2.1.2: Human tissue

This project has also utilised frozen human sections from the Norfolk and Norwich tissue bank, in collaboration with Dr. James Sington (consultant pathologist and colon cancer expert). Samples were obtained as matched pairs, in order to identify any differences between normal and tumour regions from the same patient.

2.2: Cell Culture

2.2.1: Maintenance of cell lines

Cell lines were maintained in 75cm^2 culture flasks (Nunc) within a Heraeus incubator at 37°C in a humid atmosphere containing 5% CO_2. Cell lines were obtained from the sources and grown in appropriate medium containing the indicated supplements (Table 2.1). All work was performed in a class II laminar flow tissue culture hood under sterile conditions.

Cell Line	Medium *	Supplements *	Origin
ARPE-19	DMEM/F:12 (1:1) (High Glucose, + NEAA)	10% FBS 1% L-Glutamine 2% Sodium bicarbonate	Gift: Julie Sanderson (University of East Anglia, Norwich, UK)
Caco-2	DMEM (High Glucose, + NEAA)	10% FBS 1% L-Glutamine 100 U/ml Penicillin 0.1 mg/ml Streptomycin	American Type Culture Collection HTB-37
HCT-116	DMEM (High Glucose, + NEAA)	10% FBS 1% L-Glutamine 100 U/ml Penicillin 0.1 mg/ml Streptomycin	American Type Culture Collection CCL-247
MDCK-II	DMEM (High Glucose, + NEAA)	10% FBS 1% L-Glutamine 100 U/ml Penicillin 0.1 mg/ml Streptomycin	American Type Culture Collection CCL-34
mIMCD-3	DMEM/F:12 (1:1) (High Glucose, + NEAA)	10% FBS 1% L-Glutamine	American Type Culture Collection CRL-2123

TC7	DMEM (High Glucose, + NEAA)	10% FBS 1% L-Glutamine 100 U/ml Penicillin 0.1 mg/ml Streptomycin	Gift: Elizabeth Lund (Institute of Food Research, Norwich, UK)
ARPE-19 **(GFP-α-Tubulin)**	DMEM/F:12 (1:1) (High Glucose, + NEAA)	10% FBS 1% L-Glutamine 2% Sodium bicarbonate 1 mg/ml G418	Lab-made stable cell line (Deborah Goldspink)
***** DMEM, DMEM/F:12 (Invitrogen, Paisley, Scotland). Penicillin/Streptomycin, G418, L-Glutamine, Sodium bicarbonate (Sigma, Poole, Dorset). FBS (PAA Laboratories, Yeovil, Somerset).			

Table 2.1 List of cell lines, medium and additives, and their origins

2.2.1.1: Passaging cells

Cell lines were passaged twice a week when they reached approximately 80% confluency, with seeding dilutions adjusted as required to ensure cells remained in the exponential growth phase. Reagents were warmed in a 37°C water bath prior to use. For subculture of a flask, the medium was removed and the cells washed 0.25% Trypsin/1mM Ethylenediaminetetraacetic acid (EDTA) (Sigma, Poole, Dorset). Following removal of this wash, cells were detached from the tissue culture plastic by adding a further 5ml of Trypsin/EDTA, and incubating at 37°C for 5 minutes until cells had detached, after which 8ml of medium (+FBS) was added to neutralise the trypsin. The suspended cells were pelleted by centrifugation at 800 RCF (relative centrifugal force) for five minutes, after which the supernatant was removed, and the cells resuspended in fresh medium. The resuspended cells were then diluted into fresh T75 flasks in a total volume of 10ml medium.

2.2.1.2: Freezing & thawing cells

Low passage stocks for each cell line were maintained in a liquid nitrogen dewer. These were periodically brought up to avoid potential phenotypic changes

associated with high passage numbers. To freeze cells down, a flask was passaged as above up until the step where the cell pellet was resuspended after centrifugation. At this point, pellets were instead resuspended in appropriate medium containing 10% Dimethylsulphoxide (DMSO) to act as a cryopreservant. This was aliquoted into several cryovials (Corning, Amsterdam, The Netherlands), and immediately transferred to a "Mr Frosty™" freezing container containing isopropanol and gradually frozen at -80°C. For long-term storage, cryovials were transferred to the liquid nitrogen dewer.

To bring cells up from frozen, cryovials were removed from storage and defrosted at 37°C, after which cells were immediately transferred to a prewarmed 10ml of medium and pelleted by centrifugation at 800 RCF for 5 minutes to eliminate the DMSO. The supernatant was removed and the pellet resuspended in 10ml of appropriate medium (containing 10% FBS plus relevant supplements), then transferred to a tissue culture flask. Once the flask had reached 80% confluency, the cells were passaged as per the standard maintenance procedure. For the TC7 cell line, cells were initially grown in medium containing 20% FBS, before being returned to 10% FBS at the first subculture, as the extra serum helped the cells to settle.

2.2.2: Seeding cells

Cells were seeded onto appropriate surfaces for experiments as required, including multiwell plate (Nunc, Penfield, New York, USA) plastic surfaces, 13mm diameter (No. 0 thickness) glass coverslips (VWR International, Lutterworth, Leicestershire) or ACLAR plastic strips (Agar Scientific, Stansted, Essex) in 3cm Petri dishes / 6 well plate wells for immunolabelling experiments, and glass bottomed dishes (MatTek, Ashland, Massachusetts, USA) for live fluorescence microscopy. Glass coverslips were sterilised by oven baking overnight at 180°C, whilst ACLAR pieces were sterilised in 70% ethanol and air-dried in the tissue culture hood. For seeding, cells were trypsinised as above and resuspended in fresh medium. A haemocytometer was used to calculate cell concentration, and thus the appropriate

dilution to seed at a particular density. Such seeding densities varied between different cell types, and according to experimental purpose.

2.2.3: 3D cell culture

The 3D cell culture method used here was modified from (O'Brien et al., 2006), with Matrigel™ (BD Biosciences, Oxford, Oxfordshire) used to provide the 3D matrix. Matrigel™ sets at room temperature, so the pipette tips and eppendorfs to be used were stored in the -20°C freezer prior to use, to ensure the matrix mix remained as cold as possible during preparation. Cells were diluted to $1x10^6$ cells/ml in 1% FBS medium and 20µl (20,000 cells) transferred to a 200µl ice cold Matrigel™ aliquot. Small drops of the cell-matrix mix were transferred to several glass coverslips in 24 well plate wells, taking care to keep each blob distinct. Coverslips were transferred to the 37°C incubator for 1 hour to allow the Matrigel™ to set, after which 1ml of 5% FBS medium was added to each well. Cysts were allowed to develop over a 6-8 day period, with the medium replaced every 2 days.

2.3: Drug Treatments

2.3.1: Nocodazole regrowth

Nocodazole treatments were used in microtubule regrowth assays. Nocodazole addition coupled with cold treatment was used to completely depolymerise the microtubule network. The effects of the drug are reversible, with its removal triggering microtubule regrowth.

TC7 cells were treated with normal DMEM medium containing nocodazole (Sigma, Poole, Dorset) diluted to a final concentration of 33μM for an initial one-hour on ice, followed by a further one-hour incubation at 37°C. The drug was removed by washing with ice cold DMEM for five minutes three times (all on ice, to prevent microtubule polymerisation), with the coverslips then transferred into medium prewarmed to 37°C to initiate microtubule regrowth. This warm medium was quickly changed a further two times, with cells then transferred to the 37°C incubator. Coverslips were fixed for subsequent immunolabelling before nocodazole treatment, immediately prior to drug washout, and at various timepoints throughout the recovery period.

2.3.2: Double thymidine block

The double thymidine block was used to synchronise cells, such that at a certain timepoint following release from the drug treatment, a larger proportion of cells would simultaneously undergo mitosis. Treatment with thymidine blocks the cell cycle at the G1/S border, preventing progression beyond S phase, meaning cells accumulate in G1 phase. On removal of the thymidine, the cells are released to proceed through the cell cycle, and so will enter mitosis together at a certain time following release. To increase the synchronisation effect, cells can be blocked twice. This consists of an initial block (lasting 17 hours), followed by wash out and 9 hour passage through the cell cycle, before a second 17 hour thymidine treatment, followed by final release (Bostock et al., 1971; O'Connor and Jackman, 1996).

Cells were grown to 50% confluency on glass coverslips and treated with thymidine (Sigma, Poole, Dorset) at a final concentration of 2mM, then incubated at 37°C for 17 hours. The drug was removed and the cells washed three times in medium, then incubated at 37°C in normal medium for 9 hours, releasing cells from the block. Thymidine was then reapplied at a final concentration of 2mM for a second 17-hour period. Cells were again released from the block by washing three times in medium, and allowed to progress through the cell cycle in the 37°C incubator. For optimising purposes in each cell line, coverslips were fixed and processed for immunolabelling at several time points after release from the block, in order to assess the time at which the most spindles were observed.

2.4: Cell Transfection

2.4.1: siRNA

The siRNAs (Qiagen, Manchester, Greater Manchester) used in this project were designed against human EB2 (MAPRE2) and KIF17 sequences, for use in the human ARPE-19 and HCT116 cell lines. HP Custom siRNA against EB2, Flexitube pre-designed siRNA against KIF17, and Allstar negative control (scramble) siRNA were supplied lyophilised, and dissolved in RNAse free water to give a working stock solution. The target sequences for these siRNAs are listed in Table 2.2.

Protein	siRNA ID	Target Sequence (5' -> 3')
EB2	Sequence (d)	CTCGATAACCCAAGAGACTAT
KIF17	Hs_KIF17_1	CAGCAACTACTTCCGATCTAA
	Hs_KIF17_3	CGGCTACACGCTGATGAACAA
	Hs_KIF17_4	AAGCTCAATATCAGCTGGGAA
	Hs_KIF17_5	CTGGGTGCTGCTTAACGTCTA

Table 2.2 List of siRNA sequences

siRNA was delivered into cells seeded at 40-50% confluency in six well plate wells by oligofectamine according to a two-shot protocol, in which transfections occurred at 0 and 48 hours, with experimental analysis typically at 96 hours post initial treatment. For each well at a particular time point, siRNA was diluted to a final concentration of 27nM in 180μl of Opti-MEM medium. In a second tube, 6μl of oligofectamine was added to 12μl of Optim-MEM. The two tubes were combined after five minutes, and then allowed to mix for a further 15 minutes, before being added to the appropriate well. At the 48 hour time point, cells in a single well were typically subcultured into two or three six well plate wells (depending on cell density), prior to the addition of the second siRNA treatment.

2.4.2: Plasmid DNA

Maps of the plasmid vectors used in this project for transient expression of cDNA constructs are illustrated in Appendix B. Plasmid DNA was transfected into cells using Jetprime (Polyplus, Illkirch, France) 24 hours prior to analysis. Accordingly, for rescue following siRNA depletion, plasmid transfection occurred at 72 hours post initial siRNA treatment. For a single six-well plate well, 2μg of DNA was added to an eppendorf tube containing 200μl of Jetprime buffer, followed by 4μl of Jetprime reagent. These were allowed to mix for 10 minutes before being added to the appropriate well. The medium in a transfected well was replaced with fresh medium 4 hours after transfection.

2.4.2.1: Creation of stable cell lines

New cell lines were created to stably express the mCherry-EB2 and empty pmCherry-C1 vector in MDCK cells. Cells were seeded into separate six well plate wells for each plasmid and allowed to settle overnight. They were then transfected with 2μg of appropriate DNA using Jetprime, as described above. 24 hours after transfection, cells were treated with 1mg/ml of geneticin (G418) antibiotic, to allow selection of antibiotic resistant (and therefore plasmid expressing) cells. This concentration had previously been found to be the lowest that will kill all MDCK cells in a two-week period (D. Goldspink, personal communication). The antibiotic containing medium was replaced three times a week, until all but the antibiotic resistant cells remained. Despite the antibiotic selection, not all remaining cells expressed the fluorescently tagged construct, so a further selection was made using fluorescence-activated cell sorting (FACS). FACS was performed by Dr. Andy Goldson using a Bectin Dickinson FACS ARIA II high speed cell sorter. Initially, this was used on cells transfected with either of the two plasmids to produce highly concentrated pools of mCherry fluorescence expressing cells for each treatment, which when subsequently seeded onto glass coverslips and observed were found to increase the proportion of cells visibly fluorescing to approximately 95%. This polyclonal group was maintained as the stable cell line for further experiments in empty pmCherry-C1

expressing cells, however a further selection was made for the mCherry-EB2 expressing cells, to give a monoclonal stable cell line. This was achieved by a second FACS sort (as above), with a single mCherry-EB2 cell from the polyclonal pool sorted into each separate well of a 96 well plate. These were allowed to grow over time, and were subcultured into larger wells as they reached confluency. Several clones were checked by seeding onto glass coverslips and examined by fluorescence microscopy following fixation and immunolabelling, such that the stable clone selected for further experiments had an appropriate expression level and pattern of mCherry-EB2. The selected clone was then maintained as the stable cell line for future use.

2.5: Human Tissue Samples

2.5.1: Cryostat sectioning

Ethical approval was gained (REC reference 11/H0906/17), allowing the use of frozen colon human tissue samples, obtained courtesy of James Sington from the Partners in Cancer Research Tissue Bank at the Cotman centre, Norwich. Tissue samples were obtained in matched pairs of tumour and apparently normal biopsies from the same patient. Known details of samples used are shown in Table 2.3.

	Tissue Bank Number	**Accession Number**	**Sample Site**	**Location**
Matched Pair Sample A	09TB0228	09S47054	Normal	Hemicolon (right)
			Tumour	
Matched Pair Sample B	11TB0023	11S05023	Normal	Hemicolon (right)
			Tumour	

Table 2.3 Details of human colon tissue samples

Polylysine coated slides (VWR International, Lutterworth, Leicestershire) were prepared by marking two boxed regions using a PAP pen (Sigma, Poole, Dorset), to ensure the sections when added were surrounded by a hydrophobic barrier so that reagents covered sections during staining. Tissue samples were mounted in Tissue-Tek® O.C.T™ mounting medium (Sakura, Thatcham, Berkshire) on dry ice and transferred to the cryostat microtome. Sections were cut into 10μm slices, and transferred into the regions highlighted by the PAP pen on the polylysine slides. They were then immediately transferred to a -20°C freezer and methanol added for fixation (Section 2.5). To check samples were correctly orientated, sections were quickly stained in haematoxylin and viewed under a microscope.

2.6: Sample Staining

2.6.1: Fixatives

Tissue culture cells grown on coverslips or in 3D culture, as well as cryostat sectioned tissue samples were all generally fixed in methanol at -20°C. More recently an alternative methanol-formaldehyde fix has also been used, the protocol modified from (Rogers et al., 2002). This method gave a slight increase in quality of labelling for proteins localised along microtubules such as EB2 and KIF17, and was also more effective at fixing cysts grown in 3D culture. A 3% formaldehyde solution was prepared by diluting a 37.5% formaldehyde stock solution (Sigma, Poole, Dorset) in ice cold methanol.

2.6.2: Immunofluorescent labelling

2.6.2.1: 2D culture

Cells were generally fixed by removing medium and adding methanol at -20°C for five minutes, followed by three quick washes in 1% goat serum (Sigma, Poole, Dorset) in PBS (Oxoid, Basingstoke, Hampshire). They were treated with the detergent NP40 (1% NP40 in PBS) for no longer than 2½ minutes, to permeate cell membranes, after which they were again washed three times in 1% goat serum-PBS. Alternatively, samples were fixed in methanol-formaldehyde (prepared as above) at -20°C for ten minutes, then washed for two minutes three times in 1% goat serum-PBS also containing 0.1% Triton X-100.

Following fixation, cells were blocked in 10% goat serum-PBS for 30 minutes to prevent non-specific binding of antibodies (for methanol-formaldehyde fixed samples this blocking solution also contained 0.1% Triton X-100). Primary antibodies were diluted in 1% goat serum-PBS, with a 30μl spot of appropriate primary antibody combination pipetted onto parafilm for each coverslip. A list detailing the primary antibodies used is shown in Table 2.4. Coverslips were gently inverted onto the antibody spot, cell side down, and incubated in a moist chamber for one hour at

room temperature. Cells were returned to 3cm Petri dishes (cells facing up) and washed for five minutes, six times in 1% goat serum-PBS, to remove any excess primary antibody. Secondary antibodies raised in goat and conjugated to fluorophores that would specifically target the primary antibody based on the animal it was raised in were used to visualise protein localisation. The secondary antibodies used are detailed in Table 2.5. These were diluted in 1% goat serum-PBS, and spotted onto parafilm as for the primary antibody. Coverslips were again inverted onto these drops, and incubated in a dark, moist chamber for 30 minutes. Following this, cells were again washed for five minutes, four times, to eliminate excess secondary antibody. If also staining for DNA, DAPI (Sigma, Poole, Dorset) was diluted in PBS (1:40,000), and added onto cells for five minutes, followed by three five minute washes in PBS. Samples were then mounted onto slides; coverslips were placed with cells facing upwards, and drops of hydromount (National Diagnostics Hessle, Yorkshire) containing 2.5% (w/v) of 1,4-diazabicyclo[2.2.2]octane (Sigma, Poole, Dorset) (DABCO, used to reduce photobleaching of fluorophores) were added. A long glass coverslip (0.13-0.17mm in thickness) was then gently lowered to cover the samples.

All primary antibodies used were raised in mouse, rat or rabbit. Whilst rat and rabbit or mouse and rabbit antibody combinations were mixed when diluting the primary and appropriate secondary antibodies, where samples were to be stained using both anti-rat and anti-mouse antibodies, a sequential staining procedure was used, in which the immunolabelling procedure was performed separately for each. Before use, primary antibodies were validated to check specificity.

2.6.2.2: 3D culture

3D culture coverslips were fixed in methanol at -20°C for approximately thirty minutes (until the pink coloration from the medium the cells were grown in had been eliminated from the Matrigel^{TM} spots), then washed in 1% goat serum-PBS for 20 minutes three times, transferring coverslips into a dish containing fresh solution

for each wash. They were then moved into a dish containing 1% NP40-PBS for 20 minutes, followed by three further 20 minute 1% goat-serum PBS washes, performed as outlined above. Alternatively, samples were fixed in methanol-formaldehyde at -20°C for approximately one hour (until the pink coloration had been eliminated, as above), then washed in 1% goat serum-PBS containing 0.1% Triton X-100 for 30 minutes three times, once again transferring between dishes for each wash.

Following fixation, cells were blocked in 10% goat serum-PBS for two hours (for methanol-formaldehyde fixed coverslips this blocking solution also contained 0.1% Triton X-100). Samples were stained in 24 well plate wells. Primary antibodies (Table 2.4) were diluted in 1% goat serum-PBS, as previous, and 100μl added to each coverslip, then incubated at 4°C in the cold room overnight. Samples were washed for two hours, changing the wash every 30 minutes, by moving coverslips between dishes. Secondary antibodies were prepared and added as for the primary antibodies, and incubated in the dark at room temperature for two hours. Note that where available alternative highly cross-absorbed secondary antibodies were used (see table 2.5), to reduce the possibility of background fluorescence from the matrix. Samples were washed for 90 minutes, changing the wash every 30 minutes (as above), and then transferred into DAPI (1:40,000, in PBS) for 15 minutes. Coverslips were washed in PBS three further times over a 30 minute time period, and then mounted onto slides by inverting each coverslip onto a drop of hydromount (containing DABCO, as above).

2.6.2.3: Cryostat sections

Cryostat sections were fixed in methanol as for 2D cell cultures. Following fixation, samples were blocked by adding 10% goat serum-PBS to the region encircled by the hydrophobic PAP pen, and incubating for one hour. Primary antibodies were diluted in 1% goat serum-PBS, and after pipetting off the blocking solution, 100μl antibody mix was added to each region, and incubated in a moist chamber in the cold room overnight. Samples were washed in 1% goat serum-PBS

for 10 minutes, six times. Secondary antibodies (including where available highly cross-absorbed antibodies) were diluted in 1% goat-serum-PBS and added to the samples as above, where they were incubated in a moist dark chamber for 1 hour. Following this, samples were again washed for ten minutes, four times, after which DAPI diluted in PBS (1:40,000) was added for ten minutes. After three final 5 minute PBS washes, the remaining liquid was removed and the samples mounted by adding a drop of hydromount to each region and gently lowering a long glass coverslip (0.13-0.17mm thickness) over the samples.

Secondary controls were also taken, where samples underwent the immunolabelling procedure with a particular secondary antibody without the addition of a primary antibody, to ensure staining patterns generated were not due to non-specific staining, or background autofluorescence.

2.6.3: Haematoxylin and eosin (H & E) staining

To understand the histological architecture of cryostat sections, samples were stained with haematoxylin and eosin. Tissue samples that had been cryostat sectioned and fixed in methanol were transferred into Mayers haematoxylin solution (Sigma, Poole, Dorset) for five minutes, and then washed in running tap water for twenty minutes. Slides were then placed in 0.1% eosin (Raymond A Lamb, Eastbourne, Sussex) for two minutes, followed by a further quick wash in tap water. Samples were then dehydrated by being added to each concentration of an ascending ethanol sequence (30%, 50%, 70%, 95% and 100%) for two minutes per concentration, after which they were transferred to Histochoice® clearing agent (Sigma, Poole, Dorset) for ten minutes. Finally, samples were mounted by adding a few small drops of DPX mounting medium (Sigma, Poole, Dorset), and gently lowering a long thin glass coverslip on top.

Primary Antibody	Raised In	Source	Dilution *
ACF7	Rabbit	Sigma (Poole, Dorset) (HPA013713)	IF: 1:100
APC	Mouse	Abcam (Cambridge, Cambridgeshire) (ab58)	IF, WB: 1:500
α-tubulin	Rabbit	Abcam (ab15246)	IF: 1:100, 3D: 1:50
Tyrosinated tubulin (YL1/2)	Rat	AbD Serotec (Kidlington, Oxfordshire) (MCA77G)	IF: 1:200
Detyrosinated tubulin	Rabbit	Abcam (ab48389)	IF: 1:200, WB: 1:500
Acetylated tubulin	Mouse	Sigma (T6793)	WB: 1:500
β-actin	Rabbit	Abcam (ab8227)	IF: 1:100, WB: 1:10000
β-catenin	Mouse	BD Biosciences (Oxford, Oxfordshire) (610153/4)	IF: 1:500
β-catenin	Rabbit	Sigma (C2206)	IF: 1:2000
EB1	Mouse	BD Biosciences (610535)	IF, WB: 1:500
EB1	Rabbit	Abcam (ab50188)	IF: 1:2000
EB2 (KT52)	Rat	Abcam (ab45767)	IF, WB: 1:200
E-Cadherin	Mouse	BD Biosciences (610181)	IF, 3D: 1:200
GFP	Mouse	Sigma (G6539)	IF: 1:500
γ-tubulin	Mouse	Abcam (ab11316)	IF: 1:1000
γ-tubulin	Rabbit	Abcam (ab16504)	IF: 1:1000
IQGAP1	Mouse	BD Biosciences (610611/2)	IF: 1:200
KIF17	Rabbit	Abcam (ab11261)	IF: 1:200
Ninein	Rabbit	Abcam (ab52473)	IF: 1:500, 3D: 1:250
Ninein (Pep3)	Rabbit	Made in Lab (M.Mogensen)	IF: 1:1000
Pericentrin	Rabbit	Gift: S. Doxsey (UMASS Medical School)	IF: 1:1000
RFP	Mouse	Abcam (ab65856)	WB: 1:1000
ZO-1 (R40.76)	Rat	Santa Cruz (Dallas, Texas, USA) (sc-33725)	IF: 1:200
* IF = Immunofluorescence, WB = Western Blot, 3D = 3D Culture			

Table 2.4 Detailed list of primary antibodies

Secondary Antibody	Raised Against	Source	Dilution
Alexa 488	anti-RAT IgG	Invitrogen Molecular Probes (Paisley, Scotland)	1:1000
	anti-RABBIT-IgG		
	anti-MOUSE-IgG		
Alexa 568	anti-RAT IgG		
	anti-RABBIT-IgG		
	anti-MOUSE-IgG		
Alexa 647	anti-RAT IgG		
	anti-RABBIT-IgG		
Cy5	anti-MOUSE-IgG	Jackson (Stratech, Newmarket, Suffolk)	1:500
Alexa 488 (highly cross-absorbed)	anti-RAT IgG	Jackson	1:500
	anti-MOUSE-IgG		
Alexa 647 (highly cross-absorbed)	anti-RABBIT-IgG		
HRP conjugated	anti-RAT IgG	Sigma (Poole, Dorset)	1:1000 – 1:10000
	anti-RABBIT-IgG		
	anti-MOUSE-IgG		

Table 2.5 Detailed list of secondary antibodies.

Note: all secondary antibodies were raised in goat.

2.7: Microscopy

2.7.1: Widefield

Fixed cells and tissue were imaged on a widefield upright Zeiss Axiovert 200M microscope with images captured using a monochrome CCD camera (immunofluorescence) or colour CCD camera (H&E sections). Fluorescence was detected using a 100W mercury lamp and dichroic mirror filter sets. Axiovision software (Zeiss) was used to generate multichannel images, with Photoshop CS2/7.0 (Adobe) used for further image processing.

2.7.2: Confocal

Immunolabelled cells and tissue were imaged using an inverted Zeiss LSM510 META scanning confocal microscope. Samples were excited using appropriate lasers: Enterprise UV (364nm) for DAPI, Argon (488nm) for Alexa 488 fluorophores, Helium/Neon (HeNe1, 543nm) for Alexa 568 fluorophores, and HeNe2 (633nm) for Alexa 647/Cy5 fluorophores. The pinhole was set to 1 for the channel with the highest wavelength, with the pinhole for other channels then set accordingly. Images were captured using Zeiss LSM software using unidirectional scan mode, with scan speed and number optimised for each image. Images were further processed in Volocity (Improvision) and Photoshop CS2/7.0 (Adobe) software.

For analysis of spindle orientation, Z stacks were taken at twice the optimal frame size and half the optimal slice interval (0.18μm). Images were deconvolved using a theoretical point spread function in Huygens (Scientific Volume Imaging) software, with FIJI (Image J) software used to further process images, and measure distance and angle between spindle poles. Prism (Graphpad) software was used to prepare graphs and perform statistical analysis.

2.7.3: Live Imaging

Live time-lapse microscopy was performed using a Zeiss Axiovert inverted microscope, with samples maintained in a sealed chamber containing 5% CO_2 at 37°C on a heated stage. Time-course experiments were set up using Axiovision (Zeiss) software with images captured using a monochrome CCD camera.

For experiments requiring low powered imaging (using the x10 or x20 objectives) over an extended time period (i.e. cell division analysis and migration and scratch assays), cells were seeded in multiwall plates and phase contrast images captured every ten minutes over the experimental time period from several positions for each experimental condition. Where required, fluorescence was detected using a 100W mercury lamp and dichroic mirror filter sets.

For live imaging of microtubule dynamics, GFP-α-tubulin expressing ARPE-19 cells treated with appropriate conditions were grown in glass bottomed 3cm dishes (MatTek, Ashland, Massachusetts, USA), allowing the use of an oil immersion x63 objective lens. Cells were maintained in phenol red free DMEM/F12 (Invitrogen, Paisley, Scotland) supplemented as outlined in table 2.1. Images were captured at set exposure levels every three seconds over a three minute time period. Several areas were imaged for each condition. The light required to excite the GFP was provided by a high powered LED light source, to allow rapid switches on and off without the need for opening and closing a shutter, thus allowing a short interval between successive frames.

2.7.3.1: Microtubule Dynamics Analysis

For analysis of microtubule dynamics, 12.5 x12.5 μm regions for each condition to be analysed were selected and processed in FIJI (Image J) software. Briefly, areas were treated with the unsharp mask filter, smoothed, inverted and the brightness and contrast adjusted. The length of microtubules in each frame for each region was measured, and the change in length between adjacent frames used to score as to whether a microtubule underwent a pausing, shrinking or growing event.

Movements were classed as growing or shrinking if the change in length between frames was ≥0.5μm (the approximate width of microtubule fluorescence), otherwise the event was classified as paused. For each microtubule, the percentage of time spent growing, shrinking and pausing was calculated, and the average time spent in each state recorded for all the microtubules in a particular area. Five cells were analysed for each condition and the average percentage of microtubules in a growing, shrinking or paused state at a particular moment calculated. Prism (Graphpad) software was used to prepare graphs and perform statistical analysis.

2.8: Migration & Invasion Assays

2.8.1: Sparse cell tracking

Cells were seeded sparsely (typically at 100,000 cells per well) in six well plates. Several regions for each condition were tracked by live time-lapse microscopy, with images gathered every 10 minutes over a 16 hour time period.

For each condition, the position of individual cells across several regions was tracked at each timepoint in FIJI (Image J), which was also used to prepare combined tracking traces illustrating all paths tracked for each condition analysed, and to calculate the average velocity for each cell. Data analysis and graph preparation was performed in Prism (Graphpad) software.

2.8.2: Scratch assays

Cells for each condition were seeded into 24 well plate wells, and allowed to grow to confluency, at which point they were treated with 2mM thymidine to block cell division. After allowing 24 hours for the thymidine to take effect, a single scratch was made to the sheet of cells in each well with the end of a P200 pipette tip. Regions of each scratch were imaged by live time-lapse microscopy, with images gathered every 10 minutes over a 16 hour time period.

For each scratch, analysis occurred at t=10 hours, as beyond this point the two halves of some scratches had closed. The area of scratch at the start and end of this time period was measured for each region in Axiovision software (Zeiss), and used to calculate the average area of closure for each condition. In addition, 8 cells from each region were tracked over the experimental period in FIJI (Image J) software as for the sparse cell tracking experiments, and used to calculate the average speed of cell movement at the leading edge of each region, and in turn the mean velocity of cells across each condition. Further analysis and graph preparation was performed in Prism (Graphpad) software.

2.9: Construct Generation

Mouse EB2 was cloned from the mIMCD-3 cell line and inserted into the multiple cloning site (MCS) of the pmCherry-C1 vector (Appendix B, 4).

2.9.1: Total RNA extraction

mIMCD-3 cells were seeded in a 6 well plate at 1 million cells per well, and allowed to settle for 24 hours. The cells were quickly washed in PBS, and then each well was treated with 1ml TRIzol reagent (Invitrogen, Paisley, Scotland) for 5 minutes. Cells were scraped and the contents of each well transferred to separate 1.5ml eppendorf tubes. 200μl chloroform was added to each tube, mixed, and spun at 12000 x g for 10 minutes. This process causes the samples to separate into three layers, with the total RNA content of the cells contained in the upper, aqueous phase. This phase was transferred to a fresh tube for each sample, and 500μl isopropanol added, and incubated a room temperature for 10 minutes, to allow the RNA content to precipitate. Tubes were spun at 12000 x g for 10 minutes at 4°C and the supernatants removed, after which 1ml 75% ethanol was added and vortexed to mix. Tubes were then spun at a maximum of 7500 x g for 10 minutes at 4°C and the supernatants removed. The samples were allowed to air dry for 10 minutes, then dissolved in 20μl nuclease free water by heating at 55°C for 10 minutes. RNA concentration was measured on a Nanodrop ND-1000 spectrophotometer, and samples stored at -20°C.

2.9.2: PCR

2.9.2.1: Primers

Primers were designed to clone each of the three mouse EB2 transcript variants (Appendix B, 5-6). Basic primers (without restriction sites) were used for initial checking of which variant was expressed in mIMCD-3 cells, after which primers

designed to allow the restriction digestion and ligation in frame into the XhoI (forward primer) and HindIII (reverse primer) sites of the pmCherry-C1 vector were used. Primers were purchased from Sigma, and used as a 10μM stock. The sequences of the primers used are shown in table 2.6.

Basic Primers	**Sequence** (5' -> 3')
mEB2RevBAS	TCAGTACTCCTCCTGCTGCT
mEB2ForV1BAS	CAATGCCCGGGCCGACCCAAAC
mEB2ForV2BAS	GGATGAAACAGATCAGAGATCA
mEB2ForV3BAS	GAATGGCGGTCAATGTGTATTC
Restriction Primers	
mEB2RevRD	CCCAAGCTTTCAGTACTCCTCCTGCTGCT
mEB2ForV3RD	CCGCTCGAGGAATGGCGGTCAATGTGTATTC

Table 2.6 Sequence of PCR primers for the cloning of mouse EB2.

2.9.2.2: RT-PCR

RT-PCR was performed using the Superscript-II Reverse Transcriptase Kit (Invitrogen, Paisley, Scotland) and generic primers, to produce a cDNA library for mIMCD-3 cells from the total RNA extract.

The following reaction mix was produced:

1μl 10μM dNTPs

1μl RNAse inhibitor

1μl 10μM generic primer

5μg RNA

This was made up to 13μl with nuclease free water, and the primer annealed to the template by heating at 65°C for 5 minutes, after which the samples were immediately transferred to ice. 4μl First Strand Buffer and 2μl 0.1M Dithiothreitol (DTT) were added to the samples and left at room temperature for 5 minutes, after

which 1μl Superscript enzyme was added. Mixes were heated at 42°C for 2 hours, after which the enzyme was inactivated by heating at 72°C for 15 minutes. Samples were stored at -20°C.

2.9.2.3: GoTAQ PCR

Taq PCR was performed using the GOTAQ PCR Kit (Promega, Southampton, Hampshire) using basic primers, to determine which EB2 transcript variant was expressed in the mIMCD-3 cell cDNA library.

The following 50μl reaction mix was produced for each transcript variant:

10μl 5x GoTAQ Flexi buffer

8μl 25mM $MgCl_2$

1μl dNTP mix (10mM of each dNTP)

0.5μl GoTAQ Polymerase

2μl 10μM basic forward primer (Table 2.6)

2μl 10μM basic reverse primer (Table 2.6)

DNA template (mIMCD-3 cDNA library)

Nuclease free water (to make up to 50μl total)

This was run through the following thermocycle:

Initial denaturation: 2 minutes @ 94°C

Denaturation: 30s @ 94°C
Annealing: 30s @ 60°C
Extension: 30s @ 72°C
} x35

Final Extension: 5 minutes @ 72°C

Hold: @ 4°C

On completion, samples were stored at -20°C.

2.9.2.4: High fidelity PCR

After identifying which EB2 transcript variant is present in the cDNA library, high fidelity PCR was performed with restriction primers using the Expand High Fidelity PCR System (Roche, Burgess Hill, Sussex) to accurately synthesise the required insert from the cDNA library.

Two reaction mixes were prepared:

Enzyme Mix:

5μl 10x Buffer (containing $MgCl_2$)

0.75μl Expand High Fidelity Enzyme

19.25μl Nuclease Free Water

DNA Mix:

1μl 10mM dNTPs

250ng cDNA template (mIMCD-3 cDNA library)

1μl 10μM restriction forward primer (Table 2.6)

1μl 10μM restriction reverse primer (Table 2.6)

21μl Nuclease Free Water

The DNA and enzyme mixes were combined and run through the same thermocycle as outlined above for GoTAQ PCR. Samples were stored at -20°C

2.9.3: Agarose gel electrophoresis

Samples were run on 1% agarose gels containing 0.2μgml^{-1} Ethidium bromide, made up in 1x TAE buffer diluted from a 50x TAE stock solution (Appendix A). Samples were mixed with 6x loading buffer (0.25% w/v bromophenol blue, 30% glycerol) and loaded into wells of the gel, along with a 1kb DNA ladder (Invitrogen, Paisley, Scotland). Gels were run in 1x TAE buffer at a constant 100V, until the

loading dye reached ¾ of the way down the gel. UV images were taken of the DNA banding pattern.

2.9.4: Gel purification

DNA was purified from agarose gels using the QIAEX II Gel Extraction Kit (Qiagen, Manchester, Greater Manchester). The appropriate bands were excised from an agarose gel under UV light, and 3 gel volumes of buffer QXI were added, along with 30μl QIAEX II beads and 10μl Sodium acetate. The tubes were incubated at 50°C for 10 minutes to dissolve the agarose, vortexing regularly to keep the beads in suspension. The tubes were centrifuged for 30s at maximum speed (16,100 RCF) in a tabletop centrifuge, and the supernatant removed. The beads were washed a further time with buffer QXI and twice with 500μl buffer PE, centrifuging and removing the supernatant as above between each wash. After the final wash, the beads were allowed to air dry for 30 minutes, then 20μl nuclease free water added and incubated at 50°C for 5 minutes to elute the DNA. The samples were spun as previously, and the supernatant containing the DNA transferred to a fresh eppendorf tube. The elution step was repeated on the remaining beads, to ensure maximum recovery, and the concentration of DNA measured by Nanodrop.

2.9.5: Ethanol precipitation

Ethanol precipitation preparations were carried out when DNA was of insufficient purity for purpose, or to concentrate DNA. A tenth of the sample volume of 3M Sodium acetate and 2.5x the sample volume of 100% ethanol were added and the sample transferred to the -20°C freezer for 15 minutes, before being spun at maximum speed (16,100 RCF) in a tabletop centrifuge for 15 minutes. The supernatant was decanted off, and the sample allowed to air-dry for 30 minutes. An appropriate volume of nuclease free water was added to dissolve the purified DNA, and the sample stored at -20°C.

2.9.6: Restriction digests

DNA was restricted using XhoI and HindIII restriction enzymes (Roche, Burgess Hill, Sussex) using the following reaction conditions. Total reaction volume varied between 20-50μl:

DNA: 1-5μg

XhoI: 0.5μl (5 units)

HindIII 0.5μl (5 units)

10x Surecut Buffer B: 2-5μl (according to total volume)

Nuclease free water: up to final reaction volume

Reactions were incubated in a 37°C waterbath overnight, and stored at -20°C.

2.9.7: pGEM®-T ligation

Initial attempts to directly restrict and ligate the high fidelity PCR product into the pmCherry-C1 expression vector were unsuccessful, so instead it was ligated into the pGEM®-T carrier vector (Appendix B, 3) using the pGEM-T® Easy Vector Systems kit (Promega, Southampton, Hampshire).

The following reaction mix was prepared:

4μl high fidelity PCR product

1μl (50ng) pGEM®-T vector

5μl 2x rapid ligation buffer

1μl (3 units) T4 DNA Ligase

This mix was incubated at room temperature for 1 hour, and then used to transform bacteria. A control mix containing water rather than the PCR product was also prepared.

2.9.8: DNA ligation

Gel extracted EB2 cDNA insert restricted from the pGEM®-T carrier vector was ligated into digested pmCherry-C1 (Clontech, Saint Germain en Laye, France) using Ready-To-Go T4 DNA ligase (Amersham, Little Chalfont, Buckinghamshire). Vector and insert were mixed at an approximate 1:4 ratio in a total final volume of 20μl, which was added to a vial of Ready-To-Go T4 DNA ligase, and left at room temperature for one hour. A control mix containing water rather than insert was also prepared. Both were used to transform bacteria.

2.9.9: Bacterial transformation

High (10^8) or Max (10^9) Efficiency DH5α *E. coli* were transformed by adding the ligation mixes (including control reactions) to 50μl aliquots of bacteria and incubating on ice for 20 minutes. Samples were then heat-shocked in a heat block at 42°C for 30s, transferred back to the ice for 1 minute, and 250μl SOC medium added. Samples were incubated in the shaking incubator for 1 hour before being plated onto a kanamycin (at 20μgml^{-1}) or ampicillin (at 100μgml^{-1}) resistance LB agar (Appendix A) plate (depending on the resistance gene of the plasmid the bacteria were transformed with) at an appropriate density (according to the expected efficiency of the transformation), and incubated at 37°C overnight. Transformations involving pGEM-T were performed on blue-white ampicillin resistance plates. Plates were stored at 4°C.

2.9.10: Plasmid preparation

Several transformed colonies were selected for analysis. Initially, cultures were grown and mini-prepped to isolate plasmids. These were then restricted and run on an agarose gel to check for presence of the insert. Several insert positive clones were verified by sequencing, then prepared on a large scale for use in experiments by midi-prep.

2.9.10.1: Mini-Prep

Mini preps were performed using the Wizard Plus SV miniprep DNA Purification System (Promega, Southampton, Hampshire). Potential colonies were grown in a 2ml starter culture (in LB, see Appendix A) containing appropriate antibiotics for 6 hours in the shaking incubator at 37°C, then 50μl was transferred to 3ml LB containing antibiotics, and grown overnight in the shaking incubator at 37°C.

The resulting culture was spun at 10000 x g for 5 minutes and the supernatant discarded. Pellets were resuspended in 250μl cell resuspension solution, after which 250μl cell lysis solution was added and inverted to mix. The samples was incubated for up to 5 minutes to allow the sample to clear, and 10μl alkaline protease added for a maximum of 5 minutes, followed by 350μl of neutralisation solution. The samples were then spun at maximum speed (16,100 RCF) in a tabletop centrifuge for 10 minutes.

The lysates produced were decanted into a spin column in a collection tube, and spun at maximum for 1 minute. The flow-through was discarded. The column was washed with 750μl, and then 250μl column wash solution (CWS) and spun as previously. A final spin of 2 minutes at maximum speed dried the column, after which it was transferred to a fresh eppendorf tube. 100μl nuclease free water was added to elute the DNA, and the column spun at 16,100 RCF for 1 minute. DNA concentration was measured by nanodrop, and the samples stored at -20°C.

2.9.10.2: Midi-Prep

Midi preps were performed using the HiSpeed Plasmid Midi kit (Qiagen, Manchester, Greater Manchester). Potential colonies were grown in a 10ml LB starter culture containing appropriate antibiotics for 6 hours in the shaking incubator at 37°C, then 500μl was transferred to 100ml LB (with antibiotics), and grown overnight in the shaking incubator at 37°C. The resulting culture was spun at 600 x g for 15 minutes at 4°C. Pellets were resuspended in 6ml of cold buffer P1, and 6ml of buffer P2 was added and the sample vigorously mixed and incubated for 5 minutes.

6ml of Buffer P3 was added, the sample was vigorously mixed and immediately transferred into a QIA filter cartridge, and incubated at room temperature for 10 minutes. After this, the sample was filtered through the cartridge into an equilibrated HiSpeed Tip, and allowed to pass through (DNA binds to the tip). The tip was washed with 20ml of buffer QC, and then eluted into a 50ml tube with 5ml of buffer QF. 3.5ml of isopropanol was added to the eluted DNA, and incubated for 5 minutes, then transferred to a syringe. A QIAprecipitator Midi module was attached, and the eluate filtered away. 2ml 70% ethanol was added to the syringe, and filtered through the module, followed by fresh air twice, to dry the cartridge. 1ml Nuclease free water added and filtered through the precipitator module, then transferred back and filtered through for a second time to ensure maximum elution of DNA. DNA concentration was analysed by Nanodrop, and the sample stored at -20°C.

2.9.11: Sequencing

Genome Enterprise Ltd., Norwich, performed sequencing of plasmids believed to contain the mEB2 insert, with samples prepared according to specified instructions. pGEM®-T clones were sequenced from either end using T7-20mer or SP6 primers provided by the sequencing company. pmCherry-C1 clones were sequenced starting at a point towards the end of the mCherry region and going through the insert, using the pmCherryC1_1215_Forseq primer (kindly provided by P. Powell, UEA, Norwich). This was particularly important to ensure the insert correctly orientated and in frame with the end of the mCherry sequence. Primer sequences are shown in Table 2.7.

Sequencing Primer	**Sequence** (5' -> 3')
T7-20mer	TAATACGACTCACTATAGGG
SP6	GATTTAGGTGACACTATAG
pmCherry_C1_Forseq	CATCAAGTTGGACATCACCTCC

Table 2.7 Details of sequencing primers.

2.10: Western Blotting

2.10.1: Cell lysis

100x Halt Protease/Phosphatase inhibitor cocktail (Pierce, Cramlington, Northumberland) was diluted into cell lysis buffer (Appendix A). Cells grown in multiwall plates or tissue culture flasks were rinsed with ice cold PBS and then lysed for thirty minutes on ice. 500μl lysis buffer was added to a T75 flask, whilst 100μl was added to a six well plate well. Every 15 minutes during lysis cells were scraped, with lysates then transferred to an eppendorf tube. Samples were spun at maximum speed (16,100 RCF) in a table top centrifuge at 4°C and the supernatant transferred to a fresh eppendorf, with the cell pellet discarded.

2.10.1.1: Polarisation sequence

For mIMCD-3 polarisation sequences, cells were seeded in six well plate wells, with lysates taken at several time points over a nine day period. At early time points, cells were still very sparse, therefore to ensure that lysates were of sufficiently high protein concentration for use, several plates were lysed in sequence (with the lysate from one plate being transferred to an equivalent well on the next). For day 3 lysates, three six well plates were lysed sequentially (100μl per well, 600μl lysate in total), whilst similarly for day 5 lysates two plates were processed. Days 7 and 9 had a single six well plate for each day, which was lysed as standard.

2.10.2: Protein quantification

Protein concentration was calculated using the BCA protein assay (Pierce, Cramlington, Northumberland). This is based on preparing several bovine serum albumin (BSA) standards, ranging from 0-2000μg/ml in concentration, diluted in lysis buffer. 40μl water was added to each well required in a 96 well plate. 10μl of each standard and each sample to be analysed were added to separate wells, in triplicate

for each. 200μl of working reagent (composed of 1 part reagent B diluted in 50 parts reagent A) was added to each well, and the plate incubated for 1 hour at 37°C. Absorbance readings at 550nm were taken on a spectrophotometer, with the curve generated from the BSA standards used to calculate the protein concentrations of the cell lysates measured.

2.10.3: SDS-PAGE electrophoresis

Cell lysates for each condition to be analysed were diluted in ddH_20 based on the concentrations calculated in the BCA assay, such that each sample contained equal protein content in a total volume of 40μl. To these diluted lysates, 10μl of 5x sample buffer (Appendix A) containing 12.5% β-mercaptoethanol was added, and the tubes heated at 95°C in a heat block for 1 minute.

Gels were prepared between spaced glass plates by adding a 6-8% lower resolving gel (Appendix A), and allowing this to set before adding a 5% upper stacking gel (Appendix A) and spacing comb, which was removed once the upper gel had set. Once made, gels were transferred to a mini-protean II tank (BioRad, Hemel Hempstead, Hertfordshire), which was filled with 1x SDS running buffer, diluted in ddH_2O from a 10x stock (Appendix A). The prepared samples along with 10μl of prestained protein ladder (BioRad, Hemel Hempstead, Hertfordshire) were loaded into separate wells of the gel, and electrophoresis was performed using a constant current of 30mA per gel, until the sample buffer had migrated towards the bottom of the gel.

2.10.3.1: Protein transfer

Once electrophoresis was completed, gels were moved into transfer buffer (Appendix A), along with nitrocellulose membrane (BioRad, Hemel Hempstead, Hertfordshire) and two thick pieces of filter paper (BioRad, Hemel Hempstead, Hertfordshire), which were all allowed to equilibrate for 10-15 minutes. Proteins

were transferred to the membrane using a semi-dry transfer cell (BioRad, Hemel Hempstead, Hertfordshire). Following the equilibration period, a sandwich was assembled on the apparatus, with a piece of filter paper at the very bottom, followed by the nitrocellulose membrane, then the gel, with the other piece of filter paper at the top. Each layer was rolled prior to the addition of the next, to eliminate air pockets between layers. Transfer was performed at a constant 15V for a 35 minute period.

2.10.4: Protein detection

After transfer, the membranes were processed for immunoblotting. Following an initial quick wash in 0.5% (w/v) dried milk powder (Oxoid, Basingstoke, Hampshire) in PBS-T (Appendix A), membranes were incubated in 5% (w/v) milk PBS-T on the rocker for either two hours at room temperature, or overnight in the cold room.

2.10.4.1: Antibody probing

Primary antibodies (see table 2.4) were diluted in 1ml of 0.5% milk PBS-T and added to a plastic bag containing the membrane that was then heat sealed and transferred to the cold room rocker for incubation overnight. The next morning, membranes were washed on the rocker at room temperature for 10 minutes, three times in 0.5% milk PBS-T. HRP-conjugated secondary antibodies were diluted in 10ml of 0.5% milk PBS-T, and added to appropriate membranes for 1 hour on the rocker at room temperature. Remaining excess antibody was again removed over three 10 minute washes in 0.5% milk PBS-T on the rocker at room temperature.

2.10.4.2: Immunodetection

Antibodies were detected using home made electrochemical luminescence (ECL) solutions (Appendix A). ECL solution A was mixed with ECL solution B and added to the membrane for one minute. Excess solution was removed and the membrane transferred to a cassette lined with cling-film. In the dark room, Hyperfilm ECL photographic film (Amersham, Little Chalfont, Buckinghamshire) was applied to the encased membrane for an appropriate exposure time and developed in a Xograph.

2.10.4.3: Re-probing

If wanting to examine levels of an additional protein (most commonly β-actin as a loading control), membranes were stripped and reprobed. To strip, 10x re-blot solution (Chemicon, Watford, Hertfordshire) was diluted in ddH_2O and applied to membranes for 20-25 minutes. Residual solution was washed off by adding 0.5% milk PBS-T for 5 minutes, 3 times, and desired primary antibodies applied. The protocol was then repeated as described for the first probing.

2.11: Cell Cycle Analysis

Cell cycle analysis was performed by flow cytometry. Cells for each condition were grown in six well plate wells, trypsinised, and spun down at 800 RCF for 5 minutes. Pellets were washed by resuspending in 1ml PBS and transferring to an eppendorf tube. Samples were spun at 100 RCF and the supernatant removed. Cells were resuspended in 300μl PBS, after which 700μl ice cold ethanol was added. Tubes were mixed by running over a rack and transferred to the -20°C freezer overnight.

Staining cocktail was prepared in PBS consisting of RNase A at a final concentration of 0.1mg/ml, Triton X-100 at a final concentration of 0.1% and Propidium iodide (PI) (Sigma, Poole, Dorset) at a final concentration of 20μg/ml. Cells were spun down at 100 RCF and the supernatant removed. Pellets were washed by resuspending in 1ml PBS, then spinning down and removing the supernatant. Samples were stained by resuspending each pellet in 200μl PI staining cocktail and incubated in the dark at 37°C for thirty minutes. PI fluorescence to assess DNA content was measured on an Accuri C6 flow cytometer. Analysis was performed in FloJo software, using the Watson Pragmatic model to fit distribution data to cell cycle phases, taking care to gate around the singlet population (and thus excluding any pairs or aggregates of cells that are stuck together). Further analysis and graph preparation was performed in Prism (Graphpad) software.

2.12: Statistical Analysis

Preparation of graphs and statistical analysis was performed in Graphpad (Prism) software. Two-tailed unpaired t-tests were used to compare the statistical significances of the differences between two groups. Where there was a difference in variance between the two data sets an unpaired t-test with Welch's correction was used. For experiments with multiple groups, a one-way ANOVA was performed using the Tukey's multiple comparison post-hoc test to assess the significance of any differences between two separate groups within the data set. Where data were gathered examining the proportion of cells in particular categories, a chi-squared test for interdependence was used to determine whether differences in these proportions between separate conditions was significant. For all tests, differences were regarded as significant where $p<0.05$.

Chapter III

Characterisation of Human Tissue Samples

3.1: Introduction

The innermost layer of the colon lumen is folded into distinctive crypts lined by a single cell thick sheet of apico-basally polarised columnar epithelial cells. These undergo rapid turnover, originating from stem cells at the bottom of each crypt. As they migrate away from the stem cell zone up to the surface epithelium, cells differentiate and polarise, initially as proliferative progenitor cells capable of mitosis before becoming fully differentiated by the uppermost third of the crypt. Once at the surface, cells undergo apoptosis and are shed into the lumen of the gut (Figure 1.9 C) (Sancho et al., 2004; van der Flier and Clevers, 2009). Colonic crypts are therefore an excellent model system to study differentiation processes in epithelial cells, and particularly promising for investigating the organisation and development of polarised apico-basal microtubule arrays.

Colorectal cancers originate from these crypt epithelial cells, gradually accumulating mutations as they progress along the adenoma-carcinoma sequence to develop into a malignant neoplasm, before eventually undergoing metastasis and infiltrating distant sites (Fearon and Vogelstein, 1990). A common mutation present in almost all colorectal tumours is the truncation of APC, a protein linked to Wnt signalling, but which is also an important +TIP implicated in epithelial polarisation, in addition to several other cytoskeletal roles (Hanson and Miller, 2005).

The highly organised apico-basal microtubule cytoskeleton of crypt epithelial cells is characterised by relocation of the centrosome to apical regions and the accompanying reorganisation of the microtubule array into bundles anchored by the minus end at non-centrosomal apical sites, with plus ends extending into basal regions (Mogensen, 1999). It is a particularly interesting subject for study in terms of a possible role in cancer due to the importance of the microtubule array in establishing cell polarity during differentiation (Cohen et al., 2004). Disruption of array formation could therefore potentially contribute to the development of neoplastic characteristics, in particular the loss of polarity, dedifferentiation, and the transition to a mesenchymal invasive phenotype via EMT (Polyak and Weinberg, 2009). It is therefore important to investigate microtubule organisation and the

mechanism of array formation in cancer cells, including associated microtubule interacting factors.

The formation of the non-centrosomal apico-basal microtubule array has been proposed to be driven by a release and capture mechanism (see section 1.5.3, Figure 1.7). This process is particularly associated with the redeployment of the minus end anchoring protein ninein to apical junctional sites, following initial centrosomal microtubule nucleation. This allows microtubule minus end release from the centrosome, followed by subsequent translocation of the plus end to basal regions and minus end capture by the relocated ninein at these non-centrosomal sites (Bellett et al., 2009; Moss et al., 2007). As previously outlined, there are several steps in the process, and it may be vital that all steps occur successfully to avoid array disruption in colorectal cancers. One of these key steps involves the cortical capture of microtubule plus ends in the intermediate extended radial array.

To fully understand the effects of any potential microtubule reorganisation in disease states we must develop a better understanding of the controlling mechanisms and key interactions in the release and capture mechanism under normal conditions, and then examine the process in cancer models. In particular, is there any evidence of mislocalisation of the key proteins in the release and capture mechanism (such as ninein) in cancer cells and tissues, and if so is there any change in microtubule array organisation?

Most studies in the development of the release and capture model have taken place in tissue culture systems, however, to examine the questions outlined above it is important to directly observe the internal cytoskeletal organisation of cells from both normal and diseased tissue samples. Work from a previous project involved the immunolabelling of paraffin embedded human tissue samples from healthy people and patients with FAP. These successfully demonstrated that apico-basal microtubule arrays were present in human colon epithelial tissue, and provided insight into the gross morphological changes triggered in FAP tissue such as crypt fusions, along with indications in some regions that apico-basal microtubule polarity could be disrupted (Keynton, 2011). Unfortunately, whilst paraffin sections

provide excellent tissue preservation, the fixation often leads to loss of antigenicity for certain proteins (Shi et al., 1991), including the majority of those of interest to the lab. Previous attempts at antigen retrieval in such cases have proved ineffective (Jennifer Keynton, personal communication).

An important initial objective in this project was therefore to develop an immunolabelling technique for frozen human tissue samples excised from normal and cancerous regions. Unfixed frozen surgical samples were obtained from the tissue bank, and sectioned using a cryostat, after which they were fixed in methanol and immunolabelled for various proteins of interest. Additionally, haematoxylin and eosin (H & E) staining was also performed to assess overall tissue architecture in the different samples. Initially, healthy control tissue was used to optimise the cryostat and staining procedures, whilst later matched pairs of apparently normal versus tumour tissue were obtained from colorectal cancer patients and used for comparison.

The results gathered from these various investigations are outlined in this chapter. Briefly, immunolabelling procedures were developed that proved effective for some relevant proteins (generally junctional and centrosomal targets, including importantly ninein). Specifically, the centrosomal proteins ninein and γ-tubulin were localised to the apical surface of crypt epithelial cells. These techniques were then used to investigate two tumour tissue samples, the second of which in particular demonstrated a great degree of gross tissue architectural change. Results from control samples as described in this chapter are included in (Goldspink et al., 2013a, manuscript in preparation).

3.2: Results

3.2.1: Immunolabelling of normal frozen human colon tissue samples

Techniques for cryostat tissue sectioning and cytoskeletal protein immunolabelling were developed using control tissue samples. Initially, frozen samples were sectioned by cryostat and a selection of methanol based fixatives trialled. Simple treatment with 100% methanol at -20°C for 5 minutes was ultimately found to give the most effectively fixed sections. Despite this, staining was generally inconsistent, with tissue sections extremely prone to damage. Additionally, there was evidence in some samples of autofluorescence, particularly in green and red filter channels (data not shown). Several antibodies were trialled for effectiveness, including those targeting APC and microtubules, however overall only antibodies against the junctional proteins β-catenin and E-cadherin, and the centrosomal proteins ninein and γ-tubulin were consistently effective.

Samples sectioned transversely through crypts and immunolabelled for ninein and β-catenin revealed ninein localised in distinct puncta in apical regions of crypt cells (Figure 3.1 A). Co-labelling of ninein with γ-tubulin revealed ninein dots colocalising with the γ-tubulin at centrosomal sites, but with further additional ninein staining in these apical regions not linked to γ-tubulin (Figure 3.1 B).

Sections were also labelled for secondary antibodies only to act as a control, confirming that the fluorescent patterns observed were due to staining of the target proteins rather than due to any non-specific labelling (Figure 3.1 C).

3.2.2: Analysis of cancer patient matched paired tissue samples

Two separate matched pairs of cancer patient tissue samples were analysed. Matched pairs consist of a sample derived directly from the colon tumour, and a control region from an area of epithelium adjacent to the tumour site, but apparently free of cancer cells.

Control tissue from the first sample (sample A) was cryostat sectioned, fixed and subjected to H & E staining. The transversely sectioned regions presented illustrate normal tissue architecture, with crypts appearing as a circular single layer of cells. Crypts were clearly distinct from each other and fairly evenly spaced, separated by regions of connective tissue (Figure 3.2 A). Samples for immunofluorescent labelling were sectioned longitudinally through crypts. The base of a crypt labelled for β-catenin and ninein is illustrated (Figure 3.2 B). Ninein is localised throughout the region in the same pattern of distinct points at the apex of cells as seen in the transverse sections from the previous control sample (Figure 3.1).

The matched pair tumour sample from the first patient was also sectioned and H & E stained. The overall tissue architecture was similar to that of the control region, with crypts once again consisting of a single layer of epithelial cells. There was evidence of disorganisation and a possible increase in cell density within regions of connective tissue, with crypts less evenly spaced and some evidence of crypt merging or incomplete fission (Figure 3.3 A). Samples were immunolabelled for β-catenin and ninein, with ninein localisation generally similar to that seen in the control sample. However, as illustrated in the 3D reconstruction through a longitudinal region of the base of a crypt, the ninein dots appeared in places to have moved down from the very apex, instead appearing in a location mid way down the cells imaged (Figure 3.3 B).

The control region of the second sample (sample B) had similar overall architecture to the other control regions images (data not shown). Sections were immunolabelled for ninein and the junctional protein E-cadherin. Presented is a confocal longitudinal section through the base and mid region of a single representative crypt, illustrating the previously observed pattern of ninein dots in the apical regions of cells. In places where a transverse section had been cut through the very top of a cell, single central ninein dots could be seen, suggesting centrosomal organisation. Ninein speckles located in the cytoplasm were also apparent. There was however no particularly obvious accumulation of ninein at junctional associated sites along the length of the crypt (Figure 3.4).

H & E stains from the tumour region of sample B highlight the much greater degree of architectural disorganisation compared to that observed in sample A (Figure 3.5 A), as confirmed by widefield fluorescence microscopy of an overview through a region immunolabelled for E-cadherin and ninein (Figure 3.5 B). In particular, note the multilayered nature of the epithelial wall as seen in the H & E section and the DAPI in the fluorescent images; multiple nuclei can be seen stacked on top of each other throughout the sample, and are no longer restricted exclusively to the very base of a cell, with nuclei also observed in apical regions. Further confocal images through the immunolabelled sections highlight the disorganisation of the tumour epithelial layer in regions retaining a crypt morphology (Figure 3.5 C) as well as more general connecting regions, likely to have originally been the surface epithelium (Figure 3.5 D). In particular, cells as marked by E-cadherin appear exceptionally long and thin. Interestingly, ninein was again clearly visible as distinct dots in apical regions; even in areas where it was hard to judge exactly which face would have been the apical surface, ninein was clearly lined up on one side and not the other. There was also evidence of ninein speckles in the cytoplasm throughout (Figure 3.5).

3.3: Discussion

3.3.1: Cancer tissue exhibits extensive architectural change

Although the two cancer samples analysed had very different morphologies, sample B clearly demonstrated a great degree of morphological change, in particular displaying a multilayered epithelial wall, implying a dramatic loss in control of division orientation. Sample A by contrast appeared to only show minor differences from control conditions, and may well have been from a less severe tumour.

Overall the most interesting data have come from analysing ninein localisation in control and tumour cells. Ninein consistently appears in distinct points at the apical surface of cells. Many of these have been established to colocalise with γ-tubulin, suggesting a centrosomal organisation, however they also appeared distinct from γ-tubulin, possibly indicating some accumulation at non-centrosomal sites. Unfortunately, regions of surface epithelia proved generally too damaged to fully assess ninein distribution. This is unfortunate, as recent experiments within the group have demonstrated a clear change in ninein organisation between the base of the crypt and the surface epithelium of the colon. Rat colon cryostat sections (which were quickly frozen, fixed and stained) illustrate ninein in the punctate pattern consistently seen in the human sections as discussed for the majority of the crypt, but with a distinct switch at the very top of, and extending into the surface epithelium, to instead localise strongly as a distinct band at the very apex of cells (Goldspink et al., 2013a, manuscript in preparation). Interestingly, a similar pattern was seen in isolated tissue from the small intestine, where crypts surround the base of villi. These small intestinal crypts expressed the punctate pattern characteristic of the majority of the length of colonic crypts, whilst villus tissue clearly possessed an apical band of ninein similar to that seen at the surface epithelium of the colon (Goldspink et al., 2013a, manuscript in preparation). Taken together, these observations indicate a possible change in apico-basal array organisation as cells reach the top of intestinal crypts; an apical ninein band is a classic indication of non-centrosomal minus end anchorage. This suggests that the lower sections of crypts could possess apico-basal microtubule arrays that are not

released, instead maintaining apical anchorage at the centrosome in an 'umbrella' conformation. Meanwhile, once cells have fully differentiated into absorptive cells at the colonic surface epithelium or small intestinal villus, they do undergo the classic reorganisation into non-centrosomal arrays anchored by peripheral ninein as described by the release and capture mechanism.

Interestingly, in the sample B tumour sectioning, despite no longer being a single layer thick, the epithelial cells were generally a long thin shape, more characteristic of surface epithelial cells. Ninein however still appeared to be in distinct points at the very apex of cell, implying a centrosomal localisation. Indeed, it was noticeable that despite the multicellular nature of the epithelial wall, ninein still localised to the apical luminal surface. Further, whilst ninein dots were apical but somewhat scattered in terms of exact location in control crypts, they were very much aligned at the uppermost surface in the cancer sample. It is possible though that this was due to better preservation of the tumour sample due to its increased cell density making cryostat sectioning smoother and easier, and so less prone to causing damage. Alternatively, the cancer state may mean that the epithelial cells do not fully differentiate, meaning ninein is not deployed to non-centrosomal sites, and so is only detected at apical centrosomal sites. Further experiments are clearly required, to both confirm the initial theory regarding the apparent switch in ninein location during differentiation, and to more accurately determine what is occurring in tumour situations, and thus whether ninein could be an interesting cancer target.

3.3.2: Frozen tissue samples poorly preserve cytoskeletal architecture

Overall the quality of results generated by sectioning of frozen samples was too poor to allow for many conclusions. Tissue suffers a great deal of damage, particularly in comparison to the paraffin embedded sections used in the previous study. This is clearly visible in sections immunolabelled for junctional E-cadherin and β-catenin, where it is often difficult to make out the shape of an individual cell. Additionally, the surface epithelium was rarely sufficiently preserved, a weakness as

it becomes difficult to make any comparison between the morphology of cells in the stem cell zone and those that are fully differentiated towards the surface.

Most importantly, due to this damage only a small number of proteins were usefully stained for, and these did not include microtubules or +TIP proteins such as EB1. Initially, it had been hoped a large number of samples, at different levels of dedifferentiation could have been checked for the various proteins of interest, however, due to these overall technical difficulties few meaningful conclusions can be drawn. Thus, a further future examination into *in vivo* tissue architecture is required to apply the various findings made via tissue culture experiments.

3.3.3: Summary and future work

As indicated above, cryostat sectioning of tissue bank samples clearly has severe flaws for the analysis of the cytoskeleton, as the tissue preservation is insufficient to reliably assess the fine structural details. In particular, the failure to successfully stain for microtubules themselves is a major issue. This is likely due to how samples are initially acquired during surgery. Animal tissue cryostat sectioning by other group members has proven more successful, likely due to the increased speed by which samples are initially processed. Microtubules are extremely sensitive to temperature, with cold causing depolymerisation (Breton and Brown, 1998). Samples extracted during surgery are likely to spend an amount of time waiting for processing, during which the microtubule cytoskeleton may be lost. Thus, for any future human frozen tissue sections, arrangements should be made to directly collect samples for immediate processing at the time of initial extraction.

More recently, a particularly effective method has been developed within the lab to allow high quality imaging of the cytoskeleton in gut crypts. Rather than attempting to freeze and section tissue, whole mount crypts are instead isolated in bulk directly from the small or large intestine of a rat or mouse (Belshaw et al., 2010; Whitehead et al., 1993), after which they are immediately fixed and immunolabelled. In the example images presented in Figure 3.6 (kindly provided by Deborah

Goldspink), isolated whole mount crypts have been immunolabelled and confocal sections taken through crypt bases. Labelling for β-catenin and DAPI (Figure 3.6 A) highlights the shape of the polarised cells, including both enterocytes and goblet cells, and also provides an example of a division event. Additionally, a crypt immunolabelled for microtubules importantly confirms the presence of the apico-basal microtubule array (Figure 3.6 B). Finally, a crypt stained for β-catenin and APC illustrates the striking basal localisation of APC in crypt cells (Figure 3.6 C), similar to the distribution previously observed in cochlea pillar cells, where it has been associated with plus end anchorage of apico-basal microtubule arrays (Mogensen et al., 2002). This technique has proved successful for almost all proteins tested, including +TIP proteins (Goldspink et al., 2013b; Goldspink et al., 2013a, manuscript in preparation), and so promising for further study of microtubule apico-basal array formation. As yet it has not been applied to crypts derived from tumour systems, leaving an exciting avenue for future study of any changes to microtubule organisation in cancerous tissue.

Figure 3.1 Characterisation of control human tissue samples.
Widefield fluorescent images of transverse sections through control frozen human colon tissue samples immunolabelled for **(A)** β-catenin (red), ninein (green) & DAPI (blue), **(B)** γ-tubulin (red), ninein (green) & DAPI (blue), and **(C)** DAPI (blue) and secondary antibodies only (Alexa 488, green and Alexa 568, red). **(A)** Crypts visible as a circle of polarised cells with nuclei in basal regions, surrounding a central lumen (labelled ***[L]***). Ninein can be seen localised as distinct points in apical regions of crypt cells (arrowed in inset). **(B)** Co-labelling for γ-tubulin revealed colocalisation of ninein and γ-tubulin puncta (arrowed in inset), in addition to additional ninein speckles not colocalised with γ-tubulin labelling patterns (arrowhead in inset). **(C)** Staining with secondary antibodies only was performed to act as a control for the immunolabelling process. Scale bars: **(A)** & **(B)** = 20μm, **(C)** = 50μm.

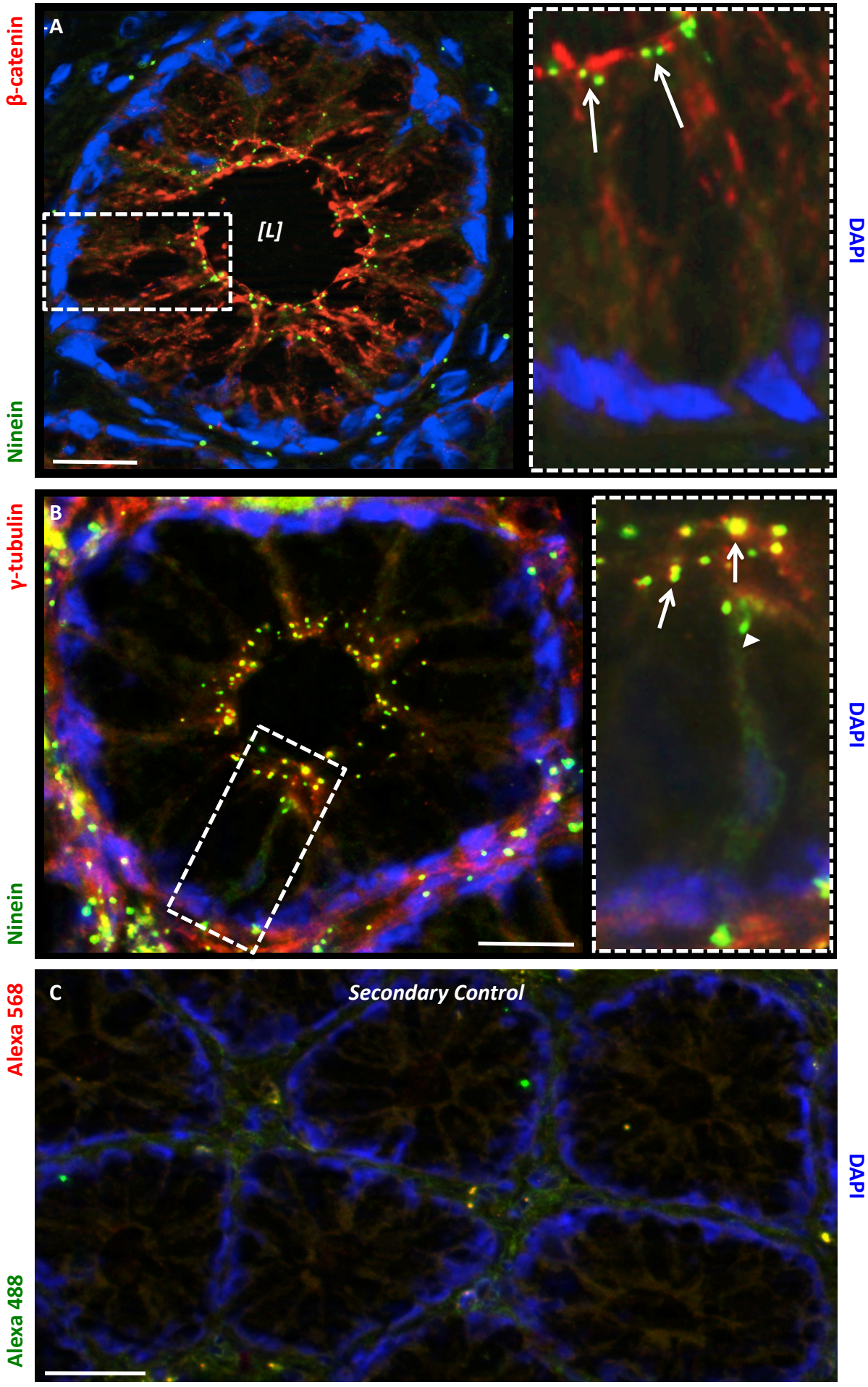
β-catenin
Ninein
A
[L]
DAPI
γ-tubulin
Ninein
B
DAPI
Alexa 568
Alexa 488
C
Secondary Control
DAPI

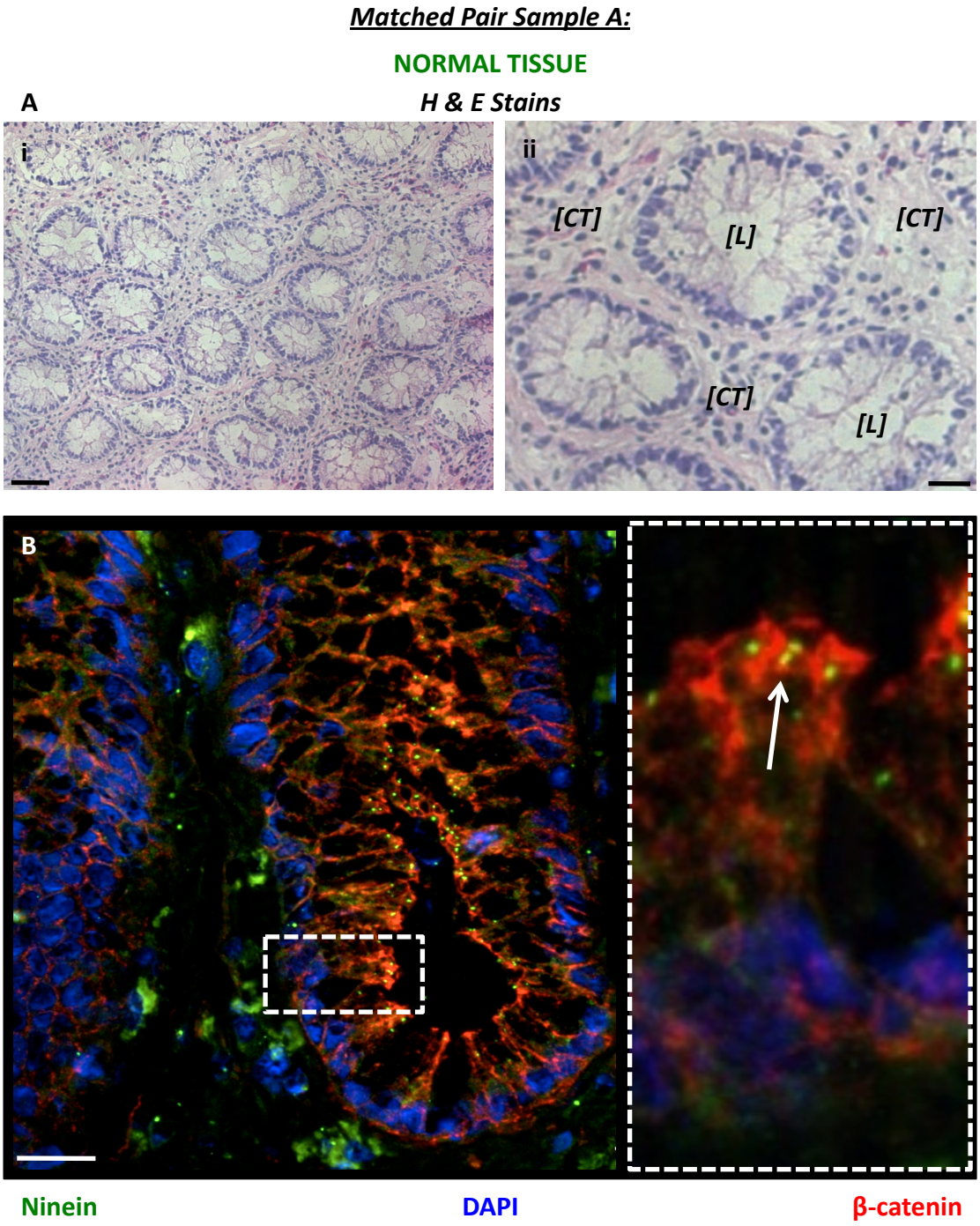

Figure 3.2 Characterisation of cancer patient tissue sections I: sample A (normal tissue)
Normal regions of frozen human colon tissue from a matched pair of samples taken from a cancer patient were sectioned, and fixed for processing. **(A)** Lateral cross-sectional views of colon crypts following H & E staining, illustrating normal tissue architecture of well spaced single crypts linked by connective tissue (labelled ***[CT]*** in **[ii]**). Note that each crypt consists of a circular single layer of cells surrounding a central lumen (labelled ***[L]*** in **(ii)**) **(B)** Longitudinal view of the base of a crypt immunolabelled for β-catenin (red), ninein (green) and DAPI (blue). Note the ninein localised as distinct points at the very apex of crypt cells (arrowed in inset). Scale bars: **(A i)** & **(B)** = 20µm, **(A ii)** = 50µm.

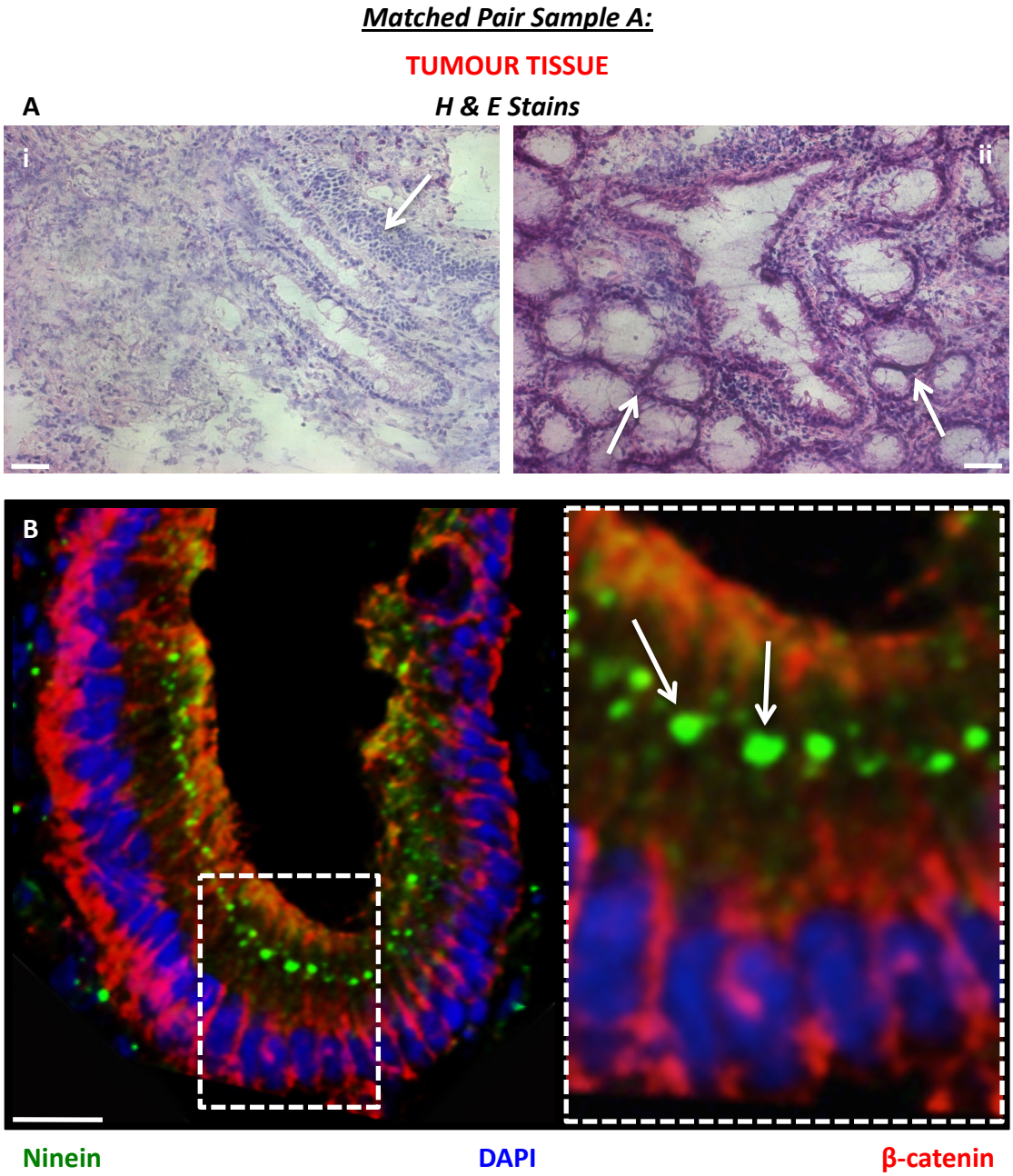

Figure 3.3 Characterisation of cancer patient tissue sections II: sample A (tumour tissue)
Tumour regions of frozen human colon tissue from a matched pair of samples taken from a cancer patient were cryostat sectioned, and fixed for processing. **(A)** Cross-sectional views following H & E staining, illustrating a possible increase in cell density of the connective tissue (arrowed in **[i]**) and disorganisation of crypt spacing, with possible merging of neighbouring crypts (arrowed in **[ii]**). Note that crypt morphology is generally similar to control samples. **(B)** 3D reconstruction of a longitudinal view of the base of a crypt immunolabelled for β-catenin (red), ninein (green) and DAPI (blue). Note the ninein puncta have localised further down crypt cells (arrowed in inset), rather than at the very apical surface. Scale bars: **(A)** = 50µm, **(B)** = 20µm.

Matched Pair Sample B:

NORMAL TISSUE

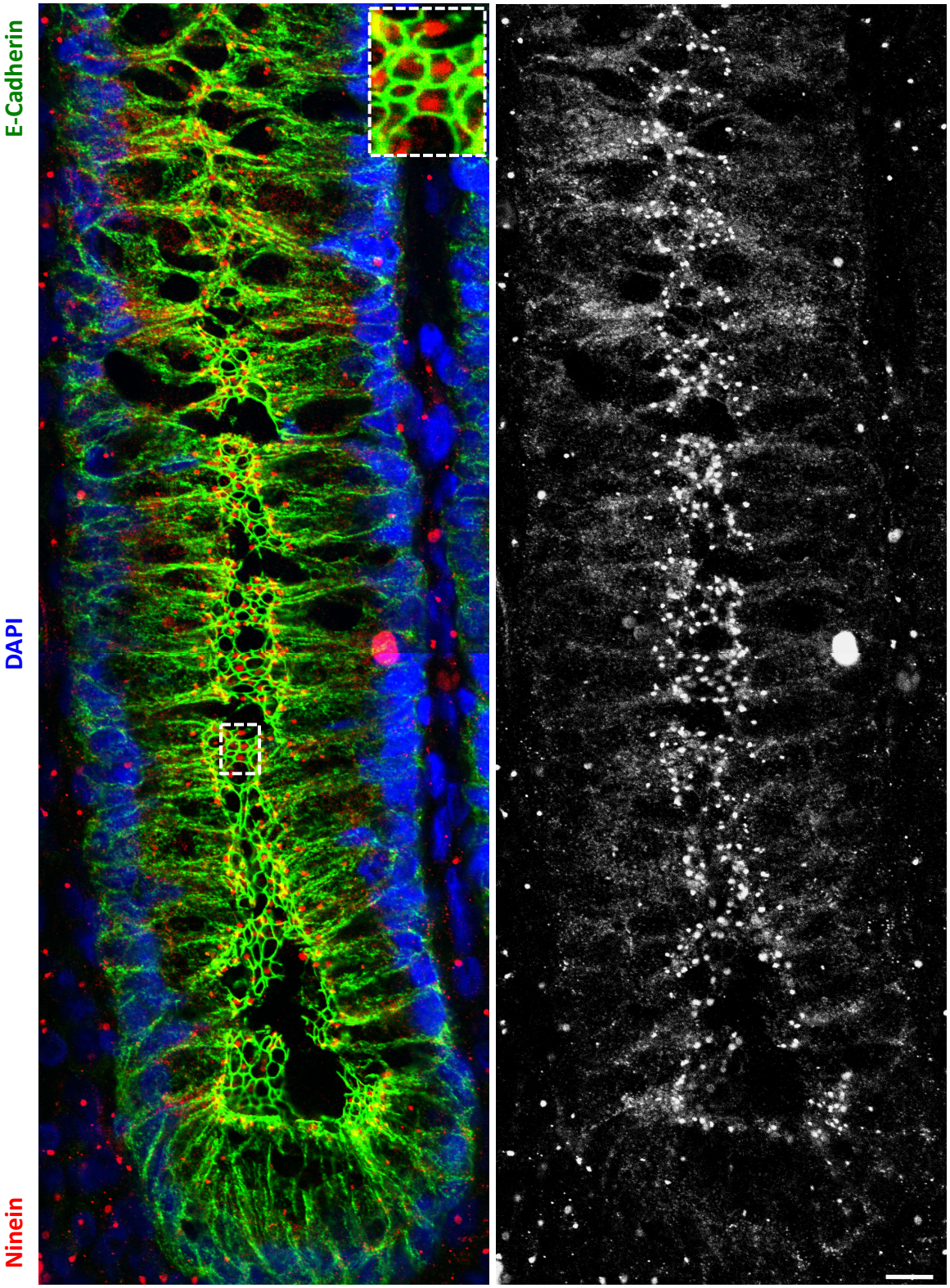

Figure 3.4 Characterisation of cancer patient tissue sections III: sample B (normal tissue)
Normal regions of frozen human colon tissue from a matched pair of samples taken from a cancer patient were cryostat sectioned, and fixed for processing. Confocal image of a longitudinal view of a crypt immunolabelled for E-Cadherin (green), ninein (red, white) and DAPI (blue). Note the ninein localised as distinct dots at the very apex of cells along the length of the crypt. Also observe the ninein visible as centrosomal dots where the very apical region if cells has been sliced through (enlarged in inset). Scale bar = 10µm.

Figure 3.5 Characterisation of cancer patient tissue sections IV: sample B (tumour tissue)
Tumour regions of frozen human colon tissue from a matched pair of samples taken from a cancer patient were cryostat sectioned, and fixed for processing. **(A)** Cross-sectional views following H & E staining, illustrating distinct disorganisation of tissue architecture. **(B)** Widefield and **(C,D)** confocal sections of regions immunolabelled for E-Cadherin (green), ninein (red, white) and DAPI (blue). Note in particular the increased number of cells in the epithelial layer at both the base of crypts **(C)** and other regions **(D)**, and the long thin shape of the cells in this epithelial wall. Also distinct is the maintenance of ninein localisation as dots at a single apical face in each of the observed regions. Scale bars: **(A)** & **(B)** = 50µm, **(C)** & **(D)** = 10µm.

Matched Pair Sample B:

TUMOUR TISSUE

H & E Stain

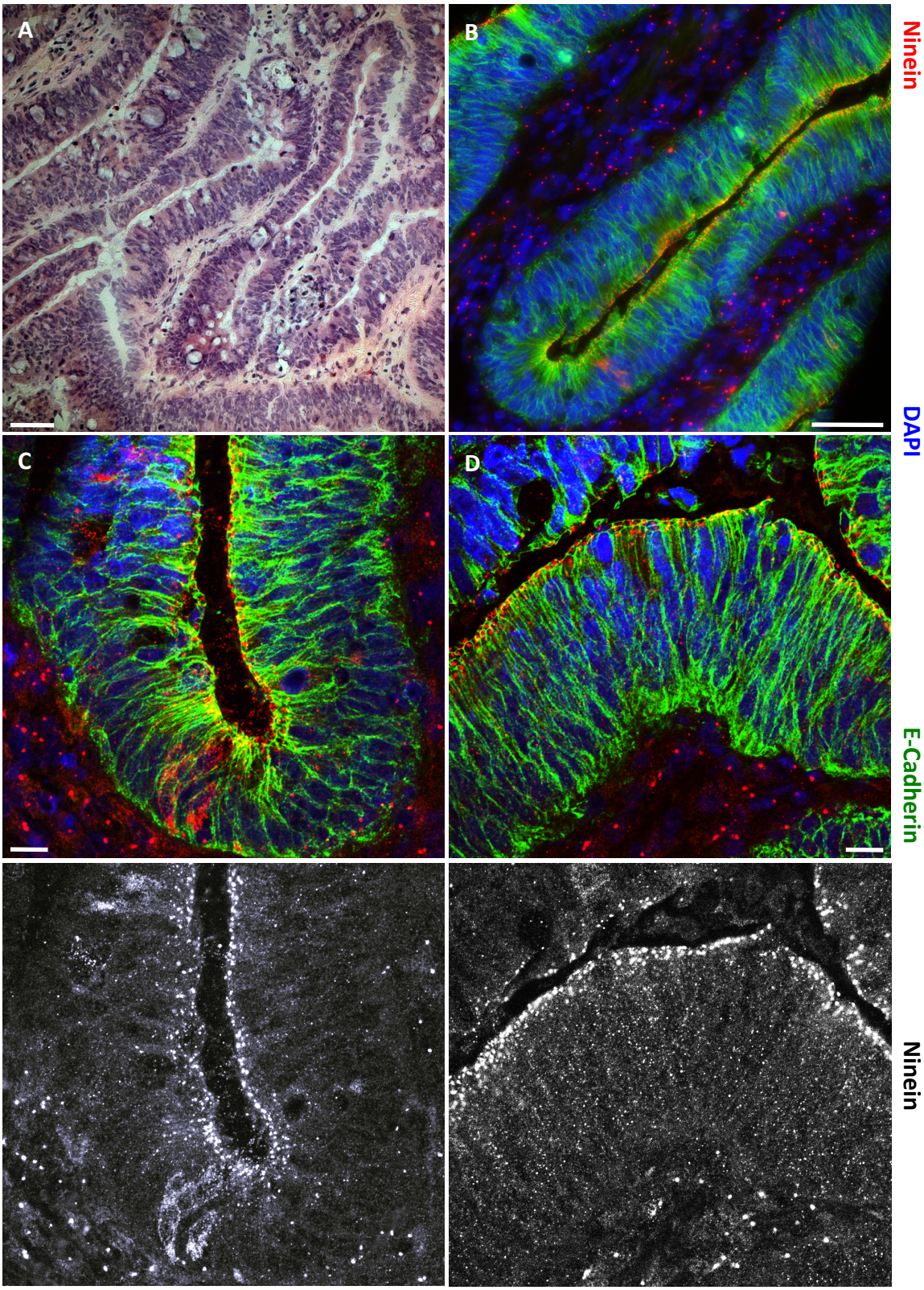

Figure 3.6 Isolated rat crypts provide an improved model for cytoskeletal immunolabelling
Confocal sections of the base of isolated rat colonic crypts, illustrate greater cell preservation and a distinct increase in quality of images following immunolabelling. **(A)** Crypt labelled for β-catenin (red) and DAPI (blue). Note the dividing cell on the right side. **(B)** Crypt labelled for microtubules (green, white) and DAPI (blue), confirming the distinctive apico-basal organisation of microtubules in crypt epithelial cells (insert). **(C)** Crypt labelled for APC (green, white), β-catenin (red) and DAPI (blue). Note the organisation of APC in baso-lateral regions (insert), with labelling especially strong at the base of crypt cells. All scale bars = 10µm.

Images courtesy of Deborah Goldspink

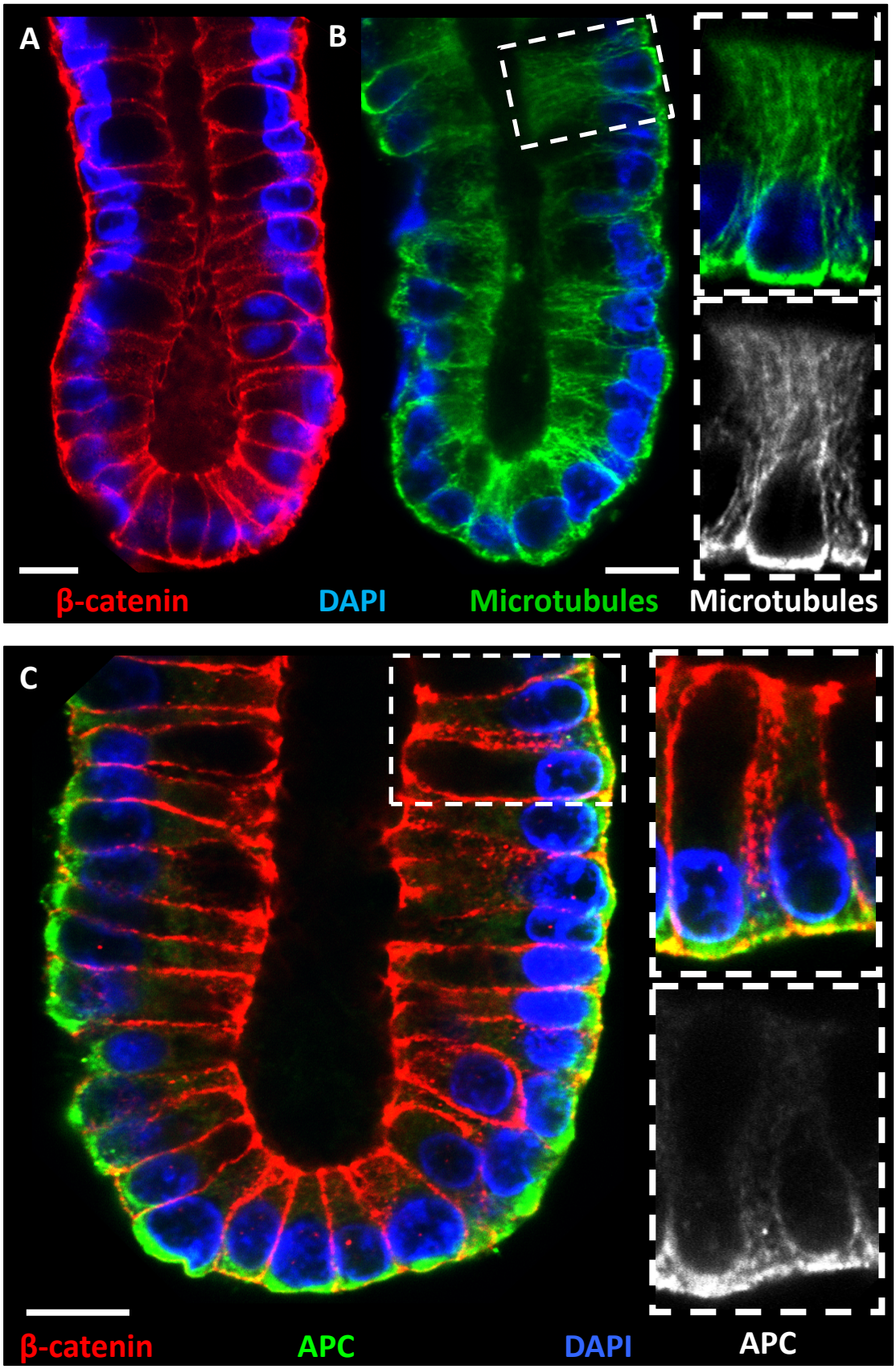

Images courtesy of Deborah Goldspink

Chapter IV

APC and Microtubule Cortical Contact

4.1: Introduction

APC is a prime candidate protein for study in the investigation of the microtubule cytoskeleton in colorectal cancer. Truncations in the APC gene have long been established as a common early defect in the disease, although these mutations have generally been linked to functions within signalling pathways important in crypt development. Increasingly however, it has been shown to have important roles in the cytoskeleton as a microtubule +TIP, where it stabilises microtubules (Mimori-Kiyosue et al., 2000) and has been associated with the formation of the apico-basal microtubule arrays present in epithelial cells (Mogensen et al., 2002). It has also been shown to be important in cell division for kinetochore attachment (Green and Kaplan, 2003), and for orientation of the spindle (Fleming et al., 2009). Interestingly, although APC can interact with microtubules through several regions, the domain responsible for direct binding and for its interaction through the +TIP EB1 is located in the C-terminal segment lost in the truncation mutations associated with colorectal cancer (Figure 1.12).

APC localises to basal regions where the plus ends of the apico-basal array cluster in highly polarised epithelial cells, such as the pillar cells of the cochlea, where it may play a role in anchoring the microtubule plus ends of the developed array (Mogensen et al., 2002). It has also been seen to localise along the lateral membrane of polarised epithelial cells in culture (Rosin-Arbesfeld et al., 2001). We have recently developed a technique to isolate and immunolabel crypts from the intestinal epithelium of adult mice and rats (Goldspink et al., 2013b), which revealed APC strongly localised in basal clusters and extending along the lateral regions of colonic rat crypt cells (Figure 3.6, D. Goldspink, unpublished data). Epithelial apico-basal microtubule arrays have been proposed to form via a release and capture mechanism (Bellett et al., 2009). An important intermediary step is the formation of an extended radial array in which microtubule plus ends dock at adherens junction associated cortical sites. APC has been described as an adaptor for microtubule cortical capture, and given its lateral localisation in epithelial cells may thus be involved as a receptor for this extended array (Figure 4.1).

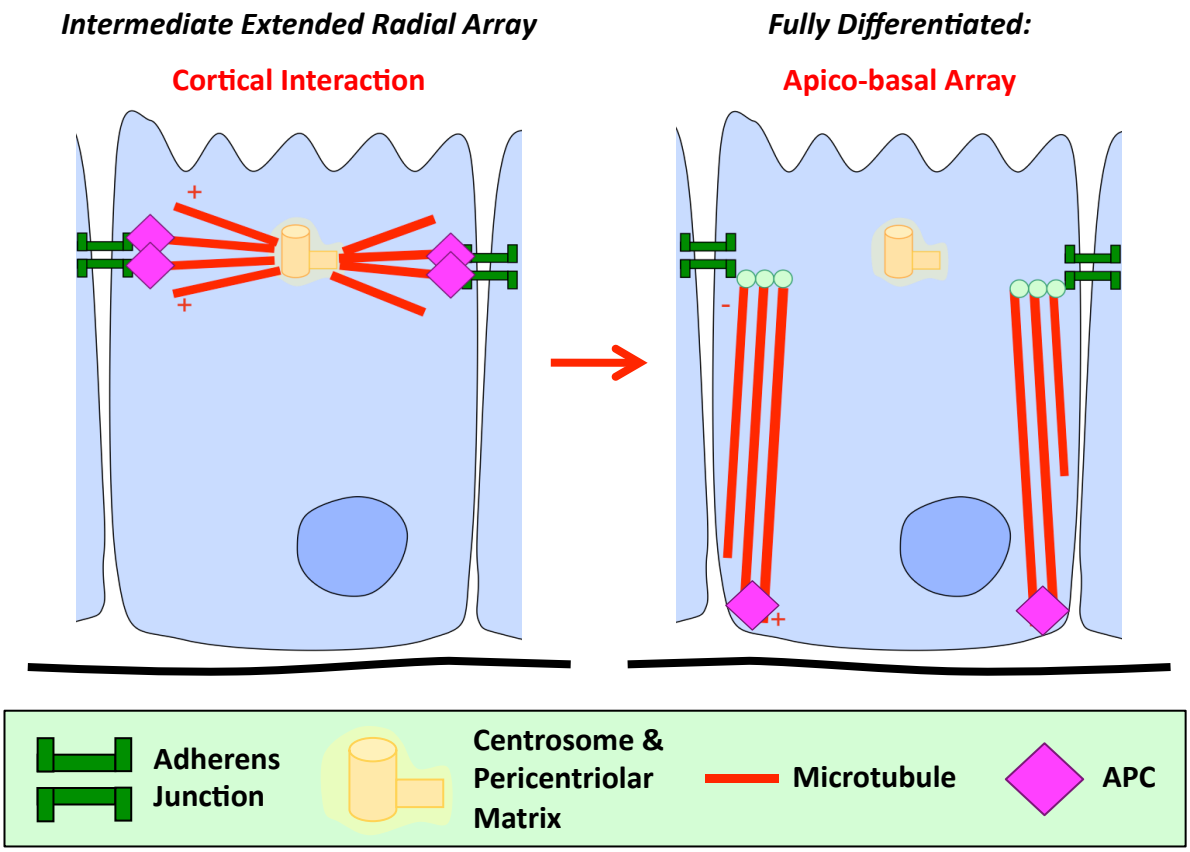

Figure 4.1 Cortical contact is an important step in the formation of apico-basal microtubule arrays
According to the release and capture model, an important intermediate step is the formation of an extended radial array organised by an apically located centrosome in which plus ends make cortical contact at adherens junction associated sites. APC is a potential cortical receptor for this interaction. Following differentiation, APC is located in basal regions where the plus ends of non-centrosomal apico-basally orientated microtubules are anchored.

The TC7 colorectal cancer cell line is derived from the widely used Caco2 cell line, and as such both have the same truncation mutation at residue 1367 of one APC allele, whilst lacking the second copy of the gene (Rowan et al., 2000). Much prior work utilising TC7 cells to investigate APC in colorectal cancer epithelial cells has been undertaken as part a PhD project by Jennifer Keynton, who carried out the initial characterisation of the cells, and developed many of the techniques and methods I have utilised here. The purpose of this part of my project was to further expand on this work. Key relevant findings from her work showed truncated APC in TC7 cells localised to the cortex, and suggested microtubules could make a transient connection with this APC, before curling away. Nocodazole regrowth experiments in polarised cells showed that following microtubule depolymerisation and nocodazole wash out the apico-basal array of TC7 cells would reform. Actin depolymerisation by Latrunculin B caused the loss of APC from the cortex and prevented microtubule cortical targeting to adherens junctions. Some initial investigations involving GFP-APC transfection and spindle orientation were also undertaken (Keynton, 2011). The fact that TC7 cells would polarise suggested that full length APC was not required, although whether the process was as efficient as in wild-type conditions was not determined.

A key issue for this previous work was the lack of a wild-type APC colon cell control. Since then, the HCT116 cell line has been acquired, which whilst derived from a tumour possesses full length APC. It does however possess a mutation in β-catenin, in the form of a point mutation of a single residue (Serine 45). This compromises a key phosphorylation site (Morin et al., 1997) rather than resulting in a large scale deletion or frame shift, meaning the mutated protein is likely able to interact with usual cytoskeletal partners, unless those interactions are dependent on its phosphorylation status. A key initial aim of my project was therefore to characterise this cell line, and then use it to investigate microtubule plus end cortical interaction in comparison to the truncated APC of TC7 cells. GFP-APC was also transfected into TC7 cells, in an attempt to rescue the phenotype observed by the expression of full-length protein.

As previously discussed (section 1.7.3.3), anchorage of astral microtubules to the cortex by APC has been suggested to be important for controlling mitotic spindle orientation in animal models (Fleming et al., 2009), however preliminary experiments in cell lines have been less conclusive. An additional aim therefore was to evaluate spindle orientation in TC7 cells, and compare this to the HCT116 cells expressing wild type APC.

Finally, kinesin-2 family microtubule motors (such as KIF3A and KIF3B/C) have been associated with the transport of APC to plus ends (Jimbo et al., 2002; Miki et al., 2005). Loss of the motor that transports APC along microtubules to cortical sites could prevent APC accumulation at junctional sites. KIF17 is another kinesin-2 family member, which has recently been implicated in the transport of APC to the cortex (Jaulin and Kreitzer, 2010). Attempts were therefore made to deplete KIF17, in order to completely remove either mutant or full length APC from junctional sites and examine whether this would further compromise microtubule interactions at the cell cortex.

To briefly summarise the data presented in this section, it was found that truncated APC compromised the formation of stable microtubule contacts with the cortex, such that following a brief initial interaction, microtubules would curl away and orientate parallel to the cell periphery. Importantly, this could be rescued in TC7 cells by the expression of a full length GFP-APC construct. Spindle orientation investigations demonstrated that whilst there was no general increase in the division plane angle in truncated APC expressing TC7 cells, there was a significant increase in the proportion of dividing cells with grossly abnormal spindle morphologies, either exhibiting a rotated phenotype or having a multipolar spindle.

4.2: Results

4.2.1: Confirmation and further exploration of the TC7 cell line as a model for the expression of truncated APC in polarised epithelial cells

TC7 cells have been characterised previously (Keynton, 2011), with the results from immunolabelling experiments of subconfluent cells as presented here confirming these established observations. TC7 cells are seen to have a disorganised microtubule network generally lacking centrosomal focus, with microtubules often appearing to run parallel to the cell cortex. Centrosomes appeared split, marked by two distinct foci (Figure 4.2 A), with pericentrin and PCM-1 dispersed into the cytoplasm (Keynton, 2011). As is typical for epithelial cells, EB1 was expressed as comets at microtubule plus ends (Figure 4.2 B), although these tended to have a slightly extended tail when compared with the other epithelial cell lines, such as ARPE-19s. TC7 cells formed both adherens and tight junctions, as evidenced by β-catenin (Figure 4.2 C) and ZO-1 (Figure 4.2 D) localisation to cortical regions. The truncated APC present was also located at cortical sites (Figure 4.2 E), where it colocalised with β-catenin (Figure 4.2 F). Finally, in common with MDCK cells (the archetypal cell line for epithelial polarisation), ninein was also found to relocate to these junctional sites (although this was not as frequent or as strong a localisation as seen in MDCKs), as well as localising to the centrosome and in the cytoplasm as speckles (Figure 4.2 G).

Caco2 and TC7 cells polarise when grown on tissue culture filter insert, although TC7 cells appear to achieve this much more quickly (E. Lund, personal communication). TC7 cells will also polarise when grown on plastic or glass, and so were studied in a polarisation series, to examine how the cytoskeleton rearranges during this process. Cells were seeded sparsely (20,000 cells per six-well plate well) and allowed to develop over a period of up to 14 days. Samples were fixed and immunolabelled on each day of the series to analyse how cells develop as they reach confluency (generally between days 5-7), and subsequently polarise (Figure 4.3). At day 3, cells were observed to be generally sparse, with few immediate neighbours. At this stage, cells often displayed a migratory arrangement, with β-actin present in

lamellipodia at the exposed edge, and in stress fibres, with microtubules more organised (Figure 4.3 A) and their plus ends (marked by EB1) extended towards the leading edge (Figure 4.3 B). By day 5, most cells had neighbours, but were still in a spread, relatively flat morphology. Actin was found localised at peripheral sites and in stress fibres, whilst the microtubule network appeared more disorganised (Figure 4.3 A), with plus ends appearing to curve around the cell periphery (Figure 4.3 B). Between days 6-8 the cells reached confluency and constrict, their cell area decreasing, and microtubule organisation appearing disorganised. They further polarised over days 9-14, with actin found localised to peripheral sites, as indicated by colocalisation with β-catenin (Figure 4.3 A), whilst EB1 localised along the lattice of the apico-basally orientated microtubule bundles (Figure 4.3 B). Importantly, throughout the differentiation process, APC was observed to localise at cortical sites (Figure 4.3 C).

4.2.2: Characterisation of HCT116 cells

For initial characterisation, HCT116 cells were seeded onto glass coverslips and immunolabelled for microtubules, EB1, and a variety of centrosomal and junctional proteins, including APC.

Cells stained for α-tubulin and centrosomal proteins (Figure 4.4 A-C) revealed relatively small, flat cells possessing a microtubule array emanating from a centrosome located adjacent to the nucleus. Although not as organised as the classical radial array exhibited by the ARPE-19 cell line, HCT116 microtubules appeared to show greater centrosomal focus than seen in TC7 or MDCK cells. Centrosomes, as marked by γ-tubulin (Figure 4.4 A) were seldom split. Ninein localised as cytoplasmic speckles but primarily at the centrosome (Figure 4.4 B) where it colocalised with γ-tubulin (Figure 4.4 D). Pericentrin was generally focussed at the centrosome where it colocalised and surrounded γ-tubulin (Figure 4.4 E). It was also localised in clusters close to the centrosome around the nucleus (Figure 4.4 C), but appeared less dispersed than in TC7 cells. PCM-1 also appeared to focus around the centrosome (data not shown), as opposed to the dispersed pattern

previously noted in TC7 cells (Keynton, 2011). Cells were also stained for EB1, which was localised at the centrosome and extended in typical plus tip comets radiating from the central focus (Figure 4.4 F).

As with MDCK and TC7 cells, the adherens junction components E-Cadherin (Figure 4.4 G) and β-catenin were found to localise at junctional sites in HCT116 cells. Interestingly, particularly in the case of β-catenin, these were often expressed in a punctate pattern at the cell periphery, rather than the continuous line at cell-cell contacts typically visible in TC7 cells (Figure 4.4 H). These punctate patterns were especially visible at sites where junction formation seemed to be taking place, as is common for the process. As opposed to MDCK and TC7 cells, HCT116 junctions did not appear as tightly arranged, with small gaps often appearing between cells in confluent regions.

Cells stained for APC (Figure 4.4 I) showed colocalisation with β-catenin at junctional sites (Figure 4.4 Ji), however, not all β-catenin junctions were accompanied by APC (Figure 4.4 Jii). APC did not exhibit a typical +TIP distribution at microtubule plus ends, however it did regularly appear to colocalise with γ-tubulin at the centrosome (Figure 4.4 K). Overall, staining for junctional components suggested the contacts were weak, which may explain why seeding HCT116 cells at confluency onto tissue culture filter inserts, failed to induce polarisation (Figure 4.4 L).

Western blotting using an N-terminal antibody was used to confirm expression of full length APC (which has a molecular weight of 310kDa) in HCT116 cells, compared against the APC truncation mutation present at residue 1367 in TC7 and its parental Caco2 cell line (Rowan et al., 2000). Bands were visible above the 150kDa marker in TC7 and Caco2 cells corresponding to the reported size of the truncated products, whilst a band above the 250kDa marker was present in the HCT116 lysate at a height observed previously to correspond to the full length protein. A small band at a similar height corresponding to full length APC was also present in the TC7 lysate. This has been previously observed (Keynton, 2011), and

suggests a small amount of full length APC remains expressed in the TC7 culture (Figure 4.5).

Finally the observation that HCT116 cells appeared noticeably smaller than other epithelial cell lines was verified by measuring the areas of 175 subconfluent TC7 and HCT116 cells. TC7 cells have an average area of 1340μm^2, which was comparable to similarly treated ARPE-19 cells (which had an average area of 1292μm^2) (Goldspink et al., 2013b). By contrast, HCT116 had a significantly smaller mean area of 425μm^2 ($p<0.0001$). TC7 area data also had a wider spread, likely due to the apical constriction that occurs as cells begin to polarise (Figure 4.6).

4.2.3: GFP-APC expression in TC7 cells

TC7 cells were seeded sparsely and transiently transfected with a GFP tagged full length APC construct twenty-four hours prior to fixation. Cells were immunostained with an anti-GFP antibody to enhance the fluorescent signal. Counterstaining with an anti-APC antibody verified the construct as APC, and demonstrated a markedly different pattern of localisation than neighbouring untransfected cells expressing the truncated endogenous APC (Figure 4.7 A). As opposed to a primarily cortical localisation, full length GFP-APC localised along microtubules, and was seen to localise especially strongly at the plus ends of microtubules exposed at the leading free edge of cells (Figure 4.7 B). It also strongly localised to protrusions between neighbouring cells (Figure 4.7 B-C). These match what has been previously observed for endogenous full length APC in cell culture (Näthke et al., 1996). Although there was no obvious change in EB1 expression, there did appear to be some accumulation in punctate patterns within the very highly GFP-APC expressing protrusions (Figure 4.7 Cii). Although the GFP-APC did not show great accumulation at cortical sites, it could be found co-localising with β-catenin at cell junctions (Figure 4.7 D, Ei), as well as along β-catenin at non-junctional sites at the free edge of cells, which may be linked to the actin cytoskeleton (Figure 4.7 Eii).

4.2.4: Analysis of microtubule orientation at the cortex

The orientation at which microtubules approached the cortex was analysed to determine whether there was any effect on microtubule plus end anchorage due to the APC truncation mutation. Acquisition of the HCT116 cell line allowed for a more direct comparison of microtubule orientation at cortical sites in colon cells expressing truncated and full length APC than had previously been possible. MDCK, HCT116, and TC7 cells, as well as TC7 cells rescued by transfecting with full length GFP-APC were fixed when subconfluent, and labelled for microtubules and junctional proteins. MDCK and HCT116 cells were selected as examples of cell lines that expressed full length APC. HCT116 cells are the obvious control for the experiment, however as they were found not to polarise, and possess a β-catenin mutation, MDCK cells were also used for comparison against TC7 cells. Transfection of TC7 cells with full length APC was performed to attempt to rescue the truncation phenotype. For each condition 10μm areas of the cortex were randomly selected, and the microtubules scored for orientation as either parallel or perpendicular to the cortex (Figure 4.8 A). For each 10μm area the percentage of microtubules orientated perpendicular to the membrane was counted, and the mean average for all areas for each condition calculated. 70 areas from 40 different cells were analysed in MDCK cells, 65 areas from 52 different cells were analysed in HCT116 cells, and 80 areas were selected from 51 different TC7 cells, whilst 70 areas from 30 TC7 cells transiently transfected with GFP-APC 24 hours prior to fixation were also analysed. It was found that there was no significant difference in the percentage of perpendicularly orientated microtubules between MDCK (57%) and HCT116 (61%) cells. However there was a significant reduction in the percentage of perpendicular microtubules in TC7 cells compared to either control cell line ($p<0.001$ for both comparisons), with only 24% of TC7 microtubules orientated at right angles to the cortex. In other words, a greater proportion of microtubules are orientated parallel to the cortex in the truncated APC expressing TC7 cells than either wild type APC controls. Interestingly, TC7 cells transfected with full length APC exhibited a rescued phenotype, with 53% of microtubules orientated perpendicular to the cortex. This was a significant increase compared to TC7 cells ($p<0.001$), and not significantly

different compared to either control cell line (Figure 4.8 B). This suggests that expression of full length APC in TC7 cells was able to rescue the compromised cortical orientation of microtubules in TC7 cells.

A nocodazole regrowth assay was performed to further analyse microtubule cortical approach. Treatment with nocodazole causes depolymerisation of microtubules, which can be reversed when the drug is removed. On nocodazole treatment, the depolymerised microtubule network is reduced to a haze of tubulin in the cytoplasm. Following wash out of the drug, microtubules repolymerise from the centrosome, forming initial asters, which extend out to the cell periphery between 10-15 minutes post drug removal, with the microtubule array closely resembling the organisation observed prior to microtubule breakdown by 30 minutes of recovery (Figure 4.9 A). Nocodazole regrowth can be used to follow the reforming of the microtubule array, and thus examine how microtubules interact with the cortex (Bellett et al., 2009). Quantification of microtubule orientation at several time points during regrowth in TC7 cells demonstrate that microtubules are initially orientated perpendicular to the cortex, with the percentage orientated parallel increasing as the reformation of the array progresses (Figure 4.9 B). These results confirm the previous observations made from similar experiments (Keynton, 2011) that the microtubules appear to approach at a perpendicular angle, make an initial transient contact with junctional sites before curling away to run parallel with the cortex (Figure 4.9 C)

4.2.5: Analysis of spindle orientation in TC7 and HCT116 cells

Orientation of the TC7 spindle was previously compared with that of MDCK cells, in which it was found that the TC7 spindle actually unexpectedly appeared to exhibit a smaller difference and variability in angle of the division plane than the MDCK control cells (Keynton, 2011). An issue with these findings however was that in order to increase the frequency of division events and thereby get sufficient numbers to analyse, the cells were seeded sparsely, and so lacked neighbouring cells, and therefore cell-cell junctions. Thus, if APC is important for the anchorage of

astral microtubules at junctional sites as hypothesised, it is important to reanalyse the spindle in confluent conditions where junctions have formed.

To get a large number of mitotic events at a particular time cell cycles were synchronised using the double thymidine block. Initially, the technique was optimised for both TC7 and HCT116 cell lines. For each, cells were synchronised as described in the material and methods, and fixed at each step in the treatment and at set time points following release from the final block, in order to calculate the length of time to leave cells following release to get the greatest number of cell in division. In TC7 cells, the percentage of cells in mitosis rose from an average baseline of 5.8% in untreated cells to a maximum of 17.7% of cells in division at 8 hours after release from the second thymidine treatment (Figure 4.10). Similarly, the time point producing the greatest proportion of cells in mitosis after release from the block was also found to be at t=8h in HCT116 cells (data not shown). All subsequent experiments for both cell lines in this section were therefore carried out this optimal point eight hours post release from the double thymidine block treatment.

For both cell lines, cells were fixed and immunostained for microtubules and γ-tubulin, to mark the spindle and spindle poles, and imaged on the confocal microscope. Z stacks were taken at double the optimum sampling and half the optimal Z slice interval (0.18μm). Images were deconvolved using a measured point spread function (PSF) in Huygens software and transferred to FIJI (Image J) software, where they were rotated such that an orthogonal XZ view passed through the centre of both spindle poles. The software was then used to measure the distance (D) between the centre of each spindle pole, and the angle (A) of the division plane (Figure 4.11 A). The results from 52 spindles in TC7 cells, and 63 in HCT116 cells, were plotted on scatter plots and the mean for each criterion calculated. There was no significant difference in the angle of the division plane (Figure 4.11 B), although as might be expected given their generally smaller size, the distance between spindle poles in HCT116 cells was significantly less ($p<0.0001$) (Figure 4.11 C). The spread of angle data was greater in HCT116 spindles.

Although there did not appear to be an overall difference in spindle angle, there did appear to be a greater variability in the phenotype of spindles observed in TC7 cells, with microtubules arranged in three distinct morphologies. The majority of spindles in both cell lines appeared normal (see Figure 1.9) when viewed in the XY plane; that is, with chromosomes as marked by DAPI arranged centrally between each half spindle and organised by a centrosome at each pole, with astral microtubules extending out to the cell periphery. In Z view, these tend to possess a small division plane angle. The second morphology was a multipolar spindle organised by multiple centrosomes. These have been ignored when measuring angle between spindle poles, due the inherent difficulty of measuring an angle for a spindle with more than two poles. The final morphology is perhaps the most interesting. On a widefield fluorescence microscope, it appears as if the spindle contains only one pole encircled by chromosomes, however an extended focus view of a confocal stack revealed two centrosomes. In Z view, it can be seen that one centrosome is distinctly above the other, with microtubule arrays emanating from each centrosome extending to the centre of the stack from above and below. As such the spindle pole angle is much greater, with the division plane appearing to be broadly parallel with the basal membrane as opposed to perpendicular as is typical (Figure 4.12). The spindles of the rotated phenotype are circled on the division plane angle and spindle distance graphs in TC7 cells, illustrating that the six largest angles and six of the smallest spindle pole distances are spindles of this rotated morphology (Figure 4.11 B, C).

To determine whether there was a difference in the ratio of the three morphologies in each cell line, spindles were scored for their spindle phenotype; 243 TC7 and 234 HCT116 spindles were analysed (Figure 4.13). TC7s cells expressed a greater percentage of both abnormal phenotypes; 93.2% of HCT116 spindles were classified as normal, whereas only 80.3% of TC7 spindles were normal. The rotated morphology accounted for 10.3% of TC7 spindles compared to 4.3% in HCT116 cells, whilst 9.5% of TC7 spindles were multipolar, with this at just 2.6% for HCT116 spindles. A chi-squared test for independence between the two cell lines confirmed these results as significant ($p=0.0002$).

4.2.6: siRNA knockdown of the kinesin motor KIF17

Whilst the truncated form of APC has lost its direct microtubule and EB1 binding sites, it can still be transported to the cell cortex by kinesin motors (see Figure 1.11). KIF17 has recently been implicated as a candidate for this process (Jaulin and Kreitzer, 2010). APC has proven difficult to knockdown in the past, and due to the diversity of its roles the cell, it is hard to be sure that any phenotypes observed after a successful knockdown are due to its cytoskeletal functions. However, knockdown of the motor responsible for its transport to junctional sites should prevent its accumulation at the cortex, and thus enable analysis of any effects on microtubule organisation caused by a loss of cortical APC. Attempts were therefore made to knockdown the KIF17 motor.

Before attempting depletion however, KIF17 expression and localisation was verified and characterised in relevant cell lines. In TC7 cells, KIF17 was found localised as speckles along microtubules (Figure 4.14 Ai), and at cortical sites, where it colocalised with APC (Figure 4.14 Aii). Similarly, in HCT116 cells, KIF17 colocalised with APC at junctional sites, and additionally at the centrosome (Figure 4.14 B). Finally, KIF17 localised along microtubules in ARPE-19 cells, and also appeared to accumulate (albeit to a lesser degree than in the other cell lines) at junctional sites. It was also evident at the exposed leading edge of cells (Figure 4.14 C).

Initial attempts to knockdown KIF17 were made utilising ARPE-19 cells, as they are also a human cell line and have been shown to be more amenable to siRNA treatment than TC7 cells. Initially, the two transfection treatment over a 96-hour time period described in the material and methods was used, however different time periods, shots and even transfection reagents were also trialled. Of the four siRNA sequences attempted, only one (Hs_KIF17_5, see Table 2.2) appeared to produce a possible knockdown, as marked by immunofluorescent labelling for KIF17 and imaging at set exposure levels. Those cells that showed a reduction in KIF17 level appeared to possess an altered microtubule arrangement in comparison to control or scramble siRNA treated cells, in which microtubules appeared to be very straight and align with each other in a fan-like arrangement (Figure 4.15 A). Additionally, EB1

appeared to localise along the microtubule lattice as opposed to the classical comet-like distribution found in control or scramble treated cells (Figure 4.15 B). These effects suggest a possible increase in microtubule stability, however they were not consistent, nor were they observed in a great number of cells, suggesting any knockdown, if even specific, was not particularly effective. Unfortunately, ARPE-19 cells do not express APC strongly, so it was impossible to judge whether its localisation had been disrupted in KIF17 siRNA treated cells (data not shown).

4.3: Discussion

4.3.1: HCT116 cells are a model for expression of full length APC

HCT116 cells were verified as expressing full length APC by Western blot, which localised to cell junctions as previously seen for the truncated APC in TC7 cells. HCT116 cells were however found not to polarise when grown on tissue culture filter insert. This is similar to ARPE-19 cells, however HCT116 cells did express E-Cadherin. Generally expression of junctional components such as β-catenin appeared more punctate than seen in polarising cell lines, with gaps between neighbouring cells often present.

As in ARPE-19 cells, the microtubule network is distinctly organised by a centrally located centrosome, with PCM components such as PCM-1 and pericentrin focussed at this site. This contrasts with the centriolar splitting, PCM spread and microtubule array disorganisation previously observed in other colon cancer cell lines, including TC7 cells (and to a lesser extent other polarising cell lines such as MDCKs) (Keynton, 2011). APC was also found localised to the centrosome in HCT116 cells, likely through EB1, which also localised to centrosomal sites, and has previously been associated with minus-end anchorage (Louie et al., 2004). Microtubule minus-end anchorage was not investigated in this project, although the interplay between anchorage and cortical capture is an important part of the release and capture mechanism, and as such it may be an interesting avenue to return to in HCT116 cells in future work.

Combined, these results suggested HCT116 cells could be used as a colon cell model for interactions with full length APC at cortical sites and in the mitotic spindle analysis. However, they would not be suitable to investigate the polarisation process in colon cancer cells as a whole.

4.3.2: Full length GFP-APC localises differentially from the APC truncation mutant in TC7 cells

As opposed to a primarily cortical location for truncated APC, the full length APC transiently transfected into TC7 cells appeared to localise along microtubules, and was particularly strong at plus ends in exposed leading edges of cells, and in cell extensions as previously seen for endogenous APC (Näthke et al., 1996). This distribution suggests a role in cell migration. APC has been associated with increased microtubule stability and links with actin in cell motility (Barth et al., 2008), although any possible effects on migration of TC7 cells were not examined in this study. These localisations are consistent with previous transfections of APC into other colon cancer cell lines such as SW480 cells, where the restoration of APC was associated with increased adhesion (Faux et al., 2004). No attempt was made to overexpress APC in HCT116 cells, although it may be interesting in the future to see whether such an experiment could increase the strength of the junctions formed between neighbouring cells, and if so whether this could promote HCT116 polarisation.

Full length GFP-APC in TC7 cells could be found at cortical sites, although such localisation did not appear to be especially strong, as it was not present at all junctional sites. APC truncation mutations have been associated with a dominant-negative behaviour (Dihlmann et al., 1999; Su et al., 1993), so it is possible that the prior localisation of the native truncated APC in TC7 cells discouraged strong GFP construct accumulation at junctions.

4.3.3: APC truncations compromise microtubule cortical contacts

Analysis of microtubule orientation at the cortex showed the percentage of microtubules perpendicular to the cortex was significantly lower in TC7 cells than in cells expressing wild type APC, either endogenously or in TC7 cells rescued with the APC construct. It is not clear whether the rescue effect is due to increased full length APC actually at the cortex, or whether the GFP-APC seen bound to the plus-end and microtubule lattice helps couple the microtubule plus end with junctional targets.

Nocodazole regrowth in TC7 cells demonstrated how microtubules initially approach the cortex at right angles, before they curl away and the disorganised array seen under control conditions forms. These results can be combined with the data from the prior project, which extensively examined the importance of APC-actin interactions at adherens junction associated sites (Keynton, 2011). Taken together a model can be proposed in which microtubules extend to the cell periphery where they are able to make an initial transitory contact, after which they curl away to run parallel to the cortex.

The importance of these combined observations in relation to the formation of the apico-basal microtubule array is yet to be fully understood. The release and capture model suggests cortical interactions during the formation of the intermediate extended radial array is vital for the efficient delivery of ninein to non-centrosomal sites during stable apico-basal array formation (Bellett et al., 2009; Moss et al., 2007). The fact that TC7 cells readily polarise and possess non-centrosomal microtubules anchored at junctional sites (as shown by EM) (Keynton, 2011) would suggest full length APC is not required for this process; it is possible that the brief initial cortical contact is sufficient for an alternative adaptor protein to couple the microtubule ends more stably to actin at junctional sites. Candidates for such a role include ACF7 (Slep et al., 2005), and IQGAP1, which can interact with the truncated version of APC (Tirnauer, 2004; Watanabe et al., 2004).

It has been observed that despite the many cellular roles for APC as an adaptor protein, it is never essential for any of them; there always seems to be an alternative protein that can compensate for the APC truncation (Nathke, 2010). Thus, the APC mutation itself contributes to cancer progression by decreasing the efficiency of many processes, and making further defects more likely, rather than directly stopping any one particular mechanism itself.

A recent paper by Lewis et al., (2012) has argued that the C-terminal region of APC associated with its microtubule related functions is not actually implicated in tumorigenesis. They found that tumours still developed in mice expressing a mutant APC that included the C-terminus, but possessed a deletion of the SAMP repeats

responsible for β-catenin binding in Wnt signalling (Lewis et al., 2012). However, whilst it is possible that the Wnt signalling implications of the APC truncation are more important in initial adenoma development and mutation accumulation, their work, based only from tissue data, fails to consider the effect that the loss of polarity and accompanying apico-basal microtubule array could have in promoting a more invasive phenotype in later steps of tumour development as it undergoes EMT, particularly as the mice used in the study had to be sacrificed early, prior to the development of invasive carcinomas.

4.3.4: Truncated APC promotes abnormal spindle phenotypes

Correct spindle orientation is important for the correct development of the colonic crypt, as it is an active tissue in terms of rapid cell turnover. The epithelial layer is a single cell thick, and this must be maintained by ensuring the plane of division remains perpendicular to the apical surface. Additionally, maintenance of asymmetric division, whereby the original centrosome and genetic material remains in the stem cell zone and the differentiating daughter cell gains the newly synthesised material is known to be important in the stem cell niche of colonic crypts, with APC influencing this orientation (Quyn et al., 2010; Yamashita et al., 2003). Astral Microtubules have been shown to play a vital role in co-ordinating the position and orientation of the spindle through interactions with dynein anchored at the cell cortex. This interaction allows the motor to exert a pulling force on the astral microtubules, and thereby control the location of each spindle pole (O'Connell and Wang, 2000). APC may be involved in this cortical capture of astral microtubule plus ends, and the resultant targetting to dynein. It has been established that APC is involved in the plus end capture of microtubules at kinetochores, and during cortical anchorage of astral microtubules (Green and Kaplan, 2003), whilst *in vivo* tissue studies in $APC^{min/-}$ mice exhibited a greater spindle angle in tumour and neighbouring regions than control mice (Fleming et al., 2009). However no previously published tissue culture data have implicated APC truncation status as a factor in the spindle orientation. In the case of previous work by Keynton (2011), the TC7 cells analysed lacked junctions, which are likely to play an important role in the anchoring of astral

microtubules as they are believed to utilise cortical dynein to pull spindle poles into the correct position (O'Connell and Wang, 2000).

In this study, it was found that some of the dividing cells analysed exhibited abnormal spindle phenotypes; multipolar spindles (likely associated with the established defective kinetochore attachments), and a rotated phenotype in which the spindle pole angle was much greater, with the division plane appearing to be rotated roughly parallel to the basal matrix, although it was impossible to say whether astral microtubules were present in such an orientation.

Interestingly and importantly, the TC7 spindles analysed possessed a significantly greater percentage of both abnormal spindle formations. Despite this, the mean spindle division plane angle was no different between TC7 and HCT116 cells, and in fact if the six data points corresponding to the rotated phenotype in TC7 cells are omitted (in other words, if only spindles of the normal morphology are analysed), the TC7 mean (± SEM) division plane angle drops from 3.909 (± 0.8183) degrees to 2.202 (± 0.2758) degrees, which is significantly less ($p=0.0007$) than the 4.419 (±0.5697) degree mean angle demonstrated by HCT116 cells. This may be due to the increased spread of angles demonstrated by HCT116 spindles compared to normally orientated TC7 spindles, which in turn could be attributed to the significantly smaller distance between spindle poles in HCT116 cells. As the spindles are smaller, the same distance in the Z plane corresponds to a greater difference in angle between the two poles than in the TC7 cells. In other words, the greater size and spread of the TC7 cells acts to flatten normally orientated spindles, reducing the effective angle of the division plane.

The observation that the spindle is not generally misorientated in TC7 cells may indicate that flat tissue culture cells (particularly TC7s relative to HCT116s) rely more on an astral microtubules interacting with the basal matrix via integrin-mediated adhesions (which have previously been shown to be dependent on the actin cytoskeleton and EB1) (Toyoshima and Nishida, 2007), rather than with dynein at the cortex. Future work should include spindle analysis in 3D cultures, although previous experiments in Caco2 cells have not demonstrated a greatly altered

orientation phenotype (Jaffe et al., 2008). It may be that rather than attributing a generally misorientated phenotype to the APC mutation, the truncation instead leads to a greater chance that correct orientation can be lost, a scenario similar to the observations in these experiments that although the majority TC7 cells have apparently normal phenotype, a greater proportion lose this, and develop the rotated morphology.

4.3.5: KIF17 colocalises with truncated and normal APC in colon cancer cell lines

The KIF17 kinesin motor has recently been associated with the transport of APC to microtubule plus ends independent of its additional ability to bind EB1, as well as a role in microtubule stabilisation during epithelial polarisation (Jaulin and Kreitzer, 2010). KIF17 was therefore examined as a potential target for knockdown, with the aim of preventing either full length or truncated APC from reaching the cortex. KIF17 was found to colocalise with microtubules (as expected for a motor protein) in all three cell lines analysed, and with both truncated and full length APC in TC7 and HCT116 cells respectively.

Unfortunately, attempts to knockdown KIF17 were generally unsuccessful. Although a phenotype change was observed in some cells using one siRNA sequence, the knockdown was inconsistent, and phenotype change of EB1 relocated along the lattice of straight microtubules extending towards the leading edge of cells is more consistent with increased microtubule stability with a possible impact on cell migration than the knockdown phenotype previously described in the literature. These effects are possibly more likely due to an off target effect of the sequence used. That said, attempting to knockdown motors responsible for APC cortical delivery should be further investigated in the future. In particular, KIF3A and KIF3B/C have been suggested to be associated with the transport of APC by interacting through the adaptor protein KAP3 (Jimbo et al., 2002; Miki et al., 2005), which binds both full length and truncated APC in a region towards the N terminus (Figure 1.11). This adaptor in particular may be a good target, as its loss may not

disrupt as many off-target pathways as risked when compromising the transport of varying cargoes following depletion of the motor protein itself, although it is important to note that KAP3 itself has several other interacting partners in addition to APC.

Figure 4.2 TC7 cell characteristics
Widefield fluorescent images of TC7 cells immunolabelled for: **(A)** α-tubulin (green) and γ-tubulin (red)**,** illustrating the disorganisation of the microtubule network and split centrosome (arrowed). **(B)** EB1 (blue) and α-tubulin (red), illustrating EB1 comet localisation at microtubule plus ends. **(C)** β-catenin (purple) and α-tubulin (green), marking junctions between neighbouring cells. **(D)** β-catenin (red, invert) and ZO-1 (green, invert) Note the enlarged boxed region highlighting the pattern of adherens and tight junctions. **(E)** APC (green), α-tubulin (red) and DAPI (blue), illustrating APC distribution at the cell periphery. **(F)** APC (green, invert), β-catenin (red) and DAPI (blue) highlighting APC colocalisation with β-catenin at junctions (boxed region, enlarged below). **(G)** APC (blue), α-tubulin (green) and ninein (red, invert) illustrating ninein relocation to junctional sites (enlarged in boxed region). All scale bars = 10μm.

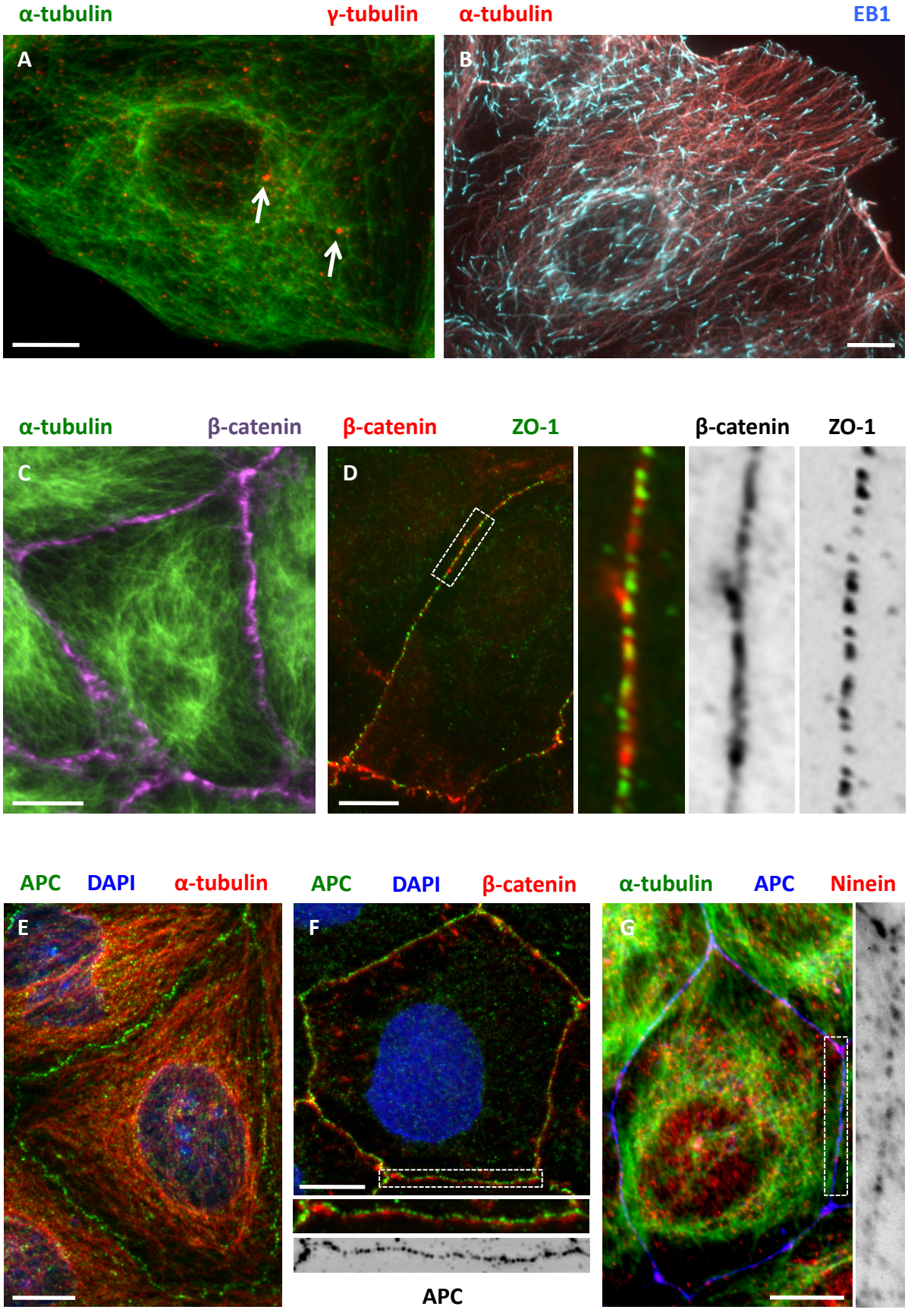
α-tubulin
γ-tubulin
α-tubulin
EB1
A
B
α-tubulin
β-catenin
β-catenin
ZO-1
β-catenin
ZO-1
C
D
APC
DAPI
α-tubulin
APC
DAPI
β-catenin
α-tubulin
APC
Ninein
E
F
G
APC
Ninein

Figure 4.3 (A-B) Characterisation of TC7 polarisation and differentiation
TC7 cells were seeded sparsely on glass coverslips and allowed to polarise over a two week period. At several points during differentiation cells were fixed and immunolabelled.
(A) Widefield fluorescent images of cells labelled for α-tubulin (red), β-catenin (green) and β-actin (blue) at days 3,5,7 and 9. At day 3, cells are subconfluent and adopt a migratory phenotype, with β-actin located at the leading edge of the cell, and microtubules extending forwards. By day 5, cells have reached confluency, and constrict as they polarise, with β-actin colocalising with β-catenin in peripheral regions.
(B) Widefield fluorescent images of cells labelled for EB1 (invert) at days 3,5,7,9 and 13. In subconfluent cells, EB1 can be seen as comets marking the microtubule plus ends. As cells reach confluency, microtubule plus ends can be seen accumulating at the periphery, whilst after cell elongation and polarisation (days 9-13), EB1 is located along the apico-basally orientated microtubule bundles. Scale bars = 10μm

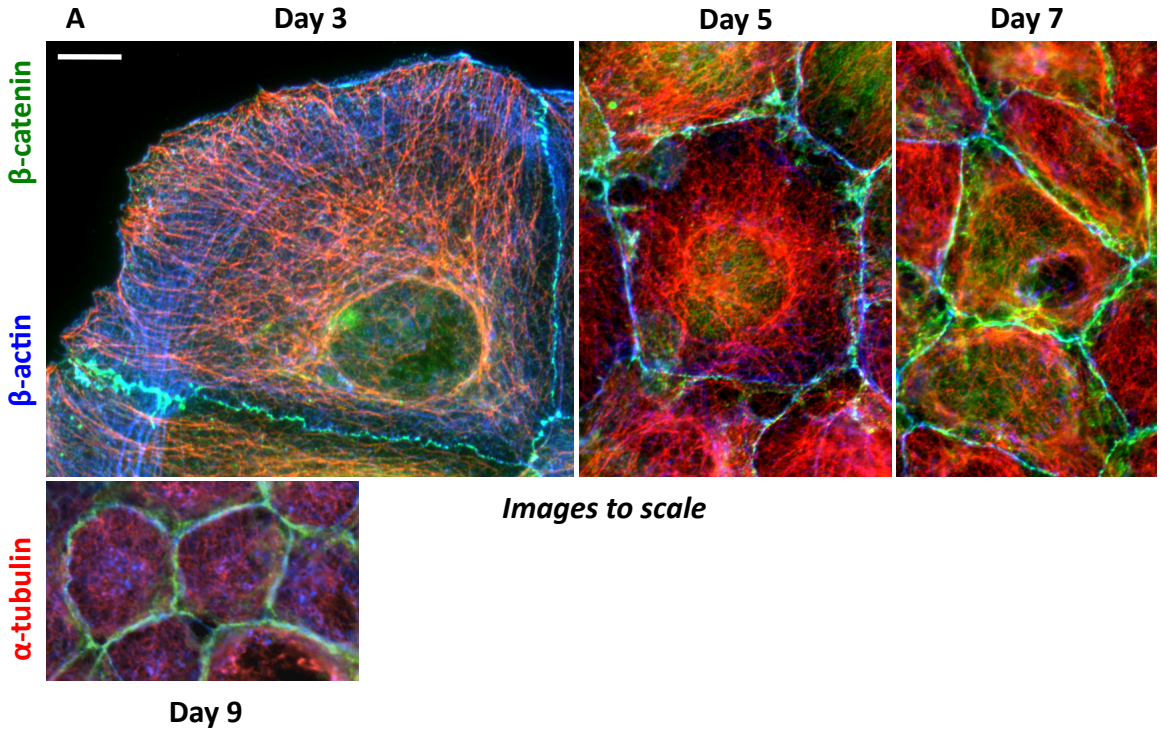
A
Day 3
Day 5
Day 7
β-catenin
β-actin
α-tubulin
Images to scale
Day 9

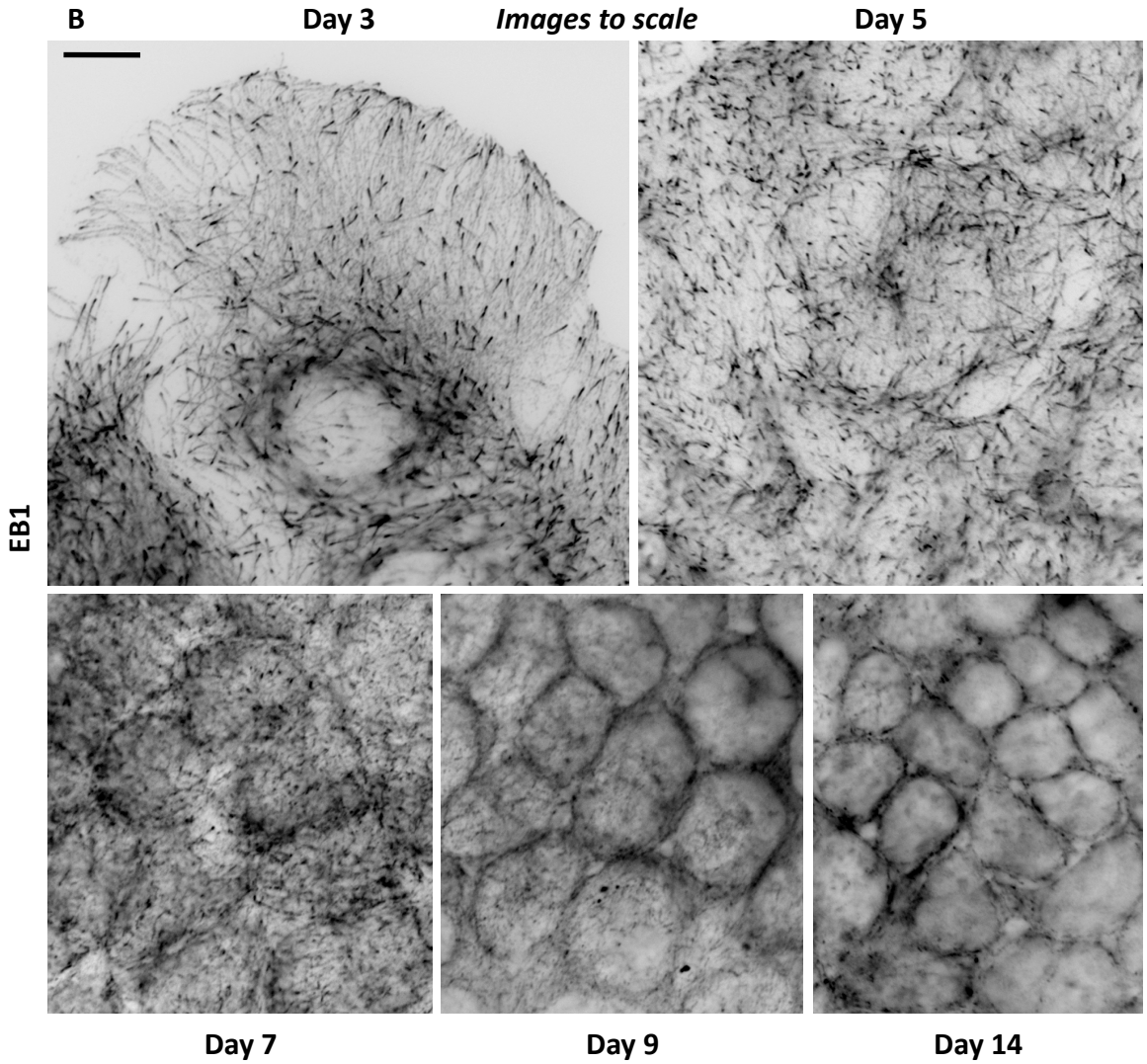
B
Day 3
Images to scale
Day 5
EB1
Day 7
Day 9
Day 14

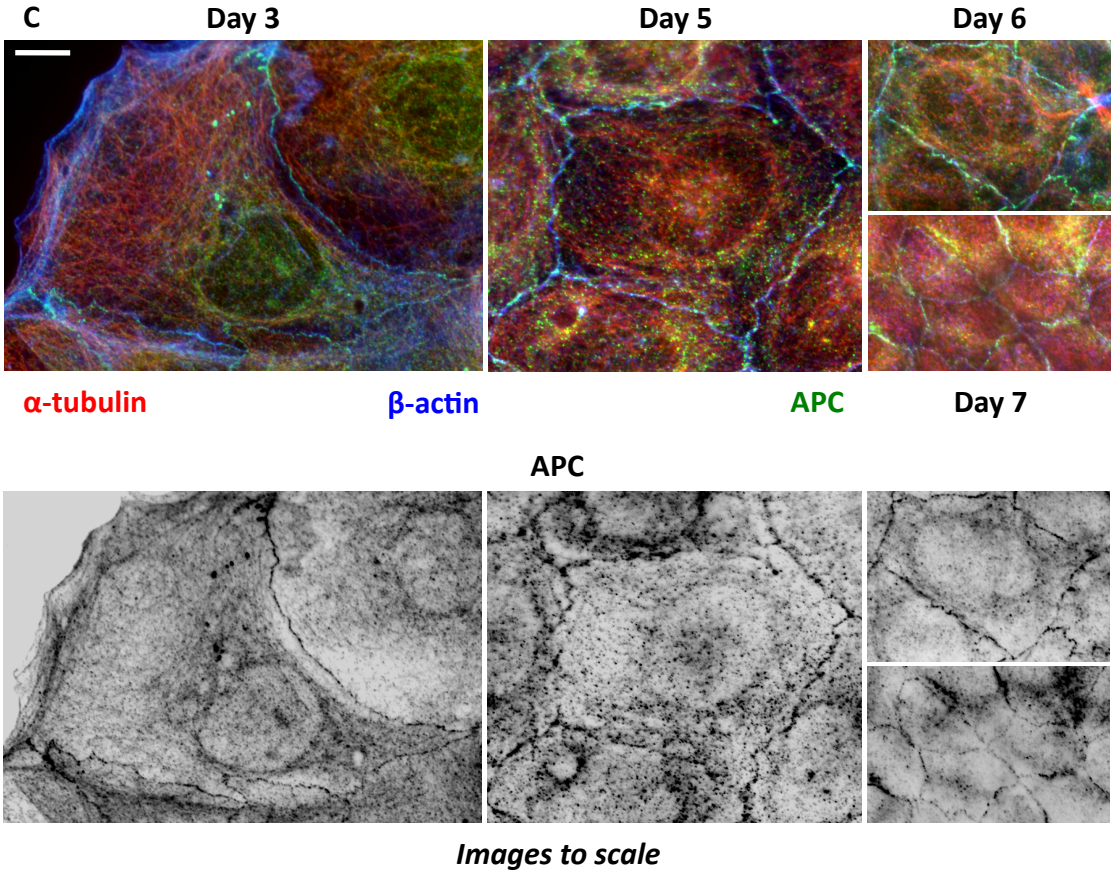

Figure 4.3 (C) Characterisation of TC7 polarisation and differentiation
TC7 cells were seeded sparsely on glass coverslips and allowed to polarise over a two week period. At several points during differentiation cells were fixed and immunolabelled.
(C) Widefield fluorescent images of cells labelled for α-tubulin (red), β-actin (blue) and APC (green, inverted below) at days 3,5,6 and 7. Note that APC is visible at the cell periphery throughout the polarisation sequence. Scale bar = 10µm.

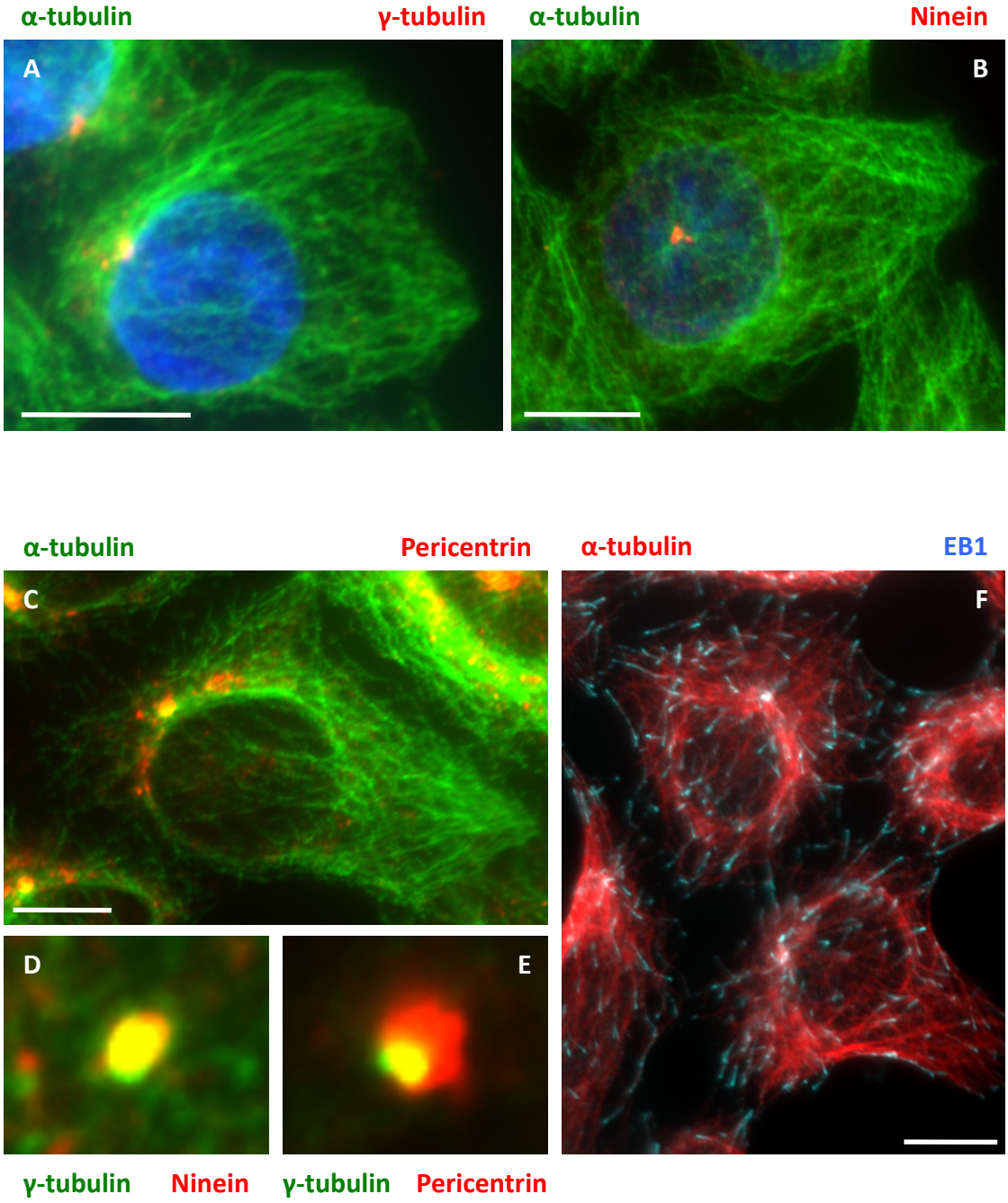

Figure 4.4 (A-F) Characterisation of HCT116 cells
Widefield fluorescent images of subconfluent HCT116 cells immunolabelled for: **(A)** α-tubulin (green) & γ-tubulin (red), and stained for DAPI (blue) **(B)** α-tubulin (green) & ninein (red) **(C)** α-tubulin (green) & pericentrin (red) **(D)** γ-tubulin (green) & ninein (red) and **(E)** γ-tubulin (green) and pericentrin (red). The images illustrate the microtubule array organised by a single central centrosome **(A-C)** at which ninein **(D)** and pericentrin **(E)** colocalise with γ-tubulin. **(F)** HCT116 cells labelled for α-tubulin (red) and EB1 (blue) demonstrating EB1 in a classic +TIP organisation at microtubule ends. Scale bars = 10μm.

Figure 4.4 (G-L) Characterisation of HCT116 cells
Widefield fluorescent images of subconfluent HCT116 cells immunolabelled for: **(G)** α-tubulin (green) & E-Cadherin (purple), and **(H)** α-tubulin (green) & β-catenin (red) and stained for DAPI (blue) illustrate adherens junction organisation. Note the punctate pattern of β-catenin. **(I)** Cells labelled for APC (invert) showing APC localised at cortical sites. **(J)** Cells labelled for APC (green) and β-catenin (red) illustrating APC colocalising with β-catenin at junctional sites (**[Ji]**, arrowed in **[Jii]**). Note however that APC is not found at all junctional sites (**[Jii]**, square brackets). **(K)** Cells labelled for APC (green) and γ-tubulin (red) illustrate APC localising to the centrosome.
(L) Confocal section of HCT116 cells seeded at confluency on a tissue culture membrane insert and immunolabelled for α-tubulin (green) and DAPI (blue) demonstrating that HCT116 cells fail to polarise.
All scale bars = 10μm.

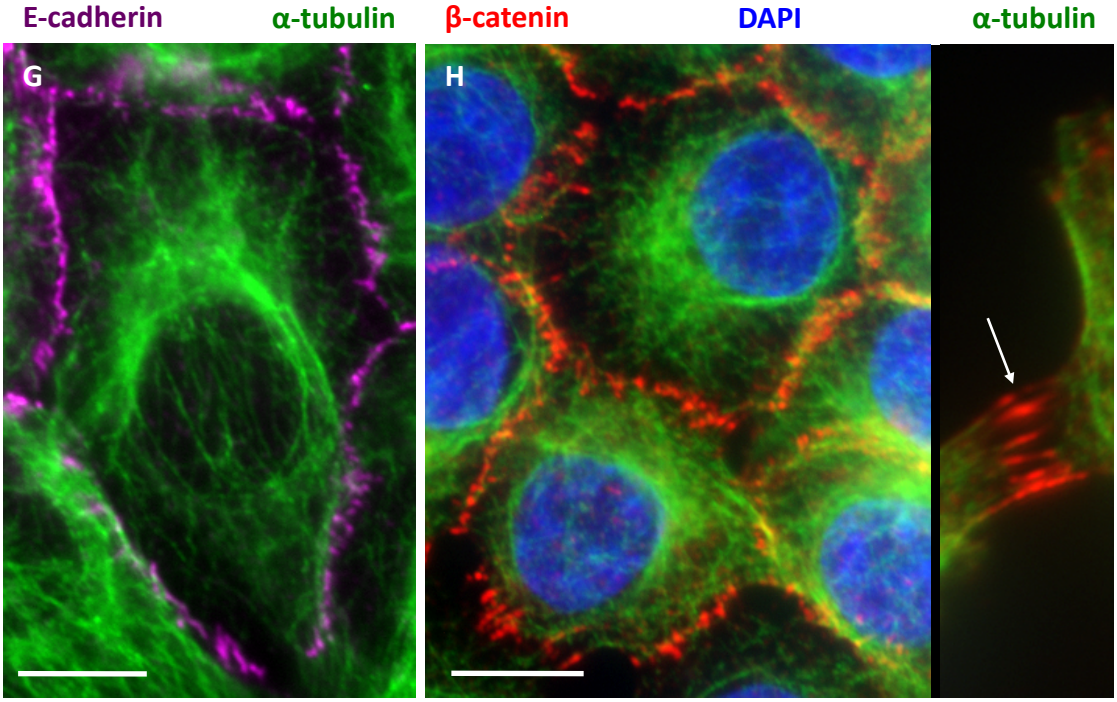
E-cadherin
α-tubulin
β-catenin
DAPI
α-tubulin
G
H

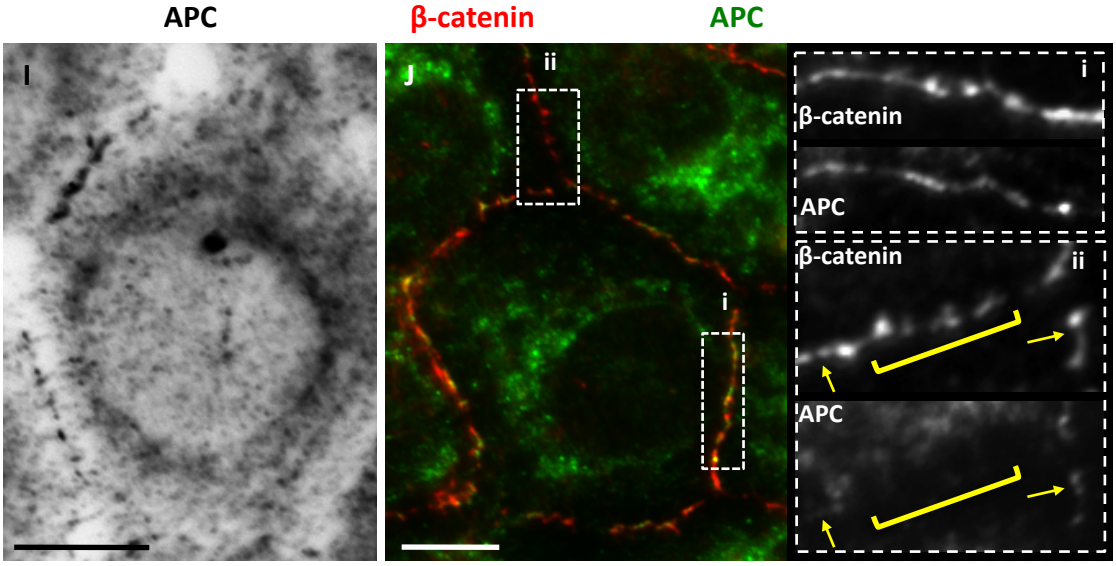
APC
β-catenin
APC
I
J
ii
i
β-catenin
i
APC
β-catenin
ii
APC

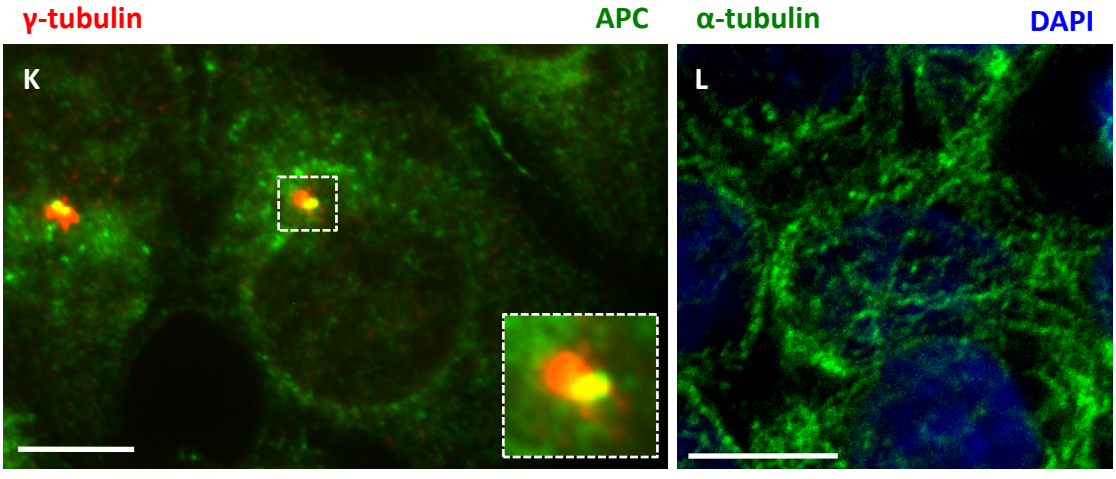
γ-tubulin
APC
α-tubulin
DAPI
K
L

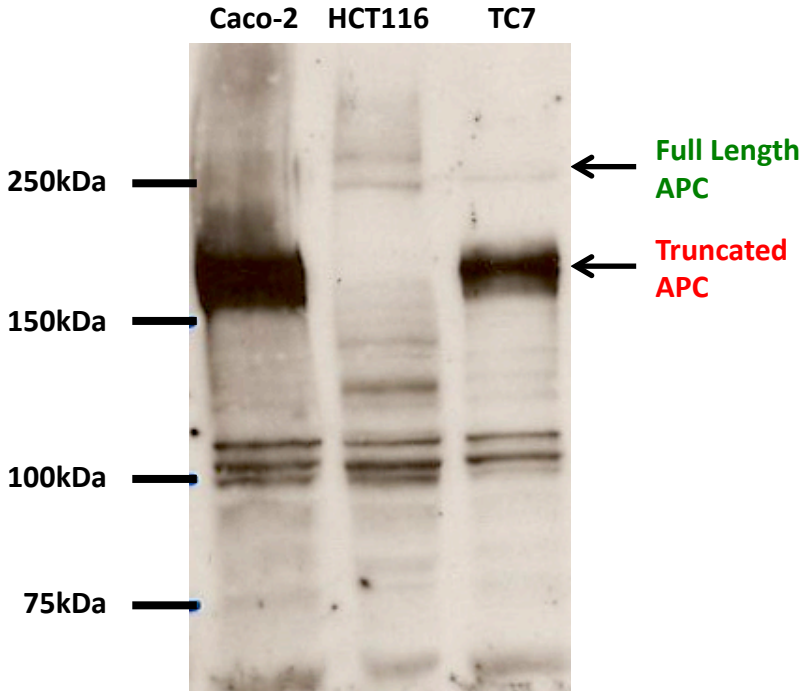

Figure 4.5 APC western of colorectal cancer cell lines
Caco-2, HCT116 and TC7 cell lysates were prepared and probed for APC. The APC truncation mutation was evident in TC7 cells and its parental Caco-2 cell line just above the 150kDa size marker, whilst full length APC was detected in HCT116 cells just above the 250kDa size marker.

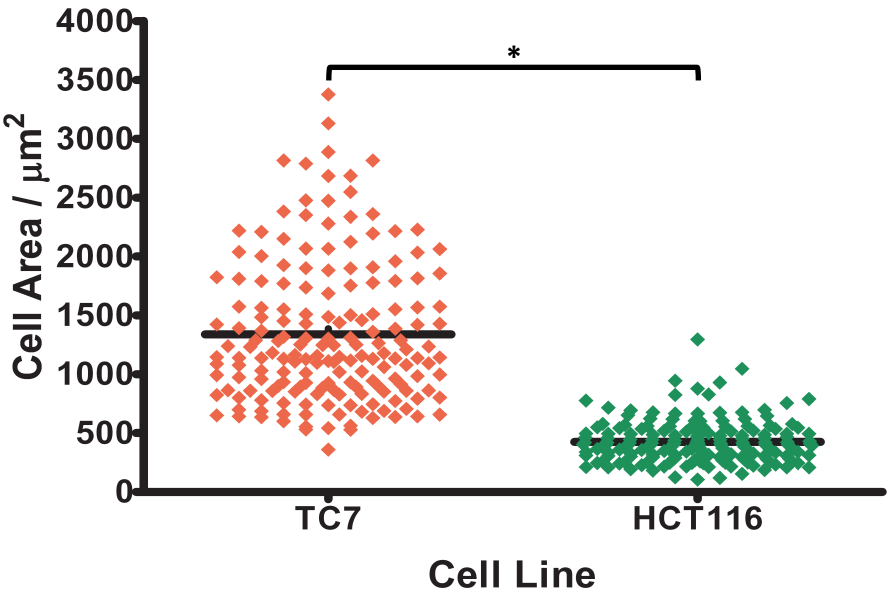

Average Cell Area (± SEM)
TC7: 1340 ± 45.83 µm^2 **HCT116:** 425.2 ± 13.71 µm^2

Figure 4.6 Relative size of HCT116 and TC7 cells
TC7 and HCT116 cells were seeded then fixed when subconfluent, and their area measured using axiovision software.
(TC7, HCT116 N=175, two-tailed unpaired t-test with Welch's correction [p<0.0001]).

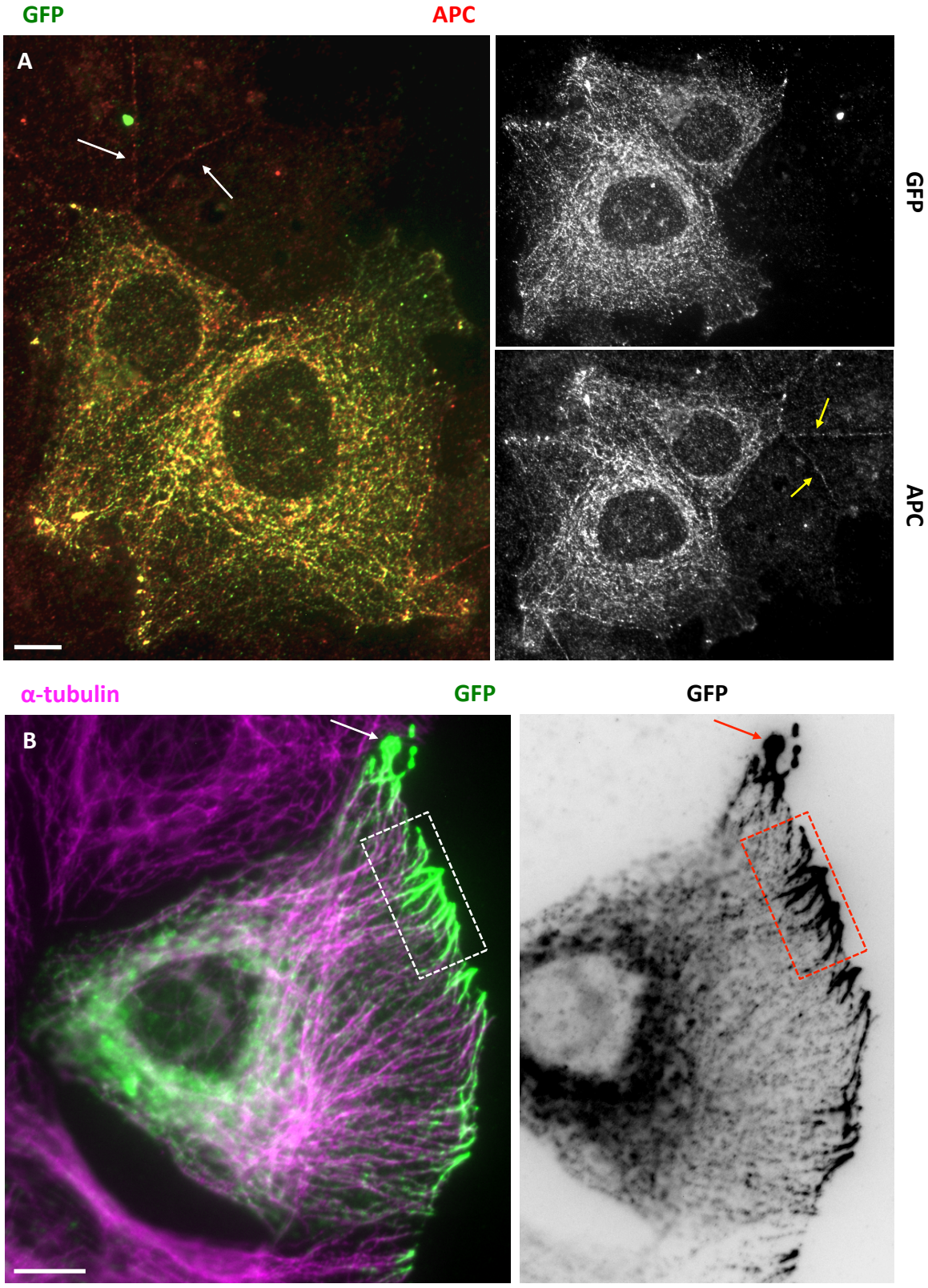

Figure 4.7 (A-B) GFP-APC expression in TC7 cells
Widefield fluorescent images of TC7 cells transfected with full length GFP-APC 24 hours prior to immunolabelling. **(A)** Cells stained for GFP (green, single channel) and APC (red, single channel), confirming APC overexpression in transfected cells. Note that GFP-APC expression appears in the cytoplasm, rather than being restricted to cell junctions as for endogenous TC7 APC (arrowed in neighbouring untransfected cells). **(B)** Cells stained for GFP (green, invert) and α-tubulin (purple) verifies full length GFP-APC localisation along microtubules, with labelling especially strong at the plus end of microtubules at the exposed leading edge of cells (boxed), and in cell extensions (arrowed). All scale bars = 10µm

Figure 4.7 (C-E) GFP-APC expression in TC7 cells
Widefield fluorescent images of TC7 cells transfected with GFP-APC 24 hours prior to immunolabelling.
(C) Cells stained for GFP (green) and EB1 (red). Note GFP-APC accumulation in cell protrusions (**[i]**, arrowed). GFP-APC colocalised with EB1 at microtubule plus ends leading into protrusions (**[ii]**, boxed), and in punctate patterns in regions of strong GFP-APC expression in these regions (**[ii]**, arrowhead).
(D) Cells stained for GFP (green) and α-tubulin (red) highlighting that in addition to localisation along microtubules, GFP-APC localised to cortical regions (enlarged in inset).
(E) Cells stained for GFP (green) and β-catenin (red), illustrating GFP-APC colocalising with β-catenin at junctional sites (**[i]**, enlarged in inset) and at the free edge of cells (**[ii]**, arrowed)
All scale bars = 10μm

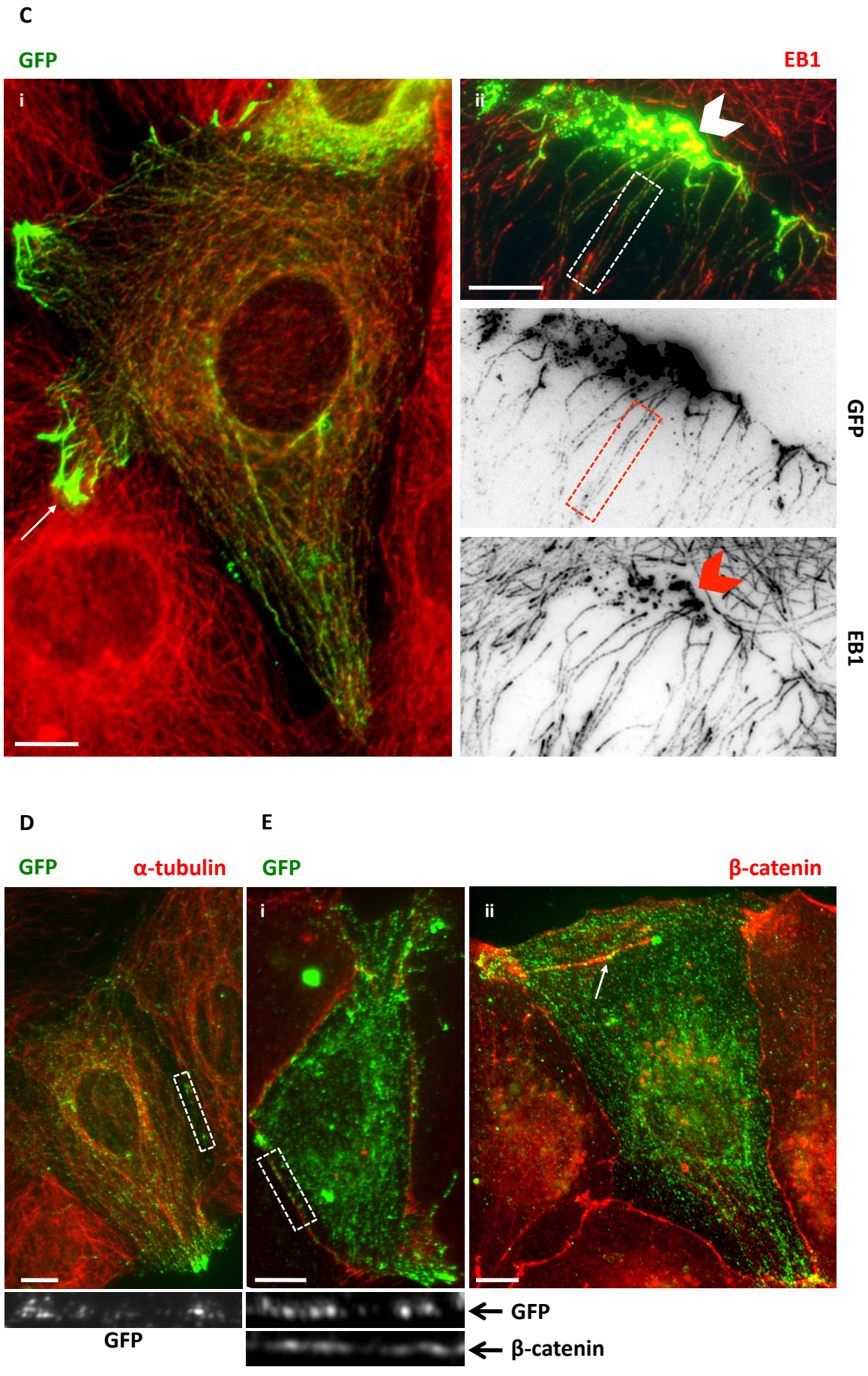
C
GFP
EB1
i
ii
GFP
EB1
D
GFP
α-tubulin
GFP
E
GFP
β-catenin
i
ii
GFP
GFP
β-catenin

Figure 4.8 Microtubule orientation and APC status

(A) Microtubule orientation at the cortex was scored as parallel or perpendicular in random 10μm sections along the cortex for each cell line. Example region immunolabelled for α-tubulin (green, invert) and β-catenin (purple). The cell lines analysed were as follows: APC full length (wild type) expressing MDCK and HCT-116 cells, the truncated APC expressing TC7 cells, and TC7 cells transiently transfected with full length GFP-APC 24 hours prior to analysis.

(B) Graph illustrating the average percentage of perpendicularly orientated microtubules in each condition. The raw data is summarised in the table. Statistical significance between each condition was assessed by one way ANOVA with Tukey's multiple comparison test. TC7 cells had significantly less microtubules orientated perpendicular to the cortex compared to either of the two full length APC expressing cell lines ($p<0.001$). This could be rescued by expression of the GFP-APC construct ($p<0.001$).

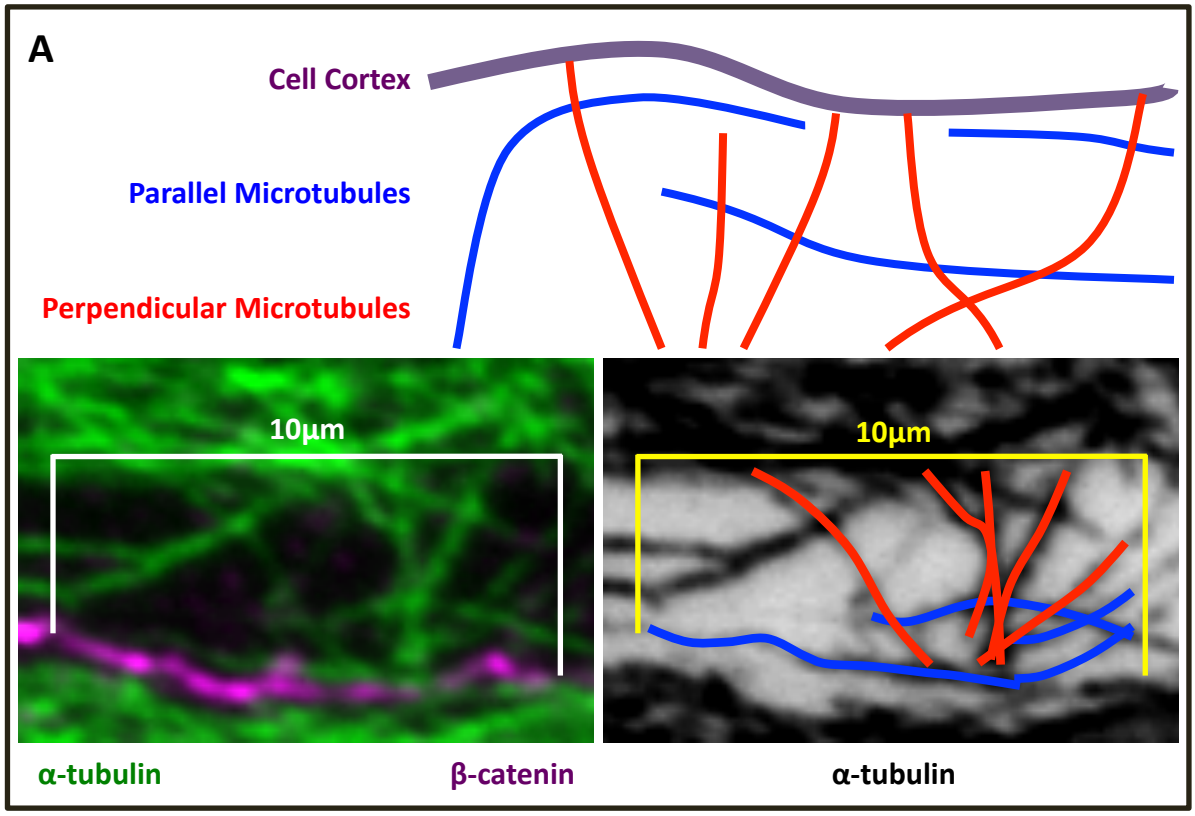

B **Percentage of microtubules orientated perpendicular to the cortex in full-length and truncated APC expressing cells**

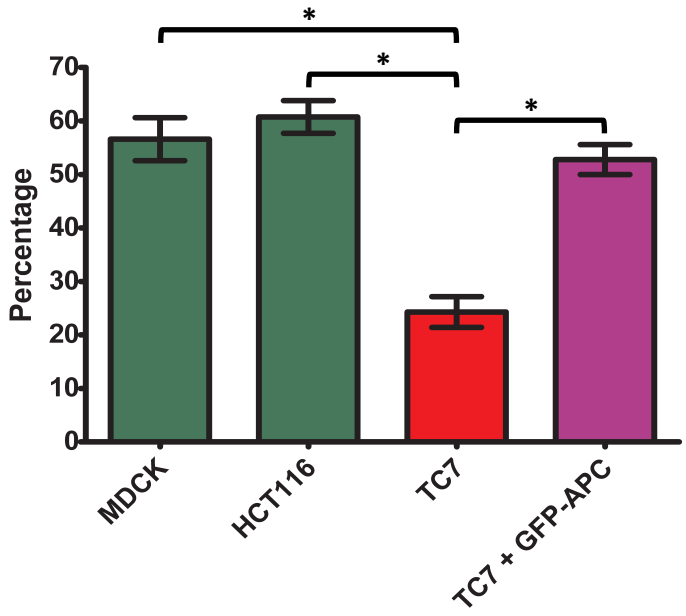

Cell Line	N	Mean ± SEM
MDCK	70	56.62 ± 4.018
HCT116	65	60.74 ± 3.061
TC7	80	24.28 ± 2.881
TC7 + GFP-APC	70	52.80 ± 2.794

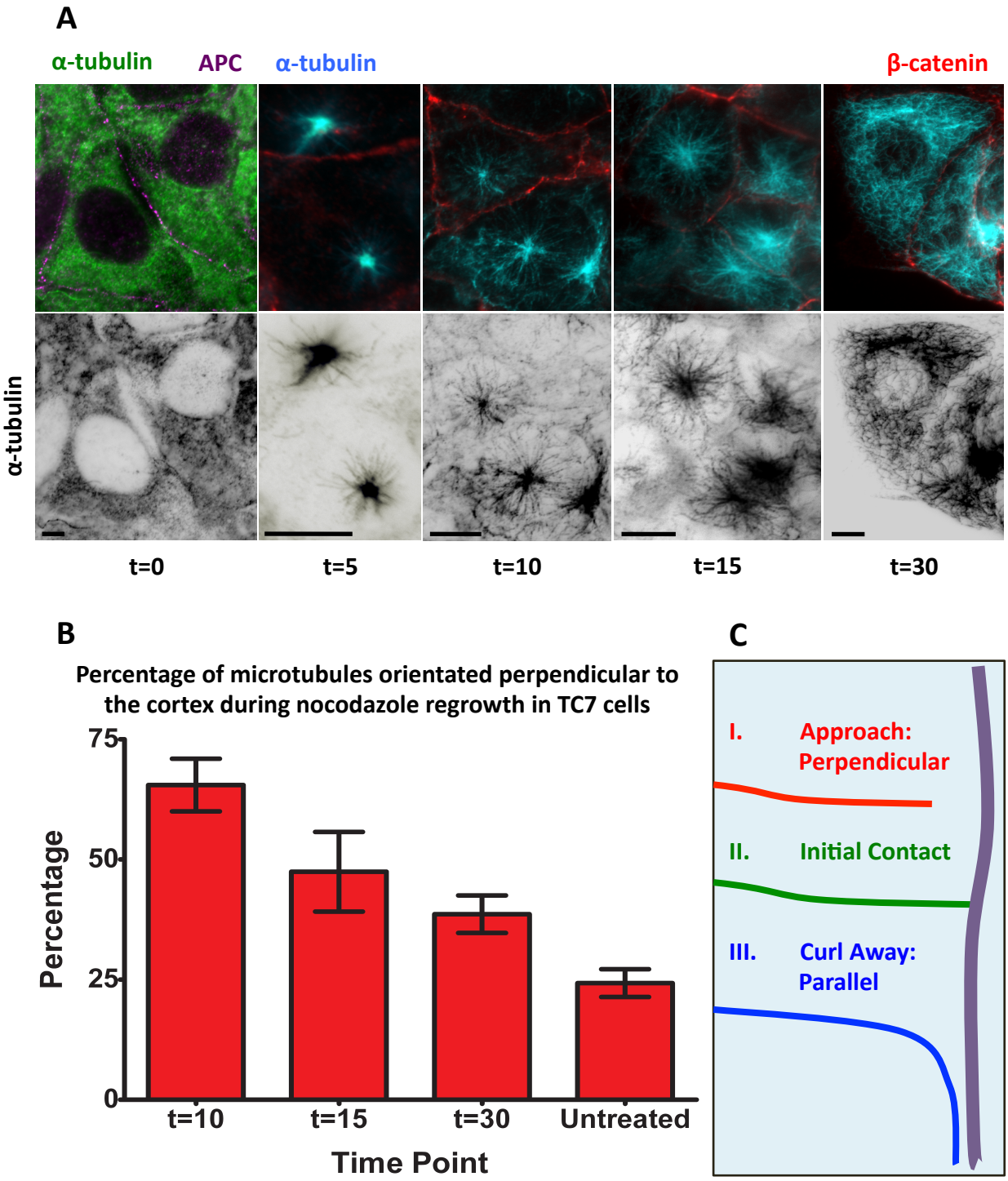

Figure 4.9 Microtubule orientation following nocodazole regrowth in TC7 cells

(A) Cells were exposed to 33μM nocodazole for two hours followed by wash out and fixed at 5, 10, 15 and 30 minutes post drug removal, then immunolabelled for α-tubulin (green, blue, inverts), and APC (purple), or β-catenin (red). Microtubule asters are visible at t=5, which elongate towards the periphery forming a radial array over the remaining timepoints until by t=30 an array resembling the original TC7 disordered microtubule network is produced. APC remains localised to the cortex in nocodazole (t=0).

(B) Quantification of microtubule orientation at t=10, 15 and 30 minutes compared to untreated control cells. Note that microtubules initially are orientated perpendicular to the cortex, but that this percentage reduces over time to approach that of untreated cells (t=10: N=37, t=15: N=11, t=30: N=36, Untreated: N=80. Error bars = SEM).

(C) Model for microtubule cortical approach in truncated APC conditions. Microtubules approach orientated perpendicularly and make an initial transient contact, but then curl away and run parallel with the cell periphery.

Figure 4.10 Optimisation of double thymidine block in TC7 cells
TC7 cells seeded onto coverslips and allowed to settle overnight, then treated with 2mM thymidine for 17 hours (Block 1), released into fresh media for 9 hours (Release 1), and reblocked in 2mM thymidine for a further 17 hours (Block 2). Cells were fixed at the end of this period (t=0), then released for a second time, and fixed at 1, 2, 3, 4, 5, 6, 8, 10, 12 and 24 hours post release, to ascertain the time point with the greatest number of mitotic events (red line). Untreated control cells were also fixed at various time points by way of comparison (blue points), and the total percentage of control cells in mitosis calculated (blue dotted line).

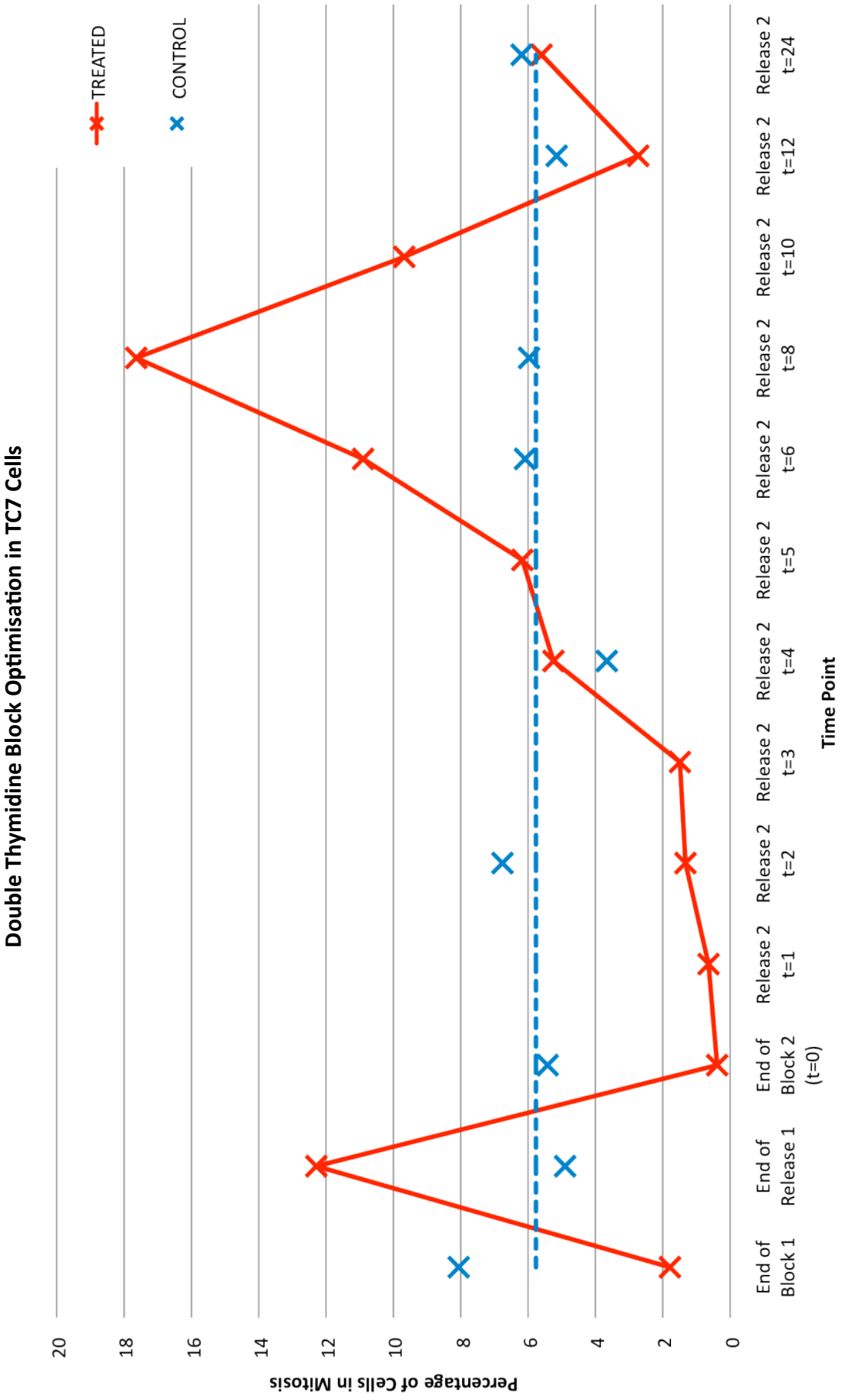
Double Thymidine Block Optimisation in TC7 Cells
TREATED
CONTROL
Percentage of Cells in Mitosis
0
2
4
6
8
10
12
14
16
18
20
End of Block 1
End of Release 1
End of Block 2 (t=0)
Release 2 t=1
Release 2 t=2
Release 2 t=3
Release 2 t=4
Release 2 t=5
Release 2 t=6
Release 2 t=8
Release 2 t=10
Release 2 t=12
Release 2 t=24
Time Point

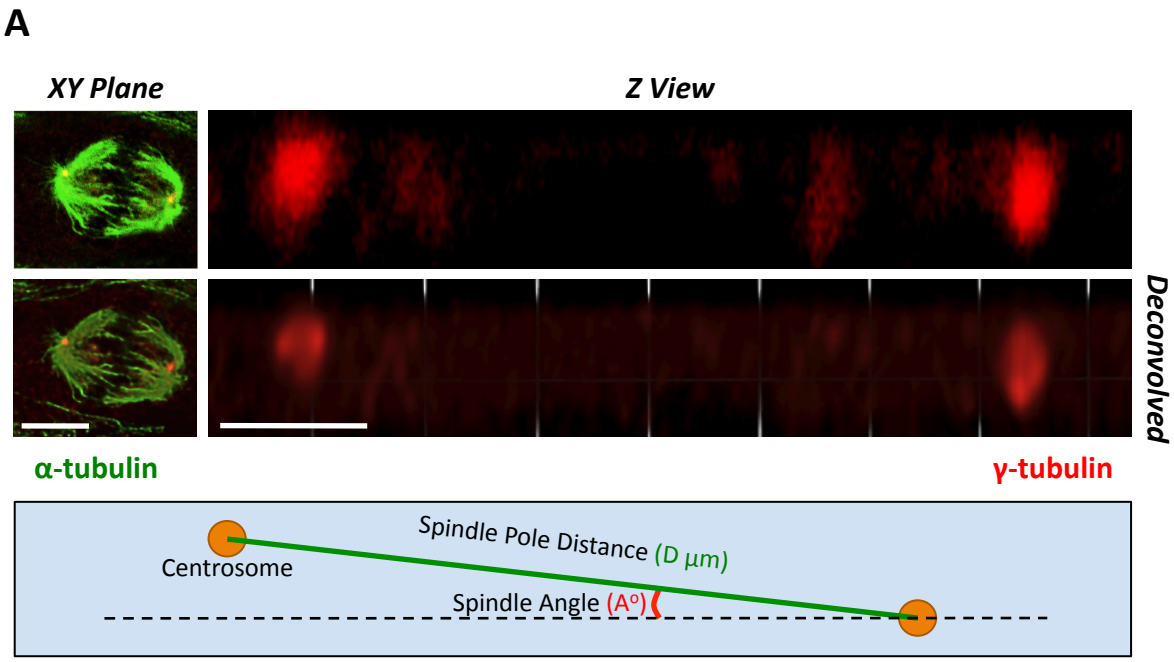

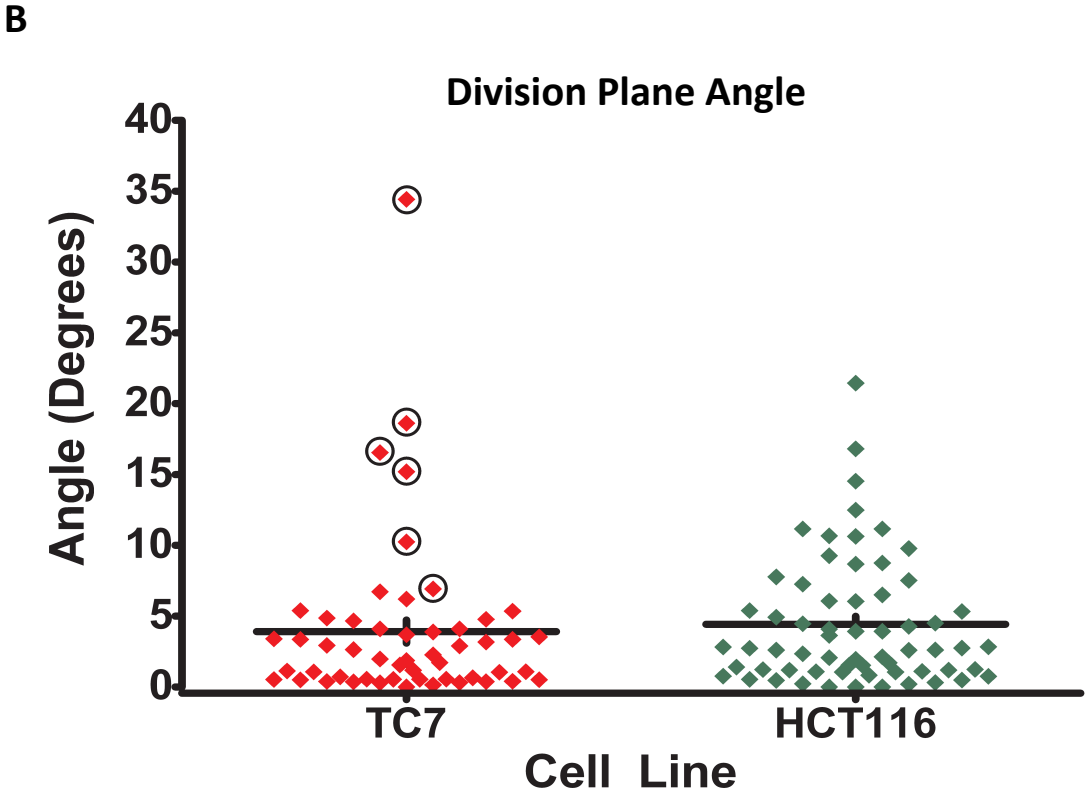

Figure 4.11 (A-B) Analysis of spindle orientation in TC7 and HCT116 cells
TC7 and HCT116 cells were treated with a double thymidine block, and fixed and stained for α-tubulin (green) and γ-tubulin (red). Optical sections through spindles were taken by confocal microscopy.
(A) Images were deconvolved, rotated, and a Z view taken through the spindle poles, which was used to calculate the spindle pole distance [D] and division plane angle [A]. XY plane scale bar = 10µm, Z view scale bar = 5µm.
(B) Scatter plot of the division plane angle [A] for the TC7 and HCT116 spindles analysed. The line represents the mean angle (+SEM). Circled points indicate TC7 spindles of the rotated phenotype.

C

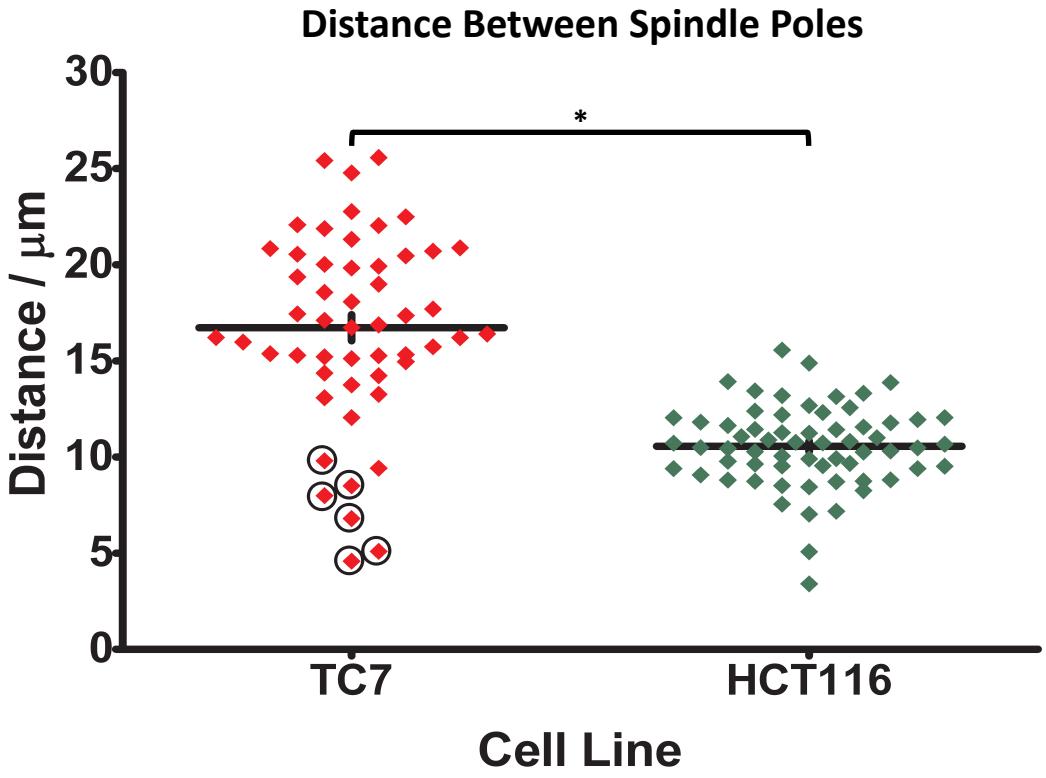

D

Cell Line	N	Mean ± SEM	
		Division Plane Angle (Degrees)	Spindle Pole Distance (µm)
TC7	52	3.909 ± 0.8183	16.73 ± 0.6823
HCT116	63	4.419 ± 0.5697	10.56 ± 0.2697
TC7: Normal Phenotype Only	46	2.202 ±0.2758	17.98 ± 0.5335

	Comparison			Unpaired t-test (Welch Correction)	F-test (variance)
Angle	TC7	*vs*	HCT116	P = 0.6101 [NS]	P = 0.0460
	TC7: Normal		HCT116	P = 0.0007	P < 0.0001
Distance	TC7		HCT116	P < 0.0001	P < 0.0001
	TC7: Normal		HCT116	P < 0.0001	P = 0.0001

Figure 4.11 (C-D) Analysis of spindle orientation in TC7 and HCT116 cells
(C) Scatter plot of the spindle pole distance [D] for the TC7 and HCT116 spindles analysed. The line represents the mean distance (+SEM). Circled points indicate TC7 spindles of the rotated phenotype.
(D) Data tables summarising the statistics. Included are comparisons of all TC7 data against HCT116 cells, and for 'normal' phenotype TC7s only, with the circled data points of the 'rotated' phenotype excluded.

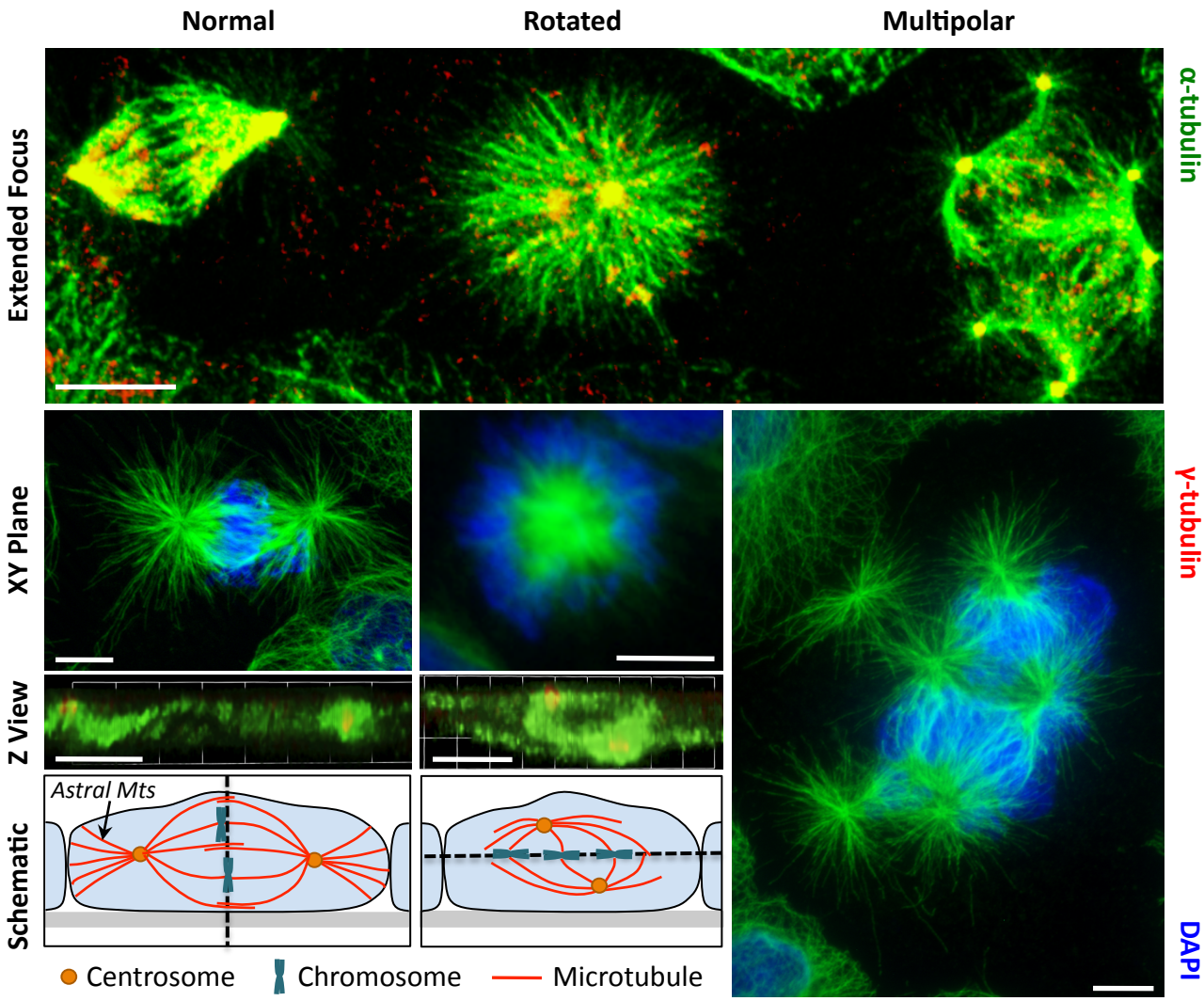

Figure 4.12 TC7 cells exhibit three spindle morphologies
TC7 spindles stained for α-tubulin (green), γ-tubulin (red) and DAPI (blue) can be found in three distinct phenotypes: normal spindles are organised by centrosomes at each spindles pole and orientate such that the division plane (dotted line in schematic) is perpendicular to the basal matrix. Astral microtubules extend out to the cell periphery. The rotated phenotype appears to have a single pole from above, though the two centrosomes can be observed by extended focus. The two halves of the spindle are seen above and below a division plane that is approximately parallel to the basal matrix. Finally, a multipolar spindle morphology is also observed. Scale bars = 10µm, except Z view scale bars = 5µm.

A

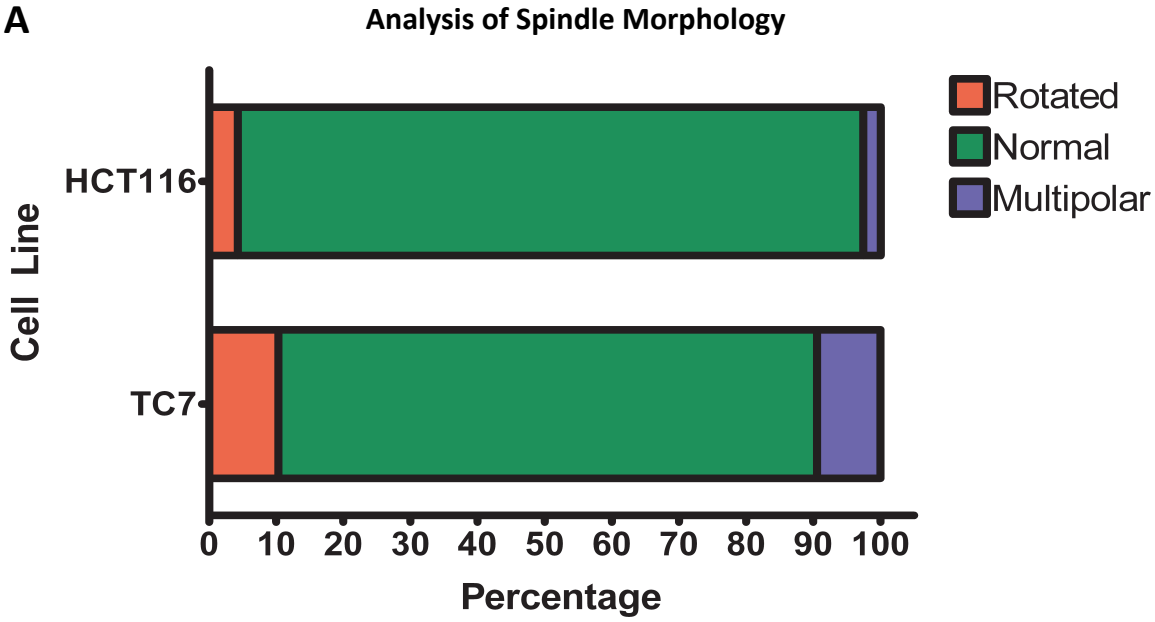

B

Spindle Type	TC7	HCT116
Normal	195 (80.3%)	218 (93.2%)
Rotated	25 (10.3%)	10 (4.3%)
Multipolar	23 (9.5%)	6 (2.6%)
Total (N)	**243**	**234**
Chi-Squared	17.51 P=0.0002	

Figure 4.13 TC7s possess a greater proportion of the abnormal spindle morphologies than HCT116 cells
Double thymidine block treated cells 8 hours after release were assessed for their spindle phenotypes, and recorded as either 'normal', 'rotated', or 'multipolar'. **(A)** Chart and **(B)** Results table outlining the data, with statistical evaluation by Chi-Squared test demonstrating that TC7 cells possessed a significantly increased proportion of both multipolar and rotated spindle phenotypes than HCT116 cells.

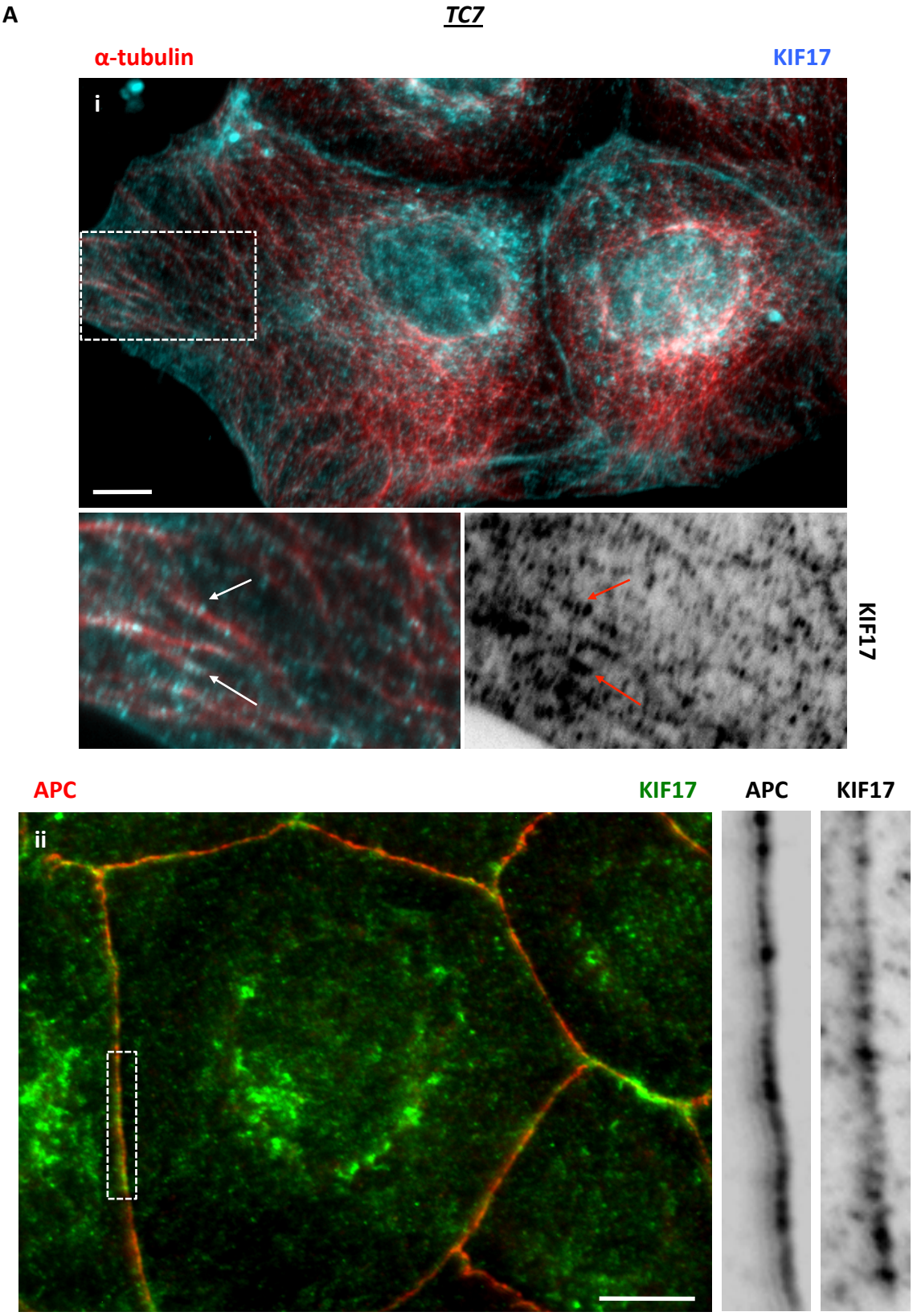

Figure 4.14 KIF17 localises along microtubules and colocalises with APC
(A) Widefield fluorescence images of TC7 cells grown on glass coverslips and immunolabelled for **[i]** KIF17 (blue, invert) & α-tubulin (red), revealing KIF17 as speckles located along the microtubule lattice (arrowed) and **[ii]** KIF17 (green, invert) and APC (red, invert), demonstrating KIF17 colocalised with TC7 truncated APC at the cell cortex (enlarged selection). Scale bars = 10µm.

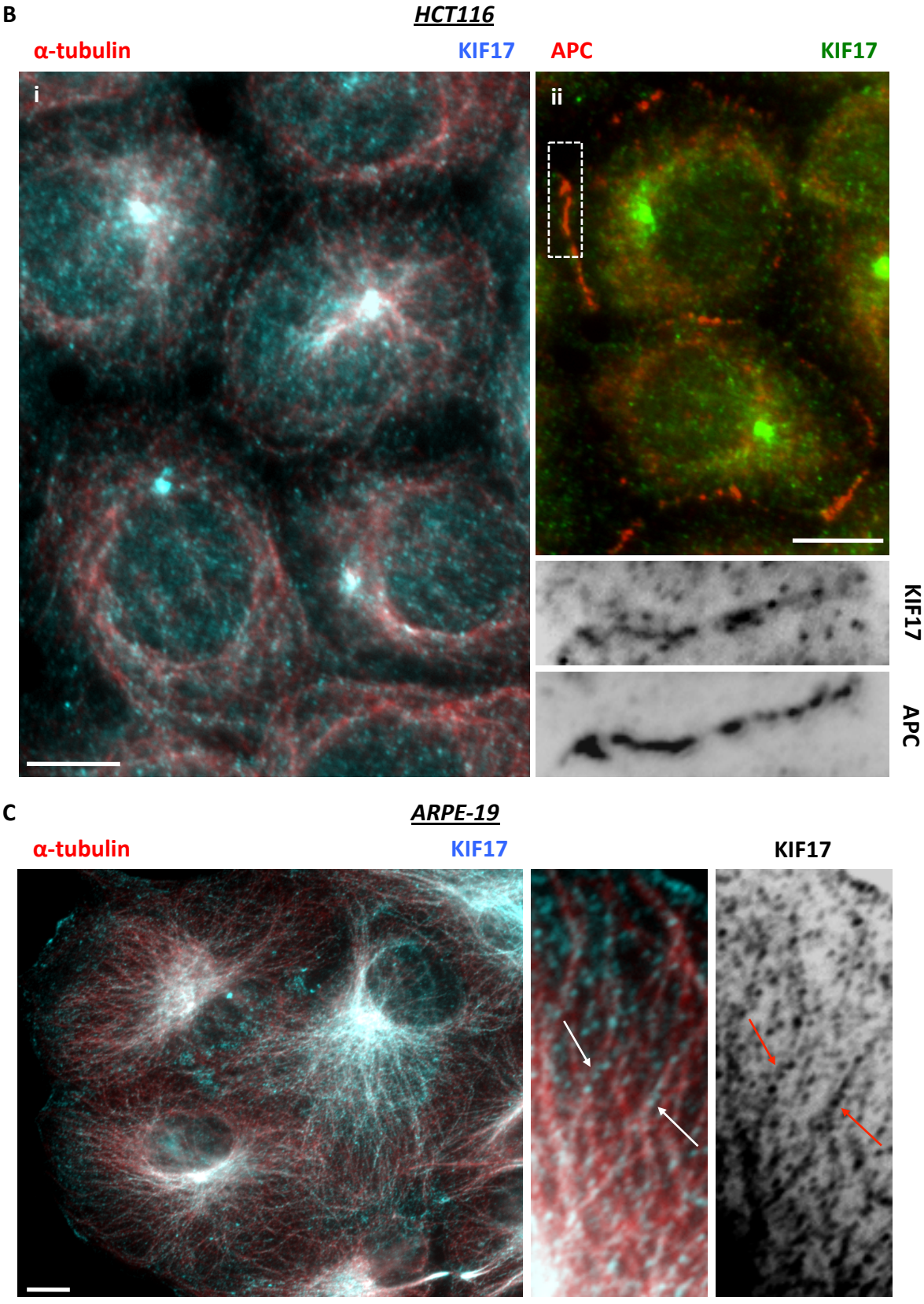

Figure 4.14 (B-C) KIF17 localises along microtubules and colocalises with APC
(B) Widefield fluorescence images of HCT116 cells grown on glass coverslips and immunolabelled for **[i]** KIF17 (blue) & α-tubulin (red), revealing KIF17 centrally located, possibly at the centrosome, and **[ii]** KIF17 (green, invert) and APC (red, invert), demonstrating KIF17 colocalised with full length APC at the cell cortex (enlarged selection). **(C)** Widefield fluorescence images of ARPE-19 cells grown on glass coverslips and immunolabelled for KIF17 (blue, invert) & α-tubulin (red), revealing KIF17 as speckles located along the microtubule lattice (arrowed). All scale bars = 10μm.

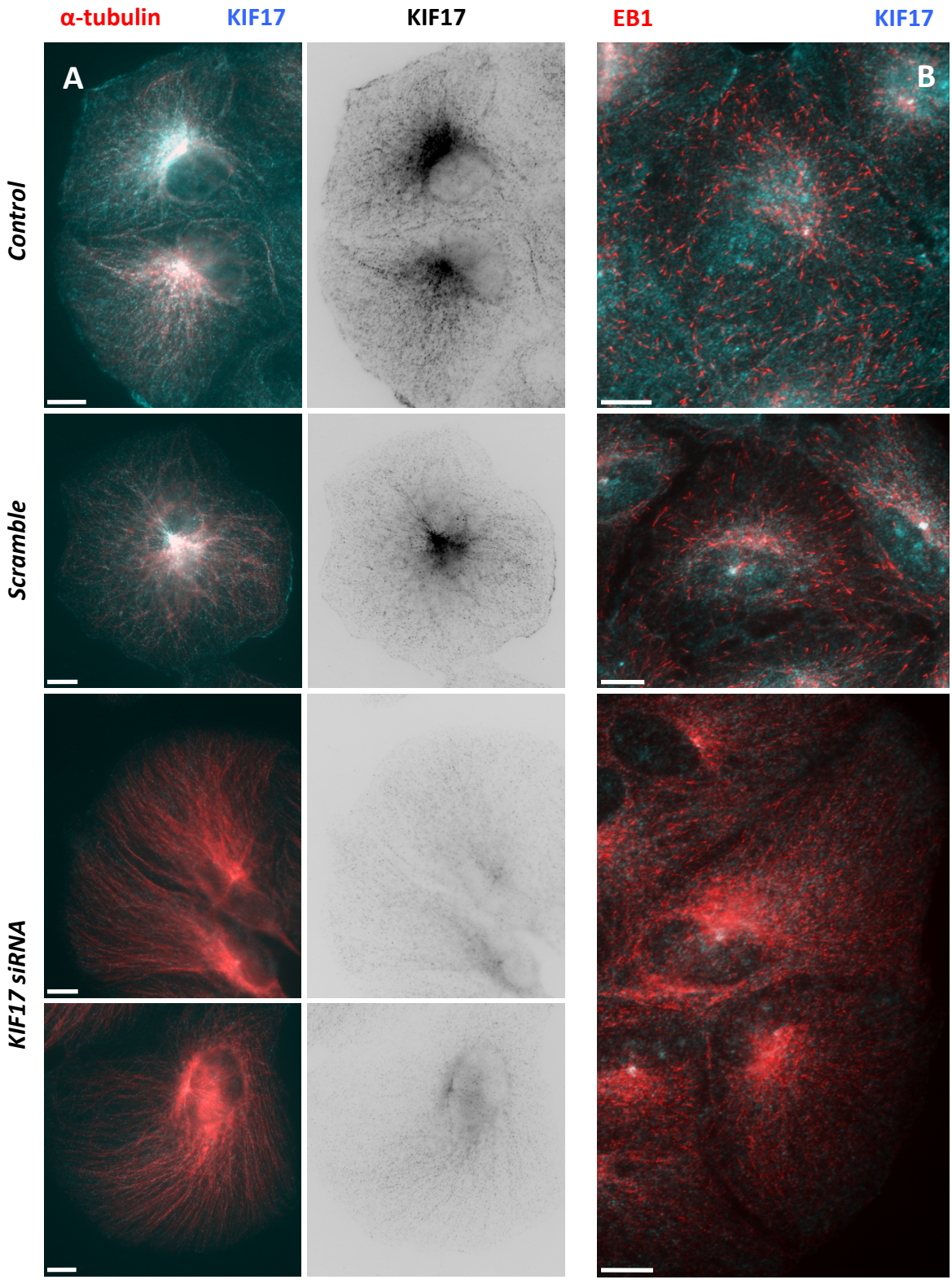

Figure 4.15 KIF17 siRNA treatment alters ARPE-19 microtubule organisation
Widefield fluorescent images of control, scramble and KIF17 siRNA treated ARPE-19 cells imaged at set exposure levels. **(A)** Cells immunolabelled for α-tubulin (red) and KIF17 (blue, invert). Regions where KIF17 appeared to be depleted resulted in straightening of microtubules at the exposed leading edge of cells, to give a fan of aligned microtubules extending to the exposed periphery. **(B)** Cells immunolabelled for EB1 (red) and KIF17 indicated a switch from the classic plus end comet arrangement as typical of control and scramble cells to a recruitment to the microtubule lattice, in cells were KIF17 appears reduced and microtubules have reorganised. Scale bars = 10µm.

Chapter V

EB2 Function in Microtubule Reorganisation & Bundle Formation

5.1: Introduction

The ability of microtubules to reorganise is crucial for the formation of the polarised apico-basal array during epithelial differentiation. It is therefore critical to understand the complex fundamental molecular processes behind this reorganisation in order to examine disregulation in cancer disease states. This ability to rearrange is driven by the dynamic nature of microtubules, with the most common group of +TIP proteins, the EB family, known to be especially important due to their influence on microtubule dynamic instability (Tirnauer and Bierer, 2000). Of the three EB family members EB1 has been most intensively studied, and has been shown to interact with, recruit, and regulate the activity of most other +TIP proteins at the microtubule plus end (Akhmanova and Steinmetz, 2008), including the microtubule-actin crosslinker ACF7 (Kodama et al., 2003; Slep et al., 2005). As such, it has been associated with the regulation of microtubule interactions with cellular structures and other cytoskeletal filaments, including actin (Lansbergen and Akhmanova, 2006).

Overexpression of EB1 causes it to decorate the microtubule lattice, and has been associated with microtubule stability and bundling (Bu and Su, 2001). Formation of stable microtubule bundles is observed during the polarisation and differentiation processes in various cell types (such as migrating fibroblasts and myoblasts), with EB1 and its relative EB3 implicated in the reorganisation of the microtubule networks involved (Straube and Merdes, 2007; Wen et al., 2004; Zhang et al., 2009). Similarly, apico-basal microtubules in epithelial cells are rearranged by the release and capture mechanism (see 1.5.3) into an array where microtubules are organised in stable bundles that are anchored at apical sites and extend down into basal regions (Bellett et al., 2009; Mogensen et al., 2002), however any contribution made by EB proteins to this mechanism remains undetermined.

In contrast to the extensive examination of EB1, investigations into the alternative two EB family members, especially EB2, have been limited. Interestingly however, whilst EB3 appears to share similar classical characteristics with EB1, EB2 demonstrates several crucial behavioural differences. Studies of the effects

exhibited by the EBs on microtubule dynamics revealed that EB2 was far less potent at promoting growth by suppressing microtubule catastrophe than either EB1 or EB3 (Komarova et al., 2009). EB proteins recognise the end of microtubules due to their affinity for GTP-tubulin displayed by the growing cap (Maurer et al., 2011; Maurer et al., 2012), coupled to electrostatic repulsion between their negatively charged C-terminal region and the microtubule lattice (Buey et al., 2011). EB2 showed less affinity for the microtubule plus end than EB1 and EB3 due to substitutions in key CH domain amino acid residues, and as such was out-competed for plus end binding by its two relatives. It was also unable to heterodimerise, unlike EB1 and EB3. As such EB2 is generally observed localised along the microtubule lattice as opposed to in a classical +TIP comet like distribution at microtubule plus ends (Komarova et al., 2009). EB2 has also been found not to interact with other +TIPs as successfully as EB1; knockdown of EB1 and EB3 together has been shown to reduce CLIP-170 expression at the microtubule plus end, and whilst this effect could be rescued by transfection with an EB1 construct, function could not be restored with an EB2 construct (Komarova et al., 2005).

EB2 has also been seen differentially expressed during cellular processes. Most interestingly, in contrast to the observations for EB1, overexpression of EB2 failed to induce microtubule bundling (Bu and Su, 2001). In addition, studies examining microtubule rearrangement during muscle differentiation, expression of EB2 was seen to be distinctly reduced (Straube and Merdes, 2007; Zhang et al., 2009), suggesting downregulation of EB2 may be essential for the formation of non-centrosomal microtubule bundles during epithelial apico-basal differentiation. If this is the case, overexpression of EB2 in cancer could have implications for the loss of epithelial polarisation and promotion of a more migratory phenotype in colon epithelial cells. Indeed, it has been demonstrated that the EB2 gene (MAPRE2) is highly overexpressed in pancreatic cancer cells, where it has been linked to perineural invasion (invasion into and along nerves), a common occurrence in pancreatic cancer often linked to recurrence of the disease (Abiatari et al., 2009).

We have recently investigated the role played by EB proteins, particularly EB2, during microtubule reorganisation in epithelial apico-basal polarisation, in

particular seeing whether the reduction in EB2 levels in muscle differentiation (as described above) is replicated in epithelial models. Initial work examined EB2 expression levels in isolated epithelial tissue explants. It was found that in the terminally differentiated cells of isolated organ of Corti from the inner ear, EB2 was highly expressed in hair cells, but distinctly reduced in supporting cells (pillar cells and Deiters), with EB1 present along microtubules (Goldspink et al., 2013b). This is significant as whilst both cell types demonstrate apico-basally orientated microtubules, they are arranged in stable bundles linked to actin filaments in supporting cells, but not in hair cells, which instead have free cytoplasmic microtubules that are dynamic (Furness et al., 1990; Goldspink et al., 2013b; Henderson et al., 1995; Slepecky et al., 1995). A similar correlation between low EB2 expression and microtubule bundle formation was observed in isolated small intestinal crypt cells. As previously established, crypt cells are not terminally differentiated, and instead undergo rapid turnover from stem cells located at the base of each crypt, producing transit amplifying cells which further divide and differentiate as they migrate to the surface epithelium (Sancho et al., 2004; van der Flier and Clevers, 2009) (Figure 1.9 C). In isolated crypts immunolabelled for EB2, it was found to be highly expressed in the stem cell zone, where apico-basal microtubules appeared to be organised in an 'umbrella' pattern, in which they are still organised by the apically located centrosome and seemed to lack bundles. Meanwhile, in the transit-amplifying and differentiated cell regions above the stem cell zone, EB1 and ACF7 were visible along clearly evident microtubule bundles, whilst EB2 expression was again dramatically reduced (Goldspink et al., 2013b).

To investigate further, experiments were carried out in epithelial tissue culture systems, particularly focussing on the effects that RNAi depletion of EB2 had on the organisation of the microtubule cytoskeleton. Work from this project has contributed to this wider investigation within our group, with some of the results outlined in this chapter included in a recently published article by Goldspink et al. (2013b). To briefly summarise the results presented here, EB2 depletion was found to cause a distinctive phenotype in which cells increased in size, with microtubules straightening and becoming decorated by EB1 and ACF7. A particular focus of this

project was to clone EB2 into a fluorescently tagged construct, which when transfected into EB2 siRNA treated cells was able to successfully rescue the various depletion phenotypes observed.

5.2: Results

5.2.1: EB2 is expressed along microtubules in epithelial cell lines

Three cell lines were used in the experiments included in this chapter. Mouse mIMCD-3 cells were used to investigate EB2 expression during polarisation and as the source cell line for the cloning of EB2. Human ARPE-19 cells were used to investigate the effects of EB2 depletion on microtubule organisation and location of microtubule interacting proteins due to their characteristic radial microtubule array, alterations from which are easily observed. HCT116 cells were used as a secondary human epithelial cell line to confirm the phenotypic effects caused by EB2 depletion in cells derived from an alternative tissue, the colon. In each, EB2 was found to localise at microtubule plus ends, but was particularly seen to associate along the microtubule lattice (Figure 5.1), in a pattern consistent with previously published data in other epithelial cell lines (Komarova et al., 2009).

5.2.2: EB2 is downregulated during mIMCD-3 polarisation

Polarisation sequences in mIMCD-3 cells were performed to investigate EB2 expression patterns as cells differentiate. These were performed in part as additional replicates to previous experiments performed by D. Goldspink, and in order to extend the experimental time from 9 to 12 days. The results presented are consistent with those from the prior experiments.

mIMCD-3 cells were seeded subconfluently and grown over a 9 to 12 day period. At several timepoints throughout the sequence, cells were immunolabelled and lysates taken for Western blotting. Cells grew from initial subconfluence (days 1-3) to confluence by day 5, at which point they started to constrict and initially differentiate. Cells further polarise over the remaining period (days 7-9). Cells immunolabelled for ACF7 revealed relocalisation from dispersed in the cytoplasm in subconfluent cells to gradual accumulation at peripheral sites as cells polarise, where it colocalised with α-tubulin and EB1. EB1 localisation also changed from typical plus

end comets to along apico-basal microtubules over the same period (Figure 5.2). EB2 meanwhile was found relatively highly expressed in subconfluent, but distinctly reduced in confluent polarised cells at days 7-9. It should also be noted that downregulation was not uniform; EB2 remained relatively highly expressed in patches of the population, surrounded by regions of low expression (Figure 5.3 A). Downregulation was confirmed by Western blotting, which showed EB2 reducing over days 7-9, whilst EB1 levels remained unchanged. Probing for tubulin PTMs associated with microtubule stability revealed levels of detyrosinated tubulin increasing over the polarisation sequence, whilst acetylated tubulin levels remained unchanged (Figure 5.3 B) (Goldspink et al., 2013b).

5.2.3: EB2 depletion causes distinctive phenotypic changes

To investigate the mechanisms by which EB2 downregulation may cause microtubule bundling and reorganisation, EB2 was depleted using siRNA in the ARPE-19 and HCT116 cell lines. Western blots of control and scramble and EB2 siRNA treated ARPE-19 lysates probed for EB2 showed that the sequence used was particularly effective, able to knock down the majority of endogenous EB2 when cells were treated twice with siRNA over a 96 hour period. Importantly, no change was seen in levels of EB1 expression in EB2 depleted cells (Figure 5.4 A).

Knockdown of EB2 in ARPE-19 cells was found to produce a distinctive set of phenotypes. Most noticeably, cells significantly increased in size, whilst microtubules appeared significantly straighter in depleted cells, and also appeared to bundle in places (Figure 5.4 B) (Goldspink et al., 2013b). EB2 depletion also caused EB1 to relocalise from the classic pattern of +TIP comets as seen in control and scramble cells to associate with the microtubule lattice. Additionally, it was found that ACF7 also reorganised to localise along the microtubule lattice, suggesting a possible recruitment by EB1 (Goldspink et al., 2013b).

HCT116 cells were used to verify the EB2 depletion phenotypes in an additional human epithelial cell line. Cells were treated with two shots of scramble

or EB2 siRNA (at 0 and 48 hours) and analysed at 96 hours, along with untreated control cells. Samples immunolabelled for EB2 confirmed successful knockdown in EB2 siRNA treated cells (Figure 5.4 C). Cell size was analysed by measuring cell area in 175 cells for each condition, which revealed that as seen in ARPE-19s, siRNA treated HCT116 cells were significantly larger than either those treated with the scramble sequence or control cells ($p<0.001$ for both comparisons, as assessed by one-way ANOVA with Tukey's multiple comparison test) (Figure 5.4 D). Similarly treated cells were also stained for α-tubulin and EB1. As standard for epithelial cells, both control and scramble treated cells exhibited the typical EB1 +TIP comet distribution. In EB2 siRNA treated cells, EB1 again markedly decorated the length of the microtubule lattice, in addition to its plus end localisation. Similarly, microtubules appeared straighter in depleted cells (Figure 5.5). Unlike ARPE-19 cells however, there was no evidence that ACF7 altered its dispersed cytoplasmic pattern in HCT116 EB2 siRNA treated cells, although ACF7 staining in HCT116 cells was never seen especially strongly (data not shown).

5.2.4: Cloning of mouse EB2

In order to verify that the phenotypes observed in EB2 siRNA treated human cell lines were due to the loss of EB2 rather than off target effects, a construct was created to rescue depleted cells by transient transfection of a plasmid vector expressing an EB2 insert. Following a sequence check, it was confirmed that mouse EB2 cDNA would be suitable for insertion into a fluorescently tagging vector, as it would be unaffected by the human siRNA sequences used for EB2 knockdown. As mIMCD-3 cells are seen to express functional EB2 along microtubules (Figure 5.1, Figure 5.3), they were selected as the source material for cloning. The pmCherry-C1 vector was selected for the insert (Appendix B, 4). The resulting construct would therefore express fluorescent mCherry tagged to the N-terminus of EB2.

There are three potential mouse EB2 (MAPRE2) transcript variants generated by alternative splicing adjacent to an alternative start codon. Two of the variants

express alternate distinct N-terminal extensions of 42 and 33 amino acids respectively, whilst the third, shortest variant originates at the alternate start codon shared by all three variants, with the transcript sequences for each identical from this point onwards (Appendix B, 5). As it was unknown which variants are expressed in mIMCD-3 cells, forward primers were designed against each possible sequence, in addition to a common reverse primer. It should be noted that as variant 3 begins at a start codon common to all three sequences, it will produce a PCR product no matter which variant is expressed in cells. Primers were designed to include XhoI and HindIII restriction sites (forward and reverse primer respectively) and appropriate flanking regions, and additionally retained two nucleotides prior to the start codon in the forward primer. Together these features were designed to allow directional insertion of EB2 into the corresponding restriction sites of the pmCherry-C1, such that on ligation, the insert is conjugated in frame with the mCherry tag (Appendix B, 6).

The first step in the cloning process was to create a cDNA library by RT-PCR using generic primers following the total RNA extraction of mIMCD cells. From this, GoTAQ PCR was performed using basic primers for each mouse EB2 variant to determine which of the variants were expressed by mIMCD cells. Basic primers lacked the restriction sites and flanking regions, consisting merely of the appropriate primer seed for each variant (Appendix B, 6). Only the variant 3 forward primer produced a PCR cDNA product, visible just below the 1000 base pair marker when run on an agarose gel (Figure 5.6 A), corresponding to the 857 nucleotides of the basic PCR product. Therefore, only the variant 3 full forward primer was used for high fidelity PCR to successfully produce a cDNA product of sufficient quality for vector insertion, as visible when run on a gel (Figure 5.6 B).

Initial attempts to restrict and ligate the gel extracted PCR product directly into pmCherry-C1 were unsuccessful, likely due to the inherent difficulty in digesting the very ends of a PCR product. Instead, the insert was blunt end ligated into the pGEM®-T non-expressing carrier vector, designed to incorporate the insert into the lacZ operon of the plasmid, enabling colony selection by blue-white screening (Appendix B, 3). A clone was successfully selected and purified, and sent for

sequencing (Genome Enterprises Limited, Norwich) through the SP6 sequencing primer, which confirmed the successful incorporation of the PCR product into the vector (Appendix C, Figure S1).

10μg of purified pGEM®-T + EB2, was fully double digested (XhoI + HindIII) overnight and run out on an agarose gel, confirming an insert of the appropriate size (Figure 5.6 C), and subsequently gel purified, then ligated into previously similarly digested pmCherry-C1. Several bacterial clones were selected and their plasmids purified and double digested with XhoI and HindIII to check for the presence of insert. A band corresponding to the size of the EB2 insert was observed in multiple clones (Figure 5.6 D), with several sent for sequencing as above, using the pmCherry-C1-1215-Forseq sequencing primer, which sequences from a point towards the end of the mCherry tag sequence through the full EB2 insert. Sequencing confirmed the successful, in frame fusion of mouse EB2 variant 3 to the mCherry fluorescent tag (Appendix C, Figure S2).

One important observation from the sequencing data from both the pGEM®-T-EB2 and pmCherry-EB2 constructs is the retention of a single deviation from the expected mouse EB2 variant 3 transcript (NM_001162942) corresponding to a 429T>C point mutation (nucleotide 328 of the transcript coding sequence), which in turn leads to a W110R substitution in the resulting translated fusion protein (Figure 1.6 E). This has the potential to be a significant change, as the natural tryptophan and mutated arginine are amino acids with very different properties; whilst tryptophan possesses a hydrophobic aromatic side-chain, arginine is positively charged polar residue.

5.2.5: Verification and characterisation of the mCherry-EB2 construct

ARPE-19 cells were transiently transfected with 2μg mCherry-EB2 construct 24 hours prior to analysis. Lysates of transfected and control cells were Western blotted for EB2 and RFP (the antibody for which also recognises the mCherry tag). Samples probed for RFP revealed a band just below the 75kDa marker, consistent

with EB2 (approximately 36kDa) conjugated to mCherry (28.8kDa). Probing for EB2 also detected the construct in transfected cells, in addition to endogenous EB2, levels of which importantly remained unaltered when compared to control cells (Figure 5.7 A). Similarly treated transfected and control cells were also fixed and immunolabelled for RFP and EB2, showing intensive colocalisation of the two fluorescent signals, and thus confirming the successful incorporation of the EB2 sequence (Figure 5.7 B).

In order to examine whether the construct was functional, ARPE-19 and HCT116 cells were transfected as above to overexpress EB2, and immunolabelled for microtubules, EB1 or ACF7. In both cell lines, mCherry-EB2 is expressed in a network and associates along microtubules. It should be noted that the construct fluorescent signal was not restricted along microtubules, but was also visible as a haze in the cytoplasm. Meanwhile, overexpression of EB2 importantly had no apparent effect on typical expression patterns of EB1 or ACF7; EB1 remained as distinct comets decorating microtubule ends, whilst ACF7 appeared in its normal dispersed localisation. This was important to establish to ensure any effects seen in rescue experiments could indeed be attributed to a rescue effect, rather than to any excessive EB2 overexpression (Figure 5.8).

5.2.6: Rescue of EB2 siRNA phenotypes

In order to verify the phenotypes observed in EB2 depleted cells, they were transiently transfected with the mCherry-EB2 construct in order to rescue the control phenotype. Both ARPE-19 and HCT116 cells were treated with two shots of EB2 siRNA at 0 and 48 hours, and assessed at 96 hours, as previously. mCherry-EB2 was added at 72 hours (24 hours prior to analysis), with only cells visibly expressing mCherry fluorescence analysed. Initially, rescue was assessed by measuring cell size in the two cell lines, as shown in the charts (Figure 5.9). In ARPE-19 cells, rescue data was assessed against size data for control, scramble and EB2 siRNA treated cells provided by D. Goldspink, revealing a significant reduction in size ($p<0.0001$, unpaired t-test) following rescue (Figure 5.9 Aii, taken from (Goldspink et al.,

2013b)). Similarly in HCT-116 cells, cell size was significantly reduced in rescued cells compared to EB2 siRNA conditions ($p<0.001$), with there being no significant difference in size of rescued cells compared to control and scramble treated cells (statistical significance assessed by one-way ANOVA with Tukey's multiple comparison test) (Figure 5.9). Microtubule straightness in ARPE-19 rescued cells was quantified by D. Goldspink by assessing the number of microtubule crossovers, which confirmed that rescue cell microtubules were significantly less straight than depleted cells, and in fact the phenotype was completely restored such that it was statistically indistinguishable in rescued cells compared to scramble treated cells (Goldspink et al., 2013b).

Next, ARPE-19 cells were immunolabelled for EB1, and transiently transfected cells expressing mCherry were assessed. Rescued cells expressing mCherry-EB1 had a restored comet phenotype, similar to control and scramble treated cells, and distinct from the EB1 lattice association evident in neighbouring unrescued EB2 siRNA treated cells (Figure 5.10). Fluorescence intensity analysis (carried out by D. Goldspink) was used to quantify EB1 lattice association. EB1 intensity was measured along randomly selected 2μm segments of microtubule lattice located away from the plus end in scramble, EB2 siRNA treated, rescued and control cells. Analysis confirmed a significant increase in intensity along the microtubule lattice in EB2 siRNA cells, which was again restored to levels statistically indistinguishable from scramble treated cells in mCherry-EB2 rescued cells (Goldspink et al., 2013b).

Finally, ACF7 lattice association was similarly analysed in mCherry-EB2 transfected ARPE-19 cells expressing observable mCherry and immunolabelled for ACF7. mCherry-EB2 expression restored depleted cells to the dispersed cytoplasmic phenotype typical in control and scramble treated conditions (Figure 5.11). As for EB1, the fluorescence intensity analysis confirmed the statistically significant shift of ACF7 to microtubule association in depleted cells that once again could be completely restored to the dispersed phenotype such that rescued cells are statistically indistinguishable from scramble treated cells (Goldspink et al., 2013b).

5.3: Discussion

5.3.1: EB2 is downregulated during epithelial polarisation

Evidence from the mIMCD-3 polarisation sequence data confirmed EB2 expression was reduced during differentiation, which supported the *in situ* data obtained from both cochlea and small intestinal crypt isolated tissue (Goldspink et al., 2013b). These combined findings imply that EB2 associates with dynamic microtubules, whilst its reduction during polarisation is necessary for microtubules to bundle and form stable apico-basal arrays decorated by EB1 and ACF7. This recruitment of ACF7 in turn suggests a link to the actin cytoskeleton during stable microtubule bundle formation.

5.3.2: EB2 depletion alters microtubule organisation, results in EB1 and ACF7 recruitment, and leads to coordination with the actin cytoskeleton

Depletion of EB2 by siRNA in ARPE-19 and HCT-116 cells produced a very distinctive set of phenotypes. A dramatic increase in cell size was observed. However, the cells were still able to proliferate over the 96 hour experimental time period, suggesting that the increase was not due to a block on cell division. Furthermore, the microtubules become straighter and frequently formed bundles. Accompanying this, EB1 relocated from its typical comet pattern to associate along microtubules, with the actin-microtubule crosslinker ACF7 also recruited to the lattice. This increase in microtubule straightness was verified by determining the number of microtubule crossover events within several randomly selected equally sized areas for each condition. Additionally, the EB1 and ACF7 lattice associations have been confirmed by fluorescence intensity measurements (Goldspink et al., 2013b). Further work has demonstrated that in EB2 depleted cells actin and microtubules co-align, with actin filaments interdigiting between microtubule bundles orientated at an angle perpendicular to the cortex (Goldspink et al., 2013b).

Together, these observations suggested a sequence where the loss of EB2 caused EB1 and ACF7 recruitment to the microtubule lattice, allowing alignment and bundling of microtubules and actin filaments, suggesting an increase in microtubule stability. Thus, the EB2 depletion phenotype closely correlated with the observations made in tissue and polarising tissue culture cells.

5.3.3: mIMCD-3 cells express mouse EB2 variant 3

PCR using primers against EB2 from the RT-PCR derived mIMCD-3 cDNA library was only successful with the variant 3 forward primer. This suggests that the cell line only expresses the shortest transcript variant, although this cannot be confirmed; the variant 3 sequence is present in all transcripts, and so should have been successfully cloned irrespective of which variants were originally expressed. It is possible that PCR conditions for the variant 1 and 2 primers were unsuitable, and required further optimisation.

An important consequence of only successfully cloning variant 3 is the potential loss from the mCherry-EB2 construct of any function provided by the N-terminal extensions present when variants 1 and 2 are expressed, although the functions of these domains are so far not known. What is known however, is that the alternative start codon from which variant 3 originates corresponds to beginning of EB1 and EB3; i.e. the start of the EB CH domain. Additionally, it has been previously found that adding the human equivalent of the longer N-terminal extension (equivalent to mouse variant 1) to the N-terminus of human EB3 had no effect on the natural EB3 activity of the hybrid construct to track microtubule plus ends and suppress catastrophe events (Komarova et al., 2009). This suggests that whatever functions the separate N-terminal extensions may possess, they do not impact on its microtubule roles. In the future however, it would be very interesting to investigate these domains, which could confer additional activity to EB2 beyond that of its other family relatives. Alternatively, these regions may have a regulatory role in controlling the expression and localisation of the protein; it has been suggested to restrict the conformational space available for folding (Buey et al.,

2011). It would also be interesting to investigate whether each variant is alternatively expressed in either different tissues, or at different stages of development, or both.

5.3.4: Mouse EB2 variant 3 was successfully cloned into pmCherry-C1

Sequencing confirmed the EB2 cDNA insert was cloned into the target vector in frame with the fluorescent mCherry tag, whilst Western blotting and immunolabelling with EB2 and RFP antibodies verified the fusion product. The sequencing however did identify a point mutation in the cloned product relative to the established sequence for mouse EB2, in which Tryptophan 110 is changed to an Arginine residue in the expressed mCherry-EB2 protein. It is not clear whether the base change originated in the PCR steps of the cloning process, or whether it was present in the original product expressed by mIMCD cells. Further, if the alteration originated in the cell line, it is not known whether it occurred during the establishment of the cell line, or whether it is found as a naturally occurring SNP in mouse EB2. Trp110 is located in the sixth α-helical region of the CH domain, where it is one of several highly conserved residues to form a common hydrophobic groove (Slep and Vale, 2007). It is shared across all three EB family members in both mouse and other species, including human sequences (Komarova et al., 2009). It is not known how disruptive to the region the change to a basic charged residue may be, although the only other two basic amino acid side chains present within the α6 helix (two lysine residues) are located in the immediate vicinity at positions 112 and 113 of the peptide.

Following transient transfection into cells, it was noticeable that the mCherry-EB2 construct was present in a haze in the cytoplasm of overexpressing cells, however it was also observed colocalising along the microtubule network in both ARPE-19 and HCT116 cell lines. Further, the ability to rescue control phenotypes verified the tagged EB2 product as functional, which has been further confirmed by a recent mass spectrometry pull-down, which successfully identified EB2 in the sample (D.Goldspink, personal communication). Importantly,

overexpression of EB2 did not noticeably effect the organisation of the microtubule network, or alter the localisation of either EB1 or ACF7.

5.3.5: mCherry-EB2 can rescue the EB2 control phenotypes

As discussed above, depletion of EB2 by siRNA in epithelial cells leads to a very distinctive set of phenotypes, in which cells dramatically increase in size and microtubules become straighter and form bundles. Accompanying this, EB1 relocates from its typical comet pattern to associate along microtubules, with the actin-microtubule crosslinker ACF7 also recruited to the lattice, and the microtubule network aligning with actin filaments.

Transient transfection of depleted ARPE-19 cells with the mCherry-EB2 construct was able to rescue the control phenotype. In particular, EB1 and ACF7 localisations were completely restored to the patterns seen in scramble and control cells, and the cell size significantly reduced. The fact that re-addition of EB2 can rescue the various effects observed in depleted cells confirms that the phenotypes seen are due to loss of EB2 expression rather than any off-target effects caused by the siRNA sequences used.

5.3.6: Summary and further work

The depleted phenotype correlates well with the characteristic changes in the microtubule network that occur following reorganisation on epithelial differentiation, in which stable bundles of apico-basally orientated microtubules decorated by both EB1 and ACF7 are produced. EB1 localisation along the lattice is well established to be associated with an increase in microtubule stability, caused by stabilisation of the lateral interprotofilamental contacts (des Georges et al., 2008; Maurer et al., 2012; Sandblad et al., 2006). Treatment with the microtubule stabilising drug taxol also caused EB1 to relocalise along the lattice (Goldspink et al., 2013b). ACF7 guides and aligns microtubules along actin filaments, and thus also

promotes stabilisation of the microtubule array in an EB1 dependant manner, as evidenced by the unbundling that occurs on ACF7 depletion (Alves-Silva et al., 2012; Kodama et al., 2003).

Crucially, EB2 expression levels were consistently seen to decrease in polarisation sequences. Meanwhile, in isolated epithelial tissue of the cochlea and gut, differing expression levels of EB2 correlated with distinct variations in organisation of the polarised apico-basal array. Low levels of EB2 were found in the transit amplifying and differentiated regions of crypts, and in cochlea pillar cells (which have bundles of apico-basal microtubule decorated with EB1 and aligned with actin filaments), whilst high expression of EB2 is seen in the stem cell zone of crypts and supporting cells of the cochlea (which despite having apico-basally orientated microtubules do not form bundles) (Goldspink et al., 2013b). Interestingly, a recent investigation into the FGF-3 receptor in cochlea epithelial cells found that loss of the receptor caused an upregulation in EB2 gene expression in pillar cells, with an accompanying reduction in microtubule bundling (Szarama et al., 2012).

Taken together, these various observations in depleted and rescued cells and tissue samples implicate down-regulation of EB2 in the establishment of stable apico-basal microtubule bundles during differentiation. Further subsequent investigations have studied the depletion of EB2 and EB1 within a polarising system. TC7 cells were depleted for either EB2 or EB1 under polarisation conditions on tissue culture filter inserts. Either depletion prevented apico-basal polarisation of treated cells, as marked by a significant reduction in average cell height. EB2 depletion also prevented the reorganisation of microtubules into peripheral rings, as would normally be seen in successfully polarising cells. Instead, microtubules appeared typical of undifferentiated TC7 cells, which were also of similar area to subconfluent cells, rather than becoming compacted as occurs on differentiation. By contrast, despite lacking the height typical of polarisation, microtubules in EB1 siRNA treated cells did reorganise to include peripheral bundles, although these were orientated incorrectly (i.e. not apico-basally). Additionally, whilst EB1 depleted cells were of greater area than control or scramble treated cells, they did show evidence of constriction, and were significantly smaller than the EB2 siRNA treated cells. This

experiment suggested that EB2 rather than EB1 expression is essential for early events in polarisation; namely apical constriction and the initial reorganisation of the microtubule array (Goldspink et al., 2013b).

From the various experiments, a model can be generated implicating a role for EB2 in the early stages of epithelial differentiation. Accordingly, it is suggested that high EB2 expression is required during the initial steps of polarisation; cell-cell contact, constriction at the apex, and the initial reorganisation of the microtubule array, where it is important that microtubules remain dynamic. However, it must then be downregulated for later steps in the differentiation process. This loss of EB2 promotes EB1 lattice association coupled to recruitment of ACF7 and the alignment of microtubules and actin filaments, and thus leads to the generation of apico-basally orientated bundles of stable microtubules as seen in *in vivo* tissue samples (Goldspink et al., 2013b).

Whilst a role for regulation of EB2 expression in epithelial differentiation has been uncovered, the regulatory and molecular mechanisms behind how the process is controlled require further future exploration. For example, by what process does EB2 downregulation cause EB1 to associate along the lattice; does the loss of EB2 merely free space along the microtubule for EB1 binding, or is there a signalling process encouraging relocalisation? Initial experiments were carried out investigating the LKB signalling pathway. This pathway acts through the MARK phosphorylation cascade, and was thought a potential target as it has been established as a polarity inducing pathway (Baas et al., 2004), and a regulator of the AMPK cascade important for cellular energy metabolism, and potentially therefore cell size (Woods et al., 2003). These experiments however failed to indicate any correlation between activation of signalling pathway components, and the EB2 related phenotypes previously observed (data not shown). More recent investigations have implicated the Rho signalling pathway and formin activation as key regulatory events (Goldspink et al., 2013b). There is still however much work to be undertaken to examine regulatory mechanisms in differentiation, and in the exploration of EB2 interacting partners.

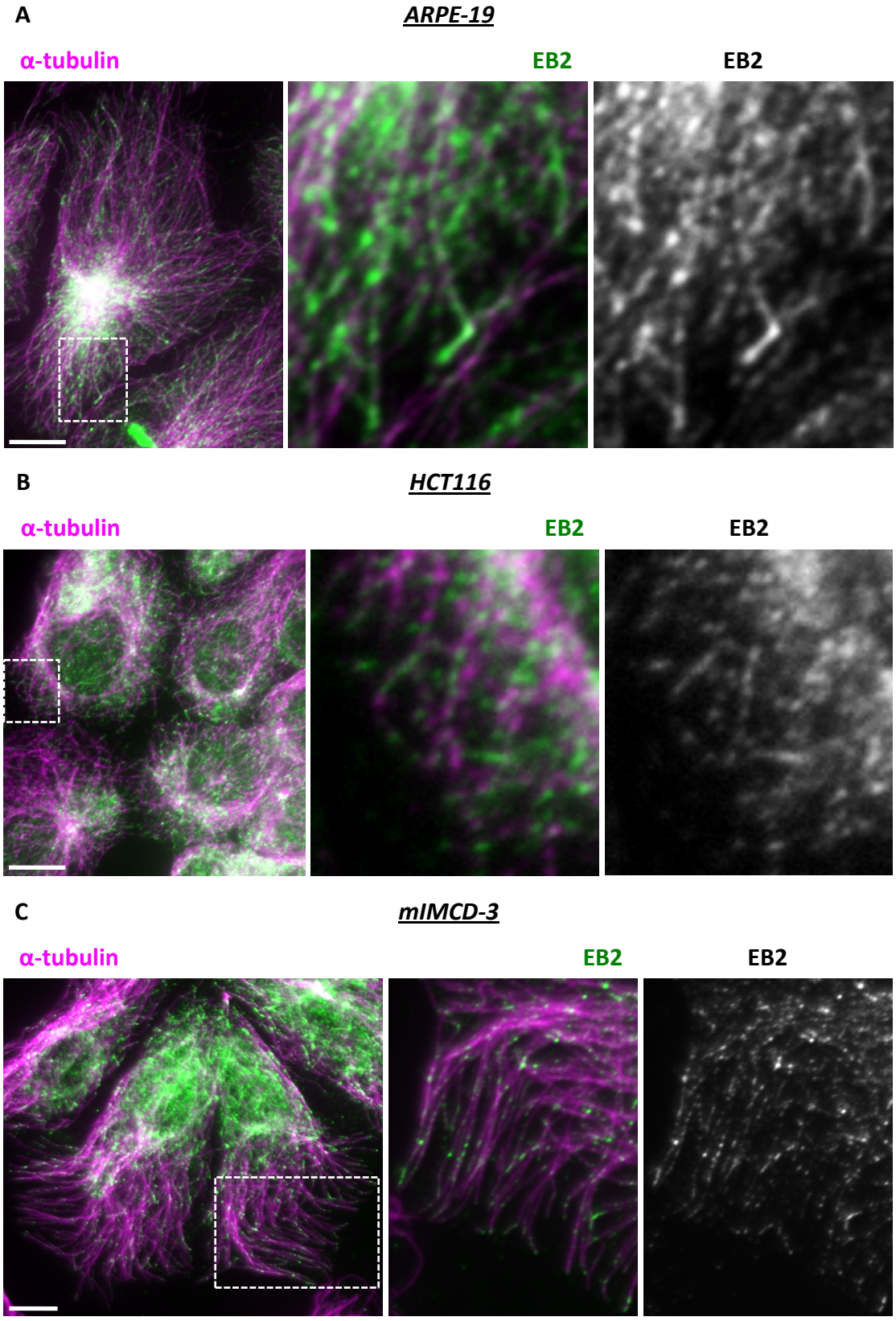

Figure 5.1 EB2 localisation in epithelial cell lines
Widefield fluorescent images of **(A)** ARPE-19, **(B)** HCT-116, and **(C)** mIMCD-3 cells immuno-labelled for α-tubulin (purple) and EB2 (green, enlarged in boxed region). In particular note that in each cell line EB2 is clearly visible along the microtubule lattice, as well as at plus ends. All scale bars = 10μm.

Figure 5.2 Polarisation sequence in mIMCD-3 cells
mIMCD-3 cells were seeded sparsely on glass coverslips and allowed to grow over a 12 day period, by which time they are highly confluent. Widefield fluorescent images of cells fixed at days 1,3,5,7,9 and 12, and immunolabelled for ACF7 (green, invert) and either **(A)** α-tubulin (purple, invert) or **(B)** EB1 (red). Cells are confluent by day 5, after which they constrict and partially polarise, forming apico-basal microtubule arrays. ACF7 is dispersed at early time-points, but gradually relocates to cortical sites as cells polarise, where it colocalises with microtubules and EB1 (enlargements). Scale bars = 10μm.

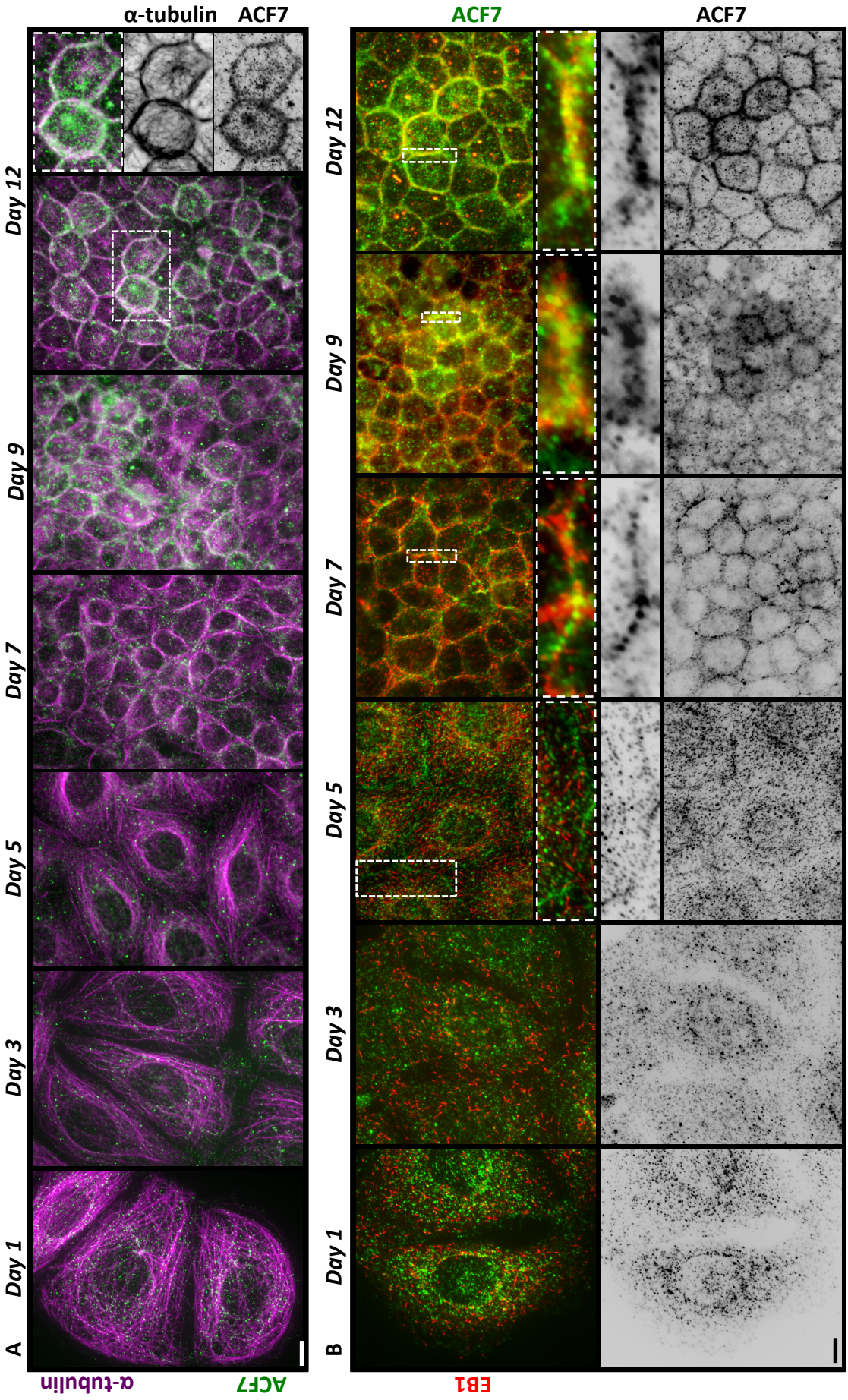
α-tubulin
ACF7
ACF7
ACF7
Day 12
Day 9
Day 7
Day 5
Day 3
Day 1
A
B
α-tubulin
ACF7
EB1

Figure 5.3 EB2 is downregulated during mIMCD-3 epithelial differentiation
mIMCD-3 cells were seeded sparsely and allowed to grow over a 12 day period. **(A)** Cells fixed and immunolabelled for α-tubulin (red) and EB1 (blue) at days 3, 7 and 9. **[i]** Widefield fluorescent images reveal EB2 expression is reduced in confluent cells (days 7-9) in comparison to subconfluent cells (day 3). Scale bar = 10μm. **[ii]** Images at lower magnification at day 7 reveal EB2 is expressed in patches, with regions of high expression surrounded by areas of low expression Scale bar = 20μm. **(B)** Western blots of cell extracts at days 3,5,7 and 9 show protein expression levels of EB2, EB1, detyrosinated tubulin acetylated tubulin and β-actin. EB2 is downregulated over the polarisation sequence, whilst levels of detyrosinated tubulin increase. Levels of EB1 and acetylated tubulin remain unchanged.

Day 7
ii
B
EB2
EB1
Detyrosinated Tubulin
Acetylated Tubulin
β-actin
DAY 9
DAY 7
DAY 5
DAY 3
50 kDa
40 kDa
40 kDa
35 kDa
50 kDa
50 kDa
50 kDa
EB2
α-tubulin
EB2
i
A
Day 3
Day 7
Day 9

Figure 5.4 (A-B) EB2 depletion in epithelial cell lines affects cell size and microtubule organisation
ARPE-19 cells were treated with scramble and EB2 siRNA and processed 96 hours post initial treatment, along with untreated controls.
(A) Western blots of ARPE-19 lysates of each condition for EB2, EB1 and the loading control β-actin. Note the complete knockdown of EB2 in the EB2 siRNA treated lane, and that levels of EB1 do not change between different treatments.
(B) Widefield fluorescent images of ARPE-19 cells for each treatment immunolabelled for α-tubulin (green) and EB2 (red, invert). Note the large size of the EB2 depleted cell and the straightness and alignment of the microtubules. In particular, observe apparent microtubule bundling (boxed region). Scale bars = 10μm.

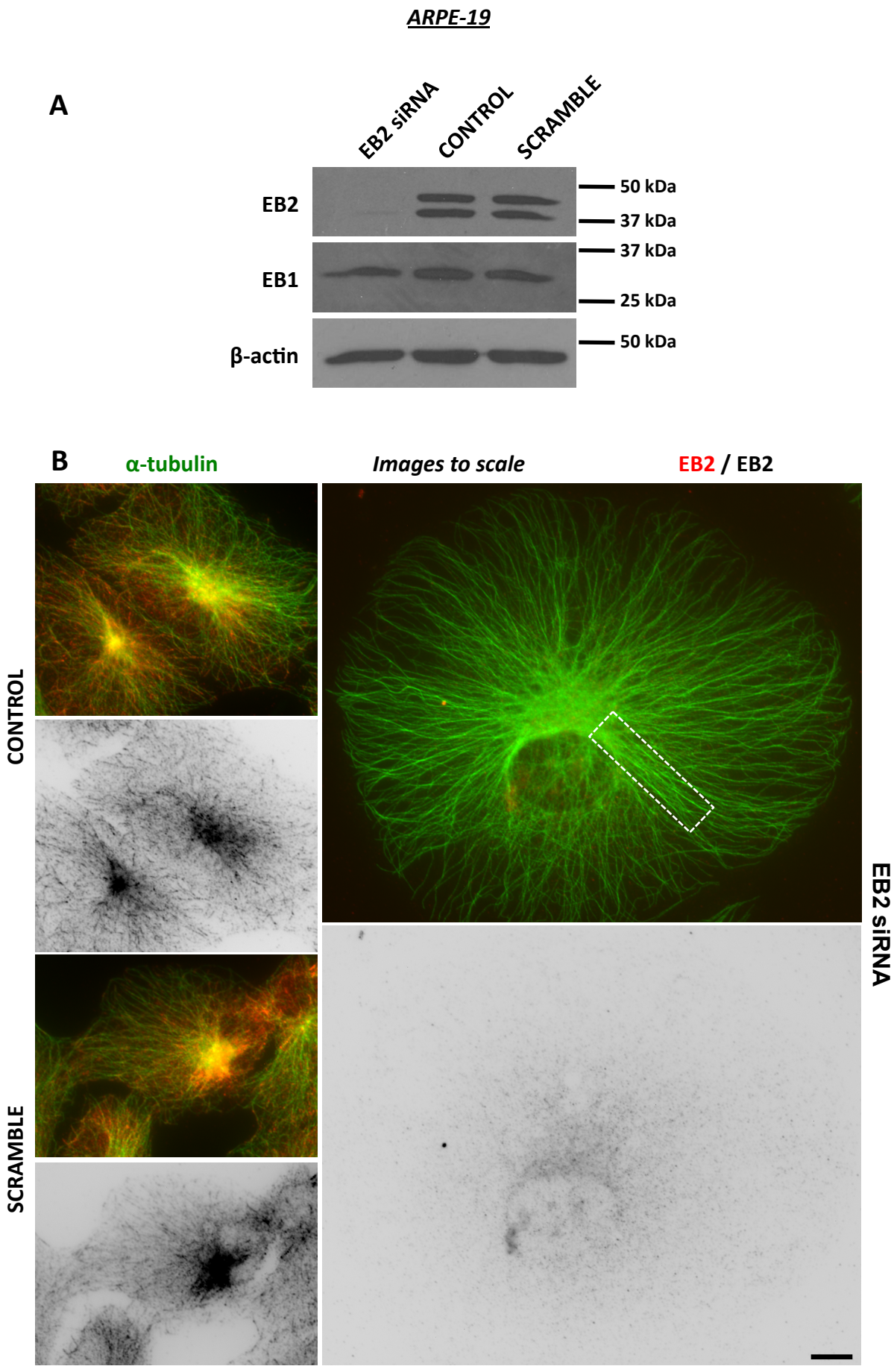
ARPE-19
A
EB2 siRNA
CONTROL
SCRAMBLE
EB2
EB1
β-actin
50 kDa
37 kDa
37 kDa
25 kDa
50 kDa
B
α-tubulin
Images to scale
EB2 / EB2
CONTROL
SCRAMBLE
EB2 siRNA

Figure 5.4 (C-D) EB2 depletion in epithelial cell lines affects cell size and microtubule organisation
HCT116 cells were treated with scramble and EB2 siRNA and processed 96 hours post initial treatment, along with untreated controls.
(C) Widefield fluorescent images of HCT116 cells for each treatment immunolabelled for α-tubulin (green) and EB2 (red, invert). Note the similar increase in size of the EB2 depleted cells as seen in the ARPE-19 depleted treatment. Scale bars = 10μm.
(D) Analysis of cell size by measuring cell area for each condition in HCT-116 cells. EB2 depleted cells show a statistically significant approximately four-fold increase in size compared to control and scramble cells (one-way ANOVA with Tukey's multiple comparison test).

HCT116

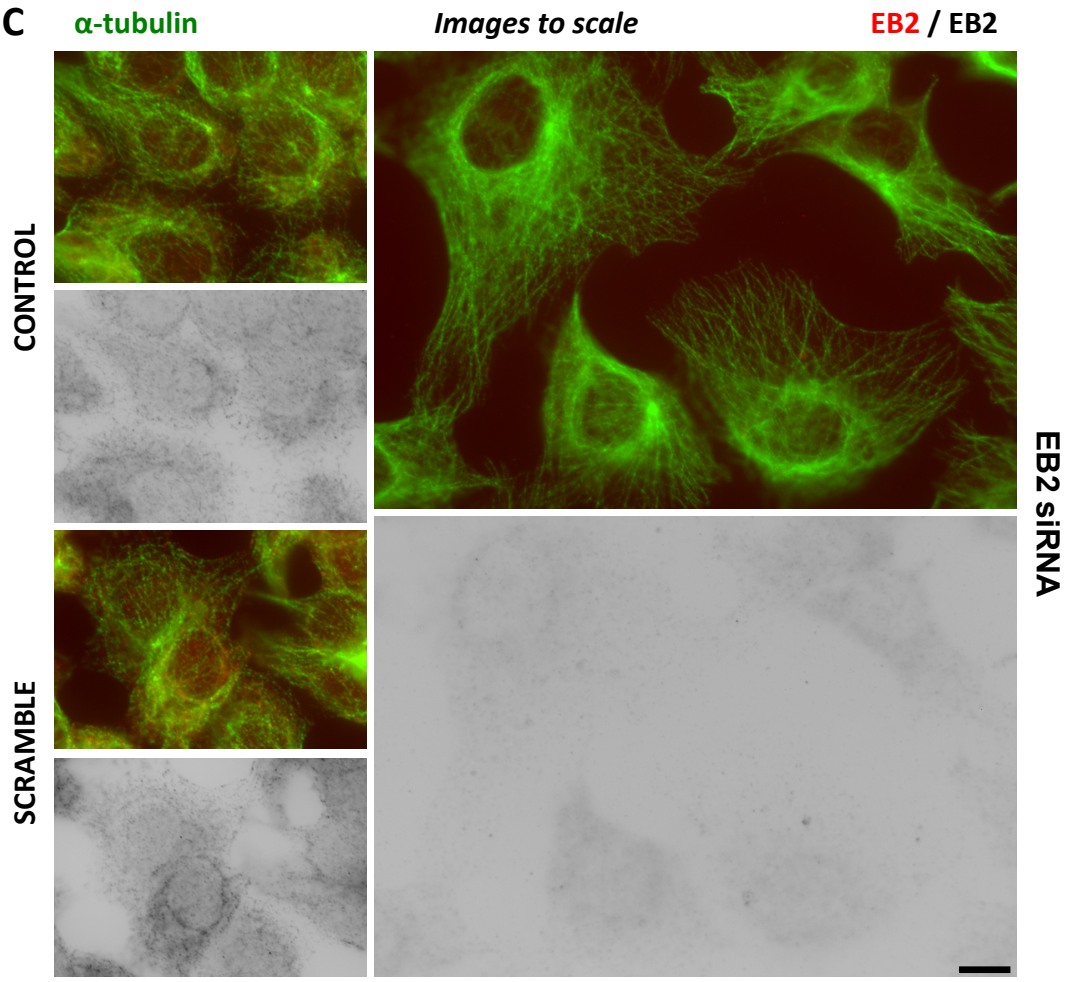

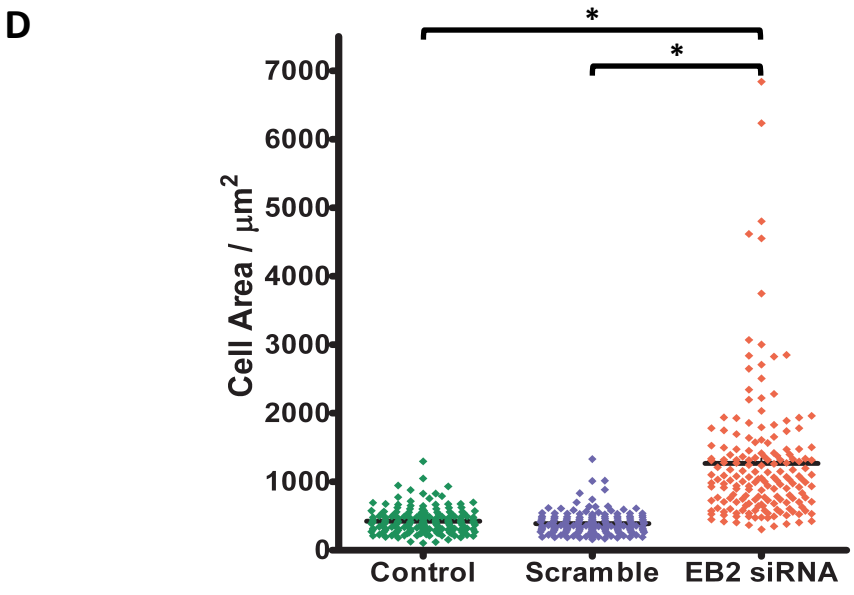

Treatment	N	Mean ± SEM (µm²)
Control	175	425.2 ± 13.71
Scramble	175	388.5 ± 12.20
EB2 siRNA	175	1268 ± 71.87

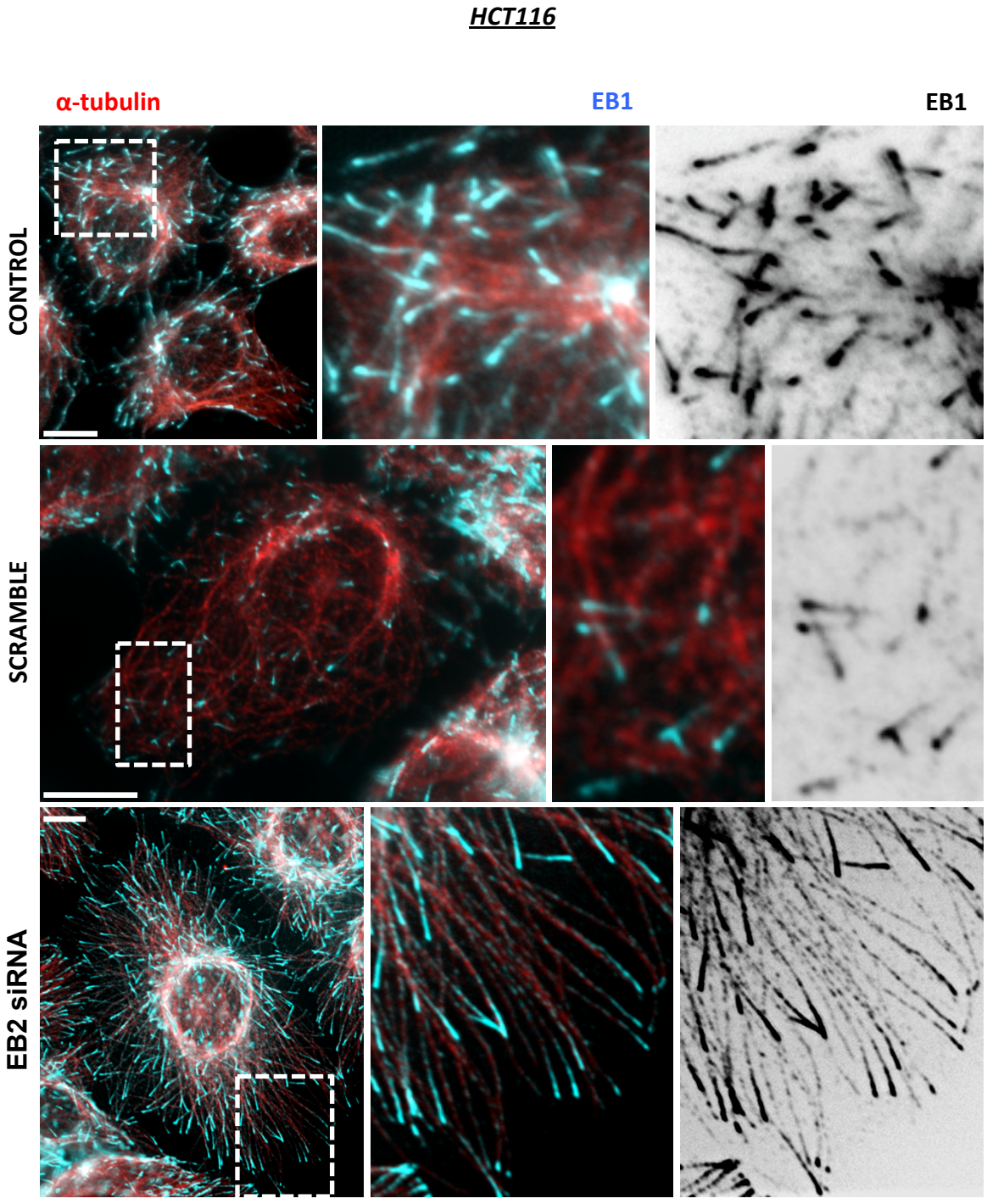

Figure 5.5 EB2 depletion causes EB1 to associate with the microtubule lattice
Widefield fluorescent images of untreated control, scramble and EB2 siRNA treated HCT116 cells fixed 96 hours post initial treatment and immunolabelled for α-tubulin (red) and EB1 (blue, invert). Enlarged selections of peripheral regions in EB2 depleted cells reveal EB1 comets extend along the microtubule lattice, in contrast to the short tails of comets in scramble treated and control cells. Scale bars = 10µm.

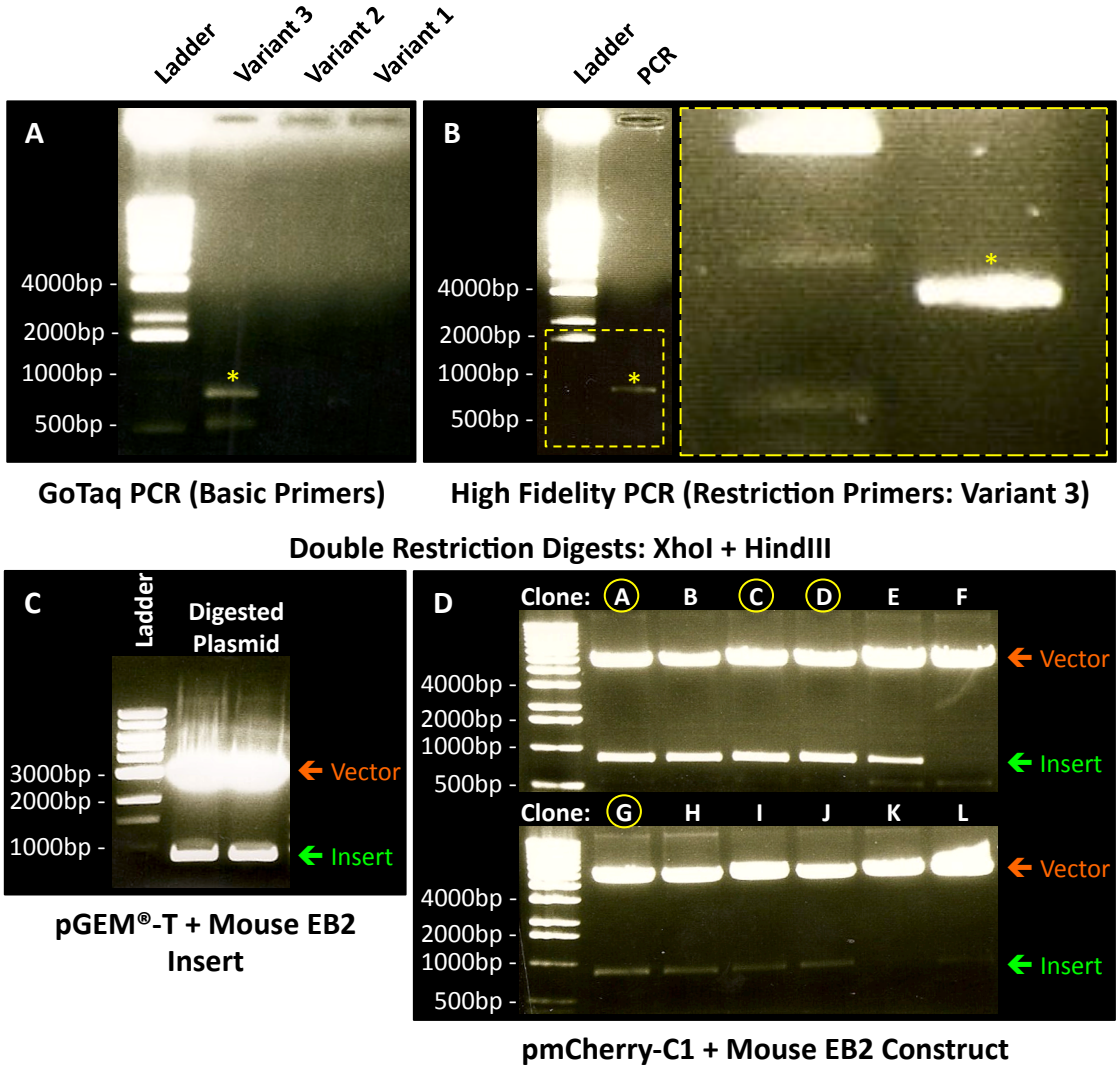

Figure 5.6 Cloning of mouse EB2 from mIMCD-3 cells
(A) GoTAQ PCR of EB2 cDNA from an mIMCD-3 RT-PCR cDNA library, using basic primers designed against each mouse EB2 transcript variant. A band corresponding to the EB2 transcript was only seen in the variant 3 lane at around 800bp (asterisk). **(B)** High fidelity PCR of mouse EB2 variant 3 (asterisk) from the mIMCD cDNA library using restriction digest primers. **(C)** Double restriction digest (XhoI & HindIII) of pGEM®-T following EB2 cDNA ligation. **(D)** Double restriction digest (XhoI & HindIII) of pmCherry-C1 from selected isolated clones following ligation of the EB2 insert. A band corresponding to the insert was observed in several clones. Selected clones (circled) were verified as containing EB2 by sequencing. **(E)** Sequencing of both pGEM®-T-EB2 and mCherry-C1-EB2 constructs revealed a point mutation (T>C) (highlighted in red) with respect to the published sequence for mouse EB2 variant 3 at base 328 of the CDS, resulting in a W110R mutation in the expressed protein (highlighted in yellow).

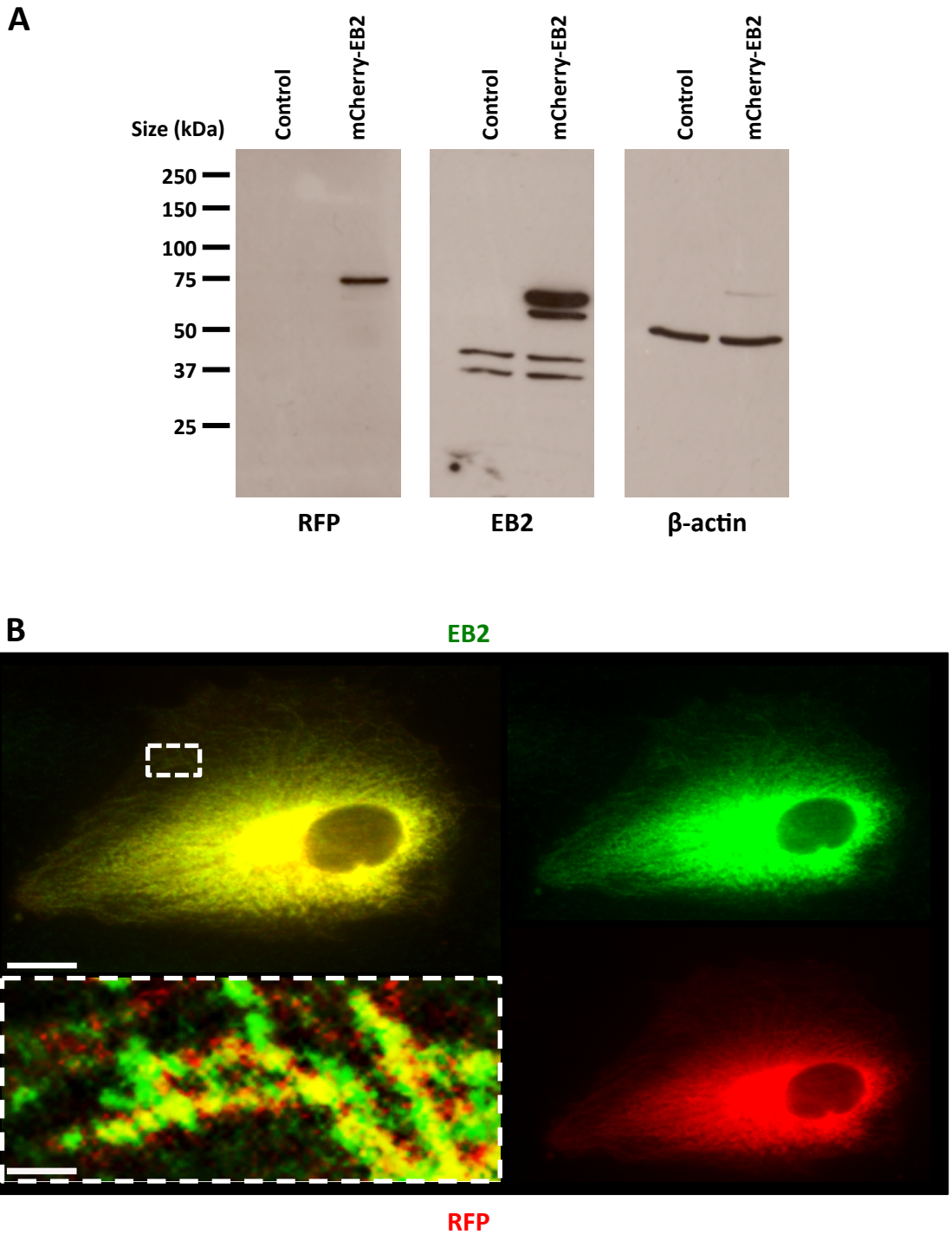

Figure 5.7 Verification of mCherry-EB2 protein expression
ARPE-19 cells were transiently transfected with the purified mCherry-EB2 construct 24 hours prior to processing. **(A)** Western blot of control and overexpressing cell lysates probed for RFP, EB2 and the loading control β-actin. Note the bands corresponding to the tagged construct at approximately 75kDa in the RFP and EB2 probed blots, and the endogenous typical EB2 bands present only on the EB2 antibody probed blot **(B)** Widefield fluorescent images of transfected cells fixed and immuno-labelled for EB2 (green) and RFP (red), illustrating co-localisation of EB2 and RFP staining in transfected cells (enlarged in boxed region, with RFP and EB2 labelling colocalising in yellow). Main scale bar = 10µm, enlargement = 1µm.

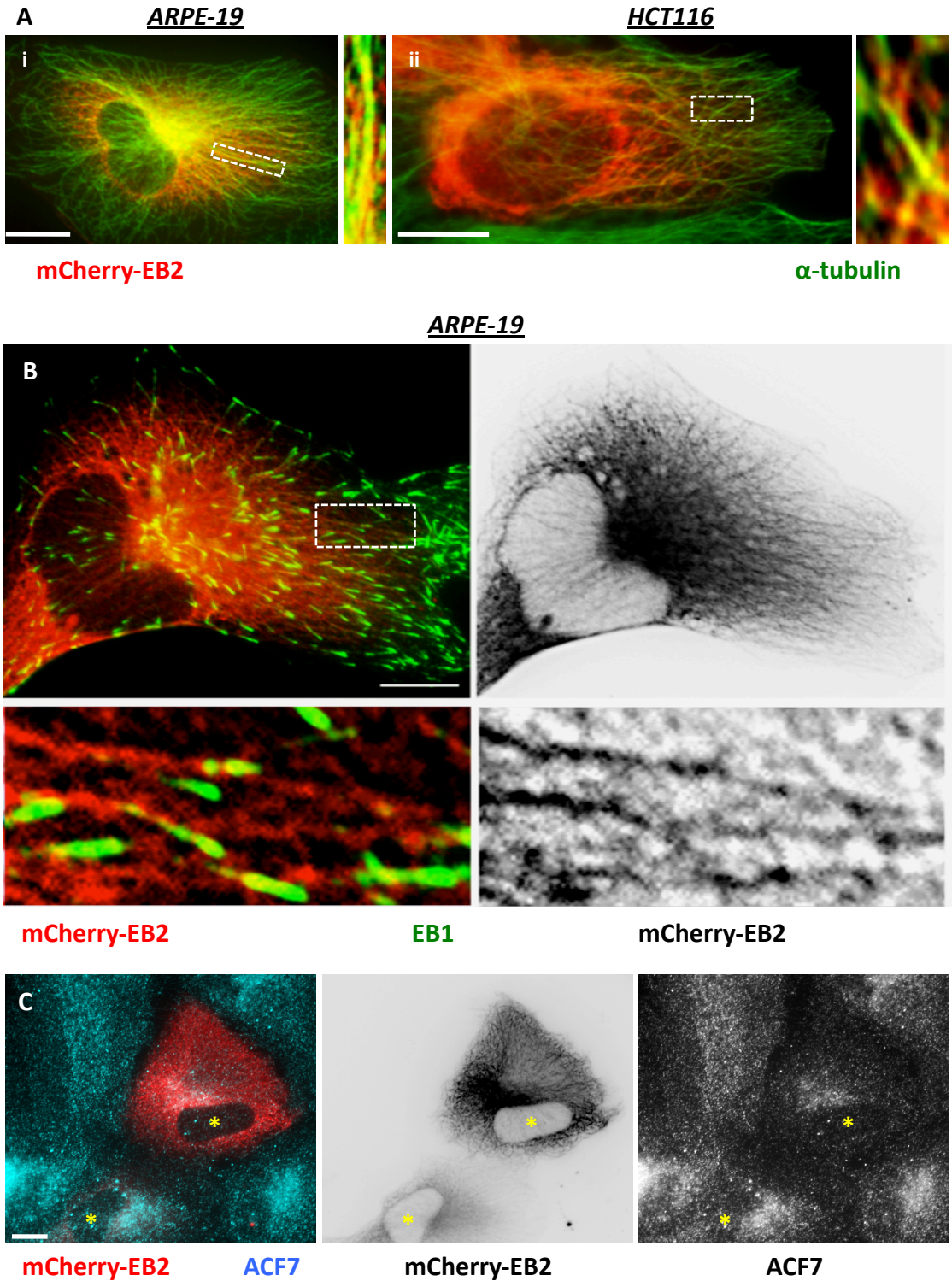

Figure 5.8 mcherry-EB2 characterisation in epithelial cell lines
Cells were transfected with mCherry-EB2 (red, invert) 24 hours prior to fixation and immunolabelling. **(A) [i]** ARPE-19 and **(ii)** HCT-116 transfected cells labelled for α-tubulin (green), revealing localisation of mCherry-EB2 (red) along microtubules (enlarged in boxed regions). **(B)** ARPE-19 transfected cell labelled for EB1 (green) showing EB1 comets located at the end of mCherry-EB2 (red, inverts) decorated microtubules (enlarged in boxed regions below). **(C)** ARPE-19 transfected cells labelled for ACF7 (blue, white), illustrating no effects of mCherry-EB2 (red, invert) overexpression (starred cells) on ACF7 localisation. Scale bars = 10µm.

Figure 5.9 Rescue of control cell size with expression of mCherry-EB2 in EB2 depleted cells
(A) ARPE-19 cells were treated with EB2 siRNA 96 hours prior to fixation and rescued by transient transfection of EB2-mCherry-EB2 construct (red) 24 hours prior to fixation. **[i]** Widefield fluorescent image of cells immunolabelled for α-tubulin (blue, invert). Scale bars = 10μm. **[ii]** Cell size analysis of control, scramble, EB2 siRNA treated and rescued cells, taken from (Goldspink et al., 2013); control, scramble and EB2 siRNA data courtesy of D. Goldspink. Control, scramble EB2 siRNA: N=311, mCherry-EB2 rescue, N=55 (statistical significance assessed by unpaired t-test, [***] $p < 0.0001$). **(B)** Cell size analysis of control, scramble, EB2 siRNA and rescued HCT-116 cells, treated as above. Control, scramble, EB2 siRNA: N=175, rescued N=70 (statistical significance assessed by one-way ANOVA with Tukey's multiple comparison test).
In both cell lines rescue with the mCherry-EB2 construct was able to reduce the size of EB2 depleted cells

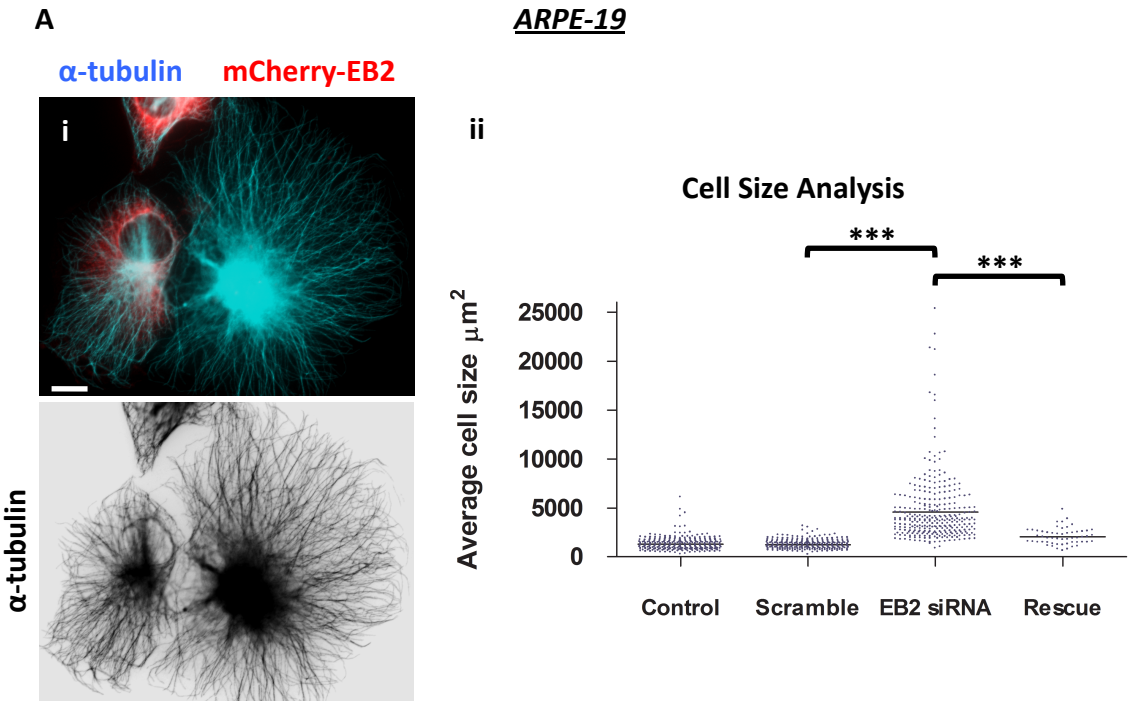

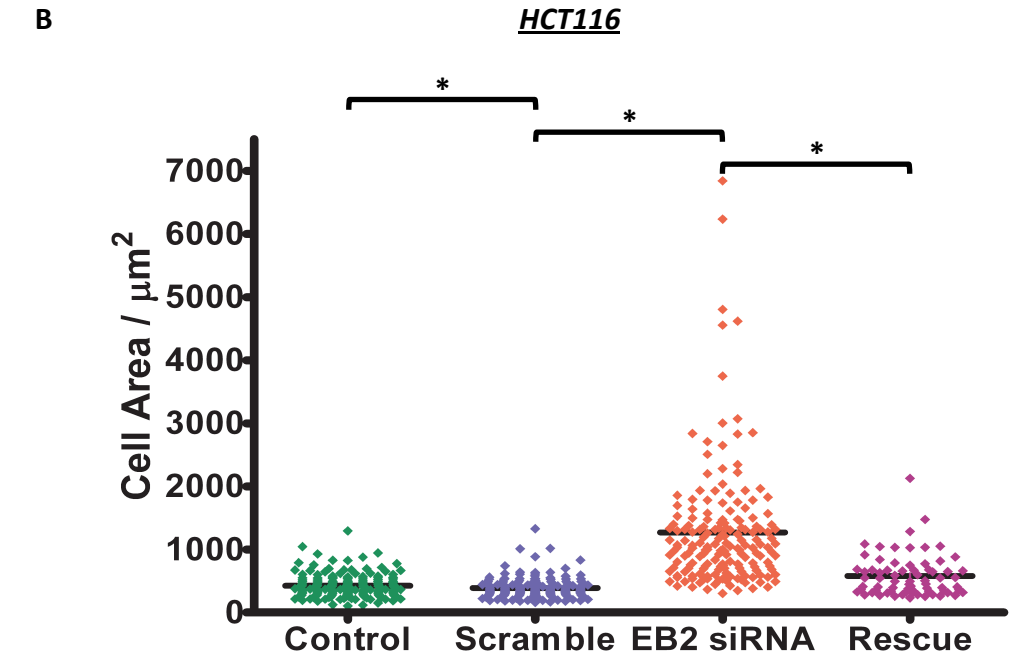

Treatment	N	Mean ± SEM (µm²)
Control	175	425.2 ± 13.71
Scramble	175	388.5 ± 12.20
EB2 siRNA	175	1268 ± 71.87
Rescue	70	580.2 ± 39.76

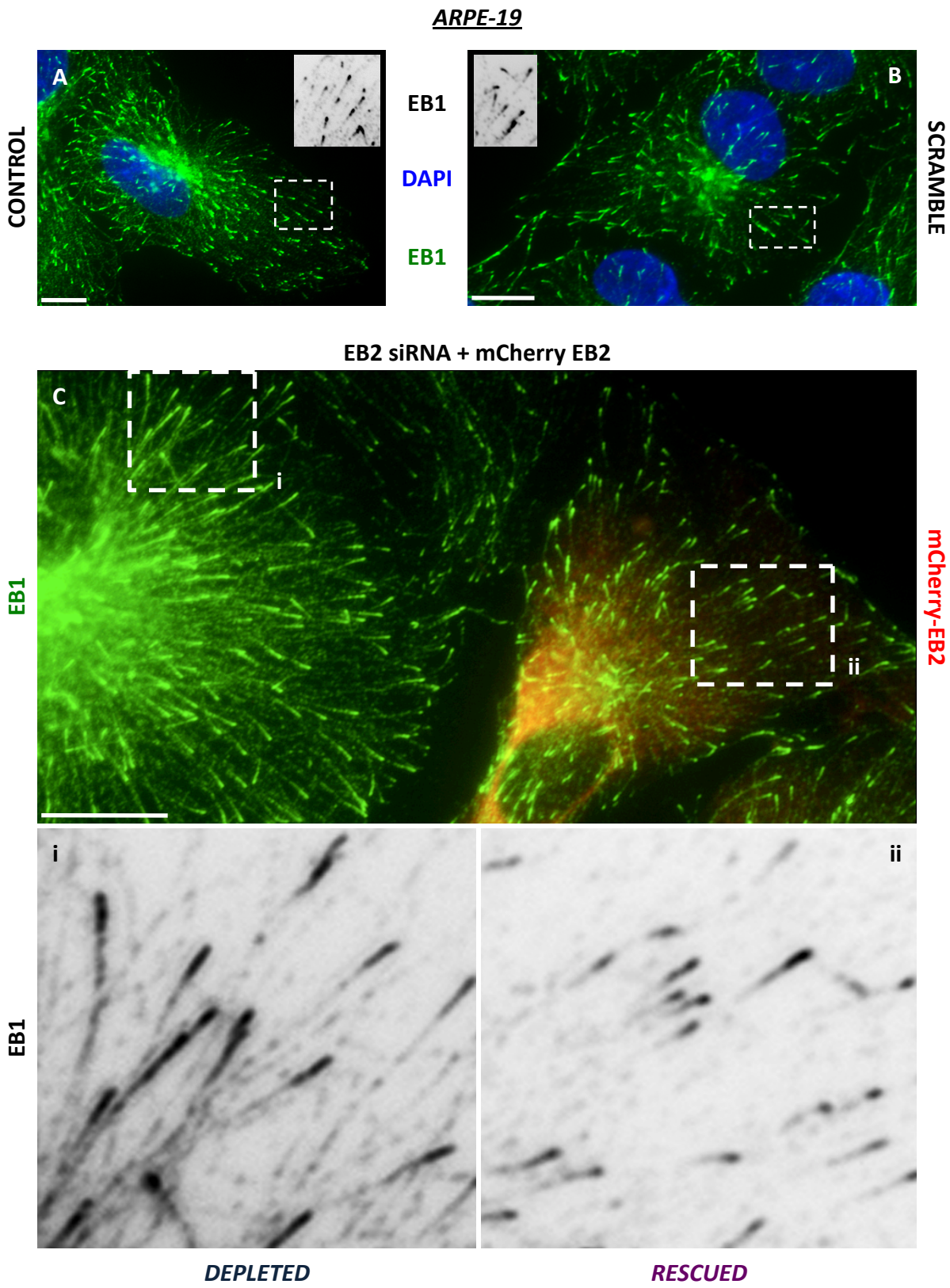

Figure 5.10 Rescue of EB1 comet localisation in mCherry-EB2 expressing EB2 depleted ARPE-19 cells
ARPE-19 cells were treated with EB2 siRNA 96 hours prior to fixation and rescued by transient transfection of EB2-mCherry-EB2 construct 24 hours prior to fixation. Widefield fluorescent images of **(A)** Control and **(B)** scramble treated cells immunolabelled for EB1 (green) and DAPI (blue), illustrating EB1 localisation as comets at microtubule plus ends (inverted insets). **(C)** mCherry-EB2 (red) transfected EB2 depleted cell immunolabelled for EB1 (green, inverts) showing that the EB1 lattice association observed in depleted cells **[i]** is lost with EB1 restored to plus end comets in the rescued cell **[ii]**. Scale bars = 10µm.

Figure 5.11 ACF7 cytoplasmic dispersed distribution can be rescued by mCherry-EB2 expression in EB2 depleted ARPE-19 cells

ARPE-19 cells were treated with EB2 siRNA 96 hours prior to fixation and rescued by transient transfection of EB2-mCherry-EB2 construct 24 hours prior to fixation. Immunofluorescent images of **(A)** Control, **(B)** scramble and **(C)** EB2 siRNA treated cells immunolabelled for α-tubulin (green), ACF7 (red, inverts) and DAPI (blue). Note the ACF7 alignment along microtubules in the EB2 depleted cell (**(C)**, arrowed), compared to the dispersed cytoplasmic speckles seen in control and scramble treated cells. **(D)** mCherry-EB2 (red) rescued EB2 depleted cells labelled for ACF7 (green, inverts). EB2 depletion causes ACF7 to relocalise along the microtubule lattice in the unrescued cell (KD, arrowed), however the dispersed pattern observed in control and scramble cells is rescued upon mCherry-EB2 expression (R). Scale bars = 10μm.

ARPE-19

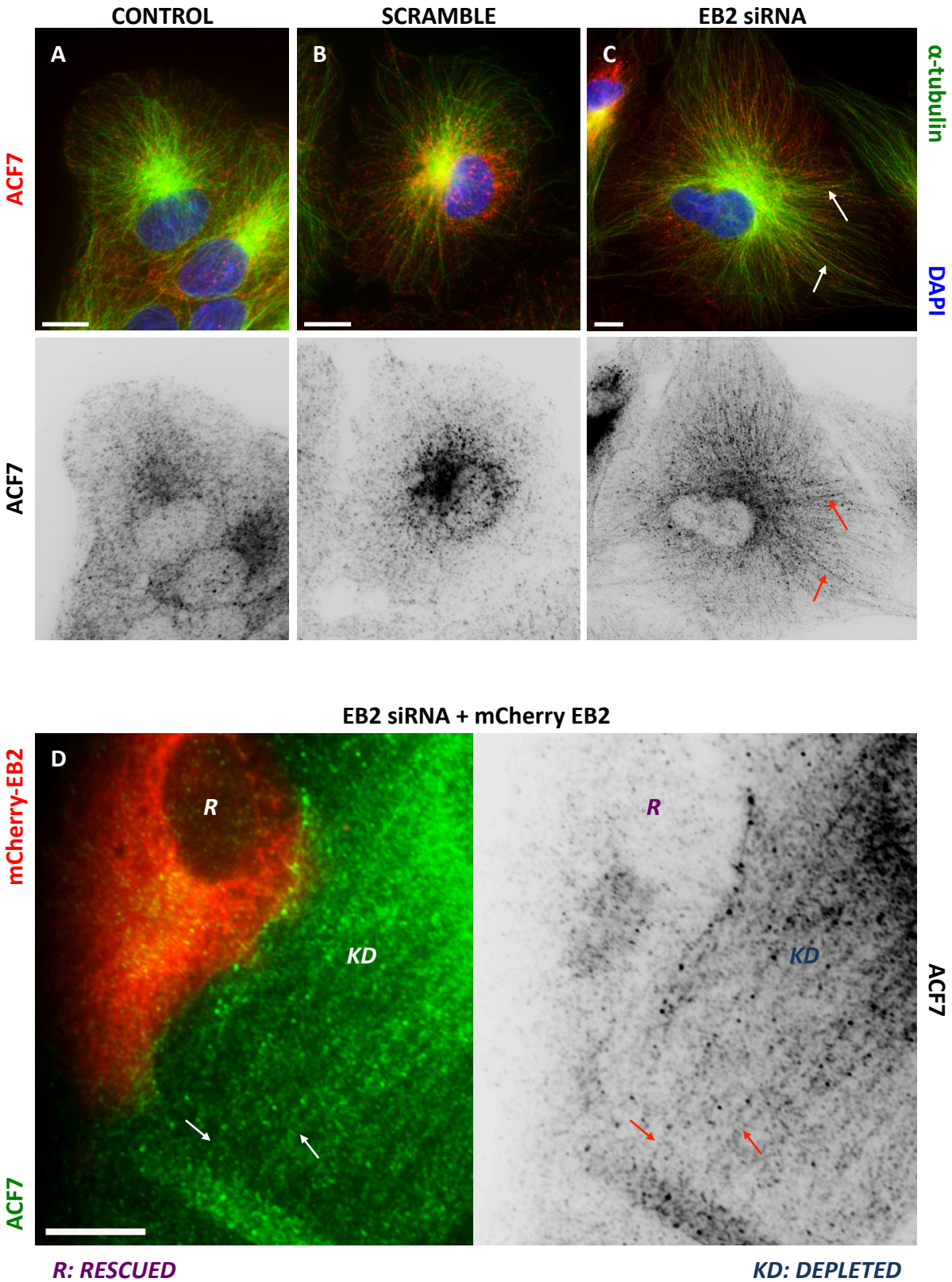
CONTROL
SCRAMBLE
EB2 siRNA
A
B
C
ACF7
α-tubulin
DAPI
ACF7
EB2 siRNA + mCherry EB2
D
mCherry-EB2
ACF7
R
KD
R
KD
ACF7
R: RESCUED
KD: DEPLETED

Chapter VI

The Role of EB2 in Microtubule Dynamics & Cell Division

6.1: Introduction

Microtubule +TIP proteins of the EB family are essential regulators of microtubule dynamic instability, important for the reorganisation of differentiated microtubule arrays (Tirnauer and Bierer, 2000). EB1 and EB3 have previously been shown to encourage microtubule dynamics by promoting growth and suppressing catastrophe events, whilst in contrast EB2 did not seem to function in the same manner (Komarova et al., 2009).

A key aspect of the phenotype observed following EB2 depletion in epithelial cell lines was the apparent reorganisation of microtubules into bundles co-aligned with actin filaments. Importantly, these observations were consistent with the arrangement of microtubule arrays seen in isolated tissue explants, where bundling correlated with low EB2 expression levels (Chapter V) (Goldspink et al., 2013b). Bundling occurs during epithelial differentiation and is associated with microtubule stability (Pepperkok et al., 1990), suggesting that EB2 may be involved in maintaining a dynamic population of microtubules. Stable microtubules have been associated with accumulation of tubulin post-translational modifications, including detyrosination (Webster et al., 1987). It was therefore important to analyse the tyrosination status and microtubule dynamics in cells depleted for EB2.

Another important change observed in cells treated with EB2 siRNA was the significant increase in cell size (Figure 5.4 D) (Goldspink et al., 2013b). Cell size regulation is a complex process important for cell function and viability, and throughout development processes. It is particularly associated with a synergy between growth and division, as the contents of the cytoplasm generally have to double in every cell cycle. Although not fully understood, it is tightly controlled such that if perturbed by a particular factor, the removal of that factor usually swiftly restores cells to their normal state (Conlon and Raff, 1999; Jorgensen and Tyers, 2004). Size appears to be regulated via several mechanisms, which often signal centrally through mTOR. It can be activated via various extracellular growth factors or the availability of nutrients and energy, and is inhibited by drug treatment (particularly rapamycin), cell stress, and starvation (Fingar et al., 2002; Guertin and

Sabatini, 2001). As an example, LKB1 signalling (which as previously noted is also associated with epithelial differentiation processes through an alternative pathway), acts to repress mTOR and restrict growth through the AMPK signalling cascade when sensing a low energy environment (Shaw et al., 2004; Woods et al., 2003). Cell size has also been directly associated with DNA content (ploidy), by either DNA replication within a single nucleus (as seen in myocardiocytes) or mitosis without cytokinesis (as occurs in some hepatocytes), which produce multinucleate cells (Conlon and Raff, 1999). Manipulations of the key components within these various influential pathways have been seen to produce a large cell size phenotype.

As indicated earlier, there is an especially strong link between size and the cell cycle. However, whilst the two are generally well co-ordinated (for example, nutrient starvation in cell culture can be used to induce G1 phase cell cycle arrest), the mechanisms controlling each are separable. This has been demonstrated in a variety of organisms including budding yeast, *Drosophila* and mammalian cell lines, where cell cycle blocking treatments (such as the inactivation or depletion of cdc regulatory genes or addition of chemical blocking agents) also cause an increase in cell size, as the underlying processes controlling cell growth remain unchecked (Fingar et al., 2002; Johnston et al., 1977; Jorgensen and Tyers, 2004; Neufeld et al., 1998). It was therefore important to analyse the cell cycle in EB2 depleted cells, and determine whether they were capable of successfully dividing, in order to ascertain whether the increase in cell size following siRNA treatment was in fact due to a block on the cell cycle.

Several experiments were performed to examine the effect of EB2 depletion on microtubule dynamics and cell division. Firstly, ARPE-19 cells stably expressing GFP-α-tubulin were depleted for EB2 and analysed by live time-lapse microscopy to determine the dynamics of microtubules in peripheral regions. Cells were also transfected with mCherry-EB2, to determine whether EB2 overexpression had any effects. To assess the cell cycle and any problems with cell division EB2 depleted cells underwent cell cycle analysis by flow cytometry, in addition to concurrent examinations by live time-lapse microscopy over an extended 48-hour period, which together were designed to determine whether the large cells observed following EB2

siRNA treatment have the ability to divide. It was found that EB2 depletion stabilised microtubules, which demonstrated increased pausing and reduced shrinking events. Additionally, EB2 depleted cells possessed detyrosinated tubulin in distinct microtubule bundles. Live imaging revealed that large EB2 depleted cells were capable of successful mitosis, however many cells appeared to die whilst attempting to divide, a phenomenon that increased in frequency over time. Cell cycle analysis by flow cytometry revealed a distinct sub-G1 peak, which correlated with the observed failed divisions. Some of the data presented in this chapter were included in (Goldspink et al., 2013b).

6.2: Results

6.2.1: EB2 depleted cells express detyrosinated tubulin in distinct microtubule bundles

ARPE-19 cells grown on glass coverslips were treated with two shots of scramble or EB2 siRNA (at 0 and 48 hours) and fixed at 96 hours, along with untreated control cells. Cells from each treatment were immunolabelled for tyrosinated and detyrosinated tubulin. Most of the α-tubulin expressed in all three conditions was tyrosinated. Expression of detyrosinated tubulin was somewhat inconsistent, particularly in scramble treated and control cells, where when expressed there was little apparent organisation; detyrosinated microtubules were often relatively curly, and expressed along subsections of the microtubule. However, on EB2 depletion detyrosination was detected particularly prominently along the length of distinct bundles of very straight microtubules extending from the central area of the cell out to the cell periphery (Figure 6.1).

Scramble and EB2 siRNA treated cells, along with untreated controls were also immunolabelled for acetylated tubulin. The presence of acetylated microtubules was variable in all three conditions, without any particular differences between EB2 siRNA and control or scramble treated cells (data not shown).

6.2.2: EB2 depletion leads to less dynamic microtubules

ARPE-19 cells stably expressing GFP-α-tubulin were used to investigate the effect of EB2 depletion on microtubule dynamics. These were grown in glass-bottomed dishes, treated with two shots of scramble or EB2 siRNA (at 0 and 48 hours) and analysed at 96 hours post initial treatment, along with untreated control cells. For each condition, cells demonstrating GFP in a distinct microtubule network were selected and imaged by live time-lapse fluorescence microscopy for a three-minute period, with frames taken every three seconds.

For analysis, peripheral regions measuring 12.5 x 12.5μm were selected from each treatment and processed. The lengths of the microtubules within each region were measured in each frame across the course of the experimental period. It should be noted microtubules were only analysed if their plus ends were initially visible and did not grow beyond the region. Microtubules that shrank beyond the region were analysed up until the point where they retracted from view.

Microtubules from multiple areas across five cells per treatment were analysed (with more than 60 microtubules assessed for each treatment). Dynamic profile graphs (in which the microtubule length at each time-point is zeroed against the original length at t=0) for all microtubules measured across each condition highlight the less dynamic microtubules in depleted cells compared to scramble and control cells. A region ±2.5μm from the original length, representing little overall change is highlighted to the right of each profile (Figure 6.2). Note the evident clustering of EB2 depleted microtubules in this region, in comparison to both control and scramble treated areas, which have a far greater spread of lines. Also note the greater number of lines in the control and scramble treated areas that terminate prior to end of the experimental period, corresponding to microtubules that have shrunk beyond the experimental frame of reference.

Movies were prepared illustrating a representative region from a scramble (Movie S1) and EB2 siRNA (Movie S2) treated cell, highlighting the location of microtubule plus ends over the period of the time-course. These distinctly show that whilst the microtubules under scramble treated conditions are highly dynamic, demonstrating clear growing and shrinking events throughout, EB2 depletion decreases dynamics; the microtubules visible spend the majority of the time paused, with very little growth or shrinkage. These observations are further illustrated in selected frames from each of the movies (Figure 6.3). Dynamic profiles of the indicated microtubules from these regions clearly demonstrate the stability of the EB2 siRNA treated cells compared to the scramble cells, as seen in the two movies. The depleted lines (red) deviate far less from the zero axis representing no length change in comparison to the scramble (blue) treated microtubules (Figure 6.4), showing the EB2 depleted microtubules are less dynamic.

To assess the degree by which dynamics have changed across the varying conditions, the microtubule length changes as measured were further analysed. For each microtubule, the degree of length change was determined by calculating the exact change in length between consecutive frames across the entire three-minute experimental period. These were than categorised into growing, pausing and shrinking events and used to calculate the percentage of each type of event over the life history of an individual microtubule. Events were classified as growing or shrinking if the change in length between consecutive frames was ≥0.5μm (the approximate measured width of the microtubules in the images), otherwise they were classed as paused. The average percentages for each event were calculated for individual cells from all the microtubules assessed in that cell, with a total of five separate cells (N=5) analysed for each treatment. There were no significant differences (as assessed by one-way ANOVA with Tukey's multiple comparisons test) between control and scramble treated cells for any of the dynamic events. Also, there was no significant difference between scramble and EB2 siRNA treatments on the percentage of microtubules undergoing growing events. In contrast, there were significantly fewer ($p<0.05$) shrinking events in depleted cells (12.1%) compared to scramble treated cells (23.9%), and in addition a significantly greater ($p<0.01$) percentage of pausing events on EB2 depletion (82.9%) than in scramble (69.0%) conditions (Figure 6.5).

Attempts were made to rescue the dynamic phenotype by transfecting EB2 siRNA treated cells with the mCherry-EB2 construct, however the combination of siRNA and construct treatments coupled to attempted fluorescent time-lapse imaging of cells already expressing a tagged construct was cytotoxic to the cells, and it proved impossible to gather images of sufficient quality for use.

To analyse whether EB2 overexpression could affect microtubule dynamics, untreated control GFP-tubulin expressing cells were seeded onto glass-bottomed dishes and transiently transfected with the mCherry-EB2 construct 24 hours prior to imaging. Analysis was conducted as for the knockdown investigation on a total of 48 microtubules across five separate cells (N=5). Statistical analysis (unpaired t-test) against untreated control cells revealed no significant difference for any of the

microtubule dynamic events (Figure 6.6). Attempts were made to use cells transfected with the empty pmCherry-C1 vector as a more appropriate control, however the quality of images gathered was too poor for reliable analysis.

6.2.3: Cell cycle analysis reveals a sub-G1 population on EB2 depletion

ARPE-19 cells treated with scramble and EB2 siRNA as described previously, along with untreated controls samples, were stained with propidium iodide (PI) 96 hours after the initial siRNA treatment, and analysed for DNA content by flow cytometry (Krishan, 1975). Debris and doublets were gated out and two separately treated samples were processed per condition for each of two experiments with >15,000 events processed per sample. Each run underwent cell cycle analysis in FloJo software using the Watson Pragmatic model (Watson et al., 1987) to fit the DNA fluorescence intensity data into the different cell cycle phases; Sub-G1, G1, S, G2/M, and super-G2, and accordingly calculate the proportion of cells in each. Histograms for control, scramble and EB2 siRNA treatments illustrating total cell fluorescence (marking relative DNA content) against event count show that the majority of cells in each are in G1 phase (as marked by the first large peak representing one copy of the genomic DNA), with a second smaller peak at double the intensity (which corresponds to the two copies of DNA in G2 or M phases). Cells in S phase are in the process of DNA duplication and so have fluorescent intensities between the G1 and G2/M peaks. Most interestingly, however, is a distinct peak in the EB2 depleted sample located at a fluorescent level below that of G1 cells, which is not found in control or scramble treated conditions (Figure 6.7). Sub-G1 peaks correspond to cells with DNA content less than a single genomic DNA copy, and can be characteristic of the DNA fragmentation seen during cell death pathways, particularly apoptosis (Furuya et al., 1997; Ziegler and Groscurth, 2004).

Cell cycle data were quantified from two individually processed runs over two separate experiments, which each gave a similar pattern of results (Results from experiment 1 are shown in Figure 6.8, those from experiment 2 are in Appendix C, Supplementary Figure S3). Significances between the proportions of cells in each

phase for each treatment were assessed by one-way ANOVA test with Tukey's multiple comparison test for each experiment. Analysis suggested a possible non-specific effect of siRNA treatment, as the scramble values differed from control cells in both experiments; in particular G1 values decreased, whilst the proportion of cells in S phase increased. In the case of experiment 2 these differences were statistically significant ($p<0.05$ for G1, $p<0.001$ for S) (Supplementary Figure S3). Interestingly these patterns appeared enhanced on EB2 siRNA treatment, which in both experiments reduced cells in G1 and increased cells in S phase to a greater extent when compared to control cells than the scramble treatment did, suggesting possible S phase arrest following EB2 depletion. In terms of statistical analysis, the effect was greater in experiment 2, where there was a significance increase in the percentage of cells in S phase in depleted cells compared to either control or scramble treated cells ($p<0.001$ for both comparisons) (Supplementary Figure S3). In experiment 1, the effect was less obvious, with only a slightly significant ($p<0.05$) increase for S phase in depleted to control cells, and no significant difference when compared to scramble cells (Figure 6.8).

Whilst the data suggesting a possible S phase arrest were inconsistent, the evidence for the sub-G1 peak observed in the histograms (Figure 6.7) is clear. In both experiments very few sub-G1 events are seen in either control or scramble conditions, whilst on EB2 depletion, there is a significant increase ($p<0.01$ in experiment 1 (Figure 6.8), $p<0.05$ in experiment 2 (Supplementary Figure S3)) when EB2 siRNA treatment is compared to either scramble or control cells. In experiment 1 there was also a clear decrease in the proportion of cells in G2/M phase on EB2 depletion ($p<0.05$ compared to either control or scramble treated cells) (Figure 6.8).

6.2.4: EB2 depleted cells divide but suffer increased division failures

To assess whether the giant cells observed on EB2 depletion were capable of mitosis, ARPE-19 cells were seeded onto a 6 well plate and treated with two shots of scramble or EB2 siRNA as previously, then analysed by live time-lapse phase contrast microscopy every 10 minutes for a 48 hour time period between 72 and 120 hours

after initial siRNA transfection. Note that all other analysis of the EB2 depletion phenotypes have occurred at 96 hours post initial treatment (Chapter V, Figures 6.1-6.5). Scramble cells were seen to divide regularly over the time-course, as illustrated in a selected representative region (Movie S3). Select frames from the movie demonstrate the key steps in the division process; namely, initial rounding, followed by cytokinesis during which two initial cells are visible, before the two daughter cells separate (Figure 6.9 A).

Large EB2 depleted cells were also seen to divide (Movie S4), with select frames illustrating the rounding, cytokinesis and separation steps (Figure 6.9 Bi). However, what was also noticeable was a number of depleted cells appearing to die, particularly later in the time-course (Movies S4 and S5). Interestingly, those that died appeared to do so whilst exiting division, as highlighted in frames from the large central cell present in Movie S5, representative of the overall phenotype. These frames illustrate an initial rounding similar to that seen during normal mitotic events, with cells spending a considerable time in a typical spheroid morphology. However, instead of then splitting into two daughter cells, cells die by appearing to explode. Interestingly however, just before final failure, two cells similar to that seen at the onset of separation can briefly be seen, raising the possibility that the cells are failing during the cytokinesis process on mitotic exit (Figure 6.9 Bii).

The number of successful and failed divisions was recorded for both treatments over the 72-96 and 96-120 hour time periods. Several regions from three separate wells were selected and analysed across both time periods for each treatment, with data recorded from 11 scramble and 29 EB2 siRNA treated regions. In total, 227 scramble and 311 EB2 siRNA treated division events were recorded between 72-96 hours, whilst 386 scramble and 387 EB2 siRNA divisions were observed between 96-120 hours post initial transfection. In scramble treated cells, very occasional death events were observed, but the vast majority (92% between 72-96 hours, 97% from 96-120 hours) of divisions appeared normal. However, following EB2 depletion, an increased number of failures was observed. At the earlier time-point, the majority of divisions (75%) still occured normally, with a quarter of observed events therefore resulting in death. This rate of failure greatly increases

when the experiment extends beyond the 96-hour time-point, with 66% of observed events between 96 and 120 hours being instances of cell death (Figure 6.10 A). Analysis by Chi-Squared test confirmed the differences between scramble and depleted cells over both time periods were significant ($p<0.0001$ for both time-points, Figure 6.10 B).

6.3: Discussion

6.3.1: Loss of EB2 decreases microtubule dynamics

Analysis of microtubule dynamics confirmed that on EB2 depletion microtubules became less dynamic and more stable, with significantly fewer shrinking and more pausing events. Coupled to this, the microtubule bundles that formed on depletion contained detyrosinated tubulin. Further data support this conclusion; cold treatment completely depolymerised microtubules in control and scramble treated cells, whilst in contrast in EB2 depleted cells several stable microtubules remained intact despite the treatment (Goldspink et al., 2013b).

As already discussed, microtubule dynamics play an essential role in the reorganisation of microtubule arrays throughout differentiation processes. Results presented here suggest that EB2 functions by maintaining a dynamic population of microtubules. EB2 downregulation by either siRNA mediated manipulation, or as part of natural epithelial differentiation, causes microtubules to form bundles, with EB1 and ACF7 association along the lattice, and co-alignment with actin filaments (as previously examined in Chapter V) (Goldspink et al., 2013b).

To summarise, the overall ability of EB2 to effect microtubule dynamic instability appears to be a key factor contributing to the mechanism by which it functions, and provides an explanation of how it may contribute to the overall epithelial differentiation process (see Chapter 8).

6.3.2: EB2 depleted cells have the ability to divide, but extended depletion causes increased cell death

An important observation made on EB2 depletion of ARPE-19 cells was the distinctive increase in cell size. Such an increase is often linked with arrest of the cell cycle, resulting in a block on cell division (Conlon and Raff, 1999). It was important therefore to investigate whether the large cells produced by EB2 siRNA treatment

had the ability to divide, and whether there was any evidence of a disrupted cell cycle.

The ability to divide was assessed very simply, by directly observing depleted cells by time-lapse microscopy. All depletion experiments throughout the project were performed at 96 hours post initial siRNA treatment, so live cell imaging was performed over a 24 hour time-period either side of this 96 hour point, to give a total experimental time of 48 hours. Importantly, division events were seen in depleted cells, indicating they were still competent for mitosis. This correlates with additional investigations; EB2 siRNA treated cells were seen to be positive for Ki-67 following immunolabelling (Goldspink et al., 2013b). Ki-67 is a marker commonly used to assess whether cells are capable of proliferation after undergoing a particular treatment (Gerdes et al., 1984).

Interestingly however, a distinct increase in the number of cells that appeared to die whilst attempting to divide was apparent. Importantly, the rate of cell death was relatively low up to the 96-hour time-point used in other analyses; indeed whilst a prior proliferation assay from 0-96 hours had identified a slight drop in proliferation in EB2 in pure numerical terms, it was not statistically significant (Goldspink et al., 2013b). Interestingly, when the proliferation assay was continued beyond the 96 hour time point until 144 hours after the initial siRNA treatment, a distinct drop in cell number was indeed detected (D. Goldspink, personal communication). That measured drop can now be explained by a significant increase in cell death in cells beyond the 96 hour cut-off point. It should be pointed out that at this stage the mechanism by which EB2 loss causes cell death is unknown. It is possible that this is due to the effect that EB2 has on microtubule stabilisation, but it is also equally possible that lack of EB2 has a hitherto unknown affect on alternative pathways.

It should be noted that as expected, the EB2 siRNA treatment produced cells of a typically increased size, with the spread of those sizes consistent with that previously measured (Figure 5.9 A) (Goldspink et al., 2013b). This size spread is characterised by both the previously discussed large cells, mixed with other smaller

cells of a size comparable to most scramble treated cells. Importantly, there were no obvious size related differences as to whether a mitotic event resulted in success or failure; both large and small sized depleted cells were seen to successfully divide, or conversely fail to complete mitosis and die.

The cells used for experiment 1 of the cell cycle analysis (Figure 6.8) were seeded at the same time from the same initial cell population as used for the 72-120 hour live cell imaging, with the flow cytometry analysis performed at the typical 96 hour time-point. There can therefore be comparisons made between the flow cytometry and the live imaging experiments. Importantly, a key finding from the flow cytometry data was the presence of a sub-G1 peak, coupled with a possible reduction in the proportion of cells in G2/M phase. such a Sub-G1 phenomenon is commonly associated with the DNA fragmentation that occurs when cells enter a cell death pathway such as apoptosis or necrosis (Ziegler and Groscurth, 2004). This correlates well with the live imaging experiments where cells were clearly seen to be dying, especially at later checkpoints.

From the live time-lapse images of observed cell deaths, it appears as if division fails during cytokinesis, although this cannot be definitively stated. This could be due to the increased stability of microtubules in the cleavage furrow preventing daughter cell separation, although such a mechanism is more normally associated with failure to separate and the formation of multiple nuclei, rather than any type of cell death (Guertin et al., 2002). Alternatively, treatment with a low concentration of the microtubule stabilising drug taxol has been seen to disrupt mitotic exit, and cause death via apoptotic pathways (Jordan et al., 1996). It is also possible that the formation of the actomyosin ring required at the cleavage furrow is disturbed.

Overall, there are many mechanisms by which cell death occurs, for example, a specialised form of cell death known as mitotic catastrophe has been identified, in which cells die during mitosis, although this mechanism generally affects multinucleate cells, with cells accumulating in G2/M phase (Castedo et al., 2004; Vakifahmetoglu et al., 2008), neither of which is apparent in the phenotypes seen in

this study. The various cell death pathways are particularly complicated, and indeed do not always have a unified definition, particularly in the case of less common modes like mitotic catastrophe. Thus, without further data, it is not possible to judge exactly how the cells are dying following the extended EB2 siRNA depletion as seen within this study.

Originally, the data from the two separate cell cycle experiments were intended to be combined to give four replicates, however it was found that whilst separate runs from the same experiment were similar, the underlying differences between the proportion of cells in G1 and S phases under control conditions were too great to fairly incorporate them together. In particular, the second experiment possessed more cells in G1 and fewer in (66% G1, 14% S) than the first (54% G1, 24% S). This is likely due to the experiments being run on different batches of cells or at slightly different confluency levels, with an accompanying small difference in the rate of division. More confluent cells divide less, and cells duplicating at a slower rate would have more cells in G1 and fewer in S phase. Additionally, there seemed to be a greater effect of siRNA treatment in the second experiment, with significant differences between control and scramble cells in G1 and S phases (Appendix C, Supplementary Figure S3). Nevertheless, both experiments produced graphs of comparable shapes, with certain common findings, particularly the presence of the sub-G1 peak. There are hints of possible S phase arrest, particularly in the second experiment, but the large differences between control and scramble numbers make it impossible to attribute this definitively to the EB2 knockdown, rather than it being a general side effect of siRNA manipulation on the cell cycle.

6.3.3: Further work

There remain several areas for future investigations, particularly in terms of the potential cell cycle and division effects of EB2 loss. Initially further cell cycle analyses should be performed to properly determine whether cells are accumulating in parts of the cell cycle other than that marked by the sub-G1 peak.

Perhaps most interesting however is to try and elucidate the mechanism by which loss of EB2 causes cell death. This is of particular interest in terms of cancer research, as EB2 could prove an interesting future target if its activation promotes proliferation whilst its loss causes death. In the first instance, it is essential to identify the actual pathway triggered; in other words, are cells undergoing programmed cell death via apoptosis, or dying via necrosis? An early way to examine this theory is to stain depleted cells for Annexin V, often used as a marker for apoptosis when analysed by flow cytometry (Vermes et al., 1995). It is also vital to decide whether the cells are indeed actually dying during division, or if the phenotypes seen via live microscopy can be explained in an alternative way.

Following identification of the appropriate death pathway, it is then important to judge whether the EB2 depletion death phenotype is actually caused by its cytoskeletal interactions, and not due to a previously unknown role in other cellular pathways, such as signalling. To that end, it may be interesting to investigate whether EB2 has any interactions with the apoptosis inhibitory protein survivin, which has been associated with the stabilisation of spindle microtubules, an interaction that has been shown induce apoptosis if disrupted (Li et al., 1998).

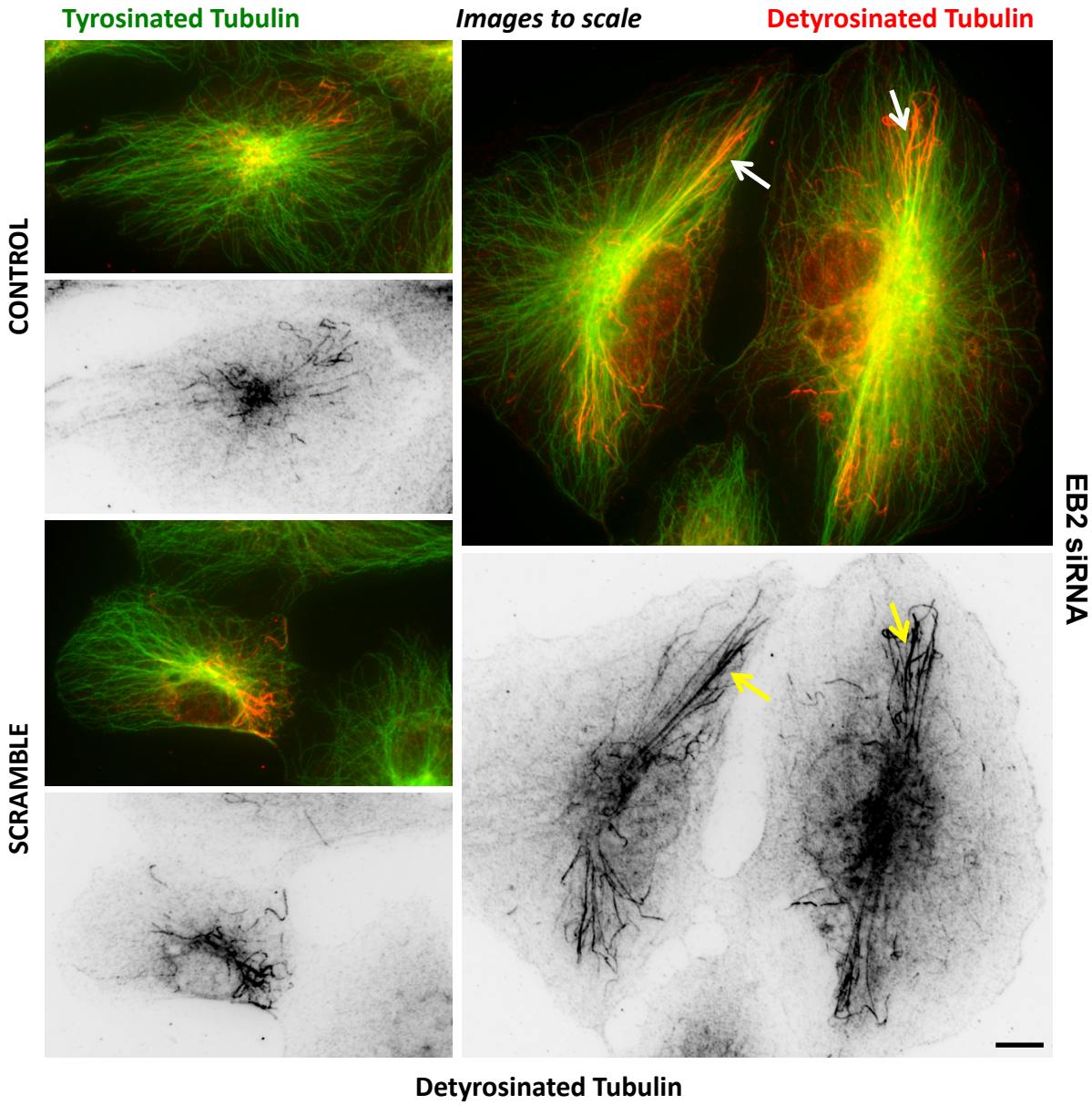

Figure 6.1 EB2 depleted ARPE-19 cells express detyrosinated tubulin in stable microtubule bundles
Widefield fluorescent images of ARPE-19 cells treated with scramble or EB2 siRNA and untreated controls fixed at 96 hours post siRNA treatment and immunolabelled for tyrosinated tubulin (YL1/2) (green) and detyrosinated tubulin (glu-tubulin) (red, invert). Detyrosinated tubulin prominently localises in distinct microtubule bundles (arrowed) in EB2 siRNA treated cells. Scale bar = 10µm.

Figure 6.2 EB2 depletion alters the dynamic profiles of microtubules
ARPE-19 cells stably expressing GFP-tubulin and treated with scramble or EB2 siRNA, in addition to untreated controls were imaged every 3 seconds over a three minute period by time-lapse widefield fluorescent microscopy. 12.5x12.5µm peripheral regions from each condition were selected for analysis. For each region microtubules were selected and their length measured in each frame across the three minute period, with a profile for each microtubule displayed in the graphs. Each line represents the change in length of a microtubule relative to its original length at t=0s. Displayed are profiles for all microtubules measured across 5 separate cells for each condition (EB2 siRNA (red lines); 11 regions, 66 microtubules, scramble (blue lines); 10 regions, 61 microtubules and control (green lines); 9 regions, 61 microtubules). For each graph, a region corresponding to a change of ±2.5µm from the original length is marked (brackets). Note the distinct lack of length changes in EB2 siRNA conditions compared to the control and scramble charts, highlighted by the greater clustering of microtubules in the marked region of the EB2 siRNA chart.

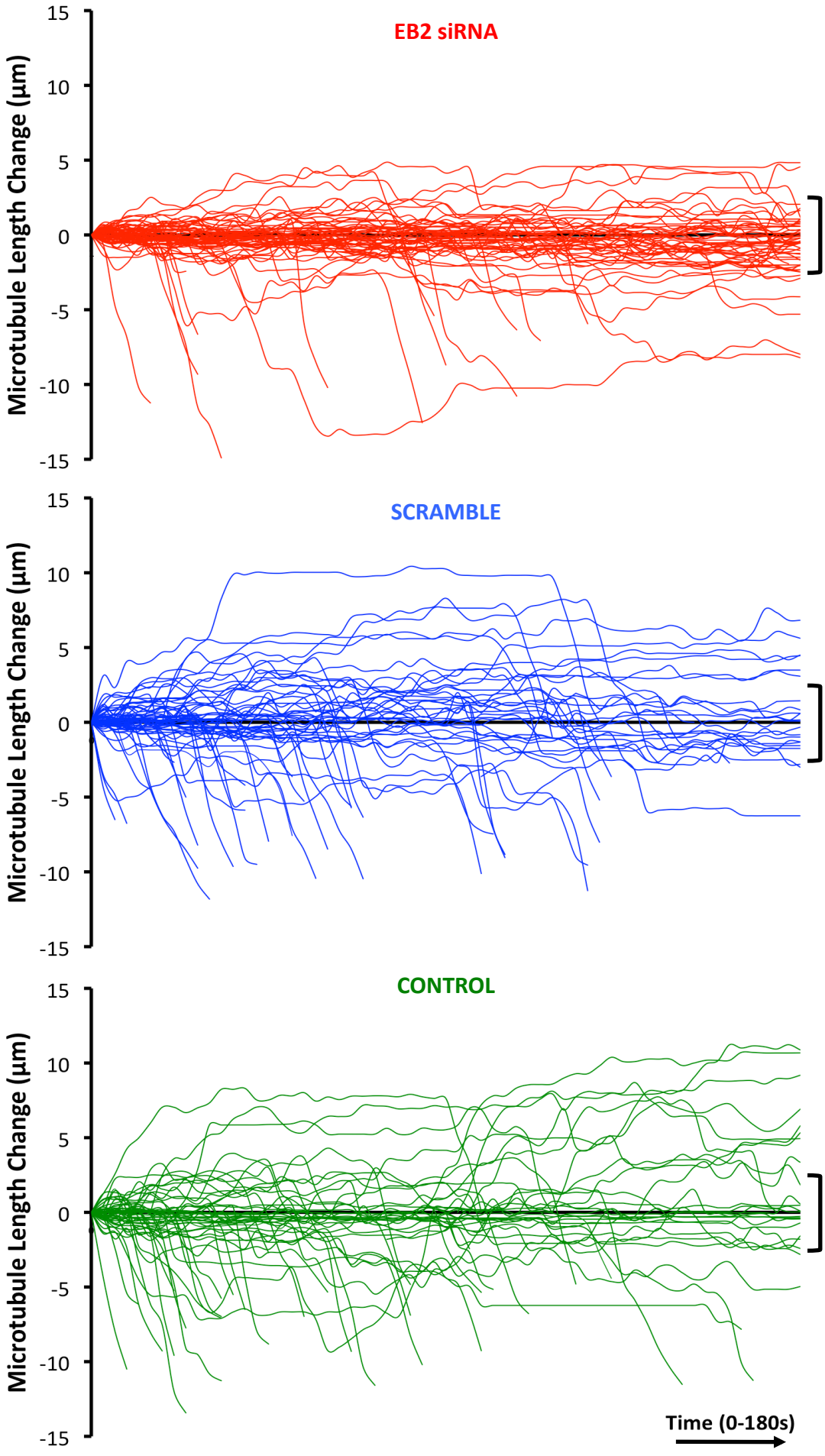
EB2 siRNA
SCRAMBLE
CONTROL
Microtubule Length Change (µm)
15
10
5
0
-5
-10
-15
Time (0-180s)

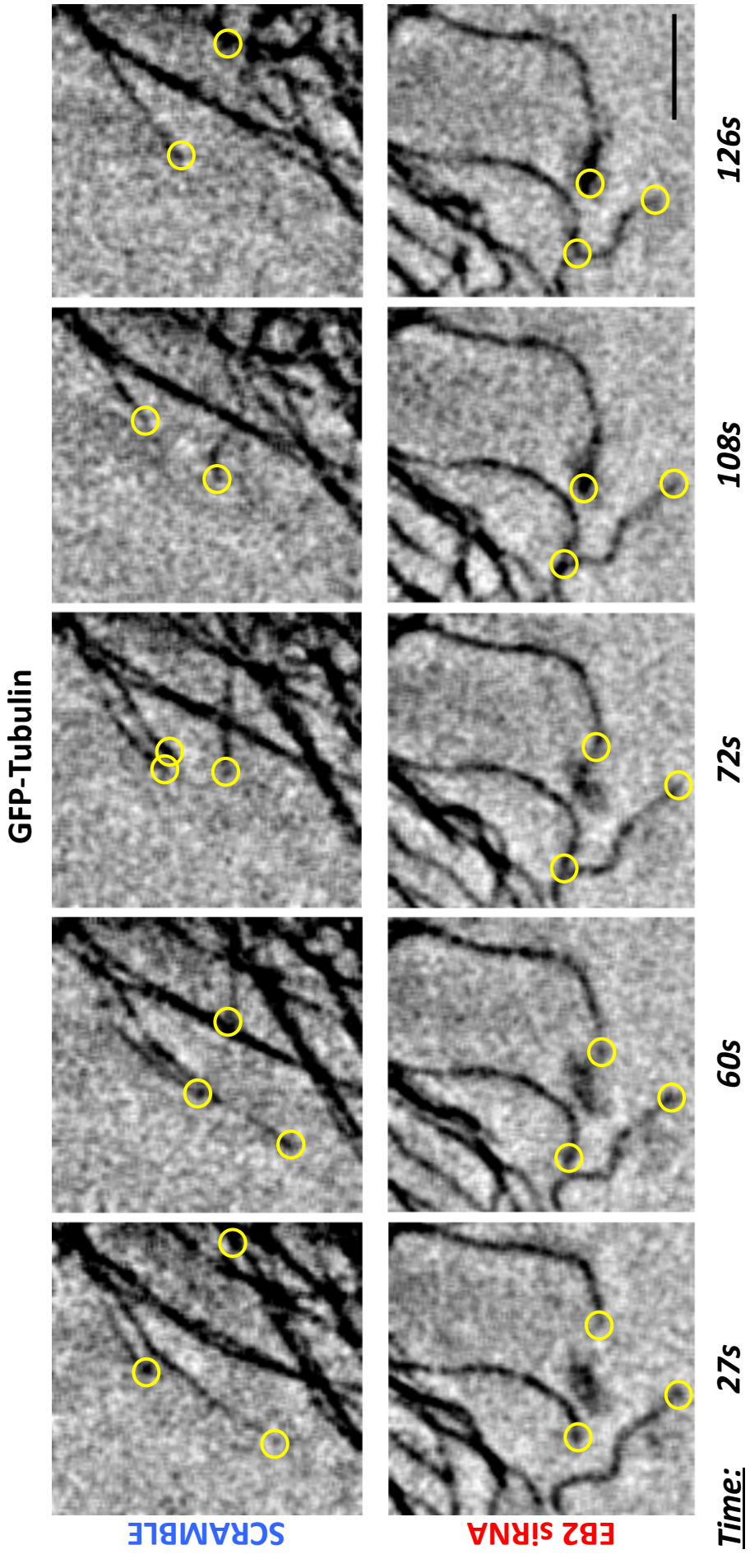

Figure 6.3 EB2 depletion decreases microtubule dynamics
ARPE-19 cells stably expressing GFP-tubulin were treated with scramble or EB2 siRNA and imaged every 3 seconds over a three minute period by time-lapse widefield fluorescent microscopy. 12.5x12.5µm peripheral regions from each condition were selected for analysis. Shown are select image frames from a representative scramble and EB2 depleted region (also see movie S1 and S2) with the position of analysed microtubule plus ends highlighted at each time point (circled). Note the dynamic microtubules in the scramble treated cell undergoing growth and shrinkage events, whilst microtubules in the depleted region are less dynamic and spend more time in a paused state. Scale bar = 5µm.

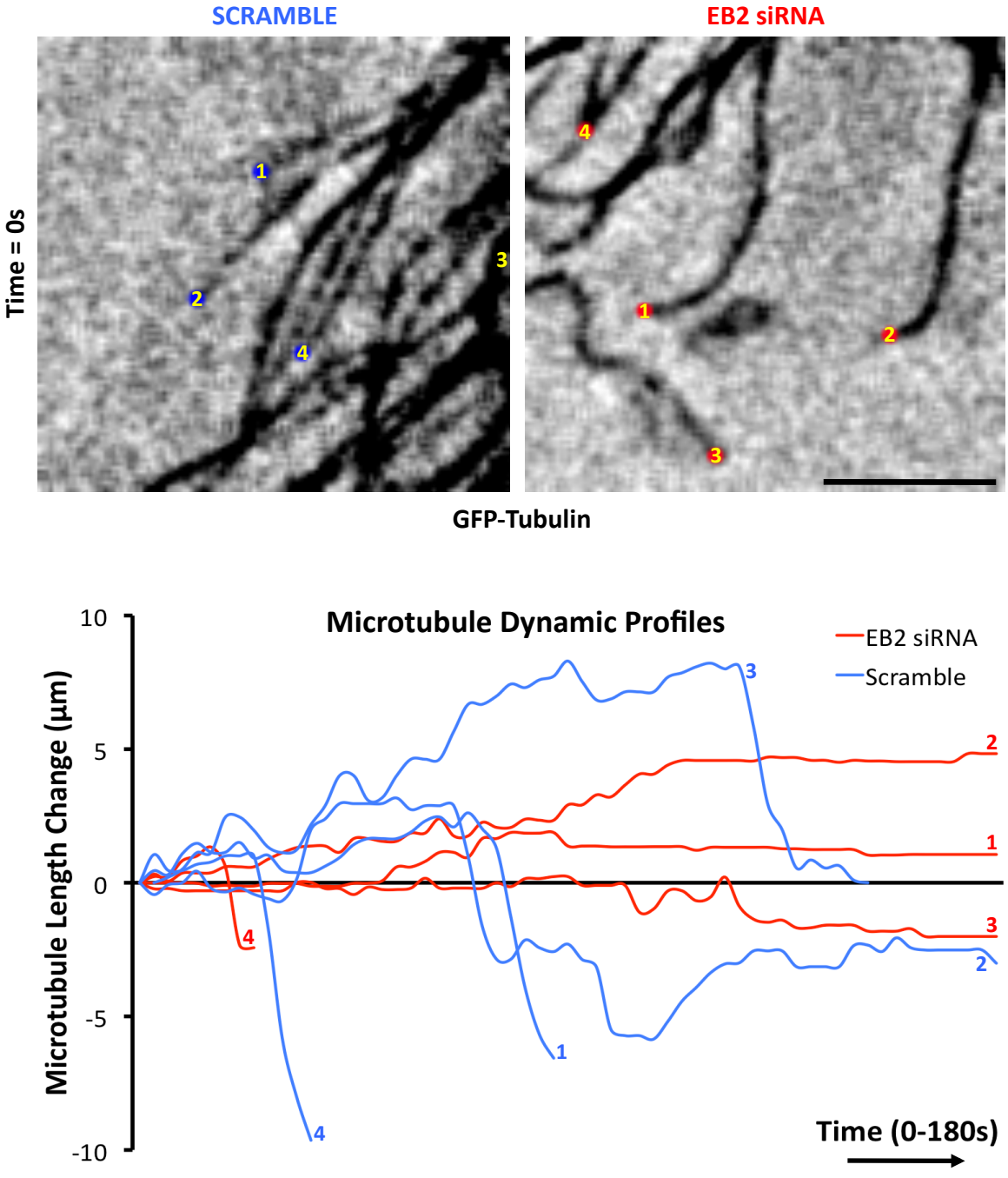

Figure 6.4 Dynamic profiles of selected microtubules
ARPE-19 cells stably expressing GFP-tubulin were treated with scramble or EB2 siRNA and imaged every 3 seconds over a three minute period by time-lapse widefield fluorescence microscopy. 12.5x12.5µm peripheral regions from each condition were selected for analysis. For each region the length of a selected microtubule was measured in each frame across the three minute period, to produce a profile representing its change in length compared to t=0s. Displayed are profiles from the microtubules selected (numbered in images) from the representative scramble and EB2 depleted regions shown in movies S1 and S2. Profile lines stop where microtubules shrink out of the frame of the selected region. Note the greater degree of length change in scramble microtubules (blue lines) compared to EB2 siRNA treated microtubules (red lines). Scale bar = 5µm.

Figure 6.5 EB2 depletion causes increased microtubule pausing and reduces shrinking events
ARPE-19 cells stably expressing GFP-tubulin and treated with scramble or EB2 siRNA, in addition to untreated controls were imaged every 3 seconds over a three minute period by time-lapse widefield fluorescent microscopy. 12.5x12.5µm peripheral regions from each condition were selected for analysis. For each region microtubules were selected and their length measured in each frame across the three minute period. The difference in length between frames was calculated and used to score for either growing, shrinking or pausing events. Microtubules were defined as growing or shrinking if the difference in microtubule length between consecutive frames was ≥0.5µm. The percentage of frames where a microtubule was in each dynamic state was calculated and averaged across the microtubules from a particular cell. Five cells were analysed for each condition (N=5), and the average percentage (±SEM) plotted for shrinking, pausing and growing events. For each event, results were statistically analysed by two tailed unpaired t-test between treatments, showing that EB2 siRNA treatment causes a significant decrease in shrinking events, and a significant in increase in pausing events compared to control or scramble treated cells (one-way ANOVA with Tukey's multiple comparison test for each event).

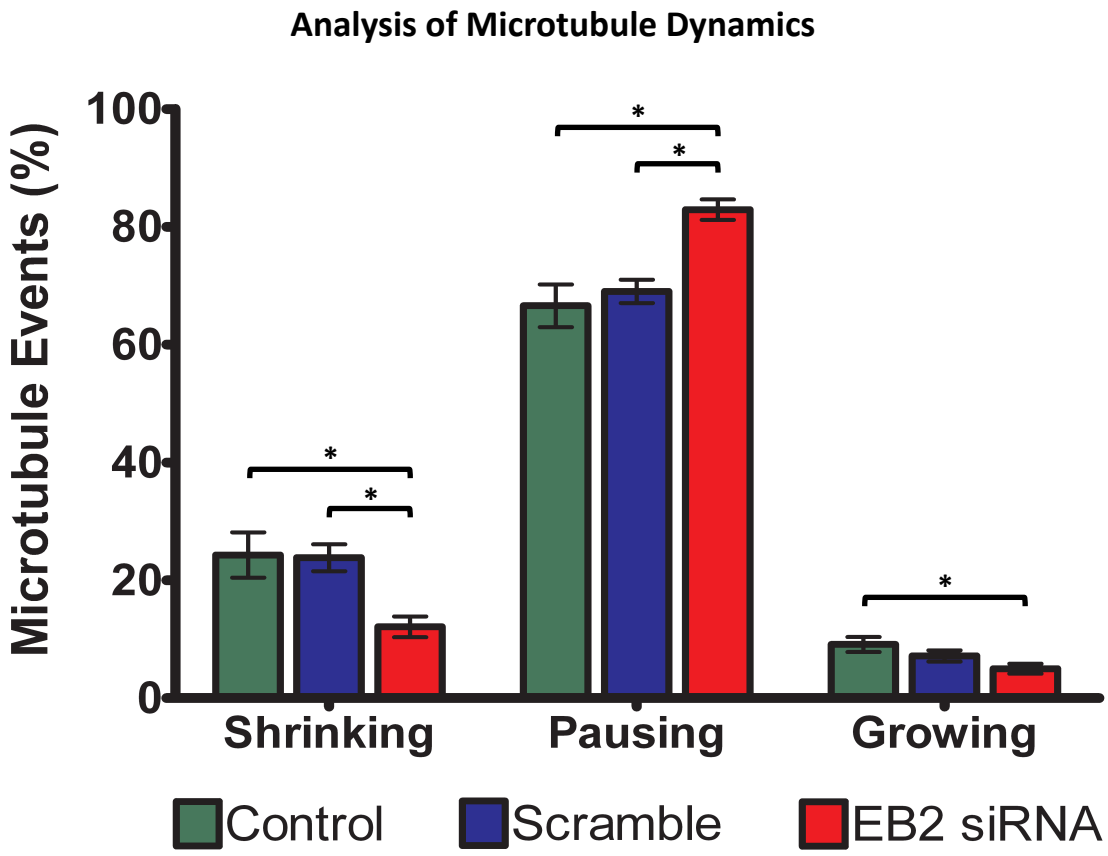

Treatment	N	Dynamic Events	Mean ± SEM (%)
Control	5	Shrinking	24.30 ± 3.8
		Pausing	66.60 ± 3.6
		Growing	9.11 ± 1.2
Scramble	5	Shrinking	23.83 ± 2.3
		Pausing	69.02 ± 2.0
		Growing	7.15 ± 1.0
EB2 siRNA	5	Shrinking	12.09 ± 1.8
		Pausing	82.90 ± 1.8
		Growing	5.01 ± 0.9

Figure 6.6 EB2 overexpression has no effect on microtubule dynamics
ARPE-19 cells stably expressing GFP-tubulin were transfected with mCherry-EB2, and imaged every 3 seconds over a three minute period by time-lapse widefield fluorescent microscopy. 12.5x12.5µm peripheral regions from each condition were selected for analysis. For each region microtubules were selected and their length measured in each frame across the three minute period, and a profile graph produced representing microtubule change in length relative to that at t=0s. **(A)** Dynamic profiles for all microtubules measured across 5 separate cells (purple lines); 10 regions, 48 microtubules. A region corresponding to a change of ±2.5µm from the original length is marked (brackets). **(B)** The difference in length between frames was calculated and used to score for either growing, shrinking or pausing dynamic events. Microtubules were defined as growing or shrinking if the difference in microtubule length between consecutive frames was ≥0.5µm. The percentage of frames where a microtubule was in each dynamic state was calculated and averaged across the microtubules from a particular cell. 5 cells were analysed for each condition (N=5), and the average percentage (±SEM) plotted for shrinking, pausing and growing events. For each event, results were statistically analysed by two tailed unpaired t-test between overexpressing and control conditions, showing that EB2 siRNA treatment caused no significant changes to the proportions of each dynamic event.

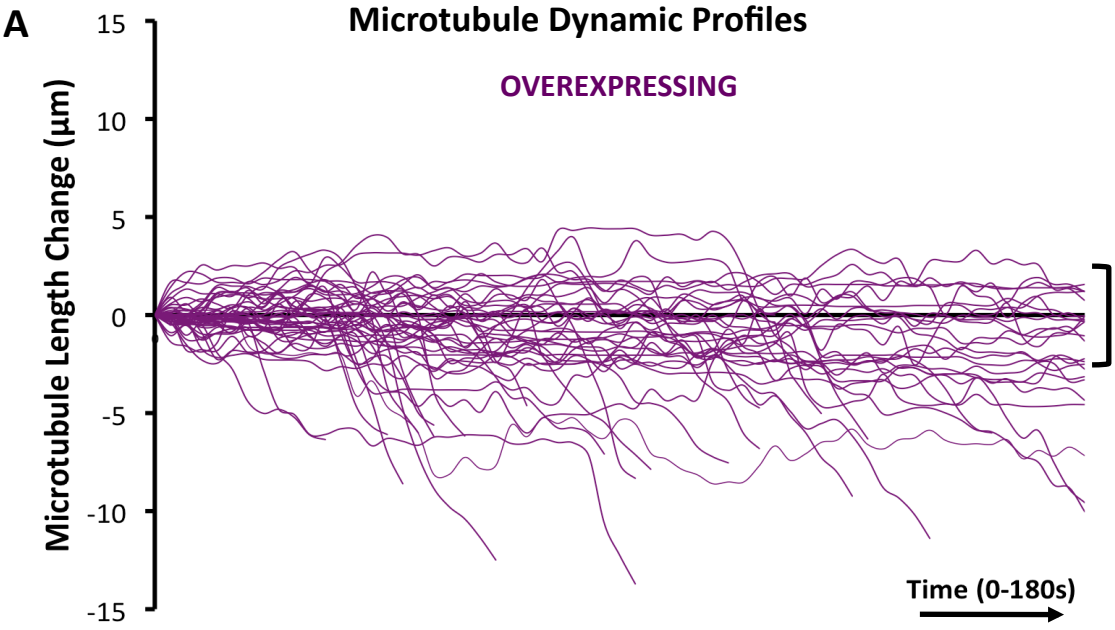

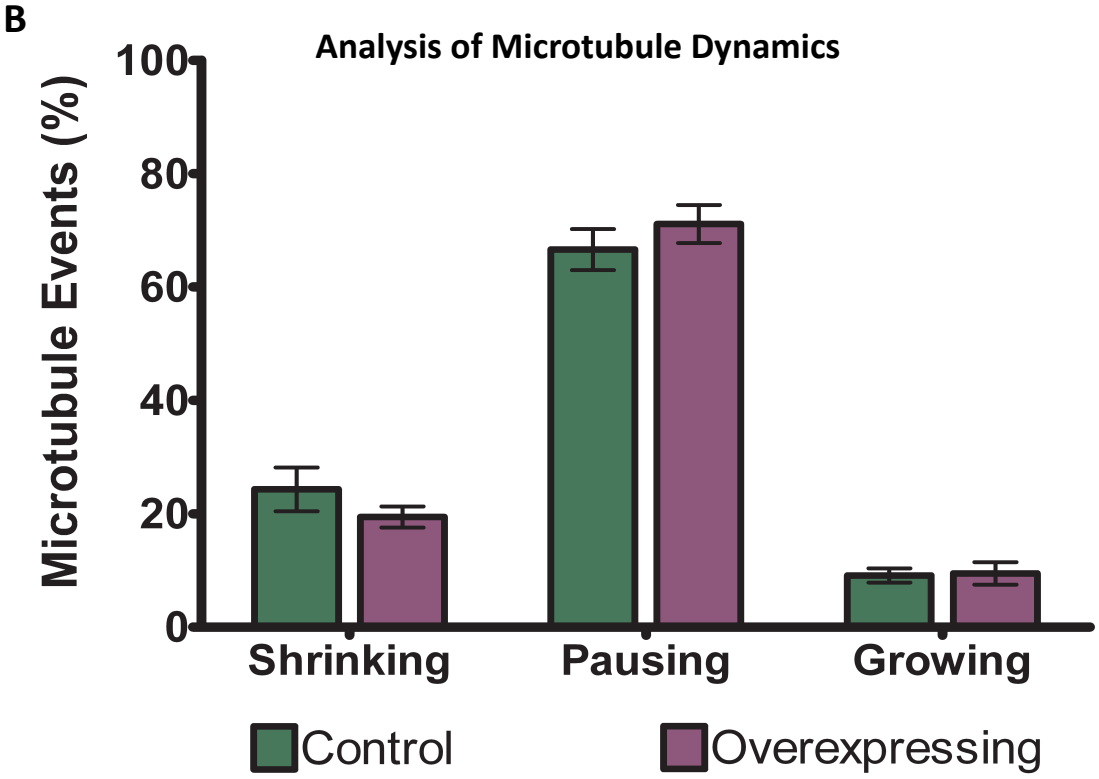

Treatment	N	Dynamic Events	Mean ± SEM (%)
EB2 Overexpressing	5	Shrinking	19.41 ± 1.9
		Pausing	71.11 ± 3.4
		Growing	9.47 ± 2.0

Dynamic Event	Two-tailed Unpaired t-test			
Shrinking	Control	*vs*	EB2 Over-expressing	[NS]
Pausing				[NS]
Growing				[NS]

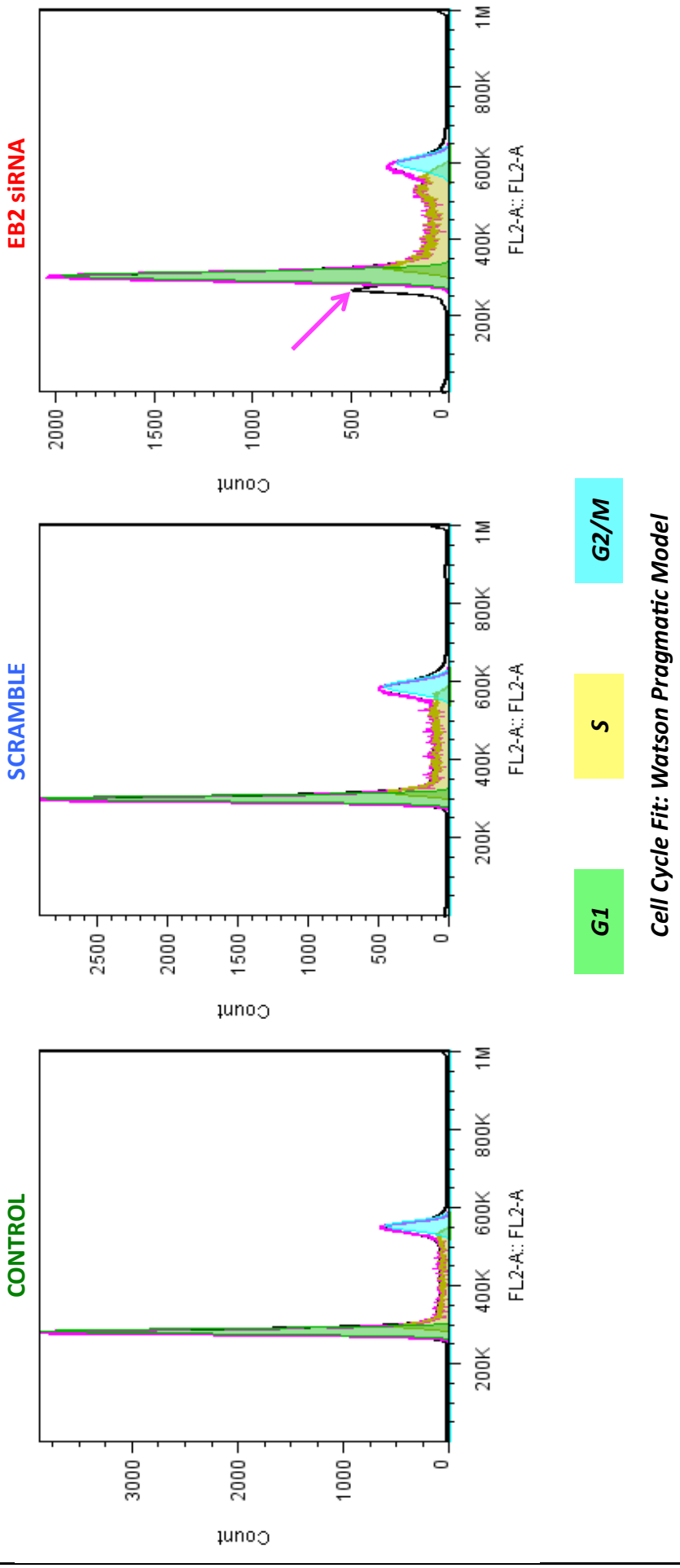

Figure 6.7 Cell cycle analysis of EB2 depleted ARPE-19 cells
Scramble and EB2 siRNA treated and untreated control samples were stained with Propidium iodide 96 hours post transfection, and analysed for DNA content by flow cytometry. Debris and doublets were excluded by gating around the singlet cell population. The histograms illustrate a representative run (>30,000 cells) for each condition. Cell cycle distribution data were fitted in FloJo software using the Watson Pragmatic model to define G1 (green), S (yellow) and G2 (blue) phases as illustrated. Note in particular the sub G1 peak visible exclusively in the EB2 depleted sample (purple arrow).

Figure 6.8 EB2 depletion causes an accumulation of cells in sub G1 and reduction in G2/M phases
Scramble and EB2 siRNA treated and untreated control samples were stained with Propidium iodide 96 hours post transfection, and analysed for DNA content by flow cytometry over two runs per condition (>15,000 cells per run, N=2). Cell cycle distribution data was fitted in FloJo software using the Watson Pragmatic model to define cell cycle phases for each run, and used to calculate the average percentage of cells in each phase. Statistical differences between treatments were analysed by one-way ANOVA with Tukey's multiple comparisons test for each phase. There was a significant increase in the percentage of cells in sub G1, and a significant reduction of cells in G2/M on EB2 depletion.

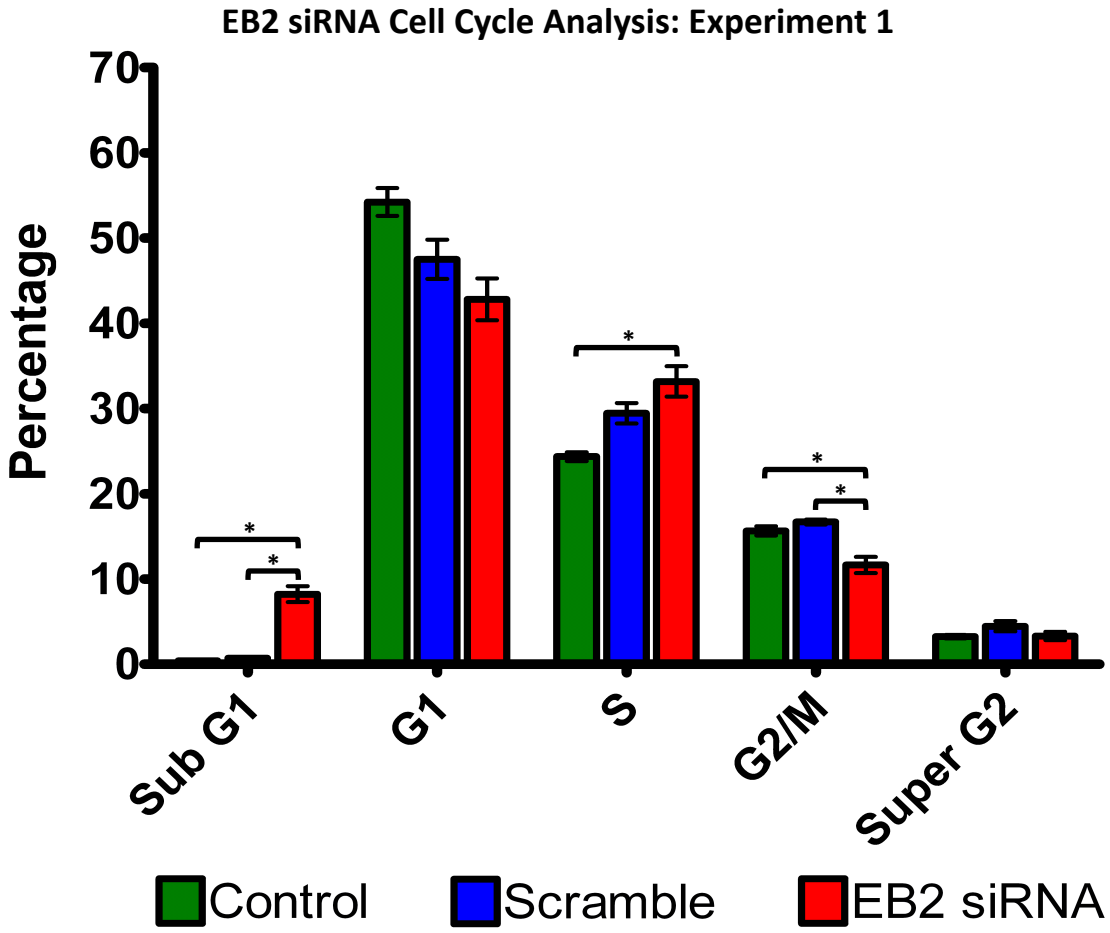

Treatment	N	Phase	Mean ± SEM (%)
Control	2	Sub G1	0.39 ± 0.1
		G1	54.23 ± 1.6
		S	24.35 ± 0.5
		G2/M	15.65 ± 0.5
		Super G2	3.23 ± 0.2
Scramble	2	Sub G1	0.70 ± 0.1
		G1	47.51 ± 2.3
		S	29.45 ± 1.2
		G2/M	16.69 ± 0.3
		Super G2	4.46 ± 0.6
EB2 siRNA	2	Sub G1	8.22 ± 0.9
		G1	42.81 ± 2.5
		S	33.17 ± 1.8
		G2/M	11.65 ± 0.9
		Super G2	3.31 ± 0.5

Figure 6.9 EB2 depleted cells are able to divide, but can fail to separate
ARPE-19 cells were treated with scramble and EB2 siRNA and observed by phase contrast live-microscopy over a 48 hour period between 72-120 hours after siRNA treatment. Selected frames from **(A)** scramble treated cells, illustrating stages of normal division (see Movie S3) & **(B)** EB2 siRNA depleted cells, showing **(i)** a large cell dividing and separating normally to produce two daughter cells (starred, see Movie S4), and **(ii)** a cell that fails to separate (see Movie S5). Note how the cell contracts to divide as normal, with two buds clearly visible (arrowed) just before the cell dies (circled).

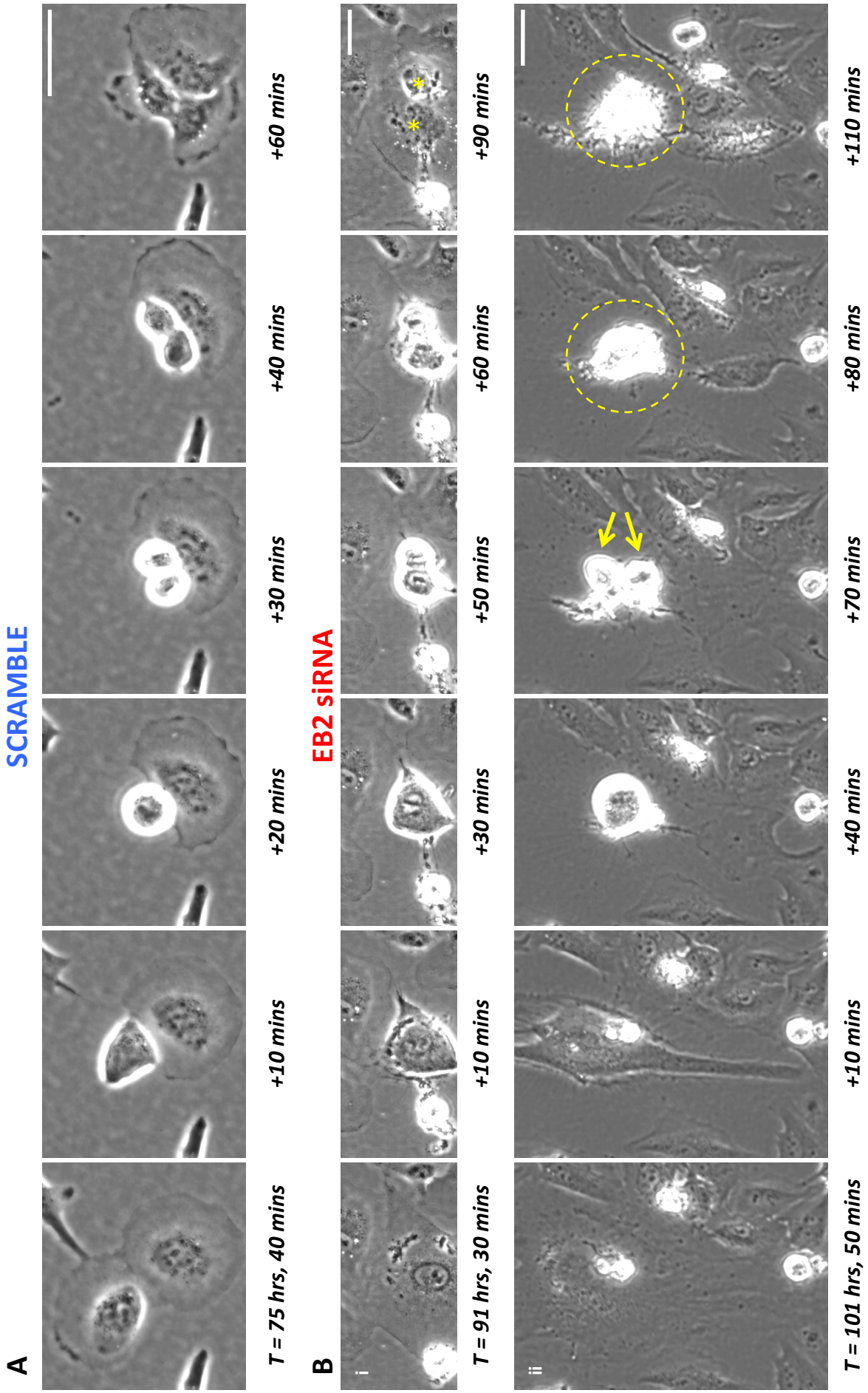
A
SCRAMBLE
T = 75 hrs, 40 mins
+10 mins
+20 mins
+30 mins
+40 mins
+60 mins
B
EB2 siRNA
i
T = 91 hrs, 30 mins
+10 mins
+30 mins
+50 mins
+60 mins
+90 mins
ii
T = 101 hrs, 50 mins
+10 mins
+40 mins
+70 mins
+80 mins
+110 mins

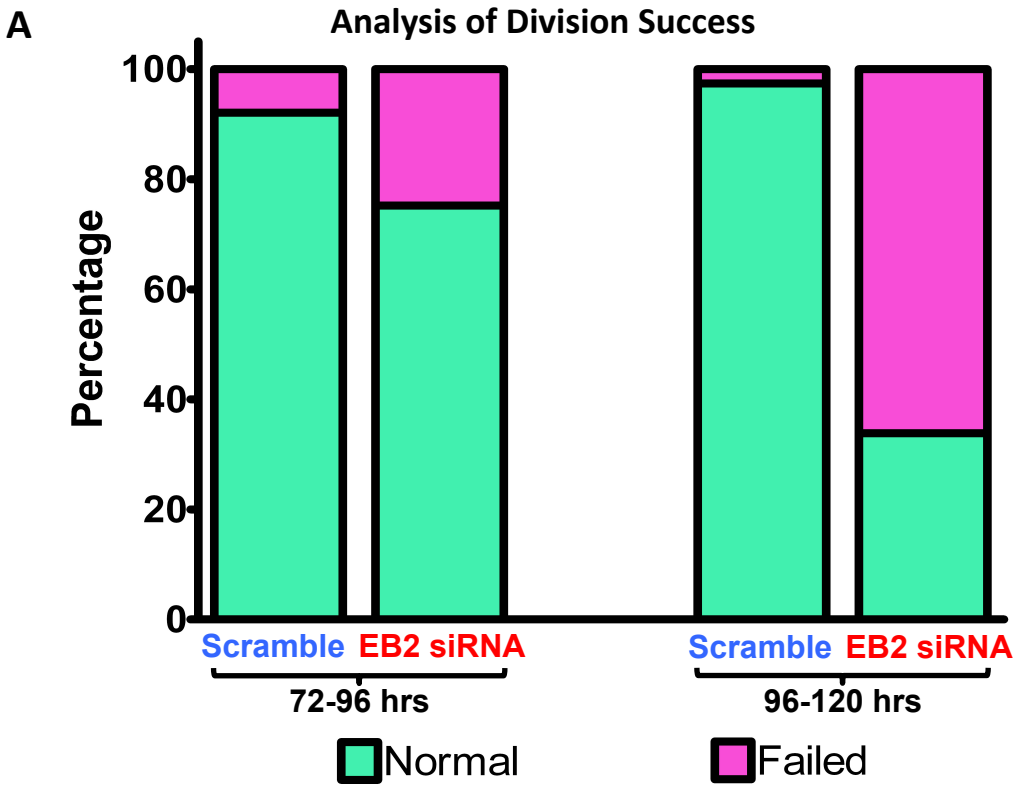

	72-96 hrs		96-120 hrs	
	Scramble	EB2 siRNA	Scramble	EB2 siRNA
Normal	209 (92.1%)	234 (75.2%)	376 (97.4%)	131 (33.9%)
Failed	18 (7.9%)	77 (24.8%)	10 (2.6%)	256 (66.1%)
Total (N)	**227**	**311**	**386**	**387**

B

	Chi-Squared			
72-96 hrs	Scramble	***vs***	EB2 siRNA	25.56 P < 0.0001
96-120 hrs	Scramble		EB2 siRNA	345.9 P < 0.0001

Figure 6.10 EB2 depletion in ARPE-19 cells causes increased instances of division failure over time
ARPE-19 cells were treated with scramble and EB2 siRNA and observed by phase contrast live-microscopy over a 48 hour period between 72-120 hours after siRNA treatment. Regions from each treatment were analysed for successful division events post treatment. **(A)** Instances of successful division (green) or division failure and death (magenta) were analysed and recorded separately for the 72-96 and 96-120 hour periods. **(B)** Differences in distribution for each time period were assessed by Chi-Squared test. For both time periods, the proportion of division events in which cells die significantly increased following EB2 depletion. Note that this failure was particularly pronounced during the second 24 hour period (96-120 hours) where the majority of observed events resulted in death.

Chapter VII

EB2 Overexpression in Polarisation & Migration

7.1: Introduction

Metastasis, the migration and invasion of tumour cells through tissues to distant sites, is a major mechanism in the cancer disease process directly linked to prognosis, with these growths at secondary locations (rather than the primary tumour) known to be responsible for the majority of cancer deaths (Chambers et al., 2002). The pathway to metastasis begins when epithelial cells undergo a switch to a mesenchymal phenotype, a transdifferentiation process termed epithelial-mesenchymal transition (EMT). In addition to its important role in tumorigenesis, EMT (along with the reverse process, MET) occurs naturally during development, and involves epithelial cells losing the key features associated with their differentiated phenotype, in particular cell-cell adhesion and apico-basal polarity, whilst in turn gaining mesenchymal characteristics such as increased apoptosis resistance, and importantly invasive and migratory properties. It is also believed to play an important role in the development of drug resistance by tumour cells (Polyak and Weinberg, 2009; Thiery et al., 2009).

EMT is a complex mechanism that can be triggered by a variety of factors, and acts in a multistep process utilising many differing cellular pathways. It is often characterised by the loss of E-cadherin (Polyak and Weinberg, 2009; Thiery et al., 2009). The cytoskeleton plays a vital role, undergoing a complete reorganisation during the radical morphological changes that occur on phenotypic transition. In particular, the stable bundles of apico-basally orientated microtubules that are a key aspect of polarised epithelial cells must be lost on transition to a mesenchymal phenotype, to be replaced by the more flexible dynamic network required for appropriate interactions with actin filaments via proteins such as APC and IQGAP1, and for controlling correct delivery of substrates to adhesion sites as needed for migratory processes (Rodriguez et al., 2003; Small et al., 2002). Indeed, microtubule stabilisation has recently been shown to impede assembly of focal adhesions and thus cell migration, in addition to causing a decrease in EMT and tumour metastasis (Li et al., 2011).

Whilst EB2 has been shown to be essential for the initial establishment of the epithelial non-centrosomal apico-basal microtubule array, its subsequent downregulation has been observed and implicated in microtubule stability and bundle formation during differentiation in a variety of model systems, including intestinal crypts (Chapter V and VI), (Goldspink et al., 2013b). It is therefore not unreasonable to speculate that a potential disruption of natural EB2 downregulation in cancer cells that results in a continuous overexpression of the protein could contribute to epithelial dedifferentiation and the establishment of the migratory and invasive phenotypes associated with EMT and resultant metastasis. Indeed, EB2 overexpression in pancreatic cancer cells has recently been implicated in perineural invasion, an important defining aspect of pancreatic cancers where cells invade into and migrate along nearby nerves. This work by Abiatari and colleagues identified the MAPRE2 gene encoding EB2 as upregulated in highly invasive pancreatic cancer cell lines and in *in vivo* human pancreatic cancer tissue samples (Abiatari et al., 2009).

To investigate the potential effects of EB2 overexpression on key aspects of EMT, a stable mCherry-EB2 overexpressing epithelial cell line was created and used to examine cell polarity, migration and invasion. Initially, polarity was assessed in 2D culture, followed by attempts to form cysts grown in a 3D Matrigel^{TM} matrix. Next, the speed of random migration in both EB2 overexpressing and depleted conditions was assessed, followed by the examination of directed migration in overexpressing cells by way of wound healing scratch assays.

To briefly summarise the results presented, it was found that EB2 overexpression did not obviously effect the cytoskeletal organisation of cells grown in 3D culture, although there was evidence that cyst formation could be disrupted, leading to the formation of unstructured aggregates within the cell matrix. There also appeared to be indications of cell protrusion from cysts and possible invasion through the 3D matrix. Overexpressed EB2 was found to colocalise with actin, IQGAP1 and APC at the leading edge of migratory cell lamellipodia. Depletion of EB2 was found to dramatically reduce the rate of cell migration, whilst in contrast the speed of both random and directed migration was found to significantly increase on EB2 overexpression, as did the degree of closure following scratch wound assays.

EB2 was thus found to have great potential for further examination as a potentially exciting new target in cancer cells, with behaviour linked to the loss of polarity and increased migration characteristic of cells undergoing EMT. As such, it could play an important role in driving tumour metastasis.

7.2: Results

7.2.1: Generation of an MDCK-II EB2 overexpressing stable cell line

To investigate the effect of EB2 overexpression in experiments requiring EB2 expression over an extended time period, including polarisation and migration studies, a cell line stably expressing mCherry-EB2 was required. MDCK-II cells were initially transiently transfected with mCherry-EB2, confirming mCherry-EB2 localised along microtubules (Figure 7.1 A), as described previously in other epithelial cell lines (see section 5.4.2, Figure 5.8).

To generate a stable cell line in a polarising system, both MDCK-II and TC7 cells were transfected with mCherry-EB2 and treated with G418 for selection of the stably incorporated construct. Whilst transfected TC7 cells failed to survive antibiotic selection (data not shown), a population of mCherry-EB2 expressing MDCK-II cells was produced. For monoclonal selection, FACS was used to seed a single fluorescent cell into separate wells of a 96 well plate. These were maintained in selective antibiotic and allowed to grow into monoclonal colonies. Once sufficient cells were generated, a sample of several clones was seeded onto glass coverslips, fixed, and imaged by widefield fluorescence microscopy to select the most suitable clone for subsequent experiments. Stable clone 133 was selected for all future work as it expressed mCherry-EB2 consistently across the cells imaged, and demonstrated mCherry-EB2 fluorescence in a distribution indicative of microtubule lattice association (Figure 7.1 B). A western blot of a clone 133 lysate probed for RFP was also performed, verifying mCherry-EB2 expression (Figure 7.1 C).

An empty vector polyclonal stable cell line was also produced for use as a suitable control. MDCK-II cells were transfected with the empty pmCherry-C1 plasmid vector and selected by maintenance in G418. FACS was used to concentrate fluorescence expressing cells, although the cell line was not further selected into a monoclonal cell line (data not shown).

7.2.2: MDCK-mCherry-EB2 cells maintain EB2 expression during polarisation sequences

MDCK-mCherry-EB2 stable cells were seeded subconfluently and grown over a 15 day time period. Samples were fixed or lysed at days 1, 5, 10 and 15 for fluorescent imaging and western blotting respectively. Overexpression of EB2 had no apparent effect on the ability of cells to apico-basally polarise as established in MDCK-II, mIMCD-3, and other epithelial cell lines (see section 5.2.2, Figure 5.2); EB2 overexpressing cells grew to confluence by day 5, after which they differentiated and polarised over the remaining time course. Fluorescent imaging demonstrated that mCherry-EB2 was expressed throughout the polarisation sequence in a pattern similar to that seen for microtubules; in particular, it appeared as a disorganised network in subconfluent cells at day 1, and reorganised into the peripheral rings characteristic of the apico-basal array by days 10 and 15 (Figure 7.2 A). Western blots probing for RFP at each time-point indicated a small increase in mCherry-EB2 expression between days 1 and 5, after which expression levels remained constant over the rest of the experimental period (Figure 7.2 B).

7.2.3: EB2 overexpression in MDCK-II 3D epithelial cultures

3D epithelial cultures have been established as an improved model system for studying polarisation in epithelial cells compared to growing cells on tissue culture filter inserts. Single cells are embedded into a 3D extracellular matrix (in this case Matrigel^{TM}), and allowed to develop into cysts with a central lumen, an architecture more akin to the natural tissue environment (O'Brien et al., 2006). This also allows for direct imaging through the apico-basal plane of polarised cells in the central regions of cysts, as opposed to relying on a Z-plane reconstruction from an XY confocal stack in filter polarised cells, thus enabling greater resolution for imaging of apico-basally orientated microtubule arrays and associated proteins.

MDCK-II cells have previously been established for 3D cell culture (O'Brien et al., 2006), with staining techniques for cytoskeletal proteins further optimised within

our lab (Goldspink et al., 2013a, manuscript in preparation). Untreated control MDCK-II cells were grown in Matrigel™ for a 14 day period, during which they successfully formed 3D cysts with a distinct lumen. Confocal imaging of cysts immunolabelled for microtubules and E-cadherin demonstrated the cells had successfully polarised, forming a distinct apico-basal microtubule array, with lateral cell junctions marked by E-cadherin expression (Figure 7.3 A). A confocal stack of optical sections through cysts immunolabelled for E-cadherin and ninein demonstrated ninein localised exclusively to apical regions of cells at both centrosomal and cortical sites (Figure 7.3 B).

The stable MDCK-mCherry-EB2 cell line was also seeded in Matrigel™ and fixed and immunolabelled following a 14 day period. Confocal sections of cysts immunolabelled for microtubules and E-Cadherin revealed a similar localisation to that observed in control cells, with cells again polarised to form an apico-basal array and E-cadherin visible at lateral junctional sites. Resolution was however insufficient to judge whether there were any subtle differences in the degree of microtubule bundling between control and overexpressing conditions (Figure 7.4 A). Cysts were also immunolabelled for ninein and microtubules, again revealing a similar apical ninein localisation, although it was hard to judge whether the ninein had redeployed to cortical regions, or whether staining was restricted to centrosomal sites (Figure 7.4 B).

Control and overexpressing 3D cultures were also imaged by phase contrast microscopy during cyst development, to examine any differences in their formation. Control cysts grew with a typical morphology of a single layer of cells encompassing a central lumen (Figure 7.5 A). Interestingly, whilst EB2 overexpressing cysts grew with the same overall morphology to control conditions, some abnormalities were revealed. In particular, there was a noticeable amount of cell aggregation in the vicinity of mature cysts, with evidence of cell extrusion from the basal region of cysts into the surrounding matrix. Additionally, a large number of potential cysts appeared to have failed to successfully form, instead appearing as a large aggregate of cells, which was not observed to such a degree under control conditions (Figure 7.5 B).

7.2.4: mCherry-EB2 localises to the leading edge of migratory cells

During initial characterisation of the mCherry EB2 construct (as outlined in section 5.3.3), ARPE-19 cells were transiently transfected with mCherry-EB2 24 hours prior to fixation and immunolabelling for microtubules or EB1. In addition to its localisation along microtubules as previously described, it was also noticeable that the mCherry-EB2 construct was expressed at the leading edge of these cells. EB1 localisation was not affected (Figure 7.6 A). Similarly, this same localisation of EB2 at the leading edge was also seen in sparsely seeded stable MDCK-mCherry-EB2 cells immunolabelled for microtubules (Figure 7.6 B).

Sparsely seeded control MDCK-II cells were fixed and immunolabelled for IQGAP1 and microtubules or β-actin. Widefield fluorescent imaging demonstrated that β-actin and IQGAP1 co-localised at the leading edge of migratory cells, with microtubule plus ends extended into this region (Figure 7.7). Similarly, stable MDCK-mCherry-EB2 cells were seeded sparsely and immunolabelled for proteins associated with the leading edge during migration, including IQGAP1, actin and APC. Microtubule organisation appeared unaffected on EB2 overexpression, whilst mCherry-EB2 was found to colocalise with each of IQGAP1, actin and APC at the leading edge (Figure 7.8).

7.2.5: EB2 overexpression in MDCK-II cells causes an increase in speed of cell migration

To assess the impact of EB2 overexpression on the speed of random cell migration, control MDCK-II cells as well as the stably expressing empty vector and mCherry-EB2 overexpressing cell lines were seeded sparsely in separate wells of a six well plate for time-lapse phase contrast and fluorescence microscopy. Images of example representative regions for control (Figure 7.9 Ai), empty vector (Figure 7.9 Bi) and EB2 overexpressing (Figure 7.9 Ci) cells at t=0 illustrate the initial seeding densities, as well as mCherry expression levels for each condition. Separate areas for

each treatment were live imaged every 10 minutes over a 16 hour period using a x10 objective.

For analysis, 20 separate areas were examined for each condition, derived form three separate experiments. For each area, five cells were analysed to give a total of 100 cells per condition (N=100). Analysis was performed utilising FIJI (Image J) software using the manual-tracking module. To allow calculation of speed, the position of each analysed cell was recorded for each frame in the time-course. Where a cell underwent mitosis, just one of the resultant daughter cells was followed for the remainder of the time-lapse. The positional data for each cell were combined in FIJI (Image J) to produce dot and line tracking trace movies illustrating the paths taken by every cell analysed for control (Figure 7.9 Aii, Movie S6), empty vector (Figure 7.9 Bii, Movie S7) and EB2 overexpressing (Figure 7.9 Cii, Movie S8) treatments separately. The dots represent the position of a cell at a particular time-point, whilst the lines illustrate the path it has taken over previous frames. These combined tracking traces illustrate the degree of movement of a cell from its original position, and indicate the directionality of movement. In particular, note the greater number of control and empty vector cells that appear to move very little, compared to cells overexpressing EB2.

From the position data of the tracking traces, the total distance covered by an individual cell over the 16 hour experimental time period, and therefore its average velocity could be calculated. This calculation was performed for each analysed cell and presented in a graph to give an overall average velocity for each condition. Statistical analysis using one-way ANOVA with Tukey's multiple comparison test revealed a significant increase in average speed in empty vector expressing cells compared to untreated control MDCK-II cells ($p<0.05$), with a further increase in speed of EB2 overexpressing cells ($p<0.05$ compared to empty vector expressing cells, $p<0.001$ compared to untreated controls). EB2 overexpressing cells moved at an average velocity of 0.3044 μm/min, a 13.5% increase from that demonstrated by pmCherry-C1 empty vector expressing cells, which travelled at an average of 0.2682 μm/min (Figure 7.10).

7.2.6: EB2 depletion in ARPE-19 cells causes a decrease in speed of cell migration

To examine the effect of EB2 depletion on migration speeds, the scramble and EB2 siRNA treated cells previously used to assess division success (which had also been imaged at a rate of one frame every 10 minutes), were further analysed for cell velocity. The first 16 hours of the time-lapse were used, beginning therefore at 72 hours post initial siRNA transfection (see section 6.2.4, Movies S3, S4 and S5). Regions for analysis were selected from three separate six well plate wells for each condition; for scramble cells, 4 cells were analysed from each of 15 separate areas, whilst for EB2 depleted cells 2 cells were used from 30 regions, to give a total of 60 cells for each treatment (N=60). Cells were tracked in FIJI (Image J) as described above, and again when a cell underwent mitosis, just one of the resultant daughter cells was followed for the remainder of the time-lapse. The combined tracking traces for all scramble (Figure 7.11 A, Movie S9) and EB2 siRNA (Figure 7.11 B, Movie S10) treated cells analysed produced a notable reduction in line density in EB2 depleted cells, implying less overall movement.

As for overexpression analysis, the position data for each cell was used to calculate its average velocity, and thus the average speed of movement for cells from both treatments. Statistical analysis by unpaired t-test revealed a significant decrease in average cell velocity speed on EB2 depletion compared to scramble treated ARPE-19 cells ($p<0.0001$). On average, EB2 siRNA treated cells migrated at a speed of 0.2111 μm/min, a 33.2% decrease from scramble cells, which moved at a mean velocity of 0.3160 μm/min (Figure 7.12).

7.2.7: EB2 overexpression in MDCK-II cells increases the rate of wound healing

Scratch assays mimic *in vitro* wound healing, and can be used to assess the closure rate of a population of cells, as well as assess the speed of directed migration

of individual cells at the leading edge of the scratch (Liang et al., 2007). Here, they were used to further assess the effect of EB2 overexpression on cell migration.

Initially, control and stable MDCK-mCherry-EB2 cells were seeded onto glass coverslips, grown to confluency and scratched with a pipette tip to produce a thin wound. Following time to heal, the coverslips were fixed and immunolabelled to examine the cytoskeletal organisation of cells located at the leading edge of the scratch. Cells from each condition labelled for γ-tubulin and microtubules shared similar organisation, with microtubules extending forwards into lamellipodia, and the centrosome (as marked by γ-tubulin) located adjacent and behind the nucleus (Figure 7.13 A). As for sparsely seeded cells, immunolabelling for β-actin revealed accumulation in the lamellipodia at the forward membrane for both treatments, with mCherry-EB2 in overexpressing cells once again colocalising with actin at the leading edge (Figure 7.13 B).

For migration analysis experiments, scratches were prepared for phase contrast time-lapse live imaging. Untreated control MDCK-II, stable empty vector expressing and stable MDCK-mCherry-EB2 cells were seeded into several separate 24 well plate wells, and allowed to grow to confluency, at which point 2mM thymidine was added to each well to prevent cell division. Division was blocked in case EB2 overexpression caused an increase in cell proliferation, which could potentially cause a misleading increase in the rate of scratch closure. Cells were maintained in thymidine for a minimum of 16 hours, before a single scratch was made with a pipette tip in each well. Plates were immediately transferred to the microscope for live time-lapse imaging. For each scratch, a representative region was selected for imaging by phase contrast and fluorescent microscopy. Frames were taken at 10 minute intervals overnight using a x10 objective lens.

For analysis purposes, a 10 hour cut off was used for all measurements and conditions. This was the earliest time-point at which a region analysed came close to having the two sides of a scratch make contact and sealing, whilst still maintaining a clear gap between the approaching edges. To assess the degree of wound closure in each condition, the area of the gap between opposite sides in each imaged scratch

region was measured at the start and end of the 10 hour experiment, and used to calculate the total area closed for each scratch, and thus the total area into which cells had migrated (Figure 7.14). A total of 16 separate scratches were measured for each treatment (N=16), and used to calculate an average amount of wound closure, and thus a relative measure of the degree of population migration, with significance between different treatments assessed by one-way ANOVA with Tukey's multiple comparisons test. There was no significant difference in closure between control and empty vector expressing cells, however EB2 overexpressing cells did close a significantly greater area ($p<0.001$ compared to empty vector expressing cells, $p<0.01$ compared to control cells). In total, whilst empty vector regions closed by an average of 3.546×10^5 μm^2, overexpressing areas closed by a mean of 4.671×10^5 μm^2, an overall increase of 31.7% (Figure 7.15).

To further analyse effects on migration rate, individual cell speeds were also assessed in each treatment. For each scratch, eight cells located at the leading edge were tracked in FIJI (Image J), using the manual tracking module in the same manner as described earlier, over the 10 hour experimental period. Dot and line tracking traces derived from the position data as previously described were prepared and overlaid onto the phase contrast time lapse frames at each time point for a representative example region from each condition; control (Figure 7.16 A, Movie S11), empty vector expressing (Figure 7.16 B, Movie S12) and EB2 overexpressing (Figure 7.16 C, Movie S13). For the purposes of analysis, the eight separate speeds for each region were averaged to produce the mean cell velocity for an individual scratch, and these were combined for each treatment to give the overall average (N=16). Statistical significance was assessed by one-way ANOVA with Tukey's multiple comparisons test. As for the area of closure measurements, there was no significant difference between the average velocity of untreated control and empty vector expressing scratches and a significant ($p<0.05$) 16.8% increase in the speed of EB2 overexpressing cells (0.4342 μm/min) compared to control (0.3717 μm/min) cells. However, whilst there was a similar 14.5% increase in average cell velocity between empty vector (0.3792 μm/min) expressing cells compared to EB2 overexpressing cells, this was not statistically significant.

7.3: Discussion

7.3.1: EB2 overexpressing cells are able to form apico-basal microtubules

Polarised differentiation sequences and successful production of 3D epithelial cultures grown in Matrigel™ using the generated stable MDCK-mCherry-EB2 cell line demonstrated that overexpression of EB2 alone does not prevent polarisation of cells or the formation of apico-basal microtubules. Interestingly, as opposed to the normal EB2 downregulation during polarisation previously described (Figure 5.3) (Goldspink et al., 2013b), western blots probing for the construct demonstrated high and consistent levels of mCherry-EB2 at each of the later timepoints in the polarisation sequence. This implies that the construct hybrid product is not affected by the natural mechanism causing EB2 loss on polarisation, suggesting it is likely a downregulation of MAPRE2 gene expression that causes loss of EB2, rather than a targeting of the protein for degradation. Alternatively, it is possible that any hypothetical degradation sequence is present in the N-terminal extension regions of the alternative EB2 splice variants, and thus not present in the construct.

Importantly, as overexpressing cells were successfully able to polarise, with E-cadherin expression clearly present in the 3D cultures generated, aberrant EB2 expression alone is unlikely to cause EMT. This is not surprising; as previously discussed, both hair cells of the cochlea and cells within the stem cell zone of the intestinal crypt possess apico-basal polarity and express EB2. Its downregulation is in turn necessary for the formation of stable microtubule bundles in highly polarised cells such as the supporting cells of the cochlea, as well as in the transit amplifying and differentiated regions of the crypt (Goldspink et al., 2013b). Thus, even if EB2 downregulation was prevented in colonic crypt cells, it is still likely that polarised cells similar to those seen in the stem cell zone would initially form, however these may be unable to form the bundles required for differentiation, and therefore may be susceptible to further alterations causing a loss of cell polarity.

The initial aim was to evaluate whether there were any differences in bundling of the apico-basal arrays in control and EB2 overexpressing 3D cysts, with the theory that unbundled arrays, whilst apico-basally orientated may not have undergone release and capture, and thus would still be anchored at the centrosome in an 'umbrella' conformation. Control and EB2 overexpressing cysts were therefore stained for microtubules and ninein to mark minus end anchoring sites, and thereby determine whether ninein had been released and translocated to non-centrosomal junctional sites as described by the release and capture model (Moss et al., 2007). Unfortunately, it was impossible to say from immunofluorescent images whether the microtubule arrays in the cysts were bundled, with no obvious differences seen between control and overexpressing cells. Additionally there was no conclusive difference in the ninein distribution between the two conditions. Further investigations into the microtubule organisation are clearly necessary; in particular, it would be interesting to subject control and EB2 overexpressing 3D cultures to imaging by transmission election microscopy, to judge the degree of microtubule bundling.

Importantly, some EB2 overexpressing cells showed invasive characteristics, as noted by the accumulation of aggregates around cysts and evidence suggesting some basal extrusion into the Matrigel^{TM} matrix. Basal extrusion has been associated with cancer cell invasion and the formation of multicellular aggregates in extracellular matrix (Hogan et al., 2009). Interestingly, APC apparently promotes apical extrusion, whilst the APC mutations so often seen in colorectal cancer have been associated with a switch to increased level of abnormal basal extrusion (Marshall et al., 2011). It is therefore vital to further examine these phenotypes in 3D invasion assays.

7.3.2: EB2 overexpression causes increased invasion and migration

Increased MAPRE2 gene expression has been linked with highly invasive cells and poor prognosis in pancreatic cancer (Abiatari et al., 2009). It was therefore interesting to observe following the initial characterisation of the mCherry-EB2

construct that it would localise to the leading edge of cells. Further immunolabelling experiments confirmed mCherry-EB2 colocalisation with proteins associated with cell motility, including β-actin, IQGAP1 and APC, in the lamellipodia of migratory cells. Actin is the vital active complex that drives forward membrane protrusion during migration (Pollard and Borisy, 2003), whilst a dynamic microtubule network is essential to allow turnover and trafficking of key proteins such as focal adhesion components (Kaverina and Straube, 2011). Importantly, the microtubule network, acting through +TIP proteins including APC via IQGAP1, plays a vital role in the activation of ARP2/3 and formin induced actin nucleation by effecting signals from Rac and Cdc42 (Fukata et al., 2002; Watanabe et al., 2004), members of the Rho GTPase family of proteins that are the essential controllers of the migration process (Ridley, 2001). Thus, potential interactions of EB2 with actin, IQGAP1 and APC at the leading edge of migratory cells suggested a possible role for EB2 in cell migration, and by extension EMT and cancer cell invasion.

To investigate this possible association, live imaging assays were performed in both EB2 depleted and EB2 overexpressing cells, with the result that EB2 expression levels were found to correlate with the speed of cell migration. EB2 depletion was seen to strongly inhibit migration, whilst overexpression increased cell movement.

As indicated, EB2 depletion was found to cause a marked reduction in migration speed of 33.2%. This is likely due to the increased microtubule stability caused by EB2 loss (see Chapter VI) (Goldspink et al., 2013b). In migration, whilst it is important for microtubules extending into lamellipodia to be stabilised, it is also essential that other microtubules are able to be dynamic, and that the switch between stable and dynamic microtubules is properly regulated (Kaverina and Straube, 2011); for example, it has been shown that the loss of EB1 will reduce cell motility (Schober et al., 2009).

For EB2 overexpression, experiments were performed to examine both directional and random cell migration, which can be driven by different internal mechanisms that control whether membrane protrusions form at the same forward

location or at different points around the cell, and is generally controlled by Rho GTPase signalling (Petrie et al., 2009). In experiments using either sparsely seeded cells for random migration, or scratch assays for directed migration and the behaviour of an epithelial sheet, EB2 overexpression was found to significantly increase the speeds by which cells moved.

Cells in a sheet with a particular coordinated direction of travel generally moved more quickly than randomly migrating cells; empty vector cells in scratch assays (average velocity = 0.3793 μm/min) moved on average 41.4% quicker than their sparsely seeded counterparts (average velocity = 0.2682 μm/min), with overexpressing cells also increasing in speed by a similar degree of 42.6% (sparse cell average speed = 0.3044 μm/min, increasing to 0.4342 μm/min in the scratch experiments). Most interestingly however, within both sparse and scratch experiments the degree to which cell speeds increased in EB2 overexpressing cells compared to empty vector controls was very similar at 13.5% and 14.5% respectively. Importantly, in the scratch experiment, this increase in speed correlated to a significant increase in the degree to which the epithelial sheet was able to close the wound; EB2 overexpressing cells were able to close on average an area 31.7% larger than that of the empty vector control.

7.3.3: Summary and further work

In summary, experiments involving overexpression of EB2 have produced extremely promising results implicating EB2 in a previously unknown role in cell migration, with further suggestions that it may similarly encourage invasion through a 3D matrix. Coupled to its newly established role in the establishment of epithelial polarity and formation of apico-basal microtubule arrays, EB2 and its regulation has emerged as a potentially exciting new target for study of EMT in cancers such as those of the colon. There is therefore much scope for further investigation to expand on these promising initial results.

Firstly, it is essential to establish whether there is indeed any difference in microtubule organisation between control and EB2 overexpressing cells in 3D culture, and indeed in tissue explants, including colonic crypts. In particular, of immediate merit is to image such samples on a TEM microscope, and examine the exact nature of the apico-basal microtubule array; are microtubule bundles formed and aligned with actin filaments in overexpressing cells, and do microtubules arrange into an 'umbrella' conformation anchored at the centrosome, rather than the non-centrosomal apically anchored arrays dictated by the release and capture model? It may also be worth examining such cysts by combining TEM with immunogold labelling, which could more accurately indicate any colocalisation with actin filaments or crosslinking proteins such as ACF7.

It is also important to assess further whether there is any alteration in expression of epithelial or mesenchymal markers, including tight junctional markers such as ZO-1, integrins, and the expression of alternate types of intermediate filaments; keratins for epithelial cells and vimentin following a switch to a mesenchymal phenotype.

In terms of examining the apparent promotion of cell motility and invasion, there are great prospects for future work. Firstly, it seems that EB2 may interact at the leading edge of migratory cells with actin, IQGAP1 or APC. This suggests a possible function in organising actin rearrangements, and may suggests some kind of role in the established Rho-GTPase pathway known to control cell migration (Ridley, 2001). In particular, Rac/cdc42 and Rho activation assays and inhibitors in control and EB2 overexpressing cells would provide an insight into the potential signalling mechanisms and control systems. It would also be interesting to investigate a potential interaction with formins such as mDia, which have previously shown to act downstream of Rho-GTPases to stabilise microtubules extending into the leading edge of migrating fibroblasts (Palazzo et al., 2001).

To further examine mechanisms of directional migration, Ibidi slides are a well-established technique for monitoring migration during chemotaxis (Blow, 2007). It is also essential to properly analyse invasion, therefore investigations in EB2

overexpressing conditions using a 3D inverted invasion assay (Murray et al., 2013) could provide interesting insights into speed and degree to which cells are able to invade through a matrix .

Finally, investigations could be made using a cell line naturally high in EB2 expression, such as the highly invasive Panc1 human cell line (Abiatari et al., 2009), which are unable to form 3D epithelial cysts, instead producing aggregates (Matsuda et al., 2010) similar to those sometimes observed in the MDCK-mCherry-EB2 overexpressing cell line. As we have already established successful knockdown of EB2 in human cell lines, it is fascinating to speculate as to whether depletion of EB2 in Panc1 cells could reduce migration speeds, and maybe even allow polarisation and 3D culture formation.

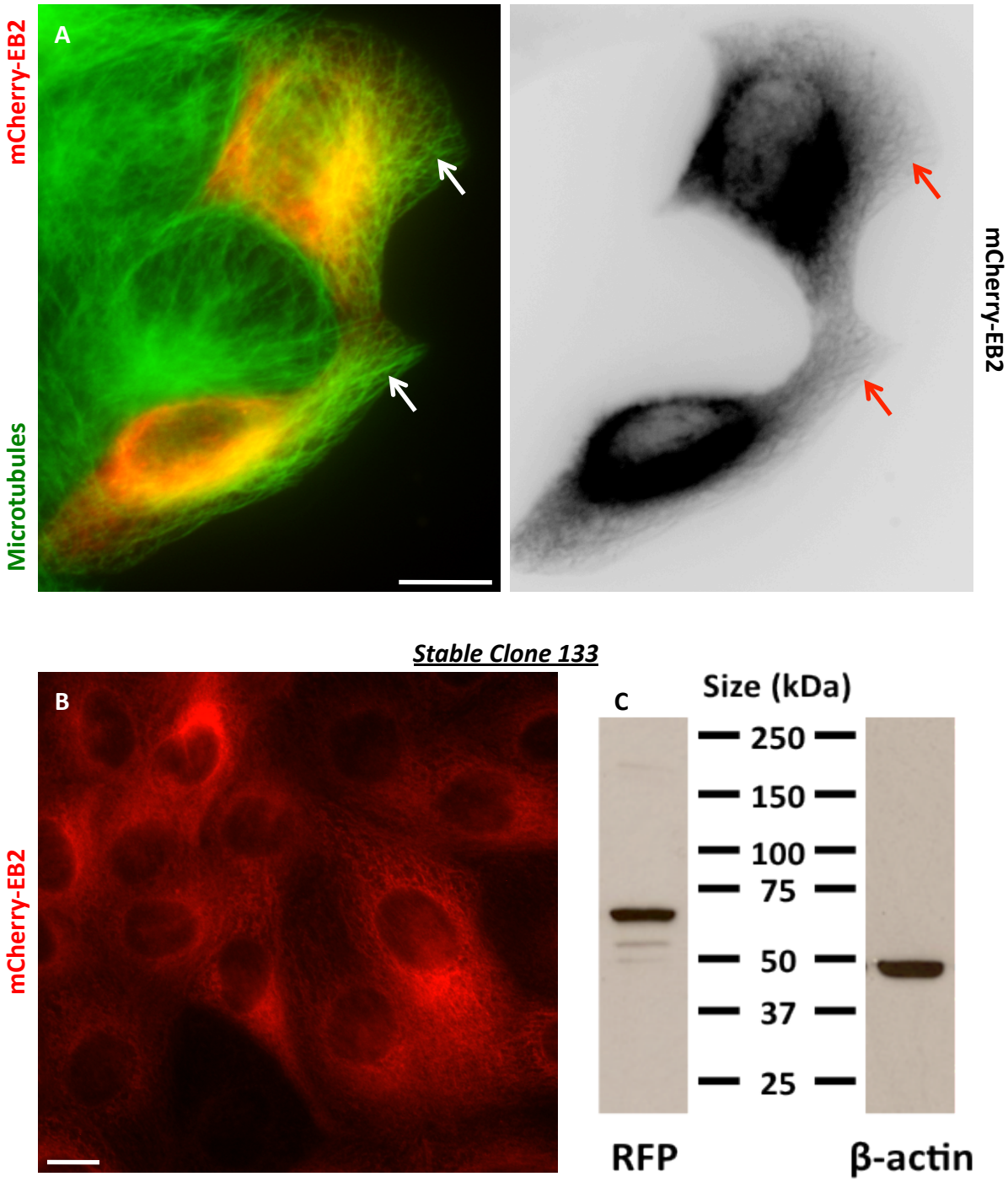

Figure 7.1 Establishment of a mCherry-EB2 expressing stable cell line
(A) MDCK-II cells were transfected with mCherry-EB2 (red, invert) 24 hours prior to fixation, and immunolabelled for microtubules (green), revealing mCherry-EB2 localised along microtubules (arrowed). **(B)** A monoclonal stable EB2 overexpressing cell line was generated by antibiotic selection from FACS sorted mCherry-EB2 (red) transfected MDCK-II cells. Several colonies were produced, from which clone 133 was selected. The image shows a representative region, illustrating mCherry-EB2 pattern indicative of localisation along microtubules. **(C)** Western blot probed for RFP and β-actin, confirming mCherry-EB2 expression in the clone 133 cell line, as indicated by the RFP band just below the 75kDa marker. All scale bars = 10µm.

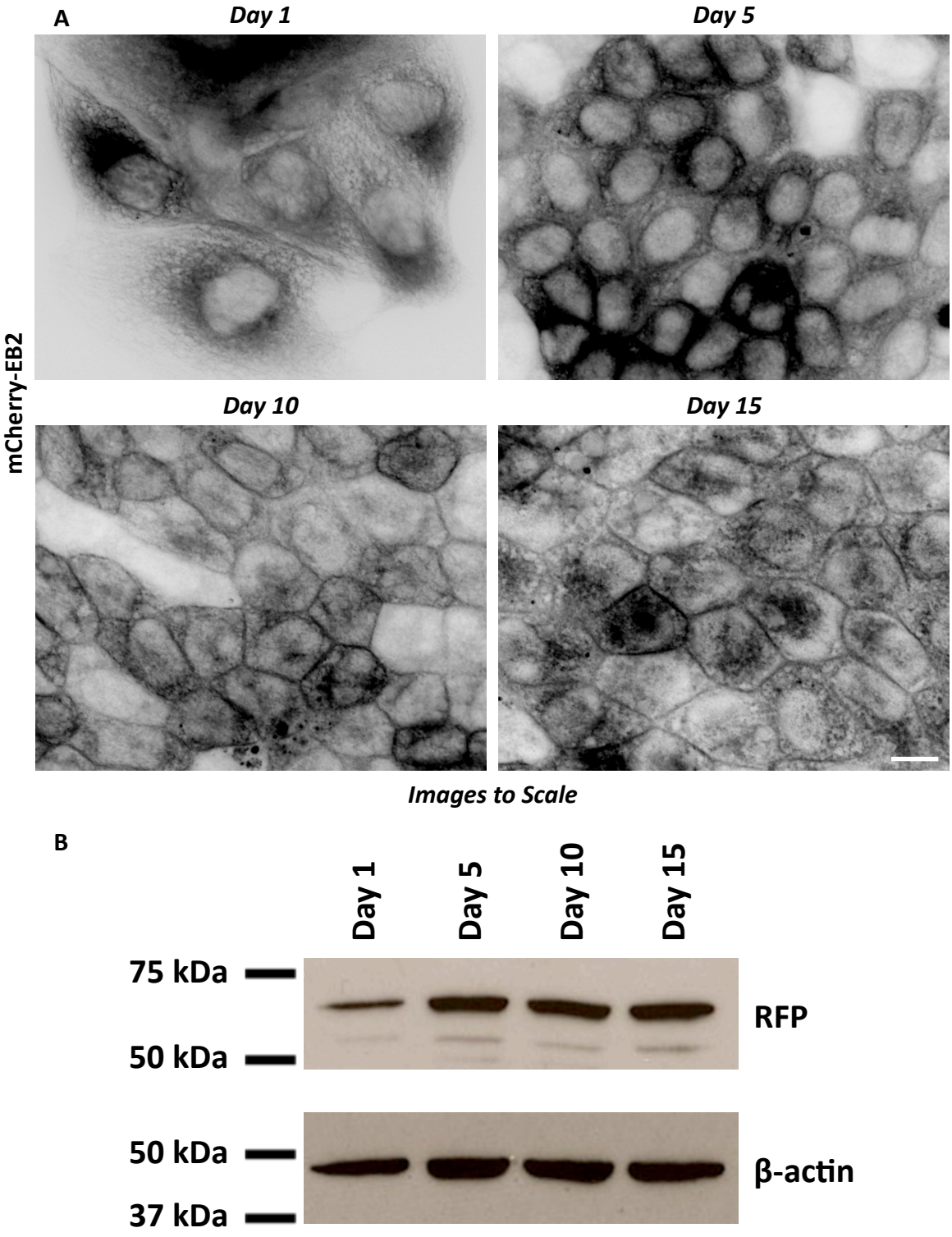

Figure 7.2 Polarisation sequence in MDCK-II cells stably overexpressing mCherry-EB2
The MDCK-mCherry-EB2 stable cell line was seeded sparsely and allowed to grow over a 15 day period, with cells processed at days 1, 5, 10 and 15. **(A)** At each time point, cells were fixed and imaged by widefield fluorescence microscopy for mCherry-EB2 (invert). EB2 was initially visible along microtubules (Day 1), and as cells polarised continued to mirror the reorganisation of microtubules into apico-basal arrays, such that by days 10 and 15, mCherry-EB2 was visible in peripheral rings similar to the microtubule organisation in polarised cells. **(B)** Western blots of extracts taken at each time point were probed for RFP and β-actin, and revealed that following an initial increase in expression level between days 1 and 5, mCherry-EB2 protein levels remained constant throughout the remaining time points. Scale bar = 10μm.

Figure 7.3 3D culture of MDCK-II cells
MDCK-II cells were seeded into matrigel drops, and allowed to grow into 3D cysts, before fixation, immunolabelling and confocal microscopy. **(A)** Cyst immunolabelled for microtubules (green) and E-Cadherin (purple), highlights the apico-basal organisation of microtubules in the polarised cells. **(B)** Cyst immunolabelled for ninein (red) and E-Cadherin (blue), viewed in the XZ orientation. **[i]** XY orientated slice through a region corresponding to the top of the cyst, to give a cross-section through the apical region of these cells. **[ii]** XY orientated slice through a region corresponding to the middle of the cyst, to give a lateral cross-section through these cells. Note in both orientations ninein located at both the centrosome (circled), and non-centrosomal apical sites (arrowed). All scale bars = 10μm.

CONTROL

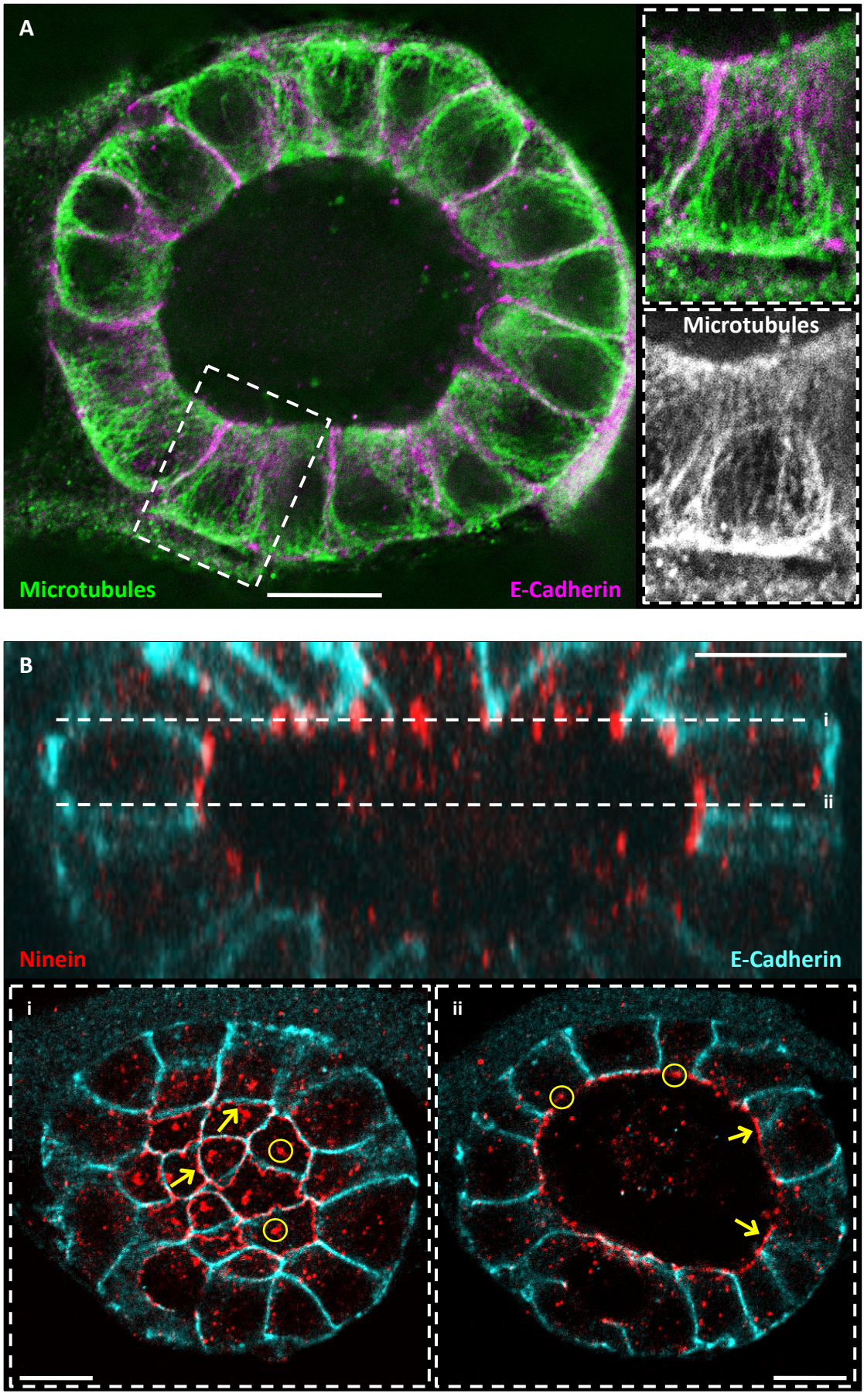
A
Microtubules
E-Cadherin
Microtubules
B
i
ii
Ninein
E-Cadherin
XZ View
XY Views
i
ii

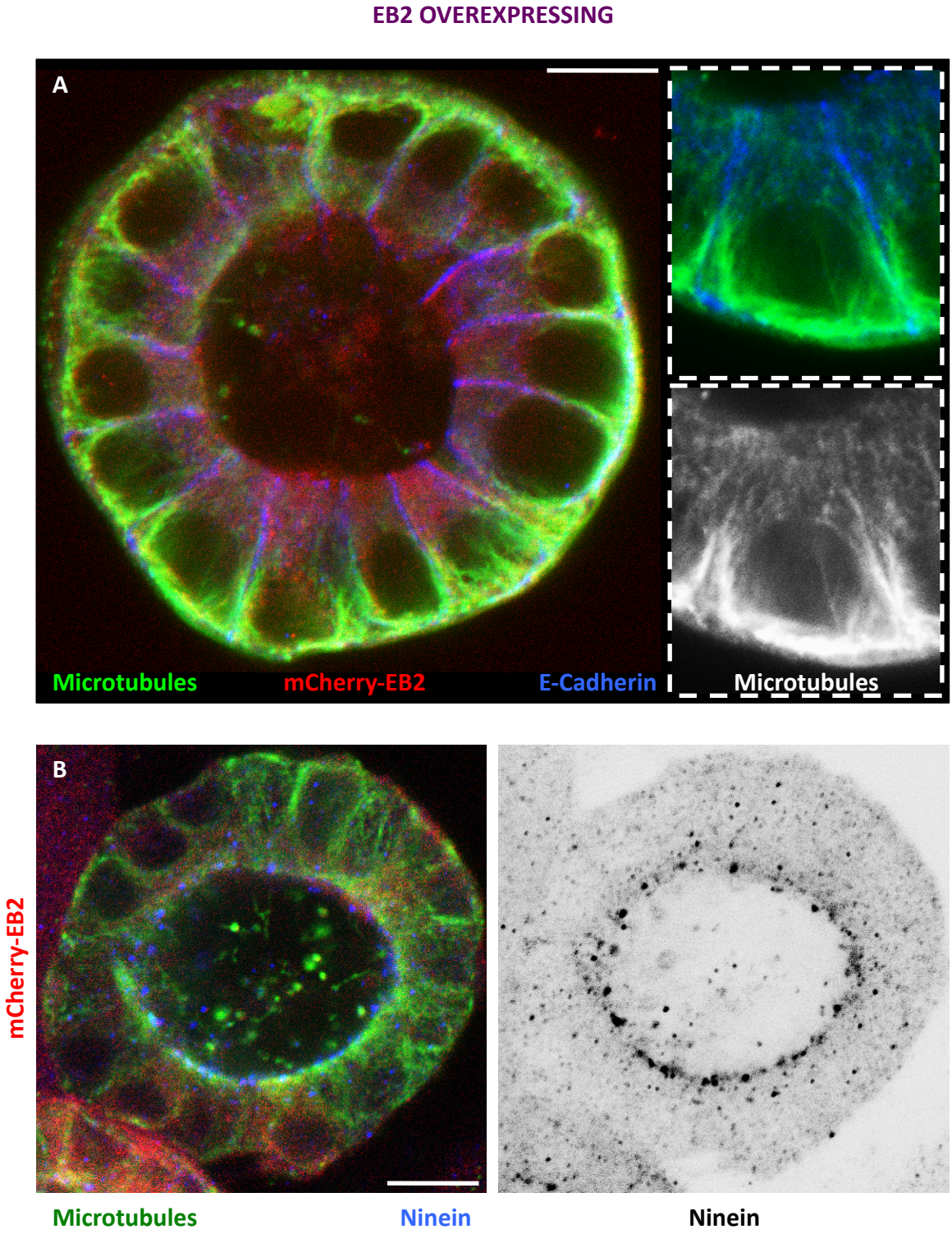

Figure 7.4 3D culture of EB2 overexpressing MDCK-II cells
Stably expressing MDCK-mCherry-EB2 (red) cells were seeded in matrigel drops, and allowed to grow into 3D culture cysts, before fixation, immunolabelling and confocal microscopy. **(A)** Cyst immunolabelled for microtubules (green) and E-Cadherin (blue), highlighting apico-basal organisation of microtubules in polarised cells, similar to that observed in control cells. **(B)** Cyst immunolabelled for ninein (blue) and microtubules (green), illustrating ninein located at apical sites in a similar pattern to that seen in control cells. All scale bars = 10µm.

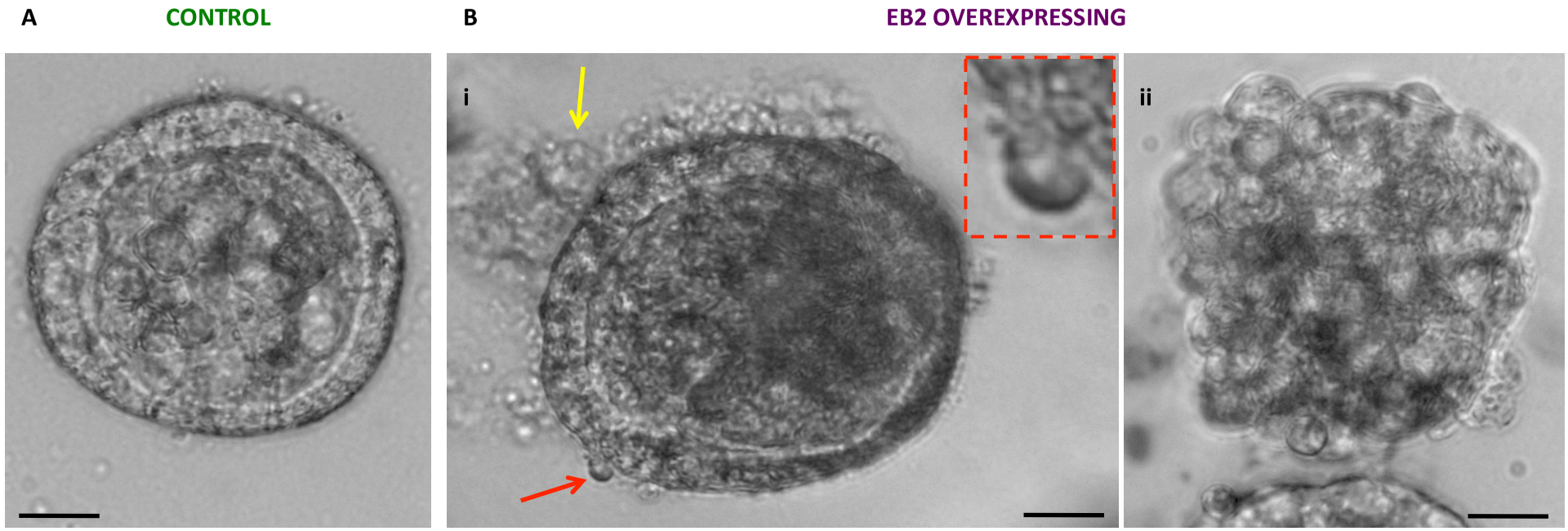

Figure 7.5 EB2 overexpression can cause cell protrusion and aggregation in 3D culture
(A) Phase contrast image of control MDCK-II cells growing in 3D culture, illustrating typical cyst morphology.
(B) Phase contrast images of MDCK-II cells stably overexpressing mCherry-EB2 growing in 3D culture. **[i]** The cyst in general is similar to the control conditions, however note the basal extrusion (red arrow), and the cell aggregates associated with the cyst (yellow arrow). **[ii]** Additionally, often it appears a cyst never successfully formed, resulting in a large aggregate of cells. Scale bars = 20µm

Figure 7.6 mCherry-EB2 localises to the leading edge of epithelial cells
(A) ARPE-19 cells were transiently transfected with mCherry-EB2 (red, invert) 24 hours prior to processing, then immunolabelled for **[i]** microtubules (blue) or **[ii]** EB1 (green). In both images, mCherry-EB2 is clearly visible at the leading exposed edge of cells (**[i]** boxed region, **[ii]** arrowed). **(B)** MDCK-II cells stably expressing mCherry-EB2 immunolabelled for microtubules (blue), revealing mCherry-EB2 localised to the leading edge of the cell. All scale bars = 10μm.

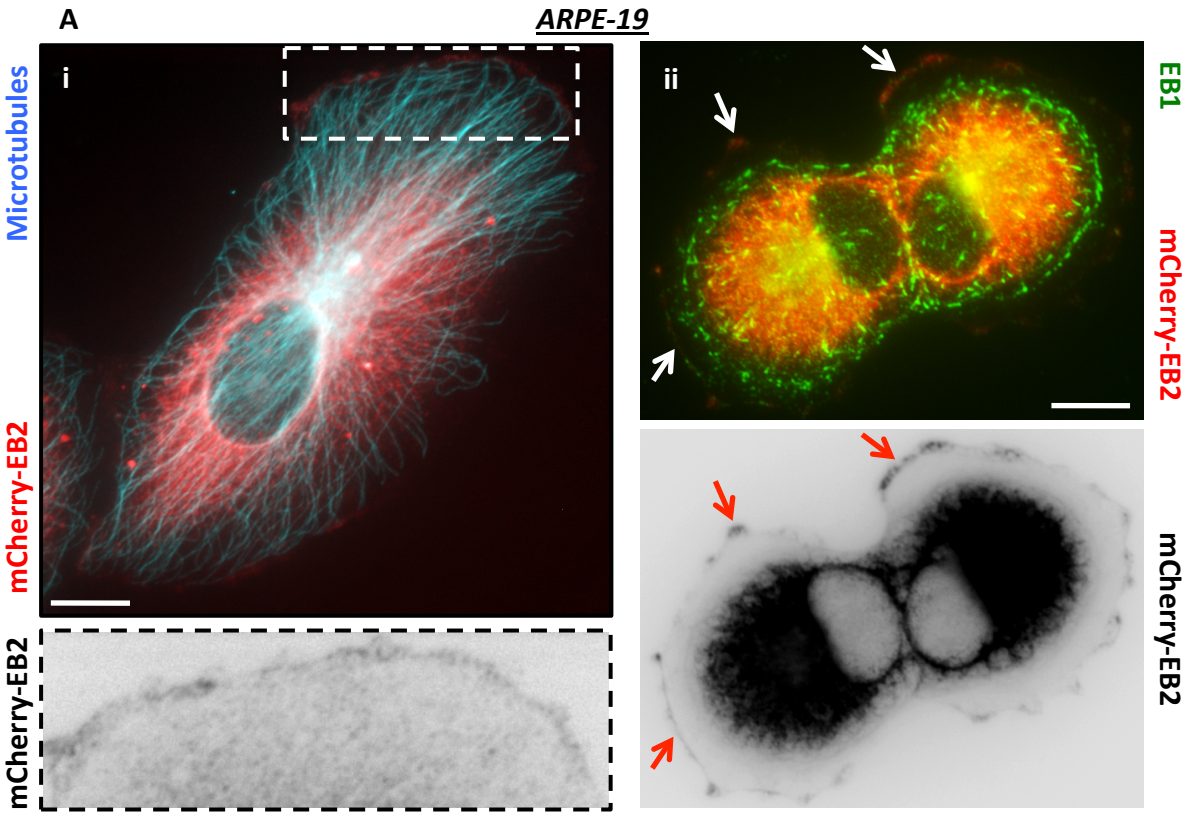
A
ARPE-19
i
ii
Microtubules
mCherry-EB2
EB1
mCherry-EB2
mCherry-EB2
mCherry-EB2

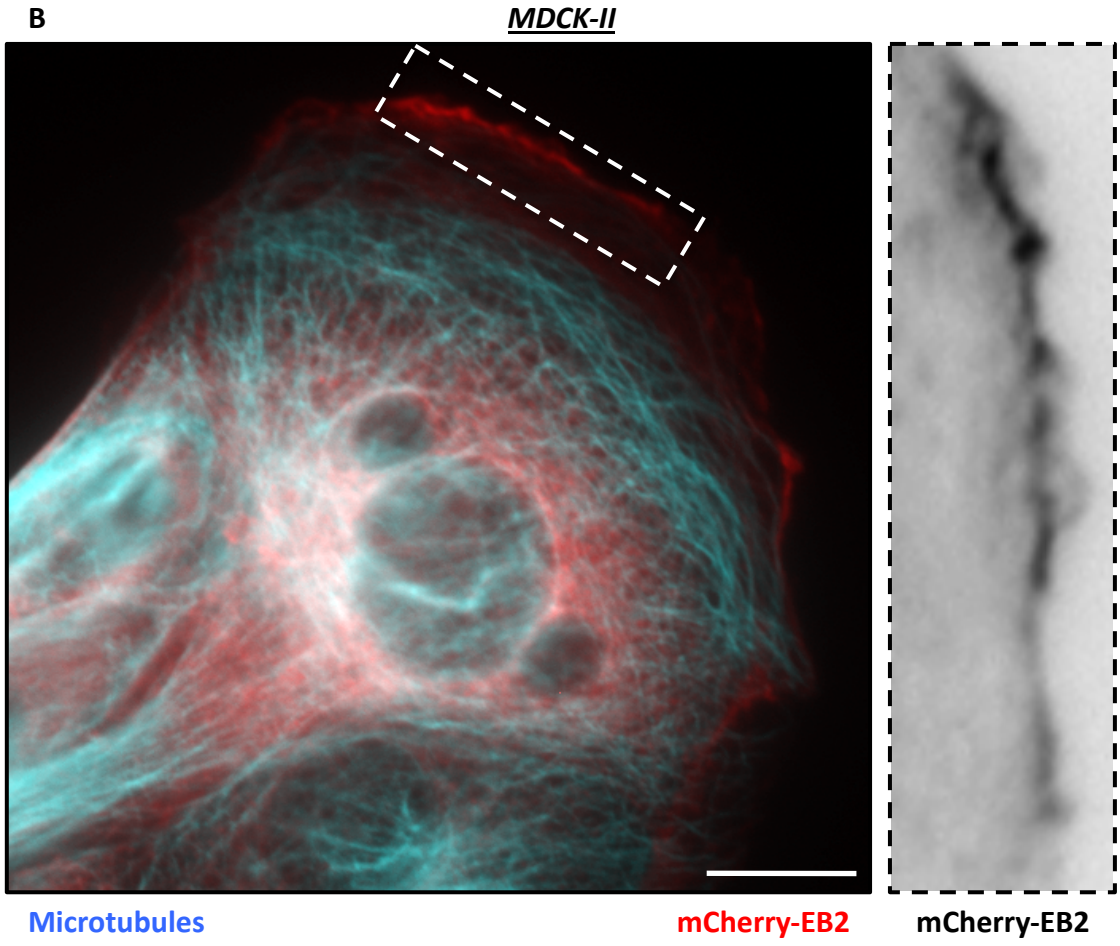
B
MDCK-II
Microtubules
mCherry-EB2
mCherry-EB2

Figure 7.7 β-actin and IQGAP1 are exposed at the leading edge of migratory MDCK-II cells
(A) Control MDCK-II cells were fixed and immunolabelled for microtubules (blue) and IQGAP1 (red, invert). Note the IQGAP1 localised at the exposed leading edge of the cell (boxed region). **(B)** Control MDCK-II cells were fixed and immunolabelled for β-actin (green) and IQGAPi (red, invert). Note the IQGAP1 at the leading edge (boxed region), where it colocalises with β-actin. All scale bars = 10μm.

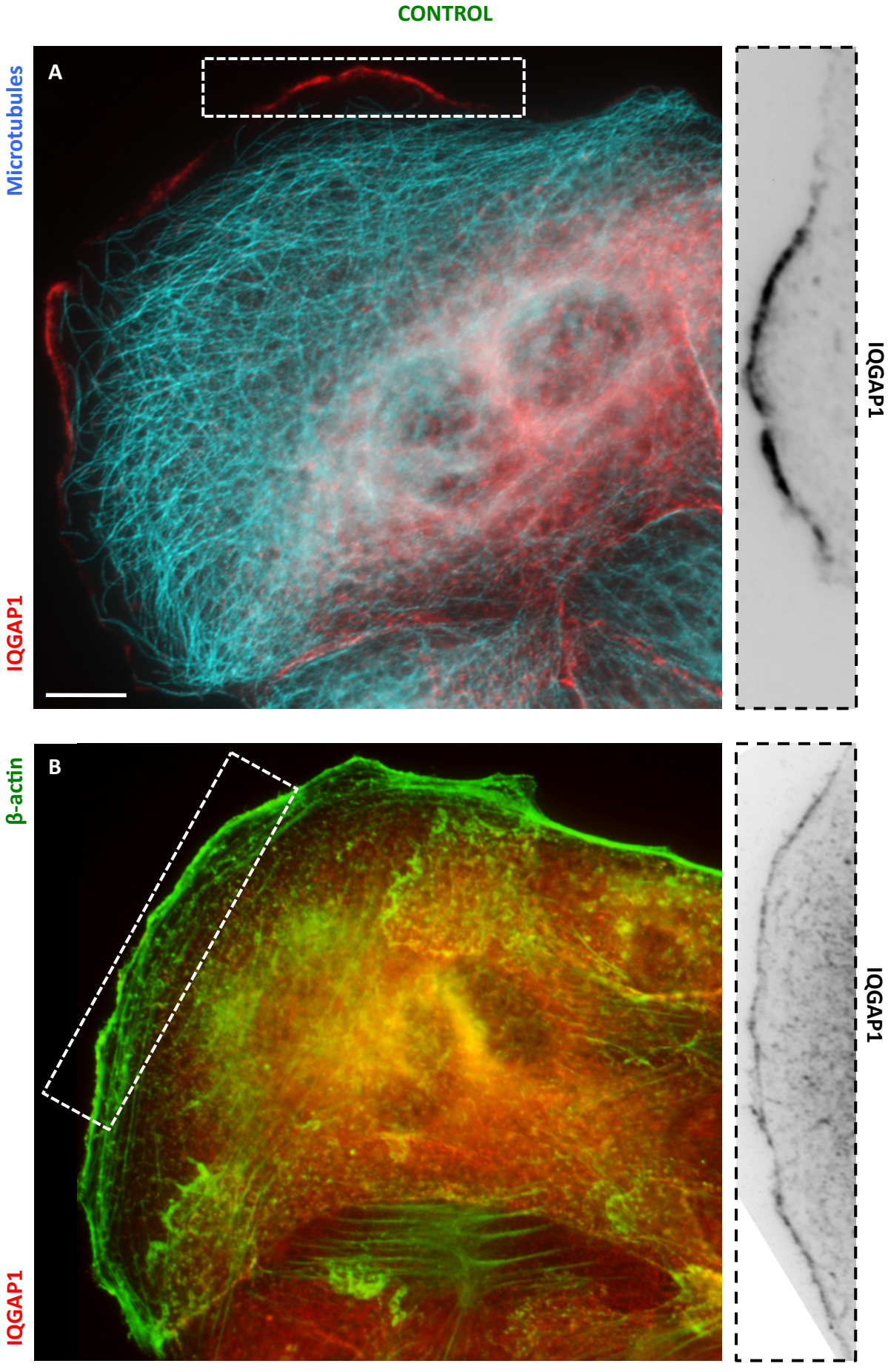
CONTROL
A
Microtubules
IQGAP1
IQGAP1
B
β-actin
IQGAP1
IQGAP1

Figure 7.8 mCherry-EB2 colocalises with IQGAP1, β-actin, and APC at the migratory leading edge
(A) Stable MDCK-mCherry-EB2 (red, invert) overexpressing cells were fixed and immunolabelled for microtubules (green) and IQGAP1 (blue, invert). Note the colocalisation of IQGAP1 and mCherry-EB2 at the leading edge. **(B)** A stable migratory MDCK-mCherry-EB2 (red, invert) overexpressing cell was fixed and immunolabelled for β-actin (green, invert) and IQGAP1 (blue, invert). Note the colocalisation of all three proteins at the leading edge. **(C)** Stable MDCK-mCherry-EB2 (red, invert) overexpressing cells were fixed and immunolabelled for APC (green, invert). Note the colocalisation of the two at the leading edge. All scale bars = 10μm.

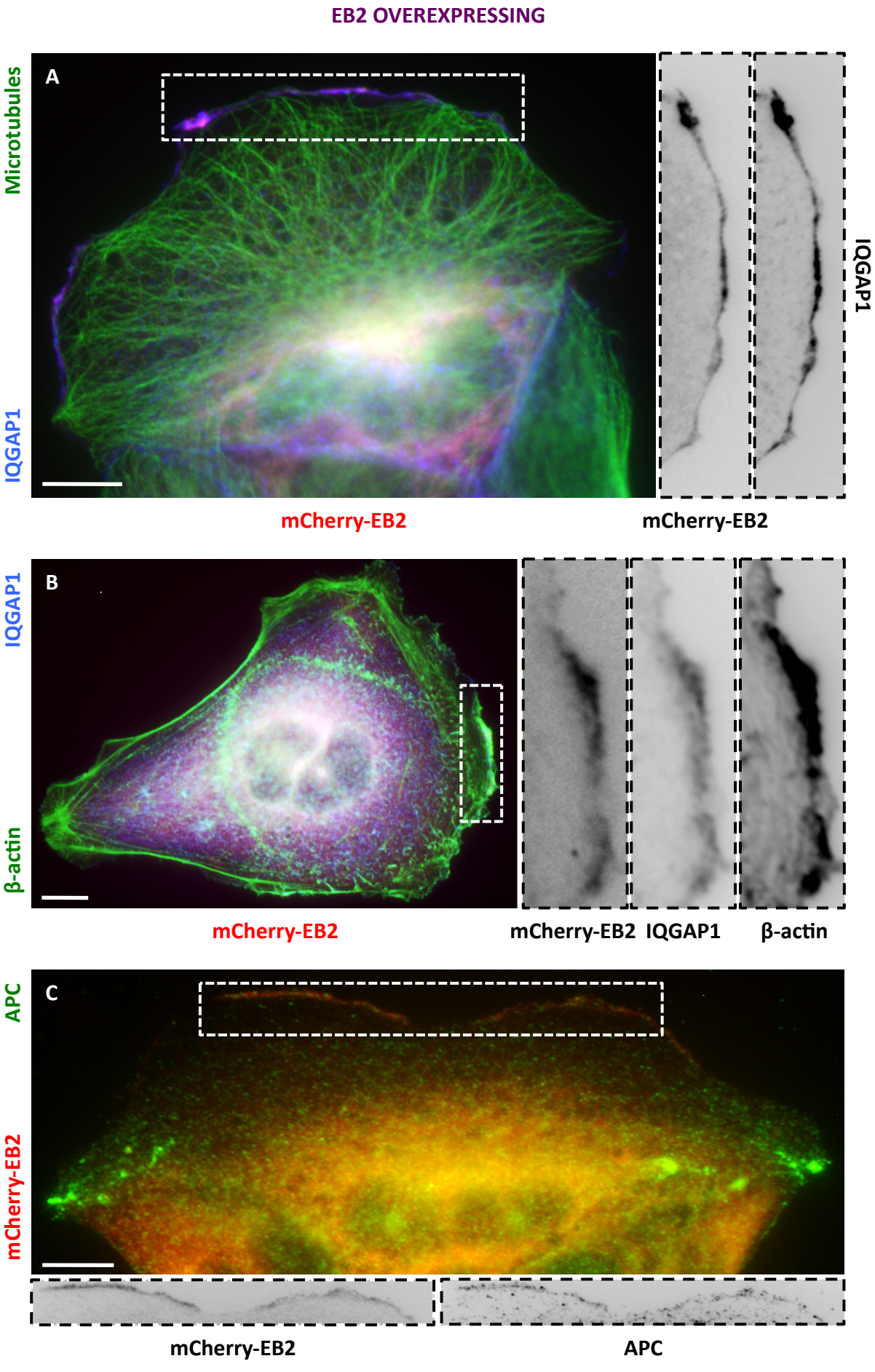
EB2 OVEREXPRESSING
A
Microtubules
IQGAP1
IQGAP1
mCherry-EB2
mCherry-EB2
B
IQGAP1
β-actin
mCherry-EB2
mCherry-EB2
IQGAP1
β-actin
C
APC
mCherry-EB2
mCherry-EB2
APC

Figure 7.9 (A) Single cell tracking of EB2 overexpressing MDCK-II cells
Control MDCK-II cells were seeded sparsely into six well plate wells and imaged by widefield time lapse microscopy for a 16 hour period, with frames taken every 10 minutes. **[i]** Image of a representative control region at t=0. **[ii]** 5 cells were analysed from each of 20 control regions (100 cells total); cell position was tracked at each time point for each cell to give a trace of position over the time-course. The traces of every cell analysed from all regions across the full time-course are combined to produce the combined tracking trace illustrated. All scale bars = 100µm.

A **CONTROL**

i **Representative Region (Time = 0 hours)**

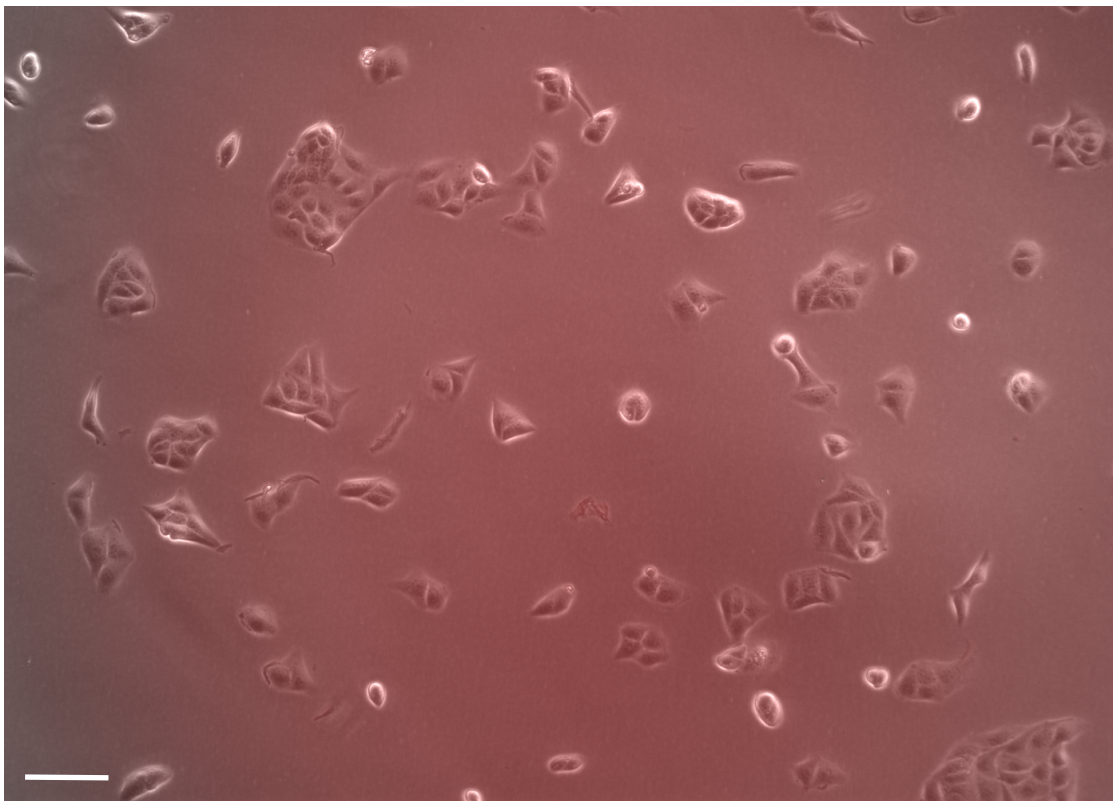

ii **Combined Tracking Trace (All Regions)**

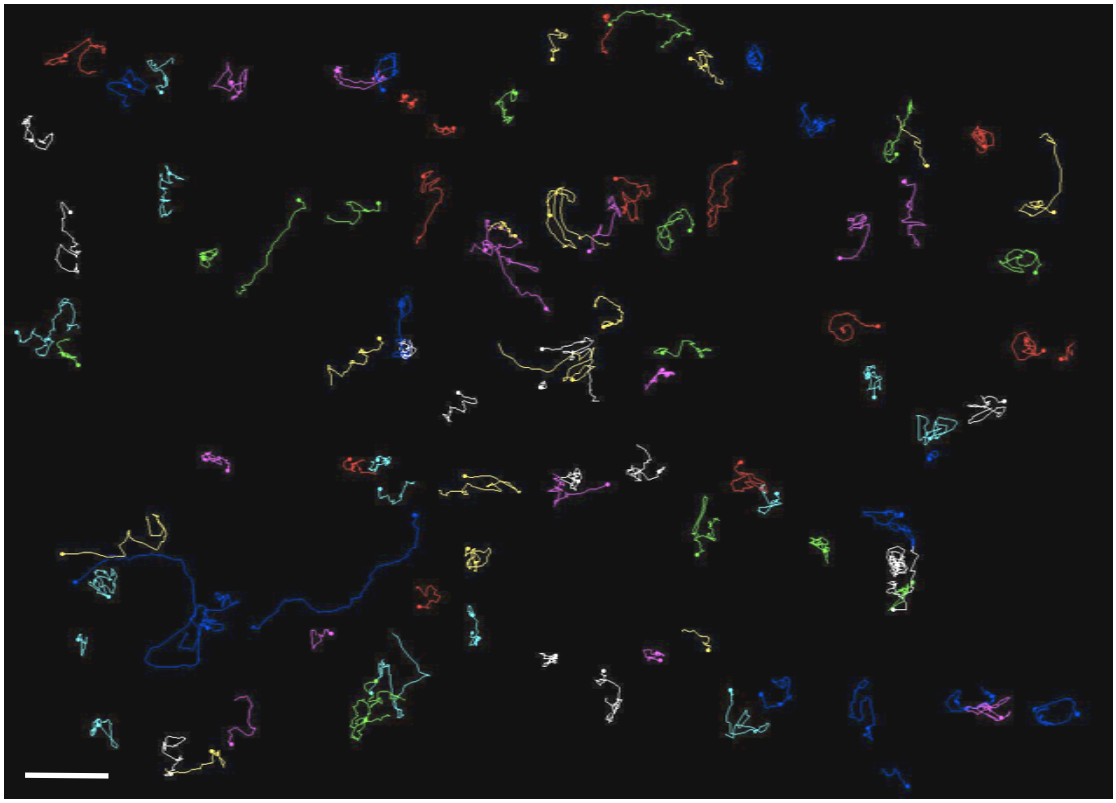

Figure 7.9 (B) Single cell tracking of EB2 overexpressing MDCK-II cells
MDCK-II cells stably expressing the empty pmCherry-C1 vector (red) were seeded sparsely into six well plate wells and imaged by widefield time lapse microscopy for a 16 hour period, with frames taken every 10 minutes. **[i]** Image of a representative empty vector region at t=0. **[ii]** 5 cells were analysed from each of 20 empty vector regions (100 cells total); cell position was tracked at each time point for each cell to give a trace of position over the time-course. The traces of every cell analysed from all regions across the full time-course are combined to produce the combined tracking trace illustrated. All scale bars = 100μm.

B **EMPTY VECTOR**

i **Representative Region (Time = 0 hours)**

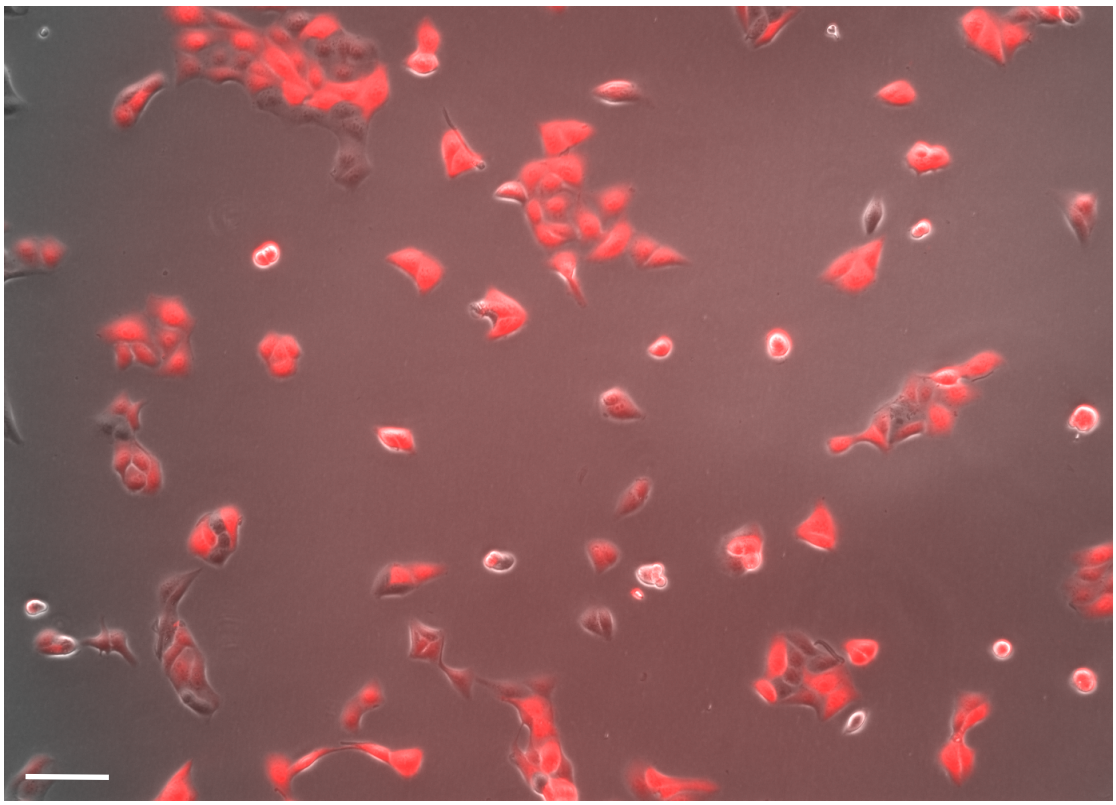

Empty pmCherry-C1

ii **Combined Tracking Trace (All Regions)**

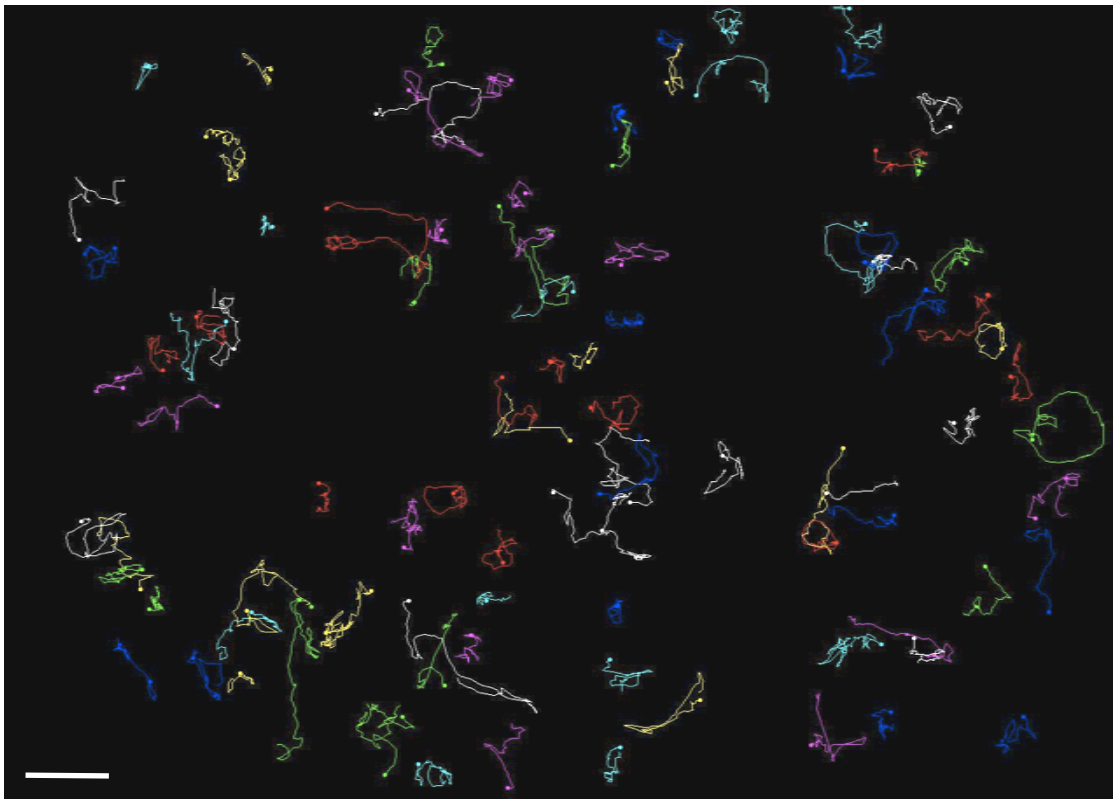

Figure 7.9 (C) Single cell tracking of EB2 overexpressing MDCK-II cells
MDCK-II cells stably expressing mCherry-EB2 (red) were seeded sparsely into six well plate wells and imaged by widefield time lapse microscopy for a 16 hour period, with frames taken every 10 minutes. **[i]** Image of a representative EB2 overexpressing region at t=0. **[ii]** 5 cells were analysed from each of 20 EB2 overexpressing regions (100 cells total); cell position was tracked at each time point for each cell to give a trace of position over the time-course. The traces of every cell analysed from all regions across the full time-course are combined to produce the combined tracking trace illustrated. Note the greater degree of movement in EB2 overexpressing cells, as marked by longer lines, and how fewer cells appear to move very little when compared to control or empty vector conditions. All scale bars = 100μm.

C EB2 OVEREXPRESSING

i Representative Region (Time = 0 hours)

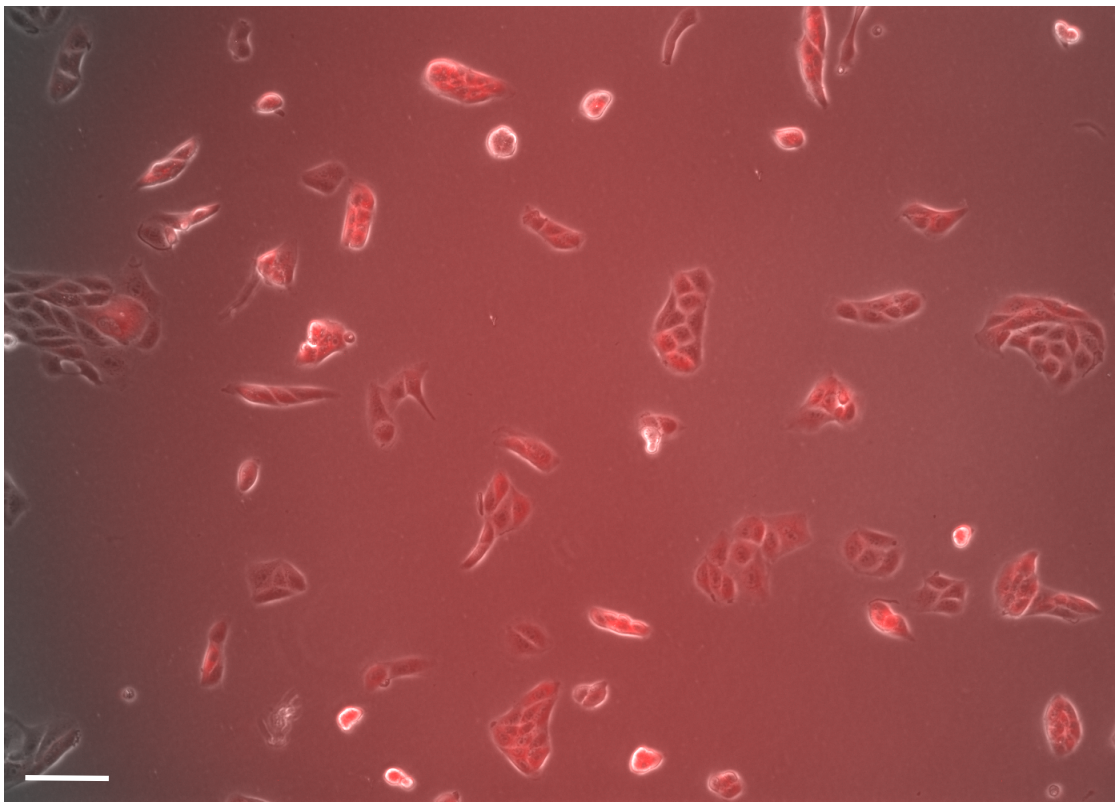

mCherry-EB2

ii Combined Tracking Trace (All Regions)

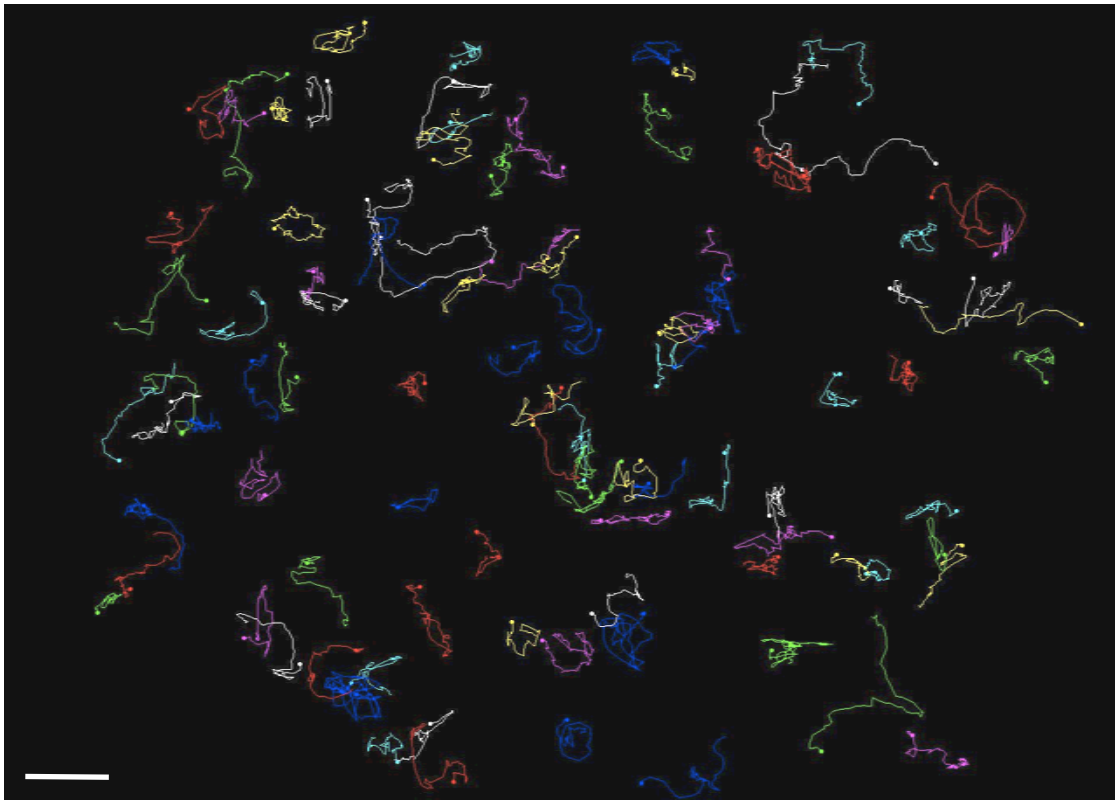

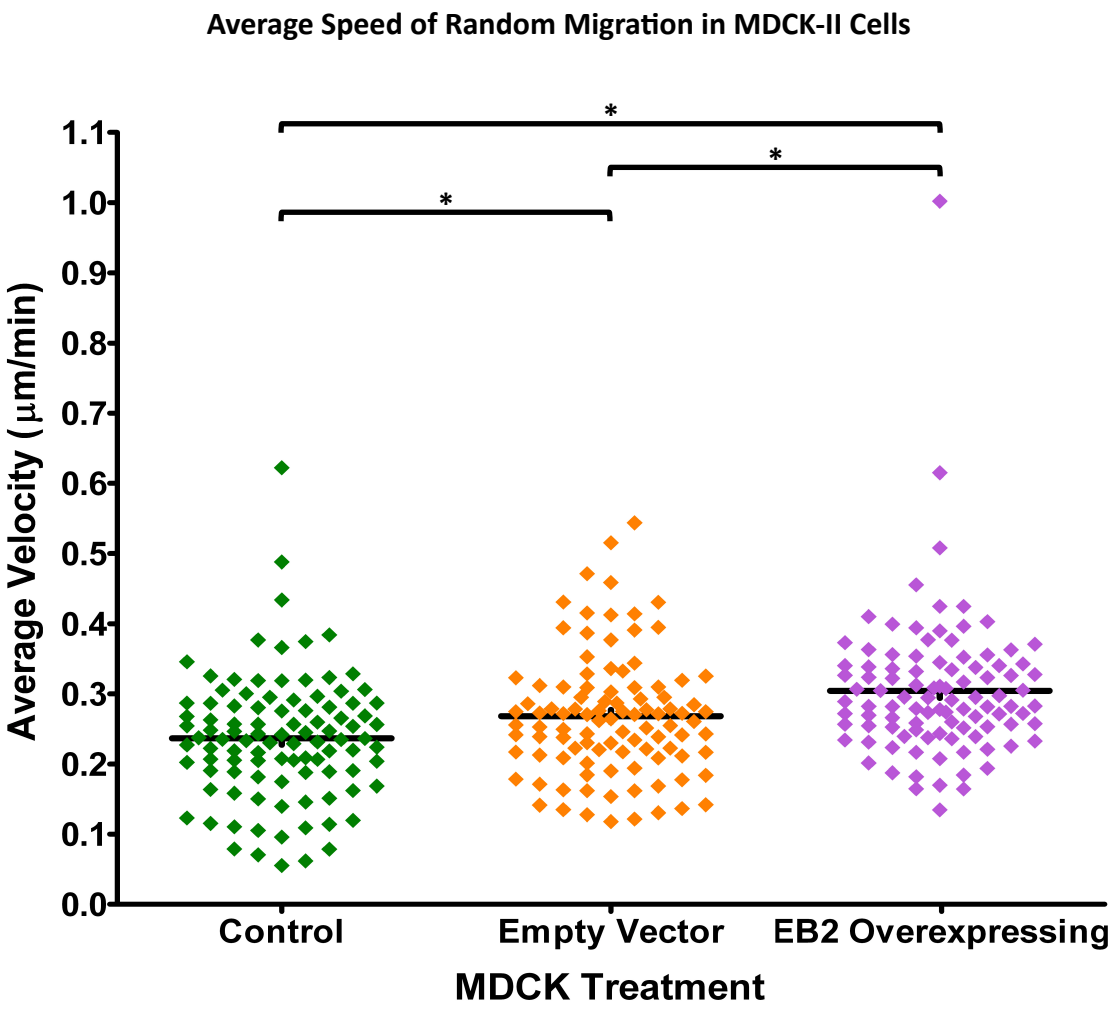

Treatment	N	Mean ± SEM (µm/minute)
Control	100	0.2366 ± 0.0090
Empty Vector	100	0.2682 ± 0.0087
EB2 Overexpressing	100	0.3044 ± 0.0135

Figure 7.10 EB2 overexpression causes increased speed of random migration in subconfluent cells
Control, pmCherry-C1 empty vector expressing and mCherry-EB2 overexpressing MDCK-II cells were analysed for migration in sparsely seeded conditions. For each treatment, 5 cells from 20 separate regions (total N=100 for each) were tracked in FIJI (ImageJ) software across each timepoint of a 16 hour time-course, with each frame captured every 10 minutes. From these data, the average velocity for each cell across the time period was calculated and plotted. Statistical significance was assessed by one-way ANOVA with Tukey's multiple comparison test, revealing a significant in speed between control and empty vector expressing cells and a further significant increase between empty vector and EB2 overexpressing cells.

Figure 7.11 Single cell tracking in EB2 depleted ARPE-19 cells
ARPE-19 cells treated with two shots of **(A)** scramble or **(B)** EB2 siRNA at 0 and 48 hours (as previous) were seeded sparsely into six well plate wells and imaged by widefield time lapse microscopy for a 16 hour period beginning 72 hours post initial transfection, with frames taken every 10 minutes. 60 cells for each treatment (from 15 scramble and 30 EB2 siRNA treated regions) were analysed; cell position was tracked at each time point for each cell to give a trace of position over the time-course. The traces of every cell analysed from all regions across the full time-course are combined to produce the combined tracking traces illustrated. Note the greater degree of movement in scramble treated cells, as marked by longer lines, compared to EB2 depleted conditions. All scale bars = 50μm.

A

SCRAMBLE

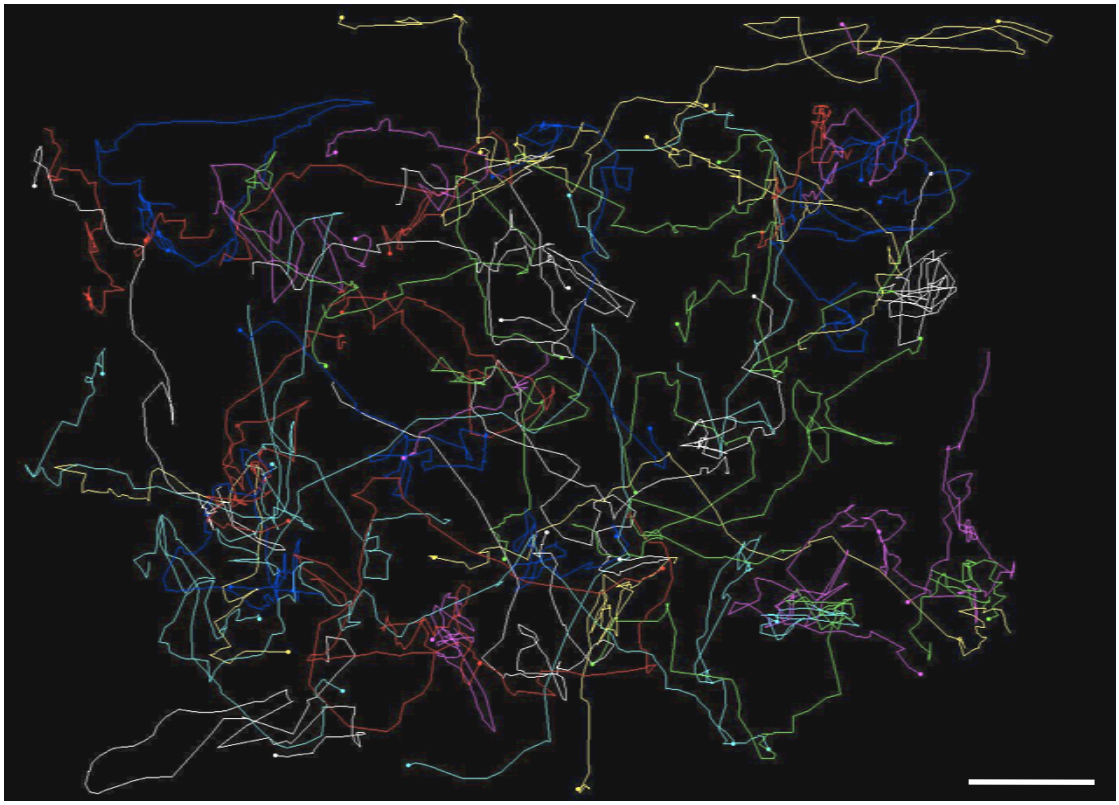

B

EB2 siRNA

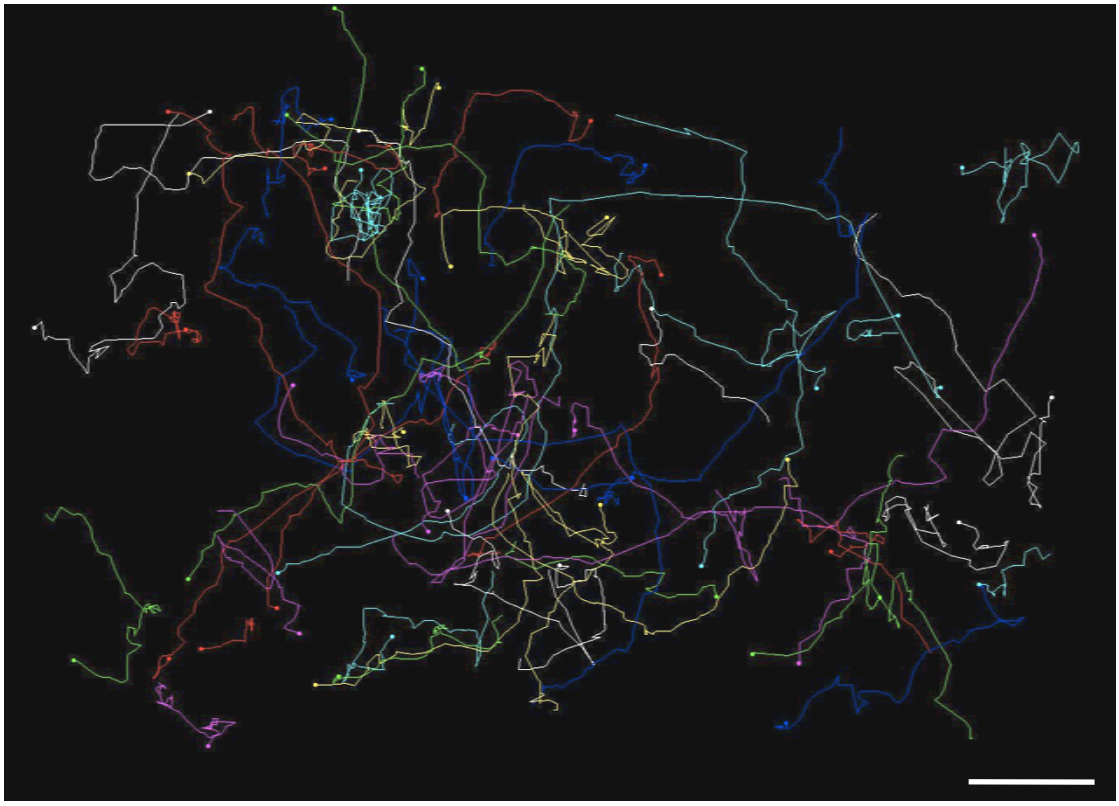

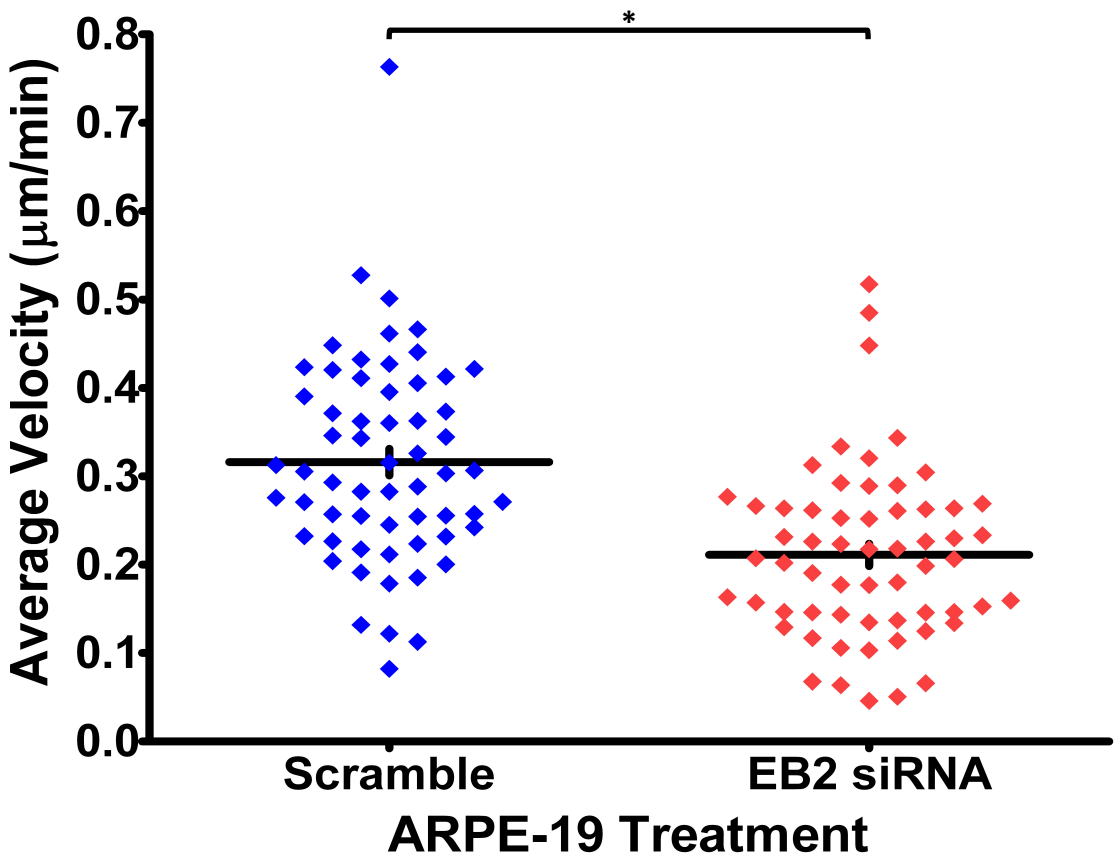

Treatment	N	Mean ± SEM (µm/minute)
Scramble	60	0.3160 ± 0.0151
EB2 siRNA	60	0.2111 ± 0.0126

Unpaired t-test			
EB2 siRNA	*vs*	Scramble	P < 0.0001

Figure 7.12 EB2 depletion causes decreased speed of random migration in subconfluent cells
ARPE-19 cells treated with two shots of **(A)** scramble or **(B)** EB2 siRNA at 0 and 48 hours (as previously) were seeded sparsely into six well plate wells and imaged by widefield time lapse microscopy for a 16 hour period beginning 72 hours post initial transfection, with frames taken every 10 minutes. 60 cells (N=60) for each treatment (from 15 scramble and 30 EB2 siRNA treated regions) were analysed. The position of each cell was tracked in FIJI (ImageJ) software for each time-point across the timecourse. From these data, the average velocity for each cell across the time period was calculated and plotted. Analysis by unpaired t-test revealed a significant decrease in cell velocity on EB2 depletion compared to scramble treated cells.

Figure 7.13 Scratch wound assays in EB2 overexpressing cells
Control and mCherry-EB2 (blue, invert) stably overexpressing cells were grown to confluence, and wounded to produce a scratch in the cell monolayer. The wound was allowed time to begin closing, and was then fixed and immunolabelled. **(A)** Widefield fluorescent images of cells for each treatment labelled for microtubules (green) and γ-tubulin (red), illustrating migratory cells at the edge of the scratch displaying centrosomes located behind the nucleus. **(B)** Widefield fluorescent images of cells for each treatment labelled for microtubules (green) and β-actin (red, invert). Note the colocalisation of mCherry-EB2 and β-actin stains. All scale bars = 10μm

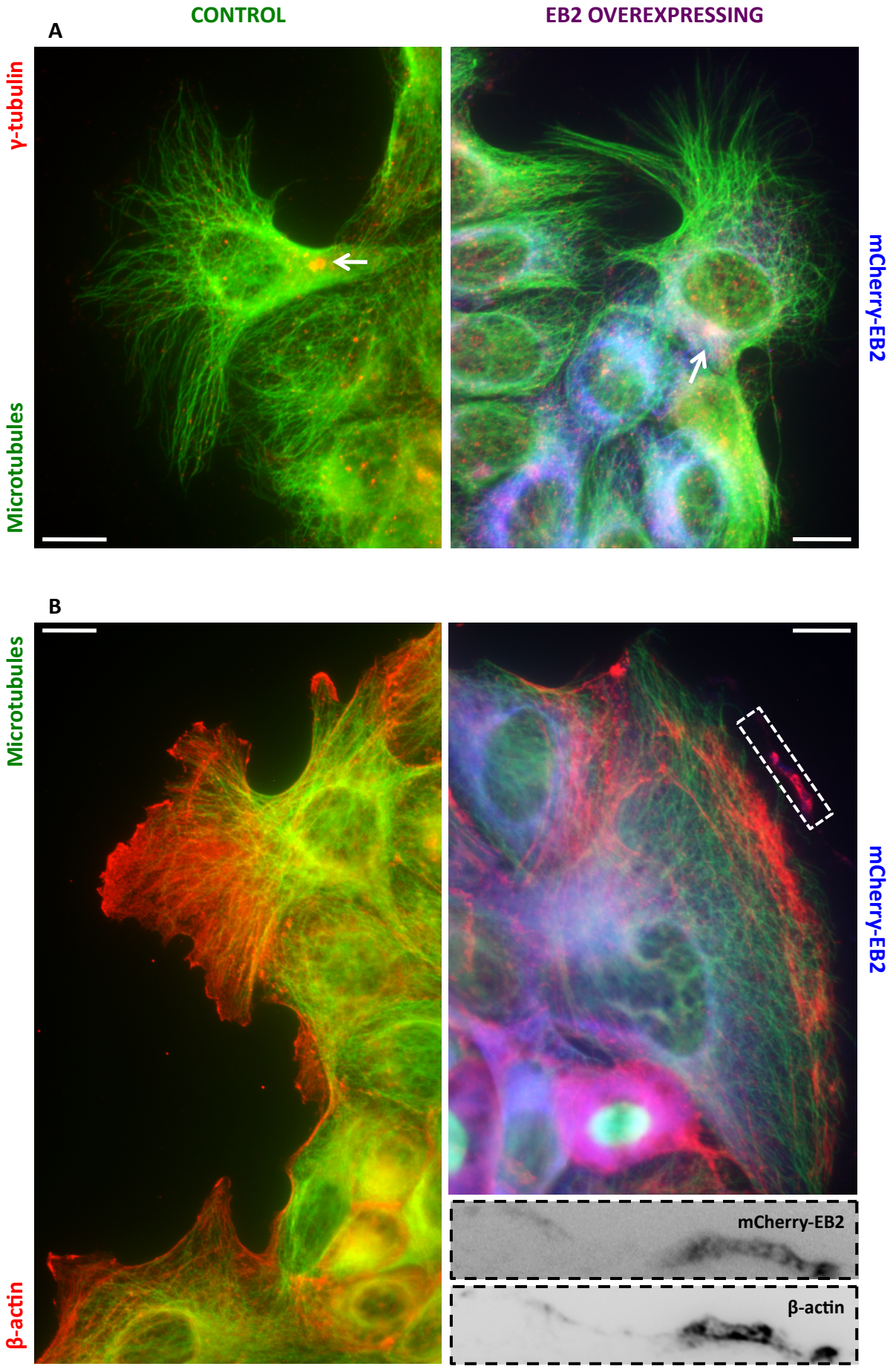
CONTROL
EB2 OVEREXPRESSING
A
γ-tubulin
Microtubules
mCherry-EB2
B
Microtubules
β-actin
mCherry-EB2
mCherry-EB2
β-actin

Figure 7.14 Measurement of area in scratch wound assays
(A) Control, **(B)** pmCherry-C1 (**[i]** red, **[ii]** white) empty vector stably expressing and **(C)** mCherry-EB2 (**[i]** red, **[ii]** white) stably overexpressing MDCK cells were seeded into 24 well plate wells and allowed to grow to confluency, then treated with thymidine to block cell division. Cells were observed by time-lapse widefield microscopy every 10 minutes for a 10 hour period. The area closed by the scratches for each condition were calculated by measuring the scratch area at t=0 hours (green lines) and at t=10 hours (blue lines) in Axiovision software. Images show representative example scratch regions. All scale bars = 100μm.

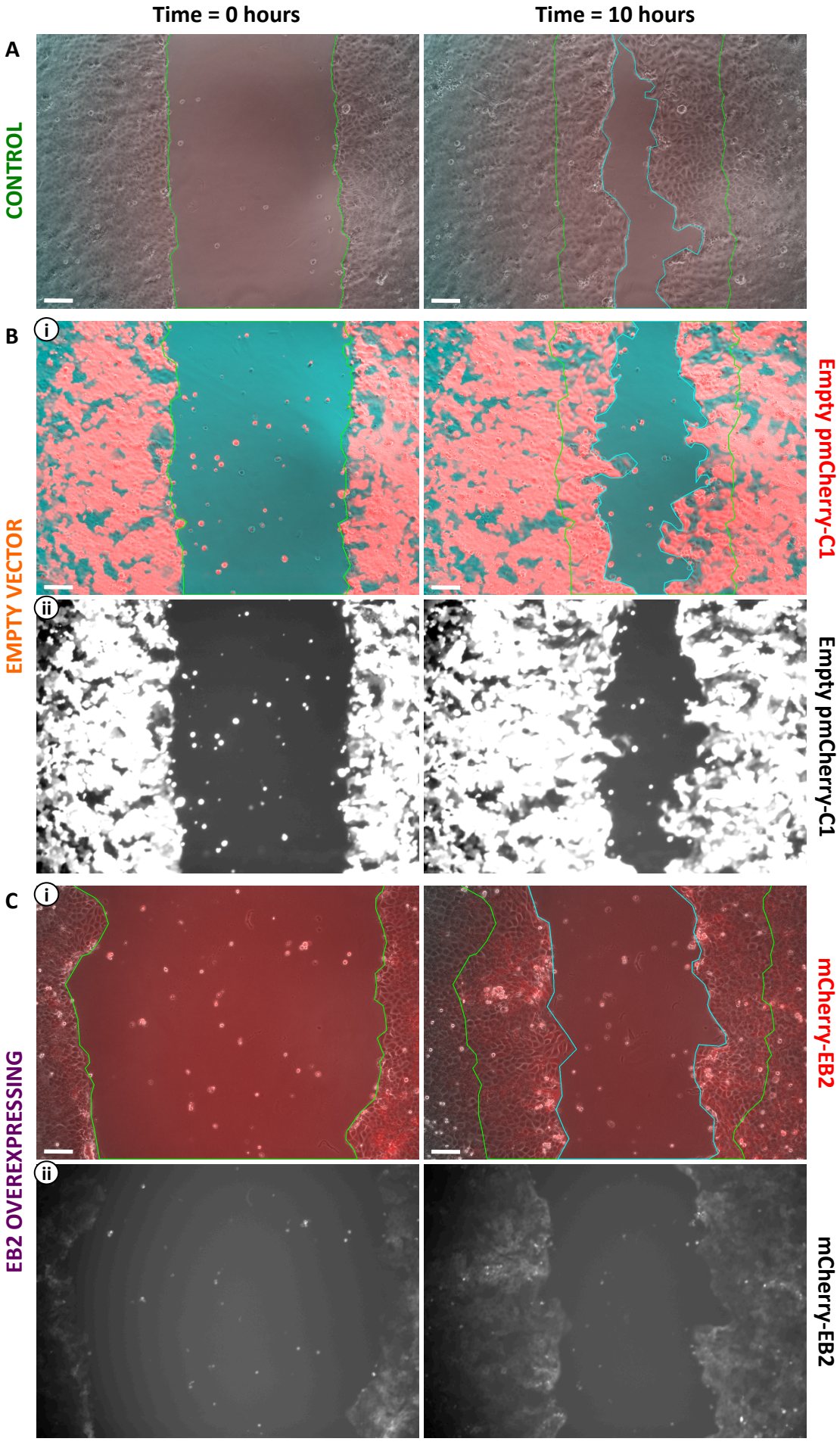
Time = 0 hours
Time = 10 hours
A
CONTROL
B
EMPTY VECTOR
i
ii
Empty pmCherry-C1
Empty pmCherry-C1
C
EB2 OVEREXPRESSING
i
ii
mCherry-EB2
mCherry-EB2

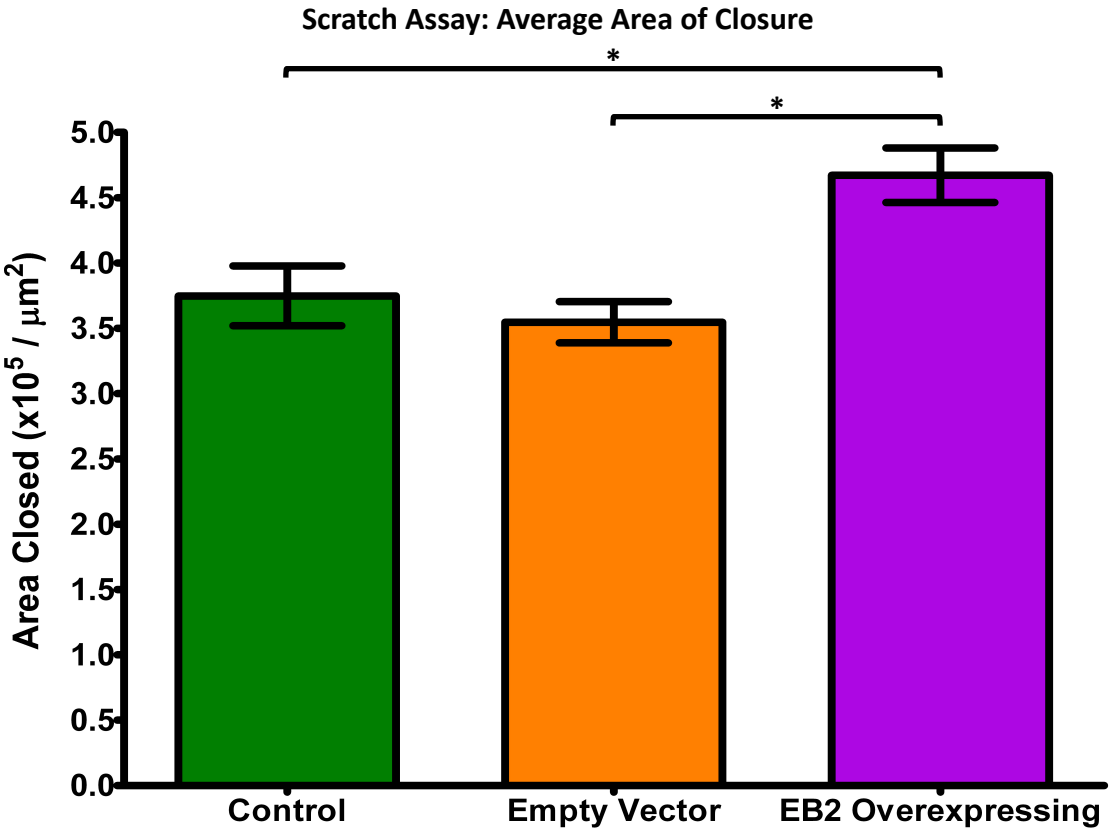

Treatment	N	Mean ± SEM (x10^5 / µm^2)
Control	16	3.748 ± 0.229
Empty Vector	16	3.546 ± 0.157
EB2 Overexpressing	16	4.671 ± 0.209

Figure 7.15 EB2 overexpression causes increased area of closure in scratch wound assays
Control, pmCherry-C1 empty vector expressing and mCherry-EB2 overexpressing MDCK cells were seeded into 24 well plate wells and allowed to grow to confluency, then treated with thymidine to block cell division. Cells were observed by time-lapse widefield microscopy every 10 minutes for a 10 hour period. The area closed by the scratches for each condition were calculated by measuring the scratch area at t=0 hours and at t=10 hours in axiovision software. 16 separate scratches for each condition were analysed (N=16) and plotted. Analysis by one way ANOVA with Tukey's multiple comparison test revealed a significant increase in the area closed in EB2 overexpressing cells compared to empty vector expressing or control cells.

Figure 7.16 Single cell tracking during scratch wound assays
(A) Control, **(B)** pmCherry-C1 empty vector expressing and **(C)** mCherry-EB2 overexpressing MDCK cells were seeded into 24 well plate wells and allowed to grow to confluency, then treated with thymidine to block cell division. Cells were observed by time-lapse widefield microscopy every 10 minutes for a 10 hour period. For each scratch, 8 cells at the leading edge were tracked at each time point to give a trace of position across the full time course. Images display example traces from representative scratch regions from each treatment. Note the longer lines in the overexpressing scratch compared to the two control conditions. All scale bars = 100µm.

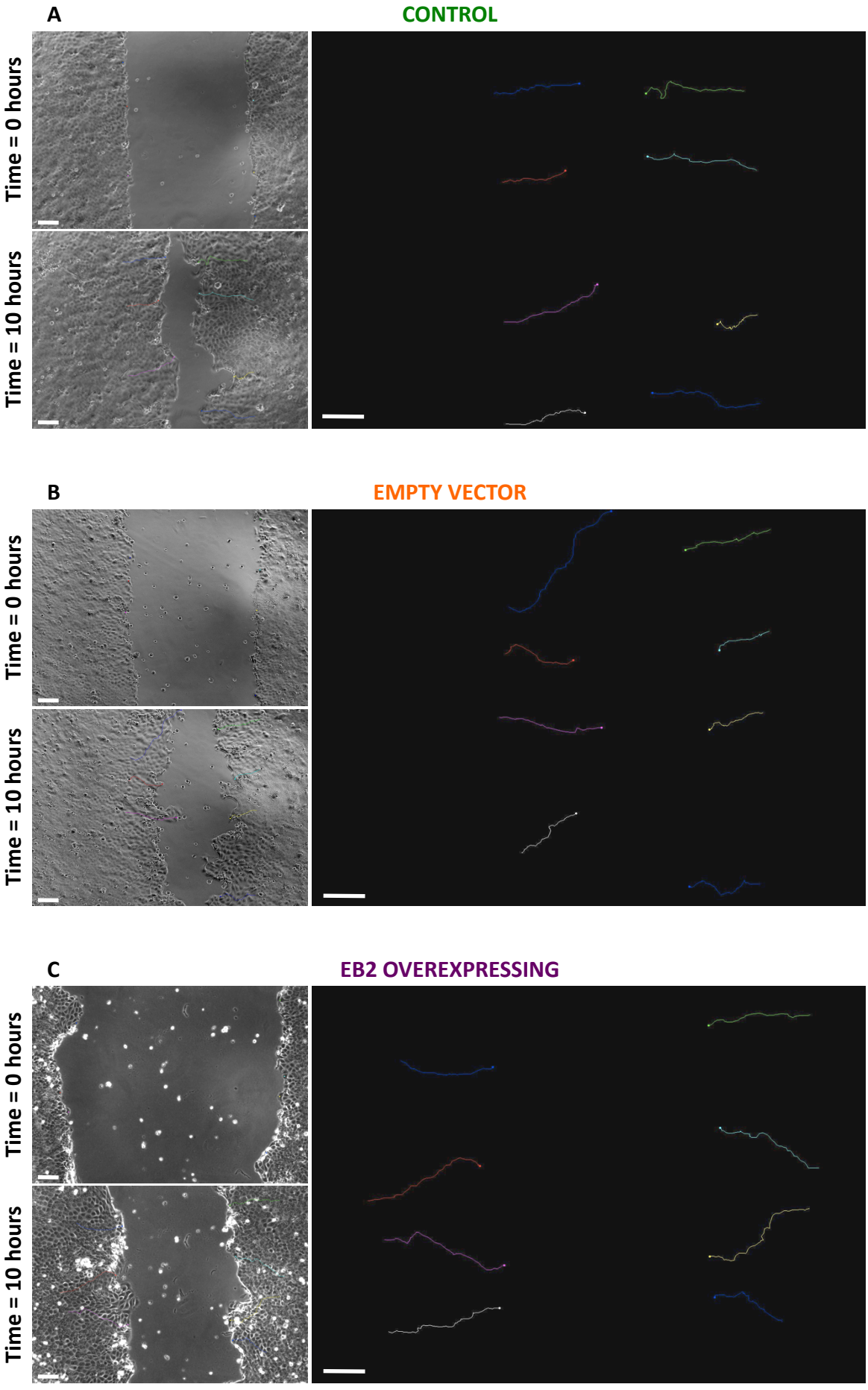
A
CONTROL
Time = 0 hours
Time = 10 hours
Tracking Trace
B
EMPTY VECTOR
Time = 0 hours
Time = 10 hours
Tracking Trace
C
EB2 OVEREXPRESSING
Time = 0 hours
Time = 10 hours
Tracking Trace

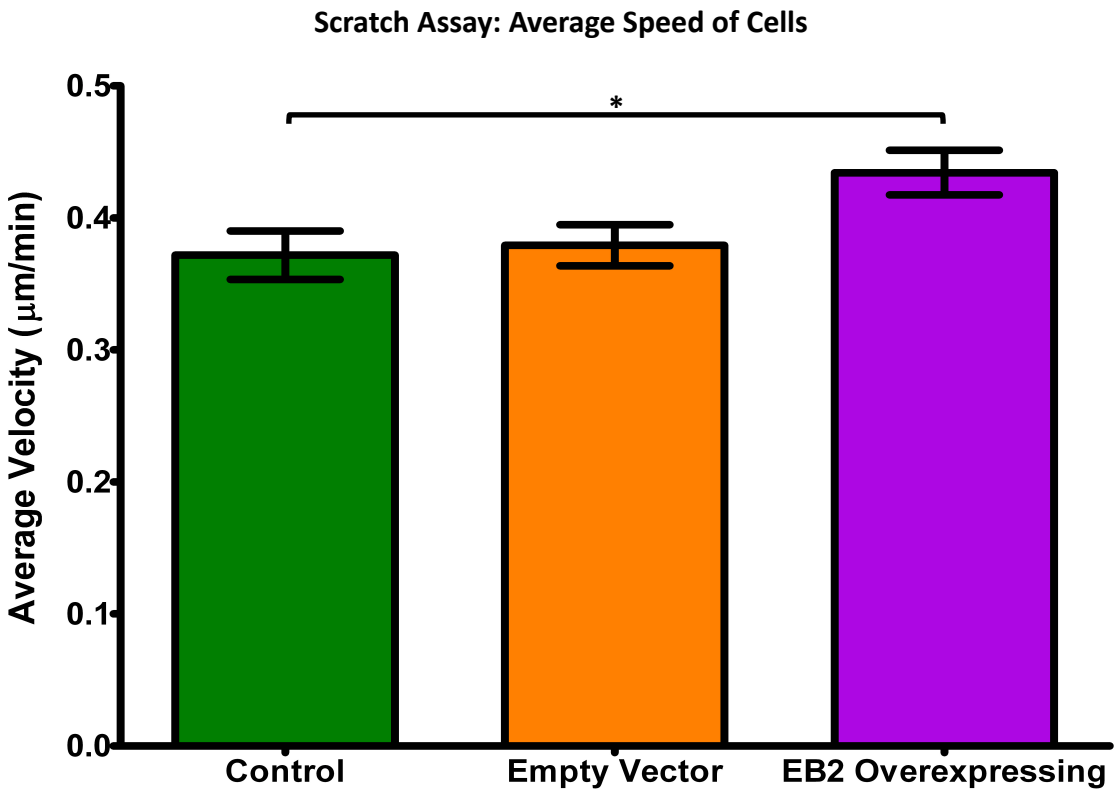

Treatment	N	Mean ± SEM (μm/minute)
Control	16	0.3717 ± 0.0184
Empty Vector	16	0.3792 ± 0.0156
EB2 Overexpressing	16	0.4342 ± 0.0169

Figure 7.17 EB2 overexpression causes increased speed of cell migration in scratch wound assays
Control, pmCherry-C1 empty vector expressing and mCherry-EB2 overexpressing MDCK cells were seeded into 24 well plate wells and allowed to grow to confluency, then treated with thymidine to block cell division. Cells were observed by time-lapse widefield microscopy every 10 minutes for a 10 hour period. For each scratch, 8 cells at the leading edge were tracked at each time point, and used to calculate the average cell velocity for each scratch. These average values from each scratch were combined to generate an overall mean individual cell velocity for each condition (N=16). Analysis by one-way ANOVA with Tukey's multiple comparison test revealed a significant increase in speed in EB2 overexpressing cells compared to control cells, although the difference was not significant when compared to empty vector expressing cells.

Chapter VIII

General Discussion

Colorectal cancer is one of the most common forms of the disease, and thus a major global health issue. There is therefore a great desire to understand the mechanisms of carcinogenesis and identify novel tumour targets that can act as either prognostic markers, or targets for future drug development. Colorectal tumours originate in the epithelial layer lining the crypts of the gut lumen and progress over many years, gradually accumulating genetic mutations and losing their differentiated polarised epithelial characteristics, before ultimately turning invasive and metastasising to secondary sites (Sancho et al., 2004).

The epithelial microtubule cytoskeleton is an interesting target for cancer research due to its importance in the establishment of polarity in the cells lining the gut (Cohen et al., 2004). It has been well established that polarised epithelial cells undergo a dramatic rearrangement in microtubule network organisation relative to the classical radial array organised by the centrosome seen in most undifferentiated epithelial cells. Polarisation occurs following the formation of cell-cell junctions, resulting in the centrosome relocating to the apical region of the cell, with microtubules subsequently rearranged into bundles anchored by their minus ends at apical non-centrosomal sites and plus ends extending into basal regions (Bacallao et al., 1989; Bre et al., 1987). The release and capture mechanism has been developed to describe the formation of epithelial non-centrosomal apico-basal arrays. In this, microtubules originate at the centrosome, and extend out to make contact with adherens junctions in apical regions, forming an intermediate extended radial array. The anchoring protein ninein is then released from the centrosome, and redeployed to these junctional sites. Cortical dynein drives microtubule minus end release from the centrosome and subsequent translocation of plus ends to basal regions where they are stabilised, with the minus ends eventually anchored by the redeployed ninein at adherens junction associated sites (Bellett et al., 2009; Mogensen et al., 2000; Moss et al., 2007).

Further understanding of the release and capture mechanism and thus the exact pathway behind apico-basal microtubule array formation is therefore important prior to investigations in cancer. In particular, would defects in microtubule network organisation, and increased microtubule dynamics encourage a

loss of epithelial polarity, and further, could they promote the transition to a more migratory phenotype?

The most important factor driving microtubule behaviour is their inherent dynamics, which allow them to undergo the dramatic rearrangements required for epithelial differentiation. Dynamics are tightly controlled by an array of microtubule interacting factors, in particular the +TIP family of proteins, which include the EB family of proteins, and APC. In addition to their role in regulating microtubule dynamic instability, +TIPs are also believed to play an important role in targeting of microtubule plus ends for cortical capture (Galjart and Perez, 2003; Lansbergen and Akhmanova, 2006), a key step in the formation of the intermediary extended radial array during the release and capture model (Bellett et al., 2009). Due to this wide network of microtubule related proteins, and their varying diversity of behaviours, there is a large pool of potential targets that if disregulated could disrupt the microtubule network in disease.

This project aimed to assess whether the formation of the apico-basal microtubule array is disrupted in colorectal cancer, and to judge what impact this could have on epithelial cell polarity. More generally, it also attempted to further enhance our knowledge of the natural mechanisms by which apico-basal epithelial networks are produced, and thereby provide a better basis for the understanding of these processes if they were found altered in disease. In particular, the investigations focused on two +TIP proteins, APC and EB2, for which interesting data has been acquired.

APC is known to be mutated in the majority of colorectal cancers, but historically has generally been studied for its signalling roles rather than its cytoskeletal interactions (Hanson and Miller, 2005; Nathke, 2004). Results from a previous project had implicated the APC truncation mutation in compromised microtubule interactions at cortical sites (Keynton, 2011). With cortical contact an important factor in both apico-basal array formation and spindle orientation, an early objective of this work was to further examine the APC truncation at the cell cortex using a more appropriate control cell line.

EB2 is a member of the EB family of +TIPs, which are generally strongly associated with promoting microtubule dynamics (Komarova et al., 2009), and have been linked to microtubule reorganisation on differentiation (Straube and Merdes, 2007; Zhang et al., 2009). Prior study of EB2 has been extremely limited, however it has demonstrated some intriguing behavioural differences compared to the other EB proteins, including less affinity for the microtubule plus end, and less potency at promoting microtubule growth (Komarova et al., 2009). Interestingly, EB2 is downregulated during differentiation of myocytes (Straube and Merdes, 2007). This project formed part of a wider ongoing investigation with the objective of examining any functions for EB2 throughout the epithelial polarisation process, given the outlined distinct behavioural differences relative to the members of its immediate family. EB2 has also been implicated in pancreatic cancer cell invasion (Abiatari et al., 2009), so a further aim was to study the overexpression of EB2 in terms of possible role in promoting EMT, invasion and migration in epithelial cancer systems.

8.1: Summary

Key findings of this project include:

1. APC truncation mutations compromise cortical contact leading to microtubules curling from the cell periphery. Expression of full length APC rescues the phenotype (Chapter IV).

2. EB2 depletion reduces microtubule dynamics (Chapter VI), and causes a distinct phenotype where EB1 and ACF7 relocalise along the microtubule lattice, co-ordinating microtubule-actin co-alignment and thereby the formation of stable microtubule bundles. This correlates with observations that EB2 is downregulated during epithelial polarisation, allowing microtubule bundle formation. Expression of the EB2 construct rescues the depletion phenotype (Chapter V).

3. Long term EB2 depletion causes activation of a cell death pathway (Chapter VI).

4. EB2 expression is linked to migration and potentially EMT; depletion reduces cell velocity, while overexpression triggers an increase in random migration speed and rate of wound healing. Overexpression may also increase cell invasiveness (Chapter VII).

8.2: APC Mediates Microtubule Cortical Interactions

8.2.1: Truncated APC compromises microtubule cortical capture

Microtubule interactions with the cortex play an important role in several systems, including at the migratory leading edge, and in apico-basal array formation (Bellett et al., 2009; Watanabe et al., 2004). Such interactions are often mediated by +TIP proteins, including dynein (Ligon et al., 2001) and CLASPs (Mimori-Kiyosue et al., 2005), and are further linked to cortical receptors such as IQGAP1, which can additionally co-ordinate with the actin cytoskeleton in peripheral regions. APC also interacts with IQGAP1 and actin, and has similarly been identified localised to the leading edge of migratory cells (Barth et al., 2008; Gundersen, 2002; Watanabe et al., 2004). Importantly, APC is truncated in the majority of colon cancers, losing the direct microtubule and EB1 binding sites at the C-terminus, but retaining N-terminal regions capable of interacting with IQGAP1 and kinesin motor proteins (Nathke, 2004).

Full length APC in epithelial tissue is found predominantly in basal regions of cells, where it is believed to anchor the plus end of apico-basal microtubule bundles (Mogensen et al., 2002), whilst in polarised cell lines it has also been localised to lateral regions in an actin dependent fashion (Rosin-Arbesfeld et al., 2001), allowing for a possible role in cortical capture of the extended radial array. Despite lacking direct EB1 and microtubule binding sites, truncated APC is also seen at the cortex following immunolabelling of TC7 cells (Chapter IV), an observation consistent with previous studies (Sharma et al., 2006).

A key flaw of previous studies was the lack of a suitable wild type APC human colon control cell line. Here HCT-116 cells have been used to address this issue. Although they were found not to polarise, with seemingly quite weak junctions, HCT-116 cells were seen to have a more ordered microtubule array anchored at the centrosome than characteristic of TC7 cells. Most importantly, the full length APC they expressed localised to cortical regions (Chapter IV). However, they are a cancer

cell line, and it should be noted that they possess a point mutation at a key phosphorylation site in β-catenin.

Analysis of microtubule cortical orientation in full-length control cell lines and truncated APC TC7 cells revealed a significant drop in the number of microtubules organised perpendicular to the cortex in truncated APC conditions. Most interestingly, rescue with a full-length GFP-APC construct transiently transfected into TC7 cells was able to restore the proportion of perpendicularly arranged microtubules towards that of the control cell lines. Nocodazole regrowth revealed microtubules initially grew out to the cortex before curling away, suggesting that they made an initial contact, but that the ability to permanently anchor to junctional sites had been lost (Chapter IV). These findings further support the model generated from the original study, which strongly linked actin with APC for stable microtubule anchorage at adherens junctions via a mechanism in which APC at the microtubule plus end guided microtubules along cortical actin to junctional sites. A lack of full length APC, actin or adherens junction components were all reported to result in microtubules that curled away from the cell periphery (Keynton, 2011).

Future study should focus on verifying potential associating partners for full length and truncated APC at cortical adherens junction associated sites. It is known that APC can link to the actin cytoskeleton via IQGAP1 (Watanabe et al., 2004), as well as interact with the microtubule-actin crosslinking protein ACF7, which it has been shown to recruit to the plasma membrane in migratory cells (Zaoui et al., 2010). These links through APC to actin filaments could play an important part in stabilising microtubule interactions at the cortex. As demonstrated during the investigation of EB2 during epithelial differentiation, ACF7 has an important role acting through EB1 in cross-linking the actin and microtubule cytoskeletons into co-aligned stable bundles (Goldspink et al., 2013b). It may therefore play a similar role in the approach to the adherens junctional sites, mediated in this instance through APC. Recent work in our lab has identified a critical association between CLIP-170 and IQGAP1 required for the delivery of ninein to the cortex, with depletion of either compromising microtubule cortical capture (Goldspink et al., 2013a, manuscript in preparation). Speculatively then, it may be that an initial transient link is made

between cortical IQGAP1 and the microtubule plus end, via CLIP-170. This transient interaction brings the microtubule plus end in proximity with the actin cytoskeleton at apical adherens junction associated sites, allowing for a more stable anchorage of microtubules to junctions mediated by APC and possibly acting via ACF7, or IQGAP1 in an additional role. This cross-linkage thus allows the formation of a sufficiently stabilised extended radial array capable of efficient ninein delivery to the cortex. Meanwhile, in cancer cells expressing truncated APC, whilst that initial transient contact is retained and may be sufficient for some ninein redeployment, the lack of full length APC to fully coordinate microtubule plus ends correctly with the actin cytoskeleton ultimately prevents cortical stabilisation, meaning microtubules lose contact and curl away from adherens junctions (Figure 8.1).

It should be noted that whilst the APC truncation clearly has an effect on microtubule cortical anchorage in flat tissue culture cells, it does not prevent polarisation from occurring, as demonstrated in TC7 cells. Additionally, immunolabelling of rat isolated crypts has not revealed APC strongly localised to apical junctional sites (although this may be due to issues with fixation). There is some doubt therefore as to whether APC mediated cortical contact is relevant to the initial formation of the apico-basal array, it may be more likely to have an effect on the embedding of microtubule plus ends in basal regions. APC has been ascribed many varied roles in epithelial cells, but never seems completely necessary for any single one (Nathke, 2010); there appears to be a lot of redundancy in its function. In the case of epithelial differentiation then, rather than directly altering microtubule array formation (which with the diversity of +TIP proteins may well have several alternative pathways to stabilise cortical capture), the APC mutation may instead reduce the overall efficiency of the system, allowing for later additional defects to have a greater impact. This would support the fact that overall, APC mutations generally occur relatively early on in the established colorectal cancer progression sequence, acting more as a destabilisation factor to exacerbate the harmful effect of further defects accumulated later in tumour progression (Cardoso et al., 2007; Fearon and Vogelstein, 1990).

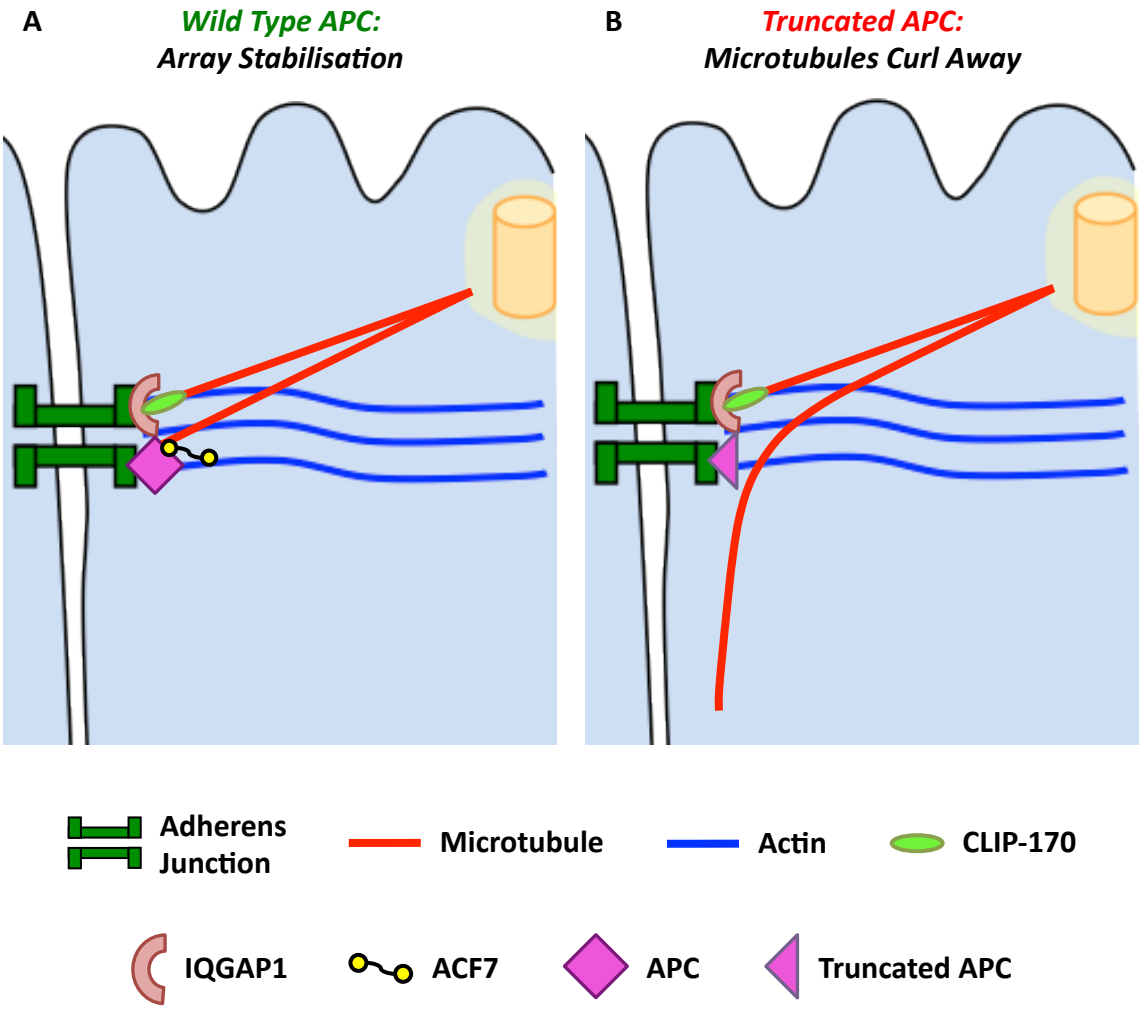

Figure 8.1 Speculative model for APC mediated microtubule cortical contact in the establishment of the extended radial array during the release and capture model
(A) In normal conditions, microtubules growing from the centrosome make initial transitory contact at adherens junction associated sites to the cortically located receptor IQGAP1 via the +TIP CLIP-170. Wild-type APC at these cortical sites co-ordinates cross-linking of microtubules to actin filaments via an adaptor such as ACF7, or IQGAP1 itself, stabilising the intermediate radial array.
(B) In cells expressing truncated APC, co-ordination with actin filaments fails to occur. Microtubules approaching the cortex still make a transitory connection to IQGAP1 via CLIP-170, but the truncated APC is unable to stabilise the link, meaning microtubules lose contact, and curl away from the cell periphery.

8.2.2: Truncated APC is associated with spindle misorientation

Correct spindle orientation and asymmetric division is essential for the correct maintenance of an epithelial monolayer in colonic crypts. Division plane rotation can produce a multilayered epithelium, disrupting the overall tissue architecture, as seen in the immunolabelled frozen cancer tissue samples (Chapter III). APC has been associated with maintaining this system (Quyn et al., 2010; Yamashita et al., 2003), as it is involved in plus end interactions with kinetochores and astral microtubule anchorage at the cortex (Green and Kaplan, 2003). Astral microtubule cortical interactions are particularly important, as they are believed to interact with junctionally associated dynein to rotate spindle poles into the correct position (O'Connell and Wang, 2000). Supporting this, experiments utilising $APC^{min/-}$ mouse tissue have shown evidence of spindle angle misalignment (Fleming et al., 2009). The spindle orientation experiments in this study do further suggest APC truncations can lead to alignment defects. Although the general angle between TC7 and wild type APC cells showed no increase, there was a significant amount of APC truncation expressing cells that became completely misaligned, demonstrating a rotated phenotype (Chapter IV). However, further study is needed to discover the exact mechanism and interacting partners involved, although it is reasonable to suppose the process could act through similar speculative pathways as outlined earlier for the formation of the extended radial array, particularly given that it has been demonstrated that the APC orthologue Kar9 contributes to spindle orientation in yeast via Myosin V translocation along actin fibres (Yin et al., 2000).

8.3: EB2 Plays an Important Role in Epithelial Differentiation

Differentiation of epithelial cells is associated with increase microtubule stability and bundling (Pepperkok et al., 1990). Meanwhile, EB proteins have been linked to microtubule stability and differentiation processes, with overexpression of EB1 known to cause the formation of stable microtubule bundles (Bu and Su, 2001). This has been demonstrated in muscle myoblast differentiation, where stable non-centrosomal microtubule bundling and differentiation is dependent on EB1 and EB3 (Straube and Merdes, 2007; Zhang et al., 2009). It is also seen in fibroblast migration where microtubule stabilisation has been linked to EB1, acting alongside APC and mDia via Rho signalling (Wen et al., 2004). In contrast, experiments have shown EB2 functioning differently than the other EB proteins; its overexpression does not cause bundling (Bu and Su, 2001), and its expression levels are seen to diminish during muscle differentiation (Straube and Merdes, 2007).

8.3.1: EB2 loss promotes microtubule stabilisation

In contrast with its EB family siblings, this study has demonstrated that a loss of EB2 leads to microtubule stabilisation. Depletion of EB2 by siRNA in ARPE-19 and HCT116 cells was found to trigger a distinct change in phenotype; cells were seen to dramatically increase in size, accompanied by a redeployment of both EB1 and ACF7 to decorate the microtubule lattice. Additionally, microtubules were seen to straighten and form bundles, which were co-aligned actin filaments. Crucially, these effects could be rescued by transfection with the created mCherry-EB2 construct (Chapter V). Taken together, these observations suggested a stabilisation of the microtubule network leading to EB1 lattice association, and bundle formation mediated by microtubule-actin cross-linking though the spectraplakin ACF7. This apparent increased microtubule stability on EB2 loss was confirmed via live time-lapse microscopy analysis of EB2 siRNA treated cells, which revealed that EB2 depletion leads to significantly increased microtubule pausing and decreased shrinking dynamic events (Chapter VI) (Goldspink et al., 2013b).

Increases in cell size can be associated with a block on mitosis, however proliferation assays and positive staining for the proliferation marker Ki-67 suggested depleted cells remained in cell growth phases (Goldspink et al., 2013b). This was verified directly by live phase contrast time-lapse imaging of EB2 siRNA treated cells, which confirmed that EB2 depleted cells retained the ability to divide. It also revealed a number of cell death events in division resembling a failure of cytokinesis, an observation supported by a notable peak sub-G1 seen during flow cytometric cell cycle analysis, which is characteristic of DNA fragmentation in death pathways (Ziegler and Groscurth, 2004). These cell death events increased in frequency with the length of EB2 depletion; at 96 hours post treatment most division events were still successful (hence the lack of a significant drop in the proliferation assays that ran to this time point), however by 120 hours of depletion approximately two-thirds of division events resulted in failure (Chapter VI). As yet, it is unclear exactly how these deaths are occurring, however it is vital in the future that the exact cell death pathway is identified, be it apoptosis, necrosis, or another alternative mechanism. One possible method is a variant of apoptosis known as mitotic catastrophe, in which cells undergo programmed cell death during the mitotic process (Castedo et al., 2004; Vakifahmetoglu et al., 2008). Intriguingly, mitotic catastrophe has recently been observed in a cytoskeletal context. Knockdown of various centrosomal proteins (interestingly, including ninein) was seen to alter microtubule spindle organisation, cause arrest in metaphase, and ultimately activate a caspase cascade leading to apoptosis either in interphase or during the actual division process itself (Kimura et al., 2013).

Whichever mechanism is ultimately identified, it is also important to investigate exactly how EB2 loss contributes to the death phenotype. For example, does the increased microtubule stability disorganise spindle microtubules or interfere with actin organisation at the cleavage furrow, causing issues with cytokinesis? Alternatively, could EB2 be involved in a hitherto unknown signalling pathway, possibly mediated by the alternatively spliced N-terminal extension regions that have yet to be characterised?

8.3.2: EB2 is a central regulator of microtubule organisation in epithelial apico-basal polarisation

Crucially, we have demonstrated a key role within the epithelial polarisation process for EB2 downregulation and resultant microtubule bundling and coordination with actin (as seen on siRNA treatment). EB2 was observed to be downregulated during mIMCD-3 cell culture polarisation sequences (Chapter V) (Goldspink et al., 2013b), whilst in both isolated small intestinal crypt and cochlea tissue explants EB2 was seen differentially expressed between different cell types within the same epithelial tissue. Cells with unbundled apico-basal arrays and dynamic microtubules (including cochlea hair cells and some cells within the crypt stem cell region) had high levels of EB2, whilst regions demonstrating stabilised microtubule bundles (crypt areas above the stem cell zone and cochlea supporting cells) demonstrated very low EB2 expression levels. Depletion studies in differentiating TC7 cells revealed that depletion of either EB1 or EB2 prevented cell apico-basal elongation (as marked by cell height in the Z-axis). However, whilst EB1 siRNA treated cells did apically constrict and possess peripheral bundles (although these were incorrectly orientated), EB2 depletion prevented reorganisation of the microtubule array into bundles, and compromised cell constriction (Goldspink et al., 2013b).

Taken together, these results implied EB2 expression was required during early differentiation to maintain a dynamic microtubule population for initial reorganisation, and to allow initial apical constriction, before its later downregulation enables EB1 lattice association, and accordingly microtubule stability, bundling, and actin crosslinking (Goldspink et al., 2013b).

A recent investigation in the cochlea has further supported these observations. FGF signalling has an important role regulating cell architecture during organ of Corti development. In particular, it was found that loss of FGF receptor 3 in supporting pillar cells compromised microtubule organisation, distinctly reducing the degree of bundle formation. Importantly, this was also accompanied by a significant increase in expression of the MAPRE2 gene (Szarama et al., 2012).

As discussed, the result of EB2 downregulation is the lattice association of EB1, and resultant link to the actin cytoskeleton via ACF7. It is important to examine this interaction further, with recent follow up work in our lab focussing on a potential role for formins in the process. Formins such as mDia are known to associate with microtubules directly through their FH2 domains , and via interactions with +TIPs, including EB1. These interactions have been shown to promote microtubule stability and lead to co-alignment of microtubules and actin filaments (Bartolini and Gundersen, 2010; Ishizaki et al., 2001; Palazzo et al., 2001; Wen et al., 2004). Formins are also able to trigger actin nucleation and cable elongation at various sites, including at adherens junctions (Kobielak et al., 2004). It was found that the treatment of EB2 depleted ARPE-19 cells with a formin inhibitor that specifically targeted the FH2 domain (Rizvi et al., 2009) was able to rescue the depletion phenotype previously outlined. In particular, microtubules were less organised and no longer straight, whilst EB1 and ACF7 distribution were restored to plus end comets and a dispersed pattern respectively. Importantly, the co-alignment of microtubules along actin filaments was also no longer apparent. Together, these observations suggested that formin activation following EB2 downregulation could play an essential role in the formation of stabilised microtubule bundles and actin co-alignment during the epithelial differentiation process (Goldspink et al., 2013b).

8.3.3: Regulation of EB2 expression levels in epithelial differentiation

The next step in understanding the role of EB2 in epithelial differentiation is to determine the mechanism by which EB2 is switched off during polarisation, and thus establish what pathways drive the formation of stabilised microtubule bundles. Importantly, overexpressed mCherry-EB2 in a stable cell line was not downregulated during polarisation sequences (Chapter VII), suggesting a switching off of gene expression rather than targeting of the protein product for degradation is the mechanism that drives EB2 loss. However, it should be noted that proteins can be targetted to the proteosome for degradation by the addition of polyubiquitin chains, and it is possible that ubiquitination sites in the EB2 portion of the construct could

be masked by the fluorescent tag, thereby preventing any hypothetical normal targeting of the hybrid product to the proteosome for degradation.

Due to the observed co-ordination between microtubule and actin networks, signalling via Rho GTPases could be a potential regulatory pathway for the EB2 mechanism. Rho GTPase activation depends on GDP exchange for GTP, and thus is regulated by GEFs (guanine exchange factors) and GAPs (GTPase activating proteins), which regulate GTP exchange and hydrolysis respectively. There are a total of 20 members in the Rho family, including the best studied examples RhoA, Rac1 and Cdc42 (Vega and Ridley, 2008). Signalling is mediated through kinase cascades involving the likes of ROCK1 and ROCK2 to activate a variety of targets (Riento and Ridley, 2003), including formins such as mDia (Ishizaki et al., 2001; Palazzo et al., 2001; Wen et al., 2004). Thus, Rho family activation has been associated with the regulation of both actin and microtubules, as well as cross-talk between the two, in both cell migration and polarity, where it has been implicated in signalling to myosin-II for apical constriction (Jaffe and Hall, 2005; Krendel et al., 2002; Siegrist and Doe, 2007; Takesono et al., 2010). In particular, Rho family members control actin organisation, and can both influence, and be influenced by microtubule dynamics; for example, inhibiting RhoA has been seen to reduce stress fibres and causes increased microtubule stability and bundling (Gao et al., 2004).

Recently, follow up work has taken place to examine the potential for involvement of Rho signalling in the mechanism controlling EB2 downregulation and stable microtubule bundle formation. It was found that treatment of ARPE-19 cells with the ROCK inhibitor Y27632 was able to partially replicate the EB2 depletion phenotype; in particular, microtubules were seen to form bundles, with EB1 relocalised along the lattice. The treatment also reduced actin stress fibres, however in contrast to EB2 depletion, ACF7 did not associate with microtubules, and accordingly, there was no obvious co-alignment along actin filaments. Taken together, these results suggested activation of a Rho signalling pathway mediated through ROCK could contribute to phenotypes associated with EB2 loss, especially decreased microtubule dynamics, possible formin activation, and cortical acto-myosin controlled apical contraction (Goldspink et al., 2013b).

8.3.4: Model for EB2 function in epithelial apico-basal array formation

The various observations from this project and more recent follow up work have produced a model illustrating the importance of EB2 as a regulator of microtubule apico-basal polarisation during epithelial differentiation, within the context of the broader release and capture mechanism (Figure 8.2).

During the early phases of polarisation, EB2 expression is required to maintain the dynamic microtubule population required for initial array rearrangement. Whilst EB1 is localised as classic +TIP comets at the microtubule plus end, EB2 is expressed along the lattice of these dynamic microtubules, which grow out from the centrosome to make contact with a cortical receptor at adherens junction associated sites and form the extended radial array, as discussed earlier (Figure 8.1). Importantly, this dynamic behaviour also enables junction formation and most likely an accumulation of relevant Rho GTPase associated factors to allow for successful acto-myosin mediated apical constriction. Meanwhile, cortically localised formins trigger actin nucleation and initial elongation from apical sites (Figure 8.2 A). As previously discussed, establishment of the extended radial array allows ninein to be redistributed to cortical sites, after which cortically anchored dynein triggers microtubule release from the centrosome and translocation towards basal regions (Bellett et al., 2009; Moss et al., 2007). Crucially, at these later stages of differentiation, EB2 expression is downregulated leading to its loss from the lattice. This allows EB1 to bind along microtubules and co-ordinate with the actin-microtubule cross-linking spectraplakin ACF7. Microtubules are thus guided along extended actin cables, resulting in the formation of stable apico-basal microtubule bundles co-aligned with actin filaments (Figure 8.2 B) (Goldspink et al., 2013b).

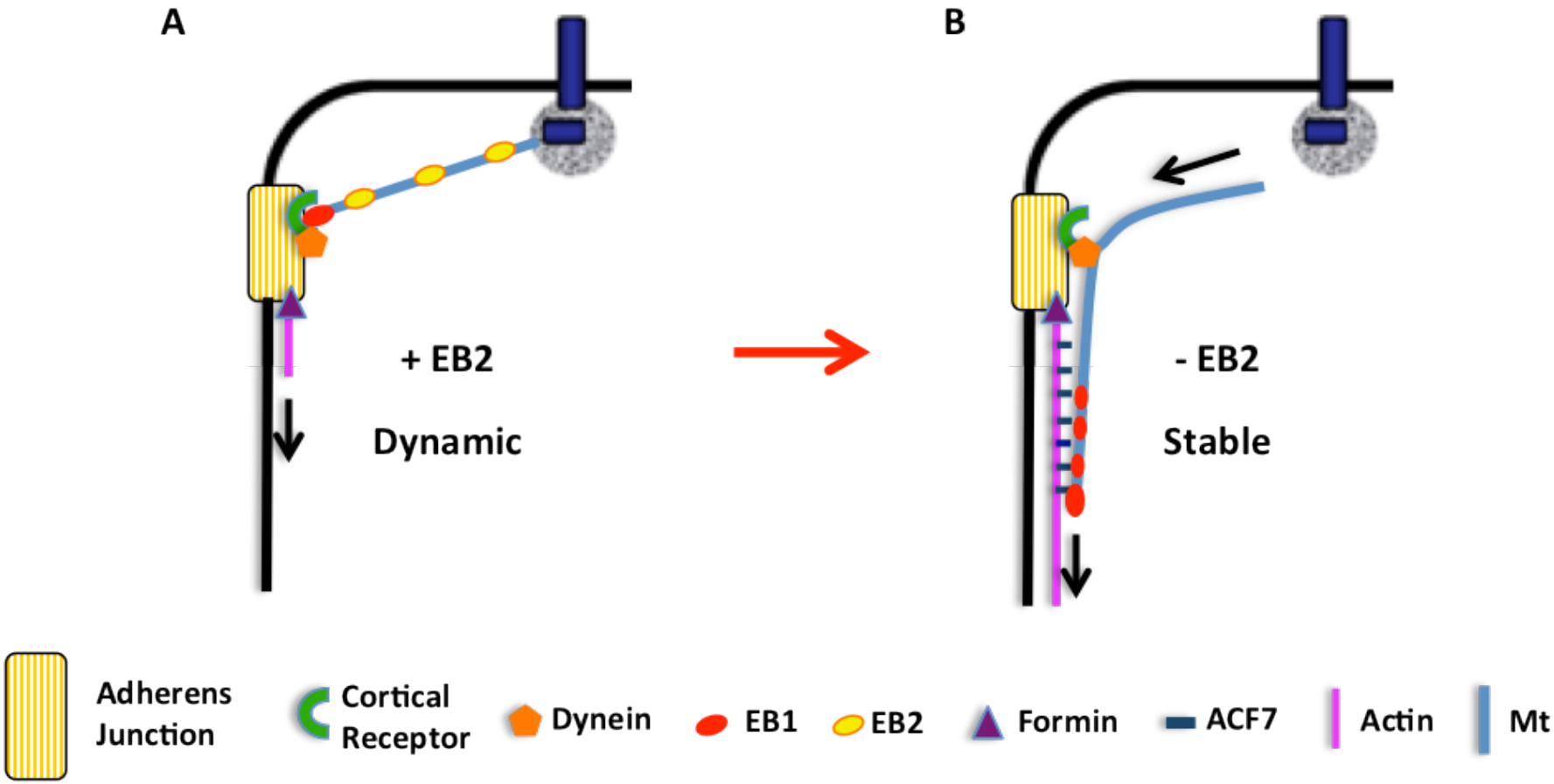

Figure 8.2 Model for EB2 in the release and capture mechanism and microtubule apico-basal bundle formation
Work from this study has contributed to the establishment of a novel role for EB2 in microtubule bundle formation during apico-basal array reorganisation via the release and capture mechanism during epithelial polarisation. **[A]** During initial stages of differentiation EB2 is expressed along the lattice, maintaining a dynamic microtubule population nucleated at the centrosome and extending out to the make contact at adherens junction associated sites, as per the release and capture mechanism. Meanwhile, formin activation at junctional sites initiates actin filament assembly and elongation. **[B]** At later stages, EB2 is downregulated, causing EB1 lattice recruitment. Dynein drives microtubules release, and these are translocated along actin cables via interactions mediated by lattice associated EB1 and ACF7 cross-linking, to form stable apico-basally orientated microtubule bundles co-aligned along actin filaments.
Taken from (Goldspink et al., 2013b)

8.4: EB2 Expression Promotes Cell Migration and Invasion

It is clear that the downregulation of EB2 plays an essential role in the formation of stabilised microtubule arrays in epithelial cells, including those of the transit amplifying region and surface epithelium of the small intestine, and most likely also the colon. It was interesting therefore to focus on what would happen if control of EB2 expression became disregulated in cancer cells, leading to persistent overexpression, and see whether this could compromise epithelial polarity. Of further interest were studies in pancreatic cancer that had illustrated an upregulation of the EB2 gene in highly invasive migratory cells (Abiatari et al., 2009). Taken together, this suggested a potential role for overexpressed EB2 in promoting EMT.

EMT is the instigating effect in cancer metastasis, and as such is an important target for potential cancer therapies. Metastasis is the key process that dictates poor tumour prognosis (Chambers et al., 2002), and thus the ability to prevent a transition to an invasive, migratory phenotype would be invaluable. As such, it is vitally important to understand how cytoskeletal factors such as EB2 overexpression could be involved in the loss of apico-basal polarity and promotion of epithelial remodelling and cell migration.

+TIPs proteins have long been associated with establishing the organisation of the microtubule network during migration; for example, APC and CLIP-170 are known to contribute to microtubule anchorage via IQGAP1 in lamellipodia (Watanabe et al., 2005). Similarly, CLASPs are also seen localised along microtubules in lamellipodia (Kumar et al., 2009), whilst EB1 has been seen coupled with APC and the formin mDia to stabilise microtubule ends and promote migration (Wen et al., 2004). As previously discussed, it is essential for efficient movement that the microtubule network is generally dynamic, but stabilised in regions extending forwards, thereby allowing trafficking of required components, whilst also maintaining correct interactions with the actin cytoskeleton (Kaverina and Straube, 2011; Ridley et al., 2003).

Here, it is demonstrated that EB2 depletion will reduce speed of random migration, whilst overexpression causes an increase in speed of movement. This is further demonstrated in scratch assays where overexpression causes an increase in individual cell velocity at the scratch leading edge that translates to a greater area of coverage during wound healing. There was also evidence of cell aggregation and basal cell extrusion from 3D cysts overexpressing EB2, suggesting EMT and a possible increase in invasive potential (Chapter VII).

It is now important to identify how EB2 is regulated, and particularly by what signalling pathways it could promote cell migration. The most likely targets are the diverse Rho GTPase family of small GTP/GDP binding proteins, which have been well associated with cell migration, with altered activity levels of the group known to be implicated in cancer development. (Ridley, 2001; Vega and Ridley, 2008). It is important to identify which family member may be involved in EB2 regulation, with an interesting initial target being RhoC. Whilst the Rho subfamily are highly related, they influence motility in different ways. For example, whilst depletion of both RhoA and RhoC reduces random migration, they give very different morphological phenotypes. Additionally, whilst RhoC loss also compromises chemotaxis and invasion through a matrix, RhoA depleted cells have been found to migrate towards a serum gradient normally, and actually cause an increase in invasive potential (Ridley, 2013). RhoC has been identified as a prognostic marker in colorectal cancer, and has been shown to increase invasion, become upregulated during EMT, and be required for cancer metastasis (Bellovin et al., 2006; Dietrich et al., 2009; Hakem et al., 2005). Intriguingly, RhoC depletion has been seen to give a somewhat similar phenotype to that seen in EB2 depleted cells in that cells become significantly more spread, as marked by an increase in cell area. Also interestingly, the formin FMNL3 has been identified as a downstream effector of RhoC involved in increased migration and invasion (Vega et al., 2011), giving a potential link to the actin and microtubule cytoskeletons, and thus the EB2 activity observed in our study. Activation of FMNL3 itself has been associated with promoting microtubule alignment and increased stability (Hetheridge et al., 2012).

8.5: Future Work & Conclusions

The exciting preliminary data indicating a possible migratory role for EB2, in addition to its examined key impact as a central regulator of microtubule apico-basal polarisation and bundling, suggests an immediate priority for further investigation is to fully examine the ability of EB2 to promote migration and invasion and potentially cause a loss of epithelial apico-basal polarity. Initially, the exact migratory behaviour pattern would be further analysed, with invasion though a matrix assessed by the inverted invasion assay, and directional migration studied by movement along a chemotactic gradient. Subsequently, it would then be vital to identify EB2 interacting partners, in order to understand its normal downregulation and activity in migratory pathways. These are most likely regulated by the Rho GTPases, with RhoC an initial target for study.

To conclude, establishment and maintenance of the apico-basal microtubule cytoskeleton is essential for the integrity of epithelial polarity. The mechanism by which microtubules are arranged into stabilised apico-basal bundles is complex and involves co-ordination with the actin cytoskeleton, with control provided by the key regulators of the microtubule plus end, the +TIPs. Disregulation of this process in cancer, especially of the colon, where differentiation processes regularly occur as cells migrate from the stem cell zone to the surface epithelium, could provide driving factors for tumour progression. In particular, compromised cortical capture following APC truncation, or altered expression patterns of the EB family member EB2 may compromise polarity and potentially trigger EMT and the promotion of the migratory, invasive phenotype critical for metastasis. Further investigations of microtubule organisation in epithelial cancers are therefore vital, and could provide various new and interesting future targets.

Appendices

Bacterial Growth Media

Lysogeny Broth (LB)

In 400ml ddH_20:

4g Tryptone

2g Yeast Extract

4g Sodium chloride

LB Agar Plates

In 300ml LB:

4.5g Agar

Melted in a microwave, appropriate antibiotic added, and poured into Petri dishes to set.

Agarose Gel Electrophoresis Solutions

0.5M EDTA

In a final volume of 500ml ddH_20:

93.1g EDTA (0.5M)

adjusted to pH 8.1

50x TAE Buffer

In a final volume of 500ml ddH_20:

141g Tris (2M)

28.5ml Glacial Acetic Acid (1M)

50ml 0.5M EDTA (50mM)

adjusted to pH 7.7

Western Blotting Solutions

Lysis Buffer

In ddH_20:

50mM HEPES

adjusted to pH 7.5

50mM Sodium chloride

1mM EDTA

10% (v/v) Glycerol

1% (v/v) Triton X-100

Sample Buffer

In ddH_20:

125mM Tris-HCl at pH 6.8

2% w/v SDS

0.02% (w/v) Bromophenol Blue

20% (v/v) Glycerol

Lower Gel Buffer

In a final volume of 250ml ddH_20:

45.375g Tris (1.5M) adjusted to pH 8.8 with Hydrocholoric acid

1g SDS (0.4% w/v)

Upper Gel Buffer

In a final volume of 250ml ddH_20:

15.125g Tris (500mM) adjusted to pH 6.8 with Hydrocholoric acid

1g SDS (0.4% w/v)

6% Lower Resolving Gel

Per gel (12ml total volume):

1.8ml 40% Acrylamide (Sigma, Poole, Dorset)

3ml Lower Gel Buffer

7.2ml ddH_2O

72µl 10% Ammonium persulphate (Sigma, Poole, Dorset)

14µl TEMED (N,N,N',N'-tetramethylethylenediamine) (Sigma, Poole, Dorset)

8% Lower Resolving Gel

Per gel (12ml total volume):

2.4ml 40% Acrylamide

3ml Lower Gel Buffer

6.6ml ddH_2O

72µl 10% Ammonium persulphate

14µl TEMED

5% Upper Stacking Gel

Per gel (8ml total volume):

1ml 40% Acrylamide

2ml Upper Gel Buffer

5ml ddH_2O

72µl 10% Ammonium persulphate

14µl TEMED

10x SDS Running Buffer

In a final volume of 5l ddH_20:

151g Tris (250mM)

720g Glycine (1.9M)

50g SDS (1% w/v)

Transfer Buffer

In a final volume of 1l:

800ml ddH_2O

2.9g Glycine (39mM)

5.8g Tris (48mM)

adjusted to pH 8.3

0.375g SDS (0.0375% w/v)

200ml Methanol (20% v/v)

PBS-T

In a final volume of 200ml PBS:

100µl Tween-20

Tris-HCl

In ddH_20:

100mM Tris

adjusted to pH 8.5 with Hydochloric acid

ECL Solution A

In 10ml Tris-HCL, pH 8.5:

45µl Coumaric acid (91mM stock solution: 0.15g in 10ml DMSO) (Sigma, Poole, Dorset)

100µl Luminol (250mM stock solution: 0.44g in 10ml DMSO) (Sigma, Poole, Dorset)

ECL Solution B

In 10ml Tris-HCL, pH 8.5:

6µl 30% Hydrogen peroxide solution

1 GFP-APC

Human APC in pEGFP-C1

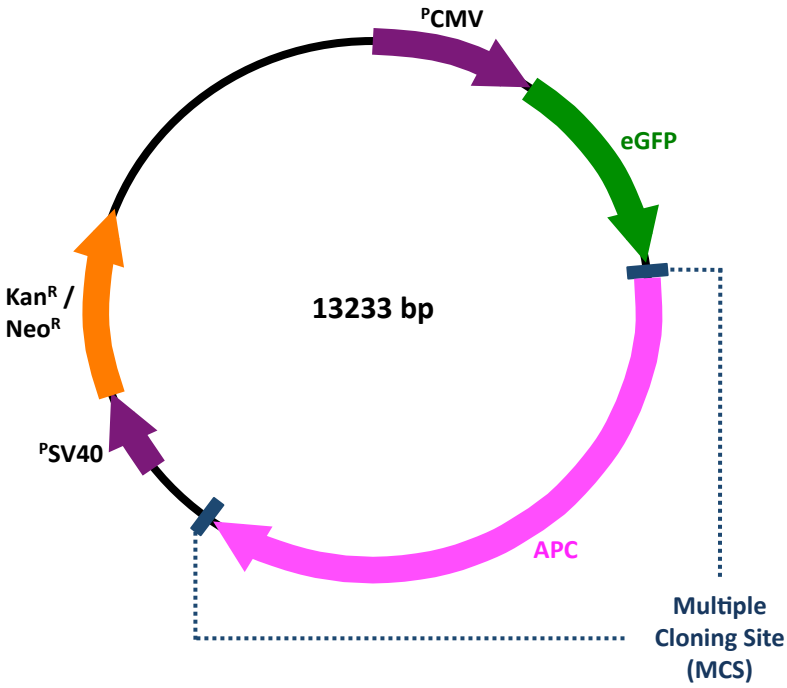

A construct map of the GFP-APC plasmid, kindly gifted by I. Nathke, University of Dundee.

2 GFP-Tubulin

Human α-tubulin in pEGFP-Tub (Clontech)

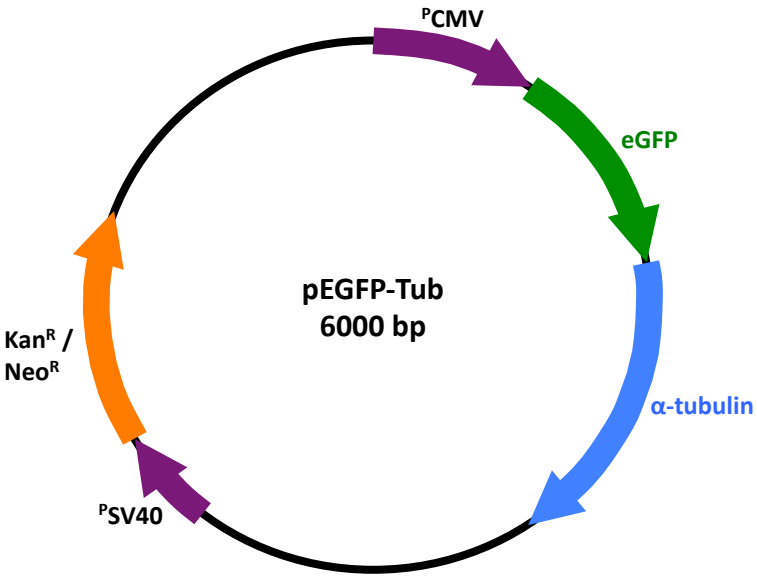

A construct map of the pEGFP-Tub plasmid, purchased from Clontech and used here to express GFP-α-tubulin in previously prepared stably expressing ARPE-19 cells.

3

pGEM®-T

Carrier vector (Promega)

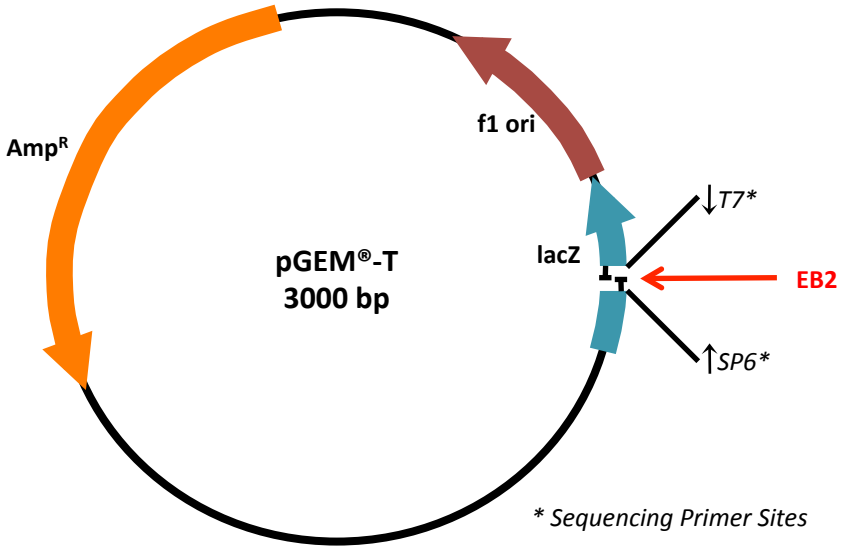

A construct map of pGEM®-T, kindly gifted by P. Powell, University of East Anglia, and used as a carrier vector in the cloning of mouse EB2 (variant 3).

4

mCherry-EB2

Mouse EB2 (variant 3) in pmCherry-C1 (Clontech)

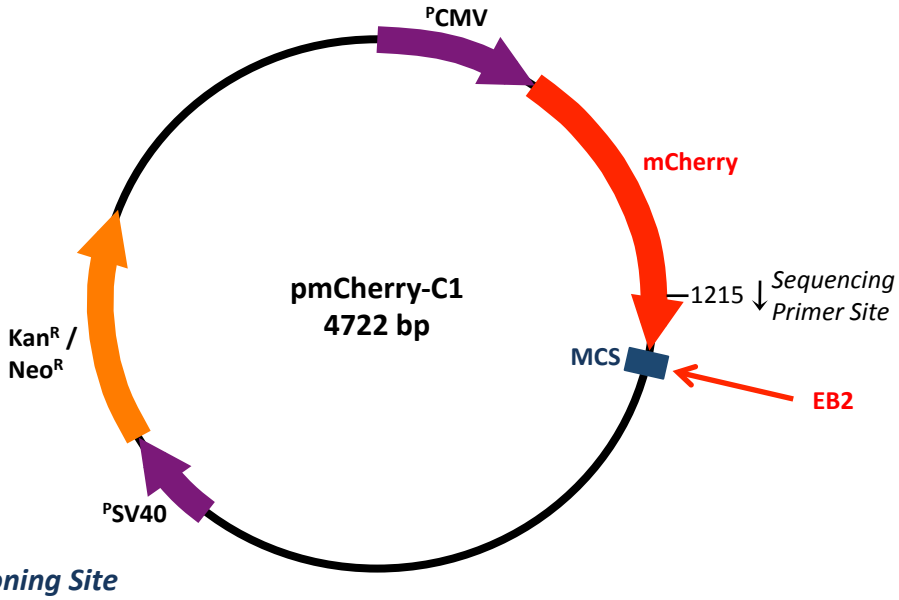

Multiple Cloning Site

```
                                    BglIII     SacI
      End mCherry  BspEI                XhoI        HindIII     EcoRI
1315   TACAAGTCCGGACTCAGATCTCGAGCTCAAGCTTCGAATTCTGCA
          KpnI          XmaI
 SalI          SacII      SmaI
 Acc1    Asp718      ApaI      BamHI            XbaI          BclI
GTCGACGGTACCGCGGGCCCGGGATCCACCGGATCTAGATAACTGATCATA   1410
```

A construct map of pmCherry-C1, kindly gifted by P. Powell, University of East Anglia, and used to directionally clone mouse EB2 (variant 3) into the MCS via the XhoI and HindIII restriction sites.

5 Mouse EB2 (MAPRE2) Transcript Variants

Variant 1: (Accession Number: NM_153058)

```
ORIGIN
        1 ggcctttgga gggcggggcc gggcacagag ctggagcaga gcgcggctgc agggtgagca
       61 gcaagcagcg gggagacaca accctccgcc ccagtcagcc accgcgtgtg ttccctctgt
      121 cgggagagcg ccaatgcccg ggccgaccca aacgttgtcc ccaaatggcg agaacaacaa
      181 cgacatcatc caggataacg ggactatcat tcctttccgg aagcacacag tgcgcgggga
      241 gcggtcctac agttgggga tggcggtcaa tgtgtattct acctcgataa cccaggagac
                                                                  … etc
Translation:

"MPGPTQTLSPNGENNNDIIQDNGTIIPFRKHTVRGERSYSWGMAVNVYSTSITQETMSRHDIIAWVNDIVSLNY
TKVEQLCSGAAYCQFMDMLFPGCISLKKVKFQAKLEHEYIHNFKLLQASFKRMNVDKVIPVEKLVKGRFQDNLDF
IQWFKKFYDANYDGKEYDPVEARQGQDAIPPPDPGEQIFNLPKKSHHANSPTAGAAKSSPASKPGSTPSRPSSAK
RASSSGSASRSDKDLETQVIQLNEQVHSLKLALEGVEKERDFYFGKLREIELLCQEHGQENDDLVQRLMEVLYAS
DEQEGQTEEPEAEEQAHDQQPQQQEEY"  => 326 Amino Acids (42 aa N term extension)
```

Variant 2: (Accession Number: NM_001162941)

```
ORIGIN
        1 tctgccctag cttaggtgca agagaagtcc agtcttgagt gaggtctaag ggacctgctt
       61 ctaatctgtg ggaaccgcgg ggtgctactt ggcggaacag gacgctagga tgaaacagat
      121 cagagatcaa cgggtaatca gaaagggtcc ccagaagcac cattcacttc aacagccagg
      181 gagagtgcct ggatgttcaa attgggga at ggcggtcaat gtgtattcta cctcgataac

Translation:

"MKQIRDQRVIRKGPQKHHSLQQPGRVPGCSNWGMAVNVYSTSITQETMSRHDIIAWVNDIVSLNYTKVEQLCSG
AAYCQFMDMLFPGCISLKKVKFQAKLEHEYIHNFKLLQASFKRMNVDKVIPVEKLVKGRFQDNLDFIQWFKKFYD
ANYDGKEYDPVEARQGQDAIPPPDPGEQIFNLPKKSHHANSPTAGAAKSSPASKPGSTPSRPSSAKRASSSGSAS
RSDKDLETQVIQLNEQVHSLKLALEGVEKERDFYFGKLREIELLCQEHGQENDDLVQRLMEVLYASDEQEGQTEE
PEAEEQAHDQQPQQQEEY"  => 317 Amino Acids (33 aa N term extension)
```

Variant 3: (Accession Number: NM_001162942)

```
ORIGIN
        1 gtggaggcgg agcgtggccg gctgaggggg tggagaaaac aaagccccca gctgtcagca
       61 gaagaaggag gcgacaacgc cggagcaggg tccccagaag caccattcac ttcaacagcc
      121 agggagagtg cctggatgtt caaattgggg aatggcggtc aatgtgtatt ctacctcgat
                                                                  … etc
Translation:

"MAVNVYSTSITQETMSRHDIIAWVNDIVSLNYTKVEQLCSGAAYCQFMDMLFPGCISLKKVKFQAKLEHEYIHN
FKLLQASFKRMNVDKVIPVEKLVKGRFQDNLDFIQWFKKFYDANYDGKEYDPVEARQGQDAIPPPDPGEQIFNLP
KKSHHANSPTAGAAKSSPASKPGSTPSRPSSAKRASSSGSASRSDKDLETQVIQLNEQVHSLKLALEGVEKERDF
YFGKLREIELLCQEHGQENDDLVQRLMEVLYASDEQEGQTEEPEAEEQAHDQQPQQQEEY"
  => 284 Amino Acids (No N term extension)
```

atgccc	N-terminal Extension	atggcg	Common Sequence	gg	Exon Boundary

6 Mouse EB2 Primer Designs

Reverse Primer (all variants)

```
… tgaccagcagccccagcagcaggaggagtactgaaccgtctcatcagctcttgacacttc …
            3′ <- tcgtcgtcctcctcatgacttcgaaccc 5′
                                    HindIII
```

Forward Primer (Variant 1):

```
          XhoI
      5′ ccgctcgagcaatgcccgggccgacccaaac -> 3′
… tctgtcgggagagcgccaatgcccgggccgacccaaacgttgtccccaaatggcgagaa …
```

Forward Primer (Variant 2):

```
          XhoI
      5′ ccgctcgaggatgaaacagatcagagatca -> 3′
… gcggaacaggacgctaggatgaaacagatcagagatcaacgggtaatcagaaagggtcc …
```

Forward Primer (Variant 3 / All Variants):

```
          XhoI
      5′ ccgctcgaggaatggcggtcaatgtgtattc -> 3′
… ggatgttcaaatggggaatggcggtcaatgtgtattctacctcgataacccaggagact …
```

KEY:

gaatgcc	**Primer Seed**
atgcccg	**CDS Template**
tga	**Stop Codon**
ccc	**Restriction Site Flanking Region**
ctcgag	**XhoI Restriction Site**
aagctt	**HindIII Restriction Site**
at	**Alternative Splice Site**

Primers were designed to clone each of the three mouse EB2 transcript variants into the XhoI and HindIII restriction sites of the pmCherry-C1 vector MCS. The alternative splice site is marked in black in the variant 3 forward primer, downstream of which each variant is identical. As such, the variant 3 primer targets all three transcript variants. To ensure the EB2 sequence is in frame with the cherry tag, two residues 5′ to the EB2 CDS were retained (red letters). Initial PCR to determine which EB2 variant was expressed by mIMCD-3 cells was performed with basic primers consisting of just the primer seeds (green). High fidelity PCR was performed with the complete primer as designed.

1 Sequencing

pGEM®-T + EB2

A Sequencing Trace

File: 1_SP6_1_1710.ab1

Geospiza
www.geospiza.com

Sample Name:	sr.3903.19	Signal Strengths:	A = 219, C = 253, G = 265, T = 277
Mobility:	KB_3730_POP7_BDTv3.mob	Lane/Cap#:	27
Spacing:	12.2284	Matrix:	n/a
Comment:	3333_19	Direction:	Native



B **BLAST Sequence Alignment**

Mouse EB2 (Mapre2) Variant 3 mRNA (NM_001162942) vs. pGEM-T + EB2 sequencing result

```
Identities = 856/857 (99%), Gaps = 0/857 (0%)
Strand=Plus/Minus

Mouse EB2  1    GAATGGCGGTCAATGTGTATTCTACCTCGATAACCCAGGAGACTATGAGCAGGCATGACA  60
               ||||||||||||||||||||||||||||||||||||||||||||||||||||||||||||
Construct  932  GAATGGCGGTCAATGTGTATTCTACCTCGATAACCCAGGAGACTATGAGCAGGCATGACA  873

Mouse EB2  61   TCATTGCATGGGTCAATGACATCGTGTCTCTAAACTACACAAAAGTGGAACAGCTCTGTT  120
               ||||||||||||||||||||||||||||||||||||||||||||||||||||||||||||
Construct  872  TCATTGCATGGGTCAATGACATCGTGTCTCTAAACTACACAAAAGTGGAACAGCTCTGTT  813

Mouse EB2  121  CAGGAGCAGCCTATTGCCAGTTCATGGACATGCTCTTCCCGGGCTGTATTAGTTTGAAGA  180
               ||||||||||||||||||||||||||||||||||||||||||||||||||||||||||||
Construct  812  CAGGAGCAGCCTATTGCCAGTTCATGGACATGCTCTTCCCGGGCTGTATTAGTTTGAAGA  753

Mouse EB2  181  AAGTAAAATTCCAAGCAAAGTTGGAGCATGAGTATATTCACAACTTTAAACTTCTGCAAG  240
               ||||||||||||||||||||||||||||||||||||||||||||||||||||||||||||
Construct  752  AAGTAAAATTCCAAGCAAAGTTGGAGCATGAGTATATTCACAACTTTAAACTTCTGCAAG  693

Mouse EB2  241  CATCCTTTAAACGGATGAATGTTGATAAGGTAATCCCAGTGGAGAAGCTGGTGAAAGGGC  300
               ||||||||||||||||||||||||||||||||||||||||||||||||||||||||||||
Construct  692  CATCCTTTAAACGGATGAATGTTGATAAGGTAATCCCAGTGGAGAAGCTGGTGAAAGGGC  633

Mouse EB2  301  GTTTCCAAGACAACCTGGATTTTATTCAGTGGTTTAAGAAGTTCTACGATGCTAACTATG  360
               |||||||||||||||||||||||||||| ||||||||||||||||||||||||||||||
Construct  632  GTTTCCAAGACAACCTGGATTTTATTCAGCGGTTTAAGAAGTTCTACGATGCTAACTATG  573

Mouse EB2  361  ACGGGAAGGAGTACGATCCTGTTGAGGCCCGACAAGGGCAAGATGCAATTCCTCCCCCTG  420
               ||||||||||||||||||||||||||||||||||||||||||||||||||||||||||||
Construct  572  ACGGGAAGGAGTACGATCCTGTTGAGGCCCGACAAGGGCAAGATGCAATTCCTCCCCCTG  513

Mouse EB2  421  ACCCTGGTGAACAGATCTTCAACCTGCCCAAGAAGTCGCACCATGCAAACTCCCCCACAG  480
               ||||||||||||||||||||||||||||||||||||||||||||||||||||||||||||
Construct  512  ACCCTGGTGAACAGATCTTCAACCTGCCCAAGAAGTCGCACCATGCAAACTCCCCCACAG  453

Mouse EB2  481  CAGGCGCGGCTAAGTCAAGTCCTGCATCTAAGCCAGGATCCACACCTTCTCGCCCCTCGT  540
               ||||||||||||||||||||||||||||||||||||||||||||||||||||||||||||
Construct  452  CAGGCGCGGCTAAGTCAAGTCCTGCATCTAAGCCAGGATCCACACCTTCTCGCCCCTCGT  393

Mouse EB2  541  CTGCCAAAAGGGCTTCATCCAGTGGCTCTGCATCCAGATCTGACAAAGATTTAGAAACGC  600
               ||||||||||||||||||||||||||||||||||||||||||||||||||||||||||||
Construct  392  CTGCCAAAAGGGCTTCATCCAGTGGCTCTGCATCCAGATCTGACAAAGATTTAGAAACGC  333

Mouse EB2  601  AGGTCATACAGCTCAACGAGCAGGTACATTCATTGAAACTCGCCCTAGAAGGTGTGGAGA  660
               ||||||||||||||||||||||||||||||||||||||||||||||||||||||||||||
Construct  332  AGGTCATACAGCTCAACGAGCAGGTACATTCATTGAAACTCGCCCTAGAAGGTGTGGAGA  273

Mouse EB2  661  AGGAGAGGGATTTCTACTTCGGGAAGTTGAGAGAGATTGAGCTGCTGTGCCAAGAACATG  720
               ||||||||||||||||||||||||||||||||||||||||||||||||||||||||||||
Construct  272  AGGAGAGGGATTTCTACTTCGGGAAGTTGAGAGAGATTGAGCTGCTGTGCCAAGAACATG  213

Mouse EB2  721  GGCAGGAGAACGATGACCTCGTGCAGCGACTAATGGAAGTGCTCTACGCTTCCGATGAAC  780
               ||||||||||||||||||||||||||||||||||||||||||||||||||||||||||||
Construct  212  GGCAGGAGAACGATGACCTCGTGCAGCGACTAATGGAAGTGCTCTACGCTTCCGATGAAC  153

Mouse EB2  781  AGGAGGGCCAAACGGAAGAGCCAGAAGCAGAGGAGCAAGCCCATGACCAGCAGCCCCAGC  840
               ||||||||||||||||||||||||||||||||||||||||||||||||||||||||||||
Construct  152  AGGAGGGCCAAACGGAAGAGCCAGAAGCAGAGGAGCAAGCCCATGACCAGCAGCCCCAGC  93

Mouse EB2  841  AGCAGGAGGAGTACTGA  857
               ||||||||||||||||
Construct  92   AGCAGGAGGAGTACTGA  76
```

C **Summary**

SP6 Primer

AGCATCAACGCGTTGGGAGCTCTCCATATGGTCGACCTGCAGGCGGCCGCGAATTCA
CTAGTGATTCCCAAGCTTTCAGTACTCCTCCTGCTGCTGGGGCTGCTGGTCATGGGC
TTGCTCCTCTGCTTCTGGCTCTTCCGTTTGGCCCTCCTGTTCATCGGAAGCGTAGAG
CACTTCCATTAGTCGCTGCACGAGGTCATCGTTCTCCTGCCCATGTTCTTGGCACAG
CAGCTCAATCTCTCTCAACTTCCCGAAGTAGAAATCCCTCTCCTTCTCCACACCTTC
TAGGGCGAGTTTCAATGAATGTACCTGCTCGTTGAGCTGTATGACCTGCGTTTCTAA
ATCTTTGTCAGATCTGGATGCAGAGCCACTGGATGAAGCCCTTTTGGCAGACGAGGG
GCGAGAAGGTGTGGATCCTGGCTTAGATGCAGGACTTGACTTAGCCGCGCCTGCTGT
GGGGGAGTTTGCATGGTGCGACTTCTTGGGCAGGTTGAAGATCTGTTCACCAGGGTC
AGGGGGAGGAATTGCATCTTGCCCTTGTCGGGCCTCAACAGGATCGTACTCCTTCCC
GTCATAGTTAGCATCGTAGAACTTCTTAAACCGCTGAATAAAATCCAGGTTGTCTTG
GAAACGCCCTTTCACCAGCTTCTCCACTGGGATTACCTTATCAACATTCATCCGTTT
AAAGGATGCTTGCAGAAGTTTAAAGTTGTGAATATACTCATGCTCCAACTTTGCTTG
GAATTTTACTTTCTTCAAACTAATACAGCCCGGGAAGAGCATGTCCATGAACTGGCA
ATAGGCTGCTCCTGAACAGAGCTGTTCCACTTTTGTGTAGTTTAGAGACACGATGTC
ATTGACCCATGCAATGATGTCATGCCTGCTCATAGTCTCCTGGGTTATCGAGGTAGA
ATACACATTGACCGCCATTCCTCGAGCGGAATCGAATTCCCGCGGCCGCCATGGCGG
CCGGGAGCATGCGACGTCGGGCCCAATTCGCCCTATAGTGAGTCGTATTACAATTCA
CTGGGCCGTCGTTTTACAACGTCGTGACTGGGAAAACCCTGGCGTTACCCAACTTAA
TCGCCTTGCAGCACATCCCCCTTTCGCCAGCTGGCGTAATAGCGAAGAGGCCCGCAC
CGATCGCCCTTCCCACAGTGCGCAGCCTGAATGCGAATGGACGCGCCCTGTAGCGCG
CATAGCGCGCGTGTGTGTTACGCGCAGCGTGACGCTACCACTGCAGGCGCCTAGCGC
CGGCTCTTCGCTTTCTCCCTCATCTCGCACGTTCGCGCTTCCCGTCAGGCTCTAAAT
CGGGTCCTAAGATTCGATTTATGCTACGACTCGACCAAAACTGCATAAGGGTA

KEY:

ATGCCCG	**EB2 CDS**
CTCGAG	**XhoI Restriction Site**
AAGCTT	**HindIII Restriction Site**
CCC	**Restriction Site Flanking Region**
G	**Deviation from Expected Sequence**

Figure S1 pGEM®-T + EB2 carrier vector sequencing data
The ligated pGEM®-T + EB2 carrier vector was sequenced through the insert via the SP6 sequencing primer by Genome Enterprise Limited™ (Norwich). **(A)** Sequencing trace, presented by FinchTV software (Geospiza). **(B)** BLAST alignment of the sequencing result against the mRNA transcript of mouse EB2 variant 3. **(C)** Summary of the sequencing result revealing the full cDNA PCR product has been successfully ligated into the plasmid (note the construct is orientated in reverse in its 3' -> 5' direction), with a single base deviation from the expected sequnce at nucleotide 328 of the EB2 CDS, base 429 of the transcript (479T>C).

pmCherry-C1 + EB2

A **Sequencing Trace**

File: plt11231_D09_sr.4033.21_073.ab1

Geospiza
www.geospiza.com

Sample Name:	sr.4033.21	Signal Strengths:	A = 104, C = 80, G = 107, T = 86
Mobility:	KB_3730_POP7_BDTv3.mob	Lane/Cap#:	73
Spacing:	12.5212	Matrix:	n/a
Comment:	3333_21	Direction:	Native

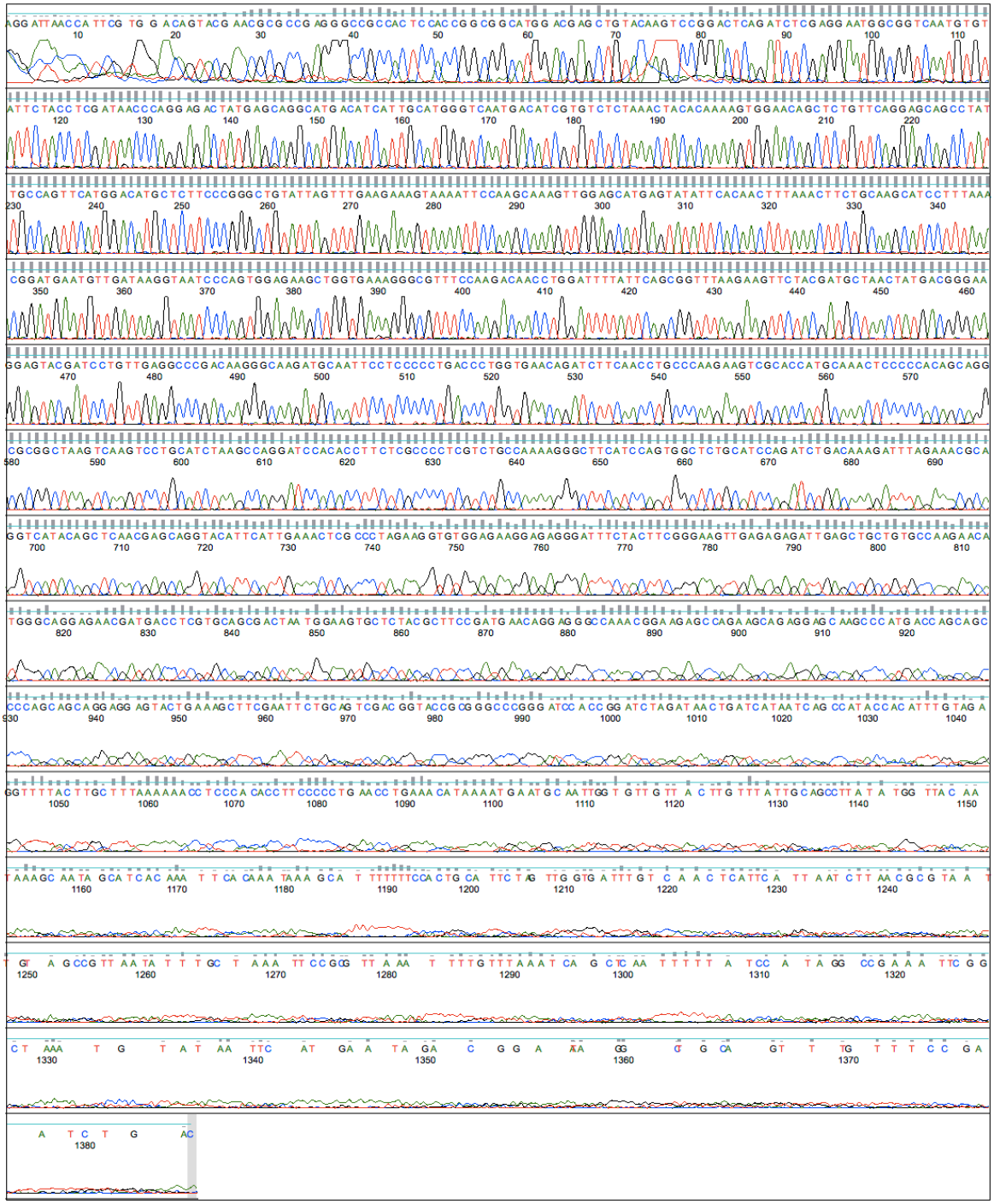

B **BLAST Sequence Alignment**

Mouse EB2 (Mapre2) Variant 3 mRNA (NM_001162942) vs. pmCherry-C1 + EB2 sequencing result

```
Identities = 856/857 (99%), Gaps = 0/857 (0%)
Strand=Plus/Plus

Construct  96   GAATGGCGGTCAATGTGTATTCTACCTCGATAACCCAGGAGACTATGAGCAGGCATGACA  155
               ||||||||||||||||||||||||||||||||||||||||||||||||||||||||||||
Mouse EB2  1    GAATGGCGGTCAATGTGTATTCTACCTCGATAACCCAGGAGACTATGAGCAGGCATGACA  60

Construct  156  TCATTGCATGGGTCAATGACATCGTGTCTCTAAACTACACAAAAGTGGAACAGCTCTGTT  215
               ||||||||||||||||||||||||||||||||||||||||||||||||||||||||||||
Mouse EB2  61   TCATTGCATGGGTCAATGACATCGTGTCTCTAAACTACACAAAAGTGGAACAGCTCTGTT  120

Construct  216  CAGGAGCAGCCTATTGCCAGTTCATGGACATGCTCTTCCCGGGCTGTATTAGTTTGAAGA  275
               ||||||||||||||||||||||||||||||||||||||||||||||||||||||||||||
Mouse EB2  121  CAGGAGCAGCCTATTGCCAGTTCATGGACATGCTCTTCCCGGGCTGTATTAGTTTGAAGA  180

Construct  276  AAGTAAAATTCCAAGCAAAGTTGGAGCATGAGTATATTCACAACTTTAAACTTCTGCAAG  335
               ||||||||||||||||||||||||||||||||||||||||||||||||||||||||||||
Mouse EB2  181  AAGTAAAATTCCAAGCAAAGTTGGAGCATGAGTATATTCACAACTTTAAACTTCTGCAAG  240

Construct  336  CATCCTTTAAACGGATGAATGTTGATAAGGTAATCCCAGTGGAGAAGCTGGTGAAAGGGC  395
               ||||||||||||||||||||||||||||||||||||||||||||||||||||||||||||
Mouse EB2  241  CATCCTTTAAACGGATGAATGTTGATAAGGTAATCCCAGTGGAGAAGCTGGTGAAAGGGC  300

Construct  396  GTTTCCAAGACAACCTGGATTTTATTCAGCGGTTTAAGAAGTTCTACGATGCTAACTATG  455
               |||||||||||||||||||||||||||| ||||||||||||||||||||||||||||||
Mouse EB2  301  GTTTCCAAGACAACCTGGATTTTATTCAGTGGTTTAAGAAGTTCTACGATGCTAACTATG  360

Construct  456  ACGGGAAGGAGTACGATCCTGTTGAGGCCCGACAAGGGCAAGATGCAATTCCTCCCCCTG  515
               ||||||||||||||||||||||||||||||||||||||||||||||||||||||||||||
Mouse EB2  361  ACGGGAAGGAGTACGATCCTGTTGAGGCCCGACAAGGGCAAGATGCAATTCCTCCCCCTG  420

Construct  516  ACCCTGGTGAACAGATCTTCAACCTGCCCAAGAAGTCGCACCATGCAAACTCCCCCACAG  575
               ||||||||||||||||||||||||||||||||||||||||||||||||||||||||||||
Mouse EB2  421  ACCCTGGTGAACAGATCTTCAACCTGCCCAAGAAGTCGCACCATGCAAACTCCCCCACAG  480

Construct  576  CAGGCGCGGCTAAGTCAAGTCCTGCATCTAAGCCAGGATCCACACCTTCTCGCCCCTCGT  635
               ||||||||||||||||||||||||||||||||||||||||||||||||||||||||||||
Mouse EB2  481  CAGGCGCGGCTAAGTCAAGTCCTGCATCTAAGCCAGGATCCACACCTTCTCGCCCCTCGT  540

Construct  636  CTGCCAAAAGGGCTTCATCCAGTGGCTCTGCATCCAGATCTGACAAAGATTTAGAAACGC  695
               ||||||||||||||||||||||||||||||||||||||||||||||||||||||||||||
Mouse EB2  541  CTGCCAAAAGGGCTTCATCCAGTGGCTCTGCATCCAGATCTGACAAAGATTTAGAAACGC  600

Construct  696  AGGTCATACAGCTCAACGAGCAGGTACATTCATTGAAACTCGCCCTAGAAGGTGTGGAGA  755
               ||||||||||||||||||||||||||||||||||||||||||||||||||||||||||||
Mouse EB2  601  AGGTCATACAGCTCAACGAGCAGGTACATTCATTGAAACTCGCCCTAGAAGGTGTGGAGA  660

Construct  756  AGGAGAGGGATTTCTACTTCGGGAAGTTGAGAGAGATTGAGCTGCTGTGCCAAGAACATG  815
               ||||||||||||||||||||||||||||||||||||||||||||||||||||||||||||
Mouse EB2  661  AGGAGAGGGATTTCTACTTCGGGAAGTTGAGAGAGATTGAGCTGCTGTGCCAAGAACATG  720

Construct  816  GGCAGGAGAACGATGACCTCGTGCAGCGACTAATGGAAGTGCTCTACGCTTCCGATGAAC  875
               ||||||||||||||||||||||||||||||||||||||||||||||||||||||||||||
Mouse EB2  721  GGCAGGAGAACGATGACCTCGTGCAGCGACTAATGGAAGTGCTCTACGCTTCCGATGAAC  780

Construct  876  AGGAGGGCCAAACGGAAGAGCCAGAAGCAGAGGAGCAAGCCCATGACCAGCAGCCCCAGC  935
               ||||||||||||||||||||||||||||||||||||||||||||||||||||||||||||
Mouse EB2  781  AGGAGGGCCAAACGGAAGAGCCAGAAGCAGAGGAGCAAGCCCATGACCAGCAGCCCCAGC  840

Construct  936  AGCAGGAGGAGTACTGA  952
               ||||||||||||||||||
Mouse EB2  841  AGCAGGAGGAGTACTGA  857
```

C **Summary**

pmCherry-C1-1215-Forseq Primer

AGGATTAACCATTCGTGGACAGTACGAACGCGCCGAGGGCCGCCACTCCACCGGCGG
CATGGACGAGCTGTACAAGTCCGGACTCAGATCTCGAGGAATGGCGGTCAATGTGTA
TTCTACCTCGATAACCCAGGAGACTATGAGCAGGCATGACATCATTGCATGGGTCAA
TGACATCGTGTCTCTAAACTACACAAAAGTGGAACAGCTCTGTTCAGGAGCAGCCTA
TTGCCAGTTCATGGACATGCTCTTCCCGGGCTGTATTAGTTTGAAGAAAGTAAAATT
CCAAGCAAAGTTGGAGCATGAGTATATTCACAACTTTAAACTTCTGCAAGCATCCTT
TAAACGGATGAATGTTGATAAGGTAATCCCAGTGGAGAAGCTGGTGAAAGGGCGTTT
CCAAGACAACCTGGATTTTATTCAGCGGTTTAAGAAGTTCTACGATGCTAACTATGA
CGGGAAGGAGTACGATCCTGTTGAGGCCCGACAAGGGCAAGATGCAATTCCTCCCCC
TGACCCTGGTGAACAGATCTTCAACCTGCCCAAGAAGTCGCACCATGCAAACTCCCC
CACAGCAGGCGCGGCTAAGTCAAGTCCTGCATCTAAGCCAGGATCCACACCTTCTCG
CCCCTCGTCTGCCAAAAGGGCTTCATCCAGTGGCTCTGCATCCAGATCTGACAAAGA
TTTAGAAACGCAGGTCATACAGCTCAACGAGCAGGTACATTCATTGAAACTCGCCCT
AGAAGGTGTGGAGAAGGAGAGGGATTTCTACTTCGGGAAGTTGAGAGAGATTGAGCT
GCTGTGCCAAGAACATGGGCAGGAGAACGATGACCTCGTGCAGCGACTAATGGAAGT
GCTCTACGCTTCCGATGAACAGGAGGGCCAAACGGAAGAGCCAGAAGCAGAGGAGCA
AGCCCATGACCAGCAGCCCCAGCAGCAGGAGGAGTACTGAAAGCTTCGAATTCTGCA
GTCGACGGTACCGCGGGCCCGGGATCCACCGGATCTAGATAACTGATCATAATCAGC
CATACCACATTTGTAGAGGTTTTACTTGCTTTAAAAAACCTCCCACACCTTCCCCCT
GAACCTGAAACATAAAATGAATGCAATTGGTGTTGTTACTTGTTTATTGCAGCCTTA
TATGGTTACAATAAAGCAATAGCATCACAAATTCACAAATAAAGCATTTTTTTCCAC
TGCATTCTAGTTGGTGATTTGTCAACTCATTCATTAATCTTAACGCGTAATGTAGCC
GTTAATATTTGCTAAATTCCGCGTTAAATTTTGTTTAAATCAGCTCAATTTTTATCC
ATAGGCCGAAATTCGGCTAAATGTATAATTCATGAATAGACGGAATAGGCTGCAGTT
TGTTTCCGAATCTGAC

KEY:

ATGCCCG	**EB2 CDS**
CTCGAG	**XhoI Restriction Site**
AAGCTT	**HindIII Restriction Site**
GTACAAG	**mCherry Sequence**
C	**Deviation from Expected Sequence**

Figure S2 pmCherry-C1 + EB2 construct sequencing data
The pmCherry-C1 purified clones were sequenced through the insert via the pmCherry-C1-1215-Forseq sequencing primer by Genome Enterprise Limited™ (Norwich). **(A)** Sequencing trace, presented by FinchTV software (Geospiza). **(B)** BLAST alignment of the sequencing result against the mRNA transcript of mouse EB2 variant 3. **(C)** Summary of the sequencing result revealing the full cDNA PCR product has been successfully ligated into the plasmid in frame with the end of the mCherry sequence.

Figure S3 Cell Cycle Analysis Expt 2: EB2 depletion causes an accumulation of cells in sub G1
Scramble and EB2 siRNA treated and untreated control samples were stained with Propidium iodide 96 hours post transfection, and analysed for DNA content by flow cytometry over two runs per condition (>15,000 cells per run, N=2). Cell cycle distribution data was fitted in FloJo software using the Watson Pragmatic model to define cell cycle phases for each run, and used to calculate the average percentage of cells in each phase. Statistical differences between treatments were analysed by one-way ANOVA with Tukey's multiple comparisons test for each phase. Once again there was a significant increase in the percentage of cells in sub G1 on EB2 depletion, with indications of possible S phase arrest. Presence of any siRNA effected the cell cycle, as evidenced by the significant decrease in percentage of cells in G1 and increase in cells in S phase when comparing scramble to control conditions. Depletion of EB2 appears to enhance these effects.

2

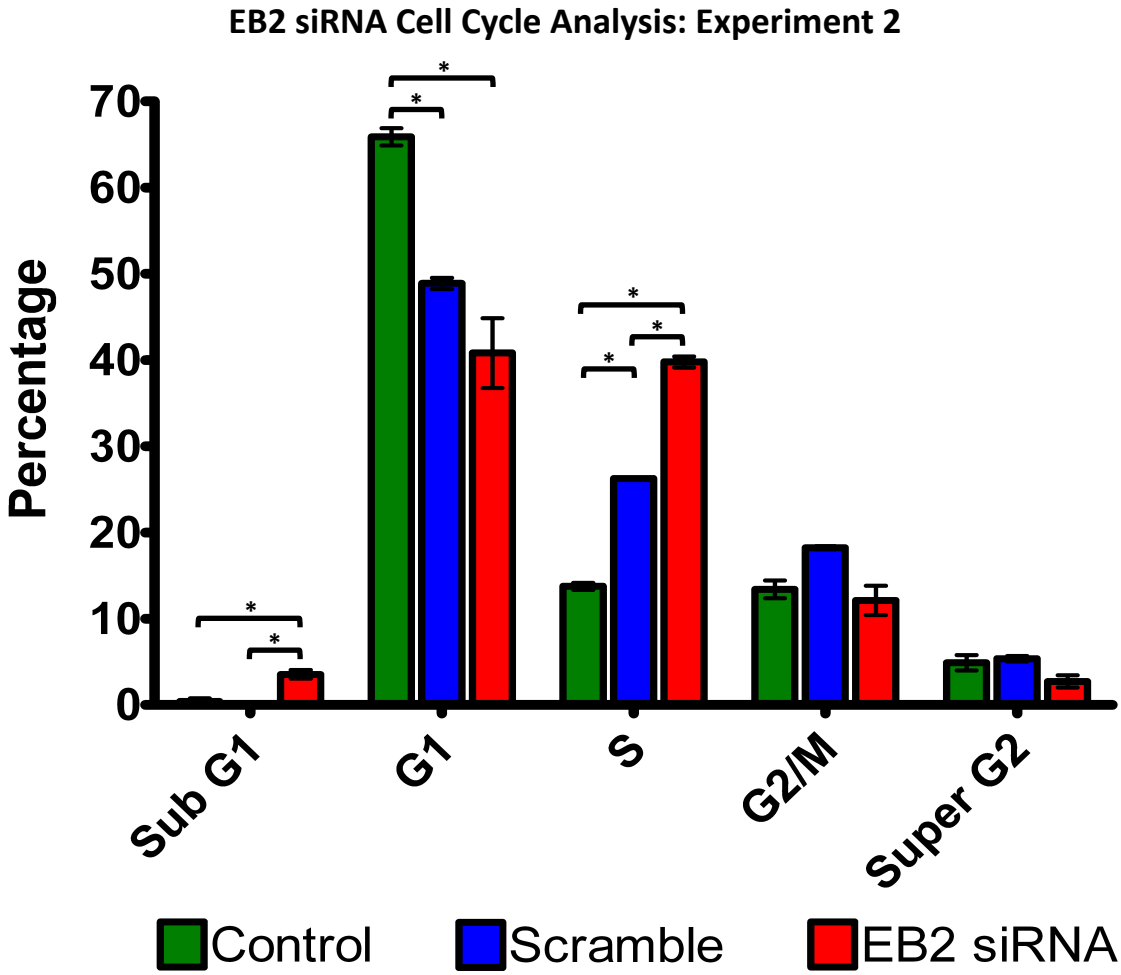

Treatment	N	Phase	Mean ± SEM (%)
Control	2	Sub G1	0.39 ± 0.4
		G1	65.88 ± 1.0
		S	13.75 ± 0.4
		G2/M	13.39 ± 1.0
		Super G2	4.88 ± 0.9
Scramble	2	Sub G1	0.11 ± 0.1
		G1	48.89 ± 0.7
		S	26.27 ± 0.1
		G2/M	18.23 ± 0.2
		Super G2	5.36 ± 0.3
EB2 siRNA	2	Sub G1	3.54 ± 0.5
		G1	40.81 ± 4.1
		S	39.78 ± 0.6
		G2/M	12.11 ± 1.7
		Super G2	2.72 ± 0.7

3 Movies

Chapter VI

Movie S1 Microtubule dynamics in a scramble treated ARPE-19 cell
Widefield fluorescent time-lapse movie of a representative peripheral 12.5x12.5µm region of a scramble treated ARPE-19 cell stably expressing GFP-α-tubulin, 96 hours after siRNA treatment. Frames were taken every 3 seconds over a 3 minute period, and are replayed at 5 frames per second. The plus ends of analysed microtubules are marked (red dots). Note the highly dynamic behaviour of the microtubules.

Movie S2 Microtubule dynamics in an EB2 siRNA treated ARPE-19 cell
Widefield fluorescent time-lapse movie of a representative peripheral 12.5x12.5µm region of an EB2 siRNA depleted ARPE-19 cell stably expressing GFP-α-tubulin, 96 hours after siRNA treatment. Frames were taken every 3 seconds over a 3 minute period, and are replayed at 5 frames per second. The plus ends of analysed microtubules are marked (red dots). Note how microtubule ends spend a significant portion of time in a paused state, with relatively few shrinking events.

Movie S3 Cell division in scramble treated ARPE-19 cells
Phase contrast time-lapse movie of scramble treated ARPE-19 cells over a 48 hour time period between 72 and 120 hours after siRNA treatment. Frames were taken every 10 minutes, and are replayed at 10 frames per second. Note the many normal mitotic events that occur throughout.

Movie S4 EB2 siRNA treated ARPE-19 cells are able to divide
Phase contrast time-lapse movie of EB2 siRNA depleted ARPE-19 cells over a 48 hour time period between 72 and 120 hours after siRNA treatment. Frames were taken every 10 minutes, and are replayed at 10 frames per second. Cells are noticeably larger compared to scramble treated cells, and are able to undergo successful mitosis; in particular note the large cells that divide in the bottom left at approximately 11s (92 hours) and middle left at approximately 27s (118 hours) into the movie. Also note the many cells that die, particularly in the second half of the movie.

Movie S5 EB2 depletion causes cell death in division
Phase contrast time-lapse movie of EB2 siRNA depleted ARPE-19 cells over a 48 hour time period between 72 and 120 hours after siRNA treatment. Frames were taken every 10 minutes, and are replayed at 10 frames per second. Several cells successfully divide throughout, whilst others appear to die. Note in particular the large cell in the centre of the frame, which gradually increases in size over the course of the movie, before contracting up to divide at approximately 18s (102 hours) into the movie. Two buds can be briefly observed, before the cell is seen to die.

Chapter VII

Movie S6 Cell tracking in subconfluent control MDCK-II cells
Time-lapse movie of the combined tracking traces for 100 untreated control MDCK-II cells, taken from 20 separate areas. For each cell, position was tracked for each frame of a 16 hour time-lapse experiment with images taken every 10 minutes using a x10 objective, and movies replayed at 10 frames per second. Dots represent current position of cells in any frame, whilst lines indicate the path the cell has taken. Position data for all cells were combined, and FIJI (Image J) software used to prepare the traces. Note in particular the relative lack of movement in many of the cells analysed.

Movie S7 Cell tracking in subconfluent empty vector expressing MDCK-II cells
Time-lapse movie of the combined tracking traces for 100 MDCK-II cells stably expressing empty pmCherry-C1, taken from 20 separate areas. For each cell, position was tracked for each frame of a 16 hour time-lapse experiment with images taken every 10 minutes using a x10 objective, and movies replayed at 10 frames per second. Dots represent current position of cells in any frame, whilst lines indicate the path the cell has taken. Position data for all cells were combined, and FIJI (Image J) software used to prepare the traces. Traces appear generally similar to those prepared for control cells.

Movie S8 Cell tracking in subconfluent EB2 overexpressing MDCK-II cells
Time-lapse movie of the combined tracking traces for 100 MDCK-II cells stably overexpressing mCherry-EB2, taken from 20 separate areas. For each cell, position was tracked for each frame of a 16 hour time-lapse experiment with images taken every 10 minutes using a x10 objective, and movies replayed at 10 frames per second. Dots represent current position of cells in any frame, whilst lines indicate the path the cell has taken. Position data for all cells were combined, and FIJI (Image J) software used to prepare the traces. Note how cells generally appear to travel over a longer path and the relative lack of cells demonstrating negligible position changes, when compared to control or empty vector traces.

Movie S9 Cell tracking in subconfluent scramble siRNA treated ARPE-19 cells
Time-lapse movie of the combined tracking traces for 60 scramble siRNA treated ARPE-19 cells, taken from 15 separate areas, beginning 72 hours after initial siRNA treatment. For each cell, position was tracked for each frame of a 16 hour time-lapse experiment with images taken every 10 minutes using a x20 objective, and movies replayed at 10 frames per second. Dots represent current position of cells in any frame, whilst lines indicate the path the cell has taken. Position data for all cells were combined, and FIJI (Image J) software used to prepare the traces. Note the degree of movement displayed by the cells tracked.

Movie S10 Cell tracking in subconfluent EB2 siRNA treated ARPE-19 cells
Time-lapse movie of the combined tracking traces for 60 EB2 siRNA treated ARPE-19 cells, taken from 30 separate areas, beginning 72 hours after initial siRNA treatment. For each cell, position was tracked for each frame of a 16 hour time-lapse experiment with images taken every 10 minutes using a x20 objective, and movies replayed at 10 frames per second. Dots represent current position of cells in any frame, whilst lines indicate the path the cell has taken. Position data for all cells were combined, and FIJI (Image J) software used to prepare the traces. Note how cells generally move at a slower rate, remaining in the same locations for greater lengths of time compared to scramble treated cells.

Movie S11 Scratch assay and cell tracking in control MDCK-II cells
Phase contrast time-lapse movie of a wound healing assay from a representative region of a control MDCK scratch. Images were taken every 10 minutes over a 10 hour time period using a x10 objective, and are replayed at 10 frames per second. Overlay lines indicate tracking traces of 8 individual cells at the edge of the wound for the course of the time-lapse. Dots represent current position of cells in any frame, whilst lines indicate the path the cell has taken. FIJI (Image J) software was used to prepare the traces. Note the degree of wound closure, and the length of the tracking lines.

Movie S12 Scratch assay and cell tracking in empty vector expressing MDCK-II cells
Phase contrast time-lapse movie of a wound healing assay from a representative region of a pmCherry-C1 stably expressing MDCK scratch. Images were taken every 10 minutes over a 10 hour time period using a x10 objective, and are replayed at 10 frames per second. Overlay lines indicate tracking traces of 8 individual cells at the edge of the wound for the course of the time-lapse. Dots represent current position of cells in any frame, whilst lines indicate the path the cell has taken. FIJI (Image J) software was used to prepare the traces. Note the degree of wound closure, and the length of the tracking lines.

Movie S13 Scratch assay and cell tracking in EB2 overexpressing MDCK-II cells
Phase contrast time-lapse movie of a wound healing assay from a representative region of an mCherry-EB2 stably overexpressing MDCK scratch. Images were taken every 10 minutes over a 10 hour time period using a x10 objective, and are replayed at 10 frames per second. Overlay lines indicate tracking traces of 8 individual cells at the edge of the wound for the course of the time-lapse. Dots represent current position of cells in any frame, whilst lines indicate the path the cell has taken. FIJI (Image J) software was used to prepare the traces. Note the increased degree of wound closure, and the greater length of the tracking lines compared to control and empty vector expressing conditions.

Abbreviations

+TIP	Plus-end tracking protein
2D	Two dimensional
3D	Three dimensional
AAA	ATPases associated with diverse cellular activities
ABP	Actin binding protein
ACF7 (MACF1)	Actin cross-linking factor 7 (Microtubule-actin crosslinking factor 1)
ADF	Actin de-polymerisation factor
ADP	Adenosine-5'-diphosphate
AMPK	5' adenosine monophosphate activated protein kinase
APC	Adenomatous polyposis coli
aPKC	Atypical protein kinase C
Arp	Actin related protein
ARPE	Retinal pigmented epithelium
ATP	Adenosine-5'-triphosphate
BBS4	Bardet-Biedl syndrome 4
BCA	Bicinchoninic acid
BRCA 1/2	Breast cancer type 1/2 susceptibility protein
BSA	Bovine serum albumin
β-TrCP	Beta-transducin repeat containing E3 ubiqiuitin protein ligase
cAMP	Cyclic adenosine monophosphate
CAP-Gly	Cytoskeleton-associated protein glycine rich
CCD	Charge-coupled device
CCP	Complement control protein
Cdc42	Cell division control protein 42
CDKs	Cyclin dependent kinases
cDNA	Complementary DNA
cGMP	Cyclic guanosine monophosphate
CH	Calponin homology domain
ch-TOG	(CKAP5) Cytoskeleton associated protein 5
CIN	Chromosomal instability
CK1α	Casein kinase 1α
CLASP 1/2	CLIP associating protein 1/2
CLIP-115/170	Cytoplasmic linker associated protein 115/170
CNap-1	Centrosomal Nek-2 associated protein 1
DABCO	1,4-diazabicyclo[2.2.2]octane
DAPI	4',6-diamadino-2-phenylindole
ddH_2O	Double distilled water
DLG-1	Discs large protein 1
DMEM	Dulbecco's modified eagle medium

DMEM/F-12	Dulbecco's modified eagle medium/nutrient mixture F-12
DMSO	Dimethylsulphoxide
DNA	Deoxyribonucleic acid
dNTPs	Deoxynucleotide triphosphates
DTT	Dithiothreitol
EB	End binding protein
EB1	End binding protein 1
EB2 (RP1)	End binding protein 2
EB3 (EBF3)	End binding protein 3 (EB1 family member 3)
EBH	End binding homology domain
ECL	Electrochemical luminescence
EMT	Epithelial-mesenchymal transition
E-cadherin	Epithelial cadherin
EDTA	Ethylenediaminetetraacetic acid
FACS	Fluorescence-activated cell sorting
F-actin	Filamentous actin
FAP	Familial adenomatous polyposis
FBS	Foetal bovine serum
FGF	Fibroblast growth factor family
FH2	Formin homology domain 2
FMNL3	Formin like protein 3
G-actin	Globular actin
GAP	GTPase activating protein
GAS2	Growth arrest specific protein 2
GCP	γ tubulin complex component
GDP	Guanosine-5'-diphosphate
GEF	Guanine nucleotide exchange factor
GFP	Green fluorescent protein
GSK3β	Glycogen synthase kinase 3β
GTP	Guanosine-5'-triphosphate
GTPγS	Guanosine-5'-O-[gamma-thio]triphosphate
γTuRC	γ tubulin ring complex
γTuSC	γ tubulin small complex
H&E	Haematoxylin and eosin staining
HDAC6	Histone deacetylase 6
HEPES	N-2-hydroxyethylpiperazine-N-2-ethane sulphonic acid
IQGAP1	IQ motif containing GTPase activating protein
JAMs	Junction adhesion molecules
KAP3	Kinesin associated protein 3
KIF	Kinesin super family
LB	Lysogeny broth

LED	Light emitting diode
LIS1	Lissencephaly protein 1
LKB1	Liver kinase B1
LRP	Lipoprotein receptor related protein
LSM	Laser scanning microscope
MAP	Microtubule associated protein
MAPRE 1/2/3	Microtubule-associated protein RP/EB family member 1/2/3
MARK	Microtubule affinity regulating kinase
MCAK	Mitotic centromere-associated kinesin
MCS	Multiple cloning site
MDCK	Madin-darby canine kidney
mDia	Diaphanous-related formin
MEC17	Mechanosensory abnormality 17
MEM	Minimum essential media
MET	Mesenchymal-epithelial transition
mIMCD	Mouse terminal inner medullary connecting duct
MIN	Mismatch repair deficiency
MMPs	Matrix metalloproteases
MTOC	Microtubule organising centre
mTOR	Mammalian target of rapamycin
NEAA	Non-essential amino acids
Nek2	NIMA (never in mitosis gene A) related kinase A
Nlp	Ninein like protein
PAGE	Polyacrylamide gel electrophoresis
PAR-1/3/6	Partitioning defective 1/3/6 homolog
PBS	Phosphate buffered saline
PCM	Pericentriolar material
PCR	Polymerase chain reaction
PI	Propidium iodide
Plk1	Polo-like kinase 1
PMT	Post-translational modification
PP1	Protein phosphatase 1
PSF	Point spread function
RCF	Relative centrifugal force
RFP	Red fluorescent protein
RNA	Ribonucleic acid
ROCK	Rho associated kinase
RT-PCR	Reverse transcription polymerase chain reaction
SDS	Sodium dodecyl sulphate
SIRT2	Human Sir2
siRNA	Small interfering RNA

SLAIN2	SLAIN motif family, member 2
SNP	Single nucleotide polymorphism
SOC	Super optimal broth
SPB	Spindle pole body
TAE Buffer	Tris-acetate-EDTA buffer
TCF	T-cell factor
TEM	Transmission electron microscopy
TGF-β	Transforming growth factor β
TOG	Tumour-overexpressed gene
Trp	Tryptophan
TTL	Tubulin-tyrosine ligase
TTLL	Tubulin-tyrosine ligase-like
UV	Ultraviolet
v/v	Volume/volume
w/v	Weight/volume
XMAP215	Xenopus microtubule associated protein 215
ZO-1/2/3	Zonula occludens 1/2/3

References

Abal, M., M. Piel, V. Bouckson-Castaing, M. Mogensen, J.B. Sibarita, and M. Bornens. 2002. Microtubule release from the centrosome in migrating cells. *Journal of Cell Biology*. 159:731-737.

Abiatari, I., S. Gillen, T. DeOliveira, T. Klose, K. Bo, N.A. Giese, H. Friess, and J. Kleeff. 2009. The microtubule-associated protein MAPRE2 is involved in perineural invasion of pancreatic cancer cells. *International Journal of Oncology*. 35:1111-1116.

Akella, J.S., D. Wloga, J. Kim, N.G. Starostina, S. Lyons-Abbott, N.S. Morrissette, S.T. Dougan, E.T. Kipreos, and J. Gaertig. 2010. MEC-17 is an α-tubulin acetyltransferase. *Nature*. 467:218-222.

Akhmanova, A., C.C. Hoogenraad, K. Drabek, T. Stepanova, B. Dortland, T. Verkerk, W. Vermeulen, B.M. Burgering, C.I. De Zeeuw, F. Grosveld, and N. Galjart. 2001. CLASPs are CLIP-115 and -170 associating proteins involved in the regional regulation of microtubule dynamics in motile fibroblasts. *Cell*. 104:923-935.

Akhmanova, A., and M.O. Steinmetz. 2008. Tracking the ends: A dynamic protein network controls the fate of microtubule tips. *Nature Reviews Molecular Cell Biology*. 9:309-322.

Akhmanova, A., and M.O. Steinmetz. 2010. Microtubule +TIPs at a glance. *Journal of Cell Science*. 123:3415-3419.

Akhmanova, A., and Michel O. Steinmetz. 2011. Microtubule End Binding: EBs Sense the Guanine Nucleotide State. *Current Biology*. 21:R283-R285.

Alberts, B. 2002. Molecular biology of the cell. Garland Science, New York.

Alves-Silva, J., N. Sánchez-Soriano, R. Beaven, M. Klein, J. Parkin, T.H. Millard, H.J. Bellen, K.J.T. Venken, C. Ballestrem, R.A. Kammerer, and A. Prokop. 2012. Spectraplakins promote microtubule-mediated axonal growth by functioning as structural microtubule-associated proteins and EB1-dependent + TIPs (tip interacting proteins). *Journal of Neuroscience*. 32:9143-9158.

Arce, C.A., J.A. Rodriquez, H.S. Barra, and R. Caputto. 1975. Incorporation of L tyrosine, L phenylalanine and L 3,4 dihydroxyphenylalanine as single units into rat brain tubulin. *European Journal of Biochemistry*. 59:145-149.

Baas, A.F., J. Kuipers, N.N. Van Der Wel, E. Batlle, H.K. Koerten, P.J. Peters, and H.C. Clevers. 2004. Complete polarization of single intestinal epithelial cells upon activation of LKB1 by STRAD. *Cell*. 116:457-466.

Bacallao, R., C. Antony, C. Dotti, E. Karsenti, E.H.K. Stelzer, and K. Simons. 1989. The subcellular organization of Madin-Darby Canine Kidney cells dueing the formation of a polarized epithelium. *Journal of Cell Biology*. 109:2817-2832.

Bahe, S., Y.D. Stierhof, C.J. Wilkinson, F. Leiss, and E.A. Nigg. 2005. Rootletin forms centriole-associated filaments and functions in centrosome cohesion. *Journal of Cell Biology*. 171:27-33.

Baird, D.H., K.A. Myers, M. Mogensen, D. Moss, and P.W. Baas. 2004. Distribution of the microtubule-related protein ninein in developing neurons. *Neuropharmacology*. 47:677-683.

Barra, H.S., C.A. Arce, J.A. Rodriguez, and R. Caputto. 1973. Incorporation of phenylalanine as a single unit into rat brain protein: reciprocal inhibition by phenylalanine and tyrosine of their respective incorporations. *Journal of Neurochemistry*. 21:1241-1251.

Barth, A.I.M., H.Y. Caro-Gonzalez, and W.J. Nelson. 2008. Role of adenomatous polyposis coli (APC) and microtubules in directional cell migration and neuronal polarization. *Seminars in Cell and Developmental Biology.* 19:245-251.

Bartolini, F., and G.G. Gundersen. 2010. Formins and microtubules. *Biochimica et Biophysica Acta - Molecular Cell Research*. 1803:164-173.

Bartolini, F., J.B. Moseley, J. Schmoranzer, L. Cassimeris, B.L. Goode, and G.G. Gundersen. 2008. The formin mDia2 stabilizes microtubules independently of its actin nucleation activity. *Journal of Cell Biology*. 181:523-536.

Bellett, G., J.M. Carter, J. Keynton, D. Goldspink, C. James, D.K. Moss, and M.M. Mogensen. 2009. Microtubule plus-end and minus-end capture at adherens junctions is involved in the assembly of apico-basal arrays in polarised epithelial cells. *Cell Motility and the Cytoskeleton*. 66:893-908.

Bellovin, D.I., K.J. Simpson, T. Danilov, E. Maynard, D.L. Rimm, P. Oettgen, and A.M. Mercurio. 2006. Reciprocal regulation of RhoA and RhoC characterizes the EMT and identifies RhoC as a prognostic marker of colon carcinoma. *Oncogene*. 25:6959-6967.

Belshaw, N.J., N. Pal, H.S. Tapp, J.R. Dainty, M.P. Lewis, M.R. Williams, E.K. Lund, and I.T. Johnson. 2010. Patterns of DNA methylation in individual colonic crypts reveal aging and cancer-related field defects in the morphologically normal mucosa. *Carcinogenesis*. 31:1158-1163.

Bhat, K.M.R., and V. Setaluri. 2007. Microtubule-associated proteins as targets in cancer chemotherapy. *Clinical Cancer Research*. 13:2849-2854.

Bieling, P., L. Laan, H. Schek, E.L. Munteanu, L. Sandblad, M. Dogterom, D. Brunner, and T. Surrey. 2007. Reconstitution of a microtubule plus-end tracking system in vitro. *Nature*. 450:1100-1105.

Blow, N. 2007. Cell migration: our protruding knowledge. *Nature Methods*. 4:589-593.

Bornens, M. 2002. Centrosome composition and microtubule anchoring mechanisms. *Current Opinion in Cell Biology*. 14:25-34.

Bostock, C.J., D.M. Prescott, and J.B. Kirkpatrick. 1971. An evaluation of the double thymidine block for synchronizing mammalian cells at the G1-S border. *Experimental Cell Research*. 68:163-168.

Bouckson-Castaing, V., M. Moudjou, D.J. Ferguson, S. Mucklow, Y. Belkaid, G. Milon, and P.R. Crocker. 1996. Molecular characterisation of ninein, a new coiled-coil protein of the centrosome. *Journal of Cell Science*. 109 (Pt 1):179-190.

Bre, M.H., T.E. Kreis, and E. Karsenti. 1987. Control of microtubule nucleation and stability in Madin-Darby Canine Kidney cells – the occurrence of noncentrosomal, stable tyrosinated microtubules. *Journal of Cell Biology*. 105:1283-1296.

Breton, S., and D. Brown. 1998. Cold-induced microtubule disruption and relocalization of membrane proteins in kidney epithelial cells. *Journal of the American Society of Nephrology*. 9:155-166.

Briggs, M.W., and D.B. Sacks. 2003. IQGAP proteins are integral components of cytoskeletal regulation. *EMBO Reports.* 4:571-574.

Brouhard, G.J., J.H. Stear, T.L. Noetzel, J. Al-Bassam, K. Kinoshita, S.C. Harrison, J. Howard, and A.A. Hyman. 2008. XMAP215 is a processive microtubule polymerase. *Cell*. 132:79-88.

Bu, W., and L.K. Su. 2001. Regulation of microtubule assembly by human EB1 family proteins. *Oncogene*. 20:3185-3192.

Bu, W., and L.K. Su. 2003. Characterization of Functional Domains of Human EB1 Family Proteins. *Journal of Biological Chemistry*. 278:49721-49731.

Buey, R.M., R. Mohan, K. Leslie, T. Walzthoeni, J.H. Missimer, A. Menzel, S. Bjelic, K. Bargsten, I. Grigoriev, I. Smal, E. Meijering, R. Aebersold, A. Akhmanova, and M.O. Steinmetz. 2011. Insights into EB1 structure and the role of its c-terminal domain for discriminating microtubule tips from the lattice. *Molecular Biology of the Cell*. 22:2912-2923.

Burridge, K., and K. Wennerberg. 2004. Rho and Rac Take Center Stage. *Cell*. 116:167-179.

Busch, K.E., and D. Brunner. 2004. The microtubule plus end-tracking proteins mal3p and tip1p cooperate for cell-end targeting of interphase microtubules. *Current Biology*. 14:548-559.

Busson, S., D. Dujardin, A. Moreau, J. Dompierre, and J.R. De Mey. 1998. Dynein and dynactin are localized to astral microtubules and at cortical sites in mitotic epithelial cells. *Current Biology*. 8:541-544.

Byers, T.J., A.H. Beggs, E.M. McNally, and L.M. Kunkel. 1995. Novel actin crosslinker superfamily member identified by a two step degenerate PCR procedure. *FEBS Letters*. 368:500-504.

Cardoso, J., J. Boer, H. Morreau, and R. Fodde. 2007. Expression and genomic profiling of colorectal cancer. *Biochimica et Biophysica Acta - Reviews on Cancer*. 1775:103-137.

Carvalho, P., J.S. Tirnauer, and D. Pellman. 2003. Surfing on microtubule ends. *Trends in Cell Biology*. 13:229-237.

Casenghi, M., F.A. Barr, and E.A. Nigg. 2005. Phosphorylation of Nlp by Plk1 negatively regulates its dynein-dynactin-dependent targeting to the centrosome. *Journal of Cell Science*. 118:5101-5108.

Casenghi, M., P. Meraldi, U. Weinhart, P.I. Duncan, R. Korner, and E.A. Nigg. 2003. Polo-like kinase 1 regulates Nlp, a centrosome protein involved in microtubule nucleation. *Developmental Cell*. 5:113-125.

Cassimeris, L. 2009. Microtubule Assembly: Lattice GTP to the Rescue. *Current Biology*. 19:R174-R176.

Castedo, M., J.L. Perfettini, T. Roumier, K. Andreau, R. Medema, and G. Kroemer. 2004. Cell death by mitotic catastrophe: A molecular definition. *Oncogene*. 23:2825-2837.

Chambers, A.F., A.C. Groom, and I.C. MacDonald. 2002. Dissemination and growth of cancer cells in metastatic sites. *Nature Reviews Cancer*. 2:563-572.

Chang, Y.C., P. Nalbant, J. Birkenfeld, Z.F. Chang, and G.M. Bokoch. 2008. GEF-H1 couples nocodazole-induced microtubule disassembly to cell contractility via RhoA. *Molecular Biology of the Cell*. 19:2147-2153.

Chausovsky, A., A.D. Bershadsky, and G.G. Borisy. 2000. Cadherin-mediated regulation of microtubule dynamics. *Nature Cell Biology*. 2:797-804.

Chen, C.H., S.L. Howng, T.S. Cheng, M.H. Chou, C.Y. Huang, and Y.R. Hong. 2003a. Molecular characterization of human ninein protein: two distinct subdomains required for centrosomal targeting and regulating signals in cell cycle. *Biochemical and Biophysical Research Communications*. 308:975-983.

Chen, H.J., C.M. Lin, C.S. Lin, R. Perez-Olle, C.L. Leung, and R.K.H. Liem. 2006. The role of microtubule actin cross-linking factor 1 (MACF1) in the Wnt signaling pathway. *Genes & Development.* 20:1933-1945.

Chen, X.Y., S. Kojima, G.G. Borisy, and K.J. Green. 2003b. p120 catenin associates with kinesin and facilitates the transport of cadherin-catenin complexes to intercellular junctions. *Journal of Cell Biology*. 163:547-557.

Chhabra, E.S., and H.N. Higgs. 2007. The many faces of actin: Matching assembly factors with cellular structures. *Nature Cell Biology*. 9:1110-1121.

Cohen, D., P.J. Brennwald, E. Rodriguez-Boulan, and A. Musch. 2004. Mammalian PAR-1 determines epithelial lumen polarity by organizing the microtubule cytoskeleton. *Journal of Cell Biology*. 164:717-727.

Cole, N.B., and L. Lippincott-Schwartz. 1995. Organization of organelles and membrane traffic by microtubules. *Current Opinion in Cell Biology*. 7:55-64.

Compton, C.C., and F.L. Greene. 2004. The staging of colorectal cancer: 2004 and beyond. *CA: A Cancer Journal for Clinicians.* 54:295-308.

Conlon, I., and M. Raff. 1999. Size control in animal development. *Cell*. 96:235-244.

Cooper, J.A., and D.A. Schafer. 2000. Control of actin assembly and disassembly at filament ends. *Current Opinion in Cell Biology*. 12:97-103.

Dammermann, A., and A. Merdes. 2002. Assembly of centrosomal proteins and microtubule organization depends on PCM-1. *Journal of Cell Biology*. 159:255-266.

Delaval, B., and S.J. Doxsey. 2010. Pericentrin in cellular function and disease. *Journal of Cell Biology*. 188:181-190.

Delgehyr, N., J. Sillibourne, and M. Bornens. 2005. Microtubule nucleation and anchoring at the centrosome are independent processes linked by ninein function. *Journal of Cell Science*. 118:1565-1575.

des Georges, A., M. Katsuki, D.R. Drummond, M. Osei, R.A. Cross, and L.A. Amos. 2008. Mal3, the Schizosaccharomyces pombe homolog of EB1, changes the microtubule lattice. *Nature Structural & Molecular Biology.* 15:1102-1108.

Desai, A., and T.J. Mitchison. 1997. Microtubule polymerization dynamics. *Annual Review of Cell and Developmental Biology*. 13:83-117.

Dietrich, K.A., R. Schwarz, M. Liska, S. GraѴü, A. Menke, M. Meister, G. Kierschke, C. Längle, F. Genze, and K. Giehl. 2009. Specific induction of migration and invasion of pancreatic carcinoma cells by RhoC, which differs from RhoA in its localisation and activity. *Biological Chemistry*. 390:1063-1077.

Dihlmann, S., J. Gebert, A. Siermann, C. Herfarth, and M. Von Knebel Doeberitz. 1999. Dominant negative effect of the APC1309 mutation: A possible explanation for genotype-phenotype correlations in familial adenomatous polyposis. *Cancer Research*. 59:1857-1860.

Dixit, R., B. Barnett, J.E. Lazarus, M. Tokito, Y.E. Goldman, and E.L.F. Holzbaur. 2009. Microtubule plus-end tracking by CLIP-170 requires EB1. *Proceedings of the National Academy of Sciences of the United States of America*. 106:492-497.

Dong, X., F. Liu, L. Sun, M. Liu, D. Li, D. Su, Z. Zhu, J.T. Dong, L. Fu, and J. Zhou. 2010. Oncogenic function of microtubule end-binding protein 1 in breast cancer. *Journal of Pathology*. 220:361-369.

Dos Remedios, C.G., D. Chhabra, M. Kekic, I.V. Dedova, M. Tsubakihara, D.A. Berry, and N.J. Nosworthy. 2003. Actin binding proteins: Regulation of cytoskeletal microfilaments. *Physiological Reviews*. 83:433-473.

Drubin, D.G., and W.J. Nelson. 1996. Origins of cell polarity. *Cell*. 84:335-344.

Dunn, K.C., A.E. Aotaki-Keen, F.R. Putkey, and L.M. Hjelmeland. 1996. ARPE-19, a human retinal pigment epithelial cell line with differentiated properties. *Experimental Eye Research*. 62:155-169.

Edde, B., J. Rossier, J.P. Le Caer, E. Desbruyeres, F. Gros, and P. Denoulet. 1990. Posttranslational Glutamylation of α-tubulin. *Science*. 247:83-85.

Faux, M.C., J.L. Ross, C. Meeker, T. Johns, H. Ji, R.J. Simpson, M.J. Layton, and A.W. Burgess. 2004. Restoration of full-length adenomatous polyposis coli (APC) protein in a colon cancer cell line enhances cell adhesion. *Journal of Cell Science*. 117:427-439.

Fearon, E.R., and B. Vogelstein. 1990. A genetic model for colorectal tumorigenesis. *Cell*. 61:759-767.

Fingar, D.C., S. Salama, C. Tsou, E. Harlow, and J. Blenis. 2002. Mammalian cell size is controlled by mTOR and its downstream targets S6K1 and 4EBP1/eIF4E. *Genes and Development*. 16:1472-1487.

Fleming, E.S., M. Temchin, Q. Wu, L. Maggio-Price, and J.S. Tirnauer. 2009. Spindle misorientation in tumors from APC min/+ mice. *Molecular Carcinogenesis*. 48:592-598.

Frixione, E. 2000. Recurring views on the structure and function of the cytoskeleton: A 300-year epic. *Cell Motility and the Cytoskeleton*. 46:73-94.

Fuchs, E., and D.W. Cleveland. 1998. A structural scaffolding of intermediate filaments in health and disease. *Science*. 279:514-519.

Fuchs, E., and I. Karakesisoglou. 2001. Bridging cytoskeletal intersections. *Genes and Development*. 15:1-14.

Fuchs, E., and K. Weber. 1994. Intermediate Filaments: Structure, Dynamics, Function and Disease. *Annual Review of Biochemistry*. 63:345-382.

Fukata, M., T. Watanabe, J. Noritake, M. Nakagawa, M. Yamaga, S. Kuroda, Y. Matsuura, A. Iwamatsu, F. Perez, and K. Kaibuchi. 2002. Rac1 and Cdc42 capture microtubules through IQGAP1 and CLIP-170. *Cell*. 109:873-885.

Furness, D.N., C.M. Hackney, and P.S. Steyger. 1990. Organization of microtubules in cochlear hair cells. *Journal of Electron Microscopy Technique*. 15:261-279.

Furuya, T., T. Kamada, T. Murakami, A. Kurose, and K. Sasaki. 1997. Laser scanning cytometry allows detection of cell death with morphological features of apoptosis in cells stained with PI. *Cytometry*. 29:173-177.

Gadde, S., and R. Heald. 2004. Mechanisms and molecules of the mitotic spindle. *Current Biology*. 14:R797-R805.

Galjart, N., and F. Perez. 2003. A plus-end raft to control microtubule dynamics and function. *Current Opinion in Cell Biology*. 15:48-53.

Gao, S.Y., C.Y. Li, J. Chen, L. Pan, S. Saito, T. Terashita, K. Saito, K. Miyawaki, K. Shigemoto, K. Mominoki, S. Matsuda, and N. Kobayashi. 2004. Rho-ROCK signal pathway regulates microtubule-based process formation of cultured podocytes - Inhibition of ROCK promoted process elongation. *Nephron - Experimental Nephrology*. 97:e49-e61.

Garnham, C.P., and A. Roll-Mecak. 2012. The chemical complexity of cellular microtubules: Tubulin post-translational modification enzymes and their roles in tuning microtubule functions. *Cytoskeleton*. 69:442-463.

Garrod, D., and M. Chidgey. 2008. Desmosome structure, composition and function. *Biochimica et Biophysica Acta - Biomembranes.* 1778:572-587.

Gennerich, A., and R.D. Vale. 2009. Walking the walk: how kinesin and dynein coordinate their steps. *Current Opinion in Cell Biology*. 21:59-67.

Gerdes, J., H. Lemke, and H. Baisch. 1984. Cell cycle analysis of a cell proliferation associated human nuclear antigen defined by the monoclonal antibody Ki-67. *Journal of Immunology*. 133:1710-1715.

Ghadimi, B.M., D.L. Sackett, M.J. Difilippantonio, E. Schröck, T. Neumann, A. Jauho, G. Auer, and T. Ried. 2000. Centrosome amplification and instability occurs exclusively in aneuploid, but not in diploid colorectal cancer cell lines, and correlates with numerical chromosomal aberrations. *Genes Chromosomes and Cancer*. 27:183-190.

Gibson, M.C., and N. Perrimon. 2003. Apicobasal polarization: epithelial form and function. *Current Opinion in Cell Biology*. 15:747-752.

Giepmans, B.N.G., and S.C.D. van Ijzendoorn. 2009. Epithelial cell-cell junctions and plasma membrane domains. *Biochimica et Biophysica Acta - Biomembranes.* 1788:820-831.

Giepmans, B.N.G., I. Verlaan, T. Hengeveld, H. Janssen, J. Calafat, M.M. Falk, and W.H. Moolenaar. 2001. Gap junction protein connexin-43 interacts directly with microtubules. *Current Biology*. 11:1364-1368.

Giles, R.H., J.H. van Es, and H. Clevers. 2003. Caught up in a Wnt storm: Wnt signaling in cancer. *Biochimica et Biophysica Acta - Reviews on Cancer*. 1653:1-24.

Goldspink, D.A., J.R. Gadsby, G. Bellett, J. Keynton, B.J. Tyrrell, E.K. Lund, P.P. Powell, P. Thomas, and M.M. Mogensen. 2013b. The microtubule end binding protein EB2 is a central regulator of microtubule reorganisation and dynamics in apico-basal epithelial differentiation. *Journal of Cell Science*.

Goldspink, D.A., B.J. Tyrrell, G. Bellett, E.K. Lund, J. Keynton, J.R. Gadsby, N. Galjart, and M.M. Mogensen. 2013a, manuscript in preparation. CLIP-170 is necessary for efficient ninein relocation to adherens junctions and formation of apico-basal microtubule bundles during epithelial differentiation.

Goshima, G., M. Mayer, N. Zhang, N. Stuurman, and R.D. Vale. 2008. Augmin: A protein complex required for centrosome-independent microtubule generation within the spindle. *Journal of Cell Biology*. 181:421-429.

Green, K.J., and J.C.R. Jones. 1996. Desmosomes and hemidesmosomes: Structure and function of molecular components. *FASEB Journal.* 10:871-881.

Green, R.A., and K.B. Kaplan. 2003. Chromosome instability in colorectal tumor cells is associated with defects in microtubule plus-end attachments caused by a dominant mutation in APC. *Journal of Cell Biology*. 163:949-961.

Guertin, D.A., and D.M. Sabatini. 2001. Cell Size Control. *In* eLS. John Wiley & Sons, Ltd.

Guertin, D.A., S. Trautmann, and D. McCollum. 2002. Cytokinesis in eukaryotes. *Microbiology and Molecular Biology Reviews*. 66:155-178.

Gundersen, G.G. 2002. Microtubule capture: IQGAP and CLIP-170 expand the repertoire. *Current Biology*. 12:R645-R647.

Gundersen, G.G., and T.A. Cook. 1999. Microtubules and signal transduction. *Current Opinion in Cell Biology*. 11:81-94.

Gundersen, G.G., M.H. Kalnoski, and J.C. Bulinski. 1984. Distinct populations of microtubules: Tyrosinated and nontyrosinated alpha tubulin are distributed differently in vivo. *Cell*. 38:779-789.

Haines, R.L., and E.B. Lane. 2012. Keratins and disease at a glance. *Journal of Cell Science*. 125:3923-3928.

Hakem, A., O. Sanchez-Sweatman, A. You-Ten, G. Duncan, A. Wakeham, R. Khokha, and T.W. Mak. 2005. RhoC is dispensable for embryogenesis and tumor initiation but essential for metastasis. *Genes and Development*. 19:1974-1979.

Hammond, J.W., D. Cai, and K.J. Verhey. 2008. Tubulin modifications and their cellular functions. *Current Opinion in Cell Biology*. 20:71-76.

Hanahan, D., and R.A. Weinberg. 2000. The hallmarks of cancer. *Cell*. 100:57-70.

Hannak, E., K. Oegema, M. Kirkham, P. Gonczy, B. Habermann, and A.A. Hyman. 2002. The kinetically dominant assembly pathway for centrosomal asters in Caenorhabditis elegans is gamma-tubulin dependent. *Journal of Cell Biology*. 157:591-602.

Hanson, C.A., and J.R. Miller. 2005. Non-traditional roles for the Adenomatous Polyposis Coli (APC) tumor suppressor protein. *Gene*. 361:1-12.

Hartsock, A., and W.J. Nelson. 2008. Adherens and tight junctions: Structure, function and connections to the actin cytoskeleton. *Biochimica et Biophysica Acta - Biomembranes.* 1778:660-669.

Hawkins, T., M. Mirigian, M. Selcuk Yasar, and J.L. Ross. 2010. Mechanics of microtubules. *Journal of Biomechanics*. 43:23-30.

Hayashi, I., A. Wilde, T.K. Mal, and M. Ikura. 2005. Structural basis for the activation of microtubule assembly by the EB1 and $p150^{(Glued)}$ complex. *Molecular Cell*. 19:449-460.

Hayward, D.G., and A.M. Fry. 2006. Nek2 kinase in chromosome instability and cancer. *Cancer Lettersers*. 237:155-166.

Henderson, C.G., J.B. Tucker, M.A. Chaplin, J.B. Mackie, S.N. Maidment, M.M. Mogensen, and C.C. Paton. 1994. Reorganization of the centrosome and associated microtubules during the morphogenesis of a mouse cochlear epithelial cell. *Journal of Cell Science*. 107 (Pt 2):589-600.

Henderson, C.G., J.B. Tucker, M.M. Mogensen, J.B. Mackie, M.A. Chaplin, N.B. Slepecky, and L.M. Leckie. 1995. Three microtubule-organizing centres collaborate in a mouse cochlear epithelial cell during supracellularly coordinated control of microtubule positioning. *Journal of Cell Science*. 108 (Pt 1):37-50.

Herrmann, H., and U. Aebi. 2004. Intermediate Filaments: Molecular structure, assembly mechanism, and integration into functionally distinct intracellular scaffolds. Vol. 73. 749-789.

Hetheridge, C., A.N. Scott, R.K. Swain, J.W. Copeland, H.N. Higgs, R. Bicknell, and H. Mellor. 2012. The formin FMNL3 is a cytoskeletal regulator of angiogenesis. *Journal of Cell Science*. 125:1420-1428.

Hogan, C., S. Dupré-Crochet, M. Norman, M. Kajita, C. Zimmermann, A.E. Pelling, E. Piddini, L.A. Baena-López, J.P. Vincent, Y. Itoh, H. Hosoya, F. Pichaud, and Y. Fujita. 2009. Characterization of the interface between normal and transformed epithelial cells. *Nature Cell Biology*. 11:460-467.

Hong, Y.R., C.H. Chen, M.H. Chuo, S.Y. Liou, and S.L. Howng. 2000. Genomic organization and molecular characterization of the human ninein gene. *Biochemical and Biophysical Research Communications*. 279:989-995.

Honnappa, S., S.M. Gouveia, A. Weisbrich, F.F. Damberger, N.S. Bhavesh, H. Jawhari, I. Grigoriev, F.J.A. van Rijssel, R.M. Buey, A. Lawera, I. Jelesarov, F.K. Winkler, K. Wüthrich, A. Akhmanova, and M.O. Steinmetz. 2009. An EB1-Binding Motif Acts as a Microtubule Tip Localization Signal. *Cell*. 138:366-376.

Honnappa, S., O. Okhrimenko, R. Jaussi, H. Jawhari, I. Jelesarov, F.K. Winkler, and M.O. Steinmetz. 2006. Key Interaction Modes of Dynamic +TIP Networks. *Molecular Cell*. 23:663-671.

Howard, J., and A.A. Hyman. 2003. Dynamics and mechanics of the microtubule plus end. *Nature*. 422:753-758.

Howard, J., and A.A. Hyman. 2007. Microtubule polymerases and depolymerases. *Current Opinion in Cell Biology*. 19:31-35.

Howard, J., and A.A. Hyman. 2009. Growth, fluctuation and switching at microtubule plus ends. *Nature Reviews Molecular Cell Biology*. 10:569-574.

Howng, S.L., H.C. Hsu, T.S. Cheng, Y.L. Lee, L.K. Chang, P.J. Lu, and Y.R. Hong. 2004. A novel ninein-interaction protein, CGI-99, blocks ninein phosphorylation by GSK3beta and is highly expressed in brain tumors. *FEBS Letters*. 566:162-168.

Hubbert, C., A. Guardiola, R. Shao, Y. Kawaguchi, A. Ito, A. Nixon, M. Yoshida, X.F. Wang, and T.P. Yao. 2002. HDAC6 is a microtubule-associated deacetylase. *Nature*. 417:455-458.

Hunter, A.W., M. Caplow, D.L. Coy, W.O. Hancock, S. Diez, L. Wordeman, and J. Howard. 2003. The kinesin-related protein MCAK is a microtubule depolymerase that forms an ATP-hydrolyzing complex at microtubule ends. *Molecular Cell*. 11:445-457.

Hyman, A.A., S. Salser, D.N. Drechsel, N. Unwin, and T.J. Mitchison. 1992. Role of GTP hydrolysis in microtubule dynamics: Information from a slowly hydrolyzable analogue, GMPCPP. *Molecular Biology of the Cell*. 3:1155-1167.

Ishizaki, T., Y. Morishima, M. Okamoto, T. Furuyashiki, T. Kato, and S. Narumiya. 2001. Coordination of microtubules and the actin cytoskeleton by the Rho effector mDia1. *Nature Cell Biology*. 3:8-14.

Jaffe, A.B., and A. Hall. 2005. Rho GTPases: Biochemistry and biology. Vol. 21. 247-269.

Jaffe, A.B., N. Kaji, J. Durgan, and A. Hall. 2008. Cdc42 controls spindle orientation to position the apical surface during epithelial morphogenesis. *Journal of Cell Biology*. 183:625-633.

Jakus, M.A., and C.E. Hall. 1947. Studies of actin and myosin. *The Journal of Biological Chemistry*. 167:705-714.

Janke, C., and J.C. Bulinski. 2011. Post-translational regulation of the microtubule cytoskeleton: Mechanisms and functions. *Nature Reviews Molecular Cell Biology*. 12:773-786.

Janke, C., K. Rogowski, D. Wloga, C. Regnard, A.V. Kajava, J.M. Strub, N. Temurak, J. Van Dijk, D. Boucher, A. Van Dorsselaer, S. Suryavanshi, J. Gaertig, and B. Eddé. 2005. Biochemistry: Tubulin polyglutamylase enzymes are members of the TTL domain protein family. *Science*. 308:1758-1762.

Jaulin, F., and G. Kreitzer. 2010. KIF17 stabilizes microtubules and contributes to epithelial morphogenesis by acting at MT plus ends with EB1 and APC. *Journal of Cell Biology*. 190:443-460.

Jaworski, J., C.C. Hoogenraad, and A. Akhmanova. 2008. Microtubule plus-end tracking proteins in differentiated mammalian cells. *International Journal of Biochemistry & Cell Biology*. 40:619-637.

Jimbo, T., Y. Kawasaki, R. Koyama, R. Sato, S. Takada, K. Haraguchi, and T. Akiyama. 2002. Identification of a link between the tumour suppressor APC and the kinesin superfamily. *Nature Cell Biology*. 4:323-327.

Joberty, G., C. Petersen, L. Gao, and I.G. Macara. 2000. The cell-polarity protein Par6 links Par3 and atypical protein kinase C to Cdc42. *Nature Cell Biology*. 2:531-539.

Johnson, M., M. Sharma, and B.R. Henderson. 2009. IQGAP1 regulation and roles in cancer. *Cellular Signalling.* 21:1471-1478.

Johnston, G.C., J.R. Pringle, and L.H. Hartwell. 1977. Coordination of growth with cell division in the yeast Saccharomyces cerevisiae. *Experimental Cell Research*. 105:79-98.

Jones, J.C.R., S.B. Hopkinson, and L.E. Goldfinger. 1998. Structure and assembly of hemidesmosomes. *Bioessays*. 20:488-494.

Jordan, M.A., D. Thrower, and L. Wilson. 1991. Mechanism of inhibition of cell proliferation by Vinca alkaloids. *Cancer Research*. 51:2212-2222.

Jordan, M.A., K. Wendell, S. Gardiner, W.B. Derry, H. Copp, and L. Wilson. 1996. Mitotic block induced in HeLa cells by low concentrations of paclitaxel (taxol) results in abnormal mitotic exit and apoptotic cell death. *Cancer Research*. 56:816-825.

Jordan, M.A., and L. Wilson. 2004. Microtubules as a target for anticancer drugs. *Nature Reviews Cancer*. 4:253-265.

Jorgensen, P., and M. Tyers. 2004. How cells coordinate growth and division. *Current Biology*. 14:R1014-R1027.

Karakesisoglou, I., Y.M. Yang, and E. Fuchs. 2000. An epidermal plakin that integrates actin and microtubule networks at cellular junctions. *Journal of Cell Biology*. 149:195-208.

Kardon, J.R., and R.D. Vale. 2009. Regulators of the cytoplasmic dynein motor. *Nature Reviews Molecular Cell Biology*. 10:854-865.

Kaverina, I., and A. Straube. 2011. Regulation of cell migration by dynamic microtubules. *Seminars in Cell and Developmental Biology*. 22:968-974.

Kawasaki, Y., R. Sato, and T. Akiyama. 2003. Mutated APC and Asef are involved in the migration of colorectal tumour cells. *Nature Cell Biology*. 5:211-215.

Kessenbrock, K., V. Plaks, and Z. Werb. 2010. Matrix Metalloproteinases: Regulators of the Tumor Microenvironment. *Cell*. 141:52-67.

Keynton, J.L. 2011. Microtubule assembly and organisation in normal and cancerous polarised epithelial cells. PhD Thesis. University of East Anglia.

Kim, J.C., J.L. Badano, S. Sibold, M.A. Esmail, J. Hill, B.E. Hoskins, C.C. Leitch, K. Venner, S.J. Ansley, A.J. Ross, M.R. Leroux, N. Katsanis, and P.L. Beales. 2004. The Bardet-Biedl protein BBS4 targets cargo to the pericentriolar region and is required for microtubule anchoring and cell cycle progression. *Nature Genetics*. 36:462-470.

Kimura, M., T. Yoshioka, M. Saio, Y. Banno, H. Nagaoka, and Y. Okano. 2013. Mitotic catastrophe and cell death induced by depletion of centrosomal proteins. *Cell Death and Disease*. 4.

Kobielak, A., H.A. Pasolli, and E. Fuchs. 2004. Mammalian formin-1 participates in adherens junctions and polymerization of linear actin cables. *Nature Cell Biology*. 6:21-30.

Kodama, A., I. Karakesisoglou, E. Wong, A. Vaezi, and E. Fuchs. 2003. ACF7: An essential integrator of microtubule dynamics. *Cell*. 115:343-354.

Kollman, J.M., A. Merdes, L. Mourey, and D.A. Agard. 2011. Microtubule nucleation by γ-tubulin complexes. *Nature Reviews Molecular Cell Biology*. 12:709-721.

Komarova, Y., C.O. De Groot, I. Grigoriev, S.M. Gouveia, E.L. Munteanu, J.M. Schober, S. Honnappa, R.M. Buey, C.C. Hoogenraad, M. Dogterom, G.G. Borisy, M.O. Steinmetz, and A. Akhmanova. 2009. Mammalian end binding proteins control persistent microtubule growth. *Journal of Cell Biology*. 184:691-706.

Komarova, Y., G. Lansbergen, N. Galjart, F. Grosveld, G.G. Borisy, and A. Akhmanova. 2005. EB1 and EB3 control CLIP dissociation from the ends of growing microtubules. *Molecular Biology of the Cell*. 16:5334-5345.

Krendel, M., F.T. Zenke, and G.M. Bokoch. 2002. Nucleotide exchange factor GEF-H1 mediates cross-talk between microtubules and the actin cytoskeleton. *Nature Cell Biology*. 4:294-301.

Krishan, A. 1975. Rapid flow cytofluorometric analysis of mammalian cell cycle by propidium iodide staining. *Journal of Cell Biology*. 66:188-193.

Kumar, P., K.S. Lyle, S. Gierke, A. Matov, G. Danuser, and T. Wittmann. 2009. GSK3β phosphorylation modulates CLASP-microtubule association and lamella microtubule attachment. *Journal of Cell Biology*. 184:895-908.

Kumar, P., and T. Wittmann. 2012. +TIPs: SxIPping along microtubule ends. *Trends in Cell Biology*. 22:418-428.

Kwon, M., S.A. Godinho, N.S. Chandhok, N.J. Ganem, A. Azioune, M. Thery, and D. Pellman. 2008. Mechanisms to suppress multipolar divisions in cancer cells with extra centrosomes. *Genes and Development*. 22:2189-2203.

L'Hernault, S.W., and J.L. Rosenbaum. 1985. Chlamydomonas α-tubulin is posttranslationally modified by acetylation on the ε-amino group of a lysine. *Biochemistry*. 24:473-478.

Lane, E.B., E.L. Rugg, H. Navsaria, I.M. Leigh, A.H.M. Heagerty, A. Ishida-Yamamoto, and R.A.J. Eady. 1992. A mutation in the conserved helix termination peptide of keratin 5 in hereditary skin blistering. *Nature*. 356:244-246.

Lansbergen, G., and A. Akhmanova. 2006. Microtubule plus end: A hub of cellular activities. *Traffic*. 7:499-507.

Lansbergen, G., Y. Komarova, M. Modesti, C. Wyman, C.C. Hoogenraad, H.V. Goodson, R.P. Lemaitre, D.N. Drechsel, E. Van Munster, T.W.J. Gadella Jr, F. Grosveld, N. Galjart, G.G. Borisy, and A. Akhmanova. 2004. Conformational changes in CLIP-170 regulate its binding to microtubules and dynactin localization. *Journal of Cell Biology*. 166:1003-1014.

Lauffenburger, D.A., and A.F. Horwitz. 1996. Cell migration: A physically integrated molecular process. *Cell*. 84:359-369.

Lawrence, C.J., R.K. Dawe, K.R. Christie, D.W. Cleveland, S.C. Dawson, S.A. Endow, L.S.B. Goldstein, H.V. Goodson, N. Hirokawa, J. Howard, R.L. Malmberg, J.R. McIntosh, H. Miki, T.J. Mitchison, Y. Okada, A.S.N. Reddy, W.M. Saxton, M. Schliwa, J.M. Scholey, R.D. Vale, C.E. Walczak, and L. Wordeman. 2004. A standardized kinesin nomenclature. *Journal of Cell Biology*. 167:19-22.

Lechler, T., and E. Fuchs. 2007. Desmoplakin: An unexpected regulator of microtubule organization in the epidermis. *Journal of Cell Biology*. 176:147-154.

Lee, S.H., and R. Dominguez. 2010. Regulation of actin cytoskeleton dynamics in cells. *Molecules and Cells*. 29:311-325.

Leighton, J., Z. Brada, L.W. Estes, and G. Justh. 1969. Secretory activity and oncogenicity of a cell line (MDCK) derived from canine kidney. *Science*. 163:472.

Lengauer, C., K.W. Kinzler, and B. Vogelstein. 1997. Genetic instability in colorectal cancers. *Nature*. 386:623-627.

Leung, C.L., K.J. Green, and R.K.H. Liem. 2002. Plakins: a family of versatile cytolinker proteins. *Trends in Cell Biology*. 12:37-45.

Lewis, A., H. Davis, M. Deheragoda, P. Pollard, E. Nye, R. Jeffery, S. Segditsas, P. East, R. Poulsom, G. Stamp, N. Wright, and I. Tomlinson. 2012. The C-terminus of Apc does not influence intestinal adenoma development or progression. *Journal of Pathology*. 226:73-83.

Li, F., G. Ambrosini, E.Y. Chu, J. Plescia, S. Tognin, P.C. Marchisio, and D.C. Altieri. 1998. Control of apoptosis and mitotic spindle checkpoint by survivin. *Nature*. 396:580-584.

Li, N., P. Jiang, W. Du, Z. Wu, C. Li, M. Qiao, X. Yang, and M. Wu. 2011. Siva1 suppresses epithelial-mesenchymal transition and metastasis of tumor cells by inhibiting stathmin and stabilizing microtubules. *Proceedings of the National Academy of Sciences of the United States of America*. 108:12851-12856.

Liang, C.C., A.Y. Park, and J.L. Guan. 2007. In vitro scratch assay: A convenient and inexpensive method for analysis of cell migration in vitro. *Nature Protocols*. 2:329-333.

Ligon, L.A., and E.L.F. Holzbaur. 2007. Microtubules tethered at epithelial cell junctions by dynein facilitate efficient junction assembly. *Traffic*. 8:808-819.

Ligon, L.A., S. Karki, M. Tokito, and E.L.F. Holzbaur. 2001. Dynein binds to beta-catenin and may tether microtubules at adherens junctions. *Nature Cell Biology*. 3:913-917.

Louie, R.K., S. Bahmanyar, K.A. Siemers, V. Votin, P. Chang, T. Stearns, W.J. Nelson, and A.I.M. Barth. 2004. Adenomatous polyposis coli and EB1 localize in close proximity of the mother centriole and EB1 is a functional component of centrosomes. *Journal of Cell Science*. 117:1117-1128.

Malumbres, M., and M. Barbacid. 2009. Cell cycle, CDKs and cancer: A changing paradigm. *Nature Reviews Cancer*. 9:153-166.

Manna, T., S. Honnappa, M.O. Steinmetz, and L. Wilson. 2007. Suppression of Microtubule Dynamic Instability by the +TIP Protein EB1 and Its Modulation by the CAP-Gly Domain of $p150^{Glued}$. *Biochemistry*. 47:779-786.

Marshall, T.W., I.E. Lloyd, J.M. Delalande, I. Näthke, and J. Rosenblatt. 2011. The tumor suppressor adenomatous polyposis coli controls the direction in which a cell extrudes from an epithelium. *Molecular Biology of the Cell*. 22:3962-3970.

Matsuda, Y., T. Ishiwata, Y. Kawamoto, K. Kawahara, W.X. Peng, T. Yamamoto, and Z. Naito. 2010. Morphological and cytoskeletal changes of pancreatic cancer cells in three-dimensional spheroidal culture. *Medical Molecular Morphology*. 43:211-217.

Matsumoto, T., P. Schiller, L.C. Dieterich, F. Bahram, Y. Iribe, U. Hellman, C. Wikner, G. Chan, L. Claesson-Welsh, and A. Dimberg. 2008. Ninein is expressed in the cytoplasm of angiogenic tip-cells and regulates tubular morphogenesis of endothelial cells. *Arteriosclerosis, Thrombosis, and Vascular Biology*. 28:2123-2130.

Maurer, S.P., P. Bieling, J. Cope, A. Hoenger, and T. Surrey. 2011. GTPγS microtubules mimic the growing microtubule end structure recognized by end-binding proteins (EBs). *Proceedings of the National Academy of Sciences of the United States of America*. 108:3988-3993.

Maurer, S.P., F.J. Fourniol, G. Bohner, C.A. Moores, and T. Surrey. 2012. EBs recognize a nucleotide-dependent structural cap at growing microtubule ends. *Cell*. 149:371-382.

Miki, H., Y. Okada, and N. Hirokawa. 2005. Analysis of the kinesin superfamily: insights into structure and function. *Trends in Cell Biology*. 15:467-476.

Mimori-Kiyosue, Y., I. Grigoriev, G. Lansbergen, H. Sasaki, C. Matsui, F. Severin, N. Galjart, F. Grosveld, I. Vorobjev, S. Tsukita, and A. Akhmanova. 2005. CLASP1 and CLASP2 bind to EB1 and regulate microtubule plus-end dynamics at the cell cortex. *Journal of Cell Biology*. 168:141-153.

Mimori-Kiyosue, Y., N. Shiina, and S. Tsukita. 2000. Adenomatous polyposis coli (APC) protein moves along microtubules and concentrates at their growing ends in epithelial cells. *Journal of Cell Biology*. 148:505-518.

Mitchinson, T., and M. Kirschner. 1984. Dynamic instability of microtubule growth. *Nature*. 312:237-242.

Mitchison, T.J., and E.D. Salmon. 2001. Mitosis: A history of division. *Nature Cell Biology*. 3:E17-E22.

Mogensen, M.M. 1999. Microtubule release and capture in epithelial cells. *Biology of the Cell*. 91:331-341.

Mogensen, M.M. 2004. Microtubule Organizing Centers in Polarized Epithelial Cells. *In* Centrosomes in Development and Disease. Wiley-VCH Verlag GmbH & Co. KGaA. 299-319.

Mogensen, M.M., J.B. Mackie, S.J. Doxsey, T. Stearns, and J.B. Tucker. 1997. Centrosomal deployment of gamma-tubulin and pericentrin: evidence for a microtubule-nucleating domain and a minus-end docking domain in certain mouse epithelial cells. *Cell Motility and the Cytoskeleton*. 36:276-290.

Mogensen, M.M., A. Malik, M. Piel, V. Bouckson-Castaing, and M. Bornens. 2000. Microtubule minus-end anchorage at centrosomal and non-centrosomal sites: the role of ninein. *Journal of Cell Science*. 113 (Pt 17):3013-3023.

Mogensen, M.M., J.B. Tucker, J.B. Mackie, A.R. Prescott, and I.S. Näthke. 2002. The adenomatous polyposis coli protein unambiguously localizes to microtubule plus ends and is involved in establishing parallel arrays of microtubule bundles in highly polarized epithelial cells. *Journal of Cell Biology*. 157:1041-1048.

Moores, C.A., and R.A. Milligan. 2006. Lucky 13 - Microtubule depolymerisation by kinesin-13 motors. *Journal of Cell Science*. 119:3905-3913.

Morin, P.J., A.B. Sparks, V. Korinek, N. Barker, H. Clevers, B. Vogelstein, and K.W. Kinzler. 1997. Activation of beta-catenin-Tcf signaling in colon cancer by mutations in beta-catenin or APC. *Science*. 275:1787-1790.

Moritz, M., and D.A. Agard. 2001. γ-tubulin complexes and microtubule nucleation. *Current Opinion in Structural Biology*. 11:174-181.

Morrison, E.E., B.N. Wardleworth, J.M. Askham, A.F. Markham, and D.M. Meredith. 1998. EB1, a protein which interacts with the APC tumour suppressor, is associated with the microtubule cytoskeleton throughout the cell cycle. *Oncogene*. 17:3471-3477.

Moss, D.K., G. Bellett, J.M. Carter, M. Liovic, J. Keynton, A.R. Prescott, E.B. Lane, and M.M. Mogensen. 2007. Ninein is released from the centrosome and moves bi-directionally along microtubules. *Journal of Cell Science*. 120:3064-3074.

Murray, M.Y., T.P. Birkland, J.D. Howe, A.D. Rowan, M. Fidock, W.C. Parks, and J. Gavrilovic. 2013. Macrophage Migration and Invasion Is Regulated by MMP10 Expression. *PLoS ONE*. 8:e63555.

Musacchio, A., and K.G. Hardwick. 2002. The spindle checkpoint: Structural insights into dynamic signalling. *Nature Reviews Molecular Cell Biology*. 3:731-741.

Musch, A. 2004. Microtubule organization and function in epithelial cells. *Traffic*. 5:1-9.

Natalwala, A., R. Spychal, and C. Tselepis. 2008. Epithelial-mesenchymal transition mediated tumourigenesis in the gastrointestinal tract. *World Journal of Gastroenterology.* 14:3792-3797.

Näthke, I.S., C.L. Adams, P. Polakis, J.H. Sellin, and W.J. Nelson. 1996. The adenomatous polyposis coli tumor suppressor protein localizes to plasma membrane sites involved in active cell migration. *Journal of Cell Biology*. 134:165-179.

Näthke, I. 2010. Inke Näthke: The ABCs of APC. Interview by Caitlin Sedwick. *Journal of Cell Biology*. 189:774-775.

Näthke, I.S. 2004. The Adenomatous Polyposis coli protein: The achilles heel of the gut epithelium. *Annual Review of Cell & Developmental Biology.* 20:337-366.

Nelson, W.J., and R. Nusse. 2004. Convergence of Wnt, beta-catenin, and cadherin pathways. *Science*. 303:1483-1487.

Neufeld, T.P., A.F.A. De La Cruz, L.A. Johnston, and B.A. Edgar. 1998. Coordination of growth and cell division in the Drosophila wing. *Cell*. 93:1183-1193.

Nigg, E.A. 2006. Origins and consequences of centrosome aberrations in human cancers. *International Journal of Cancer*. 119:2717-2723.

Nogales, E., and H.W. Wang. 2006. Structural mechanisms underlying nucleotide-dependent self-assembly of tubulin and its relatives. *Current Opinion in Structural Biology*. 16:221-229.

Nogales, E., M. Whittaker, R.A. Milligan, and K.H. Downing. 1999. High-resolution model of the microtubule. *Cell*. 96:79-88.

North, B.J., B.L. Marshall, M.T. Borra, J.M. Denu, and E. Verdin. 2003. The human Sir2 ortholog, SIRT2, is an NAD+-dependent tubulin deacetylase. *Molecular Cell*. 11:437-444.

Novák, B., J.C. Sible, and J.J. Tyson. 2001. Checkpoints in the Cell Cycle. *In* eLS. John Wiley & Sons, Ltd.

O'Brien, L.E., W. Yu, K. Tang, T.S. Jou, M.M. Zegers, and K.E. Mostov. 2006. Morphological and biochemical analysis of Rac1 in three-dimensional epithelial cell cultures. *Methods in Enzymology*. 406:676-691.

O'Connell, C.B., and Y.L. Wang. 2000. Mammalian spindle orientation and position respond to changes in cell shape in a dynein-dependent fashion. *Molecular Biology of the Cell*. 11:1765-1774.

O'Connor, P.M., and J. Jackman. 1996. Synchronization of Mammalian Cells. *In* Cell Cycle - Materials and Methods. M. Pagano, editor. Springer Berlin Heidelberg. 63-74.

Ohama, Y., and K. Hayashi. 2009. Relocalization of a microtubule-anchoring protein, ninein, from the centrosome to dendrites during differentiation of mouse neurons. *Histochemistry and Cell Biology*. 132:515-524.

Oriolo, A.S., F.A. Wald, V.P. Ramsauer, and P.J.I. Salas. 2007. Intermediate filaments: A role in epithelial polarity. *Experimental Cell Research*. 313:2255-2264.

Ou, Y., M. Zhang, and J.B. Rattner. 2004. The centrosome: The centriole-PCM coalition. *Cell Motility and the Cytoskeleton*. 57:1-7.

Palazzo, A.F., T.A. Cook, A.S. Alberts, and G.G. Gundersen. 2001. mDia mediates Rho-regulated formation and orientation of stable microtubules. *Nature Cell Biology*. 3:723-729.

Palazzo, A.F., C.H. Eng, D.D. Schlaepfer, E.E. Marcantonio, and G.G. Gundersen. 2004. Localized stabilization of microtubules by integrin- and FAK-facilitated Rho signaling. *Science*. 303:836-839.

Pepperkok, R., M.H. Bre, J. Davoust, and T.E. Kreis. 1990. Microtubules are stabilized in confluent epithelial cells but not in fibroblasts. *Journal of Cell Biology*. 111:3003-3012.

Perez, F., G.S. Diamantopoulos, R. Stalder, and T.E. Kreis. 1999. CLIP-170 highlights growing microtubule ends in vivo. *Cell*. 96:517-527.

Perez-Moreno, M., C. Jamora, and E. Fuchs. 2003. Sticky business: Orchestrating cellular signals at adherens junctions. *Cell*. 112:535-548.

Peris, L., M. Wagenbach, L. Lafanechère, J. Brocard, A.T. Moore, F. Kozielski, D. Job, L. Wordeman, and A. Andrieux. 2009. Motor-dependent microtubule disassembly driven by tubulin tyrosination. *Journal of Cell Biology*. 185:1159-1166.

Petrie, R.J., A.D. Doyle, and K.M. Yamada. 2009. Random versus directionally persistent cell migration. *Nature Reviews Molecular Cell Biology*. 10:538-549.

Pihan, G.A., A. Purohit, J. Wallace, R. Malhotra, L. Liotta, and S.J. Doxsey. 2001. Centrosome defects can account for cellular and genetic changes that characterize prostate cancer progression. *Cancer Research*. 61:2212-2219.

Pollard, T.D., and G.G. Borisy. 2003. Cellular motility driven by assembly and disassembly of actin filaments. *Cell*. 112:453-465.

Polyak, K., and R.A. Weinberg. 2009. Transitions between epithelial and mesenchymal states: Acquisition of malignant and stem cell traits. *Nature Reviews Cancer*. 9:265-273.

Qu, D., H. Qu, M. Fu, X. Zhao, R. Liu, L. Sui, and Q. Zhan. 2008. Increased expression of Nlp, a potential oncogene in ovarian cancer, and its implication in carcinogenesis. *Gynecologic Oncology*. 110:230-236.

Quinones, G.B., B.A. Danowski, A. Devaraj, V. Singh, and L.A. Ligon. 2011. The posttranslational modification of tubulin undergoes a switch from detyrosination to acetylation as epithelial cells become polarized. *Molecular Biology of the Cell*. 22:1045-1057.

Quintyne, N.J., S.R. Gill, D.M. Eckley, C.L. Crego, D.A. Compton, and T.A. Schroer. 1999. Dynactin is required for microtubule anchoring at centrosomes. *Journal of Cell Biology*. 147:321-334.

Quyn, A.J., P.L. Appleton, F.A. Carey, R.J.C. Steele, N. Barker, H. Clevers, R.A. Ridgway, O.J. Sansom, and I.S. Näthke. 2010. Spindle Orientation Bias in Gut Epithelial Stem Cell Compartments Is Lost in Precancerous Tissue. *Cell Stem Cell*. 6:175-181.

Rauchman, M.I., S.K. Nigam, E. Delpire, and S.R. Gullans. 1993. An osmotically tolerant inner medullary collecting duct cell line from an SV40 transgenic mouse. *American Journal of Physiology*. 265:F416-F424.

Raybin, D., and M. Flavin. 1977. Enzyme which specifically adds tyrosine to the α chain of tubulin. *Biochemistry*. 16:2189-2194.

Redeker, V., N. Levilliers, J.M. Schmitter, J.P. Le Caer, J. Rossier, A. Adoutte, and M.H. Bre. 1994. Polyglycylation of tubulin: A posttranslational modification in axonemal microtubules. *Science*. 266:1688-1691.

Rehberg, M., and R. Graf. 2002. Dictyostelium EB1 is a genuine centrosomal component required for proper spindle formation. *Molecular Biology of the Cell*. 13:2301-2310.

Rice, L.M., E.A. Montabana, and D.A. Agard. 2008. The lattice as allosteric effector: Structural studies of $\alpha\beta$- and γ-tubulin clarify the role of GTP in microtubule assembly. *Proceedings of the National Academy of Sciences of the United States of America*. 105:5378-5383.

Ridley, A.J. 2001. Rho GTPases and cell migration. *Journal of Cell Science*. 114:2713-2722.

Ridley, A.J. 2013. RhoA, RhoB and RhoC have different roles in cancer cell migration. *Journal of Microscopy.* 251:242-249.

Ridley, A.J., M.A. Schwartz, K. Burridge, R.A. Firtel, M.H. Ginsberg, G. Borisy, J.T. Parsons, and A.R. Horwitz. 2003. Cell migration: Integrating signals from front to back. *Science*. 302:1704-1709.

Riento, K., and A.J. Ridley. 2003. Rocks: Multifunctional kinases in cell behaviour. *Nature Reviews Molecular Cell Biology*. 4:446-456.

Rizvi, S.A., E.M. Neidt, J. Cui, Z. Feiger, C.T. Skau, M.L. Gardel, S.A. Kozmin, and D.R. Kovar. 2009. Identification and Characterization of a Small Molecule Inhibitor of Formin-Mediated Actin Assembly. *Chemistry & Biology*. 16:1158-1168.

Rizzolo, L.J., and H.C. Joshi. 1993. Apical orientation of the microtubule organizing center and associated beta-tubulin during the polarization of the retinal pigment epithelium in vivo. *Developmental Biology.* 157:147-156.

Rodriguez, O.C., A.W. Schaefer, C.A. Mandato, P. Forscher, W.M. Bement, and C.M. Waterman-Storer. 2003. Conserved microtubule-actin interactions in cell movement and morphogenesis. *Nature Cell Biology*. 5:599-609.

Rogers, S.L., G.C. Rogers, D.J. Sharp, and R.D. Vale. 2002. Drosophila EB1 is important for proper assembly, dynamics, and positioning of the mitotic spindle. *Journal of Cell Biology*. 158:873-884.

Roper, K., S.L. Gregory, and N.H. Brown. 2002. The 'Spectraplakins': cytoskeletal giants with characteristics of both spectrin and plakin families. *Journal of Cell Science*. 115:4215-4225.

Rosin-Arbesfeld, R., G. Ihrke, and M. Bienz. 2001. Actin-dependent membrane association of the APC tumour suppressor in polarized mammalian epithelial cells. *EMBO Journal.* 20:5929-5939.

Rowan, A.J., H. Lamlum, M. Ilyas, J. Wheeler, J. Straub, A. Papadopoulou, D. Bicknell, W.F. Bodmer, and I.P.M. Tomlinson. 2000. APC mutations in sporadic colorectal tumors: A mutational "hotspot" and interdependence of the "two hits". *Proceedings of the National Academy of Sciences of the United States of America*. 97:3352-3357.

Sääf, A.M., J.M. Halbleib, X. Chen, T.Y. Siu, Y.L. Suet, W.J. Nelson, and P.O. Brown. 2007. Parallels between global transcriptional programs of polarizing Caco-2 intestinal epithelial cells in vitro and gene expression programs in normal colon and colon cancer. *Molecular Biology of the Cell*. 18:4245-4260.

Sahai, E. 2005. Mechanisms of cancer cell invasion. *Current Opinion in Genetics and Development.* 15:87-96.

Salisbury, J.L. 2007. A mechanistic view on the evolutionary origin for centrin-based control of centriole duplication. *Journal of Cellular Physiology*. 213:420-428.

Sancho, E., E. Batlle, and H. Clevers. 2004. Signaling pathways in intestinal development and cancer. *Annual Review of Cell & Developmental Biology.* 20:695-723.

Sandblad, L., K.E. Busch, P. Tittmann, H. Gross, D. Brunner, and A. Hoenger. 2006. The Schizosaccharomyces pombe EB1 homolog Mal3p binds and stabilizes the microtubule lattice seam. *Cell*. 127:1415-1424.

Schiff, P.B., J. Fant, and S.B. Horwitz. 1979. Promotion of microtubule assembly in vitro by taxol. *Nature*. 277:665-667.

Schneeberger, E.E., and R.D. Lynch. 2004. The tight junction: a multifunctional complex. *American Journal of Physiology - Cell Physiology.* 286:C1213-C1228.

Schober, J.M., J.M. Cain, Y.A. Komarova, and G.G. Borisy. 2009. Migration and actin protrusion in melanoma cells are regulated by EB1 protein. *Cancer Letters*. 284:30-36.

Seeley, R.R., T.D. Stephens, and P. Tate. 2008. Anatomy & physiology. Boston : McGraw-Hill Higher Education ; [London : McGraw-Hill [distributor], c2008.

Sharma, M., L. Leung, M. Brocardo, J. Henderson, C. Flegg, and B.R. Henderson. 2006. Membrane localization of adenomatous polyposis coli protein at cellular protrusions: Targeting sequences and regulation by β-catenin. *Journal of Biological Chemistry*. 281:17140-17149.

Shaw, R.J., N. Bardeesy, B.D. Manning, L. Lopez, M. Kosmatka, R.A. DePinho, and L.C. Cantley. 2004. The LKB1 tumor suppressor negatively regulates mTOR signaling. *Cancer Cell*. 6:91-99.

Shi, S.R., M.E. Key, and K.L. Kalra. 1991. Antigen retrieval in formalin-fixed, paraffin-embedded tissues: An enhancement method for immunohistochemical staining based on microwave oven heating of tissue sections. *Journal of Histochemistry and Cytochemistry*. 39:741-748.

Siegel, R., D. Naishadham, and A. Jemal. 2012. Cancer Statistics, 2012. *CA: A Cancer Journal for Clinicians.* 62:10-29.

Siegrist, S.E., and C.Q. Doe. 2007. Microtubule-induced cortical cell polarity. *Genes and Development*. 21:483-496.

Slep, K.C., S.L. Rogers, S.L. Elliott, H. Ohkura, P.A. Kolodziej, and R.D. Vale. 2005. Structural determinants for EB1-mediated recruitment of APC and spectraplakins to the microtubule plus end. *Journal of Cell Biology*. 168:587-598.

Slep, K.C., and R.D. Vale. 2007. Structural basis of microtubule plus end tracking by XMAP215, CLIP-170, and EB1. *Molecular Cell*. 27:976-991.

Slepecky, N.B., C.G. Henderson, and S. Saha. 1995. Post-translational modifications of tubulin suggest that dynamic microtubules are present in sensory cells and stable microtubules are present in supporting cells of the mammalian cochlea. *Hearing Research*. 91:136-147.

Small, J.V., B. Geiger, I. Kaverina, and A. Bershadsky. 2002a. How do microtubules guide migrating cells? *Nature Reviews Molecular Cell Biology*. 3:957-964.

Small, J.V., T. Stradal, E. Vignal, and K. Rottner. 2002b. The lamellipodium: Where motility begins. *Trends in Cell Biology*. 12:112-120.

Stehbens, S.J., A. Akhmanova, and A.S. Yap. 2009. Microtubules and cadherins: a neglected partnership. *Frontiers in Bioscience.* 14:3159-3167.

Straube, A., and A. Merdes. 2007. EB3 Regulates Microtubule Dynamics at the Cell Cortex and Is Required for Myoblast Elongation and Fusion. *Current Biology*. 17:1318-1325.

Strnad, P., and P. Gonczy. 2008. Mechanisms of procentriole formation. *Trends in Cell Biology*. 18:389-396.

Su, L.K., M. Burrell, D.E. Hill, J. Gyuris, R. Brent, R. Wiltshire, J. Trent, B. Vogelstein, and K.W. Kinzler. 1995. APC binds to the novel protein EB1. *Cancer Research*. 55:2972-2977.

Su, L.K., K.A. Johnson, K.J. Smith, D.E. Hill, B. Vogelstein, and K.W. Kinzler. 1993. Association between wild type and mutant APC gene products. *Cancer Research*. 53:2728-2731.

Su, L.K., and Y. Qi. 2001. Characterization of human MAPRE genes and their proteins. *Genomics*. 71:142-149.

Szarama, K.B., R. Stepanyan, R.S. Petralia, N. Gavara, G.I. Frolenkov, M.W. Kelley, and R.S. Chadwick. 2012. Fibroblast growth factor receptor 3 regulates microtubule formation and cell surface mechanical properties in the developing organ of Corti. *Bioarchitecture*. 2:214-219.

Takesono, A., S.J. Heasman, B. Wojciak-Stothard, R. Garg, and A.J. Ridley. 2010. Microtubules regulate migratory polarity through Rho/ ROCK signaling in T cells. *PLoS ONE*. 5.

Tanos, B., and E. Rodriguez-Boulan. 2008. The epithelial polarity program: machineries involved and their hijacking by cancer. *Oncogene*. 27:6939-6957.

Thiery, J.P., H. Acloque, R.Y.J. Huang, and M.A. Nieto. 2009. Epithelial-Mesenchymal Transitions in Development and Disease. *Cell*. 139:871-890.

Tirnauer, J.S. 2004. A new cytoskeletal connection for APC: Linked to actin through IQGAP. *Developmental Cell*. 7:778-780.

Tirnauer, J.S., and B.E. Bierer. 2000. EB1 proteins regulate microtubule dynamics, cell polarity, and chromosome stability. *Journal of Cell Biology*. 149:761-766.

Tirnauer, J.S., S. Grego, E.D. Salmon, and T.J. Mitchison. 2002. EB1-microtubule interactions in Xenopus egg extracts: Role of EB1 in microtubule stabilization and mechanisms of targeting to microtubules. *Molecular Biology of the Cell*. 13:3614-3626.

Tirnauer, J.S., E. O'Toole, L. Berrueta, B.E. Bierer, and D. Pellman. 1999. Yeast Bim1p promotes the G1-specific dynamics of microtubules. *Journal of Cell Biology*. 145:993-1007.

Toyoshima, F., and E. Nishida. 2007. Integrin-mediated adhesion orients the spindle parallel to the substratum in an EB1- and myosin X-dependent manner. *EMBO Journal.* 26:1487-1498.

Tsou, M.F., and T. Stearns. 2006. Mechanism limiting centrosome duplication to once per cell cycle. *Nature*. 442:947-951.

Tsvetkov, A.S., A. Samsonov, A. Akhmanova, N. Galjart, and S.V. Popov. 2007. Microtubule-binding proteins CLASP1 and CLASP2 interact with actin filaments. *Cell Motility and the Cytoskeleton*. 64:519-530.

Tyrrell, B.J. 2012. The role of ninein in epithelial apico-basal differentiation. PhD Thesis. University of East Anglia.

Tyson, J.J., and B. Novak. 2008. Temporal Organization of the Cell Cycle. *Current Biology*. 18:R759-R768.

Vakifahmetoglu, H., M. Olsson, and B. Zhivotovsky. 2008. Death through a tragedy: Mitotic catastrophe. *Cell Death and Differentiation*. 15:1153-1162.

Vale, R.D., T.S. Reese, and M.P. Sheetz. 1985. Identification of a novel force-generating protein, kinesin, involved in microtubule-based motility. *Cell*. 42:39-50.

Vallee, R.B., and J.W. Tsai. 2006. The cellular roles of the lissencephaly gene LIS1, and what they tell us about brain development. *Genes and Development*. 20:1384-1393.

van der Flier, L.G., and H. Clevers. 2009. Stem Cells, Self-Renewal, and Differentiation in the Intestinal Epithelium. *In* Annual Review of Physiology. Vol. 71. Annual Reviews, Palo Alto. 241-260.

van der Vaart, B., C. Manatschal, I. Grigoriev, V. Olieric, S.M. Gouveia, S. Bjelic, J. Demmers, I. Vorobjev, C.C. Hoogenraad, M.O. Steinmetz, and A. Akhmanova. 2011. SLAIN2 links microtubule plus end-tracking proteins and controls microtubule growth in interphase. *Journal of Cell Biology*. 193:1083-1099.

Vasiliev, J.M., I.M. Gelfand, L.V. Domnina, O.Y. Ivanova, S.G. Komm, and L.V. Olshevskaja. 1970. Effect of colcemid on the locomotory behaviour of fibroblasts. *Journal of Embryology and Experimental Morphology*. 24:625-640.

Vaughan, K.T. 2005. TIP maker and TIP marker; EB1 as a master controller of microtubule plus ends. *Journal of Cell Biology*. 171:197-200.

Vaughan, K.T., and R.B. Vallee. 1995. Cytoplasmic dynein binds dynactin through a direct interaction between the intermediate chains and $p150^{GLUED}$. *Journal of Cell Biology*. 131:1507-1516.

Vega, F.M., G. Fruhwirth, T. Ng, and A.J. Ridley. 2011. RhoA and RhoC have distinct roles in migration and invasion by acting through different targets. *Journal of Cell Biology*. 193:655-665.

Vega, F.M., and A.J. Ridley. 2008. Rho GTPases in cancer cell biology. *FEBS Letters*. 582:2093-2101.

Verhey, K.J., and J. Gaertig. 2007. The tubulin code. *Cell Cycle*. 6:2152-2160.

Vermes, I., C. Haanen, H. Steffens-Nakken, and C. Reutelingsperger. 1995. A novel assay for apoptosis. Flow cytometric detection of phosphatidylserine expression on early apoptotic cells using fluorescein labelled Annexin V. *Journal of Immunological Methods*. 184:39-51.

Vinzenz, M., M. Nemethova, F. Schur, J. Mueller, A. Narita, E. Urban, C. Winkler, C. Schmeiser, S.A. Koestler, K. Rottner, G.P. Resch, Y. Maeda, and J.V. Small. 2012. Actin branching in the initiation and maintenance of lamellipodia. *Journal of Cell Science*. 125:2775-2785.

Vitre, B., F.M. Coquelle, C. Heichette, C. Garnier, D. Chretien, and I. Arnal. 2008. EB1 regulates microtubule dynamics and tubulin sheet closure in vitro. *Nature Cell Biology*. 10:415-U481.

Wang, W.S., M. Chen, and Y. Su. 2006. Colorectal carcinoma: from tumorigenesis to treatment. *Cellular and Molecular Life Sciences* 63:663-671.

Wang, X., J.W. Tsai, J.H. Imai, W.N. Lian, R.B. Vallee, and S.H. Shi. 2009. Asymmetric centrosome inheritance maintains neural progenitors in the neocortex. *Nature*. 461:947-955.

Watanabe, T., J. Noritake, and K. Kaibuchi. 2005. Roles of IQGAP1 in cell polarization and migration. *Novartis Foundation Symposiummp*. 269:92-101; discussion 101-105, 223-130.

Watanabe, T., S. Wang, J. Noritake, K. Sato, M. Fukata, M. Takefuji, M. Nakagawa, N. Izumi, T. Akiyama, and K. Kaibuchi. 2004. Interaction with IQGAP1 links APC to Rac1, Cdc42, and actin filaments during cell polarization and migration. *Developmental Cell*. 7:871-883.

Watson, J.V., S.H. Chambers, and P.J. Smith. 1987. A pragmatic approach to the analysis of DNA histograms with a definable G1 peak. *Cytometry*. 8:1-8.

Webster, D.R., G.G. Gundersen, J.C. Bulinski, and G.G. Borisy. 1987. Differential turnover of tyrosinated and detyrosinated microtubules. *Proceedings of the National Academy of Sciences of the United States of America*. 84:9040-9044.

Wen, Y., C.H. Eng, J. Schmoranzer, N. Cabrera-Poch, E.J.S. Morris, M. Chen, B.J. Wallar, A.S. Alberts, and G.G. Gundersen. 2004. EB1 and APC bind to mDia to stabilize microtubules downstream of Rho and promote cell migration. *Nature Cell Biology*. 6:820-U821.

Wheelock, M.J., and K.R. Johnson. 2003. Cadherin-mediated cellular signaling. *Current Opinion in Cell Biology*. 15:509-514.

Whitehead, R.H., P.E. Vaneeden, M.D. Noble, P. Ataliotis, and P.S. Jat. 1993. Establishment of conditionally immortalized epithelial cell lines from both colon and small intestine of adult H-2Kb-tsA58 transgenic mice. *Proceedings of the National Academy of Sciences of the United States of America*. 90:587-591.

Wiese, C., and Y. Zheng. 2006. Microtubule nucleation: γ-tubulin and beyond. *Journal of Cell Science*. 119:4143-4153.

Wittmann, T., A. Hyman, and A. Desai. 2001. The spindle: A dynamic assembly of microtubules and motors. *Nature Cell Biology*. 3:E28-E34.

Wittmann, T., and C.M. Waterman-Storer. 2001. Cell motility: Can Rho GTPases and microtubules point the way? *Journal of Cell Science*. 114:3795-3803.

Wodarz, A., and I. Nathke. 2007. Cell polarity in development and cancer. *Nature Cell Biology*. 9:1016-1024.

Woods, A., S.R. Johnstone, K. Dickerson, F.C. Leiper, L.G.D. Fryer, D. Neumann, U. Schlattner, T. Wallimann, M. Carlson, and D. Carling. 2003. LKB1 Is the Upstream Kinase in the AMP-Activated Protein Kinase Cascade. *Current Biology*. 13:2004-2008.

Wu, X., A. Kodama, and E. Fuchs. 2008. ACF7 Regulates Cytoskeletal-Focal Adhesion Dynamics and Migration and Has ATPase Activity. *Cell*. 135:137-148.

Yamashita, Y.M., D.L. Jones, and M.T. Fuller. 2003. Orientation of asymmetric stem cell division by the APC tumor suppressor and centrosome. *Science*. 301:1547-1550.

Yan, X.M., R. Habedanck, and E.A. Nigg. 2006. A complex of two centrosomal proteins, CAP350 and FOP, cooperates with EB1 in microtubule anchoring. *Molecular Biology of the Cell*. 17:634-644.

Yeaman, C., K.K. Grindstaff, and W.J. Nelson. 1999. New perspectives on mechanisms involved in generating epithelial cell polarity. *Physiological Reviews*. 79:73-98.

Yin, H., D. Pruyne, T.C. Huffaker, and A. Bretscher. 2000. Myosin V orientates the mitotic spindle in yeast. *Nature*. 406:1013-1015.

Zaoui, K., K. Benseddik, P. Daou, D. Salaün, and A. Badache. 2010. ErbB2 receptor controls microtubule capture by recruiting ACF7 to the plasma membrane of migrating cells. *Proceedings of the National Academy of Sciences of the United States of America*. 107:18517-18522.

Zhang, T., K.J.M. Zaal, J. Sheridan, A. Mehta, G.G. Gundersen, and E. Ralston. 2009. Microtubule plus-end binding protein EB1 is necessary for muscle cell differentiation, elongation and fusion. *Journal of Cell Science*. 122:1401-1409.

Zhu, Z.C., K.K. Gupta, A.R. Slabbekoorn, B.A. Paulson, E.S. Folker, and H.V. Goodson. 2009. Interactions between EB1 and microtubules: Dramatic effect of affinity tags and evidence for cooperative behavior. *Journal of Biological Chemistry*. 284:32651-32661.

Ziegler, U., and P. Groscurth. 2004. Morphological features of cell death. *News in Physiological Sciences*. 19:124-128.

Zumbrunn, J., K. Kinoshita, A.A. Hyman, and I.S. Näthke. 2001. Binding of the adenomatous polyposis coli protein to microtubules increases microtubule stability and is regulated by GSK3 beta phosphorylation. *Current Biology*. 11:44-49.

Zyss, D., and F. Gergely. 2009. Centrosome function in cancer: guilty or innocent? *Trends in Cell Biology*. 19:334-346.

The microtubule end-binding protein EB2 is a central regulator of microtubule reorganisation in apico-basal epithelial differentiation

Deborah A. Goldspink[1], Jonathan R. Gadsby[1], Gemma Bellett[1], Jennifer Keynton[1], Benjamin J. Tyrrell[1], Elizabeth K. Lund[1], Penny P. Powell[2], Paul Thomas[1] and Mette M. Mogensen[1,*]

[1]School of Biological Sciences, University of East Anglia, Norwich Research Park, Norwich, NR4 7TJ, UK
[2]Norwich Medical School, University of East Anglia, Norwich Research Park, Norwich, NR4 7TJ, UK

*Author for correspondence (m.mogensen@uea.ac.uk)

Accepted 31 May 2013
Journal of Cell Science 126, 4000–4014
© 2013. Published by The Company of Biologists Ltd
doi: 10.1242/jcs.129759

Summary

Microtubule end-binding (EB) proteins influence microtubule dynamic instability, a process that is essential for microtubule reorganisation during apico-basal epithelial differentiation. Here, we establish for the first time that expression of EB2, but not that of EB1, is crucial for initial microtubule reorganisation during apico-basal epithelial differentiation, and that EB2 downregulation promotes bundle formation. EB2 siRNA knockdown during early stages of apico-basal differentiation prevented microtubule reorganisation, whereas its downregulation at later stages promoted microtubule stability and bundle formation. Interestingly, although EB1 is not essential for microtubule reorganisation, its knockdown prevented apico-basal bundle formation and epithelial elongation. siRNA depletion of EB2 in undifferentiated epithelial cells induced the formation of straight, less dynamic microtubules with EB1 and ACF7 lattice association and co-alignment with actin filaments, a phenotype that could be rescued by inhibition with formin. Importantly, *in situ* inner ear and intestinal crypt epithelial tissue revealed direct correlations between a low level of EB2 expression and the presence of apico-basal microtubule bundles, which were absent where EB2 was elevated. EB2 is evidently important for initial microtubule reorganisation during epithelial polarisation, whereas its downregulation facilitates EB1 and ACF7 microtubule lattice association, microtubule-actin filament co-alignment and bundle formation. The spatiotemporal expression of EB2 thus dramatically influences microtubule organisation, EB1 and ACF7 deployment and epithelial differentiation.

Key words: EB2, EB1, ACF7, Epithelia, Microtubules, Cochlea, Intestinal crypt, Actin filaments

Introduction

Microtubule reorganisation is critical for differentiation, tissue formation and function and this is particularly evident during apico-basal polarisation of epithelial cells such as those of the kidney, intestine and inner ear. A radial microtubule array focused on a centrally located centrosome is typical of many undifferentiated epithelial cells. Here the microtubule minus-ends are anchored at the centrosome and the plus-ends extend towards the cell cortex. Cell-to-cell contact and polarisation trigger a dramatic reorganisation of these microtubules leading to the formation of an apico-basal array no longer anchored at the centrosome. The minus-ends of the apico-basal microtubules become anchored at apical, non-centrosomal sites associated with adherens junctions (Bacallao et al., 1989; Bellett et al., 2009; Mogensen et al., 2002; Moss et al., 2007). Evidence based on both *in situ* inner ear epithelial cells and *in vitro* cultures of Madin-Darby canine kidney (MDCKII) cells show that the microtubules of the apico-basal arrays originate from the centrosome but how they are subsequently reorganised remains to be determined (Bellett et al., 2009; Gierke and Wittmann, 2012).

EB1 is often referred to as the master controller of plus-end tracking proteins (+TIPs) being able to track the plus-end of growing microtubules and interact with most other +TIPs (Lansbergen and Akhmanova, 2006; Morrison et al., 1998). EB1 is evolutionary conserved, and three family members EB1, EB2 and EB3, encoded by separate (MAPRE) genes, are expressed in mammalian cells (Bu and Su, 2003; Su et al., 1995; Su and Qi, 2001). EB1 and EB3 influence microtubule dynamics by promoting growth and suppressing catastrophe whereas EB2 apparently does not (Komarova et al., 2009; Li et al., 2011; Tirnauer and Bierer, 2000; van der Vaart et al., 2009). However, relatively little is known about EB2's function in cells. EBs form dimers and bind microtubules via their N-terminal calponin homology (CH) domain and recent evidence suggest that tip recognition is due to a high affinity for GTP–tubulin, which is prominent at the growing end of microtubules (Dimitrov et al., 2008; Maurer et al., 2011; Maurer et al., 2012). Repulsive forces between the negatively charged C-terminus and the microtubule lattice are also likely to contribute to the plus-end localisation (Buey et al., 2011). EB1 and EB3, but to a lesser extent EB2, interact via the C-terminus with most other +TIPs including APC (adenomatous polyposis coli), CLIPs (cytoplasmic linker proteins), CLASPs (CLIP-associated proteins) and the microtubule-actin cross-linking spectraplakin ACF7 (MACF1). Hence, they regulate interactions of microtubules with the cell cortex, actin filaments, kinetochores and organelles (Kodama et al., 2003; Komarova et al., 2005; Lansbergen and Akhmanova, 2006; Wu et al., 2008). EBs may

Journal of Cell Science

Journal of Cell Science

thus influence microtubule reorganisation by regulating their dynamics and ability to interact with other structures.

Microtubule reorganisation and generation of apico-basal bundles is also likely to involve cytoskeletal cross-talk. The Rho GTPases are key regulators of the microtubule and actin cytoskeleton. They both regulate and are regulated by microtubule dynamics and control actin filament assembly and organisation. Microtubule depolymerisation by Nocodazole, for example, activates RhoA/ROCK and destabilises microtubules due to release of the Rho effector GEF-H1 from microtubules. RhoA/ROCK inhibition, on the other hand, induces microtubule stability and bundle formation as well as reducing stress fibres (Chang et al., 2008; Cheng et al., 2012; Gao et al., 2004; Kadir et al., 2011; Krendel et al., 2002; Scaife et al., 2003; Takesono et al., 2010).

Skeletal muscle, like differentiation of epithelial cells involves a major reorganisation of the microtubule network transforming the radial array of myoblasts into non-centrosomal parallel bundles in differentiated myotubes (Tassin et al., 1985). Intriguingly, a marked downregulation in EB2 expression has been reported during muscle differentiation while EB1 levels remained constant (Straube and Merdes, 2007). This suggests that downregulation of EB2 may be a prerequisite for microtubule bundle formation. We therefore focused our investigation on the role of EB2 in microtubule reorganisation and apico-basal bundle formation during epithelial differentiation.

Here we establish for the first time a role for EB2 in microtubule reorganisation during apico-basal epithelial differentiation. We report that EB2, but not EB1, expression is critical for microtubule reorganisation during early stages of epithelial differentiation whereas EB1 is important for apico-basal microtubule bundle formation and epithelial elongation. EB2 downregulation during latter stages of differentiation facilitates EB1 lattice association, ACF7 recruitment and microtubule-actin filament co-alignment and bundle formation. Furthermore, inhibition of the formin FH2 domain with SMIFH2 in EB2-depleted cells rescues the control phenotype.

Results

EB2 is expressed during early stages of apico-basal epithelial differentiation but downregulated in most cells at later stages

Mouse inner medullary kidney (mIMCD-3) cells were grown for 9 days resulting in highly confluent (partially polarised) epithelial

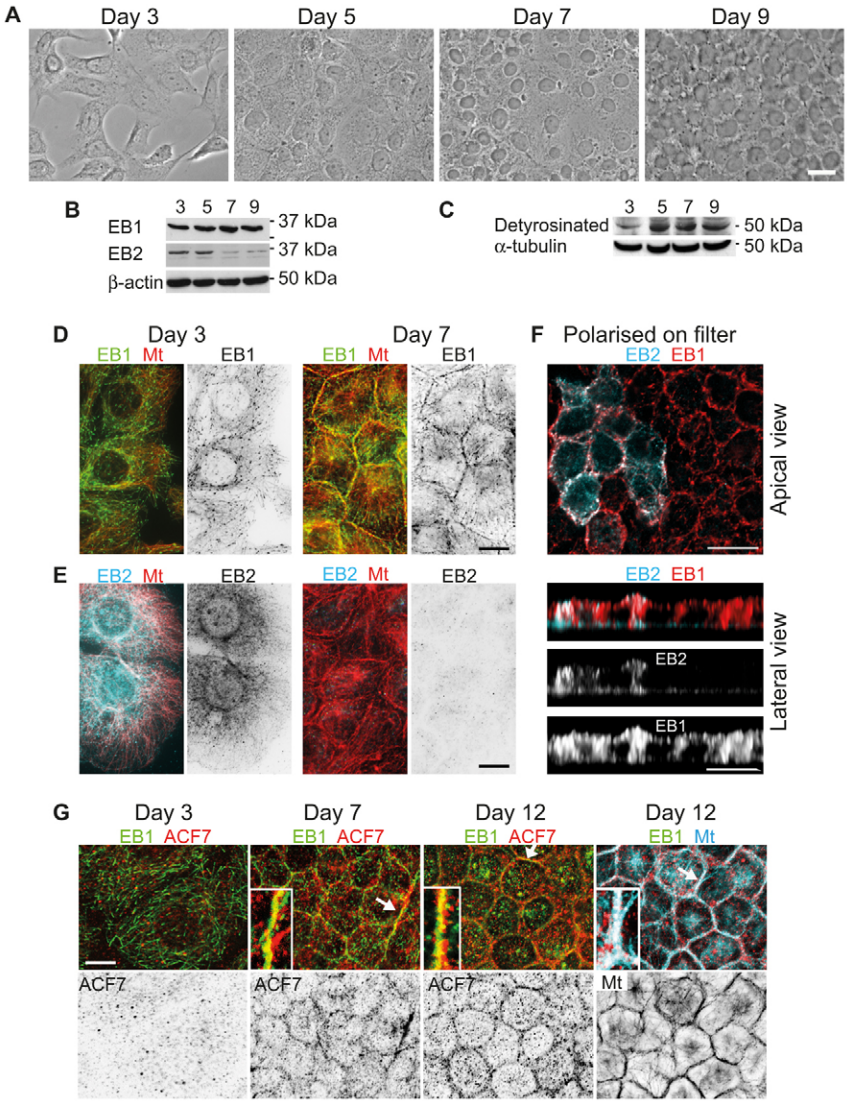

Fig. 1. EB2 is downregulated in most mIMCD-3 cells during apico-basal epithelial differentiation. (**A**) Phase-contrast images of cells at different stages of differentiation from subconfluent at day 3 to highly confluent (partially polarised) at day 9. (**B**,**C**) Western blots showing EB1, EB2 and β-actin protein levels at days 3, 5, 7 and 9 (B), and detyrosinated and total tubulin levels in (C). (**D**) Widefield fluorescence microscope images show distinct EB1 (rabbit pAb, green/invert) comets at microtubule (YL1/2, red) plus-ends at day 3 and peripheral accumulation at day 7. (**E**) Cells immunolabelled for α-tubulin (red) and EB2 (blue/invert) reveal relatively high expression of EB2 in subconfluent cells (day 3) but low expression in confluent cells (day 7). (**F**) Confocal optical sections of polarised cells grown on filter at day 7 showing a patch of high-expression EB2 (blue) cells surrounded by low-expression cells, whereas EB1 (rabbit pAb, red) expression is prominent in all. (**G**) Confocal sections of cells immunolabelled for ACF-7 (red) and either EB1 (mouse mAb, green) or tubulin (YL1/2, blue) showing dispersed ACF7 at day 3, but cortical ACF7 co-localising with EB1 and microtubules (arrows and enlargements in insets) at days 7 and 12. Scale bars: 20 µm (A); 10 µm (D–G). Mt, microtubule.

sheets (Fig. 1A). Western blots and immunolocalisation using highly specific antibodies (Komarova et al., 2005) showed that EB1 is stably expressed during epithelial differentiation while EB2 is downregulated (Fig. 1B,D,E). An increase in microtubule stability was indicated by an increase in detyrosinated tubulin as cells reached confluence (Fig. 1C). Although, EB1 protein levels remained the same during this differentiation period, EB1 localisation changed from microtubule plus-end in subconfluent cells (day 3) to mainly peripheral and apico-basal in confluent (day 7) and fully polarised cells (Fig. 1B,D,F). Interestingly, ACF7 localisation also changed from cytoplasmic and dispersed in subconfluent cells (day 3) to peripheral, co-localising with EB1 and microtubules in differentiated cells (days 7 and 12) (Fig. 1G). All subconfluent and early differentiating (days 3–5) cells showed relatively high EB2 expression, while the vast majority of confluent and fully polarised cells revealed very low expression of EB2 suggesting that downregulation of EB2 may be associated with epithelial differentiation (Fig. 1B,E,F). Interestingly, a few patches of confluent and polarised cells showed high levels of EB2 expression suggesting a heterogeneous population (Fig. 1F; supplementary material Fig. S1A). Confocal optical cross-sections and lateral views of Z stacks revealed that in EB2-expressing polarised cells EB2 showed a similar distribution to EB1 and co-localised with the apico-basal microtubules (Fig. 1F; supplementary material Fig. S1B). Both high and low EB2 expressing differentiated cells had elongated when grown on filters and appeared to assemble apico-basal microtubules. However, the precise organisation of the microtubules could not be defined due to lack of Z resolution.

siRNA depletion of EB2 induces formation of straight, bundled and less-dynamic microtubules

In order to determine whether EB2 downregulation affects microtubule organisation EB2 was depleted using siRNA in human retinal pigment epithelial cells (ARPE-19) as these contain a classic radial microtubule organisation and deviations from this pattern are easily detected (Bellett et al., 2009). ARPE-19 cells showed EB2 localisation in patches along microtubules and at plus-ends as previously reported for other cell lines (Fig. 2A) (Komarova et al., 2009). Four siRNA sequences (a–d) resulted in complete knockdown of EB2 at 96 hours after double transfection (0 and 48 hours) (Fig. 2B; supplementary material Fig. S1C). EB2 depletion produced a distinct phenotype with significantly larger cells containing straighter and often bundled microtubules compared to control (untreated) and scramble siRNA cells (Fig. 2C,D,E). Similar results were observed in U2OS, TC7 and HCT116 epithelial cells following EB2 knockdown (data not shown). EB2-depleted ARPE-19 cells were on average 3.7 times larger than scramble siRNA cells based on cell area (Fig. 2E). Cell proliferation assays and Ki-67 staining (Gerdes et al., 1984) revealed no significant differences between EB2-depleted and scramble siRNA cells within the 96 hour analyses period (supplementary material Fig. S2A,B,C). Live time-lapse imaging showed that even relatively large EB2-depleted cells were able to complete cell division (supplementary material Movies 1, 2).

Microtubule straightness was analysed by determining the number of microtubule crossover events within 10×10 μm squares. Significantly fewer crossover events were evident in EB2-depleted compared to control and scramble siRNA cells thus suggesting that EB2 depletion results in straighter microtubules (Fig. 2F). The possibility that the increase in straightness could be due to an increase in microtubule density was also assessed by determining the number of microtubules within the squares. However, no significant difference in microtubule numbers was observed between EB2 siRNA and scramble siRNA cells (supplementary material Fig. S2D). In order to verify these results a mCherry-tagged EB2 expression vector was generated using the mouse sequence, which is unaffected by the human siRNA sequences (supplementary material Fig. S2E,F). The mCherry–EB2 expressed in EB2-depleted cells associated with the microtubule lattice and successfully rescued both cell size and microtubule crossover event phenotypes (Fig. 2E,F,G). The average size of the rescued cells was significantly less than the EB2-depleted cells and the microtubules had more crossover events and were similarly organised to control/scramble siRNA cells (Fig. 2E,F).

Epithelial differentiation is known to be associated with an increase in microtubule stability (Pepperkok et al., 1990). In EB2-depleted ARPE-19 cells detyrosinated tubulin was particularly prominent in microtubule bundles (Fig. 3A). Increased microtubule stability was confirmed with cold treatment, with resistant microtubules evident in EB2-depleted, but not in control/scramble siRNA, cells (Fig. 3B, and data not shown). Furthermore, live time-lapse imaging of GFP–tubulin expressing ARPE-19 cells depleted for EB2 revealed a marked reduction in microtubule dynamics compared to control and scramble siRNA cells (Fig. 3C,D,E; supplementary material Movies 3, 4). Analyses (based on >60 microtubules per condition) revealed that EB2 depletion had no effect on microtubule growth but did cause a significant reduction in microtubule shrinking and an increase in pausing events (Fig. 3D). Graphic representation of microtubule profiles in terms of length changes over time showed minimal deviations, demonstrating reduced dynamics in EB2-depleted compared to scramble siRNA cells (Fig. 3E; supplementary material Fig. S2G). An increase in microtubule stability and bundle formation and a decrease in microtubule dynamics are evidently associated with EB2 depletion.

siRNA depletion of EB2 leads to EB1 association along the microtubule lattice

Epithelial differentiation in mIMCD-3 cells showed no change in the level of EB1 expression but a change in its distribution (Fig. 1). EB1 localisation was therefore investigated in ARPE-19 EB2-siRNA-treated cells. Both control and scramble siRNA cells showed the classic EB1 plus-end localisation (Fig. 4A). However, a marked change in EB1 deployment was observed in EB2-depleted cells with EB1 associating not only at the plus-ends but also along the length of the microtubule lattice (Fig. 4A). EB1 lattice association was also observed following EB2 depletion in U2OS, TC7 and HCT116 epithelial cells (data not shown). Predominant EB1 plus-end localisation could be rescued by expression of mCherry–EB2 in EB2-depleted cells (Fig. 4B). Both EB2 depletion and rescue phenotypes were verified by fluorescence intensity measurements. The fluorescence signal from random 2 μm segments along microtubules (but away from the plus-ends) revealed a significant increase in EB1 fluorescence intensity along the microtubule lattice in EB2-depleted compared to scramble siRNA cells while rescued cells showed a return to control fluorescence intensity levels (Fig. 4C).

Journal of Cell Science

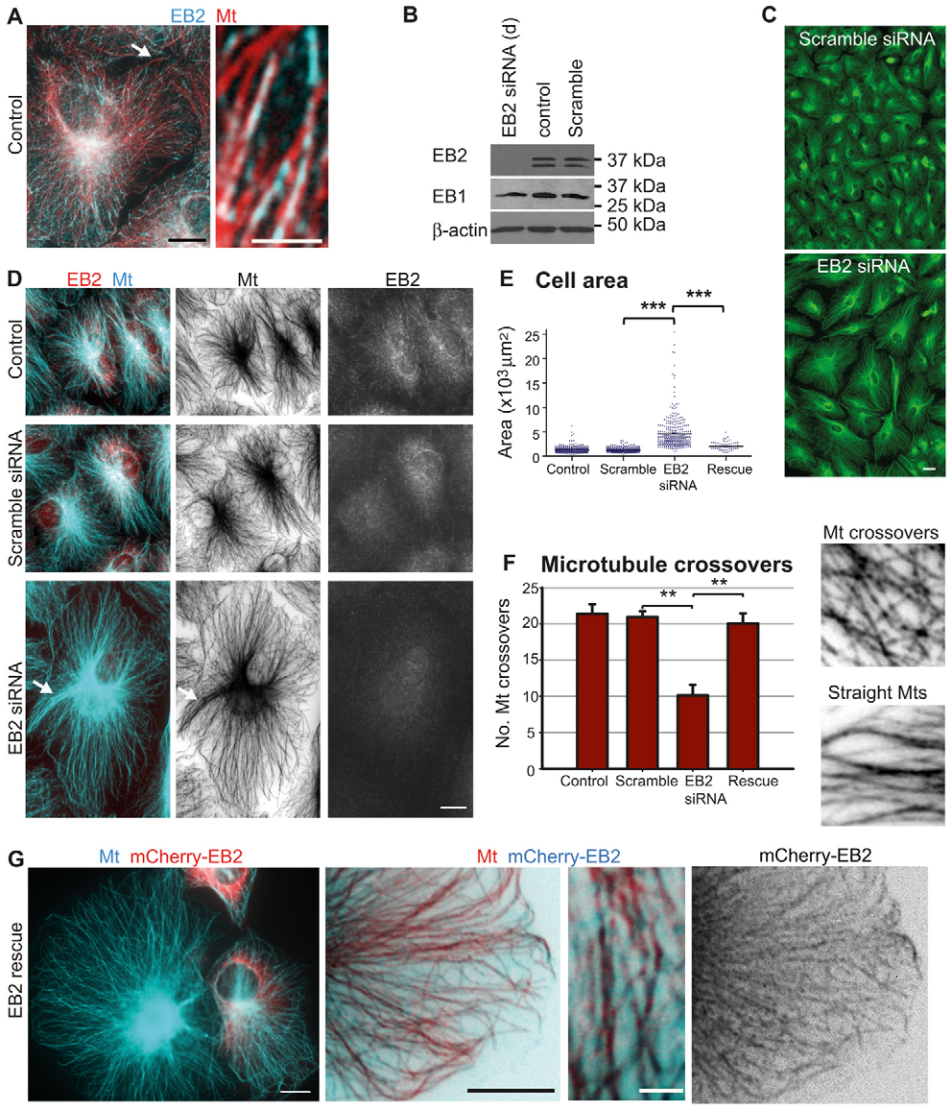

Fig. 2. siRNA depletion of EB2 in ARPE-19 cells leads to straight and bundled microtubules and increased cell size. (**A**) Widefield fluorescence images of an untreated control cell (enlarged region arrowed) showing EB2 (blue) at the plus-ends and along the microtubule (α-tubulin, red) lattice. (**B**) Western blots of cell lysates of control, scramble, EB2 siRNA (sequence d) at 96 hours post initial treatment showing EB2, EB1 and β-actin expression levels. (**C**) Image overviews highlight striking differences in cell size between scramble and EB2 siRNA-treated (sequence d) cells. Cells were fixed in paraformaldehyde to minimise cell shrinkage and were labelled for α-tubulin (green). (**D**) Widefield fluorescence images of control, scramble and EB2-siRNA-treated cells labelled for EB2 (red/single channel) and α-tubulin (blue/single channel) showing increased cell size, straight radial microtubules with some bundling (arrow). (**E**) Analysis of cell size based on cell area in control (n=311), scramble (n=311), EB2-siRNA-treated (sequence d, n=311) and mCherry–EB2 rescued (n=55) cells. (**F**) Average number of microtubule crossover events based on 15 peripheral squares (10×10 µm) in five cells, data averaged (±s.e.m.) from three independent experiments for each treatment. Images show typical examples of microtubule organisation in squares selected for analysis from control or scramble (microtubule crossovers) and EB2 siRNA-treated (straight microtubules) cells. (**G**) EB2-siRNA-depleted cell with straight and bundled microtubules (α-tubulin, blue) next to an mCherry–EB2-expressing (red) rescued cell showing curvy microtubules. Enlarged regions from an mCherry–EB2-expressing cell with mCherry–EB2 (blue, invert) associated along microtubules (red). See supplementary material Table S1 for summary of data and statistical testing. ***P<0.001, **P<0.01. Scale bars: 10 µm (A,D,G); 20 µm (C); 2 µm (A,G enlargements). Mt, microtubule.

We also found that Taxol induced microtubule stabilisation and bundle formation in ARPE-19 cells caused EB1 to become associated along microtubules as previously reported (Shannon et al., 2005). However, EB2 very rarely associated with the microtubule lattice in Taxol-induced bundles and remained cytoplasmic. EB3 did associate along microtubules, but to a lesser extent than EB1 (supplementary material Fig. S3A and data not shown). Furthermore, inactivation of the Rho effector ROCK with Y27632 in ARPE-19 cells, which is noted for inducing microtubule stability, resulted in microtubule bundling and formation of microtubule-rich cell protrusions as previously reported (Darenfed et al., 2007; Gao et al., 2004) but also led to a significant increase in EB1 lattice association compared to untreated controls (supplementary material Fig. S3B). This suggests that EB1 associates with the lattice of stable microtubules.

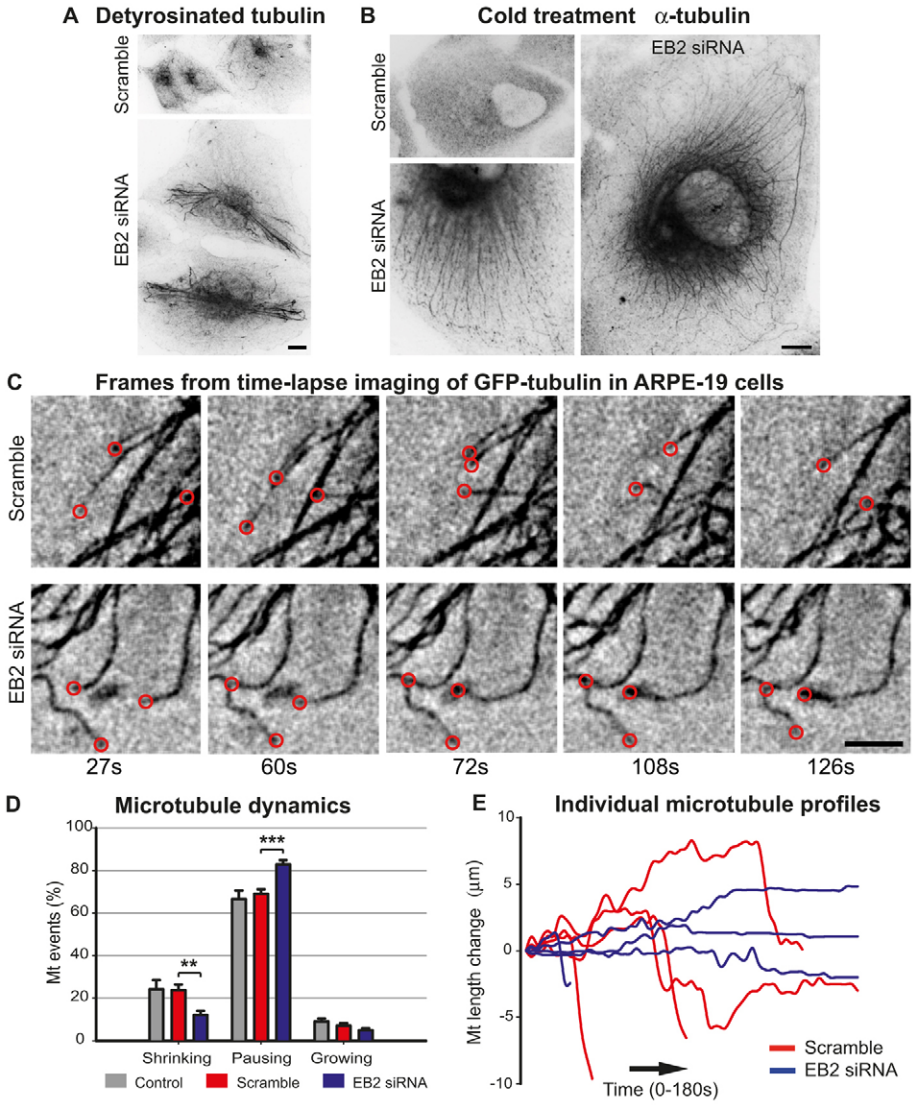

Fig. 3. EB2-siRNA-depleted ARPE-19 cells have more stable and less dynamic microtubules. (**A**) Scramble and EB2-siRNA-treated cells showing detyrosinated tubulin. (**B**) Cold-treated cells showing total loss of microtubules (α-tubulin) in scramble siRNA but resistant microtubules in EB2-depleted cells. (**C–E**) Control, scramble and EB2-siRNA-treated cells stably expressing GFP–α-tubulin imaged every 3 seconds for 3 minutes using a widefield fluorescence microscope. A total of 30 peripheral regions (12.5×12.5 μm) were analysed from $n=5$ control, scramble and EB2-depleted cells. (C) Image frames selected from a representative scramble and EB2-depleted region (see also supplementary material Movies 3,4). The microtubule plus-ends (red circles) show dynamic microtubules undergoing growth and shrinkage in the scramble siRNA cell, whereas the EB2-depleted cell shows less dynamic microtubules with many pausing events. (D) Analysis of average ($n=5$ cells ± s.e.m.) microtubule events scored every 3 seconds as either growing, shrinking or pausing in control (61 microtubules), scramble (61 microtubules) and EB2 siRNA (66 microtubules) cells. (E) Dynamic profiles of the microtubules selected in C from supplementary material Movies 3 and 4 for scramble and EB2-depleted cells, respectively. See supplementary material Table S1 for summary of data and statistical testing. ***$P<0.001$, **$P<0.01$. Scale bars: 10 μm (A,B), 5 μm (C). Mt, microtubule.

siRNA depletion of EB2 leads to ACF7 recruitment to microtubules and co-alignment with actin filaments

ACF7 has been reported to bind both microtubules and EB1, to cross-link microtubules and actin filaments, especially in the vicinity of cell junctions, and has been linked to increased microtubule stability (Karakesisoglou et al., 2000; Kodama et al., 2003; Wu et al., 2008). Our epithelial polarisation data showed a change in ACF7 distribution from dispersed at day 3 to cortical and co-localising with EB1 and microtubules at day 7 and 12 (Fig. 1) suggesting that EB1 binding along the microtubule lattice could recruit ACF7 and facilitate microtubule bundle formation. ACF7 localisation in control and scramble siRNA ARPE-19 cells was diffuse whereas distinct alignment along microtubules and some co-localisation with EB1 was observed in EB2-depleted cells (Fig. 5A). Again this phenotype could be rescued with mCherry–EB2 (Fig. 5B). The significant shift in ACF7 distribution from dispersed in control/scramble siRNA cells to alignment along microtubules in EB2-depleted cells and the subsequent rescue by mCherry–EB2 expression was confirmed by fluorescence intensity analyses (Fig. 5C). We were unable to determine whether this change in ACF7 localisation was associated with an increase in ACF7 expression or merely a redistribution of the existing pool. EB1 binding along the microtubule lattice and ACF7 association with microtubules, either directly or via EB1, could thus facilitate microtubule-actin filament co-alignment, cross linkage and bundle formation. Indeed, actin reorganisation was apparent with control/scramble siRNA cells showing mainly cortical actin and stress fibres while EB2-depleted cells revealed a reduction in stress fibres and increase in actin filaments and bundles oriented perpendicular to the cortex (Fig. 5D). Furthermore, using both confocal and electron microscopy microtubule-actin filament co-alignment was evident in EB2-depleted cells with microtubule bundles interdigitating with bundles of actin filaments (Fig. 5D,E). In the electron microscope single microtubules could also be seen aligned parallel to actin filaments and actin filaments were evident within microtubule bundles (Fig. 5E).

However, in Taxol induced bundles in ARPE-19 cells, which do not contain interdigitating actin filaments, ACF7 remained cytoplasmic and did not appear to align along microtubules as EB1 did (supplementary material Fig. S3A). Similarly, ROCK inhibition with Y27632 did not result in ACF7 recruitment to the

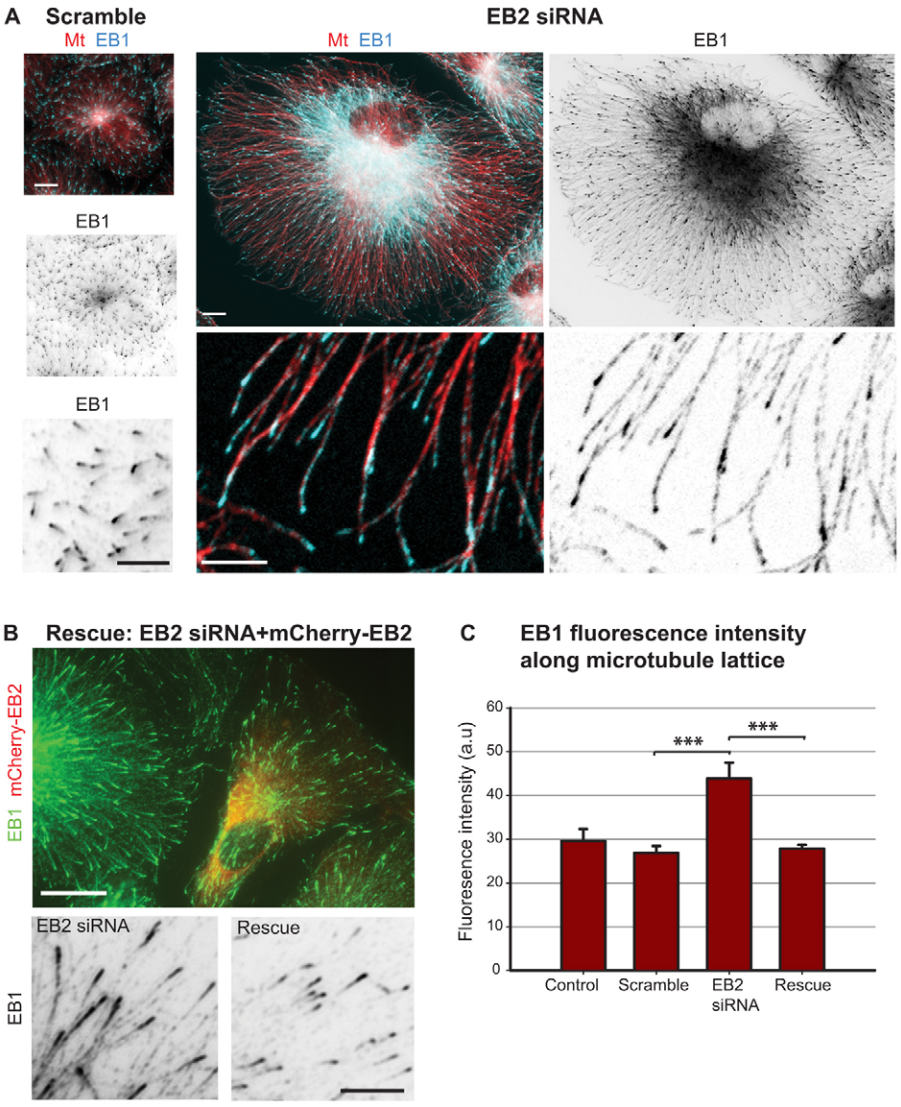

Fig. 4. EB1 associates with the microtubule lattice in EB2-siRNA-depleted ARPE-19 cells. (**A**) Scramble and EB2-siRNA-treated cells labelled for EB1 (mouse mAb, blue/inverts) and α-tubulin (red). Enlarged peripheral region of scramble cell shows distinct EB1 (invert) comets with little or no tail. Enlarged region of EB2-depleted cell shows EB1 (blue, invert) at plus-end and along the microtubule (red) lattice. (**B**) EB2-siRNA-depleted cells transiently transfected with mCherry–EB2 (red) 24 hours before fixation and labelled for EB1 (mouse mAb, green/invert) showing an mCherry–EB2 rescued cell next to a depleted cell. Invert images show EB1 localisation along microtubules in the depleted cell and plus-end comet restoration in the rescued cell. (**C**) Data analysis showing average (n=25 microtubules ±s.e.m.) EB1 fluorescence intensity in control, scramble, EB2-siRNA-treated and rescued cells. See supplementary material Table S1 for summary of data and statistical testing. ***P<0.001. Scale bars: 10 µm (A,B); 5 µm (enlargements). Mt, microtubule.

microtubule lattice nor did it lead to preferential co-alignment of microtubules and radial actin filaments, except within cell projections that also contained actin filaments (supplementary material Fig. S3B,C,D and data not shown). This suggests that microtubule stability and EB1 lattice association is not sufficient to recruit ACF7 and facilitate microtubule-actin filament co-alignment. Furthermore, it seems that ACF7 recruitment to microtubules requires actin filaments.

Double depletion of EB2 and EB1 does not rescue the control phenotype but reveals EB3 compensation

The importance of lattice associated EB1 in terms of microtubule organisation and ACF7 recruitment and co-alignment with actin filaments was further investigated in ARPE-19 cells by double depletion of EB2 and EB1. Double depletion would be expected to rescue the control phenotype if EB1 lattice association is central to the EB2 depletion phenotype.

Simultaneous double transfection (0 and 48 hours) with siRNAs for EB2 and EB1 resulted in knockdown of both proteins (Fig. 6A). No discernable differences in microtubule straightness or organisation were evident in double-depleted cells compared to EB2 only depleted cells (compare Fig. 6A,C,E and Fig. 2D; Fig. 4A and Fig. 5A). Microtubule bundles were evident in EB2/EB1 double-depleted cells as also found in EB2-depleted cells (Fig. 6A,E). The microtubules appeared straighter in EB2/EB1 double-depleted cells compared to scramble siRNA cells as confirmed by microtubule crossover event analysis which revealed significantly fewer crossover events in double-depleted compared to scramble siRNA cells (Fig. 6B).

Interestingly, EB3 associated along the length of the microtubules as well as at the plus-ends in cells double depleted for EB2 and EB1 (Fig. 6C). This is unlike control, scramble and EB2-siRNA-treated ARPE-19 cells, which showed dispersed cytoplasmic distribution of EB3 (Fig. 6C and data not shown). Increased EB3 microtubule lattice association in EB2/EB1 double-depleted cells was verified by fluorescence intensity measurements (Fig. 6D). Furthermore, an increase in ACF7 association along the length of microtubules was evident in double-depleted cells as found for EB2-depleted cells and this was verified by fluorescence intensity analyses (Fig. 6E,F).

This suggests that EB3 can compensate for EB1, associate along the microtubule lattice and maintain the EB2-depleted phenotype.

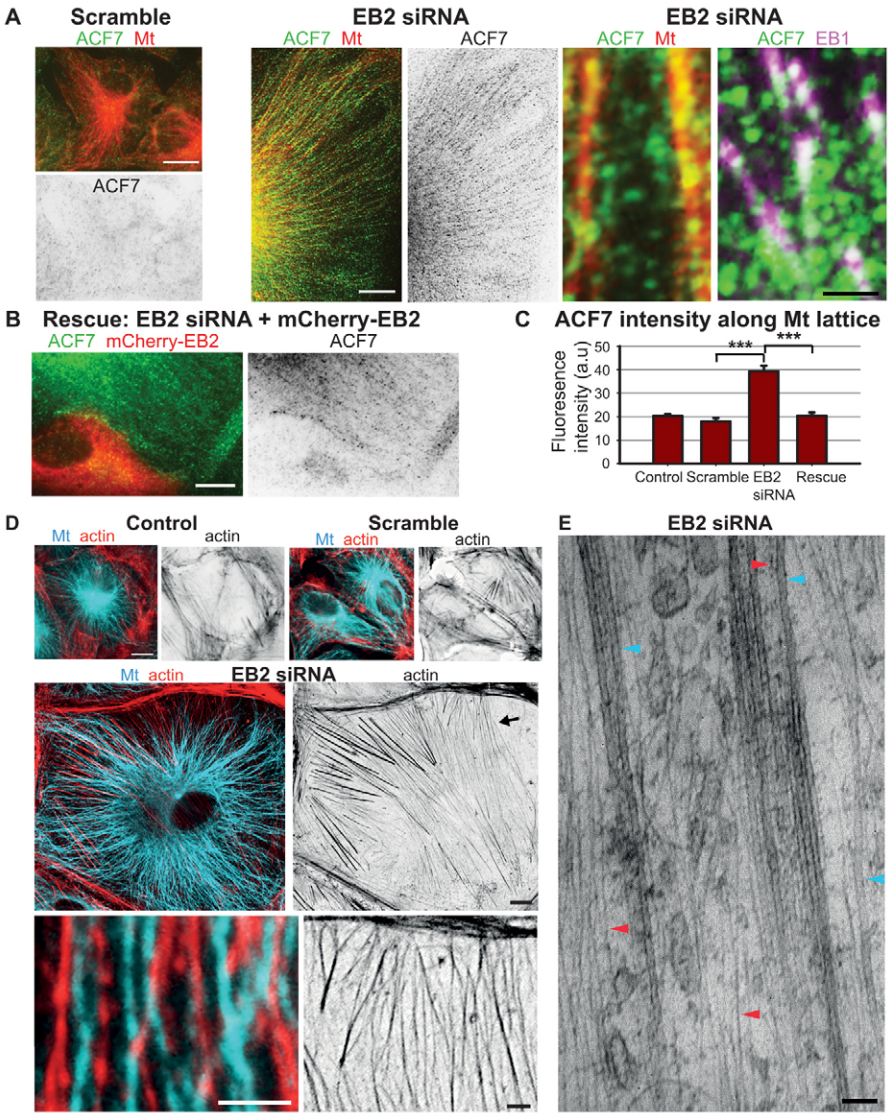

Fig. 5. EB2 depletion in ARPE-19 cells leads to ACF7 localisation along microtubules and co-localisation with EB1 and microtubule-actin filament co-alignment. (**A**) Scramble and EB2-siRNA-treated cells labelled for ACF7 (green/invert) and tubulin (YL1/2, red). ACF7 is dispersed in scramble siRNA cells but is associated along the microtubule lattice and co-localises with EB1 (mouse mAb, purple) in EB2-depleted cells (highlighted in enlarged images). (**B**) EB2-siRNA-depleted cells transiently transfected with mCherry–EB2 (red) 24 hours before fixation showing loss of ACF7 (green/invert) microtubule association in the rescued cell. (**C**) Data analysis showing average (n=25 microtubules ± s.e.m.) ACF7 fluorescence intensity in control, scramble siRNA, EB2-siRNA-treated and rescued cells. (**D**) Control, scramble and EB2-siRNA-treated cells stained for actin (phalloidin, red/invert) and α-tubulin (blue) showing mainly peripheral actin and stress fibres, and little alignment with microtubules in control and scramble siRNA cells, whereas microtubule–actin filament co-alignment is prominent in depleted cells. Enlarged regions of EB2-depleted cells show radial actin filaments oriented perpendicular to the cortex and microtubule-actin filament co-alignment and interdigitation. (**E**) Transmission electron micrograph from EB2-siRNA-depleted cell showing microtubule (blue arrowheads) and actin filament (red arrowheads) bundles co-aligned, as well as single actin filaments within microtubule bundles. See supplementary material Table S1 for summary of data and statistical testing. ***P<0.001. Scale bars: 10 μm (A,B,D); 2.5 μm (enlargements); 50 nm (E).

Unfortunately, triple depletion of EBs is lethal and could thus not be used to determine the role of EB1/EB3 in microtubule straightness and bundle formation (Komarova et al., 2009).

siRNA depletion of EB2 but not EB1 prevents initial microtubule reorganisation during apico-basal epithelial differentiation, whereas depletion of either inhibits microtubule bundle formation and epithelial elongation

Our findings show that low EB2 expression promotes microtubule stability, EB1 lattice binding and bundle formation. Therefore EB2 expression may be required to ensure a dynamic microtubule population to enable reorganisation. To further investigate the role of EB2 and EB1 in microtubule reorganisation and apico-basal bundle formation EB2 and EB1 were depleted separately in differentiating human colonic epithelial (TC7) cells as they readily polarise producing 10–12 μm tall cells when grown to confluence.

EB1 or EB2 siRNA triple treatments (0, 48 and 96 hours) of TC7 cells resulted in knockdown of both proteins (Fig. 7A). Lateral views of three-dimensional reconstructions of optical confocal sections revealed a lack of apico-basal elongation in both EB1- and EB2-depleted cells (Fig. 7B). Single optical cross-sections through apical, medial and basal regions of scramble siRNA cells showed typical polarised epithelial microtubule organisation with apical and basal networks and apico-basal bundles as evidenced by peripheral rings in medial cross-sections (Fig. 7C). This was lost in EB2-depleted cells. Instead, the microtubule networks were typical of undifferentiated epithelial cells (Fig. 7C). Unlike EB2 knockdown, optical cross-sections of EB1-depleted cells showed similar apical and basal microtubule organisation to that of scramble siRNA cells and some peripheral microtubules in medial sections. However, the peripheral bundles were not oriented apico-basally (Fig. 7C). Furthermore, both EB1 and EB2 depletion caused significant decrease in cell height and increase in area compared to scramble treatment (Fig. 7B,C,D). However, while EB1 depletion caused some cell constriction this was not the case for EB2 depletion, which resulted in cells with large surface areas typical of subconfluent cells (Fig. 7C,D).

These findings suggest that EB2 but not EB1 expression is critical for initial microtubule reorganisation and cell constriction whereas EB1 is important for apico-basal microtubule bundle

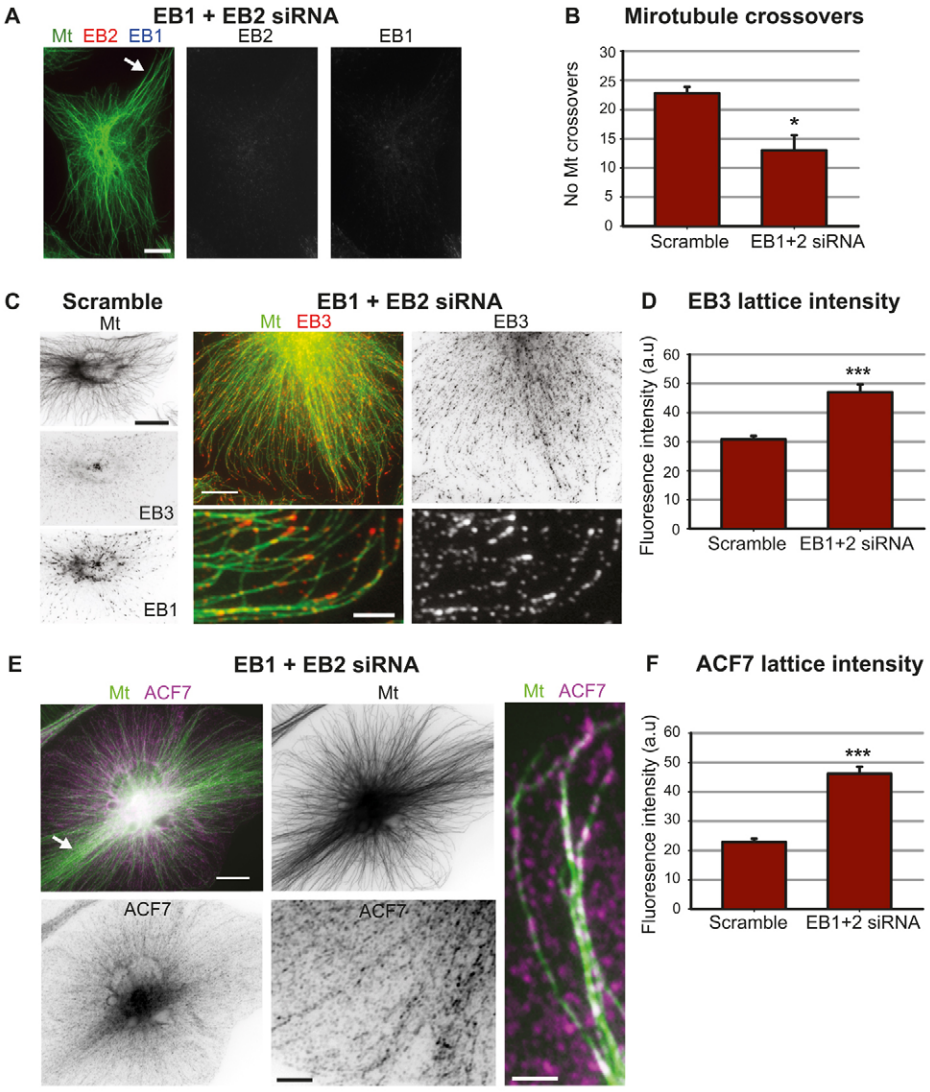

Fig. 6. Double depletion of EB2 and EB1 in APRE-19 cells does not rescue the control phenotype but reveals EB3 compensation. (**A**) Widefield fluorescence images (exposure levels set to scramble cells not shown) showing a cell treated with both EB1 and EB2 siRNA, labelled for α-tubulin (green), EB2 (red channel) and EB1 (mouse mAb blue channel), showing knockdown of both proteins and microtubule bundling (arrow). (**B**) Average number of microtubule crossover events based on 15 peripheral squares (10×10 µm) in five cells with data averaged (± s.e.m.) from three independent experiments for each treatment. (**C**) Inverted images of microtubules (α-tubulin), EB3 (KT36) and EB1 (mAb) in a scramble siRNA cell. EB1- and EB2-siRNA-depleted cell showing α-tubulin (green) and EB3 (KT36, red, invert). Enlarged region showing EB3 (red, single channel) localisation to microtubule plus-ends and along the lattice. (**D**) Data analysis showing average (n=25 microtubules ± s.e.m.) EB3 fluorescence intensity along microtubule lattice in scramble and EB1- and EB2-siRNA-treated cells. (**E**) EB1- and EB2-depleted cell showing α-tubulin (green, invert) and ACF7 (purple/invert). Enlarged regions highlights ACF7 localisation along the microtubule lattice. (**F**) Data analysis showing average (n=25 microtubules ± s.e.m.) ACF7 fluorescence intensity along the microtubule lattice in scramble and EB1- and EB2-siRNA-treated cells. See supplementary material Table S1 for summary of data and statistical testing. *P<0.05, ***P<0.001. Scale bars: 10 µm (A,C,E); 2.5 µm (enlargements).

formation and epithelial elongation. Furthermore, the results suggest that while EB3 may be able to compensate for lack of EB1 during early stages of microtubule reorganisation it can not for apico-basal bundle formation.

Formin inhibition in EB2-depleted cells rescues the control phenotype

Increased microtubule stability, actin filament reorganisation and co-alignment of microtubules and actin filaments following EB2 knockdown or downregulation suggest involvement of the Rho GTPases and their downstream effectors, the formins. The perpendicular actin bundles evident in the EB2-depleted cells (Fig. 5D) resemble dorsal/radial filaments associated with lamellipodia that are activated by Rac1 and assembled by mDia formins. In addition, expression of the FH1/FH2 domains of several formins have been shown to induce microtubule stability as well as co-alignment with actin filaments (Bartolini and Gundersen, 2010; Gasteier et al., 2005; Ishizaki et al., 2001; Kobielak et al., 2004; Kovac et al., 2013; Oakes et al., 2012; Ryu et al., 2009; Thurston et al., 2012; Yang et al., 2007). The role of formins in microtubule straightness, co-alignment with actin filaments and EB1 and ACF7 lattice association in EB2-depleted cells was therefore investigated. EB2-depleted cells were treated with the formin inhibitor SMIFH2 (Rizvi et al., 2009), which specifically inhibits the FH2 domain and affects both actin filament assembly and formin interactions with microtubules.

Formin inhibition with 10 µM SMIFH2 for 40 minutes in EB2-depleted ARPE-19 cells resulted in less-organised microtubules that lacked co-alignment with actin filaments and showed predominant EB1 plus-end and cytoplasmic ACF7 localisation (Fig. 8). SMIFH2 caused a reduction in radial actin filaments oriented perpendicular to the cortex and an increase in stress fibres (Fig. 8A). The microtubules often curled at the periphery and analysis of crossover events revealed a significant increase in SMIFH2-treated EB2-depleted compared to EB2-depleted (+DMSO) cells, but not compared to scramble siRNA (+DMSO) cells (Fig. 8A,C). Predominant EB1 plus-end localisation was restored with EB1 lattice fluorescence intensities showing a significant decrease in SMIFH2-treated EB2-depleted compared to EB2-depleted (+DMSO) cells while not compared to scramble siRNA (+DMSO) cells (Fig. 8B,D). Furthermore, a significant reduction in ACF7 fluorescence

Journal of Cell Science

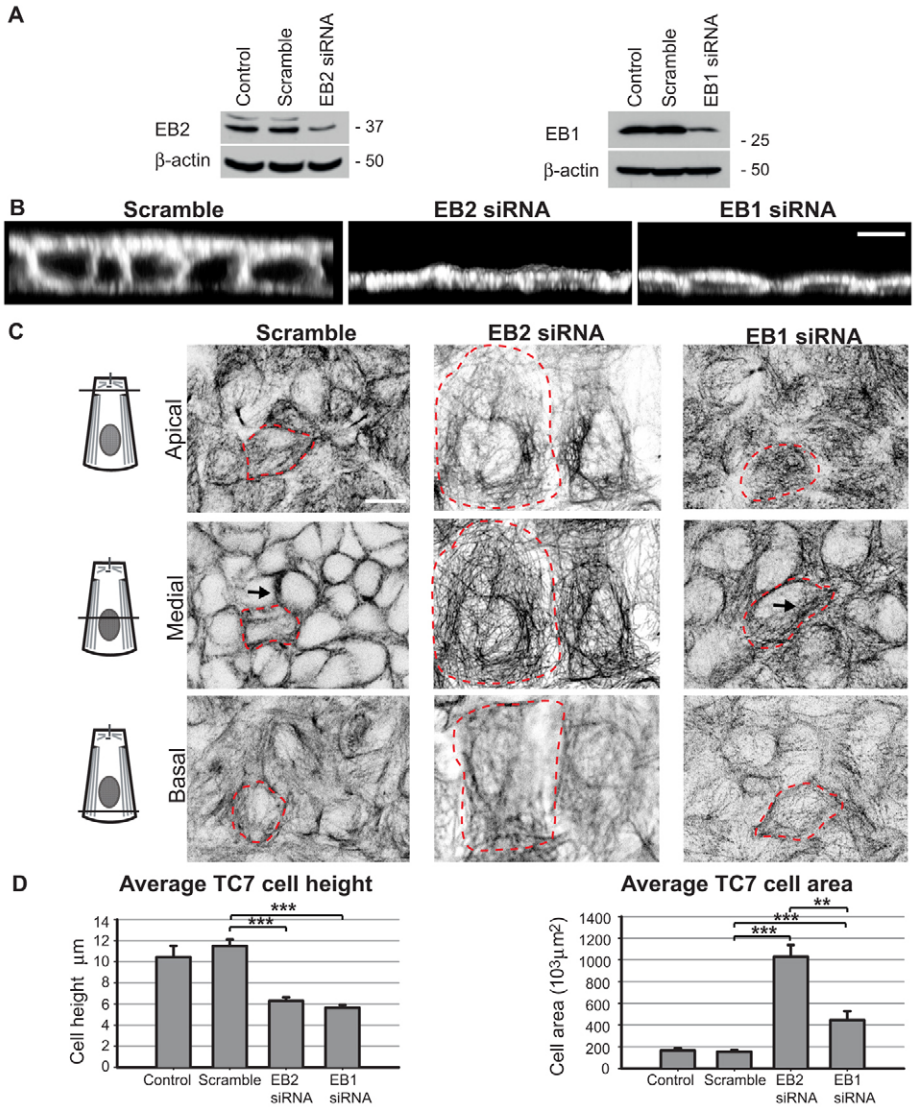

Fig. 7. EB2 depletion in TC7 cells prevents microtubule reorganisation and apico-basal elongation, whereas EB1 depletion affects elongation but not reorganisation. (**A**) Western blots of extracts taken at 144 hours from control, scramble, EB2- and EB1-siRNA-treated (0 hours, 48 hours, 96 hours) cells, showing EB2, EB1 (mouse mAb) and β-actin expression. (**B**) Lateral views of 3D reconstructions of scramble, EB2- and EB1-siRNA-treated cells (to scale) labelled for α-tubulin showing a reduction in cell height in EB2-depleted and EB1-depleted cells. (**C**) Confocal optical cross-sections through apical, medial and basal regions (see diagrams, line represents level of section) of representative scramble, EB2 and EB1 siRNA cells stained for α-tubulin. One cell from each condition is highlighted (red dotted line) in each section. All sections show large cell areas and lack of cellular constriction in EB2-depleted cells compared with scramble siRNA and EB1-depleted cells. Medial sections show distinct peripheral microtubule rings (arrow) representing cross-sections of the apico-basal microtubules in scramble cells; there is a total lack of these in EB2-depleted cells and mis-oriented bundles (arrow) in EB1-depleted cells. (**D**) Analysis of epithelial differentiation in terms of cell height and area in 143 µm×143 µm boxed regions in control (height, area $n=3$), scramble (height $n=8$, area $n=6$), EB1-siRNA-treated (height, area $n=4$) and EB2-siRNA-treated (height $n=9$, area $n=6$) cells. Data pooled from three separate experiments. See supplementary material Table S1 for summary of data and statistical testing. $^{**}P<0.01$, $^{***}P<0.001$. Scale bar: 10 µm.

intensity along microtubules was evident in SMIFH2-treated EB2-depleted compared to EB2-depleted (+DMSO) cells while not compared to scramble siRNA (+DMSO) cells (Fig. 8B,E). Formin inhibition of EB2-depleted cells thus seemed to rescue the control/scramble siRNA phenotype by increasing microtubule crossover events, decreasing co-alignment with actin filaments and restoring predominant EB1 plus-end and cytoplasmic ACF7 localisation.

The data suggest that formin activation is involved in creating the EB2-depleted phenotype in epithelial cells.

Inner ear and intestinal epithelia reveal a direct correlation between low EB2 expression and the presence of distinct apico-basal microtubule bundles

The *in vitro* cultured epithelial cell data suggest that EB2 downregulation or knockdown promotes microtubule bundle formation, EB1 lattice binding, ACF7 recruitment and co-alignment with actin filaments. However, it is important to determine *in vivo* whether there is a correlation between low level EB2 expression and the presence of distinct apico-basal microtubule bundles in polarised epithelial cells. The organ of Corti in the inner ear contains highly organised rows of sensory hair (mechanoreceptors) and supporting cells (transmit sound induced vibrations to the hair cells) (Fig. 9A). Both cell types are apico-basally polarised and terminally differentiated but only the supporting cells contain stable apico-basal microtubule bundles with interdigitating actin filaments (Fig. 9Ai,ii,vii,viii). By contrast, the majority of the microtubules in the hair cells are dynamic and free in the cytoplasm (Fig. 9Ai, iii) (Bane et al., 2002; Furness et al., 1990; Mogensen et al., 2002; Slepecky et al., 1995; Tucker et al., 1992). A distinct pattern of EB2 expression was evident in the organ of Corti with high expression of EB2 in all hair cells but very low level of expression in the supporting cells (Fig. 9Aiv,v). EB1 was also found to associate along the microtubule bundles in the supporting cells (Fig. 9Avi).

Unlike the inner ear cells the epithelium of the intestinal crypt is not terminally differentiated but undergoes rapid turnover and contains both proliferating and differentiating epithelial cells. Stem cells located at the base of the crypt give rise to transit-amplifying cells that divide, differentiate and migrate up the crypt (van der Flier and Clevers, 2009). Immunolabelling for EB2 again showed a distinct pattern with high levels of EB2 expression in cells located within the basal stem cell region while

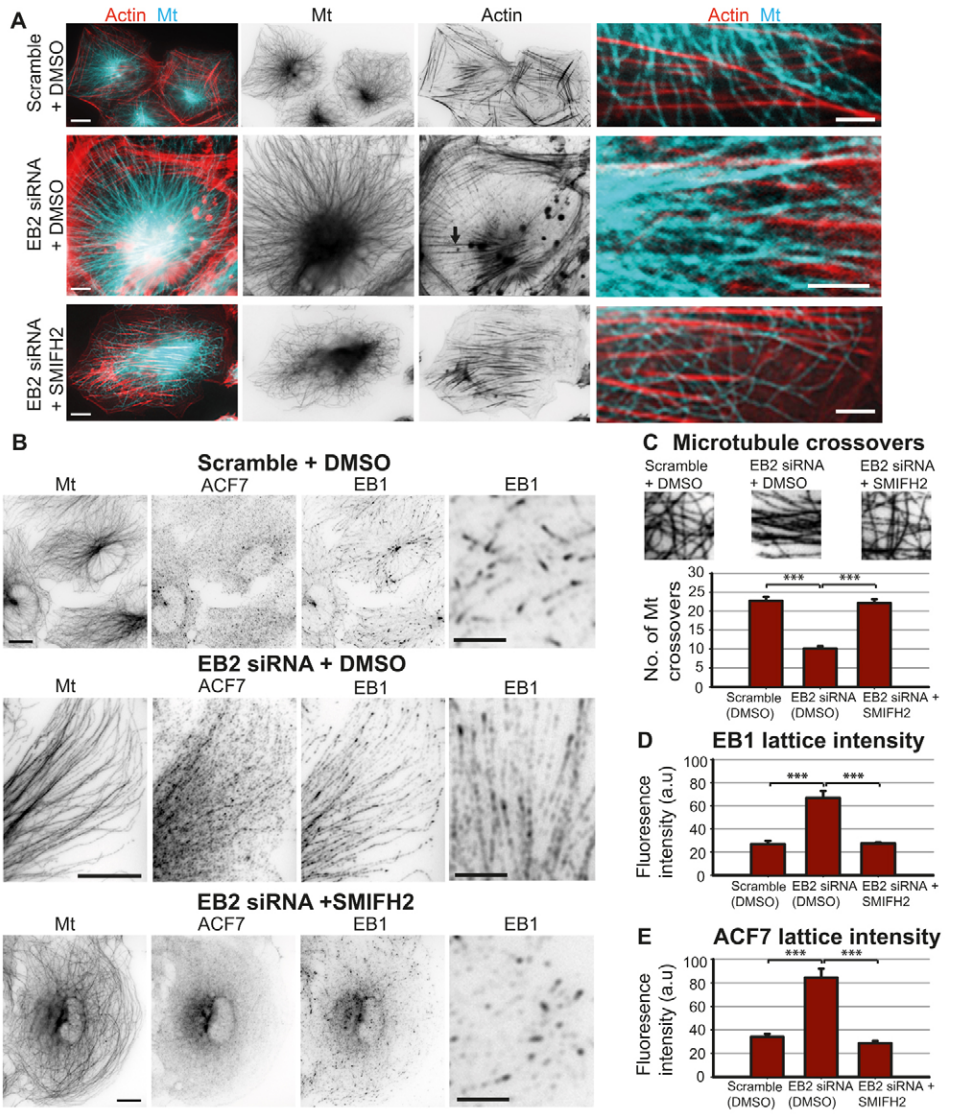

Fig. 8. Formin inhibition in EB2-depleted cells rescues the control phenotype. (**A**) Scramble (+DMSO), EB2-depleted (+DMSO) and formin-inhibited (10 μM SMIFH2 for 40 minutes) EB2-depleted ARPE-19 cells stained for α-tubulin (blue, invert) and actin (phalloidin, red, invert). Lack of straight microtubules and radial actin filaments oriented perpendicular to the cortex (arrow) are evident in SMIFH2-treated EB2-depleted cells. Enlarged regions highlight reversion to the scramble phenotype in SMIFH2-treated EB2-siRNA-depleted cells with a lack of microtubule–actin filament co-alignment. (**B**) Scramble (+DMSO), EB2-depleted (+DMSO) and formin-inhibited (10 μM SMIFH2 for 40 minutes) EB2-depleted ARPE-19 cells labelled for microtubules (YL1/2 invert), ACF7 (invert) and EB1 (mouse mAb, invert). Formin-inhibited EB2-depleted cells show extensive microtubule curving, dispersed ACF7 and a lack of EB1 microtubule lattice association similar to scramble cells (see enlarged regions of EB1 staining). (**C**) Average (n=3, ±s.e.m.) number of microtubule crossover events based on 15 peripheral squares (10×10 μm) in five cells from three independent experiments for scramble (+DMSO) treated, EB2-siRNA (+DMSO)-depleted and formin-inhibited EB2-siRNA (10 μM SMIFH2 for 40 minutes) cells. (**D**,**E**) Average (n=25 microtubules ±s.e.m.) microtubule lattice fluorescence intensities of EB1 (D) and ACF7 (E) in scramble (+DMSO), EB2 siRNA (+DMSO) and formin-inhibited EB2-siRNA-depleted cells. See supplementary material Table S1 for summary of data and statistical testing. ***P<0.001. Scale bars: 10 μm (A,B); 5 μm (enlargements).

low expression was evident in the cells above this region (Fig. 9Bi,iii). Interestingly, the apico-basal microtubules in cells within the basal region were curly and did not form distinct bundles (Fig. 9Biv). Instead, they displayed an umbrella-like organisation with microtubules focused on an apical centrosome (Fig. 10Ai). However, distinct apico-basal microtubule bundles were evident in the cells above this region where EB2 expression was low (Fig. 9Bi,ii; Fig. 10Aii). Both EB1 and ACF7 localised along the apico-basal microtubule bundles in the transit-amplifying and differentiated cells while EB1 was evident mainly along the baso-lateral and basal sides in cells within the basal region (Fig. 9Bii,iv; supplementary material Fig. S4).

A correlation between EB2 downregulation and the presence of distinct apico-basal microtubules is thus apparent in both terminally differentiated (inner ear) and proliferating (intestinal crypt) polarised epithelial tissue. The *in situ* data also indicated that EB2 expression is prominent in cells with dynamic microtubules.

Discussion

Dynamic behaviour of microtubules is essential for their reorganisation during apico-basal epithelial differentiation. Our findings suggest that EB2 expression during early stages of differentiation helps to maintain microtubule dynamics. EB2 downregulation leads to increased microtubule stability, the association of EB1 along the lattice and bundle formation, as well as ACF7 recruitment and co-alignment of microtubules and actin filaments. Similar results were obtained from both *in vitro* epithelial differentiation and *in situ* epithelial tissue analyses. siRNA depletion, rescue and microtubule dynamics studies further confirmed the central role of EB2 in epithelial differentiation.

Analyses of epithelial differentiation revealed that EB2 is expressed during early stages of differentiation when cell–cell contacts, apical constriction and major microtubule reorganisation occur whereas it is downregulated in most confluent and polarised epithelial cells. EB2 depletion during early stages of differentiation inhibited microtubule reorganisation, apical cell constriction and thus also apico-basal elongation. Lack of microtubule reorganisation is most likely due to less dynamic microtubules. This is supported by our data from cold induced depolymerisation and live cell imaging of GFP–tubulin-expressing ARPE-19 cells where EB2 depletion resulted

Journal of Cell Science

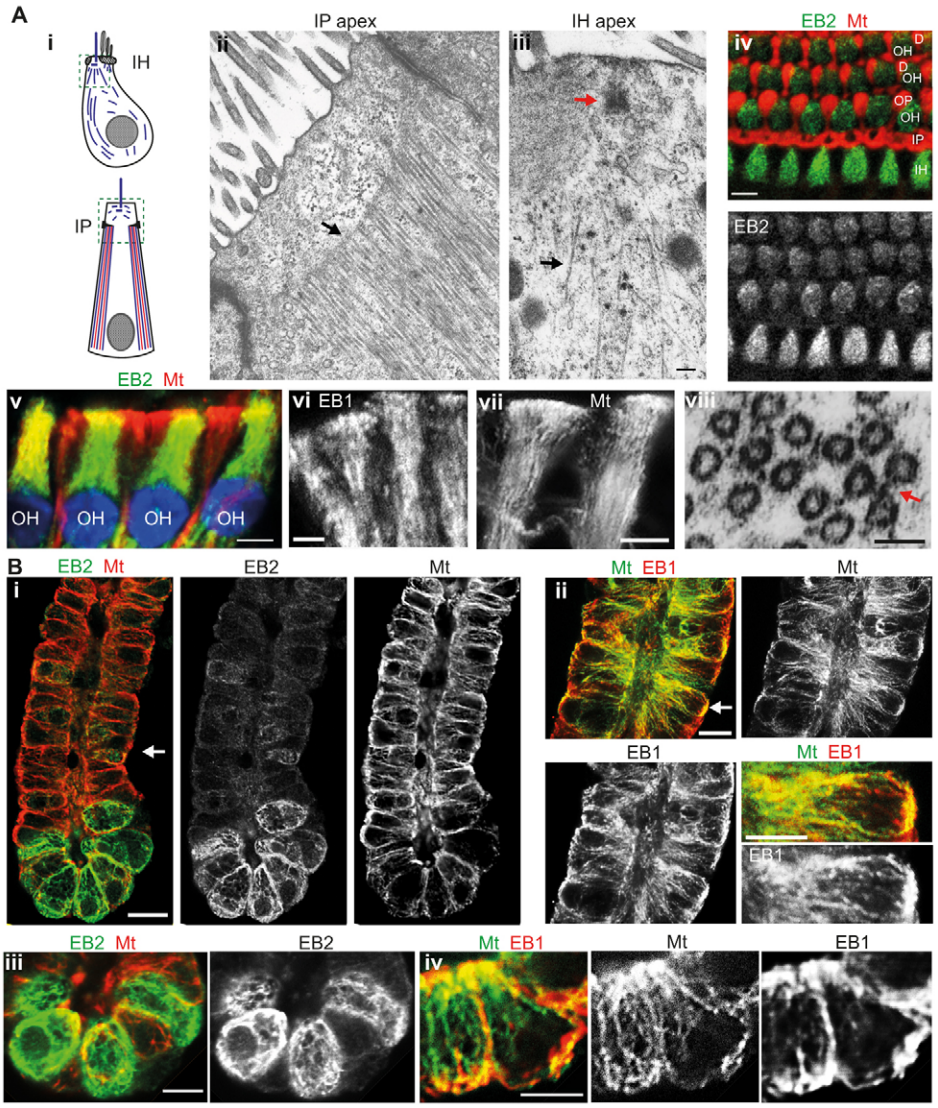

Fig. 9. Isolated inner ear (organ of Corti) and intestinal (crypt) epithelia reveal a correlation between low EB2 expression and the presence of distinct apico-basal microtubule bundles. (**A**) Isolated P4 mouse Organ of Corti. (i) Schematic diagrams of inner hair (IH) and inner pillar (IP) cells with microtubules in blue, actin filaments in red and non-centrosomal anchoring sites in black. The IH cell contains mainly free cytoplasmic microtubules (based on Furness et al., 1990), whereas the IP cell contains an apico-basal bundle of microtubules with interdigitating actin filaments, anchored at non-centrosomal sites. Boxed regions indicate the areas covered in TEM images (ii,iii). (ii) Electron micrograph of the apical region in an inner pillar cell showing part of the apico-basal bundle of microtubules anchored at non-centrosomal sites (arrow). (iii) Electron micrograph of the apical centrosomal/basal body (red arrow) region of an inner hair cell showing a fascicle (black arrow) of microtubules and lack of bundling. (iv) Apical view of Organ of Corti with rows of inner hair (IH), outer hair (OH) and supporting cells [inner pillar (IP), outer pillar (OP) and Deiters (D)] showing high EB2 (green/single channel) expression in IH and OH cells, whereas the expression of EB2 is low in all supporting cells (α-tubulin, red). (v) Lateral view showing OH and supporting cells with EB2 (green) co-localising with microtubules (red) in the OH cells, whereas supporting cells are low in EB2 expression. (vi) Lateral view of apical region of pillar cells showing EB1 (rabbit pAb) along the apico-basal microtubules. (vii) Lateral view of apical region of pillar cells showing apico-basal microtubule (α-tubulin) bundles. (viii) TEM image showing part of a cross-section through a pillar cell with actin filaments between microtubule and cross-links evident (red arrow). (**B**) Isolated adult mouse small intestinal crypts. (Bi) Lateral view of crypt labelled for α-tubulin (red, single channel) and EB2 (green, single channel) showing high EB2 expression in basal cells. (ii) Transit-amplifying region (arrow in i) showing low EB2 expression with EB1 (red, single channel) along apico-basal microtubules (YL1/2, green, single channel). Enlarged region (arrow) highlights EB1 localisation along apico-basal microtubule bundles. (iii) Basal crypt epithelial cells expressing EB2 (green, single channel) showing EB2 along curvy microtubules (YL1/2, red), (iv) Basal crypt epithelial cells showing curvy microtubules (YL1/2 green, single channel), lack of straight bundles and umbrella-like organisation with EB1 (red, single channel) mainly restricted to cortical areas. Scale bars: 100 nm (Aii,iii); 5 μm (Aiv–vii; B); 50 nm (Aviii).

in more stable and less dynamic microtubules. Decreased microtubule dynamics may also lead to mis-localisation and inactivation of Rho/ROCK/myosinII signalling required for apical actomyosin cortical contraction thus resulting in less cell constriction as observed in EB2-depleted cells (Siegrist and Doe, 2007).

Analyses of *in situ* inner ear and intestinal crypt epithelial tissue revealed a striking correlation between low EB2 expression

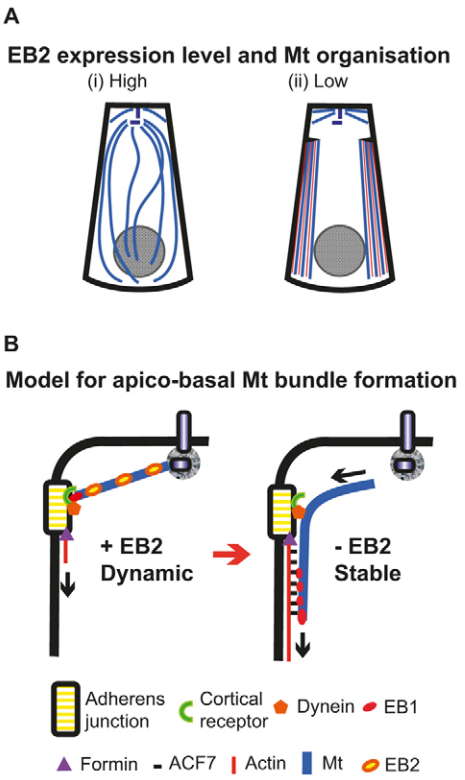

Fig. 10. Models for EB2 expression and apico-basal microtubule bundle formation. (A) EB2 expression level and apico-basal microtubule organisation. Schematic diagrams of microtubule organisation on the basis of EB2 expression levels. (i) High-EB2-expressing cell with unbundled curvy microtubules (blue) organised in an umbrella-like fashion (ii) Low-EB2-expressing cell with distinct apico-basal microtubule (blue) bundles co-aligned with actin filaments (red). (**B**) Model for apico-basal microtubule bundle formation. EB2 expression (+EB2) maintains a dynamic microtubule population during the early stages of differentiation. The centrosome nucleated microtubule elongates towards the cell periphery with EB2 associated along the lattice. The microtubule plus-end is captured at the adherens junction, a process mediated by +TIPs and cortical receptors (Bellett et al., 2009). Activation of junction-associated formin initiates actin cable assembly and elongation. The downregulation of EB2 (−EB2) at latter stages of differentiation facilitates bundle formation. Cortical-anchored dynein mediates microtubule release from the centrosome, and actin cables guide microtubules downwards facilitated by EB1 and ACF7. EB1 lattice binding and ACF7 cross-linkage lead to microtubule–actin filament co-alignment and the formation of a stable apico-basal bundle. Mt, microtubule.

and the presence of distinct apico-basal microtubule bundles that co-aligned with actin filaments and high EB2 expression and lack of such bundles. Interestingly, high expression of EB2 in polarised epithelial cells did not prevent apico-basal microtubules from forming but it did prevent them from organising into distinct straight bundles. This is supported by recent data on FGF (Fibroblast Growth Factor) signalling in cochlear development where loss of function of FGF-Receptor3 has been linked to EB2 (MAPRE2) gene upregulation and reduced microtubule bundle formation in cochlear pillar cells (Szarama et al., 2012).

The expression level of EB1 remained constant during epithelial differentiation. However, a distinct shift from a mainly plus-end to microtubule lattice association was evident and this coincided with an increase in microtubule stability. This was particularly evident following EB2 siRNA depletion. EB1 lattice association has been reported in differentiated myotubes and Sertoli cells and EB1 lattice binding has been suggested to enforce lateral protofilament interactions and thus increase microtubule stability (des Georges et al., 2008; Sandblad et al., 2006; Vitre et al., 2008; Wang et al., 2008; Wen et al., 2004; Zhang et al., 2009). EB1 lattice association was also observed along Taxol and Y27632 stabilised microtubules suggesting that stabilisation may facilitate EB1 lattice binding and this may in turn lead to further stabilisation. Interestingly, GTP–tubulin patches have been identified within the microtubule lattice and with EB1s affinity for this stable form an increase in GTP–tubulin could facilitate EB1 lattice binding (Dimitrov et al., 2008). This is supported by studies on axonal microtubules that have shown co-localisation of GFP–EB1 with patches of GTP–tubulin along the lattice (Nakata et al., 2011).

EB2 depletion also resulted in ACF7 association along the microtubules and differentiated epithelial crypt cells showed ACF7 along the apico-basal bundles. ACF7 and the *Drosophila* homologue Shot have previously been reported to bind along microtubules, acting as a MAP to stabilise microtubules. Most interestingly, ACF7 and EB1 have been suggested to guide microtubules along actin filaments with ACF7 depletion leading to unbundled and disorganised microtubules (Alves-Silva et al., 2012; Kodama et al., 2003; Wu et al., 2008). However, EB1 association along the microtubule lattice is not sufficient to recruit ACF7 as Taxol and Y27632 stabilised microtubules did not contain ACF7 along their length. Only cell projections that contained microtubules and actin filaments showed ACF7 localisation suggesting that actin filaments influence ACF7 deployment. It is also possible that the observed redeployment of ACF7 is linked to an upregulation in ACF7 triggered by EB2 depletion or downregulation but future investigations are needed to resolve this.

Cross-talk between microtubules and actin filaments is partly determined by the spatiotemporal activation of the Rho GTPases. Our formin inhibition data may suggest that EB2 downregulation is associated with formin activation. The perpendicular actin bundles in the EB2-depleted cells resemble Rac1 induced dorsal/radial filaments associated with lamellipodia that are assembled by mDia2. Interestingly, activation of the mDia pathway can lead to Rac1 activation (Kovac et al., 2013; Oakes et al., 2012; Ryu et al., 2009; Tsuji et al., 2002; Yang et al., 2007). Alternatively, the balance between Arp2/3 nucleated actin networks and formin activated linear actin cables or bundles may be shifted towards formin induced actin filament assembly and thus perpendicular actin bundles emanating from the cortex become prominent. In confluent and apico-basal polarising epithelial cells localised activation of junction located formin could trigger nucleation of actin bundles and initiate microtubule–actin filament co-alignment, a process most likely facilitated by ACF7 (Kodama et al., 2003). This is supported by our data on formin inhibition in EB2-depleted cells, which rescued the control phenotype inducing loss of microtubule–actin filament co-alignment and microtubule-associated ACF7 in EB2-depleted cells.

Diaphanous formins bind microtubules directly via their FH2 domain and are also known to stabilise microtubules (Bartolini and Gundersen, 2010; Thurston et al., 2012). EB1 binds to mDia and has been suggested to function downstream of Rho and mDia (Bartolini and Gundersen, 2010; Palazzo et al., 2001; Wen et al., 2004). Here we show that formin inhibition with SMIFH2 in EB2

depleted cells resulted in decreased EB1 lattice association. This suggests that EB1 may need to interact with formin in order to bind along the microtubule lattice or that formin-induced microtubule stabilisation facilitates EB1 lattice binding. Repulsive forces due to negative charges between the C-terminus of EB1 and the microtubule surface has been suggested to favour EB1 binding at the plus-end (Buey et al., 2011). It will be interesting in the future to determine whether formin binding to EB1 or microtubules reduces the repulsive forces and thus makes EB1 lattice association more favourable. A combination of increased GTP–tubulin within the microtubule lattice and reduced repulsive forces may thus facilitate EB1 lattice binding.

The precise temporal and spatial expression of EB2 and EB1 during epithelial differentiation is evidently critical for apico-basal microtubule bundle formation and epithelial differentiation. EB2 expression and binding along the length of microtubules, as particularly evident in the stem cell region of the crypt, for example, may prevent EB1 formin interaction, lattice binding and bundle formation and thus maintain a dynamic microtubule population. The fact that overexpression of EB2 does not induce microtubule bundles, while EB1 does, supports this idea (Bu and Su, 2001). EB1 depletion during epithelial differentiation did not prevent initial microtubule reorganisation and cell constriction possibly due to compensation by EB3 as shown by our double depletion studies of EB2 and EB1. However, lack of EB1 did inhibit apico-basal microtubule bundle formation suggesting that although EB3 can associate along the microtubule lattice it can not fully compensate for EB1's role in apico-basal bundle formation.

Here our findings suggest a model for apico-basal bundle formation dependent on EB2 expression levels. EB2 expression at early stages of differentiation maintains a dynamic microtubule population important for cell–cell junction formation, apical localisation of Rho effectors and activation of Rho/ROCK/myosinII for apical constriction and for initial microtubule reorganisation. Subsequent EB2 downregulation favours formin mediated actin filament assembly, microtubule stabilisation and co-alignment with actin filaments and EB1 and ACF7 lattice recruitment. We propose that EB1 and ACF7 lattice association play a dual role in guiding and cross-linking microtubules to formin nucleated linear actin bundles resulting in the generation of stable apico-basal bundles and that this process is dependent on the downregulation of EB2 (Fig. 10B).

Materials and Methods

Cell culture and drug treatment

Cells lines were maintained at 37℃ in 5% CO^2 and passaged twice weekly. ARPE-19 cells (human retinal pigment epithelial) and mIMCD-3 (inner medullary collecting duct) cells were cultured in DMEM/F12 containing 5 mM Hepes, 2% sodium bicarbonate and 2.5 mM L-glutamine (Invitrogen) supplemented with 10% FBS. TC7 (sub-clone of human colorectal adenocarcinoma cell line Caco-2), U2OS (human Osteosarcoma) and HCT-116 (human colorectal cancer) cells were cultured in DMEM (Invitrogen) containing 10% FBS, 1% L-glutamine and 0.1 mg/ml streptomycin and 100 units/ml penicillin. mIMCD-3 and TC7 cells were grown on 0.4 μm pore polycarbonate cell culture inserts (Nunc) for 5–7 days to stimulate epithelial polarisation. For differentiation analysis mIMCD-3 cells were seeded at 0.24×10^4 cells in 6-well plates and were fixed and lysed every other day for 12 days. For cold treatment analysis ARPE-19 cells were incubated on ice for 90 minutes. Microtubule stability was induced in the ARPE-19 cells by treatment with 2 μM of Taxol (Sigma) for 12 hours. For ROCK inhibition ARPE-19 cells were treated with either 10 μM or 30 μM of Y27632 (Tocris) for 24 hours. Formin inhibition was performed in ARPE-19 cells and cells were treated with 10 μM of SMIFH2 (Sigma) for 40 minutes, a DMSO control was used for each treatment.

Immunolabelling and tissue isolation

Fixation and immunolabelling of cultured cells were performed as previously described (Bellett et al., 2009). Rabbit polyclonal antibodies against ACF7 (HPA013713 Sigma), α-tubulin (ab15246 Abcam) and Ki-67 (Leica Microsystems) were used at 1:100, antibodies against detyrosinated tubulin (ab48389 Abcam) and β-actin (ab8227 Abcam) at 1:200 and antibodies against EB1 (ab50188 Abcam) at 1:2000. Mouse monoclonal antibodies against EB1 (BD biosciences) were used at 1:500. Rat monoclonal antibodies against EB2 clone k52 (Abcam) and EB3 clone KT36 (Abcam) were used at 1:200 and antibodies against tyrosinated tubulin clone YL1/2 (Abcam) at 1:1000. For actin staining phalloidin conjugated to AlexaFluor 488 (Invitrogen) was used at 1:200. Secondary antibodies conjugated to AlexaFluor 488, 568, or 647 (Invitrogen) were used at 1:1000. For isolated tissue staining highly cross-absorbed secondary antibodies conjugated to Dylight 488 and 647 (Jackson) were used at 1:800.

Organ of corti isolation and immunolabelling was performed as previously described (Mogensen et al., 2000). Small intestine and colon was fractioned as previously described (Belshaw et al., 2010; Whitehead et al., 1993). Isolated fractions were fixed in cold −20℃ methanol for 10 minutes and stained as above.

SDS PAGE and immunoblotting

Cells were lysed in lysis buffer (50 mM Hepes, 50 mM NaCl, 1 mM EDTA, 10% Glycerol, 1% TritonX100, 1 mM PMSF, 10 μg/ml aprotinin) at 4℃. Equal proteins concentration was determined using a BCA assay (Pierce) and samples were run using SDS PAGE. Proteins were transferred onto nitrocellulose membrane (BioRad), which was blocked in PBS-T [PBS containing 0.5% milk powder (oxoid) and 0.05% Tween20] overnight at 4℃. The membrane was probed for primary antibodies diluted as indicated in PBS-T. Rabbit polyclonal antibodies against β-actin were used at 1:10,000, α-tubulin and detyrosinated tubulin at 1:500. Mouse monoclonal antibodies against EB1 and RFP (ab65856 Abcam) were used at 1:500 and 1:1000 respectively. Rat polyclonal antibodies against EB2 clone K52 were used at 1:200. The membrane was washed and then incubated with secondary HRP-conjugated antibodies (Sigma) used at 1:10,000. For reprobing, membranes were stripped (Chemicon) and antibody incubation and detection was repeated.

RNAi transfection

ARPE-19, HCT-116 and U2OS cells were treated with 27 nM of siRNA (Qiagen) whereas TC7 cells were treated with 72 nM of siRNA. All siRNA was delivered by Oligofectamine (Invitrogen) as per manufacturer's protocol at indicated timepoints. For negative controls Allstar scramble siRNA sequence (Qiagen) was used. Human EB1 target sequence ACCAATTGCATCCCAGCTAAA. Human EB2 siRNA target sequences; EB2 siRNA (a) CAGCAGGTGC-AGCTAAARCAA, EB2 siRNA (b) AACGCAGGTCATACAGCTTAA, EB2 siRNA (c) GACCTTATTAATAGGAGCATA, EB2 siRNA (d) CTCGATAACC-CAAGAGACTAT. For simultaneous depletion of EB1 and EB2 mRNA, ARPE-19 cells were treated with 54 nM of siRNA (27 nM of each siRNA) at 0 hours and 48 hours.

For ARPE-19 cell size analysis; cells were grown to confluence and the area of 310 control, scramble and EB2-depleted cells and 55 rescued cells were measured blindly. For cell proliferation analysis ARPE-19 cells were seeded at 0.1×10^6 per well (multiwall plate, 6) before each siRNA treatment (0 and 48 hours) and cell population was measured 24 hours and 48 hours later. For apico-basal array analysis, TC7 cells were treated with siRNA at 0 hours, 48 hours and 96 hours. At 102 hours cells were seeded at 0.3×10^6 onto coverslips in 24-well plates and left for a further 42 hours before fixation/lysis.

mCherry–EB2 generation and cDNA transfection

EB2 cDNA was cloned from mIMCD-3 cells using Expand High Fidelity PCR System (Roche). Primers based on NM_001162942 were designed in frame and with restriction sites for cloning into the pmCherry-C1 vector (Clontech). The insert was restricted by *Xho*I and *Hin*dIII (Roche), purified by gel extraction (Qiagen), and ligated using T4 DNA Ligase (Amersham Biosciences) into pmCherry-C1. For transient transfection jetPRIME (Polyplus) was used according to manufacturer's protocol to deliver 2 μgs of mCherry–EB2 cDNA into ARPE-19 cells for overexpression and rescue experiments.

Widefield, confocal and electron microscopy

Electron microscopy was performed as previously described in Bellett et al. (Bellett et al., 2009). Fixed and immunolabelled cells were imaged on a widefield upright Zeiss Axiovert 200M microscope. Images were taken using a monochrome CCD camera and processed using Axiovision (Zeiss) and Photoshop (Adobe) software. Polarised cells and isolated tissues were imaged using a Zeiss LSM510 META scanning confocal microscope. Images were taken using Zeiss LSM software and processed using Volocity (Improvision) and Photoshop (Adobe) software. For live microscopy cells were maintained on a heated stage at 37℃ with 5% CO^2. For analysis of cell division, scramble and EB2-siRNA-treated ARPE-19 cells were grown in six-well plates and phase contrast images were captured using a ×20 objective every 10 minutes for a 24 hour period, beginning at 72 hours after

Journal of Cell Science

Journal of Cell Science

siRNA treatment. For analysis of microtubule dynamics, untreated, scramble and EB2-siRNA-treated ARPE-19 cells stably expressing GFP–α-tubulin (Clontech) were maintained in phenol red free DMEM/F12 (Invitrogen) medium supplemented with 10% FBS (Invitrogen), 2.5 mM L-glutamine (Invitrogen), 5 mM Hepes and 2% sodium bicarbonate (Invitrogen), in a 3 cm glass-bottomed Petri dish (MatTek), 96 hours after siRNA treatment. Images were captured at set exposure levels using a ×63 objective every 3 seconds for 3 minutes. 12.5×12.5 µm areas were selected and processed in FIJI (Image J) software; briefly, areas were treated with the unsharp mask filter, smoothed, inverted and the brightness and contrast adjusted. Microtubule length in each frame was manually measured in FIJI. Individual frames were annotated in Adobe Photoshop, and assembled into movies using Time-lapse (Microprojects). Adobe illustrator CS6 was used for final figure production.

Statistical analysis

A two-tailed unpaired *t*-test with Welch's correction was used to determine statistical significance for cell area analysis of EB2 siRNA in ARPE-19 cells. Cell height and size of differentiating TC7 was measured and averaged from boxed regions (143 µm×143 µm). Multiple regions were then further averaged for each treatment and statistical significance was determined using a two-tailed unpaired *t*-test. For fluorescence intensity analysis of EB1 and ACF7 along the microtubule lattice, average intensity along 2 µm sections of 25 random microtubules (using tubulin channel) was measured from set exposure images (from the same experiment) using AndorIQ (Andor), statistical significance was determined using a two-tailed unpaired *t*-test. Microtubule dynamics were analysed using length between frames, where movements $\geq \pm 0.5$ µm (width of fluorescence of microtubule) were scored as growth or shrinkage. For each microtubule the percentage of time spent growing, shrinking and pausing was calculated. Using a two-tailed unpaired *t*-test statistical significance was determined from data averaged from five cells (total of 60+ microtubules per treatment). To assess microtubule straightness the average number of microtubule crossover events in cortical 10 µm×10 µm boxes were counted in five cells (three boxes per cell) for each experiment ($n=3$) and significance was determined using a two tailed unpaired *t*-test. For cell proliferation assessment cell growth and Ki-67 expression was analysed using a two-tailed unpaired *t*-test. Summaries of data and significance can be found in supplementary material Table S1.

Acknowledgements

The authors wish to thank James Perkins for help with tissue culture, Richard Evans-Gowing for help with Electron Microscopy, Selina Catto for help with diagrams, Uli Mayer for advice and Paul Wright for IT assistance. We also thank Alan Prescott for helpful discussions and Jelena Gavrilovic and Jeremy Hyams for helpful discussions and comments on the manuscript.

Author contributions

D.A.G., J.R.G., G.B. and M.M.M. conceived and designed the experiments. D.A.G., J.R.G. and G.B. performed experiments and analysed data. D.A.G. and J.R.G. assisted with figure preparations and D.A.G. with writing the manuscript. J.K. and B.J.T. assisted with design and performance of experiments. P.P.P. and E.K.L. provided expertise and training in construct work and crypt isolation respectively. P.T. provided expertise and assistance with microscope imaging and analyses. M.M.M. analysed data, directed the project and wrote the manuscript. All authors read and edited the manuscript.

Funding

This project was supported by the Biotechnology and Biological Sciences Research Council (BBSRC) [grant numbers BB/D012201\1 to M.M.M. and G.B.; BB/J009040/1 to M.M.M. and D.A.G.; and BBS/B/00689 to P.P.P.]; the Anatomical Society (AS) (studentship support to D.A.G.); the BigC Appeal (Studentship supports to J.R.G. and J.K.); and the BBSRC (Studentship support to B.J.T.).

Supplementary material available online at
http://jcs.biologists.org/lookup/suppl/doi:10.1242/jcs.129759/-/DC1

References

Alves-Silva, J., Sánchez-Soriano, N., Beaven, R., Klein, M., Parkin, J., Millard, T. H., Bellen, H. J., Venken, K. J., Ballestrem, C., Kammerer, R. A. et al. (2012). Spectraplakins promote microtubule-mediated axonal growth by functioning as structural microtubule-associated proteins and EB1-dependent +TIPs (tip interacting proteins). *J. Neurosci.* **32**, 9143-9158.

Bacallao, R., Antony, C., Dotti, C., Karsenti, E., Stelzer, E. H. and Simons, K. (1989). The subcellular organization of Madin-Darby canine kidney cells during the formation of a polarized epithelium. *J. Cell Biol.* **109**, 2817-2832.

Bane, B. C., MacRae, T. H., Xiang, H., Bateman, J. and Slepecky, N. B. (2002). Microtubule cold stability in supporting cells of the gerbil auditory sensory epithelium: correlation with tubulin post-translational modifications. *Cell Tissue Res.* **307**, 57-67.

Bartolini, F. and Gundersen, G. G. (2010). Formins and microtubules. *Biochim. Biophys. Acta* **1803**, 164-173.

Bellett, G., Carter, J. M., Keynton, J., Goldspink, D., James, C., Moss, D. K. and Mogensen, M. M. (2009). Microtubule plus-end and minus-end capture at adherens junctions is involved in the assembly of apico-basal arrays in polarised epithelial cells. *Cell Motil. Cytoskeleton* **66**, 893-908.

Belshaw, N. J., Pal, N., Tapp, H. S., Dainty, J. R., Lewis, M. P., Williams, M. R., Lund, E. K. and Johnson, I. T. (2010). Patterns of DNA methylation in individual colonic crypts reveal aging and cancer-related field defects in the morphologically normal mucosa. *Carcinogenesis* **31**, 1158-1163.

Bu, W. and Su, L. K. (2001). Regulation of microtubule assembly by human EB1 family proteins. *Oncogene* **20**, 3185-3192.

Bu, W. and Su, L. K. (2003). Characterization of functional domains of human EB1 family proteins. *J. Biol. Chem.* **278**, 49721-49731.

Buey, R. M., Mohan, R., Leslie, K., Walzthoeni, T., Missimer, J. H., Menzel, A., Bjelic, S., Bargsten, K., Grigoriev, I., Smal, I. et al. (2011). Insights into EB1 structure and the role of its C-terminal domain for discriminating microtubule tips from the lattice. *Mol. Biol. Cell* **22**, 2912-2923.

Chang, Y. C., Nalbant, P., Birkenfeld, J., Chang, Z. F. and Bokoch, G. M. (2008). GEF-H1 couples nocodazole-induced microtubule disassembly to cell contractility via RhoA. *Mol. Biol. Cell* **19**, 2147-2153.

Cheng, I. K., Tsang, B. C., Lai, K. P., Ching, A. K., Chan, A. W., To, K. F., Lai, P. B. and Wong, N. (2012). GEF-H1 over-expression in hepatocellular carcinoma promotes cell motility via activation of RhoA signalling. *J. Pathol.* **228**, 575–585.

Darenfed, H., Dayanandan, B., Zhang, T., Hsieh, S. H., Fournier, A. E. and Mandato, C. A. (2007). Molecular characterization of the effects of Y-27632. *Cell Motil. Cytoskeleton* **64**, 97-109.

des Georges, A., Katsuki, M., Drummond, D. R., Osei, M., Cross, R. A. and Amos, L. A. (2008). Mal3, the Schizosaccharomyces pombe homolog of EB1, changes the microtubule lattice. *Nat. Struct. Mol. Biol.* **15**, 1102-1108.

Dimitrov, A., Quesnoit, M., Moutel, S., Cantaloube, I., Poüs, C. and Perez, F. (2008). Detection of GTP-tubulin conformation in vivo reveals a role for GTP remnants in microtubule rescues. *Science* **322**, 1353-1356.

Furness, D. N., Hackney, C. M. and Steyger, P. S. (1990). Organization of microtubules in cochlear hair cells. *J. Electron Microsc. Tech.* **15**, 261-279.

Gao, S. Y., Li, C. Y., Chen, J., Pan, L., Saito, S., Terashita, T., Saito, K., Miyawaki, K., Shigemoto, K., Mominoki, K. et al. (2004). Rho-ROCK signal pathway regulates microtubule-based process formation of cultured podocytes—inhibition of ROCK promoted process elongation. *Nephron. Exp. Nephrol.* **97**, e49-e61.

Gasteier, J. E., Schroeder, S., Muranyi, W., Madrid, R., Benichou, S. and Fackler, O. T. (2005). FHOD1 coordinates actin filament and microtubule alignment to mediate cell elongation. *Exp. Cell Res.* **306**, 192-202.

Gerdes, J., Lemke, H., Baisch, H., Wacker, H. H., Schwab, U. and Stein, H. (1984). Cell cycle analysis of a cell proliferation-associated human nuclear antigen defined by the monoclonal antibody Ki-67. *J. Immunol.* **133**, 1710-1715.

Gierke, S. and Wittmann, T. (2012). EB1-recruited microtubule +TIP complexes coordinate protrusion dynamics during 3D epithelial remodeling. *Curr. Biol.* **22**, 753-762.

Ishizaki, T., Morishima, Y., Okamoto, M., Furuyashiki, T., Kato, T. and Narumiya, S. (2001). Coordination of microtubules and the actin cytoskeleton by the Rho effector mDia1. *Nat. Cell Biol.* **3**, 8-14.

Kadir, S., Astin, J. W., Tahtamouni, L., Martin, P. and Nobes, C. D. (2011). Microtubule remodelling is required for the front-rear polarity switch during contact inhibition of locomotion. *J. Cell Sci.* **124**, 2642-2653.

Karakesisoglou, I., Yang, Y. and Fuchs, E. (2000). An epidermal plakin that integrates actin and microtubule networks at cellular junctions. *J. Cell Biol.* **149**, 195-208.

Kobielak, A., Pasolli, H. A. and Fuchs, E. (2004). Mammalian formin-1 participates in adherens junctions and polymerization of linear actin cables. *Nat. Cell Biol.* **6**, 21-30.

Kodama, A., Karakesisoglou, I., Wong, E., Vaezi, A. and Fuchs, E. (2003). ACF7: an essential integrator of microtubule dynamics. *Cell* **115**, 343-354.

Komarova, Y., Lansbergen, G., Galjart, N., Grosveld, F., Borisy, G. G. and Akhmanova, A. (2005). EB1 and EB3 control CLIP dissociation from the ends of growing microtubules. *Mol. Biol. Cell* **16**, 5334-5345.

Komarova, Y., De Groot, C. O., Grigoriev, I., Gouveia, S. M., Munteanu, E. L., Schober, J. M., Honnappa, S., Buey, R. M., Hoogenraad, C. C., Dogterom, M. et al. (2009). Mammalian end binding proteins control persistent microtubule growth. *J. Cell Biol.* **184**, 691-706.

Kovac, B., Teo, J. L., Mäkelä, T. P. and Vallenius, T. (2013). Assembly of non-contractile dorsal stress fibers requires α-actinin-1 and Rac1 in migrating and spreading cells. *J. Cell Sci.* **126**, 263-273.

Krendel, M., Zenke, F. T. and Bokoch, G. M. (2002). Nucleotide exchange factor GEF-H1 mediates cross-talk between microtubules and the actin cytoskeleton. *Nat. Cell Biol.* **4**, 294-301.

Lansbergen, G. and Akhmanova, A. (2006). Microtubule plus end: a hub of cellular activities. *Traffic* **7**, 499-507.

Li, W., Miki, T., Watanabe, T., Kakeno, M., Sugiyama, I., Kaibuchi, K. and Goshima, G. (2011). EB1 promotes microtubule dynamics by recruiting Sentin in Drosophila cells. *J. Cell Biol.* **193**, 973-983.

Maurer, S. P., Bieling, P., Cope, J., Hoenger, A. and Surrey, T. (2011). GTPgammaS microtubules mimic the growing microtubule end structure recognized by end-binding proteins (EBs). *Proc. Natl. Acad. Sci. USA* **108**, 3988-3993.

Maurer, S. P., Fourniol, F. J., Bohner, G., Moores, C. A. and Surrey, T. (2012). EBs recognize a nucleotide-dependent structural cap at growing microtubule ends. *Cell* **149**, 371-382.

Mogensen, M. M., Malik, A., Piel, M., Bouckson-Castaing, V. and Bornens, M. (2000). Microtubule minus-end anchorage at centrosomal and non-centrosomal sites: the role of ninein. *J. Cell Sci.* **113**, 3013-3023.

Mogensen, M. M., Tucker, J. B., Mackie, J. B., Prescott, A. R. and Näthke, I. S. (2002). The adenomatous polyposis coli protein unambiguously localizes to microtubule plus ends and is involved in establishing parallel arrays of microtubule bundles in highly polarized epithelial cells. *J. Cell Biol.* **157**, 1041-1048.

Morrison, E. E., Wardleworth, B. N., Askham, J. M., Markham, A. F. and Meredith, D. M. (1998). EB1, a protein which interacts with the APC tumour suppressor, is associated with the microtubule cytoskeleton throughout the cell cycle. *Oncogene* **17**, 3471-3477.

Moss, D. K., Bellett, G., Carter, J. M., Liovic, M., Keynton, J., Prescott, A. R., Lane, E. B. and Mogensen, M. M. (2007). Ninein is released from the centrosome and moves bi-directionally along microtubules. *J. Cell Sci.* **120**, 3064-3074.

Nakata, T., Niwa, S., Okada, Y., Perez, F. and Hirokawa, N. (2011). Preferential binding of a kinesin-1 motor to GTP-tubulin-rich microtubules underlies polarized vesicle transport. *J. Cell Biol.* **194**, 245-255.

Oakes, P. W., Beckham, Y., Stricker, J. and Gardel, M. L. (2012). Tension is required but not sufficient for focal adhesion maturation without a stress fiber template. *J. Cell Biol.* **196**, 363-374.

Palazzo, A. F., Cook, T. A., Alberts, A. S. and Gundersen, G. G. (2001). mDia mediates Rho-regulated formation and orientation of stable microtubules. *Nat. Cell Biol.* **3**, 723-729.

Pepperkok, R., Bré, M. H., Davoust, J. and Kreis, T. E. (1990). Microtubules are stabilized in confluent epithelial cells but not in fibroblasts. *J. Cell Biol.* **111**, 3003-3012.

Rizvi, S. A., Neidt, E. M., Cui, J., Feiger, Z., Skau, C. T., Gardel, M. L., Kozmin, S. A. and Kovar, D. R. (2009). Identification and characterization of a small molecule inhibitor of formin-mediated actin assembly. *Chem. Biol.* **16**, 1158-1168.

Ryu, J. R., Echarri, A., Li, R. and Pendergast, A. M. (2009). Regulation of cell-cell adhesion by Abi/Diaphanous complexes. *Mol. Cell. Biol.* **29**, 1735-1748.

Sandblad, L., Busch, K. E., Tittmann, P., Gross, H., Brunner, D. and Hoenger, A. (2006). The Schizosaccharomyces pombe EB1 homolog Mal3p binds and stabilizes the microtubule lattice seam. *Cell* **127**, 1415-1424.

Scaife, R. M., Job, D. and Langdon, W. Y. (2003). Rapid microtubule-dependent induction of neurite-like extensions in NIH 3T3 fibroblasts by inhibition of ROCK and Cbl. *Mol. Biol. Cell* **14**, 4605-4617.

Siegrist, S. E. and Doe, C. Q. (2007). Microtubule-induced cortical cell polarity. *Genes Dev.* **21**, 483-496.

Shannon, K. B., Canman, J. C., Ben Moree, C., Tirnauer, J. S. and Salmon, E. D. (2005). Taxol-stabilized microtubules can position the cytokinetic furrow in mammalian cells. *Mol Biol Cell* **16**, 4423-4436.

Slepecky, N. B., Henderson, C. G. and Saha, S. (1995). Post-translational modifications of tubulin suggest that dynamic microtubules are present in sensory cells and stable microtubules are present in supporting cells of the mammalian cochlea. *Hear. Res.* **91**, 136-147.

Straube, A. and Merdes, A. (2007). EB3 regulates microtubule dynamics at the cell cortex and is required for myoblast elongation and fusion. *Curr. Biol.* **17**, 1318-1325.

Su, L. K. and Qi, Y. (2001). Characterization of human MAPRE genes and their proteins. *Genomics* **71**, 142-149.

Su, L. K., Burrell, M., Hill, D. E., Gyuris, J., Brent, R., Wiltshire, R., Trent, J., Vogelstein, B. and Kinzler, K. W. (1995). APC binds to the novel protein EB1. *Cancer Res.* **55**, 2972-2977.

Szarama, K. B., Stepanyan, R., Petralia, R. S., Gavara, N., Frolenkov, G. I., Kelley, M. W. and Chadwick, R. S. (2012). Fibroblast growth factor receptor 3 regulates microtubule formation and cell surface mechanical properties in the developing organ of Corti. *Bioarchitecture* **2**, 214-219.

Takesono, A., Heasman, S. J., Wojciak-Stothard, B., Garg, R. and Ridley, A. J. (2010). Microtubules regulate migratory polarity through Rho/ROCK signaling in T cells. *PLoS ONE* **5**, e8774.

Tassin, A. M., Maro, B. and Bornens, M. (1985). Fate of microtubule-organizing centers during myogenesis in vitro. *J. Cell Biol.* **100**, 35-46.

Thurston, S. F., Kulacz, W. A., Shaikh, S., Lee, J. M. and Copeland, J. W. (2012). The ability to induce microtubule acetylation is a general feature of formin proteins. *PLoS ONE* **7**, e48041.

Tirnauer, J. S. and Bierer, B. E. (2000). EB1 proteins regulate microtubule dynamics, cell polarity, and chromosome stability. *J. Cell Biol.* **149**, 761-766.

Tsuji, T., Ishizaki, T., Okamoto, M., Higashida, C., Kimura, K., Furuyashiki, T., Arakawa, Y., Birge, R. B., Nakamoto, T., Hirai, H. et al. (2002). ROCK and mDia1 antagonize in Rho-dependent Rac activation in Swiss 3T3 fibroblasts. *J. Cell Biol.* **157**, 819-830.

Tucker, J. B., Paton, C. C., Richardson, G. P., Mogensen, M. M. and Russell, I. J. (1992). A cell surface-associated centrosomal layer of microtubule-organizing material in the inner pillar cell of the mouse cochlea. *J. Cell Sci.* **102**, 215-226.

van der Flier, L. G. and Clevers, H. (2009). Stem cells, self-renewal, and differentiation in the intestinal epithelium. *Annu. Rev. Physiol.* **71**, 241-260.

van der Vaart, B., Akhmanova, A. and Straube, A. (2009). Regulation of microtubule dynamic instability. *Biochem. Soc. Trans.* **37**, 1007-1013.

Vitre, B., Coquelle, F. M., Heichette, C., Garnier, C., Chrétien, D. and Arnal, I. (2008). EB1 regulates microtubule dynamics and tubulin sheet closure in vitro. *Nat. Cell Biol.* **10**, 415-421.

Wang, F., Zhang, Q., Cao, J., Huang, Q. and Zhu, X. (2008). The microtubule plus end-binding protein EB1 is involved in Sertoli cell plasticity in testicular seminiferous tubules. *Exp. Cell Res.* **314**, 213-226.

Wen, Y., Eng, C. H., Schmoranzer, J., Cabrera-Poch, N., Morris, E. J., Chen, M., Wallar, B. J., Alberts, A. S. and Gundersen, G. G. (2004). EB1 and APC bind to mDia to stabilize microtubules downstream of Rho and promote cell migration. *Nat. Cell Biol.* **6**, 820-830.

Whitehead, R. H., VanEeden, P. E., Noble, M. D., Ataliotis, P. and Jat, P. S. (1993). Establishment of conditionally immortalized epithelial cell lines from both colon and small intestine of adult H-2Kb-tsA58 transgenic mice. *Proc. Natl. Acad. Sci. USA* **90**, 587-591.

Wu, X., Kodama, A. and Fuchs, E. (2008). ACF7 regulates cytoskeletal-focal adhesion dynamics and migration and has ATPase activity. *Cell* **135**, 137-148.

Yang, C., Czech, L., Gerboth, S., Kojima, S., Scita, G. and Svitkina, T. (2007). Novel roles of formin mDia2 in lamellipodia and filopodia formation in motile cells. *PLoS Biol.* **5**, e317.

Zhang, T., Zaal, K. J., Sheridan, J., Mehta, A., Gundersen, G. G. and Ralston, E. (2009). Microtubule plus-end binding protein EB1 is necessary for muscle cell differentiation, elongation and fusion. *J. Cell Sci.* **122**, 1401-1409.

Journal of Cell Science